

Raghu Prakash
Vikram Jayaram
Ashok Saxena *Editors*

Advances in Structural Integrity

Proceedings of SICE 2016

Advances in Structural Integrity

Raghu Prakash · Vikram Jayaram
Ashok Saxena
Editors

Advances in Structural Integrity

Proceedings of SICE 2016

 Springer

Editors

Raghu Prakash
Department of Mechanical Engineering
Indian Institute of Technology Madras
Chennai, Tamil Nadu
India

Ashok Saxena
Department of Mechanical Engineering
University of Arkansas
Fayetteville, AR
USA

Vikram Jayaram
Department of Materials Engineering
Indian Institute of Science
Bangalore, Karnataka
India

ISBN 978-981-10-7196-6 ISBN 978-981-10-7197-3 (eBook)
<https://doi.org/10.1007/978-981-10-7197-3>

Library of Congress Control Number: 2017958620

© Springer Nature Singapore Pte Ltd. 2018

This work is subject to copyright. All rights are reserved by the Publisher, whether the whole or part of the material is concerned, specifically the rights of translation, reprinting, reuse of illustrations, recitation, broadcasting, reproduction on microfilms or in any other physical way, and transmission or information storage and retrieval, electronic adaptation, computer software, or by similar or dissimilar methodology now known or hereafter developed.

The use of general descriptive names, registered names, trademarks, service marks, etc. in this publication does not imply, even in the absence of a specific statement, that such names are exempt from the relevant protective laws and regulations and therefore free for general use.

The publisher, the authors and the editors are safe to assume that the advice and information in this book are believed to be true and accurate at the date of publication. Neither the publisher nor the authors or the editors give a warranty, express or implied, with respect to the material contained herein or for any errors or omissions that may have been made. The publisher remains neutral with regard to jurisdictional claims in published maps and institutional affiliations.

Printed on acid-free paper

This Springer imprint is published by Springer Nature
The registered company is Springer Nature Singapore Pte Ltd.
The registered company address is: 152 Beach Road, #21-01/04 Gateway East, Singapore 189721, Singapore

Foreword

I am delighted to note that the first International Structural Integrity Conference and Exhibition (SICE 2016) organized by the Indian Structural Integrity Society (InSIS) along with Indian Institute of Science, Bangalore and Indian Institute of Technology Madras, Chennai had made a modest beginning by a young professional Society. It was also convened as the Inter-Quadrennial conference of International Congress on Fracture. It was a grand success with more than 130 technical papers and 6 keynote lectures been presented during the 3-day event. I am delighted to release this Lecture Notes in Mechanical Engineering brought out by Springer Publishing consisting of selected 57 papers that were chosen after peer review by a panel of experts in the domain.

Structural integrity and its longevity studies in our country have found India-centric as well as generic solutions that can be applied worldwide. The fact that India provides engineering solutions to many multi-national companies dealing with energy, transportation, refining, and materials development is a testimony to this; there is always a quest for knowledge in this domain considering that India has embarked on “Make in India” mission for major infrastructural projects like advanced ultra-supercritical power plants. Apart from dealing with conventional mechanics, material characterization, and defect analysis, the field of structural integrity has expanded to structural health and condition monitoring, reliability and risk analysis, etc., over the last three decades since the 6th International Congress on Fracture conference held at New Delhi in 1984.

The conference proceedings covers many aspects of structural integrity—Fatigue and Fracture Mechanics; Creep–Fatigue Interactions; Structural Health Monitoring; Failure Analysis; Experimental Techniques; Computation Methods; Metals, Composites, and New Generation Materials. Many novel concepts have been applied to practical situations in diverse domains such as bioengineering, aerospace structures, civil engineering structures, power plants, and transportation.

As a professional involved in this domain, I experience and find that the quality of papers presented in this conference is of high caliber and would serve the

immediate and future needs of researchers and engineers working in this domain. I congratulate the Indian Structural Integrity Society, the organizers of this conference, and the editors of this volume for establishing this tradition and wish many more such events to happen in the near future for the purpose of pursuit of knowledge dissemination and enhancing collaborations.

A handwritten signature in black ink, reading "Baldev Raj". The signature is written in a cursive style with a prominent initial 'B' and a long, sweeping tail on the 'j'.

Bangalore, India

Baldev Raj

Preface

This book contains selected papers from the presentations made at the first international Structural Integrity Conference and Exhibition (SICE 2016) held at Hotel Le Meridien, Bangalore, during July 4–6, 2016. The conference, exhibition, and pre-conference workshop were organized jointly by the Indian Structural Integrity Society (InSIS), Indian Institute of Science, Bangalore, and Indian Institute of Technology Madras, Chennai. The timing of the conference was particularly appropriate, given the critical role of total structural integrity in the new manufacturing initiatives of the Government of India, such as the “Make in India” program. Of the 134 oral and poster presentations, a total of 57 were finally selected for publication after a peer review.

The conference attracted nearly 220 registrants from seven countries (India, Japan, USA, Russia, Ukraine, Switzerland, and UK) apart from the 56 registrants for the 2-day pre-conference workshop held during July 2–3, 2016 at IISc, Bangalore, and BiSS Research, Bangalore. SICE2016 was also convened as the Inter-Quadrennial Conference of the International Congress on Fracture (IQ-ICF).

The SICE 2016 conference focused on all aspects relating to Structural Integrity, including Fatigue and Fracture Mechanics; Creep–Fatigue Interactions; Structural Health Monitoring; Failure Analysis; Experimental Techniques; Computation Methods; Metals, Composites, and New Generation Materials. The range of applications covered bioengineering, aerospace structures, civil engineering structures, power plants, and transportation. The conference spanned 3 days with 6 plenary lectures, 23 invited lectures, and 93 contributed papers delivered by researchers working in the domain of structural integrity in three parallel sessions. There were 12 poster presentations, mostly from research scholars.

About 85 authors were invited to submit full-length manuscripts after the conference deliberations, and the same was reviewed by a team of 60 domain experts from various organizations. The high quality of the final selection of papers is due to the hard work put in by all the reviewers and volunteers, and we acknowledge their support. We hope this volume will serve as a good reference for practicing researchers in the domain and as a good source of material for budding engineers and scientists.

The conference was sponsored by several agencies such as Department of Science and Technology, Defence Research and Development Organization, and Atomic Energy Regulatory Board of the Government of India; BiSS Research, Bangalore; MTS Systems Corporation, USA, along with its local distributor Techno Testing Instruments; ABS Systems, Chennai; Altair Corporation; Honeywell Corporation; and Hysitron NanoTechnology India Pvt Ltd, Thiruvananthapuram. Springer provided support in the form of merit prizes for the best poster papers presented at the conference and is proud to be associated with bringing out this collection of selected papers as a book in Lecture Notes in Mechanical Engineering.

This conference provided a platform for practicing scientists and engineers to disseminate their knowledge and learn from one another's experience. We hope that this tradition will continue and that the Biennial SICE / IQ-ICF conferences will play a key role in advancing knowledge in this critical domain of structural integrity.

Chennai, India
Bangalore, India
Fayetteville, USA

Raghu Prakash
Vikram Jayaram
Ashok Saxena

Contents

High-R Fatigue Crack Growth Threshold Stress Intensity Factors at High Temperatures	1
Stuart R. Holdsworth and Zhen Chen	
Part I Aerospace	
Fracture Mechanics Analysis of Fuselage Structural Joints with Cracks	15
H. Ramesha, N. C. Mahendra Babu and H. V. Lakshminarayana	
Effect of Silica Nanoparticles on the Fatigue Life of a Glass Fiber Reinforced Epoxy Composite Under an Aircraft Spectrum Load Sequence	27
N. Jagannathan, K. Sakthivel, Ramesh Bojja and C. M. Manjunatha	
Fatigue Life Estimation of Typical Fighter Aircraft Main Landing Gear Using Finite Element Analysis	39
T. Sivaranjani, D. V. T. G. Pavan Kumar, C. M. Manjunatha and M. Manjuprasad	
Designing for Strength: ASME’s DBA Guidelines and Beyond	53
Kotur S. Raghavan	
Premature Fatigue Failures in the Hot Zone of Low Pressure Turbine Rotor (LPTR) Blades of Aero-Engine	65
M. Madan, R. Bharathanatha Reddy, K. Raghavendra, M. Sujata and S. K. Bhaumik	
Fatigue Life Prediction of Composite Airframe Panel	77
P. K. Sahoo, Shriram Gujar and M. Manjuprasad	
Integrity Evaluation of Feature Level Test Specimen of an Aircraft Primary Composite Structure	93
S. Venkatesh, S. C. Lakshminarayana and Byji Varughese	

A Study on the Effect of Crack Stopper for Enhanced Damage Tolerance Behavior of a Fuselage Stiffened Panel	103
G. Akshitha, A. Shailesh Rao, N. Srinivasan and M. Mohan Kumar	
Failure Analysis of a Squirrel Cage Bearing of a Gas Turbine Engine	117
Swati Biswas, Jivan Kumar, V. N. Satishkumar and S. N. Narendra Babu	
Part II Civil Structures	
On-line Deformation Monitoring of Building Estate Above Mining	129
R. Tsvetkov, Igor Shardakov, A. Shestakov and V. Yepin	
Mechanical Properties of Nano Concrete	137
Ajaysinh R. Vaghela and Gaurang R. Vesmawala	
Estimation of Critical Microcrack Length in Concrete by Considering Interfacial Properties	147
Keerthy M. Simon and J. M. Chandra Kishen	
Fracture Analysis and Remaining Life Assessment of Ultra High Strength Concrete Beams	157
A. Ramachandra Murthy, N. R. Iyer and B. K. Raghu Prasad	
Part III Composites	
Rupture in Abdominal Aortic Aneurysm	169
Qusay Alfaori, Ashok Saxena, Hanna Jensen and Morten Jensen	
Damage Tolerance Assessment of Laminated Composite Plates Subjected to Ballistic Impact	183
H. L. Vinayaka and Shivashankar R. Srivatsa	
Prediction of Mode II Delamination Onset Life Under Spectrum Fatigue Loads Using Equivalent Strain Energy Release Rate Concept	195
A. R. Anilchandra, M. Seshagirachari, Ramesh Bojja, N. Jagannathan and C. M. Manjunatha	
Dependence of Crack Velocity on Stress Intensity Factor in PMMA Using Single-Edge-Notched Clamped Beams	205
G. R. Rahul, V. Jayaram and S. Bose	
Effect of Wrap Thickness and Ply Orientation on Cracking and Failure of FRP-Wrapped Columns	215
Pradeep B. Kodag and Gaurang R. Vesmawala	

Studies on Fracture Features and Fracture Toughness of CFRP Composites Fabricated by Resin Infusion Technique 225
 K. Panbarasu, M. Suresh Kumar, V. R. Ranganath and R. V. Prakash

Numerical and Experimental Analysis of Double-Sided Stepped Lap-Repaired CFRP Laminates Under Tensile Loading 235
 Matta Seshadri and M. Ramji

Part IV Computational Mechanics

Lower and Upper Bound Estimates of Material Properties of Pristine Graphene: Using Quantum Espresso 253
 T. Chaitanya Sagar and Viswanath Chinthapenta

Studies on Behaviour of Steel Tubular Compression Members Subjected to Accelerated Corrosion 267
 A. Cinitha, P. K. Umesha and G. S. Palani

Effect of Delamination Defects on Buckling Behavior of Wind Turbine Blades 279
 Vinodkumar Boniface

Analysis of the Performance of the Cantilever-Type Piezoelectric Generator Based on Finite Element Modeling 291
 A. N. Soloviev, I. A. Parinov, A. V. Cherpakov,
 V. A. Chebanenko, E. V. Rozhkov and L. V. Duong

Energy Absorption Characteristics of AA7075-T6 Tube Filled with Aluminum Foam 303
 S. Vignesh, C. Lakshmana Rao and Simhachalam Bade

Strain Intensity Factor and Interaction of Parallel Rigid Line Inclusion in Elastic Matrix Using FEA 315
 Prataprao Patil, S. N. Khaderi and M. Ramji

Part V Creep-Fatigue

Creep-Fatigue Damage Assessment of Reactor Hot Pool Components During Crash Cooling 325
 Rosy Sarkar, S. Jaladeen and K. Velusamy

The Influence of Prior Plasticity on the Creep Resistance of Two Elevated Temperature Power Plant Steels 341
 Valliappa Kalyanasundaram and Stuart R. Holdsworth

Structural Integrity Mechanics and Creep Life Prediction of 304HCu Austenitic Stainless Steel Under Multiaxial State of Stress 353
 Kanhu Charan Sahoo, Sunil Goyal, P. Parameswaran, S. Ravi and K. Laha

Stress Analysis for Integrity Assessment of High-Energy Hot Reheat Pipe Bends of 210 MW Coal-Fired Unit	369
Rajesh Daga and Mahendra Kumar Samal	
Part VI Energy and Transportation	
Structural Integrity Study for Additional Piles on an Existing Jacket Structure in Western Indian Offshore	385
Praveen Bhat and Bakul Master	
Structural Integrity Assessment of a Reactor Pressure Vessel Using State-of-the-Art Methodologies—A Case Study	395
V. Chaudhry, S. M. Ingole, A. K. Balasubrahmanian and U. C. Muktibodh	
Sodium-Free Level Fluctuations: Concern on Structural Integrity for the Pool-Type Sodium-Cooled Fast Breeder Reactor	407
V. R. Chandan Reddy, R. Suresh Kumar, Anil Kumar Sharma, K. Velusamy and P. Selvaraj	
Monotonic Fracture Studies on Bi-metallic Pipe Weld Joints Having Circumferential Through-Wall Crack	419
G. Raghava, S. Vishnuvardhan, M. Saravanan, P. Gandhi, Suranjit Kumar, P. K. Singh, I. A. Khan and V. Bhasin	
Part VII Experimental Techniques	
Assessment of Strain in a Corrosive Environment of Structural Steel	437
A. Cinitha, P. K. Umesha and K. Kesavan	
A Test Stand for Studying Subcritical and Critical States of Full-Size Reinforced Concrete Structures	451
Igor Shardakov, Irina Glot, Aleksey Shestakov, R. Tsvetkov and V. Yepin	
Mode I SIF Determination of Orthotropic Laminates with Double-Ended Cracks Using a Single-Strain Gage	461
Debaleena Chakraborty, D. Chakraborty and K. S. R. K. Murthy	
Mechanical Testing of Elevated Temperature PMC, Metallic, and CMC Coupons	469
Erik A. Schwarzkopf and Michael J. Shepard	
In Situ Measurement of Deformation Under Tension of ABPBI and Its Composites	481
Abhijeet Dhiman, F. G. S. Wasim, M. Neergat and Krishna N. Jonnalagadda	

Determination of Effectiveness of Viscoelastic Dampers in Controlling the Seismic Response of Piping System by Shake Table Testing 493
 R. K. Verma, P. N. Dubey and G. R. Reddy

Experimental Study of Deformation Processes in Reinforced Concrete Beams Strengthened with a Carbon Fiber Sheet 503
 Anton Bykov, Igor Shardakov, Aleksey Shestakov and Irina Glot

Partial Delamination Detection and Quantification in Composite Laminates Using Laser Doppler Vibrometer 517
 Yashdeep P. Nimje and Gangadharan Raju

FEA and Experimental Analysis on Buckling and Post-buckling Behavior of CFRP Composite Panel Using Digital Image Correlation Technique 527
 Muhammad Shuaib NK, Ramji M, Naresh Reddy Kolanu and Gangadharan Raju

Part VIII Fatigue

High Cycle Fatigue Strength of Spring Steel with Small Scratches 541
 Yoshiro Nishimura, Masahiro Endo, Keiji Yanase, Yuichi Ikeda, Susumu Miyakawa and Nobuyuki Miyamoto

Estimation of Load Sequence Effect on Fatigue Crack Growth Life According to Various Prediction Models 549
 A. N. Savkin, A. A. Sedov, A. V. Andronik and K. A. Badikov

SHM—Prognostic Analysis of Tapered Attachment Lugs Under Fatigue Loading 559
 K. Bharath, B. V. Sravan Kumar, L. Chikmath and B. Dattaguru

Experimental Study on Fatigue–Vibration Interactions of Cyclically Loaded FRP Composite Cantilever Beams Made of Glass/Carbon-Layered Arrangements 579
 R. Murugan, R. Ramesh and K. Padmanabhan

Investigation of Cyclic Stress–Strain Behavior in FCC Single Crystals 593
 Nipal Deka and Krishna N. Jonnalagadda

Analysis of the Plastic Zone Size Ahead of the Crack Tip in Notched Components and Its Application to Fatigue Problems 599
 Masahiro Endo and Keiji Yanase

Effect of Loading Frequency on the Fatigue Crack Growth Rate of Type 304L(N) Material	611
Mukhar Sharma, Punit Arora, P. K. Singh, D. K. Sahoo, Gargi Choudhuri and V. Bhasin	
Fatigue Life Characterization of Additively Manufactured Acrylic like Poly-Jet Printed Parts	623
J. A. Suresh, Gurunathan Saravana Kumar, Palaniappan Ramu and Jayaganthan Rengaswamy	
Part IX Material Processing	
Influence of Machining Process on Surface Integrity and Fatigue Life of a Turbine Rotor Blade	635
Benudhar Sahoo, S. K. Panigrahi and R. K. Satpathy	
Spark Plasma Sintering Process as a Tool for Achieving Microstructural Integrity	649
P. Parameswaran, T. Ezhilarasi, Srinivasa R. Bakshi, V. Thomas Paul and E. Mohandas	
Part X Structural Health and Condition Monitoring	
On Increasing Quality of Measurement Results at Testing State of Construction Materials	663
I. P. Miroshnichenko and I. A. Parinov	
Damage Growth Study in Unidirectional CFRP Composites Using Infrared Thermography	673
Sukanta Das, Naresh Reddy and Gangadharan Raju	
Online Damage Detection in Metallic Cylindrical Shells Using Guided Wave Modes by Time Reversal Method	685
P. Jayesh and Christudas R. Bijudas	
Author Index	695
Subject Index	699

About the Editors



Dr. Raghu Prakash is currently working as Professor in Department of Mechanical Engineering, Indian Institute of Technology Madras (IIT Madras); he specializes in the areas of fatigue, fracture of materials (metals, composites, hybrids), structural integrity assessment, remaining life prediction of critical components used in transportation and energy sectors, apart from new product design. He has more than 25 years of professional experience in the field of fatigue and fracture and has more than 80 journal, chapter publications, 100 conference publications and has edited 2 book volumes. He has developed test systems for use in academia, R&D, and industry during his tenure as Technical Director at Bangalore Integrated System Solutions (BiSS) Research, Bangalore, and teaches courses relating to Fracture Mechanics, Design with Advanced Materials, Product Design, Design for Manufacture and Assembly (DFMA) at IIT Madras. He is a voting rights member of the ASTM International (Technical Committees, D-30, E-08, and E-28) and has won several prestigious awards (Binani Gold Medal, Indian Institute of Metals), scholarships, and Erasmus Mundus Fellowships. He is the recipient of Distinguished Fellow of the International Conference on Computational and Experimental Engineering and Sciences (ICCES) 2015.

He received his bachelor's degree in Mechanical Engineering from College of Engineering, Guindy, Madras (now Chennai), in first class with distinction. He obtained his master's degree (by Research) and Ph.D. from the Department of Mechanical Engineering,

Indian Institute of Science, Bangalore. He is a member of several technical societies (Indian Structural Integrity Society, Society for Failure Analysis, Indian Institute of Metals, to name a few).



Vikram Jayaram is Chair of the Division of Mechanical Sciences and Professor in Materials Engineering at the Indian Institute of Science, Bangalore. He received his Ph.D. in Materials Science and Engineering from Stanford University, USA, in 1985 and his bachelor's degree in Natural Sciences from Cambridge University, UK, in 1978. His current research covers the mechanical behavior and testing of systems at small-length scales, including fracture and creep. He also works on the low-temperature processing of ceramic composites. Earlier, he had worked on the non-equilibrium processing of ceramics and the fabrication of ceramic-metal composites through infiltration methods. He is an elected fellow of all the major science and engineering academies in India, Indian Institute of Metals, and of the American Ceramic Society. He is a recipient of the JC Bose Fellowship of Department of Science and Technology of Government of India and has authored over 150 publications.



Dr. Ashok Saxena most recently (until January 3, 2017) served as the Provost and Vice-Chancellor of Academic Affairs at the University of Arkansas, Fayetteville, USA. He is currently working as Distinguished Professor of Mechanical Engineering and Dean Emeritus. He also served as the Dean of Engineering and the Raymond and Irma Giffels' Chair at the University of Arkansas.

He previously held the position of Regents' Professor and Chair of the School of Materials Science and Engineering at the Georgia Institute of Technology in Atlanta, USA, and was a Fellow Scientist at the Westinghouse Research and Development Center in Pittsburgh, USA. He also served as the Vice-Chancellor of Galgotias University in India for a 2-year period between 2012 and 2014.

He received his MS and Ph.D. degrees from University of Cincinnati in 1972 and 1974, respectively, in Materials Science and Metallurgical Engineering and his B.Tech. degree in Mechanical Engineering from the Indian Institute of Technology Kanpur in 1970.

His area of research interest is mechanical behavior of materials focusing on linear and nonlinear fracture mechanics and fracture in materials at high temperatures under the conditions of creep and creep-fatigue. He is the recipient of numerous awards and recognitions that include the George Irwin Medal (1992) from the American Society for Testing and Materials (ASTM) for his pioneering contributions to creep-fracture mechanics, the ASTM Award of Merit and Fellow (1994), Fellow of ASM International (1996), Fellow of International Congress on Fracture (2009), and Georgia Tech Outstanding Research Author Award (1993). He is a recipient of the Wohler Fatigue Medal from the European Structural Integrity Society (ESIS) in 2010 and the Paris Gold Medal from the International Congress of Fracture (2017) and is an elected Fellow of the European Academy of Sciences (2016). He is the author/co-author/editor of 8 books and over 250 research publications.

High- R Fatigue Crack Growth Threshold Stress Intensity Factors at High Temperatures

Stuart R. Holdsworth and Zhen Chen

Abstract While knowledge relating to the determination and practical application of fatigue crack growth threshold stress intensity factors for defect assessment is relatively well established for many circumstances, this is not the case for materials and conditions which are sensitive to time-dependent mechanisms. There are two well-established international standard procedures for the determination of this fracture mechanics parameter, although their respective crack growth rate criteria differ by an order of magnitude. Unfortunately neither specifically addresses determination of the property for very high- R (K_{\min}/K_{\max}) ratios, under conditions when the environment can be influential, and ΔK_{th} can be even more sensitive to the $da/dN(\Delta K)$ criterion adopted for its determination. In addition to a general state of knowledge review, particular attention is paid to circumstances concerning high- R ΔK_{th} in power plant steels at high temperatures for which oxide-induced crack closure and creep cracking can be influential. Evidence for low-alloy 1%Cr, martensitic 9%Cr and austenitic 17%Cr steels is examined.

Keywords High- R · High temperature · ΔK_{th} · Oxide-induced crack closure
Creep cracking

Nomenclature

a	Crack depth
A	Constant in Paris mid- K regime power law
B	Specimen thickness
CT	Compact tension (specimen)
CTOD	Crack opening displacement
da/dN	Fatigue crack growth rate
DCPD	Direct current potential drop (electrical crack monitoring instrumentation)

S. R. Holdsworth (✉) · Z. Chen
Swiss Federal Laboratories for Materials Science and Technology (EMPA),
Überlandstrasse 129, 8600 Dübendorf, Zurich, Switzerland
e-mail: stuart.holdsworth@empa.ch

f	Frequency
FIB	Focussed ion beam
HCFCG	High-cycle fatigue crack growth (typically for $80 < f < 100$ Hz)
TDFAD	Time-dependent failure assessment diagram
k_p	Oxidation parabolic growth constant
k'	Inelastic strain constant in $\varepsilon(\sigma)$ relationship
$K, \Delta K$	Stress intensity factor, range of stress intensity factor
K_c	Critical stress intensity factor responsible for unstable fracture
K_{mat}^C	Material creep toughness (for a given temperature and time)
K_{max}	Maximum stress intensity factor (in cycle)
K_{min}	Minimum stress intensity factor (in cycle)
K_r	K Ratio representing proximity to fracture
ΔK_{th}	Fatigue crack growth threshold stress intensity factor
$d\Delta K_{\text{th}}^{\text{ox}}$	Enhancement to ΔK_{th} due to oxide-induced crack closure
L_r	Stress ratio representing proximity to plastic collapse or creep rupture
m	Exponent in Paris mid- K regime power law
N	Number of cycles
R	Load ratio ($K_{\text{min}}/K_{\text{max}}$)
$R_{p0.2}$	0.2% proof strength
R_m	Ultimate tensile strength
R_R	Creep-rupture strength
$R_{0.2}^C$	0.2% creep strength (stress responsible for 0.2% inelastic strain for a given temperature and time)
RT	Room temperature
SEM	Scanning electron microscope
t	Time
W	Specimen width
x	Oxide thickness
β	Inelastic strain exponent in $\varepsilon(\sigma)$ relationship
$\varepsilon, \varepsilon_{\text{ref}}$	Strain, Reference strain
$\sigma, \sigma_{\text{ref}}$	Stress, Reference stress
$\sigma_{\text{ref}}^{\text{max}}$	Maximum reference stress (in cycle)
ν	Poisson's ratio

1 Background and Introduction

High-cycle fatigue crack growth (HCFCG) behaviour may conveniently be considered in terms of three regimes, Fig. 1a. These are a low- ΔK regime close to the fatigue crack growth threshold ΔK_{th} , a mid- K regime in which fatigue crack growth rates are represented by a power law [1], and a high- ΔK regime in which da/dN is high and K_{max} approaches the critical stress intensity factor responsible for unstable

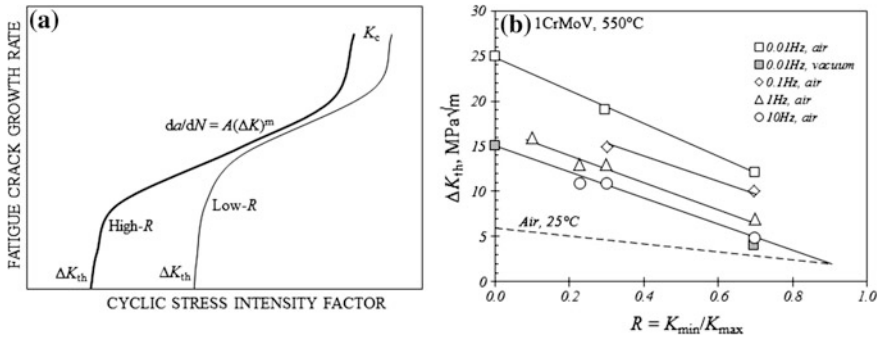


Fig. 1 a Schematic representation of high-cycle fatigue crack growth rate characteristics in low-, mid- and high- ΔK regimes; and b the influence of frequency, environment and R ratio on fatigue crack growth threshold values for 1CrMoV at 550 °C [2, 5]

fracture, K_c [2]. The focus of the following paper is behaviour in the low- ΔK regime, in particular for high- R (K_{min}/K_{max}) load ratios at high temperatures.

Conceptually, ΔK_{th} is the maximum ΔK associated with no fatigue crack extension. Experimentally, it is assumed to be the ΔK consistent with $da/dN 1 \times 10^{-10}$ m/c [3] or $da/dN 1 \times 10^{-11}$ m/c [4]. At low temperatures, the ΔK_{th} criteria difference may not be important, but this is not the case at high temperatures as will become apparent in the following paper.

In the low- ΔK regime, low da/dN and ΔK_{th} are sensitive to load ratio ($R = K_{min}/K_{max}$), with the magnitude of ΔK_{th} decreasing with increasing R (Fig. 1a). At ambient temperature (RT), higher ΔK_{th} values at low- R are primarily the consequence of plasticity-induced crack closure, but may also be due to contributions from fracture surface roughness-induced closure and fretting oxide-induced closure.

At high temperatures, $\Delta K_{th}(R)$ profiles become increasingly elevated with reducing frequency [2, 5], with the evidence for 1CrMoV steel at 550 °C (which also includes data collected at 0.01 Hz in vacuum), clearly indicating the enhancement of ΔK_{th} to be mainly the consequence of oxide-induced crack closure, Fig. 1b, although plasticity-induced closure is influential at lower R due to lower $R_{p0.2}$ at higher temperatures.

New high-temperature ΔK_{th} results for three steels with different oxidation characteristics (respectively containing 1%Cr, 9%Cr and 17%Cr) have been assessed in terms of fracture surface oxide thickness measurements and a $K(CTOD)$ analysis.

During the course of the study, it became apparent that creep cracking could occur at very low $da/dN(\Delta K)$ close to ΔK_{th} under high- R conditions at high temperatures, even for high frequencies not normally expected to be affected by time-dependent cracking processes. A time-dependent failure assessment diagram (TDFAD) approach is adopted to predict the incidence of creep cracking at the tips of very slowly propagating high- R high-cycle fatigue cracks.

2 High-Temperature Fatigue Crack Growth Thresholds

High temperature ΔK_{th} values were determined in accordance with [3] for three steels with different chromium levels, namely 1CrMoV, 9CrMoCo and 17Cr12Ni. As a generality, tests were conducted using compact tension (CT) specimens instrumented with electrical DCPD crack monitoring instrumentation at a frequency (f) of ~ 80 Hz. Typically, the tests were performed using proportional $W(2B)$ CT specimens with thicknesses (B) of 12.5 or 25 mm. The results determined for a temperature of 550 °C are summarised as a function of R and K_{max} in Fig. 2. The high-temperature values are compared with RT values when available and/or the lower bound RT ΔK_{th} trend line defined in [6].

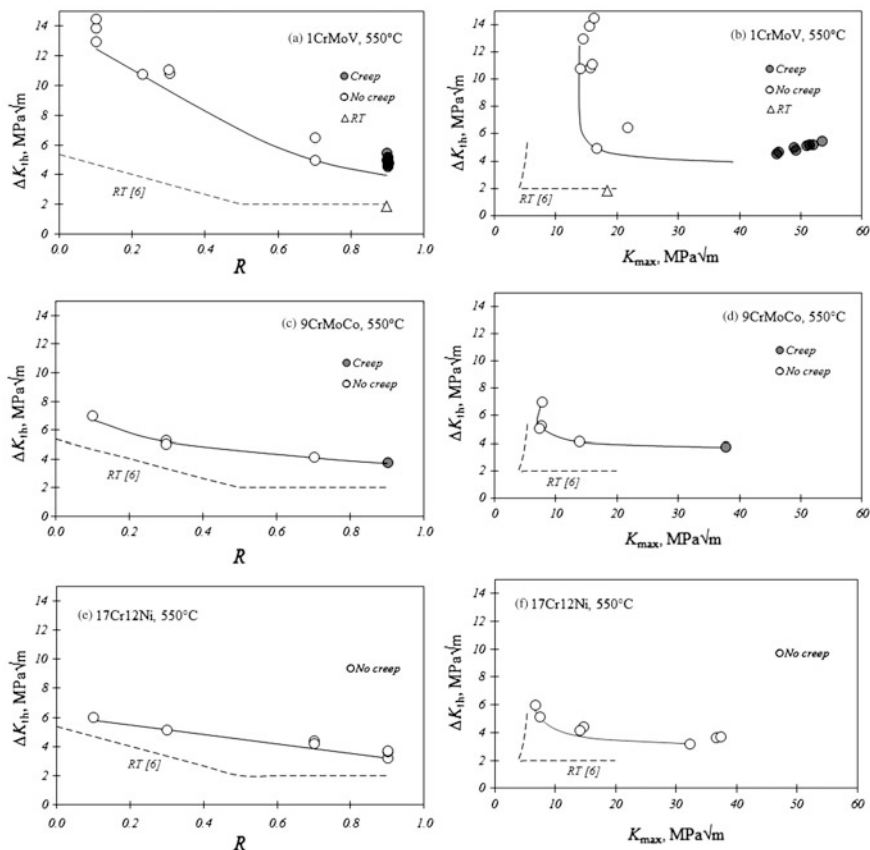


Fig. 2 Variation of ΔK_{th} with R and K_{max} , respectively, at 550 °C for **a, b** 1CrMoV, **c, d** 9CrMoCo and **e, f** 17Cr12Ni (with filled data points representing those tests involving creep crack development when high-cycle fatigue cracking was almost stationary)

As will be considered later, evidence of creep cracking in certain circumstances could be observed at high-*R* high-cycle fatigue ΔK_{th} test crack tips (when K_{max} and/or σ_{ref}^{max} were high). The filled ΔK_{th} data points in Fig. 2 acknowledge the incidence of creep cracking associated with these tests.

For each steel, there is indication of a ΔK_{th} enhancement, which at high-*R* can almost exclusively be attributed to oxide-induced crack closure. The extent of high-*R* ΔK_{th} enhancement ($d\Delta K_{th}^{ox}$) is not the same for each steel (Table 1) and appears to be related to the chromium content. This is examined further in the following section.

3 Oxide-Induced Crack Closure

The growth of oxide scales in air at elevated temperatures on the surfaces of many steels may be predicted with some certainty up to a thickness of $\sim 100 \mu\text{m}$ by adopting parabolic growth kinetics, i.e.

$$x^2 = k_p \cdot t \quad (1)$$

where upper bound k_p values for 1%Cr, 9%Cr and 17%Cr steels for a temperature of 550 °C are summarised in Table 1 [7]. For oxide thicknesses above $\sim 100 \mu\text{m}$, spallation becomes increasingly probable, and adoption of the listed k_p^{UB} values should be with caution. Typically, oxidation kinetics are relatively insensitive to chromium content up to $\sim 10\%$, above which there is a significant increase in oxidation resistance to $\sim 12\%$ Cr, before a relative stabilization, Fig. 3. The variation in oxidation kinetics is accompanied by the changes in scale formation mechanism shown as insets in Fig. 3 which are likely to be influential in their contribution to $d\Delta K_{th}^{ox}$.

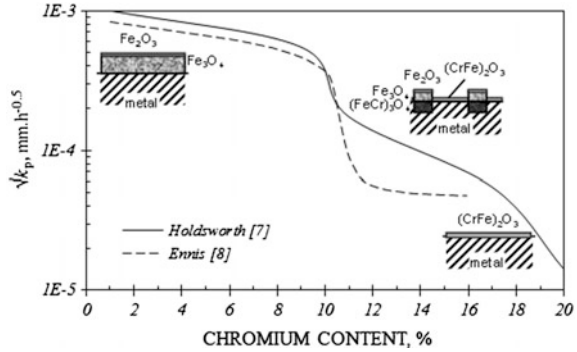
Fracture surface oxide thickness measurements for the three steels were made immediately adjacent to the final crack tips established during ΔK_{th} measurement

Table 1 Summary of oxide-induced crack closure data (550 °C)

Steel	$d\Delta K_{th}^{ox}$ MPa $\sqrt{\text{m}}$	k_p^{UB} [7] mm ² /h	$\sqrt{(k_p^{UB} t)}$ μm	$x(\text{FIB})$ μm	$R_{p0.2}^{550^\circ\text{C}}$ MPa	$E^{550^\circ\text{C}}$ MPa	$K(\text{CTOD})$ [9] MPa $\sqrt{\text{m}}$
1% Cr	2.7	1×10^{-6}	2.5	3.51	445	160,800	2.5
9% Cr	(1.8)	3×10^{-7}	2.7	0.51	483	159,078	1.0
17% Cr	(1.2)	3×10^{-9}	0.5	0.46–1.47	197	165,405	0.4–0.7

$d\Delta K_{th}^{ox}$ values given in parentheses are estimates with reference to the BS7910 RT ΔK_{th} lower bound [6] and are likely to be higher than in practice. NB ΔK_{th} defined in accordance with [3]

Fig. 3 Variation of oxide growth kinetics with chromium content in steels at 550 °C [8]



campaigns conducted in accordance with [3]. With fracture surface oxide thicknesses being in the range 0.5–3.5 μm as a consequence of being exposed for ~ 24 h during the final very low $da/dN(\Delta K)$ phase of high- R ΔK_{th} determination, an SEM-FIB drilling technique had to be adopted for maximum measurement accuracy. This involved FIB drilling a small trench, typically 1–2 mm deeper than the anticipated oxide scale thickness, with one vertical face and one stepped face. Prior to drilling, a platinum coating was locally sputter-deposited on the fracture surface to provide edge protection and a marker at the position of excavation. Following ‘rough’ drilling, the ion beam was used to polish the vertical surface of the trench. The sample could then be tilted for oxide thickness measurement directly in the SEM.

Observed FIB-determined oxide thickness measurements compare reasonably well with those calculated using the k_p^{UB} values established in [7], Table 1.

The apparent $d\Delta K_{\text{th}}^{\text{ox}}$ enhancements experienced by the three steels at 550 °C (Fig. 2) are consistent with the oxide-induced crack closure K_s which may be predicted using the plane strain Rice relationship [9], i.e.

$$\text{CTOD} = 0.225(K/R_{p0.2})^2 \quad (2)$$

The degree of consistency is evident in Table 1 and Fig. 4. An alternative and widely adopted $K(\text{CTOD})$ formulation is that proposed by Stewart [10] (Eq. 3), although $d\Delta K_{\text{th}}^{\text{ox}}$ predictions appear to be excessive using this relationship (Fig. 4).

$$\text{CTOD} = \frac{K^2(1 - \nu^2)}{2ER_{p0.2}} \quad (3)$$

4 Creep Cracking

An additional mechanism interaction which may be encountered in high-temperature high- R ΔK_{th} tests is creep cracking (Fig. 5). Experience has shown that the incidence of creep cracking ahead of very slowly growing

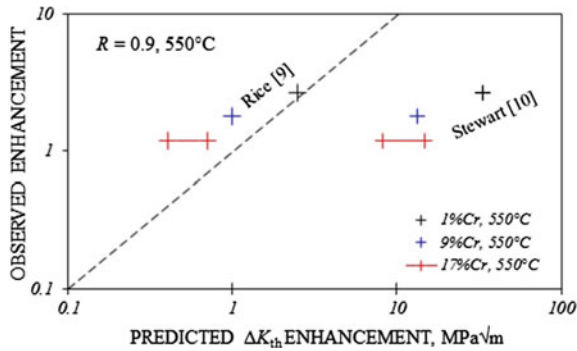


Fig. 4 Comparison of observed $d\Delta K_{th}^{ox}$ for 1%Cr, 9%Cr and 17%Cr steels at 550 °C with predictions based on Rice and Stewart $K(CTOD)$ formulations (respectively, Eqs. 2 and 3)

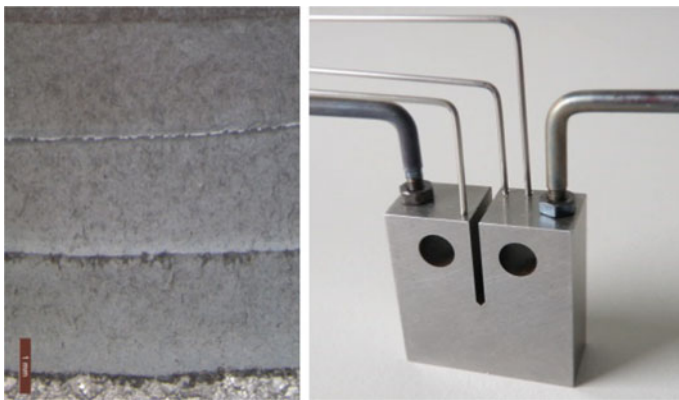


Fig. 5 Evidence of creep cracking (dark bands) at the ends of three high-R ΔK_{th} fatigue cracking campaigns in a $W(2B)12.5$ CT specimen (with inset showing $W(2B)12.5$ CT specimen with DCPD instrumentation attached)

high-cycle fatigue cracks may go undetected by examination only of $da/dN(\Delta K)$ test records. Three additional examples are shown in Fig. 6. Perhaps surprisingly, in these circumstances, fracture surface post-test examination may be the only way to reveal the presence of creep cracking with certainty (e.g. Fig. 6c). However, it is shown that when fracture surface examination is not possible, a TDFAD approach may be adopted to predict the existence of creep cracking when K_{max} approaches K_c^{mat} and/or σ_{ref} approaches $R_{0.2}^C$.

While there are two types of high-temperature failure assessment diagram [11], the one favoured for this application is the R5 TDFAD construction [12]. The failure envelope for this diagram is defined by:

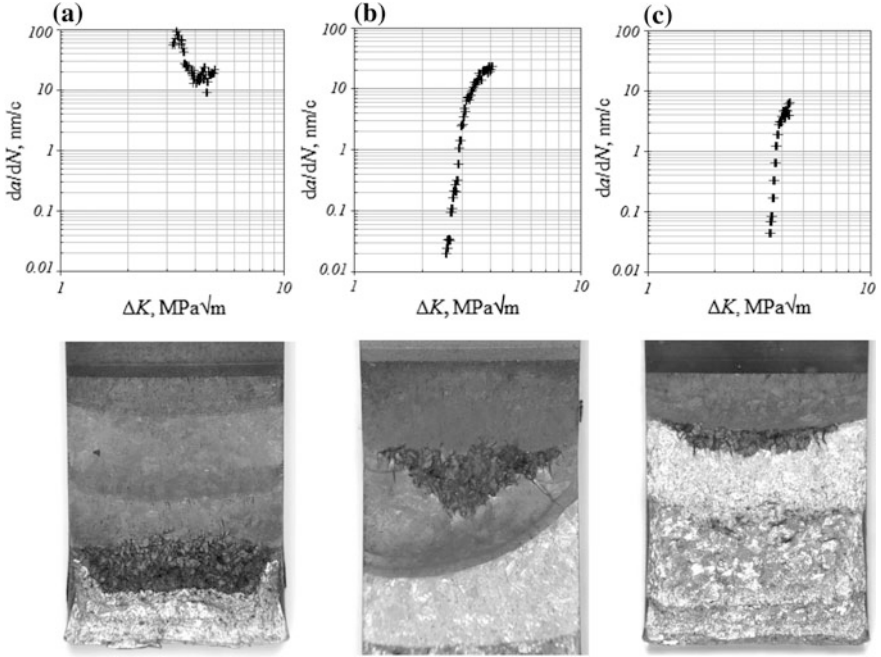


Fig. 6 Examples of high- R high-cycle $da/dN(\Delta K)$ records (with accompanying post-test fracture surfaces) for ΔK_{th} tests during which creep cracking has occurred with; **a** expected $da/dN(\Delta K)$ response, **b** a discernible but unexpected $da/dN(\Delta K)$ response and **c** a hardly discernible $da/dN(\Delta K)$ response ($W(2B)12.5$ CT specimens are 12.5 mm thick)

Table 2 Summary of TDFAD material parameter data (550 °C)

Steel	k'	β	K_{mat}^C MPa√m	$R_{0.2}^C$ MPa
1%Cr	730	9	48	366
9%Cr	1200	5	42	345
17%Cr	331.9	11.4	130	123

$$K_r = \left[\frac{E \varepsilon_{ref}}{L_r R_{0.2}^C} + \frac{(L_r)^3 R_{0.2}^C}{2E \varepsilon_{ref}} \right] \quad \text{for } L_r \leq L_r^{\max} \quad (4)$$

$$K_r = 0 \quad \text{for } L_r > L_r^{\max}$$

where $K_r = K/K_{mat}^C$, $L_r = \sigma_{ref}/R_{0.2}^C$ and $L_r^{\max} = R_R/R_{0.2}^C$. The parameters used for TDFAD construction for the three steels considered in this study at 550 °C are summarised in Table 2.

Important information for construction of the TDFAD envelope (Eq. 4) is isochronous $\varepsilon(\sigma, t)$ data for the time period of interest. Typically, for ΔK_{th} tests involving an ASTM $da/dN(\Delta K)$ criteria [3], high-cycle fatigue cracks can be almost

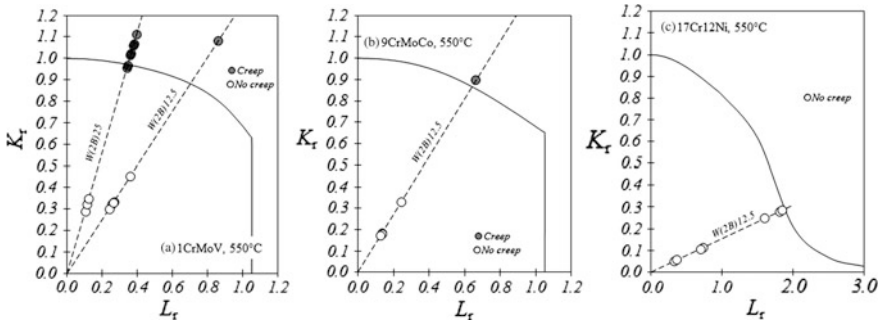


Fig. 7 TDFAD constructions for 1CrMoV, 9CrMoCo and 17Cr12Ni steels at 550 °C (with filled data points representing those tests involving creep crack development when high-cycle fatigue cracking was almost stationary)

stationary for ~ 24 h, and $\varepsilon(\sigma)$ for this period are modelled from data from various sources (e.g. [11, 13]), Table 2, using:

$$\varepsilon = \frac{\sigma}{E} + \left(\frac{\sigma}{k'}\right)^\beta \tag{5}$$

TDFADs for the three steels at 550 °C are given in Fig. 7. As in Fig. 2, filled co-ordinates are used to represent those high-R ΔK_{th} tests involving creep crack development when high-cycle fatigue cracking is almost stationary. The TDFAD envelope acceptably predicts creep crack development in high-R ΔK_{th} tests for the 1CrMoV and 9CrMoCo steels at 550 °C. There is not yet the same evidence for 17Cr12Ni in Fig. 7, primarily because 550 °C is low in the creep range for this steel.

5 Practical Implications

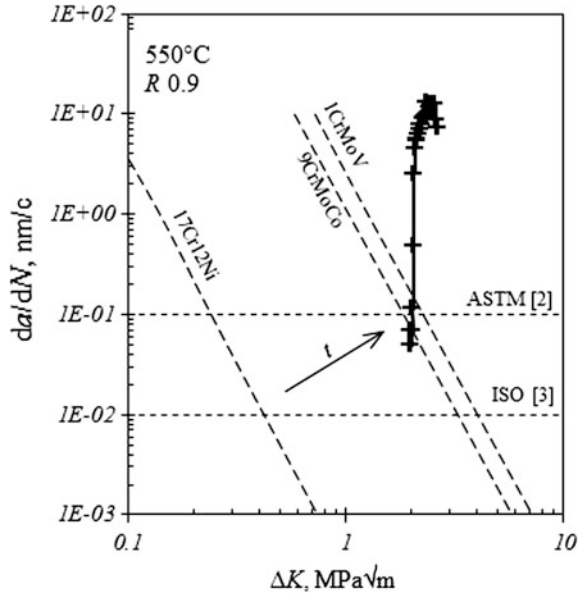
5.1 $da/dN(\Delta K_{th})$ Criterion Sensitivity: Oxidation

It has already been acknowledged that there are two international standards covering the determination of ΔK_{th} with very different da/dN criteria defining fatigue crack growth threshold stress intensity factor. The ΔK_{th} da/dN criterion in the ASTM standard is 1×10^{-10} m/c [3], whereas that in the ISO standard is 1×10^{-11} m/c [4].

While this anomaly is unlikely to have a big influence at low temperatures for materials tested in what for them are relatively inert conditions, the evidence indicates that the situation is very different at high temperatures.

Depending on the oxidation resistance of a material at a given temperature, ΔK_{th} can be significantly enhanced as a consequence of oxide-induced crack closure. For example, for a ΔK_{th} da/dN criterion of 1×10^{-10} m/c, high-cycle fatigue cracking

Fig. 8 Influence of time (oxidation) on $da/dN(d\Delta K_{th}^{ox})$ (diagonal broken lines for three steels) and ultimately on material independent high- R $da/dN(\Delta K)$ (connected black crosses), and the consequence of different ΔK_{th} da/dN criteria [3, 4] (for crack size resolution of 0.25 mm [3])



can be close to stationary for ~ 24 h, and $d\Delta K_{th}^{ox}$ is ~ 2.7 $\text{MPa}\sqrt{\text{m}}$ for 1CrMoV at 550 °C (Table 1). For a ΔK_{th} da/dN criterion of 1×10^{-11} m/c , high-cycle fatigue cracking may be close to stationary for >100 h, and, in these circumstances, $d\Delta K_{th}^{ox}$ could be >4 $\text{MPa}\sqrt{\text{m}}$ for 1CrMoV at 550 °C (i.e. with $\Delta K_{th} > 6$ $\text{MPa}\sqrt{\text{m}}$ for $R = 0.9$).

The situation is illustrated in Fig. 8. This shows a relatively material independent reducing high- R $da/dN(\Delta K)$ record representative of time insensitive conditions (connected black crosses). It also shows three diagonal iso- $da/dN(d\Delta K_{th}^{ox})$ lines (one for each of the Cr steels) representing crack size resolution (~ 0.25 mm [3]) and minimum test times (with the iso- $da/dN(d\Delta K_{th}^{ox})$ reference lines being determined by substituting $dt = da(dN/da)/f$ into Eq. 2).

With longer test times at temperature, the diagonal $da/dN(d\Delta K_{th}^{ox})$ lines move towards the right (Fig. 8). The consequence of this is enhanced ΔK_{th} values. Importantly, if the adopted ΔK_{th} test ΔK reduction rates are slower than the oxidation rates, $da/dN(\Delta K)$ can be prevented from reducing to the standard defined ΔK_{th} da/dN criteria.

5.2 $da/dN(\Delta K_{th})$ Criterion Sensitivity: Creep Cracking

The evidence in Fig. 7 indicates that, while it could have been possible to predict the incidence of creep cracking during high- R ΔK_{th} determinations for the 1CrMoV steel with only a knowledge of K_{mat}^C , it would not for the 9%Cr and in 17%Cr steels, for which a TDFAD analysis is required.

6 Concluding Remarks

High-R high-cycle fatigue crack growth thresholds for power plant steels are enhanced at high temperatures due to oxide-induced crack closure.

The extent of any enhancement of ΔK_{th} due to oxide-induced crack closure depends on time at low da/dN , temperature and material/oxidation mechanism. Consequently, the adopted standard defined $da/dN(\Delta K_{th})$ criterion becomes increasingly important with increasing temperature.

High-R ΔK_{th} values are increasingly influenced by the development of creep cracking at very low da/dN with increasing temperature. While this may only be possible to detect with certainty by fracture surface examination, evidence is presented to show that creep cracking in these circumstances may be predicted using a TDFAD analysis.

References

1. P.C. Paris, F. Erdogan, A critical examination of crack propagation laws. *J. Basic Eng.* **85**(4), 528–533 (1963)
2. S.R. Holdsworth, in *High Temperature Fatigue Crack Growth*, ed. by J.B. Marriott. High Temperature Crack Growth in Steam Turbine Materials, (Commission European Communities, COST Monograph EUR 14678EN, 1994), pp. 129–176
3. E 647, in *Standard Test Method for Measurement of Fatigue Crack Growth Rates*, (ASTM Standard, ASTM International, West Conshohocken, PA, US)
4. ISO 12108, in *Metallic Materials—Fatigue Testing—Fatigue Crack Growth Method*, International Standard
5. R.P. Skelton, J.R. Haigh, Fatigue crack growth rates and thresholds in steels under oxidising conditions. *Mat. Sci. Eng.* **36**, 17–25 (1978)
6. BS 7910, in *Guide to Methods for Assessing the Acceptability of Flaws in Metallic Structures*, (British Standards Institution, 2013)
7. S.R. Holdsworth, in *Review of Air Oxidation Kinetics for a Range of Low and High Alloy Steels*, unpublished (2000)
8. P.J. Ennis, W.J. Quadackers, Mechanisms of steam oxidation in high strength martensitic steels. *Int. J. Pres. Ves. Pip.* **84**, 75–81 (2007)
9. J.R. Rice, in *The Mechanics of Crack Tip Deformation and Extension by Fatigue*. Fatigue Crack Propagation, vol. 415 (ASTM STP 1967), pp. 247–311
10. A.T. Stewart, The influence of environment and stress ratio on fatigue crack growth at near threshold stress intensities in low alloy steels. *Eng. Fract. Mech.* **13**(3), 463–478 (1980)
11. D.W. Dean, R.D. Patel, A. Klenk, F. Mueller, Comparison of procedures for the assessment of creep crack initiation. *OMMI* **3**(3), (2004)
12. R5, An Assessment Procedure for the High Temperature Response of Structures, EDF Energy, 3 (2003)
13. ASME, in *Boiler and Pressure Vessel Code III, Rules for construction of nuclear facility components, Class 1 components in elevated temperature service, Division 1—Subsection NH*, ASME (2004)

Part I
Aerospace

Fracture Mechanics Analysis of Fuselage Structural Joints with Cracks

H. Ramesha, N. C. Mahendra Babu and H. V. Lakshminarayana

Abstract Fracture mechanics provides a methodology for prediction, prevention and control of fracture in materials, components, and structures. Fracture mechanics analysis is the backbone of damage tolerant design. Objectives of fracture mechanics analysis are: (1) stress analysis of cracks to derive crack tip stress field equations and define crack tip stress intensity factors, (2) determination of SIF solutions as function of crack length, orientation and applied loads for a given geometry, (3) prediction of mixed mode fracture under static, dynamic, and sustained loads, (4) prediction of residual strength as a function of crack length. The focus of this paper is on fracture mechanics analysis of longitudinal and circumferential joints of aircraft fuselage structure with cracks. The loading is by internal pressure. Commercial FEA software ANSYS and a special purpose post-processing subprogram called 3MBSIF are used to determine mixed mode membrane and bending SIF solutions. Residual strength prediction is based on the use of strain energy density theory of fracture. Significant results of this study are graphically presented and discussed in this paper.

Keywords Fuselage · Structural integrity · Longitudinal joint · Circumferential joint · Crack · Residual strength · Stress intensity factor

Nomenclature

t	Thickness
E	Modulus of elasticity
ν	Poisson's ratio
a_0	Initial half crack length

H. Ramesha (✉) · H. V. Lakshminarayana
Department of Mechanical Engineering, Dayananda Sagar College of Engineering,
Bangalore 560078, India
e-mail: bharatavarsh@gmail.com

N. C. Mahendra Babu
Department of Mechanical and Manufacturing Engineering, MSRUEAS,
Bangalore 560058, India

a_{cr}	Critical half crack length
K_1	Mode 1 stress intensity factor
K_2	Mode 2 stress intensity factor
K_3	Mode 3 stress intensity factor
ΔK_1	Mode 1 stress intensity factor range
ΔK_2	Mode 2 stress intensity factor range
N	Number of cycles

1 Background

Fuselage of commercial transport aircraft is a complicated structure designed to withstand aircraft loads. Parts and assembly need to be designed to give more life to the structure there by reducing high replacement costs. Nowadays, more research is going on in extending the life of aircraft beyond its designed life. Fracture mechanics analysis helps in this aspect by determining the structural integrity, remaining life, and residual strength of the structure.

Longitudinal and circumferential joints formed on fuselage structure are more susceptible to fatigue damage [1]. As aircraft undergoes pressurization cycles, the parts are subjected to cyclic load which leads to initiation and growth of cracks at joint regions. After number of flight cycles, these cracks coalesce and will lead to failure of the structure [2]. Inspection of structure using NDT tests and damage tolerance analysis helps in analyzing the structure ensuring the safety of passengers and aircraft.

Experimental investigation of fuselage structure is a costly, tedious, and time-consuming process. However, in the absence of suitable reliable analytical means, many such investigations are carried out throughout the world, and a few of these results are also available in open literature [3, 4].

In this work, effort is made for fracture mechanics analysis of curved stiffened panels with longitudinal and circumferential joint using commercial FEA software ANSYS.

2 Problem Statement

Longitudinal and circumferential joints of fuselage structure are considered for fracture mechanics analysis. The specific problem was chosen for investigation, because complete geometry, dimensions, material property, applied loads, static test results, fracture test results, and fatigue crack growth test results are readily available in a report [4]. This is essential for validation and verification of predictions made in this study.

Analysis is carried out in following steps

- Stress analysis
- Evaluation of crack tip stress intensity factors
- Prediction of residual strength

2.1 Longitudinal Joint

A segment of fuselage structure shown in figure is considered for the analysis. Figure 1a shows details of the joint, consisting of outer skin, inner skin, outer doubler plate, inner doubler plate, and stringer bonded together. Evidently, the structure is quite complicated demanding finite element modeling for fracture mechanics analysis.

Figure 1b shows views of curved panel with lead crack. The assembly detail of parts is also shown in the same Fig. 1. A lead crack in the skin panel at joint row A is considered. Fracture mechanics analysis of the panel for various crack lengths is the main objective of this work.

2.2 Circumferential Joint

Figure 2a shows the details of a circumferential joint configuration in a fuselage structure consisting of skin, finger doubler plate, and tapered doubler plate. Location of starter crack can be observed between frame assemblies as shown in Fig. 2b..

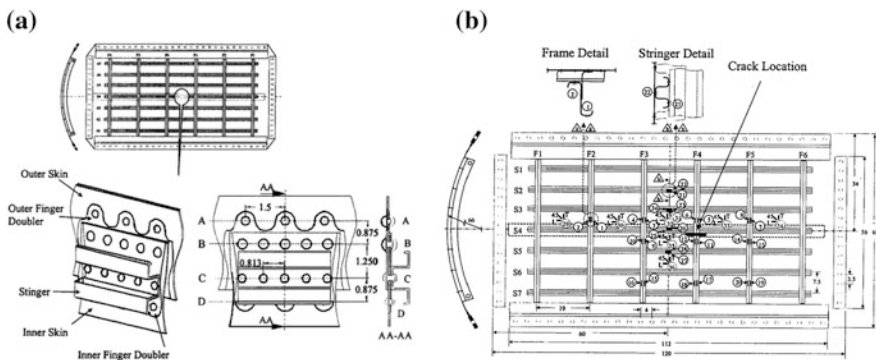


Fig. 1 a Longitudinal joint configuration; b curved panel with a starter crack [4]

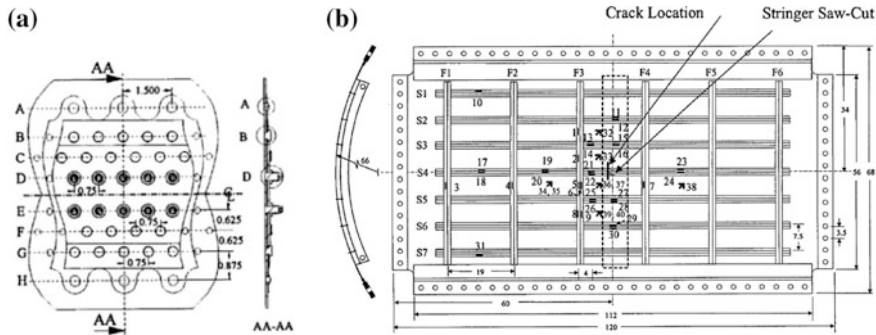


Fig. 2 a Circumferential joint configuration; b Circumferential joint in a curved panel with a starter crack [4]

A segment of Circumferential joint with seven stringers, six frame assemblies, two skin layers, and doubler plates shown in Fig. 2b is considered for the analysis [4]. A lead crack in the skin panel at joint row A is considered. Fracture mechanics analysis of the panel for various crack lengths is the main objective of this work. Analysis of the curved stiffened panel is carried out in following steps

- FEA of the curved panels (without crack)
- Validation of results with available experimental data
- Fracture mechanics analysis of the curved panels

3 FE Modeling for Stress Analysis and Validation

3.1 Introduction

Finite element modeling is defined here as the analyst's choice of material models (constitutive relations and failure criteria), finite elements (types, shapes, orders), meshes, constraint equations, analysis procedures, governing matrix equations and their solution methods, specific pre- and post-processing options available in a chosen commercial FEA software (ANSYS) for the intended analysis (LEFT analysis) of the candidate component. The finite element model is developed as per dimensions and material property data extracted from reference [4]. Analysis is carried out for internal pressure of 0.06937 N/mm^2 with symmetric boundary conditions on all four sides. Thickness and material property data of curved panel components are shown in Table 1.

Table 1 Material property and thickness of parts

Part name	t (mm)	Material	E (MPa)	ν
Skin	1.6	Al 2024-T3	72,395	0.33
Stringer-middle	1.8	Al 7075-T3	71,016	0.33
Stringer	1.6	Al 7075-T3	71,016	0.33
Shear clip	1.6	Al 7075-T5	71,016	0.33
Frame	1.8	Al 7075-T4	71,016	0.33
Finger doubler	3.1	Al 2024-T3	72,395	0.33
Tapered doubler	0.6–1.6	Al 2024-T3	72,395	0.33

3.2 Longitudinal Joint

The geometry used to compute stress distribution and deformation is presented in Figs. 3a, b, and 4. Evidently, it is a very tough task even with the best preprocessor capability available in ANSYS.

For the specific panel under investigation, measured strains using strain gages for various applied pressure loads are reported in reference [4]. The measured and computed strain on frame assembly near the joint region is presented in Table 2. The agreement is good enough to accept the proposed FE model for further investigations.

Figure 5a displays the resulting deformations at the maximum pressure. Figure 5b presents contour plots of von Mises equivalent stress for the whole panel and identifies a maximum value of 485.77 MPa for internal pressure of 0.06937 N/mm². The graphical post-processing capability in ANSYS enables us to locate the region where it occurs as a reentrant corner in a frame close to the maximum deformation region in the panel.

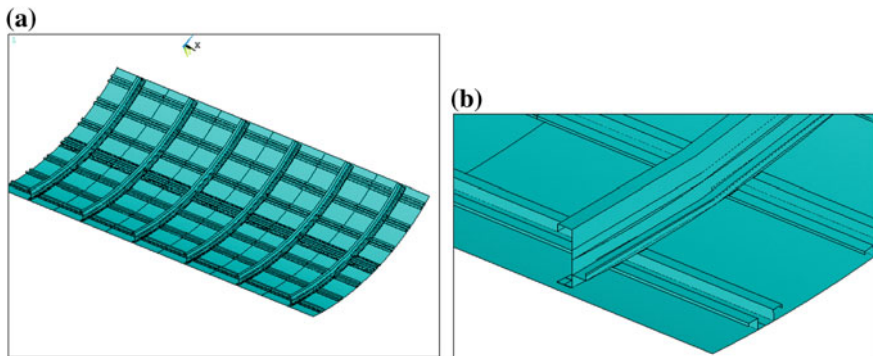


Fig. 3 a Curved panel considered for analysis; b assembly showing frame, stringer, and skin panel

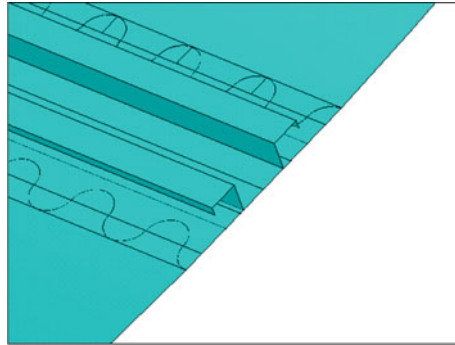


Fig. 4 Assembly showing stringer, doubler plates, outer and inner skin panels

Table 2 FE model validation using measured strain

Strain ($\mu\epsilon$) experiment [4]	Strain ($\mu\epsilon$) analysis	% Error
605.4	586.02	3.201

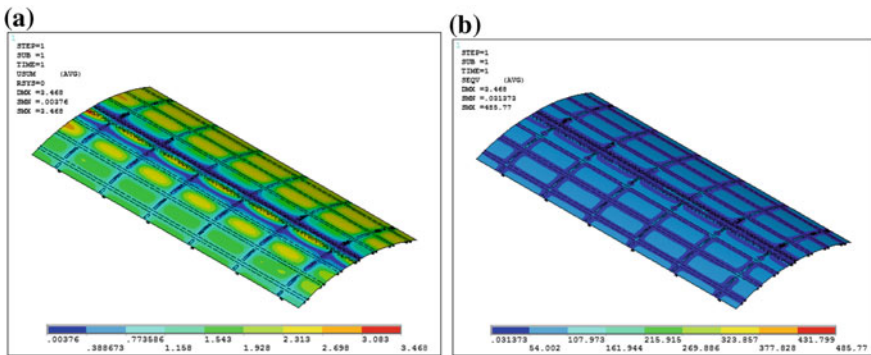


Fig. 5 a Contour plots of resultant displacement; b von Mises stress contour

3.3 Circumferential Joint

The geometry used to compute stress distribution and deformation is presented in Figs. 6a, b, and 7 highlights circumferential joint region of the panel. The computed and measured strain value on frame assembly near the joint region is presented in Table 3. The proposed FE model is used for further investigations.

Figure 8a displays the resulting deformations for internal pressure of 0.06937 N/mm^2 . Figure 8b presents contour plots of von Mises equivalent stress for the whole panel and identifies a maximum value of 488.434 MPa in stringer near frame assemblies.

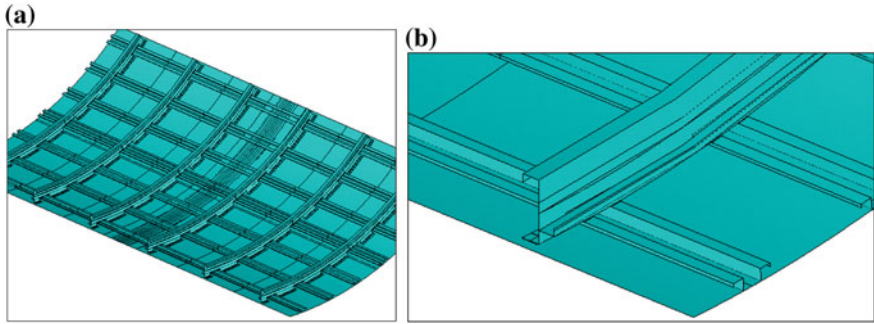


Fig. 6 a Curved panel considered for analysis; b assembly showing frame, stringer, and skin panel

Fig. 7 Circumferential joint

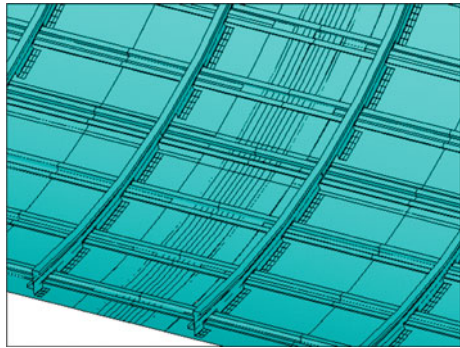


Table 3 FE model validation using measured strain

Strain ($\mu\epsilon$) experiment [4]	Strain ($\mu\epsilon$) analysis	% Error
357.03	303.4	15.02

4 Fracture Mechanics Analysis

4.1 Sub-Modeling and Computation of SIF's

4.1.1 Longitudinal Joint

ANSYS sub-modeling capability is used for evaluation of stress distribution and stress intensity factors at crack tips. Figure 9a shows the sub-model region considered for fracture mechanics analysis. Location of longitudinal lead crack in the curved panel can be observed from Fig. 9b.

It is to be noted that a single element type namely eight noded quadrilateral element quadratic in order (SHELL 281) is exclusively used. Around each crack tip, a refined mesh of singular elements (S-TRIA 6) with $NS = 20$, $\Delta a = a/50$, and 'a'

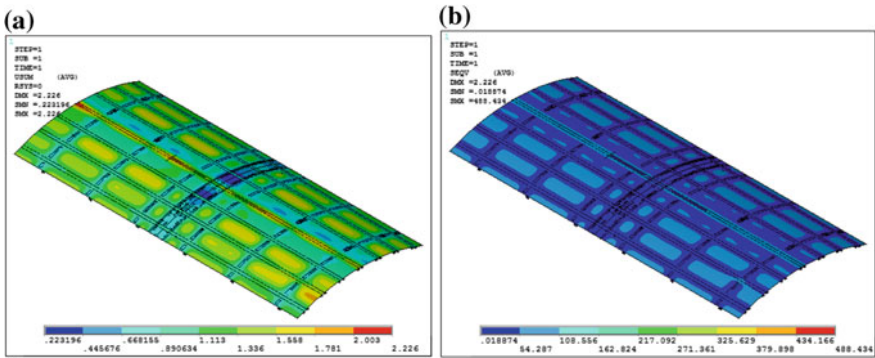


Fig. 8 a Contour plots of resultant displacement; b von Mises stress contour

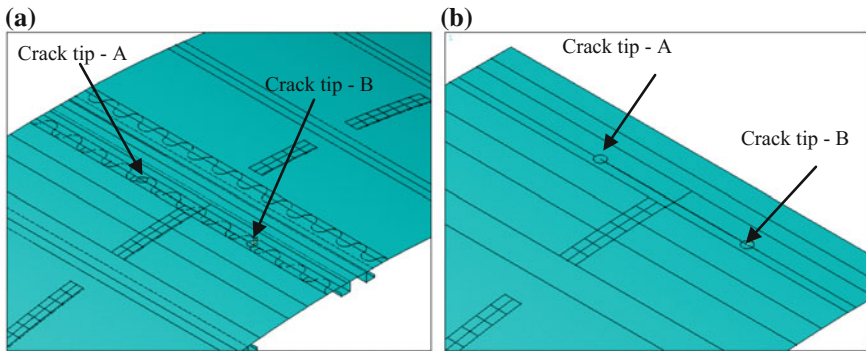


Fig. 9 a Sub-model for detailed analysis; b modeling of crack in outer skin panel (rivet row A)

is half crack length, and a compatible mesh of regular elements (QUAD 8 and TRIA 6) is used. The pre-processing command KSCON is exclusively used here. Parametric design language capability is used to model cracks of different lengths. Macros are written to generate FE models for given crack lengths.

Figure 10a, b displays von Mises stress contours around crack tips A and B. It is possible to identify the mode of fracture and estimate crack tip plastic zone shape and size from these figures. These data are essential for the choice of fracture criteria and prediction of fracture pressure and crack growth directions.

ANSYS software provides a post-processing command KCALC to compute mixed mode Stress Intensity Factors (K_I , K_{II} , K_{III}). The computed SIFs are presented in Fig. 11a, at the maximum pressure equal to 0.06937 N/mm². These results are essential for the prediction of residual strength. Figure 11b provides ΔK values predicted for load range (Minimum/Maximum) equal to 0.1.

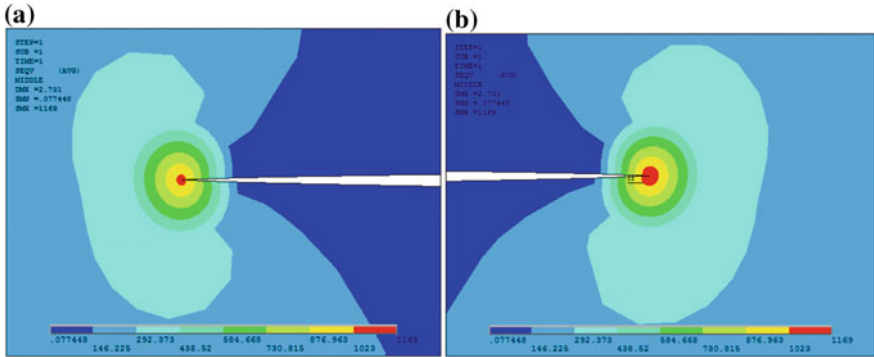


Fig. 10 **a** von Mises stress contour at crack tip—A; **b** von Mises stress contour at crack tip—B

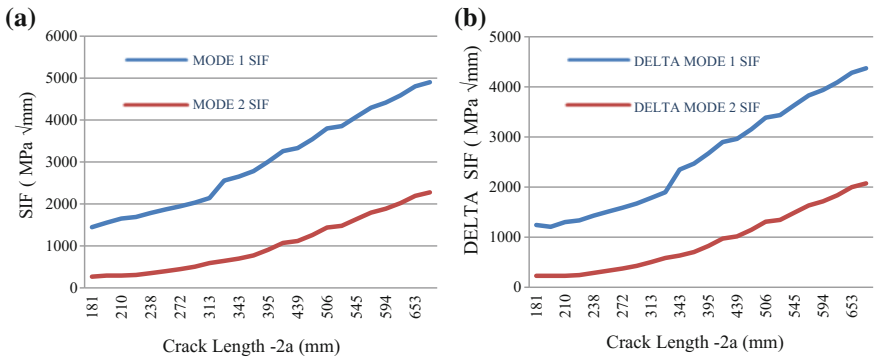


Fig. 11 **a** Stress intensity factor as a function of crack length; **b** stress intensity factor range as a function of crack length

4.1.2 Circumferential Joint

ANSYS sub-modeling capability is used for evaluation of stress distribution and stress intensity factors at crack tips. Figure 12a shows the sub-model region considered for fracture mechanics analysis. Location of circumferential lead crack in the curved panel can also be observed in the same figure.

Figure 13a, b displays von Mises stress contours around crack tips A and B. It is possible to identify the mode of fracture and estimate crack tip plastic zone shape and size from these figures. These data are essential for the choice of fracture criteria and prediction of fracture pressure and crack growth directions.

ANSYS software provides a post-processing command KCALC to compute mixed mode Stress Intensity Factors (K_1 , K_2 , K_3). The computed SIFs are presented in Fig. 14a, at the maximum pressure equal to 0.06937 N/mm^2 . These results are essential for the prediction of residual strength. Figure 14b provides ΔK values predicted for load range (Minimum/Maximum) equal to 0.1.

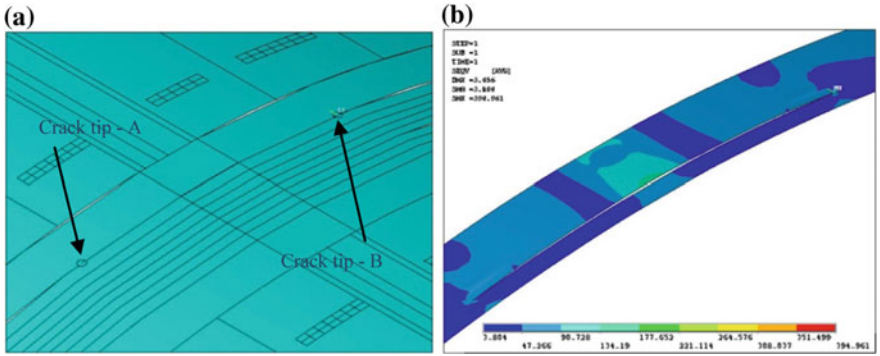


Fig. 12 a Sub-model for detailed analysis; b von Mises stress contour in the skin panel near crack location

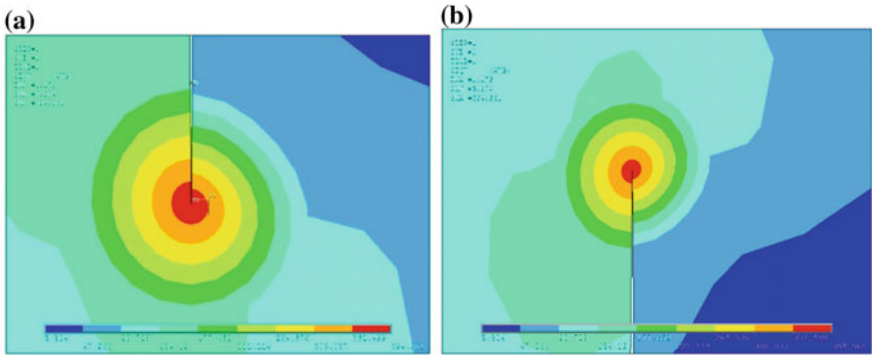


Fig. 13 a von Mises stress contour at crack tip—A; b von Mises stress contour at crack tip—B

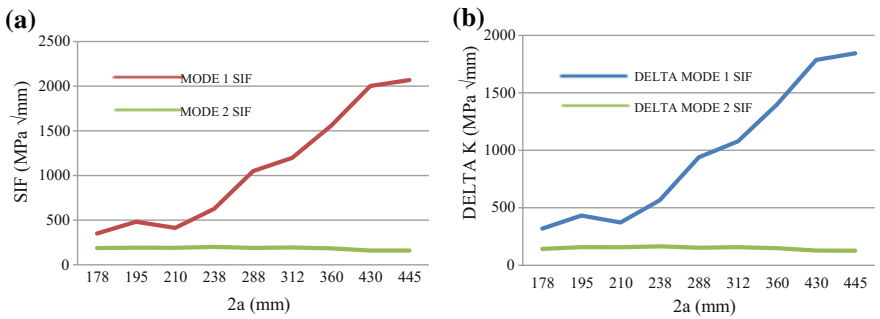


Fig. 14 a Stress intensity factor as a function of crack length; b stress intensity factor range as a function of crack length

4.2 Residual Strength Prediction and Correlation with Test Data

This section presents prediction of residual strength for longitudinal and circumferential joint curved panels using strain energy density theory of fracture. According to this crack extension will occur in the direction of minimum strain energy density (S_{min}), and the extension will occur when it reaches a critical value (S_{cr}) which is a material dependent parameter [5].

4.2.1 Longitudinal Joint

Figure 15a shows variation of strain energy density factor with respect to crack length. Critical SED factor for skin panel material is 30.072. From the figure, it is evident that Minimum SED factor reaches critical value for crack length equal to 585 mm, which can be termed as critical crack length. From this analysis, it is found that catastrophic failure of the structure occurs when lead crack at the longitudinal joint region grows to its critical length of 585 mm. Figure 15b shows variation of residual strength for different crack lengths.

4.2.2 Circumferential Joint

Figure 16a shows variation of strain energy density factor with respect to crack length. Its value gradually increases to 17.12 for crack length equal to 550 mm on further increase in crack length SED factor deviates from its path and remained constant as shown. This is due to stringer underneath the crack which resists its growth. So crack will not extend unless this stringer fails. Similar observation is

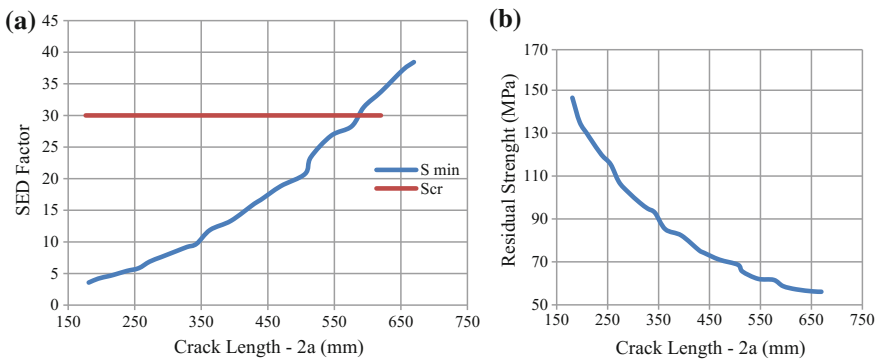


Fig. 15 a Variation of SED factor for different crack lengths; b variation of residual strength for different crack lengths

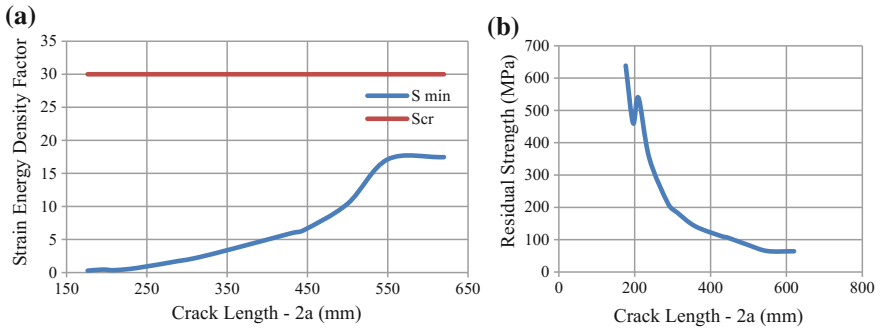


Fig. 16 **a** Variation of SED factor for different crack lengths; **b** variation of Residual strength for different crack lengths

found in experimental investigation, crack grows steadily till 560 mm and on further increase of load, the stringer underneath the crack breaks. Figure 16b shows variation of residual strength for different crack lengths. At crack length equal to 210 mm, a slight increase in residual strength can be observed, which is due to resistance by stringers located on either side of the crack.

References

1. S. Pitt, R. Jones, Multiple-site and widespread fatigue damage in ageing aircraft. *Eng. Fail. Anal.* **4**(4), 237–257 (1997) (Elsevier)
2. G. Samavedam, D. Hoadley, Fracture and fatigue strength evaluation of multiple site damaged aircraft fuselages—curved panel testing and analysis. Final Report, DOT/FAA/CT-94/10, DOT-VNTSC-FAA-93-8 (1994)
3. G. Samavedam, D. Hoadley, J. Davin, in *Structural Integrity of Ageing Airplanes*, Test Facility for Evaluation of Structural Integrity of Stiffened and Jointed Aircraft Curved Panels, (Springer, 1991), pp. 321–337
4. J. Bakuckas, Full-scale testing and analysis of fuselage structure containing multiple cracks. Report DOT/FAA/AR-01/46, (2002)
5. D.Y. Jeong, O. Orringer, G. C. Sih, Strain energy density approach to stable crack extension under net section yielding of aircraft fuselage. *Theor. Appl. Fract. Mech.* 127–137 (1995) (Elsevier)

Effect of Silica Nanoparticles on the Fatigue Life of a Glass Fiber Reinforced Epoxy Composite Under an Aircraft Spectrum Load Sequence

N. Jagannathan, K. Sakthivel, Ramesh Bojja and C. M. Manjunatha

Abstract Two types of glass fiber reinforced plastic (GFRP) composites viz., (i) GFRP employing unmodified LY556 epoxy matrix (GFRP-neat), and (ii) GFRP incorporated with 10 wt% of well-dispersed silica nanoparticles in the LY556 epoxy matrix (GFRP-nano), were tested to determine their fatigue life under mini-FALSTAFF, a standard fighter aircraft spectrum load sequence. Spectrum fatigue tests were conducted on standard test specimens in a 50 kN servo-hydraulic test machine with sinusoidal waveform at an average frequency of 3 Hz. Tests were conducted on both types of GFRP composites with various reference stresses to determine the fatigue life expressed as number of blocks required for failure. The fatigue life of GFRP-nano composite was observed to be about four times higher than that of GFRP-neat composite over the entire range of reference stresses investigated. For a given number of applied load cycles, both the matrix crack density and stiffness reduction rates were observed to be lower in GFRP-nano composite when compared to that of GFRP-neat composite. Presence of silica nanoparticles in the epoxy matrix of GFRP appear to reduce matrix cracking and also retard crack growth rate in the composite leading to enhanced fatigue life. Further, using constant fatigue life diagrams of these materials, the spectrum fatigue life under mini-FALSTAFF load sequence was predicted. Good correlation was observed between the predicted and experimental fatigue life for both types of composites.

Keywords Glass fiber · Polymer composite · Spectrum fatigue
Silica nanoparticle

N. Jagannathan (✉) · K. Sakthivel · R. Bojja · C. M. Manjunatha
Structural Technologies Division, Fatigue and Structural Integrity Group,
CSIR-National Aerospace Laboratories, Bengaluru 560017, India
e-mail: njagan@nal.res.in

© Springer Nature Singapore Pte Ltd. 2018
R. Prakash et al. (eds.), *Advances in Structural Integrity*,
https://doi.org/10.1007/978-981-10-7197-3_3

1 Introduction

Continuous fiber reinforced polymer (FRP) composites are replacing conventional metallic alloys in many structural applications such as airframe, wind turbine, ship hull. Since engineering structures experience cyclic fatigue loads in service, the fatigue performance of such composites assumes significant importance in design, safety, damage tolerance, and durability issues of these structures. Although FRP composites exhibit high specific strength and stiffness with good fatigue resistance, the continuous demand for high-performance structural materials has resulted in use of nanotechnology to further improve mechanical properties of composites.

FRP composites containing nano fillers in the epoxy matrix, called as nanocomposites, have gained tremendous importance in recent times [1, 2]. Significant improvements in static mechanical properties such as tensile and compressive strength, stiffness, interlaminar shear strength, flexural strength, and fracture toughness have been obtained by addition of various types of nanofillers such as SiO_2 , SiC, Al_2O_3 , and TiO_2 particles, carbon nanotubes, and carbon nanofiber [3–10]. Epoxies modified with layered fillers such as clay, graphite platelets, and fullerene have also been shown to improve the mechanical properties of epoxies and FRPs based upon such modified epoxies [11–15].

The fatigue behavior of bulk epoxies modified with nanofillers has been investigated. Presence of silica nanoparticles, carbon nanotubes, and carbon nanofibers in the epoxy improves constant amplitude fatigue life [16–19]. Further, the use of nano-modified epoxies as the matrices in FRPs has been observed to improve the fatigue properties of the FRPs. The addition of small amounts of carbon nanotubes [20], carbon nanofiber [21], silica nanoparticles [16, 22], and nanoclay [12] has been shown to enhance the fatigue properties of FRP composites.

Hybrid-modified epoxy composites wherein two or more different types or sized fillers added have been developed recently which dramatically improve fracture toughness and fatigue properties of polymer composites. Various hybrid combinations such as nano- and micro-sized silica particles [23], nano-silica and nano-rubber [17], nano-silica and micron rubber [24–28], nano-silica and MWCNT [29], carbon nanotubes and graphite nanoplatelets [30] have been employed to significantly improve fracture toughness and fatigue properties of composites.

Most of the fatigue studies on nanocomposites have been limited to constant amplitude fatigue but spectrum fatigue studies which simulate real service loads have not been studied in detail. Recently, we have observed that a polymer nanocomposite containing silica nanoparticles exhibit improved constant amplitude fatigue life [16] as well as enhanced fatigue life under a wind turbine spectrum load sequence [31]. The main aim of this investigation was to measure and predict the fatigue behavior of a GFRP-nano composite, under a standard aircraft spectrum load sequence. Fatigue life was determined experimentally and compared with predictions through empirical equations.

2 Experimental

2.1 Material

Two types of glass fiber reinforced polymer (GFRP) composites were considered in this study viz., (i) GFRP with unmodified LY556 epoxy matrix (termed as GFRP-neat), and (ii) GFRP with modified epoxy matrix containing 10 wt% silica nanoparticles (termed as GFRP-nano). The complete details of the materials used and the processing employed to fabricate the GFRP composites can be found in Manjunatha et al. [16]. However, for the sake of completeness, they are briefly explained here.

The epoxy resin used was a diglycidyl ether of bisphenol A (DGEBA) resin. The silica (SiO_2) nanoparticles were obtained as a colloidal silica sol. with a concentration of 40 wt% in a DGEBA resin. The curing agent was an accelerated methylhexahydrophthalic acid anhydride. The E-glass fiber cloth used was a non-crimp-fabric. The required quantity of the neat epoxy resin and the calculated quantities of silica nanoparticle-epoxy resin to give 10 wt% of nano-silica in the final resin were all individually weighed, degassed, and mixed together, and a stoichiometric amount of curing agent was added to produce a resin mix. This resin mixture was used to prepare the GFRP composite laminate by resin transfer molding technique.

E-glass fiber fabric pieces were cut and laid up in a quasi-isotropic sequence $[(+45/-45/0/90)_s]_2$. The resin mixture was infused into the glass-cloth layup and cured at 100 °C for 2 h and post-cured at 150 °C for 10 h. In this way, two types of GFRP composites were fabricated, i.e., GFRP-neat and GFRP-nano. The laminates produced were about 2.5–2.7 mm thick and had a fiber volume fraction of about 57%.

The silica particles of about 20 nm in diameter were evenly distributed in the epoxy as shown in atomic force microscopic image [16] in Fig. 1. The tensile and compressive properties of the composite laminates [31] are shown in Table 1. Both the strength and stiffness of GFRP-nano composite are slightly higher in both tension and compression due to the presence of hard silica nanoparticles in the epoxy matrix.

2.2 Fatigue Testing

Fatigue tests on composites were conducted under a standard spectrum load sequence. The load sequence considered in this investigation was a fighter aircraft loading standard for fatigue evaluation, mini-FALSTAFF [32, 33] shown in Fig. 2. It is a short version of standard FALSTAFF load spectrum, which is a standardized variable-amplitude test load sequence developed for the fatigue analysis of materials used for fighter aircraft. In Fig. 2, the normalized stress is plotted against peak/

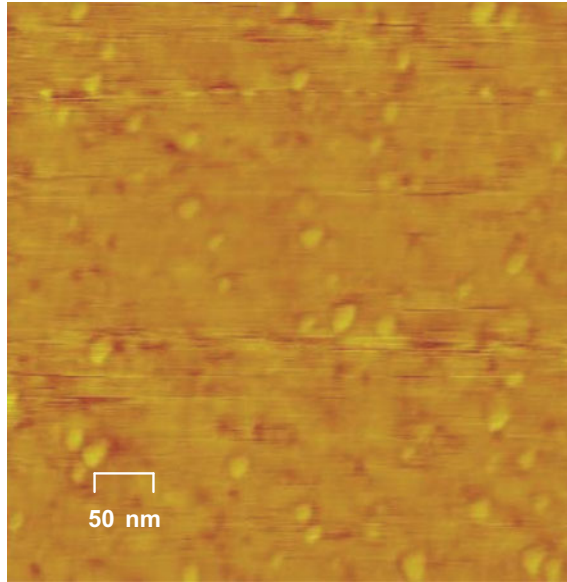


Fig. 1 Atomic force microscopy image of a 10 wt% silica nanoparticle-modified bulk epoxy polymer [31]

Table 1 Mechanical properties of the GFRP composites [31]

Type of test	Mechanical property	Material		% change
		GFRP-neat	GFRP-nano	
Tension	σ_{UTS} (MPa)	365 ± 13	382 ± 12	+4.65
	E_T (GPa)	17.5 ± 0.1	18.8 ± 1.7	+7.42
Compression	σ_{UCS} (MPa)	355 ± 47	361 ± 28	+1.69
	E_C (GPa)	21.3 ± 0.4	22.6 ± 0.4	+6.10

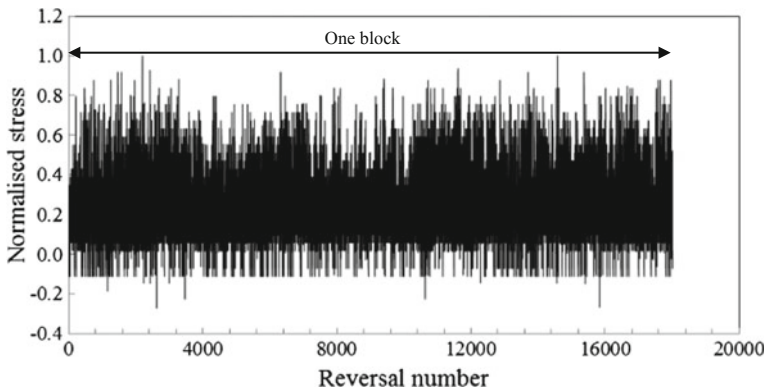


Fig. 2 Standard mini-FALSTAFF spectrum load sequence [32]

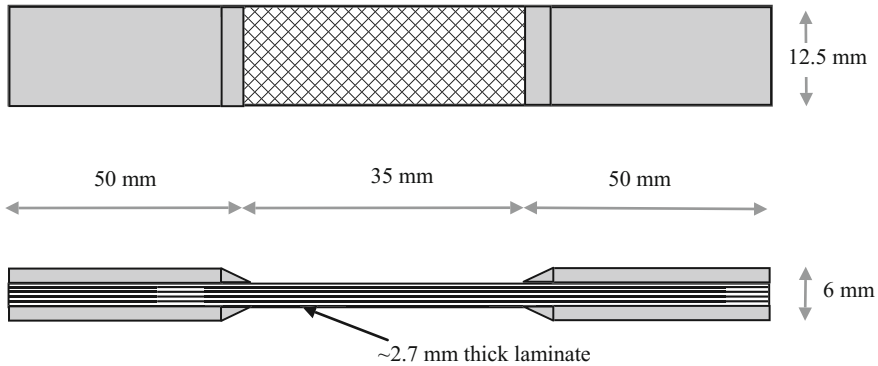


Fig. 3 Schematic diagram showing the dimensions of the fatigue test specimens

trough points of load sequence. One block of this load sequence consists of 18,012 reversals at 32 different stress levels and represents loading equivalent of 200 flights. The stress sequence for our experiments was obtained by multiplying with a constant reference stress value, σ_{ref} for all the peak/trough points in the entire block.

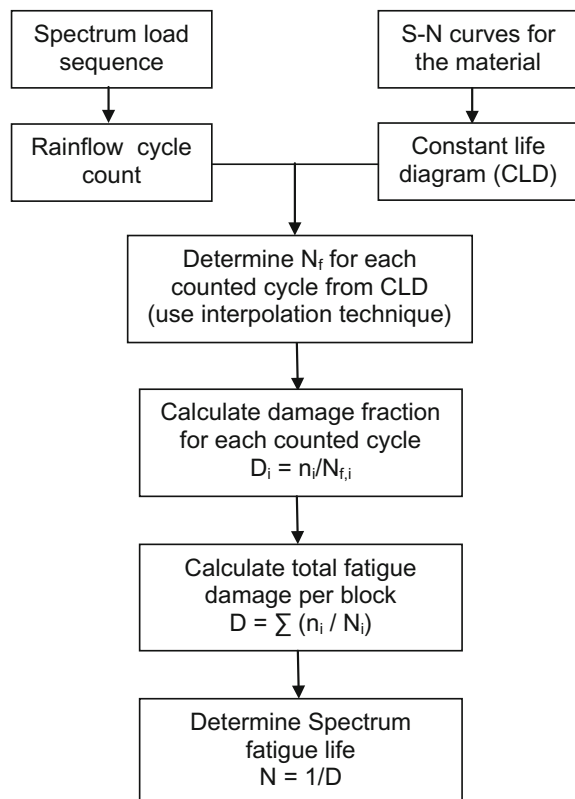
Spectrum fatigue tests with various reference stress levels were conducted on both GFRP composites. The geometry and dimensions of the test specimens employed for spectrum fatigue tests are shown in Fig. 3. Tests were conducted in a computer controlled 50 kN servo-hydraulic test machine. Sinusoidal waveform with an average frequency of 3 Hz (six reversals per second) was employed in the tests. For any given reference stress, the number of load blocks required to fail the test specimen, N_b , was determined. Whenever a specimen failed in-between a full block, it was rounded-off to the nearest complete block number.

The stiffness variation of the specimen subjected to spectrum fatigue loads was determined during the test as a function of the number of applied load blocks. Whenever stiffness measurement data were required, the fatigue test was intermittently stopped, a load cycle with $\sigma_{max} = 0.5 \sigma_{ref}$ and stress ratio $R = \sigma_{min} / \sigma_{max} = 0$ was applied, the load versus displacement data were obtained and then analyzed. Considering the large number of load cycles in one block, insertion of this one cycle was assumed not to alter the fatigue damage in the material significantly. For the purpose of comparison, the normalized stiffness of the specimen was defined as the ratio of measured stiffness at any given time to the initial stiffness (obtained before application of the first spectrum load block). For one particular test with $\sigma_{ref} = 250$ MPa, the specimens were dismantled at the end of the application of three complete load block, and photographs showing matrix cracks were obtained, as explained in [16].

2.3 Fatigue Life Prediction

The fatigue life of the GFRP composites under the mini-FALSTAFF load sequence was predicted and compared with the experimental results. The general methodology followed in prediction of fatigue life under spectrum loads in composites may be found elsewhere [31, 34]. A schematic of flow chart for life prediction is shown in Fig. 4 which involves [31]: (i) the rainflow counting of the fatigue cycles in the spectrum load sequence, (ii) the determination of the cycles to failure, N_f , for each of the counted load cycles using a constant life diagram (CLD) of the material, (iii) the calculation of the damage fraction for each of the counted load cycles as the ratio of cycle count to N_f obtained from the CLD, and finally (iv) the determination of the total fatigue damage per load block by summation of the damage fraction. The material is assumed to fail when the total damage fraction reaches 1.0, and, hence, the fatigue life under the spectrum load sequence is equal to the reciprocal of the total damage estimated per load block. This procedure was followed in the present study for estimation of fatigue life.

Fig. 4 Schematic diagram showing the procedure for prediction of spectrum fatigue life [31]



3 Results and Discussion

3.1 Experimental Spectrum Fatigue Life

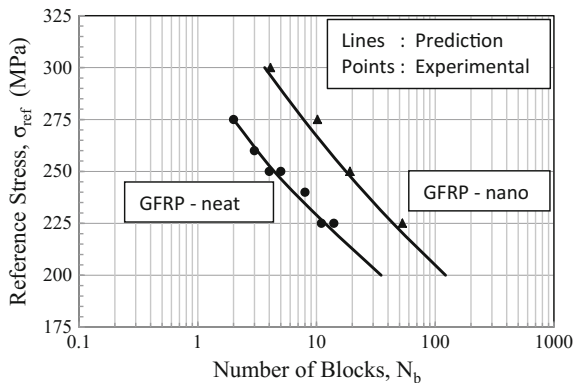
The experimentally determined spectrum fatigue life of GFRP composites under mini-FALSTAFF load sequence at various reference stresses is shown in Fig. 5. The fatigue life was observed to increase with a reduction in the reference stress in both GFRP composites, as observed in many other investigations [31, 35, 36]. It may also be seen that for any given reference stress level, the GFRP-nano composite shows higher fatigue life compared to that of GFRP-neat composite by about three times. The spectrum fatigue life enhancement is observed over the entire range of reference stress levels investigated.

The normalized stiffness of the specimen as a function of spectrum load blocks determined for the fatigue test with $\sigma_{ref} = 250$ MPa, for both GFRP composites is shown in Fig. 6. The stiffness reduction trend observed in these materials is similar to generally observed behavior in FRP composites [37–42]. It may be seen that the stiffness reduction rate is quite high in the GFRP-neat composite than in GFRP-nano composite.

Photographs of the matrix cracks observed on the surface of the composite subjected to thee complete load block of the mini-FALSTAFF spectrum load sequence with $\sigma_{ref} = 250$ MPa are shown in Fig. 7. Initiation and growth of such matrix cracks under cyclic fatigue loads in GFRP composite have been reported by others [16, 42]. The GFRP-neat composite exhibits more severe cracking than GFRP-nano composite suggesting suppression of matrix cracks by nano modification of epoxy matrix.

The fatigue failure mechanisms under cyclic loads in polymer composites have been investigated extensively. The generally accepted mechanisms include [37, 40] (i) initiation and growth of matrix cracks, (ii) initiation and growth of disbonds and delaminations, and (iii) individual fiber breaks throughout the fatigue life. Studies have clearly shown that the fatigue crack growth rate of the bulk epoxy containing

Fig. 5 Experimental and predicted fatigue lives of the GFRP composites under the mini-FALSTAFF spectrum load sequence



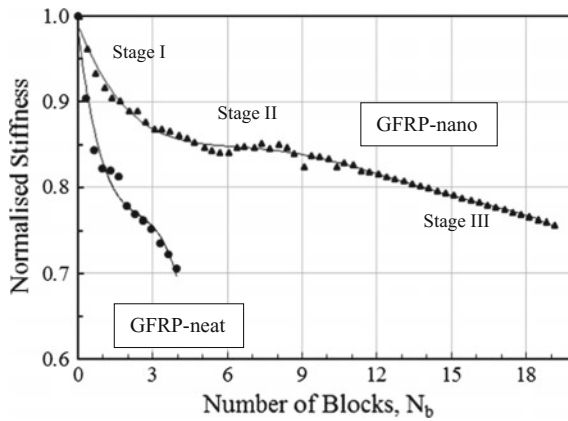


Fig. 6 Variation of the normalized stiffness for the GFRP composites determined under the mini-FALSTAFF spectrum load sequence, with $\sigma_{ref} = 250$ MPa

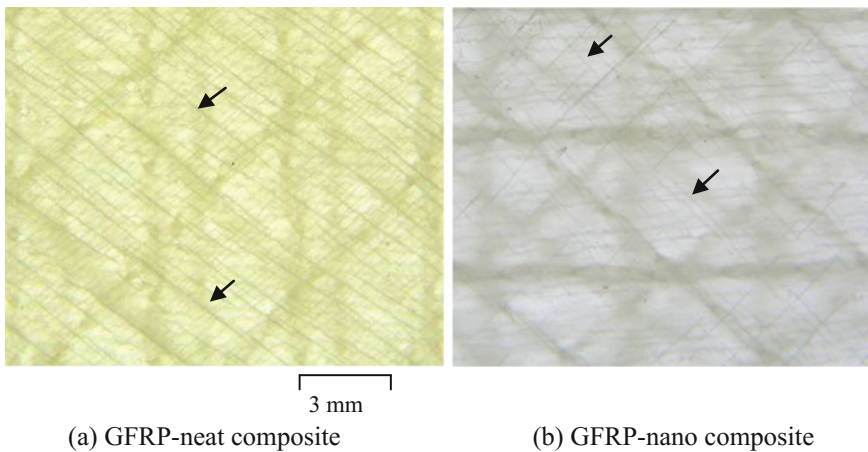


Fig. 7 Photographs showing matrix cracks (indicated by the arrows) in the GFRP composites subjected to three complete mini-FALSTAFF spectrum load blocks with $\sigma_{ref} = 250$ MPa

nano-silica particles is over an order of magnitude lower than that of the neat epoxy [43, 44]. Further, it has been shown that the use of such particles to formulate a modified epoxy matrix in a GFRP composite material enhances the constant amplitude fatigue life due to suppressed matrix cracking, delayed initiation of delamination, and reduced crack/delamination growth rate [16].

The stiffness loss in stage I and stage II results primarily from matrix cracking. Once the matrix crack density saturates and attains the characteristic damage state (CDS), the disbands and delaminations created due to the coalescence of primary and secondary matrix cracks grow, and this leads to a further loss in stiffness. The

present results show that when both composites are subjected to the same number of spectrum load blocks, the crack density is lower in the GFRP-nano composite compared to the GFRP-neat composite. Thus, the stiffness loss curves shown in Fig. 6 indicate the underlying mechanisms, i.e., suppressed matrix cracking, delayed initiation of delamination, and a reduced crack/delamination growth rate. All these mechanisms lead to an improvement in the spectrum fatigue life of the GFRP-nano composite.

3.2 Spectrum Fatigue Life Prediction

The fatigue life of GFRP-neat and GFRP-nano composites was predicted following the procedure shown in Fig. 4. The constant life diagrams (CLDs) for the GFRP composites determined in an earlier investigation [31] are shown in Fig. 8. Rainflow counting of the fatigue cycles in the spectrum load sequence was performed following the ASTM standard specified procedure [45]. Since each of the rainflow-counted load cycles will be of different load amplitude and mean stress, it is necessary to interpolate and determine N_f for all these load cycles using the CLD. A piecewise linear interpolation technique [46] was used in the present investigation. For damage accumulation model, the Miners' linear damage accumulation rule [47] was used:

$$D = \sum (n_i/N_i) \quad (1)$$

where D is the damage fraction, n_i is the cycle count, and N_i is the cycles to failure for a given load cycle amplitude. Thus, the total damage per load block was estimated following the above procedure, and the spectrum fatigue life was predicted for the GFRP composites.

The fatigue life predicted as a function of the reference stress following the above procedure is shown in Fig. 5, along with the experimental results. It may be observed from these results that very good agreement exists between the experimental and the predicted fatigue lives for both GFRP composites. Thus, the predictions also suggest an improvement in the fatigue life of GFRP-nano composite by about four times over that of GFRP-neat composite.

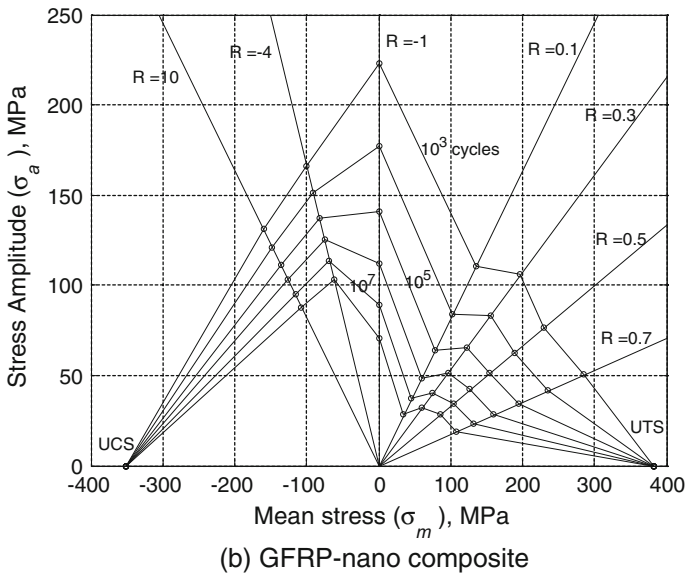
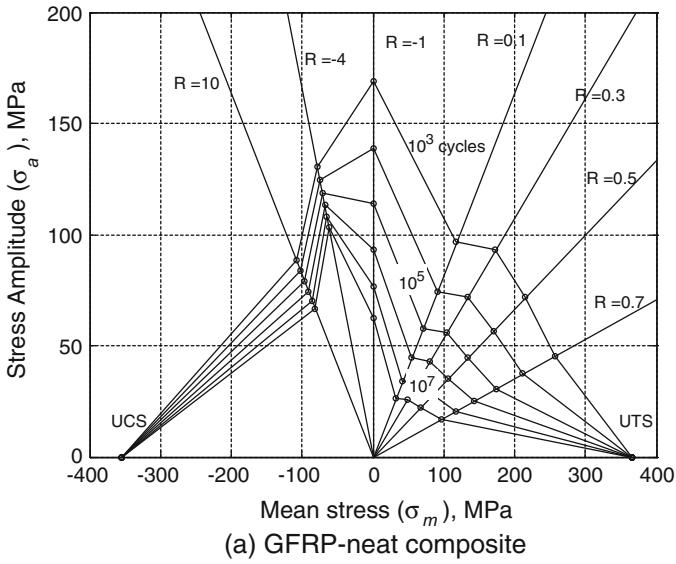


Fig. 8 Constant life diagrams (CLDs) for the GFRP composites [31]

4 Conclusions

Based on the results obtained in this investigation, the following conclusions may be drawn:

1. The addition 10 wt% of silica nanoparticles to the epoxy matrix of a GFRP composite improves the fatigue life under mini-FALSTAFF spectrum load sequence by about four times.
2. The suppressed matrix cracking and retarded crack and delamination growth rate in the silica nanoparticle-modified epoxy matrix of the GFRP composite appear to enhance the spectrum fatigue life.
3. The predicted fatigue lives under the mini-FALSTAFF spectrum load sequence are in very good agreement with the experimental observations for both the GFRP-neat and GFRP-nano composites.

Acknowledgements The authors from CSIR-NAL wish to thank Mr. Shyam Chetty, Director and Dr. Satish Chandra, Head, Structural Technologies Division, CSIR-National Aerospace Laboratories, Bangalore, India, for their constant support and encouragement during this work. The laminates were fabricated in the department of Mechanical Engineering, Imperial College, London, UK. Thanks to Prof. A.J. Kinloch and Dr. A.C. Taylor for their assistance and encouragement during this work. The authors also wish to thank the technical support staff members of the Department of Mechanical Engineering and the Composites Centre of the Aeronautics Department, Imperial College London, and the Materials Evaluation Lab, STTD, NAL, Bangalore, for their assistance in the experimental work.

References

1. E.T. Thostenson, C. Li, T.W. Chou, *Comp. Sci. Tech.* **65**, 491 (2005)
2. F. Hussain, M. Hojjati, M. Okamoto, R.E. Gorga, *J. Comp. Mater.* **40**, 1511 (2006)
3. J. Ma, M.S. Mo, X.S. Du, P. Rosso, K. Friedrich, H.C. Kuan, *Polymer* **49**, 3510 (2008)
4. C.M. Manjunatha, A.C. Taylor, A.J. Kinloch, S. Sprenger, *J. Mater. Sci.* **44**(16), 4487 (2009)
5. N. Chisholm, H. Mahfuz, V.K. Rangari, A. Ashfaq, S. Jeelani, *Compos. Struct.* **67**, 115 (2005)
6. S. Zhao, L.S. Schadler, H. Hillborg, T. Auletta, *Compos. Sci. Tech.* **68**, 2976 (2008)
7. B. Wetzel, P. Rosso, F. Hauptert, K. Friedrich, *Eng. Fract. Mech.* **73**, 2375 (2006)
8. F.H. Gojny, M.H.G. Wichmann, B. Fiedler, W. Bauhofer, K. Schulte, *Compos. A: Appl. Sci. Manufac.* **36**, 1525 (2005)
9. Z. Spitalsky, D. Tasis, K. Papagelis, C. Galiotis, *Prog. Polym. Sci.* **35**, 357 (2010)
10. C.M. Manjunatha, A.C. Taylor, A.J. Kinloch, S. Sprenger, *J. Mater. Sci.* **44**(1), 342 (2009)
11. Y. Zhou, V. Rangari, H. Mahfuz, S. Jeelani, P.K. Mallick, *Mater. Sci. Eng. A* **402**, 109 (2005)
12. S.U. Khan, A. Munir, R. Hussain, J.K. Kim, *Compos. Sci. Tech.* **70**, 2077 (2010)
13. Y. Zhou, M. Hosur, S. Jeelani, P. Mallick, *J. Mater. Sci.* **47**, 5002 (2012)
14. J. Cho, J.Y. Chen, I.M. Daniel, *Script. Mater.* **56**, 685 (2007)
15. A.M. Rafiee, F. Yavari, J. Rafiee, N. Koratkar, *J. Nano. Part Res.* **13**, 733 (2011)
16. C.M. Manjunatha, A.C. Taylor, A.J. Kinloch, S. Sprenger, *Compos. Sci. Tech.* **70**, 193 (2010)
17. G.T. Wang, H.Y. Liu, N. Saintier, Y.W. Mai, *Eng. Fail. Anal.* **16**, 2635 (2009)
18. N. Yu, Z.H. Zhang, S.Y. He, *Mater. Sci. Eng. A* **494**, 380 (2008)

19. D.R. Bortz, C. Merino, I. Martin-Gullon, *Compos. Sci. Tech.* **71**, 31 (2011)
20. C. Grimmer, C. Dharan, J. Mater. Sci. **43**, 4487 (2008)
21. D.R. Bortz, C. Merino, I. Martin-Gullon, *Compos. Sci. Tech.* **72**, 446 (2012)
22. L. Böger, J. Sumfleth, H. Hedemann, K. Schulte, *Compos. Part A: Appl. Sci. Manufact.* **41**, 1419 (2010)
23. T. Adachi, M. Osaki, W. Araki, S.C. Kwon, *Acta Mater.* **56**, 2101 (2008)
24. Y.L. Liang, R.A. Pearson, *Polymer* **51**, 4880 (2010)
25. A.J. Kinloch, R.D. Mohammed, A.C. Taylor, C. Eger, S. Sprenger, D. Egan, *J. Mater. Sci.* **40**, 5083 (2005)
26. A.J. Kinloch, R.D. Mohammed, A.C. Taylor, S. Sprenger, D.J. Egan, *J. Mater. Sci.* **41**, 5043 (2006)
27. A.J. Kinloch, K. Masania, A.C. Taylor, S. Sprenger, D. Egan, *J. Mater. Sci.* **43**, 1151 (2008)
28. C.M. Manjunatha, S. Sprenger, A.C. Taylor, A.J. Kinloch, *J. Compos. Mater.* **44**, 2095 (2010)
29. L. Böger, J. Sumfleth, H. Hedemann K. Schulte, *Compos. Part A: Appl. Sci. Manufact.* **41**, 1419 (2010)
30. J. Li, P.S. Wong, J.K. Kim, *Mater. Sci. Eng. A* **483**, 660 (2008)
31. C.M. Manjunatha, R. Bojja, N. Jagannathan, *Mater. Perf. Char.* **3**(1), 327 (2014)
32. G.M. Van Dijk, J.B. de Jonge, National Aerospace Laboratory NLR, Netherlands, NLR MP 75017 U (1975)
33. P. Heuler, H. Klatschke, *Int. J. Fat.* **27**, 974 (2005)
34. N.L. Post, S.W. Case, J.J. Lesko, *Int. J. Fat.* **30**, 2064 (2008)
35. T.P. Philippidis, A.P. Vassilopoulos, *Compos. Part A: Appl. Sci. Manufact.* **35**, 657 (2004)
36. C.M. Manjunatha, Ramesh Bojja, N. Jagannathan, A.J. Kinloch, A.C. Taylor, *Int. J. Fat.* **54**, 25 (2013)
37. R. Talreja, *Proc. Roy. Soc. London. A. Math. Phys. Sci.* **378**, 461 (1981)
38. J.S. Tate, A.D. Kelkar, *Compos. B* **39**, 548 (2008)
39. K.L. Reifsnider, R. Jamison, *Int. J. Fat.* **4**, 187 (1982)
40. S.W. Case, K.L. Reifsnider, in *Fatigue of Composite Materials*, eds. I. Milne, R.O. Ritchie, B. Karihaloo. *Comprehensive Structural Integrity*, vol. 4 Cyclic loading and fatigue, (Elsevier Science, Amsterdam, 2003)
41. A. Gagel, B. Fiedler, K. Schulte, *Compos. Sci. Tech* **66**, 657 (2006)
42. A. Gagel, D. Lange, K. Schulte, *Compos. A* **37**, 222 (2006)
43. H.Y. Liu, G. Wang, Y.W. Mai, *Compos. Sci. Tech.* **72**(13), 1530 (2012)
44. C.M. Manjunatha, N. Jagannathan, K. Padmalatha, A.C. Taylor, A.J. Kinloch, *Int. J. Nanosci.* **10**, 1095 (2011)
45. Standard Practices for Cycle Counting in Fatigue Analysis, ASTM E1049, Annual book of ASTM Standards, American Society for Testing and Materials, PA, vol. 15.03, (2003)
46. A.P. Vassilopoulos, B.D. Manshadi, T. Keller, *Int. J. Fat.* **32**, 659 (2010)
47. M.A. Miner, *J. Appl. Mech.* **12A**, 159 (1945)

Fatigue Life Estimation of Typical Fighter Aircraft Main Landing Gear Using Finite Element Analysis

T. Sivaranjani, D. V. T. G. Pavan Kumar, C. M. Manjunatha
and M. Manjuprasad

Abstract Fatigue analysis of main landing gear of typical fighter aircraft was carried out using MSC Fatigue software considering the strain spectra measured at critical location during the flight starting from taxiing, take-off to landing. In the absence of load information on the landing gear, a methodology was proposed to calculate the equivalent load system from measured strains and verified. Fatigue life of landing gear was obtained using various stress spectra based on stress-life approach and was compared with the fatigue life calculated using constant life diagram (CLD) approach. Fatigue life estimation using Gerber mean stress correction was found to be in good agreement with the fatigue life estimation using CLD approach. Fatigue analysis using maximum absolute principal stress criterion and linear damage rule give the conservative fatigue life, and hence, these criteria may be used as fatigue life estimation criteria for design.

Keywords Main landing gear · Fatigue life · Stress spectra · Goodman and Gerber mean stress corrections · Maximum absolute principal stress

1 Introduction

Landing gear system is one of the critical systems of an aircraft and is configured along with the aircraft structure because of its substantial influence on the aircraft structural configuration itself. Landing gear and its attachments are one of the principal structural elements and are useful for aircraft during taxiing, take-off and landing. Principal structural element's failure results in catastrophic failure. The main failure mechanisms in landing gear are fatigue, corrosion-related problems and overload failures. Fatigue failure is brittle-like (relatively little plastic deformation)—even in normally ductile materials and hence, it is sudden and catastrophic.

T. Sivaranjani · D. V. T. G. Pavan Kumar (✉) · C. M. Manjunatha · M. Manjuprasad
Structural Technologies Division, CSIR-National Aerospace Laboratories, HAL Airport
Road, Bangalore 560017, India
e-mail: pavan@nal.res.in

Catastrophic metal fatigue can lead to aircraft tearing apart in mid-flight. Estimation of fatigue life for the landing gear system is mandatory in order to certify the landing gear and frame the schedule for maintenance.

Beaudet and Roth [1] assessed the trends in failure mechanisms of landing gear components and their causes. The different failure causes identified were fatigue, corrosion and overload failures. Design deficiencies and manufacturing defects led mainly to fatigue failures, while poor material selection and improper field maintenance are the principal origins of corrosion-related failures. They emphasized that fatigue can be best addressed by improving the manufacturing quality and better characterizing the service and manufacturing stresses. Khondker et al. [2] showed that the composite material structure is having high efficiency and reduced weight. Imran et al. [3] showed that composite material landing gear is suitable for structural safety for both static and spectrum loads. Divakaran et al. [4] presented a work dealing with the various stages of landing gear design and development. They showed the current technology landscape and how they are going to meet the challenges in the development of landing gear and demonstrated design tools to reduce the time and cost.

The fatigue failures can be figured out mostly through non-destructive testing in the landing gear. These kinds of fatigue failures will result in the catastrophic failure of aircraft whether it is transport or military aircraft. Hence, there is a need to study the fatigue phenomena of landing gear, and it is mandatory to consider the fatigue effects on the landing gear during the design phase itself. Among the various parts present in the landing gear, oleo strut is one of the critical components under fatigue condition. In the present fatigue analysis study, the main landing gear outer cylinder nothing but the shock absorbing strut cylinder was taken into consideration.

2 Static Analysis of Main Landing Gear

As a preliminary step towards modelling and analysis of landing gear, a simple case of landing gear reported in the literature [2] was studied using finite element (FE) method. The landing gear model was made up of standard steel having Young's modulus of 200 GPa, Poisson's ratio of 0.266 and yield strength of 250 MPa.

During landing, the piston in the landing gear retracts inside by compressing the fluid in the chamber. The pressure caused by the compression is the input load for this analysis, and its magnitude is 20.68 MPa. The piston was clamped at the bottom end in this analysis. The landing gear was modelled using four-noded tetrahedral elements using Altair HyperMesh [5], the static analysis was performed using MSC Nastran [6], and the results are shown in Fig. 1. The hoop stress obtained from the finite element static analysis is 1030 MPa.

Since the pressure load was applied on the cylinder, the hoop stress can be calculated analytically as $PD/2t = 1034$ MPa, where 'P' is the applied pressure, 'D' is the mean diameter, and 't' is the thickness of the cylinder. The FE hoop stress

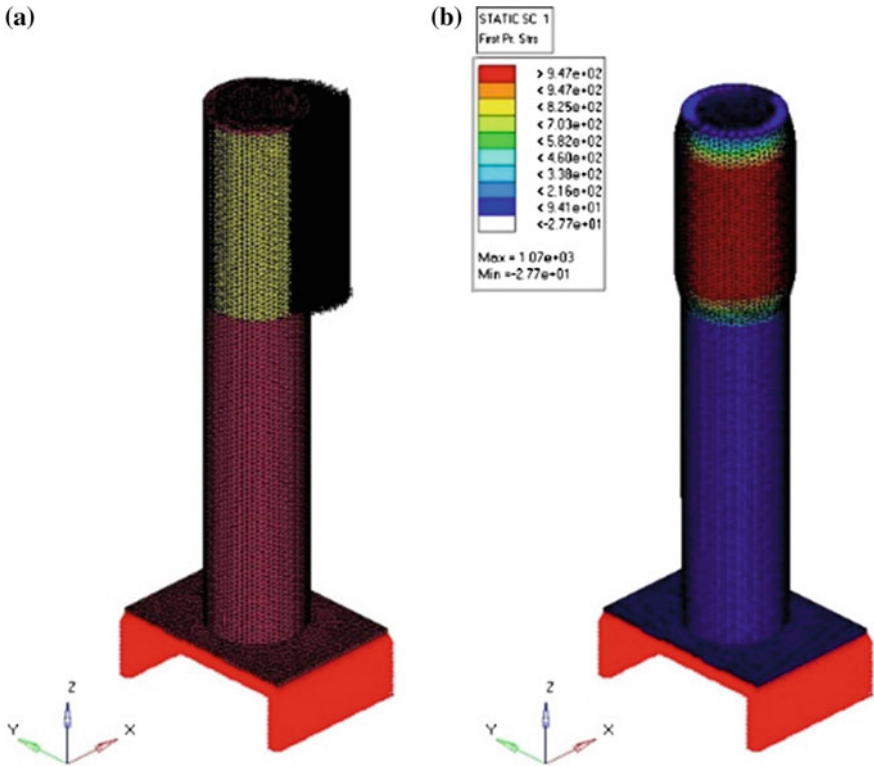


Fig. 1 Landing gear model with boundary conditions and stress contour

value is in good agreement with the analytical hoop stress value. Since, using four-noded tetrahedral elements, the finite element results are agreeing with the analytical results, the same elements were used further for the static and fatigue analysis of a fighter aircraft main landing gear.

2.1 Modelling of Main Landing Gear

A typical fighter aircraft main landing gear was considered. The landing gears are constructed using low alloy steel, and its general composition in weight percentage is C: 0.27–0.33, Si: 0.9–1.2, Mn: 1.0–1.3, Cr: 0.9–1.2, Ni: 1.4–1.8, Cu: 0.25 max, S: 0.025 max and P: 0.025 max. The mechanical properties such as ultimate tensile strength, yield strength, Young’s modulus and Poisson’s ratio are 1141 MPa, 1010 MPa, 202 GPa and 0.33, respectively. The CAD model was generated using the geometric dimensions measured from the actual landing gear. The geometry and the CAD model of the landing gear outer cylinder are shown in Fig. 2. The upper

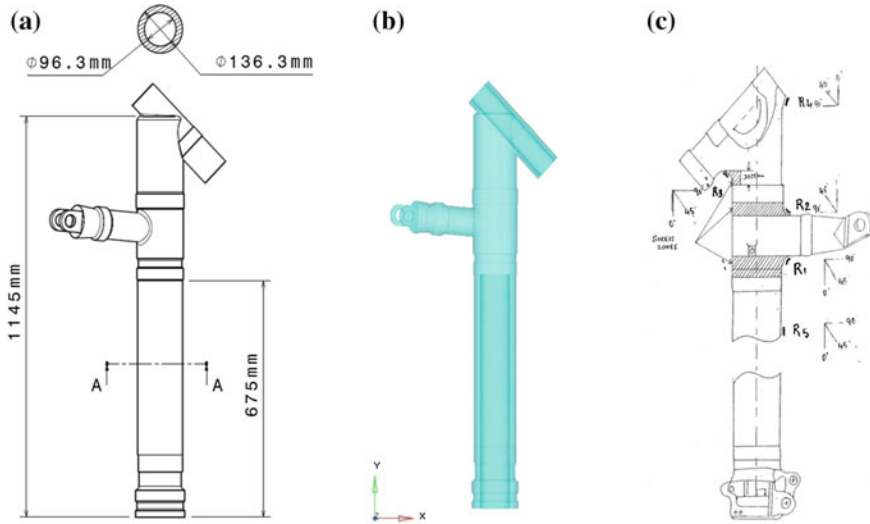


Fig. 2 Geometric dimensions, CAD model and strain gauge locations of main landing gear cylinder

portion of the landing gear was assumed as solid, and the lower portion of the landing gear was modelled as a hollow cylinder (Fig. 2). During landing or take-off or taxiing, the piston in the landing gear compresses or decompresses the fluid present inside the strut and hence the internal pressure gets generated. The pressure magnitude is not known for this main landing gear cylinder. But there are strain values available at the critical points measured from the experiment. Using those strain values, the pressure load applied in the main landing gear cylinder was calculated.

Among the five gauges shown in Fig. 2, four gauges (R1, R2, R3 and R4) were bonded at the upper portion of the landing gear. Since there was an assumption in the modelling of upper portion, the strain gauge at the lower portion only was considered. R5 is the location present in the lower hollow portion of the cylinder, and the strain values at that point for 0° , 45° and 90° directions are $-120 \mu\epsilon$, $215 \mu\epsilon$ and $570 \mu\epsilon$, respectively [7].

2.2 Load Calculation from Strain Measurements

The procedure proposed/used to calculate the load from the experimentally measured strain values is given here. Principal strains were calculated from 0° , 45° and 90° directions strain measurements, and then, the principal stresses were calculated. After that, the reference coordinate system stresses were calculated from the principal stresses, and they are longitudinal stress, hoop stress and shear stress having

the magnitude of 15 MPa, 120 MPa and 1 MPa, respectively. Since the strain values are from the main landing gear experiment subjected to static compressive load on the piston, there should be only internal pressure generated and hence mainly the hoop stress alone should occur. The longitudinal stress on the main landing gear cylinder may be due to the bending effect caused by the eccentricities in load application. In the absence of these eccentricity details, for simplicity, an equivalent axial load instead of bending load was assumed in order to get back the measured stress and strain values.

Finally, the loads were calculated from the reference coordinate system stresses using the hoop stress, axial stress and shear stress formulae, and their values are 60 MPa pressure, 112 kN axial load and 4 kN shear force. The shear force calculated here is just 3.6% of the axial load, and when compared to the hoop stress of 120.26 MPa, the shear stress of 1.588 MPa is 1.3% only. Hence, this shear stress was considered as negligible in the analysis carried out here.

2.3 *Finite Element Analysis*

The full landing gear finite element model (Fig. 3) was modelled using four-noded tetrahedral elements as per the dimensions shown in Fig. 2. The constrained boundary condition was applied at the top portion of the cylinder based on the laboratory experiment carried out earlier. The calculated internal pressure load of 60 MPa was applied to the inner wall of the cylinder. From the stress analysis, the hoop stress at the inner wall is 171 MPa and at the outer wall is 119 MPa. The stress at the outer wall of the cylinder is in good agreement with the calculated stress value from the measured strains. The longitudinal stress obtained is 2 MPa which is not in agreement with the experimental value. So, there should be some load other than internal pressure acting in the cylinder. The static pressure of 60 MPa was applied internally at the cylinder portion, an axial tensile load of 112 kN was applied at the bottom portion of the cylinder, the static stress analysis was carried out, and the results are shown in Fig. 3. The FE stresses obtained are hoop stress and longitudinal stress with the magnitude of 119 MPa and 13 MPa, respectively, and are in good agreement with the calculated stresses from the experimentally measured strains. The comparison between the finite element and experimental strain values is shown in Table 1.

From the above results, the load boundary conditions are clearly understood for the main landing gear cylinder, i.e. by using the equivalent load system comprising of internal pressure load and the axial load, so that the original landing gear behaviour can be achieved. In this way, from the static analysis of main landing gear, the boundary and loading conditions to be applied on the landing gear were obtained and verified. With the above-obtained information, fatigue analysis was carried out using the measured strain spectrum data.

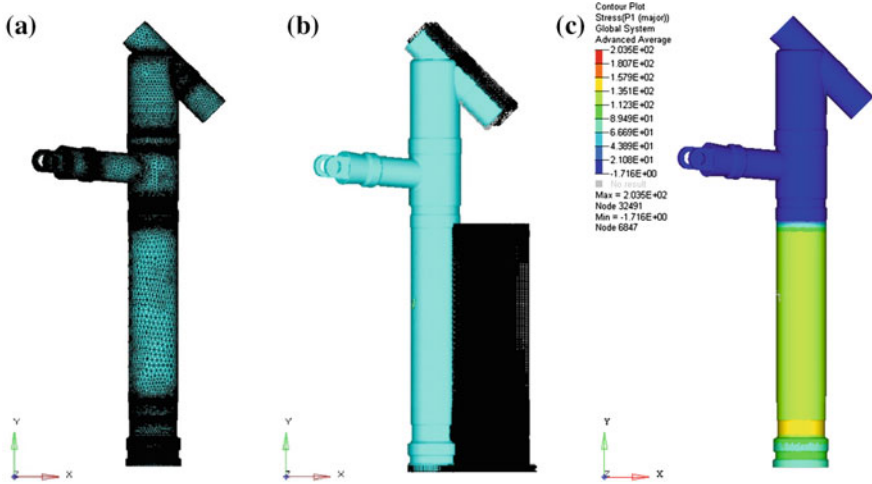


Fig. 3 Static analysis of main landing gear cylinder

Table 1 Comparison of finite element analysis (pressure and axial load) results with experimental results for main landing gear cylinder

Direction	FEA stress (MPa)	Experimental stress (MPa)	FEA strain ($\mu\epsilon$)	Experimental strain ($\mu\epsilon$)
Hoop	119	120	576	570
Longitudinal (axial)	13	15	-122	-120

3 Fatigue Analysis of Main Landing Gear

The fatigue analysis of main landing gear was carried out, considering the spectrum loads obtained from the in-flight data measured during taxiing, take-off and landing using MSC Fatigue tool. For the low alloy steel landing gear, the fatigue material properties such as Fatigue Strength Coefficient and Fatigue Strength Exponent values are $S_f = 6839$ MPa and $b = -0.264$, respectively.

The strain gauges were bonded at the critical locations (Fig. 2), and the corresponding strain values were measured during the flight using the data acquisition system. Among the five gauge locations, only the R5 location's strain spectra (Fig. 4) at the starboard side of landing gear were taken into consideration for the fatigue analysis study.

Since the strain spectra were measured starting from taxiing, take-off and landing stages, the loads acting on the landing gear during those three stages have to be considered. In general, landing gear is subjected to vertical load, drag load and side load as shown in Fig. 5. The landing gear types, landing load cases and the corresponding combination of landing and ground loads are available in detail in MIL

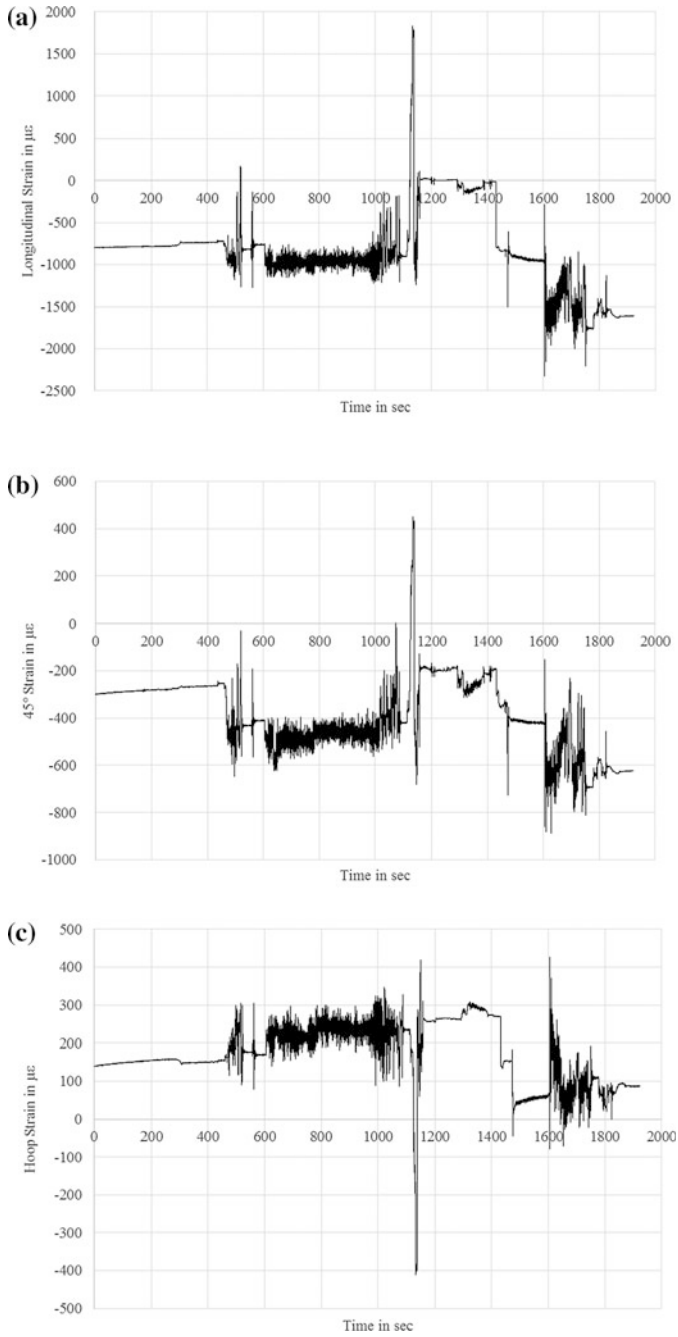


Fig. 4 Strain spectra measured at R5 location along 0°, 45° and 90° directions on the main landing gear

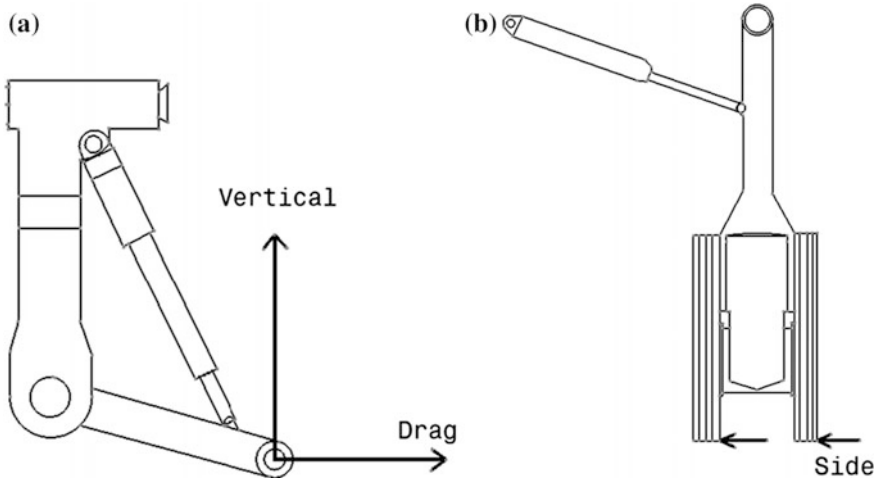


Fig. 5 Typical loads on the landing gear

standards [8] and FAR 25 regulations [9]. Based on the type of landing cases such as two-point landing, tail-down landing and single-point landing, the loads acting on the landing gear will differ. For example, in the case of drift landing [8], the vertical ground reaction shall be one half of the maximum vertical load resulting from all symmetrical landing conditions. The side load on the main gear in drift landing is 60–80% of the vertical load. Similarly, for each landing case, the load combinations among the vertical, drag and side loads will differ.

The landing load case information of the above-measured strain spectra was not available. The longitudinal stress at the R5 location may be due to the bending loads acting on the cylinder. In the absence of distance of the R5 location from the ground based on the piston position and wheel diameter, the bending stress at R5 location cannot be calculated. Hence, in the present work, for simplicity, an equivalent axial load instead of bending load was assumed to be acting on the outer cylinder of the landing gear to reproduce the measured longitudinal stress. Hence, the axial load on the outer cylinder acting along the axis of the shock absorbing strut and the internal pressure load were considered for the landing gear static and fatigue analysis.

From the strain spectra, stress spectra were generated using the procedure discussed in the Sect. 2.2. From the stress spectrum, initial and peak point values were extracted and the equivalent loads were calculated. Using the calculated equivalent loads at various time instances, static stress analyses were carried out on the landing gear by applying both the pressure load and the longitudinal load using MSC Nastran. The respective stress and strain results are presented in Table 2 and can be observed that FE stress/strain values obtained from the analysis of landing gear are in good agreement with the calculated stress/strain values. Hence, with the application of equivalent load system, the original behaviour of the landing gear was

Table 2 Comparison of measured/calculated stress and strain values and FEA stress and strain values

Time (s)	0		1133		1605		1642	
	-14 MPa and -1245 kN		22 MPa and 2814 kN		-39 MPa and -3617 kN		-67 MPa and -2948 kN	
Calculated equivalent loads (internal pressure and axial load)	Measured/ calculated	FEA	Measured/ calculated	FEA	Measured/ calculated	FEA	Measured/ calculated	FEA
Stress/strain								
Longitudinal strain (0°) (µε)	-798	-797	1835	1833	-2324	-2323	-1778	-1775
Hoop strain (90°) (µε)	140	139	-412	-410	427	424	-6	-12
Maximum principal strain (µε)	141	138	1900	1833	433	421	4	-16
Minimum principal strain (µε)	-799	-797	-442	-408	-2300	-2323	-1788	-1775
Maximum principal stress (MPa)	-28	-28	390	384	-76	-77	-133	-134
Minimum principal stress (MPa)	-171	-170	39	44	-496	-493	-405	-401
von-Mises stress (MPa)	159	159	371	365	462	462	358	358
Hoop stress (MPa)	-28	-28	44	44	-77	-76	-134	-133
Longitudinal stress (MPa)	-170	-170	385	385	-495	-493	-404	-401

achieved. This verified finite element model was used to carry out the fatigue analysis using the calculated spectra.

3.1 Fatigue Life Estimation—Hoop and Longitudinal Stress Spectra

The landing gear is one of the critical components in the aircraft, and hence, it should be designed under the category of safe life components. If the design life of the landing gear component is expired, then that component should get replaced even though there is no damage. There is no repair technology used in the case of safe life components. The component should not lose its strength or stiffness before it gets replaced. Because of this, stress-life (S-N) approach was considered for the fatigue analysis of main landing gear cylinder using MSC Fatigue software [10]. In the stress-life approach, the mean stress corrections available are Goodman, Gerber and Soderberg. Since the stress spectra calculated here are having different R ratios and the fatigue material properties are available for R ratio ‘ -1 ’, mean stress corrections should be considered to account for the different mean stresses present in the spectrum. Among the three mean stress corrections, Goodman mean stress correction and Gerber mean stress correction were used here. The stresses obtained from the finite element static analyses were considered as inputs for the fatigue analyses. Furthermore, in the fatigue life calculations using MSC Fatigue, normalization of stress spectrum approach was used. This means the given stress spectrum was normalized using the maximum stress value of the spectrum (scale factor to normalize stress spectrum) so that maximum normalized stress of unity is available in the normalized spectrum. During the fatigue analysis, the stress obtained at the point of interest in FEA gets multiplied with the unit value in the spectrum at the maximum point. The normalized spectrum should contain the values ranging from -1 to $+1$. So, we have to use the maximum stress available in the spectrum to normalize and hence the load case corresponding to maximum stress (-67 MPa internal pressure load for hoop stress spectrum and 3616 kN longitudinal compressive load for longitudinal stress spectrum) was used in this approach. Using the hoop stress spectrum and longitudinal stress spectrum, the fatigue lives were calculated, by applying the pressure load and axial load in the static analysis, and are given in Table 3.

In the actual landing gear, both the loads are acting simultaneously. Hence, it is required to calculate the fatigue life by applying both the stress spectra simultaneously. In order to incorporate the effect of both the stress spectra in the fatigue life calculation, linear damage rule was used here.

Table 3 Fatigue life of main landing gear based on normalized hoop and longitudinal stress spectra

Static analysis	Fatigue analysis			
	Stress spectrum	Scale factor	Fatigue life (landings)	
			Goodman	Gerber
-67 MPa (internal pressure)	Hoop stress spectrum	-134	9.328×10^6	8.278×10^6
3616 kN (axial compressive load)	Longitudinal stress spectrum	-496	35,914	28,946

3.2 Fatigue Life Estimation—Linear Damage Rule

According to Miner’s linear damage rule, the damage occurred in the landing gear due to the application of the stress spectra independently was calculated using the following formula:

$$D_i = \frac{n_i}{N_{i,f}} \tag{1}$$

where n_i denotes the number of load cycles applied, and $N_{i,f}$ denotes the number of cycles required for the component to fail under the applied load cycle. The fatigue lives estimated using normalized hoop and longitudinal stress spectra with the corresponding loads applied independently in static analysis are given in Table 3.

$$\text{Damage due to hoop stress spectrum} = \frac{1}{9.328 \times 10^6} = 1.072 \times 10^{-7} \tag{2}$$

$$\text{Damage due to longitudinal stress spectrum} = \frac{1}{35,914} = 2.7844 \times 10^{-5} \tag{3}$$

Damage due to the longitudinal stress spectrum is very high compared to the hoop stress spectrum.

$$\text{Accumulated Damage} = \text{Damage}_{\text{hoop}} + \text{Damage}_{\text{longitudinal}} \tag{4}$$

$$\text{Fatigue Life} = \frac{1}{\text{Accumulated Damage}} = \frac{1}{2.79512 \times 10^{-5}} = 35776 \text{ Landings} \tag{5}$$

The longitudinal stress is the critical stress when compared to the hoop stress in this analysis, and hence, the accumulated damage is closer to the damage due to the longitudinal stress spectrum. Therefore, the equivalent axial load acting on the landing gear is more critical when compared to the internal pressure load in the equivalent load system considered. It may be noted here that above fatigue life estimation is based on Goodman mean stress correction.

3.3 Fatigue Life Estimation—Principal Stress Spectra

The fatigue analysis was carried out in MSC Fatigue using the calculated principal stress spectra. The load corresponding to the maximum/minimum principal stress value in the spectrum was applied in the static analysis, and the corresponding spectra were used in the fatigue analysis. In the MSC Fatigue software, appropriate stress combination and the corresponding spectra were considered for the fatigue analysis. The fatigue life estimation using normalized spectrum was carried out, and the results were compared with the fatigue life estimated using constant life diagram (CLD) approach. In CLD approach [7], the S-N curves for different R ratios were generated experimentally and they were used to calculate the life for each and every cycle in the spectrum. The R ratio for which S-N curve is not available could be calculated using the interpolation or extrapolation techniques. The comparison between the fatigue lives obtained from the MSC Fatigue and CLD approach is given in Table 4.

From Table 4, it is clear that MSC Fatigue tool with Gerber mean stress correction can be used to perform fatigue analysis and predict the fatigue life of metallic components as it gives comparable/similar fatigue life that can be obtained from CLD approach.

3.4 Summary of Fatigue Analyses of Main Landing Gear

The fatigue analysis of main landing gear cylinder of typical fighter aircraft was carried out using the normalized longitudinal, hoop, maximum principal, minimum principal, von-Mises and maximum absolute principal stress spectra (maximum value of absolute principal stress at each and every point of time in the stress spectrum) by considering both the Goodman and Gerber mean stress correction methods in MSC Fatigue. The fatigue life results obtained using all the spectra are presented in Table 5.

Table 4 Comparison of fatigue life obtained from MSC fatigue and CLD approach

Stress spectrum	Fatigue life based on CLD (landings)	Fatigue life based on normalized spectrum (landings)	
		MSC fatigue (Goodman)	MSC fatigue (Gerber)
<i>Load applied (22 MPa internal pressure and 2813 kN axial tensile load)</i>			
Maximum principal stress	2.28×10^5	1.579×10^5	2.357×10^5
<i>Load applied (-38 MPa internal pressure and 3616 kN axial compressive load)</i>			
Minimum principal stress	1.28×10^5	2.088×10^5	1.235×10^5

Table 5 Fatigue analysis/life of main landing gear using MSC fatigue

Normalized spectrum	Fatigue life (landings)	
	Goodman	Gerber
Maximum principal stress	1.579×10^5	2.357×10^5
Minimum principal stress	2.088×10^5	1.235×10^5
von-Mises stress	6.7731×10^4	1.427×10^5
Maximum absolute principal stress	3.9397×10^4	3.2033×10^4
Linear damage rule (hoop and longitudinal stress)	3.5776×10^4	2.8845×10^4

From the fatigue analysis of main landing gear results presented in Table 5, it may be said that the fatigue life estimated using maximum absolute principal stress spectrum is in good agreement with the fatigue life estimated using linear damage rule (combination of longitudinal and hoop stress spectra). Hence, it is advisable to use either the maximum absolute principal stress spectrum or linear damage rule as the fatigue life estimation criterion for design, since both of them yield the conservative fatigue life when compared to the fatigue lives from other criteria.

4 Conclusions

Fatigue life estimation of typical fighter aircraft main landing gear was explored using MSC Fatigue for various stress spectra/criteria. In the absence of load information on the landing gear, a methodology was proposed to calculate the equivalent load system from measured strains and verified using static analysis of landing gear. The approach using the normalized stress spectrum (only the signature of the spectrum was used) along with the finite element stress distribution was explored to calculate the fatigue life. Linear damage accumulation rule was also used to incorporate the effect of two independent stress spectra in the fatigue life. Fatigue life of landing gear was obtained using various stress spectra based on stress-life approach and was compared with the fatigue life calculated using constant life diagram (CLD) approach. Among the Goodman and Gerber mean stress corrections, fatigue life estimation using Gerber mean stress correction was found to be in good agreement with the fatigue life estimation using CLD approach. Furthermore, maximum absolute principal stress spectrum/criterion and linear damage rule give the conservative fatigue life and hence these criteria may be used as fatigue life estimation criteria for design.

Acknowledgements The authors would like to thank Head, Structural Technologies Division, CSIR-NAL and the Director, CSIR-NAL for their support and encouragement to carry out the work reported in this paper. The authors would also like to express their thanks to the people who contributed to this work directly or indirectly.

References

1. P. Beaudet, M. Roth, in *Failure analysis case histories of canadian forces aircraft landing gear components*. Landing Gear Loads, AGARD Conference Proceedings, 484 (1990)
2. M. Khondker, A.K.M. Lutful Kabir, A. Younes, Md Shelimuzzaman, S. Islam, in *Landing Gear Shock Absorber Design*, Concordia University, Summer 2009
3. M. Imran, R.M. Shabbir Ahmed, M. Haneef, Static and dynamic response analysis for landing gear of test air crafts. *Int. J. Innovative Res. Sci. Eng. Technol.* **3**(5) (2014)
4. V.N. Divakaran, G.V.V. Ravi Kumar, P. Srinivasa Rao, *Aircraft landing gear design and development*, Infosys, 2015
5. Altair HyperMesh software, version 12.0, Altair HyperWorks
6. MSC Nastran solver, version 2012, MSC Software
7. C.M. Manjunatha, *Inflight strain data acquisition and fatigue life assessment of aircraft landing gear* (Project Report, CSIR-NAL, 2013)
8. Military Specification—Airplane Strength and Rigidity Ground Loads for Navy Acquired Airplanes, MIL-A-8863B (AS), 6 May 1987
9. Part 25: Airworthiness Standards: Transport Category Airplanes Special Federal Aviation Regulations, SFAR No. 13, SFAR No. 109
10. Fatigue module in MSC Patran, version 2001, MSC Software

Designing for Strength: ASME's DBA Guidelines and Beyond

Kotur S. Raghavan

Abstract Finite element stress analysis is carried out with the aim of assessing the strength of structural and other load-bearing components. It is an essential feature of structural mechanics that the stress values cannot be taken at their face value. Damage which can be caused by stress of a given magnitude is strongly dependent on the nature of stress distribution and the loads causing them. These issues are addressed in ASME's Boiler and Pressure Codes, Section VIII, Div. 2 which is referred to as Design by Analysis (DBA) guidelines. In this paper, the guidelines are assessed by carrying out elastic-plastic analysis.

Keywords Design · Strength · ASME · DBA · Stress linearization

1 Introduction

In a great majority of cases, we use finite element analysis for structural or machine design whether it is the case of new design development or verification of an existing design. Further, in a significantly high percentage of the studies that are carried out focus is on strength. In relatively smaller percentage of studies, the focus is on other design considerations such as free vibration, buckling, transient dynamics, creep.

Historically speaking, structures and machines have been built from time immemorial. Many have withstood the test of time. In comparison, finite element method can be considered to be a baby. The method came into existence exactly sixty years ago with the development of constant strain triangle (CST), which is considered to be the mother of all finite elements. Widespread application of the method, facilitated by commercially available analysis packages, is still more recent being not more than four decades old.

K. S. Raghavan (✉)
Cyient Limited, Gachibowli, Hyderabad 500032, India
e-mail: kotur.raghavan@cyient.com

Having said this, it needs to be stated here that finite element method has not made great inroads into design practices. Design approaches vary depending on the industry practices which are product dependent. Design by rules based of elementary mechanics and strength of materials are still in vogue in many industries. Boiler and pressure vessel (B and PV) codes of American Society of Mechanical Engineers (ASME) are a case in question. The present paper is concerned with finite element analysis and design for strength. The paper centres on ASME's B and PV codes. However, the contents and concepts are of general nature.

2 ASME's Boiler and Pressure Vessel Codes

American Society of Mechanical Engineers is world's premier engineering institution. It was founded about 130 years ago. The society's B and PV codes are about a century old. ASME came out with mandatory design guidelines for all pressure vessels used in process and power industry. The first edition contained a little over one hundred pages. The codes have gone continuous evolution ever since, and as of today, the codes span more than twenty thousand pages in nearly thirty volumes. The codes cover all aspects related to design, manufacturing and material selection and testing. Of particular, relevance here is the Section VIII of the codes. This section has three divisions. Division 1 provides guidelines for design by rules. Division 2 and Division 3 provide guidelines for design by analysis (DBA). Division 2 was released in mid-sixties, and this was developed as it was realized that Div. 1 rules were too conservative and the components were becoming too bulky.

There are two routes in Div. 2. They are the linear or elastic route and the nonlinear or elastic-plastic route. ASME recommends the use of latter to overcome any ambiguities or conflicts. ASME further recommends that decisions based on the elastic-plastic approach override those based on the elastic route. Thus, on the whole, there are three approaches available to the designer: one of Div. 1 and two of Div. 2. They are design by rules (DBR), design by analysis-elastic (DBA-E) and design by analysis-elastic-plastic (DBA-EP). Conceptually, DBR is based on peak stress values. The guidelines are akin to what we normally find in text books on machine design and structural design. DBA-E is based on the principle of "damage potential" of stresses. The damage caused by a stress of given magnitude is a function of the nature of stress distribution and the loads causing that stress. The guidelines consider section on the whole. On the other hand, DBA-EP takes into account stress redistribution effects.

3 Earlier Work and Scope of the Present Work

In an earlier work [1], the present author addressed the issues concerned with DBA codes. The paper focused on a few ambiguities, inadequacies and limitations of the elastic analysis guidelines. On the basis of a number of case study problems, a strong case was made for making the nonlinear route (DBA-EP) mandatory instead of giving option to the designer. One of the reasons for arriving at this recommendation was that nonlinear structural analysis is not a challenge in the present day scenario.

The main recommendation of the cited paper still holds. In the current work, more studies are carried out which provide more insights into the guidelines of DBA. These findings further reinforce the earlier recommendations.

4 Design by Analysis

The essence of DBA-E guidelines is classification of stress into membrane–bending–peak and primary–secondary categories. Different categories of stress will have different allowable stress values. Membrane stress caused by primary (mechanical) loads has the highest damage potential, and hence, the allowable stress for this category is the lowest (say S). The allowable bending stress is $1.5 * S$, and allowable secondary stress is $3 * S$. Secondary stresses are self-limiting stresses generally caused by thermal loads and structural discontinuities.

There is no issue as far as membrane stress is concerned. It is the uniform component of the stress across a section (thickness) also equal to the average stress across the section. There are, however, three different definitions for the so-called bending stress to be found in the literature. The three definitions are as follows:

1. Bending stress is the non-uniform component of the stress across a section. The variation may or may not be linear.
2. Bending stress is the linearly varying component of stress across a section. Also, bending stress is that component of stress which is proportional to the distance from the centroid of the section.
3. Bending stress is the linearly varying component of stress if peak stress (stress raiser) is present. Otherwise, it is equal to the difference between maximum stress and the membrane stress.

ASME's Section VIII codes of 2007 and later [2] contain definitions 1 and 2. It is notable that only the first definition is to be found even in the latest edition of Section III (Nuclear, Class 1). In relevant documents of ANSYS [3], the second definition is to be found. This definition is not precise as one faces uncertainties in transition regions. In documents related to ABAQUS [4] program, we find the third definition. This definition is essentially same as the first one but without vagueness as it makes distinction between two different scenarios.

The foregoing definitions are easily realized in two-dimensional structures (plane stress or axisymmetric). Both ANSYS and ABAQUS programs contain capabilities for computing membrane and bending components along specified paths using procedure known as “linearization”. The calculations are just algebraic, and the programs compute for any path whether meaningful or not. In fact, one can easily carry out linearization using Microsoft EXCEL program. One has to use engineering judgment in order to extract numbers which make sense. Thus, one of the limitations of the elastic route guidelines is that it is difficult to apply for three-dimensional domains.

5 “Bending” Stress and Strength

In this section, the effect of bending, actually the maximum value of membrane plus bending stress on the component stress is assessed under different geometry conditions. Only two-dimensional geometries are considered, and use is made of linearization capability available in ANSYS. Strength is assessed by carrying out elastic-plastic analysis. Materials are assumed to follow elastic-perfectly plastic rule. The strength is evaluated by taking into account the response trend, divergence behaviour and nature of stress distribution at critical regions.

Strength is assessed with DBA guideline as reference. As already stated, If S is the permissible (von Mises) stress for primary membrane (M) component, then the allowable membrane plus bending component (MB) is $1.5 * S$. This is based on the fact that a section yields only when the entire section and not just the extreme fibres becomes plastic.

5.1 *Parabolically Tapering Cantilever Beam*

As a first case study, a parabolically tapering cantilever beam with tip load is considered. Geometry and elastic analysis results for unit load are in Fig. 1. The figure also contains the stress contours and linearization plot. This is case of pure bending. Maximum unit stress under unit load is 0.3. Elastic-plastic analysis is next carried out. The material yield stress is 200 MPa. The section is expected to yield when the extreme fibre stress reaches 300 MPa. The tip load at section yield is 1000 N. Actually, the load applied is twice this value.

Nonlinear response is shown in Fig. 2. Here, the X -axis denotes tip load non-dimensionalized with respect to elastic limit load which is 1000 N. It is seen that the structure has not reached instability even at twice the elastic limit load although it is obvious that plastic flow has set in at non-dimensional load of unity. We also see that the beam has undergone very large deformation at full load.

A study of two-colour stress contours shown in Fig. 3 is informative. At full load, a very small part of the span has become fully plastic. Because of the

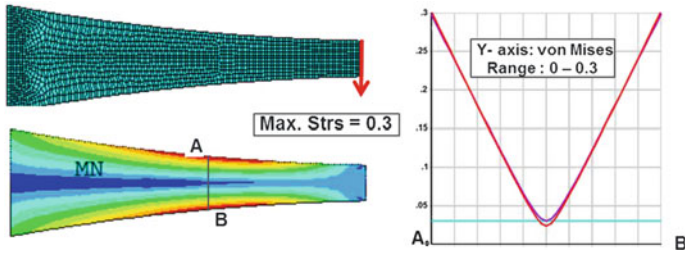


Fig. 1 Tapering cantilever beam, elastic analysis results

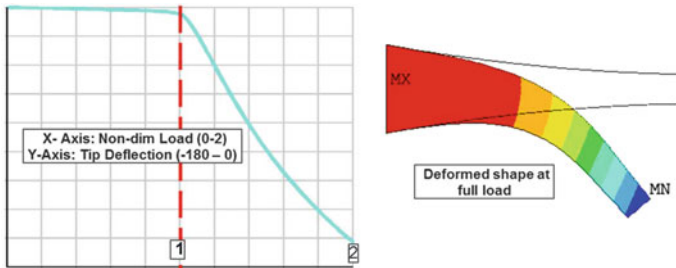


Fig. 2 Nonlinear response and deformation at full load

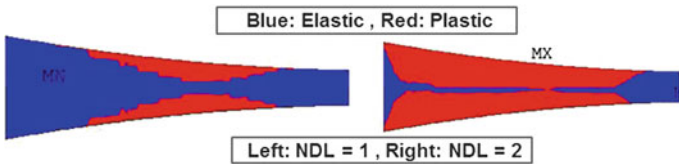


Fig. 3 Two colour von Mises stress contours

geometry, there is lot of stress redistribution taking place along the length and that is why the beam has not reached instability in spite of very large deflection. From strength point of view, however, load corresponding to non-dimensional load of unity is of design significance.

5.2 Perforated Ring

Half sector of a perforated ring subject to internal pressure is the next case study problem. Geometry, elastic stresses and linearized curves are shown in Fig. 4. These are for unit pressure application. There are two load paths here, and the inner path is more highly stressed. MB component is a little more than 1.5 times the

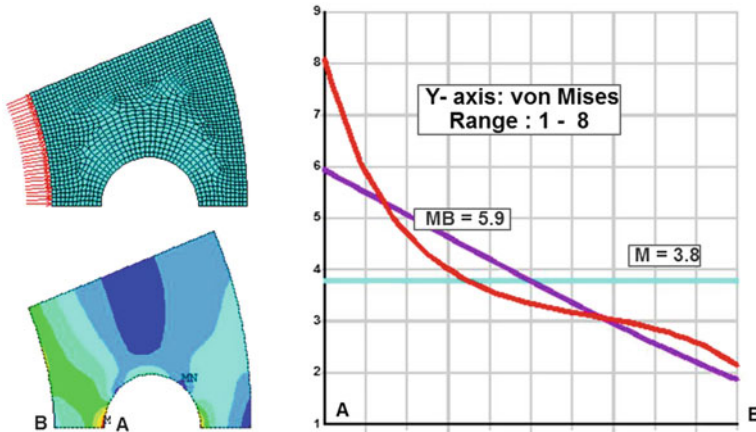


Fig. 4 Perforated ring, diameter ratio = 0.5. Geometry and stress description for unit pressure

membrane component. Going by DBA guidelines, the strength is governed by MB component. Pressure for nonlinear analysis is appropriately chosen.

Results of nonlinear analysis are presented in Fig. 5. Most importantly, instability is seen to set in at a non-dimensional pressure of 1.2 and not unity. A part of the reason for this is the outer ligament, which is also a load path, supporting the load almost equally at failure or instability. The other reason is that MB components tend to be overestimated along sections involving peak stress. Another reason is that the classification line is across a partial load path, and bending stress about the midpoint may not be physically meaningful.

For this configuration, the pressure limit (for $YS = 200 \text{ MPa}$) based on nonlinear analysis is $(300/5.9 * 1.2)$ which works out to about 61 MPa. Based on DBA-E, the pressure limit is about 51 MPa. A designer or an analyst without recourse to (or knowledge of) linearization or nonlinear analysis would perhaps estimate on the basis of highest stress magnitude which is 8 MPa (Fig. 4) and the corresponding pressure limit would be 25 MPa.

In order to get a little more insight, parametric results are presented in Table 1. The parameter is the ratio of whole diameter to the width. The second column numbers signify whether membrane or MB component governs the strength depending on whether the number is less than or greater than 1.5. The last three columns denote the strength in terms of pressure. The fourth column values are based on DBA elastic route. The last column values refer to membrane basis assessment. The message of this table is that membrane stress has dominant influence on strength. The pressure limits computed by nonlinear analysis are higher by 10–20% because of the load sharing between the inner and outer ligament sections.

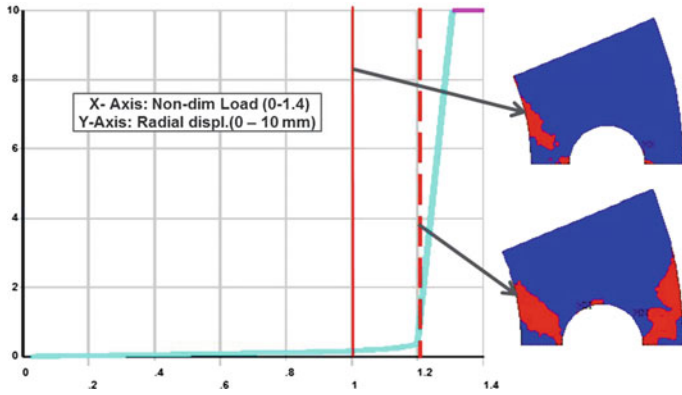


Fig. 5 Nonlinear response. Contours at theoretical and actual failure loads

Table 1 Perforated plate parametric analysis results

D/W ratio	MB-U/ M-U	Pressure limits		
		DBA-EP	DBA-E	DBA-E-MEMB
0.3	1.24	82.40	74.91	74.91
0.4	1.41	71.38	64.31	64.31
0.5	1.57	60.61	50.51	52.91
0.6	1.71	49.39	36.32	41.41

5.3 Analysis of Fillet Welds

A common fillet-welded configuration is shown in Fig. 6. The structure is obliquely loaded as shown, with angle with the horizontal being an analysis parameter. The bottom welded will be more highly stressed for angles greater than zero. Linearized stresses are typically as shown on the right-hand side of the figure for the path chosen along the path shown. The peak stress is spurious and is due to stress singularity.

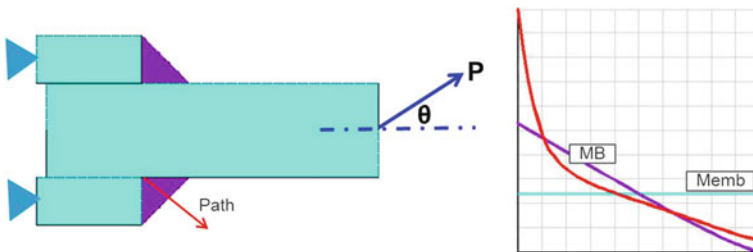


Fig. 6 Structural member with fillet welds

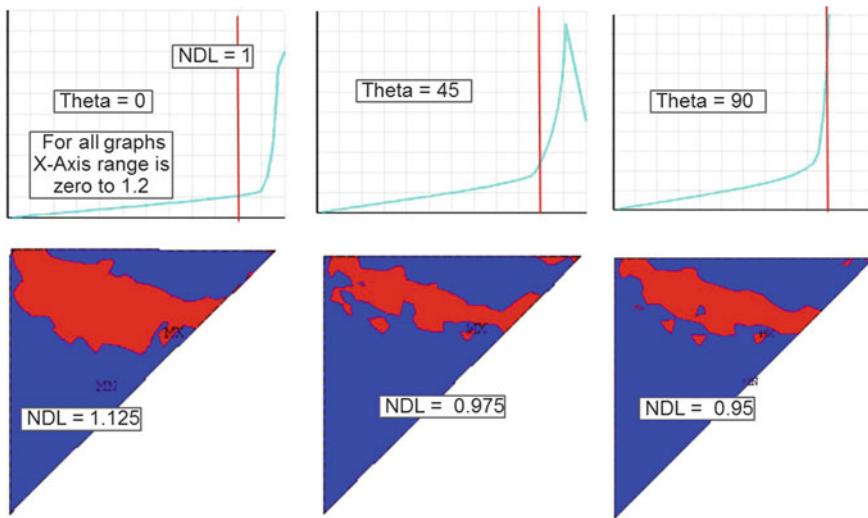


Fig. 7 Nonlinear analysis results for three load orientations

Elastic-plastic analysis results for three load orientations are presented in Fig. 7. For horizontally applied load, membrane plus bending component gives conservative results. For other two cases, it is seen to be slightly non-conservative. It is notable that failure planes are closer to the horizontal line. They are away from the throat (45° plane) which is considered in design (also in this problem for linearization).

5.4 Tension Members with Groove

The last problem in this section pertains to a tension member with a groove. The geometry and loading are as shown on the left-hand side of Fig. 8. Two cases are considered. The first case pertains to plane stress condition (strip). The second case is that of axisymmetry with XX as the axis of symmetry (grooved shaft). Non-dimensional depth ($=D/W$) is a parameter.

Stress distribution along the critical path is typically as shown on the right-hand side of Fig. 8. In all the cases, $(M + B)$ component was more than 1.5 times the membrane component. Hence, strength is governed by $(M + B)$ component. Analysis was carried out for four values of non-dimensional depth of groove, and consolidated results for plane stress and axisymmetric cases are presented in Fig. 9. Here, the ordinates correspond to non-dimensional limit loads from nonlinear analysis. A value of unity corresponds to DBA-E limits. For the plane stress condition, the bending stresses are genuine ones. The bottom curve is thus genuine. The strength is within $\pm 10\%$ of the DBA-E limit. The same is not true, however,

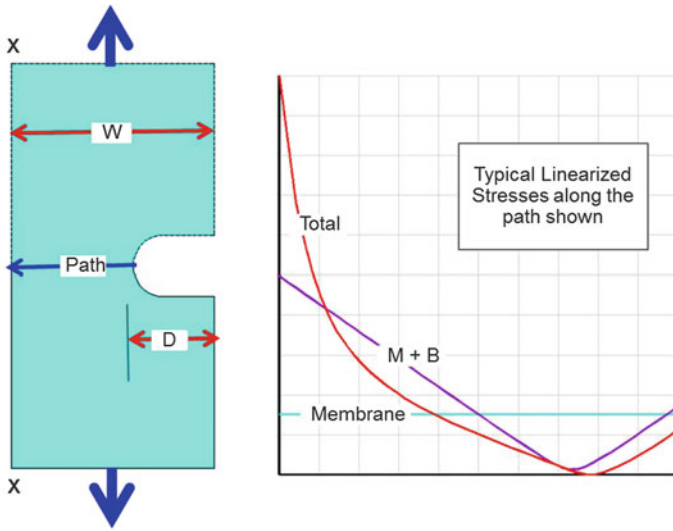
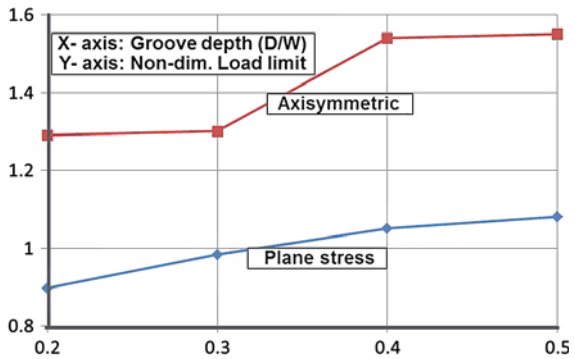


Fig. 8 Tension member with a groove

Fig. 9 Non-dimensional load limits for grooved bar



for the axisymmetric condition. By definition, bending stress is the component of stress which is proportional to the distance from the centre of the path. In axisymmetry condition, there is no such deformation taking place. The bending stress which is computed in axisymmetric cases is due to non-uniformity of stress across the section resulting from stress concentration and thus is spurious. Any design evaluation involving bending stress in axisymmetry conditions will result in undue conservatism. This is a very important point which is often overlooked by analysts and designers. ASME codes are also silent about this aspect.

6 Other Concerns

One of the provisions of DBA-E guidelines is related to “secondary” stresses. They are caused by thermal loads and geometric discontinuities. Secondary stresses are classified as “self-limiting”, and allowable value is more as compared to those for mechanical loads (three times the value allowable for primary membrane). The main concern is that the allowable limit for secondary stress has no theoretical basis. This has been addressed by the present author in Ref. [1] where it was established that stresses due to thermal loads cause no plastic flow. In a structure subject to pure thermal load, response will be linear well beyond the design limit as shown at the left of Fig. 10.

Another concern is related to limited applicability for problems involving 3D elements. In general, it can be stated that the only way of assessing the strength of 3D solid structures is elastic-plastic analysis. Using nonlinear analysis, it is possible to develop interaction curves for multi-axial load conditions like those shown on the right side of Fig. 10. This figure pertains to biaxial bending of a beam of square cross-section. The figure contains three interaction lines. The outermost is generated by way of nonlinear analysis. The middle one is DBA-E based and considers plastic moment into consideration but not redistribution. The innermost line is based on strength of materials using only the yield moment. This is the most conservative. This figure graphically presents relative impacts of the three approaches available to the analyst according to Section VIII, Divisions 1 and 2. It is worth stating here that “design by rules” and machine design textbook procedures are akin to one another.

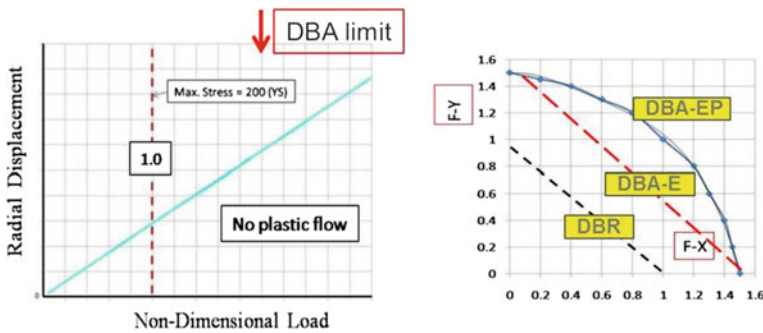


Fig. 10 Left: response to thermal load, right: biaxial bending, interaction curves

7 Summary

The purpose of the paper was to assess and evaluate DBA-E guidelines. Main focus has been on the meaning, application and interpretation of bending stress. A few simple case studies have established that the bending stress is not meaningful in all situations. Caution is needed while taking design decisions where in “bending” stresses happen to be critical. In situations where it is meaningful, the design may become slightly non-conservative. In situations where it is not meaningful, the design may become over-conservative.

Recourse to nonlinear route is highly recommended for all design problems.

8 Further Work

In this work, the strength is evaluated by joint interpretation of response pattern, nature of stress distribution at critical sections and divergence trends. ASME's codes, on the other hand, suggest consideration of only the collapse load. There may be some ambiguities in this regard. This aspect remains to be addressed.

References

1. Raghavan, K.S, in *An Evaluation of ASME's Design by Analysis Guidelines*. Proceedings ASME's GTINDIA Conference, (Bangalore, 2013)
2. American Society of Mechanical Engineers, Boiler and Pressure Vessel Code, Section VIII, Division 2, 2010
3. ANSYS Mechanical APDL User's Manual, ANSYS Inc., www.ansys.com
4. ABAQUS/CAE User's Manual, <http://www.3ds.com/products-services/simulia/products/abaqus/>

Premature Fatigue Failures in the Hot Zone of Low Pressure Turbine Rotor (LPTR) Blades of Aero-Engine

M. Madan, R. Bharathanatha Reddy, K. Raghavendra, M. Sujata and S. K. Bhaumik

Abstract Generally, the fatigue failures in gas turbine blades occur at 1/3rd height of the airfoil, where the bending stresses on the blades are maximum. In contrast, the creep and the stress-rupture damages are observed at around 2/3rd height of the blade, which is the maximum temperature zone on the leading edge. However, irrespective of the mechanism of crack generation, the major part of the crack propagation in the turbine blades takes place by fatigue mechanism because of the cyclic nature of the loads. Therefore, identification of the primary mechanism of crack initiation while analyzing these failures is of prime importance. Unless this is established unambiguously, identification of the primary cause of failure is not possible. In this paper, analysis of a prematurely failed low pressure turbine rotor (LPTR) blade is presented. Although the fracture in the blade occurred by fatigue mechanism, the initial crack initiation in the blade was found to be by stress-rupture mechanism. Detailed metallurgical investigation showed that the stress-rupture in the blade was promoted due to overheating of the blades for short durations. The reason for overheating of the blades was due to failure elsewhere in the system which resulted in faulty feedback on the actual engine temperature during operation.

Keywords Superalloy · Gas turbine blades · Overheating · Stress-rupture Fatigue

1 Introduction

Premature failures in gas turbine blades of aero-engine are of serious concern for the reliability and safety of the aircraft. In most of the cases, the specific mechanism of failure is dependent on either the defects in the material that have been present in the blade from the manufacturing stage or those generated during the service life.

M. Madan · R. Bharathanatha Reddy · K. Raghavendra · M. Sujata (✉) · S. K. Bhaumik
Materials Science Division, CSIR-National Aerospace Laboratories, Bangalore 560017, India
e-mail: msujata@nal.res.in

Most common failure mechanisms in the gas turbine blades are fatigue and creep rupture [1–4]. There are numerous studies on the effect of service exposure on the microstructure and mechanical properties of the blade materials [5, 6]. Some of the microstructural changes that influence the creep and fatigue strength of the blades include excessive precipitation of carbides and/or brittle topological close-packed (TCP) phases, rafting of γ' precipitate phase, and void formation at the triple or grain boundaries. The extent of microstructural changes that occurs in the blade material depends on time, temperature, and stress during service. In this paper, failure of low pressure turbine rotor (LPTR) blades of an aero-engine has been reported. The blades were manufactured from Nimonic 115 alloy by closed die forging.

2 The Failure

There was an incident of engine surge in a fighter aircraft. On strip examination of the engine, one of the LPTR blades was found fractured. The LPTR blades were in service for 1123:50 h against a total technical life of 1200 h. Examination revealed that the fracture in the airfoil occurred at a distance of about 20 mm from blade shroud. Only a small part of the fractured and dislodged part of the blade was retrieved from the engine during strip examination. Following the fracture, the dislodged part of the blade resulted in severe damages to the engine. Examination of the engine revealed cracks in a few more LPTR blades. The fractured and cracked LPTR blades along with a HPTR blade were subjected to detailed metal-lurgical failure analysis (Fig. 1) for establishing the primary cause of failure.

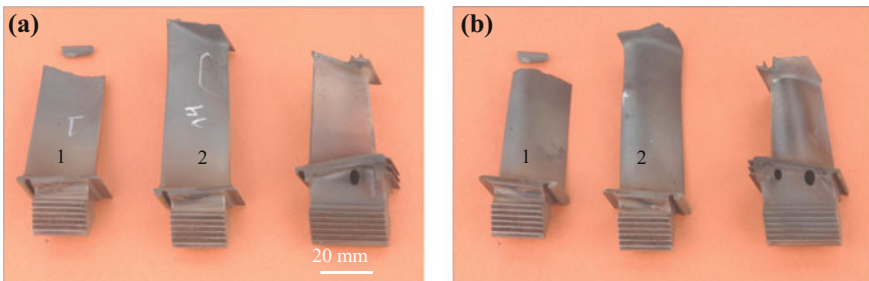


Fig. 1 Failed LPTR blades (marked 1 and 2) and the HPTR blade of the aero-engine: **a** concave surface, and **b** convex surface

3 Laboratory Investigation

3.1 Macroscopic Features of Fractured LPTR Blade

Figure 2a shows the fractured LPTR blade. The blade had fractured in the airfoil section at a height of about 50 mm from the blade root platform. Examination did not reveal the presence of any incipient cracks in the airfoil or leading edge or trailing edge. Apart from the fracture, the blade did not have any other damages. Figure 2b shows the fracture surface of the blade. Examination of the fracture surface at low magnification showed that the crack had initiated at the leading edge and there were three distinctive fracture zones. Over a length of about 4 mm from the leading edge, the fracture surface was irregular in appearance. Following this, the fracture surface showed a smooth appearance over a length of 2.5 mm with a semi-circular crack front, typical of progressive crack propagation by fatigue mechanism. The rest of the fracture surface showed intergranular mode of crack propagation, typical of overload failure in superalloy components at elevated temperatures. In the first two zones of crack propagation, that is, over 6.5 mm length from the leading edge, the fracture surface was found severely oxidized compared to the rest of the fracture surface.

3.2 Mode of Crack Propagation and Fracture Mechanism

Typical appearance of the fracture surface in the zone I is shown in Fig. 3a, b. At the leading edge, over about a length of 250 μm , the crack propagation was purely by cleavage mode. Following this, the crack propagation was by mixed mode of transgranular and intergranular fracture, and this region extended up to a length of about 600 μm . The remaining part of the zone I revealed intergranular fracture features (Fig. 3b). The fracture features in zone II showed predominantly transgranular mode of crack propagation. Vaguely delineated crack arrest marks with semi-circular crack fronts were found present in this zone. Due to severe oxidation, the micro-fractographic features were not clearly discernible. However, the gross fracture features confirmed that the crack propagation in this zone was by

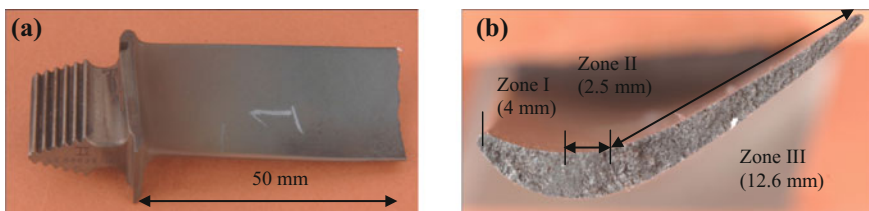


Fig. 2 a Fractured LPTR blade, b fracture surface showing three zones of crack propagation

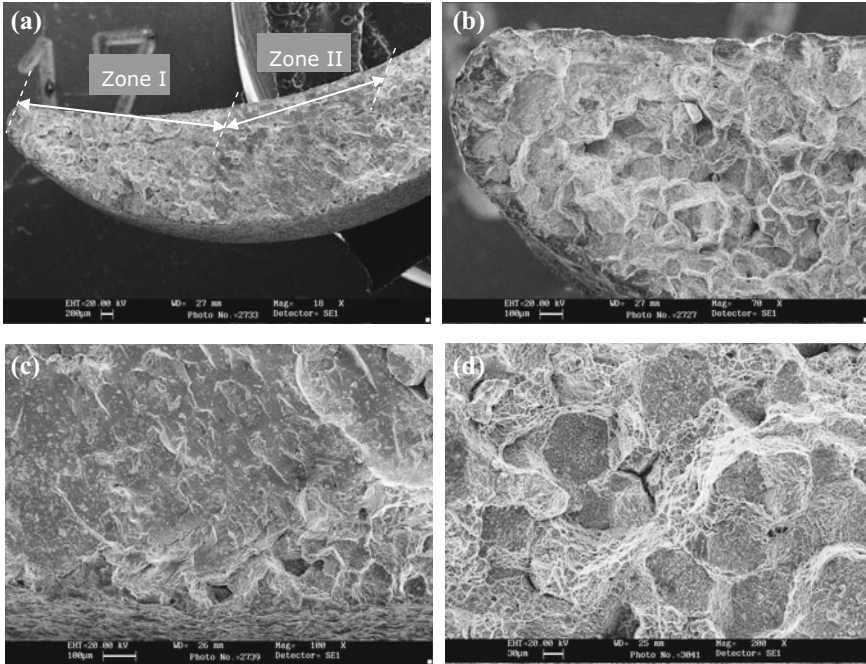


Fig. 3 Scanning electron fractographs: **a** zone I and II, **b** magnified view showing transgranular cleavage fracture up to a depth of 250 μm , **c** crack arrest marks in zone II, and **d** intergranular fracture in zone III

progressive fatigue mechanism. A transition in the fracture mode from zone II to zone III involving transgranular mode of crack propagation to intergranular mode of crack propagation was clearly identified. In the zone III, the crack propagation was purely by intergranular mode. Fine dimples on the grain facets were also observed in this region (Fig. 3d). Such features are typical of overload fracture in superalloys at elevated temperatures.

3.3 Microstructural Examination and Phase Analysis

3.3.1 Optical Microscopy

A transverse section was cut from the fractured LPTR blade at approximately 2 mm below the fracture and metallographically prepared for microstructural study. Figure 4 shows the optical microstructures of the blade at the leading and trailing edges. The microstructures consisted of γ' precipitate phase (Ni_3Al) in a Ni-rich γ matrix. The blade surface showed the presence of an oxide layer, and this was followed sequentially by a diffused zone, a thin γ' depleted zone, and the base material of the blade.

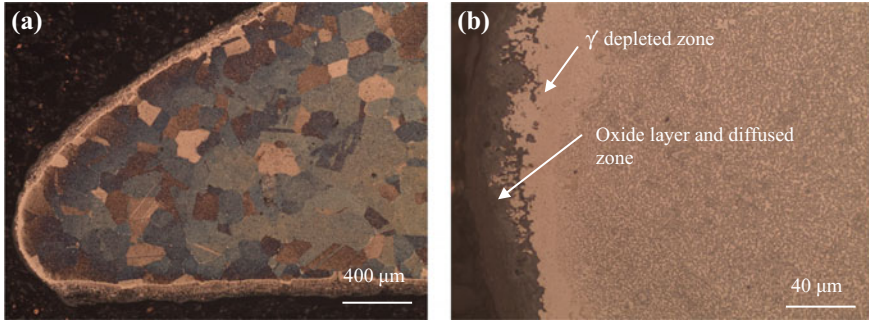


Fig. 4 a, b Optical microstructures of the leading edge of the fractured LPTR blade at different magnifications

3.3.2 Scanning Electron Microscopy

Figure 5 shows the secondary electron microstructures at the leading and trailing edges of the blade. The γ' depleted zone between the diffused layer and the base material of the blade can be seen. In the base material of the blade, no abnormal microstructural changes such as complete dissolution or excessive coarsening of either the γ' precipitate phase or the carbide phases were observed. A similar observation was also made on the concave and convex surfaces of the blade. The dimensions of the different zones of microstructure, that is, oxide and diffused layers and γ' depleted zone at different locations of the blade cross section were measured. The study revealed that the thickness of the oxide layer and the diffused layer together was significantly less at the leading edge compared to that a little away and on the concave and convex surface sides of the leading edge. The presence of oxide layers at these locations suggested that there was continuous erosion and formation of the oxide layer on the surface of the leading edge during the service. The microstructures of the broken blade were compared with those of the standard microstructures provided by the engine manufacturer. A comparative

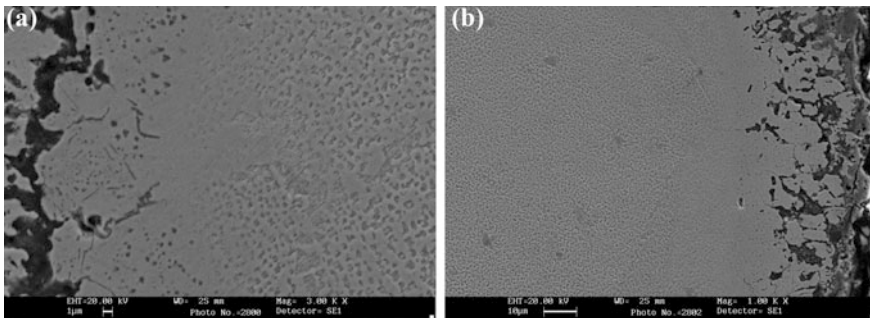


Fig. 5 Secondary electron micrographs of LPTR blades: a leading edge, and b trailing edge

study showed that the microstructural changes observed in the hotter section of the blade after 1123:50 h of service were within the acceptable limit. The microstructures did not suggest running of the engine persistently well above the normal operating temperatures.

3.3.3 Analysis of Phases Present at the Blade Surface

Analysis showed that the oxide layer on the convex and concave surfaces of the LPTR blades consisted of a mixture of oxides, namely, Al_2O_3 , Cr_2O_3 , and/or TiO_2 (Fig. 6a). The metallic phases within the diffused zone were found to be rich in Ni and Co and depleted in Al and Cr compared to the base material (Fig. 6b). In contrast, the leading edge of the blade showed the presence of a very thin diffused

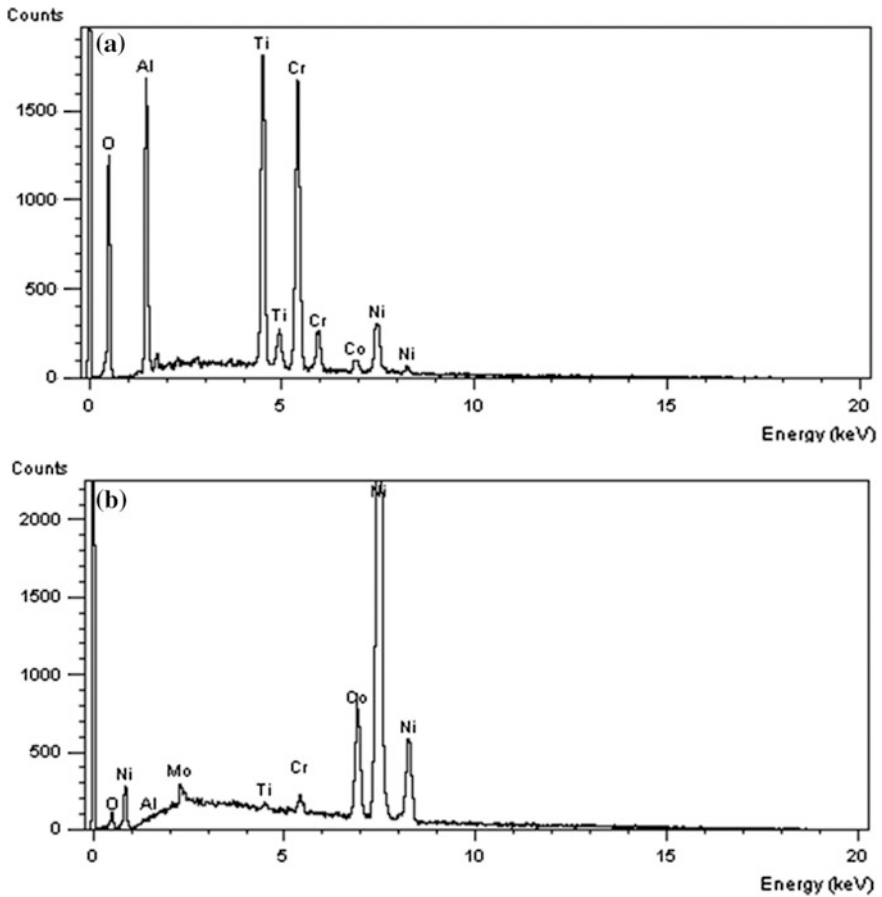


Fig. 6 Energy dispersive X-ray (EDX) spectrums: **a** oxide layer on convex surface, and **b** γ' -denuded layer

layer, and the outer surface was found to contain predominantly a Si–Ca–O rich layer.

3.4 Cracked LPTR Blade

Figure 7a shows the cracked LPTR blade received for investigation. Examination revealed that the blade had developed two cracks at the leading edge located at 52 and 48 mm distance from the blade root platform. The length of the cracks on the convex surface was measured to be 1.5 and 2.0 mm, respectively. The cracks were pulled open for further study, and a typical fractograph of the resulting fracture surfaces is shown in Fig. 7b. Examination revealed that the crack initiation and the propagation were by mixed mode of transgranular and intergranular fracture. There was no region on the crack surface which could be indicative of fatigue mode of crack propagation. The crack surfaces were found covered with thick oxide layers suggesting presence of the cracks over a prolonged period of time. In the freshly opened region, the fracture surface showed faceted, intergranular features with fine dimples on the grain facets.

3.5 HPTR Blade

Visual observation did not show any damages on the HPTR blade (Fig. 1). However, examination of the blade at low magnification showed severe surface oxidation at the hotter region on the leading edge. The blade was subjected to detailed metallurgical investigation to examine whether or not there were any abnormal microstructural changes in the material of construction.

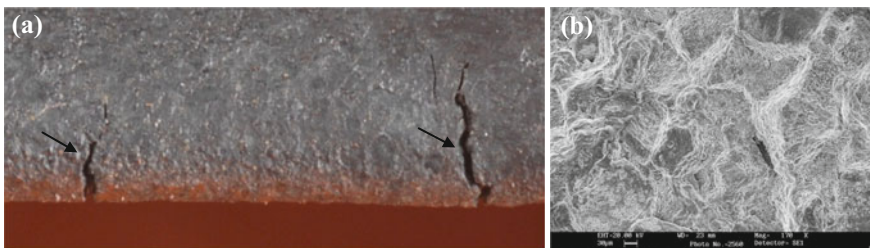


Fig. 7 **a** Cracks on the leading edge of the HPTR blade, and **b** fracture surface showing transgranular cleavage

3.5.1 Microstructure, Thermal Barrier Coating, and Composition

The microstructures of the blade at the root region and the hot zone are shown in Fig. 8. Observations revealed coarsening of the γ' precipitate phase at the hot zone of the blade. Figure 8 also shows the thermal barrier aluminide coating on the leading edge of the blade at the root region as well as in the hot zone. Examination showed rafted microstructure in the hot zone of the blade on the leading edge (Fig. 8b). Precipitation of TCP phases was also observed at a few places adjacent to the aluminide coating (Fig. 8c, d). The coating thickness including the diffusion zone was measured to be about 50 and 90 μm at the root region and hot zone of the blade, respectively.

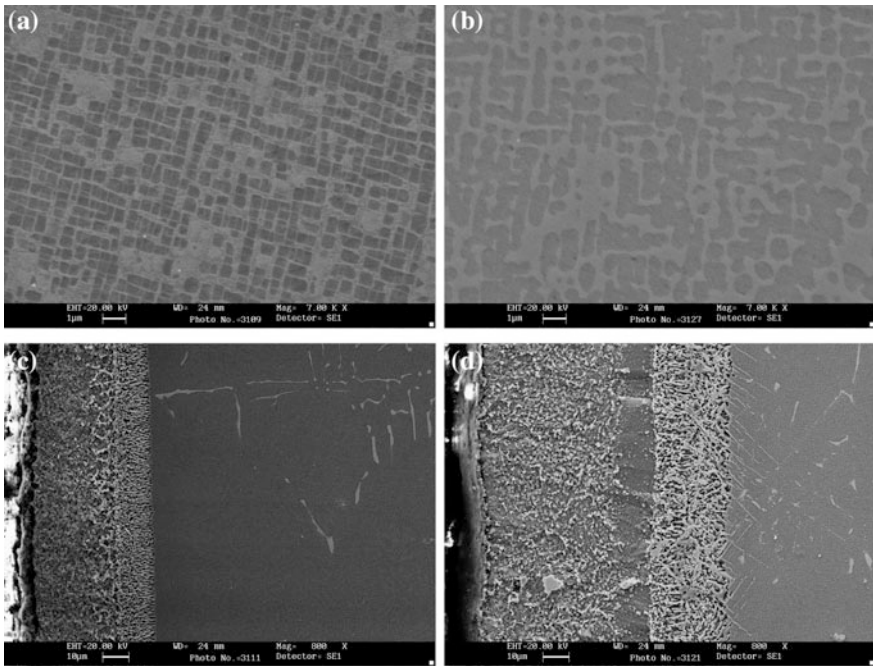


Fig. 8 Secondary electron microstructures at the leading edge of HPTR blade showing **a, b** γ' in a γ -matrix, and **c, d** thermal barrier coating; **a, c** root region, **b, d** hot zone

4 Analysis of Failure

4.1 Failure Mechanism

Fracture surface of the broken LPTR blade showed three stages of crack propagation, namely (i) crack initiation by mixed mode of transgranular and intergranular fracture, (ii) progressive fatigue crack propagation by transgranular mode, followed by (iii) final fracture by intergranular mode. These fractographic features confirmed that the failure in the blade was progressive in nature. Laboratory studies showed that there were two distinct mechanisms for the crack initiation and the subsequent crack propagation. From the fracture features, it could be clearly established that following the initiation, further crack propagation was by fatigue mechanism. The fatigue crack propagated to a critical length before giving way to final overload fracture.

In the cracked blade, there were multiple crack initiations at the leading edge at a height of 48–52 mm from the blade root platform. This region is the hot zone of the blade, and the mode of crack initiation in this blade was similar to that observed in the fractured blade. In this blade, the crack surface displayed mixed mode of fracture up to a depth of 2 mm.

4.2 Micromechanism(s) of Crack Initiation

In both the LPTR blades, the crack initiation occurred at the leading edge at a height between 48 and 52 mm from the blade root platform, which is essentially the hotter region of the blade. This clearly indicates that the crack initiation in the blades was by a thermally activated process. Examination of the remaining LPTR blades of the engine revealed the presence of cracks in seven more LPTR blades. In all the seven blades, cracking occurred at the hotter region of the leading edge, located in and around a height of 50 mm from the blade root platform. These observations suggested that the failure was not blade specific. Rather, it was because of reason(s) which was global in nature and related to the engine operating conditions.

The predominant mechanisms for temperature-assisted failures in superalloy turbine blades are (a) creep, (b) stress-rupture, (c) thermal fatigue, and (d) thermal shock. However, each of these mechanisms of failure has characteristic features which can be distinctively identified through fractography and microstructure studies. In the context of the present failure, these are discussed below.

- Creep: Generally, the creep failure in turbine blades is associated with detectable deformation surrounding the crack initiation region. Also, during creep deformation, grain-boundary sliding results in the generation of wedge-shaped cracks at the triple points, which can be readily identified through metallographic examination. Examination of the LPTR blades in the present case did not show

any such characteristic features, and hence, the possibility of failure by creep mechanism is ruled out.

- **Stress-rupture:** The stress-rupture fracture may be macroscopically either brittle or ductile in nature. Brittle fracture is intergranular and occurs with no elongation or necking. Ductile fracture is transgranular and is accompanied by discernible elongation or necking. But superalloy gas turbine blades are generally designed based on about 1% creep, and hence, they show low stress-rupture ductility. As a result, the fracture surface in this case often shows a mixture of transgranular and intergranular fracture features. Also, stress-rupture results in fracture surfaces which are generally irregular in nature, and they show uniform discolouration or oxidation. The fracture features seen at the leading edge in the present LPTR blades resemble these characteristics to a large extent.
- **Thermal shock:** Crack generation by thermal shock occurs in the hot zone of the blade and may occur on either the trailing edge or the leading edge. Generally, such cracking takes place in multiple blades in a similar fashion. The crack surface in this case is generally irregular in appearance with a mixed mode of transgranular and intergranular fracture. Thermal shock may result in generation of closely spaced multiple cracks in a single blade.

4.3 Primary Cause for Crack Initiation

Fracture features and microstructural examination clearly established that the crack initiation in the LPTR blades was by a thermally activated process, involving either thermal shock or stress-rupture. The crack initiation in the blades by these mechanisms would have been possible only if there were variations in the engine operating temperatures in excess of the normal. In Ni-base superalloys, the fractographic features on the crack surfaces generated by thermal shock and stress-rupture are very similar and not clearly distinguishable [4]. However, at times, it may be possible to distinguish between these mechanisms of failure through careful analysis of the fractographic features and microstructural changes in the material of construction together.

4.3.1 Oxide Layer on the Blades Surface

In the present case, uncoated blades made of Nimonic 115 alloy were used in the low pressure turbine section of the aero-engine. The surface oxidation of the LPTR blades during engine operation is, therefore, normal. At high temperatures and in oxidizing atmosphere, a surface oxide layer is formed on the LPTR blades. The primary constituents in the surface oxide layer are Al_2O_3 , Cr_2O_3 , and TiO_2 . The elements Al and Cr diffuse out of the blade material at the surface to form these oxides, resulting in a diffused zone in the blade comprising base material depleted

in Al and Cr interspersed with oxide phases Al_2O_3 and Cr_2O_3 . Hence, it is often difficult to assess the possibility of over-temperature in the blades unambiguously based on the characteristics of the oxide layer on the blades' surface.

4.3.2 Microstructural Changes in the Material of Construction

Microstructural changes do take place in the turbine blades, especially in the hotter regions of the blade airfoil, during engine running. Although, these changes are unavoidable even under the normal operating conditions, they do not reduce the material properties beyond acceptable limits within the technical life of the blades. Overheating of the blades beyond acceptable limit, if any, results in abnormal microstructural changes in the material which are identifiable through microstructural examination. In the present case, considering that the LPTR blades were in service for 1123:50 h, the microstructural changes observed were within the acceptable limit as per the engine overhaul manual. Also, there were no abnormal changes in the microstructure of the blades which could be suggestive of persistent running of the engine well above the normal operating temperatures. But, the presence of rafting and TCP phase in the HPTR blade material adjacent to the coating clearly indicated possible over-temperature in the engine.

4.4 Follow-Up of the Laboratory Investigation

As a follow-up of the laboratory investigation, the manufacturer subjected the aero-engine to detailed inspection. During this time, it was found that two out of the six thermocouples used for measuring the exhaust gas temperature were broken. It is important to note that the engine works on a feedback system wherein the fuel supply to the engine is controlled based on the exhaust gas temperature. In the present engine, the average value of the temperatures measured by the six individual thermocouples was the input. Because of the failure of the two thermocouples, the average temperature of the exhaust gas fed to the feedback system was less than the actual temperature. Hence, more fuel was supplied to the engine, and as a result, the engine temperature was naturally higher than that of the normal operating temperature for a substantial period of time. This was further confirmed through study of the flight data recorder (FDR). Following this study, it was possible to conclude that the failure in the LPTR blades was by stress-rupture mechanism as a consequence of engine over-temperature.

5 Conclusions

- (a) The fracture/cracking of the LPTR blades occurred by stress-rupture. In the broken blade, after initiation, the crack had propagated by fatigue mechanism before giving way to final overload fracture.
- (b) The crack initiation in the LPTR blades by stress-rupture was due to persistent over-temperature in the engine and not due to any metallurgical deficiencies in the material of construction.
- (c) The primary reason for the over-temperature in the engine was due to failure in two of the six thermocouples that were used for measuring the engine exhaust temperature. The faulty feedback to the engine operating system due to failure of the thermocouples led to more fuel supply to the engine resulting in over-temperature.

References

1. J. Hou, B.J. Wicks, R.A. Antoniou, An investigation of fatigue failures of turbine blades in gas turbine engine by mechanical analysis. *Eng. Fail. Anal.* **9**, 201–211 (2002)
2. J. Blachnio, W.I. Pawlak, Damageability of gas turbine blades-evaluation of exhaust gas temperature in front of the turbine using a non-linear observer, in E. Benini (ed.) *Advances in Gas Turbine Technology*. InTech. ISBN: 978-953-307-611-9 (2011)
3. D.P. Walls, R.E. deLanauville, S.E. Cunningham, Damage tolerance based life prediction in gas turbine engine blades under vibratory high cycle fatigue. *J Eng. Gas Turbines Power* **11**, 143–146 (1997)
4. T.M. Maccagno, A.K. Koul, J.P. Immarigeon, L. Cutler, R. Allem, G. L'Esperance, *Met Trans A* **21A**, 3115–3125 (1990)
5. Z. Shi, S. Liu, X. Wang, X. Yue, J. Li, Effect of melting temperature on the microstructure stability of a Ni-based single crystal superalloy. *Proc Eng.* **99**, 1415–1420 (2015)
6. X.W. Jiang, W. Wang, G. Xie, H. Li, L.H. Lou, J. Zhang, The effect of long term thermal exposure on the microstructure and stress rupture property of a directionally solidified Ni-based superalloy. *Met. Trans. A* **45A**, 6016–6026 (2014)

Fatigue Life Prediction of Composite Airframe Panel

P. K. Sahoo, Shriram Gujar and M. Manjuprasad

Abstract Fatigue failure analysis of pristine composite laminates and composite laminates with circular cut-outs made of CFRP T300/5208 with stacking sequence $\{0\}_{5s}$, $\{90\}_{5s}$, $\{0/90/0/90/0\}_s$ and $\{+45/-45/0/90/0\}_s$ are carried out. Fatigue damage model using physics-based approach based on multicontinuum theory and kinetic theory of fracture considering matrix cracking failure criterion is developed to calculate the fatigue life of above-mentioned composite laminates. Following the above model, $S-N$ curves are derived for different stress ratios for the pristine composite laminates and laminates with circular cut-outs. The proposed fatigue model has been validated by comparing the predicted results with experimental results available in the literature. The results show that the fatigue life to failure of pristine composite laminates is more as compared to the laminates with circular cut-outs. For different stress ratio values, the stress-life ($S-N$) curves move upward indicating that fatigue life is more as the stress ratio decreases for all the laminates. The physics-based approach can be used as an alternative approach for predicting fatigue life of composites. This analytical approach minimizes expensive testing activities significantly. The studies are important and essential to evaluate the structural integrity of composite airframe structures.

Keywords CFRP composite laminates · Fatigue life · Matrix cracking
Multicontinuum theory · Kinetic theory of fracture

1 Introduction

In new generation civilian/military aircrafts, polymer matrix composite (PMC) materials such as CFRP/GFRP are widely used in aircraft structures such as fuselage, wing and control surfaces due to their several benefits and abilities to be

P. K. Sahoo (✉) · S. Gujar · M. Manjuprasad
Structural Technologies Division, CSIR-National Aerospace Laboratories,
HAL Airport Road, Bangalore 560017, India
e-mail: pks@nal.res.in; sahoopradeepk1@gmail.com

© Springer Nature Singapore Pte Ltd. 2018
R. Prakash et al. (eds.), *Advances in Structural Integrity*,
https://doi.org/10.1007/978-981-10-7197-3_7

tailored for specific stiffness and strength properties requirements. They offer superior performances over the traditional materials such as Aluminium alloy (Al 2024-T3) in terms of lightweight, high specific strength, high stiffness and good fatigue and corrosion resistance.

The aircraft structural failure in service is mainly due to fatigue loadings. Therefore, the main consideration, while designing aircraft structures, is greatly concerned with fatigue life evaluation of structural components. Failure mechanism in CFRP composites is a very complex phenomenon. Various failure modes such as matrix yielding, matrix cracking, fibre/matrix interface debonding, fibre pull-out, fibre fracture and inter-ply delamination could occur either separately or simultaneously. Interface delamination is of particular interest in view of the relatively weak ply-to-ply interface strength, and the large interface shear stresses developed during loading. Interface delamination failure leads to significant loss of the load-carrying capacity and occurs even in the absence of any visible damage of the CFRP composite.

The composites in aircraft structures were, earlier (1970), used marginally in tertiary and secondary aircraft structural elements. Now, these are most preferred materials for large primary structures in modern frontline advanced aircraft in both combat and transport category.

Fertig and Kenik [1] presented a physics-based methodology for predicting fatigue life of composite structures using minimal coupon level data for characterization. Methodology is based on multicontinuum theory for extracting constituent stresses from a composite stress and applies the kinetic theory of fracture for predicting fatigue life of the matrix constituent. Kinetic theory of fracture in combination with a damage variable accurately predicts the fatigue life of a composite. Jen and Lee [2] investigated the static and fatigue behaviour of AS4/PEEK APC-2 laminates using extended Tsi-Hill fatigue failure criterion. Naderi and Maligno [3] developed a three-dimensional finite-element model to predict the progressive fatigue damage and the life of a carbon/epoxy flat laminates (9AS4/3501-6) based on the longitudinal, transverse and in-plane shear fatigue characteristic. The model uses fatigue failure analysis, stress analysis, random distribution and material property degradation. Fertig and Kenik [4] presented a multiscale physics based fatigue life prediction methodology for composite structures, which requires minimal fatigue characterization and computationally efficient, also taking into account arbitrary loads and load histories. Liu and Mahadevan [5] proposed a new damage accumulation model for multidirectional composite laminates to predict the fatigue life. The model is built on the ply level, and a new multi-axial damage index has been used to consider the damage caused by different stress components. With the help of proposed model and making use of the experimental results of the unidirectional laminates, the fatigue life has been predicted. Wu and Yao [6] presented a phenomenological fatigue damage model by making the use of the stiffness degradation rule of composites having two material parameters. The fatigue damage model is capable of describing the nonlinear damage development in the whole fatigue life period of the materials. Attia et al. [7] proposed a methodology and studied growth of damage in and fatigue life of I-beams made of

CFRP composite using finite-element analysis in conjunction with experiments (to obtain fracture mechanics data). Eason and Ochoa [8] modelled composite structures using the plate/shell elements, which capture a three-dimensional state of stress for damage progression incorporating a shear deformable composite element with built-in progressive damage capability into a commercial finite-element programme, ABAQUS. Varvani-Farahani et al. [9] developed an energy-based criterion to evaluate the fatigue damage of unidirectional CFRP/GFRP composites. The suggested fatigue damage model effectively linked fatigue lives of unidirectional composites at various off-axis angles h and stress ratios Lian and Yao [10] performed three-dimensional finite-element simulations for plain E-glass/epoxy to simulate the fatigue life. Papanikos et al. [11] developed a progressive fatigue damage model for predicting damage accumulation and life of CFRP laminates with arbitrary geometry and stacking sequences subjected to constant amplitude loading. The model consists of components of stress analysis, fatigue failure analysis and fatigue material property degradation. Ratwani and Kan [12] studied the effect of stacking sequence on failure modes and damage growth in composite laminates of AS4/3501-6 material. Experiments were conducted for coupons with four different stacking sequences and were investigated under X-ray radiography.

The existing fatigue models can be classified into three different categories: fatigue life model ($S-N$ curves), residual stiffness or residual strength model and progressive damage model [6, 7]. The first two models used in fatigue analysis of composites are at the macroscopic level, while third one, the progressive failure model takes into account local damage mechanisms, such as fibre breakage, local ply buckling and delamination. Micromechanics model based on Mori-Tanaka method was attempted by Reifsnider and Gao to predict fatigue failure of composite materials [13].

The literature studies show that considerable amount of work has been carried out on static strength and fatigue life evaluation of metallic airframe at both component and full-scale levels using either experimental or computational approach. As for fatigue evaluation studies of composite airframes, there exist few such studies using experimental/NDT techniques. However, there is no significant or visible amount of work carried out on fatigue life estimation of composite airframe using the computational technique. Therefore, it is necessary to develop a fatigue damage model for composites to predict fatigue life.

2 Problem Statement

Fatigue failure analyses are carried out on both pristine composite laminates and laminates with circular cut-outs using the physics-based fatigue model as detailed in Eq. (13). The MATLAB code of this model considering different stress ratios ($R = 0.1$ and $R = -0.1$) is developed. The laminates are made of CFRP (T300/5208) material.

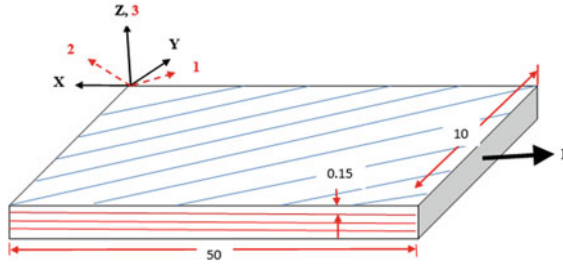


Fig. 1 Schematic draw and dimension of the laminate (all dimensions are in mm)

Table 1 Mechanical and thermal properties for CFRP T300/5208 lamina

	E_1 (GPa)	E_2 (GPa)	G_{12} (GPa)	G_{23} (GPa)	ν_{12}	ν_{23}	$\alpha_1 (10^{-6}/^\circ\text{C})$	$\alpha_2 (10^{-6}/^\circ\text{C})$
Composite (T300/5208) lamina	136	8.729	6	3.1175	0.36	0.4	-0.1134	25.236
T300 Carbon fibre	207	11.382	24.226	40.706	0.33	0.21	-0.51	10.08
5208 Epoxy	4.556	4.556	1.631	1.631	0.4	0.4	41.4	41.4

The dimensions and stacking sequences are as follows, dimensions: length 50 mm, width 10 mm, ply thickness 0.15 mm; stacking sequences: $\{0\}_{5s}$, $\{90\}_{5s}$, $\{0/90/0/90/0\}_s$ and $\{+45/-45/0/90/0\}_s$ with 10 plies for each sequence.

The schematic draw of the laminate is shown in Fig. 1. The mechanical and thermal properties of T300/5208 CFRP composite material, T300 carbon fibre and 5208 epoxy are given in Table 1 [1, 14]. The lamina properties shown in the table indicate that lamina is transversely isotropic because elastic properties in second and third direction are same, i.e. $E_2 = E_3$, $G_{12} = G_{13}$, $\nu_{12} = \nu_{13}$. Elastic properties are different in all three directions indicate laminate is orthotropic.

3 Problem Formulation and Procedures

The initiation of damage in FRP composites occurs mainly due to the kinetic process of microcrack accumulation and coalescence. After a critical density of microcracks is attained, a macroscopic crack forms and leads into ultimate failure. This kind of fatigue failure can be modelled by making use of the kinetic theory of fracture (KTF). In FRP composite materials, the stress values in matrix are not same as those in the composite. For applying KTF to the polymer composites, determination of matrix stresses from composite stresses is essential. For extracting matrix stress from composite stress, a methodology called multicontinuum theory (MCT) has been used [1].

- Multicontinuum theory

The most numerically efficient theory to be implemented for a failure analysis of composites is the MCT approach. In this approach, the macroscopic composite stress state is efficiently decomposed to the constituent level. This multiscale decomposition allows for easy identification between fibre and matrix failure states [15].

According to continuum mechanics, any physical quantity of interest can be evaluated at a material point by averaging the quantity over a representative volume element that surrounds the point of interest. The size of this representative volume element (RVE) must be very small compared to the overall physical dimensions of the material body, yet large enough to provide an accurate statistical representation of the quantity within the body’s material microstructure. A continuum point for a continuous fibre composite at lamina scale is shown in Fig. 3a. The macroscopic value used for characterizing the stress tensor at this point in a single continuum is derived by taking a volume average of all stresses as

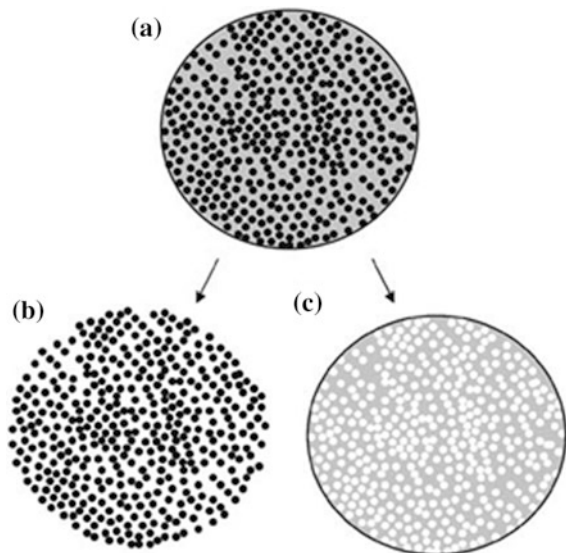
$$\sigma = \frac{1}{V} \int_D \sigma(x) dV \tag{1}$$

where the volume averaging occurs over both matrix and fibre constituents.

Let us consider a continuous fibre composite material where the fibres (*f*) and matrix (*m*) are permitted for retaining their identity in the continuum, as shown in Fig. 2. Using Eq. (1) for each constituent, we get

$$\sigma_f = \frac{1}{V_f} \int_{D_f} \sigma(x) dV \tag{2}$$

Fig. 2 Multicontinuum decomposition



$$\sigma_m = \frac{1}{V_m} \int_{D_m} \sigma(x) dV \quad (3)$$

Assuming the continuum forms of σ_m and σ_f therefore taking them as the original variables. Combining Eqs. (1)–(3) gives

$$\sigma = \phi_f \sigma_f + \phi_m \sigma_m \quad (4)$$

where ϕ_m and ϕ_f are the volume fractions of matrix and fibre, respectively. Similarly for strains,

$$\epsilon = \phi_f \epsilon_f + \phi_m \epsilon_m \quad (5)$$

The capability of decomposing lamina level continuum fields to the constituent level involves a relationship between constituent elastic constants and composite. The relation between material properties is obtained by making use of a finite-element micromechanics model of a representative composite microstructure. The multicontinuum analysis described takes into account the internal stress states of each constituent. The main advantage of the multicontinuum approach is that it allows the use of physics-based theories that have been recognized for polymers directly to the matrix material of the composite [16].

- Linking composite stress with matrix

For applying kinetic theory to composite structures, the stress in the matrix and fibre constituents need to be determined. In this study, the main focus is on matrix dominated fatigue failure, so σ_m exact value of average stress in the matrix constituent can be written as

$$\sigma_m = Q_m \sigma_c - \lambda_m \Delta T \quad (6)$$

where,

$$\begin{aligned} Q_m &= C_m \{ C_c (\phi_m I + \phi_f A) \}^{-1} \\ \lambda_m &= C_m \phi_f [(C_c - C_f) (\phi_m I + \phi_f A)]^{-1} a + \eta_m - (\phi_m I + \phi_f A)^{-1} \eta_c \\ A &= -\frac{\phi_m}{\phi_f} (C_c - C_f)^{-1} (C_c - C_m) \\ a &= C_c \eta_c - \phi_f C_f \eta_f - \phi_m C_m \eta_m \end{aligned} \quad (7)$$

In Eqs. (6) and (7), σ_c is the six-component composite stress vector; ΔT is the temperature change from the stress free state; C_i ($i = m, f, c$) is the reduced stiffness matrices for matrix, fibre and composite, respectively; ϕ_m and ϕ_f are the matrix and fibre volume fractions, respectively; and η_i ($i = m, f, c$) is the thermal expansion

coefficients of the matrix, fibre and composite, respectively, written as six-component strain vectors where the shear components are zero.

- Kinetic theory of fracture (KTF)

KTF gives a description of bond breaking via thermally activated processes. It predicts fatigue failure in the matrix constituent, which translates to composite failure. After obtaining composite stress state or stress history, MCT can be used to determine the average matrix stress. All atoms and molecules that are having temperatures greater than absolute zero oscillate with a frequency proportional to ν_0 given by Planck’s Law [17].

$$\nu_0 = kT/h \tag{8}$$

where,

ν_0 Oscillation frequency of the atom

h Planck’s constant ($h = 6.626068 \times 10^{-34}$ J s/K atom)

kT Thermal energy, described by the product of the Boltzmann constant k ($k = 1.3806504 \times 10^{-23}$ J/K atom) and the absolute temperature T

The thermal energy linked with each oscillation is not a single number but rather a distribution; there may be a possibility that any given oscillation will have sufficient energy for overcoming the energy barrier U and move from one equilibrium state to another. The chances of this occurrence for any given oscillation is given by the known exponential form $\exp(-U/kT)$. The bond-breaking rate K_b can be written as

$$K_b = \nu_0 \exp\left(-\frac{U - \gamma\sigma}{kT}\right) \tag{9}$$

The stress is acting to ease the bond-breaking process; therefore, it must reduce the energy barrier to bond breaking. The amount of this reduction is determined by the volume of material γ the activation volume, over which the process occurs so that the reduction in the activation energy is only the product of activation volume and the stress. Adjusting Eq. (9) to reflect the effect of an applied stress results in

$$K_b = \frac{kT}{h} \exp\left(-\frac{U - \gamma\sigma}{kT}\right) \tag{10}$$

Equation (10) is the baseline equation for the KTF that is used to predict composite fatigue. The above equation with multicontinuum theory and kinetic theory of fracture is put together to get an algorithm for performing fatigue failure analysis of composites.

Kinetic theory of fracture in conjunction with MCT gives a bond-breaking rate in the matrix, provided that U and γ are appropriately calibrated. The only remaining effort is to link the bond-breaking rate with a macroscopic measurement of damage.

A differential equation to evaluate the damage variable n with time t , where the evolution of the damage variable is directly related to the bond rupture rate as:

$$\frac{dn}{dt} = (n_0 - n)K_b \quad (11)$$

where

$$n_0 = \frac{e}{e - 1}$$

The damage variable, representing the fraction of microcrack density essential for fracture, is zero initially ($n(t = 0) = 0$) and unity at failure ($n(t = t_f) = 1$). Merging Eqs. (10) and (11) gives the initial equation for determining the fatigue life of a polymer.

$$\frac{dn}{dt} = (n_0 - n)K_b \frac{KT}{h} \exp\left[-\frac{U - \gamma\sigma(t)}{kT}\right], \quad n(0) = 0 \quad (12)$$

Assuming a sawtooth-shaped load history having frequency f , maximum stress σ_{\max} and minimum stress σ_{\min} , and as a first-order approximation, assuming that the stiffness properties are not degrading with increasing n , as saw in some experimental work on composites [16]. Using these assumptions and solving Eq. (12) gives the number of cycles to fatigue failure N_f .

$$N_f = \frac{fn\gamma(\sigma_{\max} - \sigma_{\min})}{(kT)^2} \exp\left(\frac{U}{kT}\right) \left[\exp\left(\frac{\gamma\sigma_{\max}}{kT}\right) - \exp\left(\frac{\gamma\sigma_{\min}}{kT}\right) \right]^{-1} \quad (13)$$

The above formula (Eq. 13) is used to calculate fatigue life of polymers and has been implemented in this study to calculate the fatigue life of composite laminates.

3.1 Fatigue Analysis Algorithm

The flow chart for stress calculations and fatigue analyses of both pristine and laminate with circular cut-outs is described in Fig. 3. For pristine laminates, stresses at each ply were calculated by inputting load, lamina properties and stacking sequences to MATLAB programming; whereas, for laminate with circular cut-outs, peak stresses at stress critical locations (around cut-out region) were obtained from ABAQUS FEA code output results. Then, the maximum stress values at respective ply for both types of laminates (pristine and laminate with cut-outs) were used in fatigue analysis model to calculate fatigue life.

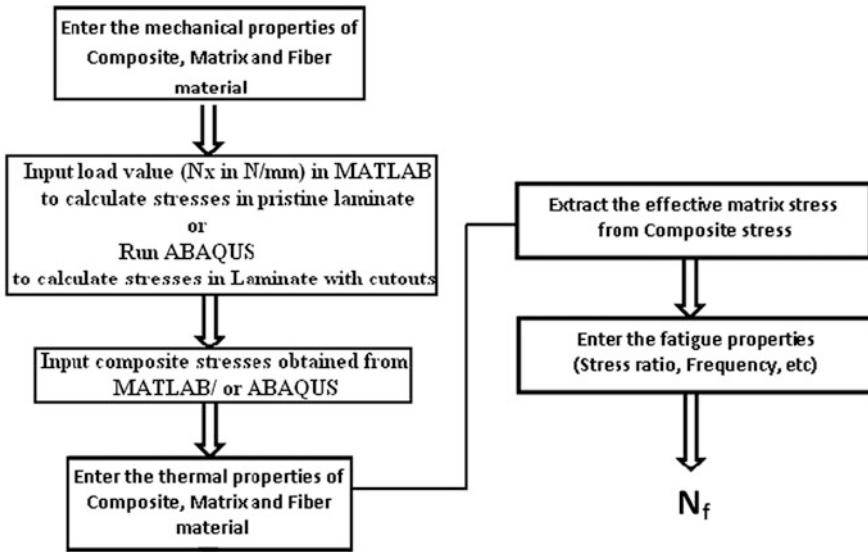


Fig. 3 Process flow chart for fatigue analysis

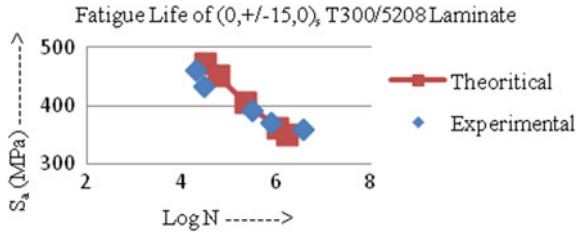
4 Results and Discussion

Fatigue analyses have been carried out for pristine composite laminates and laminates with circular cut-outs made of CFRP T300/5208 composite materials with different stacking sequences for different stress ratios ($R = 0.1$ and -0.1). The fatigue model using a physics-based approach is developed, and the MATLAB code of this model is developed. Stress-life ($S-N$) data are generated by increasing or decreasing the load values and determining the corresponding number of cycles to failure. Thus, $S-N$ curve is plotted by considering the maximum stress values occurring in a lamina to the corresponding number of cycles to failure for pristine composite laminates and laminates with circular cut-outs (stress concentrations at cut-out sections).

4.1 Model Validation

In order to validate the proposed theoretical model, fatigue life results of $(0, \pm 15, 0)$ T300/5208 laminate for stress ratio, $R = 0.1$ have been compared with experimental ones from literature [1] as shown in Fig. 4. The comparison shows that both theoretical and experimental results are in good agreement.

Fig. 4 Comparison of fatigue life prediction results with experimental



4.2 Stress-Life (S-N) Plots for Pristine T300/5208 Composite Laminates with Different Stacking Sequence

Figures 5, 6, 7 and 8 show the S-N curve for pristine T300/5208 composite laminates for stacking sequences $\{0\}_{5s}$, $\{90\}_{5s}$, $\{0/90/0/90/0\}_s$ and $\{+45/-45/0/90/0\}_s$, respectively, with different stress ratios ($R = 0.1$ and -0.1).

Fig. 5 S-N curve for $\{0\}_{5s}$ pristine composite laminate

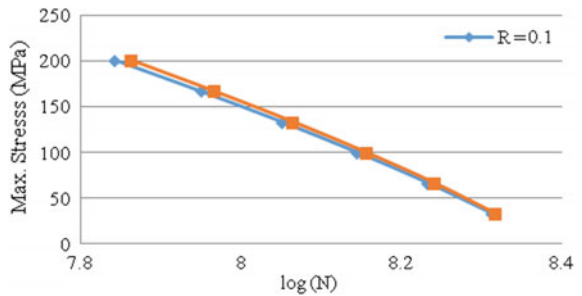


Fig. 6 S-N curve for $\{90\}_{5s}$ pristine composite laminate

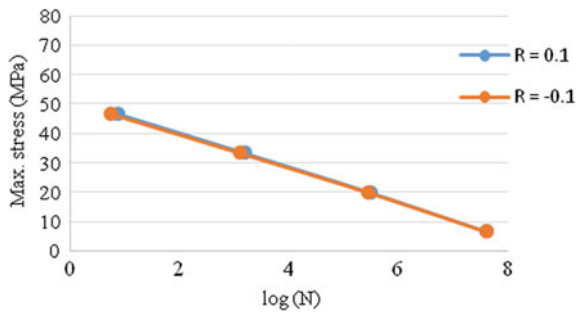


Fig. 7 S-N curve for $\{0/90/0/90/0\}_s$ pristine composite laminate

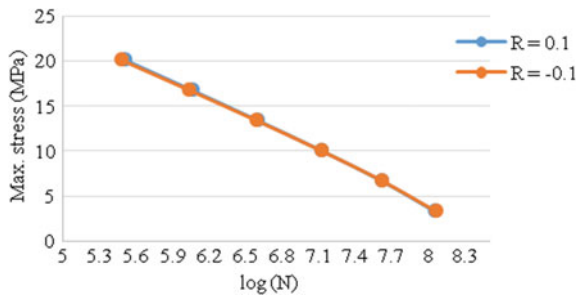
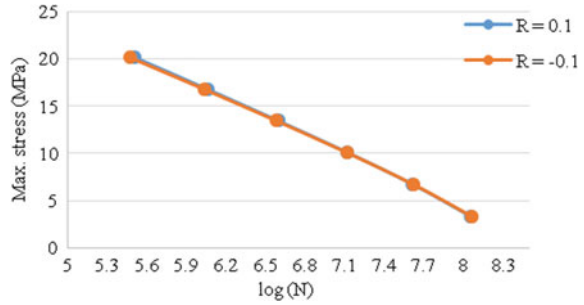


Fig. 8 *S-N* curve for $\{+45/-45/0/90/0\}_s$ pristine composite laminate



It is observed, in $\{0\}_{5s}$ pristine composite laminates (Fig. 5) that fatigue life is more for the laminates having stress ratio -0.1 compared to laminate at stress ratio 0.1 . This trend is quite acceptable by observing the fact that, the trend is similar to that established for metals. However, the difference in fatigue life is not that significant. For $\{90\}_{5s}$, $\{0/90/0/90/0\}_s$ and $\{+45/-45/0/90/0\}_s$ pristine composite laminates (Figs. 6, 7 and 8), it is observed that both the fatigue curves almost coincide at both stress ratios ($R = 0.1$ and -0.1). The possible reasons for such trend might be due to the fact that $\{0\}_{5s}$ pristine laminates fail due to failure of 0° ply, whereas other pristine composite laminates $\{90\}_{5s}$, $\{0/90/0/90/0\}_s$ and $\{+45/-45/0/90/0\}_s$ fail due to the failure of 90° lamina.

4.3 Stress-Life (S-N) Plots for T300/5208 Composite Laminate with Circular Cut-Outs with Different Stacking Sequences

Figures 9, 10, 11 and 12 show the *S-N* curves for T300/5208 composite laminate with circular cut-outs for stacking sequences $\{0\}_{5s}$, $\{90\}_{5s}$, $\{0/90/0/90/0\}_s$ and $\{+45/-45/0/90/0\}_s$, respectively, with different stress ratios ($R = 0.1$ and -0.1).

It may be seen from Figs. 9, 10, 11 and 12 that similar trend of fatigue life for different stress ratios for T300/5208 composite laminate with circular cut-outs as

Fig. 9 *S-N* curve for $\{0\}_{5s}$ composite laminate with circular cutout

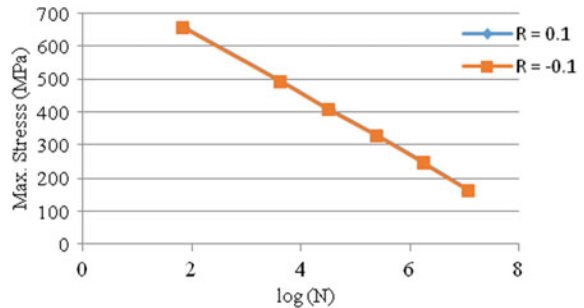


Fig. 10 *S-N* curve for $\{90\}_{5s}$ composite laminate with circular cutout

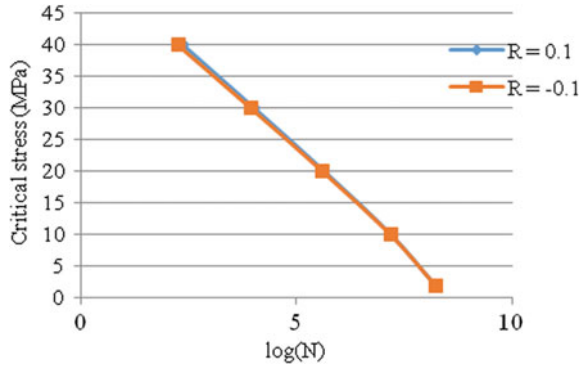


Fig. 11 *S-N* curve for $\{0/90/0/90/0\}_s$ composite laminate with circular cutout

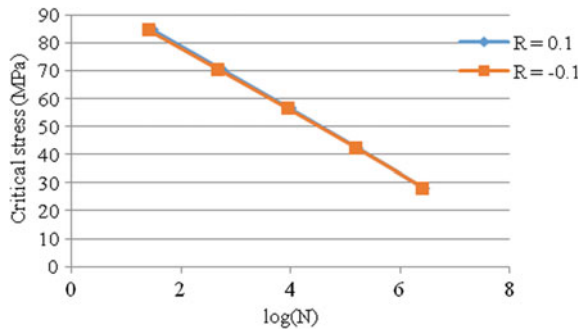
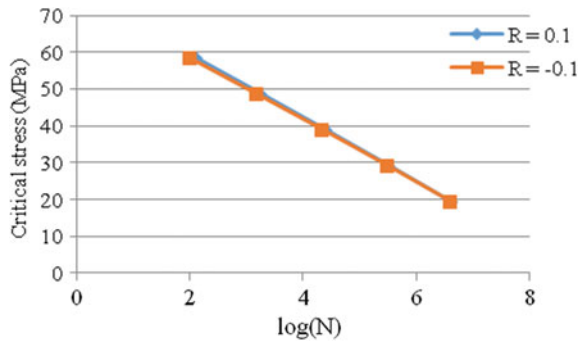
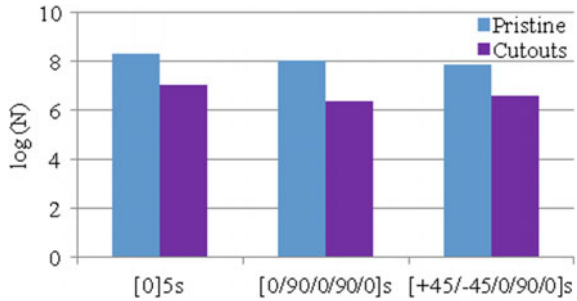


Fig. 12 *S-N* curve for $\{+45/-45/0/90/0\}_s$ composite laminate with circular cutout



discussed earlier for pristine composite laminates. It is observed that the fatigue life of laminates has decreased due to the presence of stress concentration around cut-out region, which is more prone to the damage initiation.

Fig. 13 Fatigue life comparison for pristine composite laminates and laminates with circular cut-outs



4.4 Comparison of Fatigue Lives

Figure 13 shows the comparison of fatigue life of pristine composite laminates and laminates with circular cut-outs under same load (50 N/mm) and at the same stress ratio ($R = 0.1$) for all the stacking sequences considered.

It is observed that fatigue life of pristine composite laminates is much higher compared to the fatigue life of composite laminates with circular cut-outs. This is due to the presence of stress concentrations around cut-out regions, and damage initiates first for laminates with cut-outs in comparison with pristine laminate.

5 Concluding Remarks

Finite-element stress analysis results are post-processed using multicontinuum theory and kinetic theory of fracture to obtain the fatigue lives of composite pristine laminates and laminates with cut-outs. Multicontinuum theory was used for extracting matrix stresses from composite stresses. Effective matrix stress values are processed using KTF to predict fatigue life of composite material for two different stress ratios 0.1 and -0.1 .

Fatigue lives are estimated for CFRP T300/5208 pristine composite laminates and laminate with circular cut-outs subjected to specified loading with different stress ratios ($R = 0.1$ and -0.1) and frequency ($f = 10$ Hz). The fatigue failure cycles are obtained at different stress levels, and $S-N$ curves are derived for all the laminates considered. It is observed that pristine laminates have higher cycles to failure compared to laminates with circular cut-out due to the cut-out region experiencing higher stress concentrations and the damage initiation occurs first at those locations.

Fatigue failure analysis results show that $\{0\}_5$ s pristine laminates fail due to the failure of 0° ply, whereas $\{90\}_5$ s, $\{0/90/0/90/0\}_s$ and $\{+45/-45/0/90/0\}_s$ pristine composite laminates fail due to failure of 90° lamina. Fatigue life is more for the laminate having stress ratio -0.1 as compared to laminate at stress ratio 0.1. It is observed that pristine laminates have higher cycles to failure compared to laminates

with circular cut-outs. This is due to the cut-out region experiencing higher stress concentrations, and the damage initiation occurs first at those locations. The fatigue life of laminates decreases due to the presence of stress concentration around cut-out region. This method can be used as an alternative approach to obtain stress-life ($S-N$) curves for composite laminates for predicting fatigue life of aerospace composites, thus minimizing expensive testing activities.

Acknowledgements The authors kindly acknowledge the financial support of council of Scientific and Industrial Research (CSIR) under ASTA grant ESC-02-12-03. They would like to thank the Director, CSIR-National Aerospace Laboratories, Bangalore and Dr. Satish Chandra, Head, STTD, CSIR-NAL, Bangalore for encouragement and permitting them to present and publish the work.

References

1. R.S. Fertig III, D.J. Kenik, in *Predicting Composite Fatigue Life Using Constituent Level Physics*, Presented at the 52nd AIAA/ASME/ASCE/AHS/ASC Structures, Structural Dynamic Material, Denver (Colorado, 2011)
2. M.H.R. Jen, C.H. Lee, Strength and life in thermoplastic composite laminates under static and fatigue loads. Part I: experimental. *Int. J. Fatigue* **20**, 605–615 (1998)
3. M. Naderi, A.R. Maligno, Fatigue life prediction of carbon/epoxy laminates by stochastic numerical simulation. *Compos. Struct.* **94**, 1052–1059 (2012)
4. D.R.S. Fertig III, D.J. Kenik, Physics Based Fatigue Life Prediction of Composite Structures
5. Y. Liu, S. Mahadevan, Probabilistic fatigue life prediction of multidirectional composite laminates. *Compos. Struct.* **69**, 11–19 (2005)
6. F. Wu, W. Yao, A fatigue damage model of composite materials. *Int. J. Fatigue* **32**, 134–138 (2010)
7. O. Attia, A.J. Kinloch, F.L. Matthews, Modelling the fatigue life of polymer–matrix fibre-composite components. *Compos. Sci. Technol.* **61**, 2273–2283 (2001)
8. T.G. Eason, O.O. Ochoa, Modeling progressive damage in composites: a shear deformable element for ABAQUS[®]. *Compos. Struct.* **34**, 119–128 (1996)
9. A. Varvani-Farahani, H. Haftchenari, M. Panbechi, An energy-based fatigue damage parameter for off-axis unidirectional FRP composites. *Compos. Struct.* **79**, 381–389 (2007)
10. W. Lian, W. Yao, Fatigue life prediction of composite laminates by FEA simulation method. *Int. J. Fatigue* **32**, 123–133 (2010)
11. P. Papanikos, K.I. Tserpes, S.P. Pantelakis, Modelling of fatigue damage progression and life of CFRP laminates. *Fatigue Fract. Eng. Mater. Struct.* **26**, 37–47 (2003)
12. M.M. Ratwani, H.P. Kan, in *Effect of Stacking Sequence on Damage Propagation and Failure Modes in Composite Laminates*, ed. by K. Reifsnider, Damage in Composite Materials (ASTM STP 775, ASTM, 1982), pp. 211–228
13. K.L. Reifsnider, Z. Gao, A micromechanics model for composites under fatigue loading. *Int. J. Fatigue* **13**, 149–156 (1991)
14. D.E. Bowles, in *Micromechanics Analysis of Space Simulated Thermal Deformations and Stresses in Continuous Fiber Reinforced Composites*. ed. by M.Y. University C. Langley Research. NASA Technical Memorandum, National Aeronautics and Space Administration, Langley Research Center
15. A.C. Hansen, E.E. Nelson, D.J. Kenik, A comparison of experimental data with multicontinuum failure simulations of composite laminates subjected to tri-axial stresses. *J. Compos. Mater.* (2013)

16. E.E. Nelson, J.A. Gies, R.S. Fertig III, The Virtues of Multicontinuum Mechanics for Composites Analysis, in *Presented at the Structural Dynamics and Materials Conference*, Palm Springs, California (2009)
17. H. El Kadi, F. Ellyin, Effect of stress ratio on the fatigue of unidirectional glass fibre/epoxy composite laminae. *Composites*, **25**, 917–924 (1994)

Integrity Evaluation of Feature Level Test Specimen of an Aircraft Primary Composite Structure

S. Venkatesh, S. C. Lakshminarayana and Byji Varughese

Abstract It is well known to the aircraft designers that the design of structure using only metals or only composite materials can be realized with higher confidence level based on the database or tools available present in their aircraft design bureau. However, data availability for design of primary structural element/joint using metal, composites, and mechanical fasteners is minimal, and many of them are proprietary; moreover, they are depending on type of design. There is a need to design and test a feature level test specimen with appropriate boundary and loading conditions, which simulates behavior of full-scale component. Primary structural joint for actuator mounting on the composite fin has been considered for feature level testing. The purpose of the tests was to demonstrate the validity of the structural joint by applying static limit and ultimate loads. The feature level test specimen consists of composite and metal joints was successfully loaded to the ultimate design load without evidence of failure. The global behavior predicted by the finite element (FE) model of the test arrangement was in close agreement with the experimental results as evidenced by the strain and displacement results. The success of the testing program demonstrated the importance of feature level test in the design stage of primary composite structural joints of a civil transport aircraft.

Keywords Feature level test • Composite • FE analysis • Actuator assembly

S. Venkatesh (✉) · B. Varughese
Advanced Composites Division, CSIR-NAL, Bangalore 560017, India
e-mail: venkateshs@nal.res.in

B. Varughese
e-mail: byji@nal.res.in

S. C. Lakshminarayana
Centre for Civil Aircraft Design and Development Division,
CSIR-NAL, Bangalore 560017, India
e-mail: sclnara@nal.res.in

1 Introduction

Over the last two decades, CSIR-National Aerospace Laboratories (CSIR-NAL) has developed primary components for both civil and military aircraft programmes using composite materials. The application of composite materials to primary aircraft structures requires proven design concepts and certification procedures to demonstrate their structural integrity during service life. Development phase of structural design for civil and military aircraft involves an enormous amount of design and qualification tests before building a full-scale component for testing. In the preliminary design phase of an aircraft, structural designer would like to know the adequacy of the design parameters for all primary components/features/joints in aircraft. The design parameters include strength, stiffness, and number/type of fasteners used [1, 2]. Composites have a more linear load–strain response, a greater sensitivity to stress concentrations and environments, higher data scatter, and a multiplicity of potential failure modes. Application of the metallic certification database to composite structures is limited by the inherent differences between composites and metals. In order to have confidence in the compliance of composite structural design, it is imperative to generate the database of primary structural joints of composite and metal. This is achieved by interpretation of feature level tests at the development phases.

The design of feature level test specimen and testing requires a lot of effort and brings challenges in terms of technical study/understanding, design and detailing of joints, application of proper software tools, and simulation using testing equipments to capture the strain, displacement, and local damage/structural collapse. In this study, one of the primary composite structural joint on fin is considered for feature level testing [3]. This paper presents the importance of feature level test, test design, and test-FE correlation of a primary composite structural joint of a fin component of civil transport aircraft.

2 Geometry and Structural Features of Test Component

In many of the Light Transport Aircrafts, a T-tail configuration of the empennage in which horizontal tail (HT) is mounted on fin. For variable incidence horizontal stabilizer, the actuation of the horizontal stabilizer is done by either an electromechanical or a hydraulic actuator with its fixed end mounted in the fin structure and the actuation/moving end connected to the horizontal stabilizer. These joints are classified under primary joints; any failure of such a joint would cause loss of aircraft. For this design, horizontal stabilizer trim actuator (HSTA), which is an electromechanical linear actuator, is used. HSTA consists of two load paths, the primary load path works under normal conditions, and the secondary load path works after the failure of the primary load path, and therefore, HSTA has built-in fail-safe design feature. Therefore, installation of this HSTA on an aircraft is very

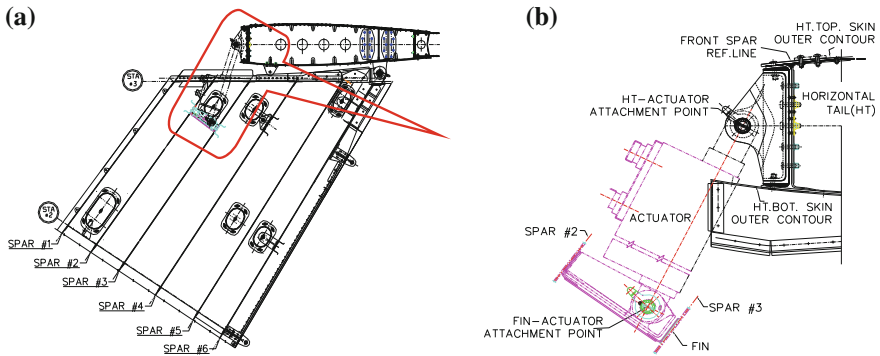


Fig. 1 a Actuator installation on HT and fin; b detail view of the attachment

important and considered to be the primary joint and hence requires proven design. Fixed or actuator end of the HSTA is connected to the composite fin structure between the spar #2 and spar #3. Hinge or movable end of the actuator connected to the horizontal stabilizer front spar, top, and bottom skins as shown in Fig. 1a. Details of the actuator attachment on HT and fin are shown in Fig. 1b.

Fin actuator fitting assembly is a critical joint, and an experimental testing of the same has to be performed before installation. The complete fin cannot be considered for experimental testing as the complete setup is huge, and the materials used are very expensive, and this joint should be validated before fabrication of the full-scale component; thereby, any changes found after the testing can be implemented in the design before fabrication of full-scale component. Hence, in this study, a segment of the fin close to the actuator fitting assembly has been considered instead of the complete fin. A feature level test model of fin actuator fitting assembly was developed to demonstrate the composite and metal joints for design ultimate loads. Feature level test specimen was designed using finite element tools. Basic understandings with the global behavior of the fin for the critical load cases were studied. Stress parameters were considered in deriving the boundary and loading conditions. Finally, required components fabricated and assembled as per the airworthiness requirements.

3 Finite Element Modeling and Stress Analysis

Finite element (FE) preprocessing and post-processing of the structure was done using hypermesh. The analysis was carried out using MSC/NASTRAN [4]. In this section, FE modeling of the global structure and the test specimen is described. The

global FE model of the fin structure with actuator assembly is shown in Fig. 2a. The structural members such as spar, skin, stiffeners, and metallic brackets were modeled using the CQUAD4 and CTRIA3 elements in MSC/NASTRAN. All composite parts were treated as 2D orthotropic layered shell structural elements modeled with PCOMP property in NASTRAN. Test configuration derived from the global FE model is shown in Fig. 2b. Parts of spar #2 and spar #3 at the actuator bracket fitting assembly, top and bottom skins, and bracket fitting assembly were considered for the test model analysis. The FE models of the components of fin and actuator fitting assembly were generated by idealizing the skin, spars, ribs, and surfaces of actuator fitting assembly by shell elements as the thickness of these components is small as compared to the other dimensions. The rivets and flanges were idealized by bar and rod elements, respectively.

The configuration of the test specimen was derived based on the configuration of spar, rib, and skins of the composite fin. The loading and boundary conditions of the test specimen should result in similar strain conditions as computed by FE analysis for the composite fin. To achieve this, a combination of actuator forces has to be determined, which gave an optimum correspondence between strains in the fin structure and in the test specimen. Boundary conditions place a very important role in achieving the same. The end fittings of the test specimen attached to the mounting brackets of the test rig were designed to take the test loads and transfer in the intended direction. To understand the structural behavior of the global model and feature level test article, displacement, von-Mises stress patterns and failure indices were studied. The failure index was calculated based on the Yamada-Sun failure criteria. Finally, the Feature level test article was designed to capture the global behavior of the fin structure.

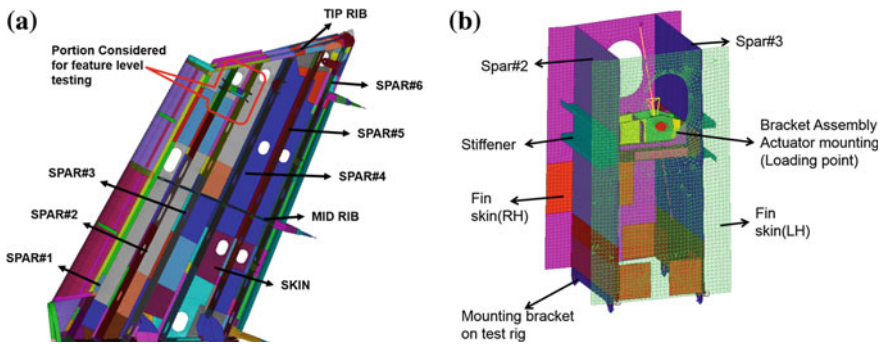


Fig. 2 a Global FE model, b Feature level test specimen

3.1 Loads and Boundary Conditions

The FE modeling was carried out to cater for the application of loads as per the test loads. The design limit load (DLL) on this actuator mounting point along the actuator axis in the neutral axis is 2000 kg, and design ultimate load (DUL) is 3000 kg [5]. The load reacted at this point due to aerodynamic load on the horizontal stabilizer is lower than the DLL of 2000 kg which is used to design the actuator. Therefore, actuator supporting structure should be able to withstand the DLL of 2000 kg and DUL of 3000 kg. The displacement boundary conditions for the feature level test model with respect to the global axes were constrained as $U_X = 0$, $U_Y = 0$ and $U_Z = 0$ in the FE model. The applied load and boundary conditions on the feature level test model are shown in Fig. 2b.

3.2 Material Properties

The materials used for fin actuator fitting assembly and bracket fitting assembly were aluminum alloy steel, bushes, and pins were made out of corrosion resistant steel. The spars, ribs, and skins of fin were made of UD prepreg (carbon-epoxy) composites with ‘quasi-isotropic’ layup sequence.

4 Test Configuration

The feature level test was conducted in the specially built test rig. It is a steel frame supported in all direction to provide the rigidity for the test loads. The test article was mounted on the test rig at the mounting brackets. The mounting brackets were designed to take the test loads and capture the global behavior of the fin structure. Figure 3 shows the schematic view of the test setup and loading arrangement of the test article.

A hydraulic jack was connected to the actuator mounting bracket through which load was applied. Design limit load of ± 2000 kg (compression and tensile) was applied on the actuator mounting point using hydraulic actuator. Test carried out for tension and compression load of 2000 kg was applied in steps of 10% DLL. Subsequently, the DUL test was carried out for tension load of 3000 kg (2000×1.5). This case is more critical for composite and metal joints. The load was applied in steps of 10% DLL up to 160% (i.e., 10% above DUL) and unloaded to zero in steps of 10% DLL. Figure 4 shows the photography of the test setup.

Strain and dial gauge locations were selected on composite skin and metal fitting assembly by understanding the finite element stress analysis. Strains and deflection were recorded at every load step during loading and unloading. Rosettes were used to measure strains, and dial gauges were used to measure the deflections.

Fig. 3 Test setup with loading arrangement

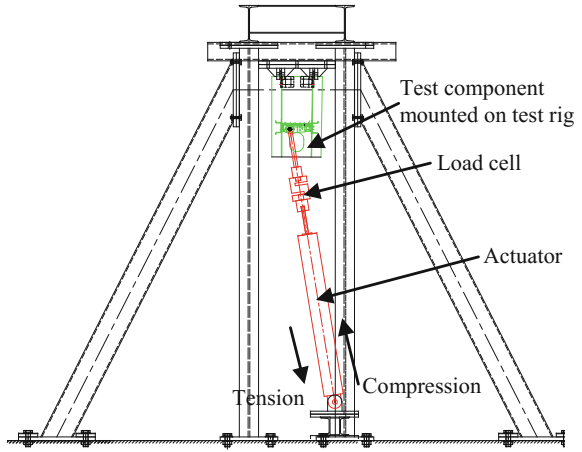


Fig. 4 Photography of the test setup



5 Test Results Comparison and Discussion

Displacement and strains were recorded during the test at various locations are compared with the finite elemental analyses results. Displacements are small in magnitude, and it is more appropriate to compare the relative displacement or twist of the test article. This eliminates the influence of test rig deflections. Maximum

deflection measures under compression and tensile load cases at DLL was 2.83 mm, and from FE, it was 1.59 mm. Displacement measured from ultimate load test (160% of DLL) for the tensile case was 2.63 mm and FE estimate was 2.54 mm as shown in Fig. 5. It has observed that the comparison between test and FEM deflections is quite good. Both deflections are showing similar profile. This shows that the FE model is capturing global elastic behavior very well. It has observed that deflection from DLL test for tension shows little deviations as compared to DUL test. Furthermore, the variation observed in DLL test can be attributed to fixture and component fittings stabilization during DUL test.

The strains recorded during the test at various locations were compared with FE strains determined from the ply strain output from MSC Nastran. The FE strains were extracted, and it is compared with test strain gauge data. The ply shear strains were derived from the strains measured in all three elements. Comparisons between experimental and FE strains are presented for the gauges at the maximum strain at two locations for the compression case (DLL) as shown in Fig. 6 and for the tensile case (DUL) as shown in Fig. 7. The strains measured from the test were within the allowable limit of 3300 $\mu\epsilon$. In general, there is a good correlation between the FE and test results. The trend observed in test and FE is similar. As the strains are low at many locations, there is no real concern for the integrity of the structure. The

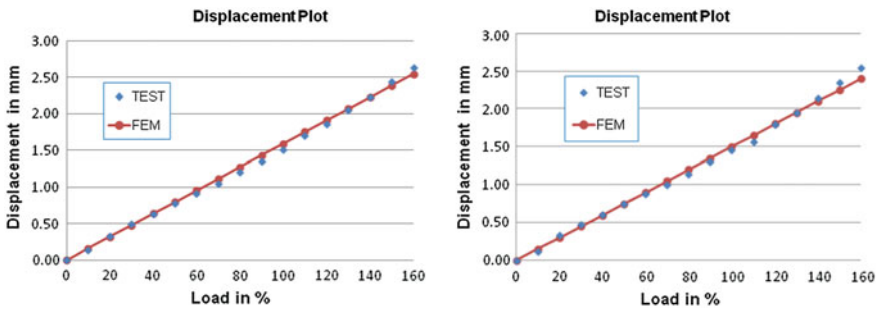


Fig. 5 Comparison of test and FE displacement for tensile case (DUL) for dial gauge 1 and dial gauge 2

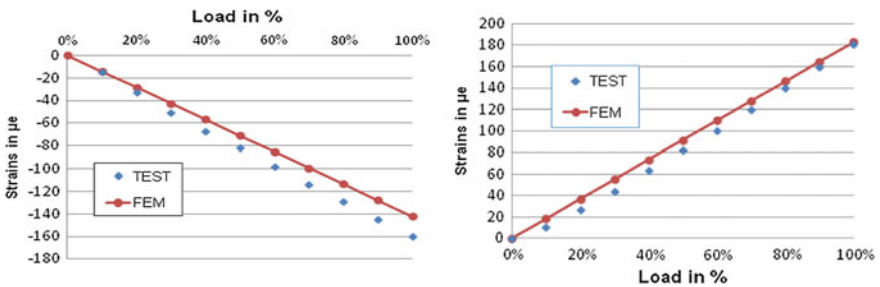


Fig. 6 Comparison of test and FE strains for the compression case (DLL)

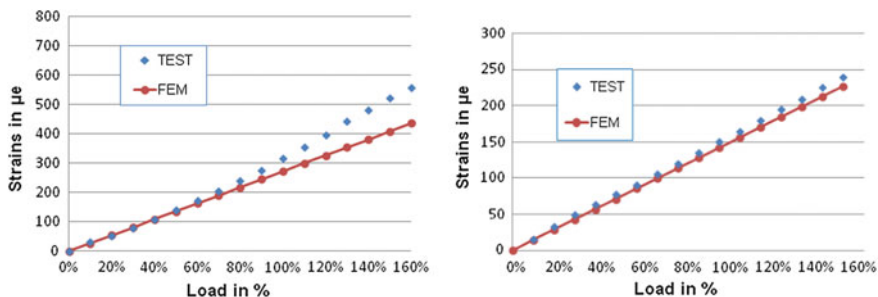


Fig. 7 Comparison of test and FE strains for the tensile case (DUL)

actuator assembly was subjected to ultrasonic inspection after the static test and results showed no debonds or delaminations on the tested article.

6 Conclusion

The structural static testing of critical joints is an essential activity to prove the integrity of composite aerospace parts. In this paper, requirements, importance in design of feature level test component, and testing were discussed. Static testing of fin actuator fitting assembly was carried out to prove the structural integrity of the joint and its attachment to the surrounding composite structure. The component was tested up to design limit load both in tension and compression loads and up to design ultimate load (up to 160% DLL) for tensile load. The deflection and strains are monitored during the DLL tests, and DUL test was compared with those from FE analysis. A good correlation between test and analysis results was observed at most locations. This proved the integrity of the structure for the load which it is designed. It may be noted that the selected geometrical size of the feature level test component and the boundary conditions chosen proved to be proper throughout the test. Hence, it may be concluded that the design of test specimen and its validation is acceptable.

Acknowledgements Authors would like to express their gratitude to Director, CSIR-National Aerospace Laboratories (NAL) and Heads of Advanced Composites Division (ACD) and Centre for Civil Aircraft Design and Development Division (C-CADD), NAL for their encouragement. Authors also thank all staff members of ACD, NAL for their unstinted support in various stages of this work.

References

1. H.G.S.J. Thuis, C. Biemans, Design, fabrication and testing of a composite bracket for aerospace applications. *Compos. Struct.* **38**(1–4), 91–98 (1997)
2. K.I. Tserpes, R. Ruzek, R. Mezihorak, G.N. Labeas, Sp.G. Pantelakis, The structural integrity of a novel composite adhesively bonded flap-track beam. *Compos. Struct.* **93**, 2049–2059 (2011)
3. B. Ramanaiah, H.V. Ramachandra, S. Sanjeev Kumar, M.G. Kotresh, B. Varughese, R. Sundaram, Challenges in static testing of co-cured co-bonded composite aircraft structure, in *National Conference on Scientific Achievements of SC & ST Scientists & Technologists*, National Aerospace Laboratories, Bangalore-17, 14–16 Apr 2009
4. R.S. Lahey, M.P. Miller, M. Reymond, *MSC/NASTRAN Version 70 Reference Manual* (The MacNeal-Schwendler Corporation, 2003)
5. M.C.-Y. Niu, *Airframe Stress Analysis & Sizing*, 2nd edn. (Hong Kong Conmilit Press Ltd, Jan 1999)

A Study on the Effect of Crack Stopper for Enhanced Damage Tolerance Behavior of a Fuselage Stiffened Panel

G. Akshitha, A. Shailesh Rao, N. Srinivasan and M. Mohan Kumar

Abstract During the design and development phase of a large transport aircraft, a considerable amount of parametric analysis and testing is carried out to bring out an optimum structure. Two-bay longitudinal crack arrest feature is the main aspect of design for damage tolerance of the pressurized fuselage cabin. Under fuselage pressurization load cycles, fatigue cracks develop at location of maximum tensile stress. There are locations on the airframe which are favorable for the initiation of longitudinal cracks. This investigation identifies one such location in a fuselage panel from where a longitudinal crack can initiate and studies the fast fracture and crack arrest features under the action of uniaxial hoop stress. The main crack arresting features are the bulkheads and crack stopper straps. A finite element modeling and analysis approach will be used for simulating stiffened panel with and without the presence of tear strap and their role in the two-bay crack arrest capability of the aircraft fuselage is assessed. Stress intensity factor for progressive crack lengths and the fatigue crack growth rate of the cracked stiffened panel was estimated. A tear strap crack stopper was introduced for evaluating the damage tolerance capability of the stiffened panel again fatigue crack growth rate was estimated for a realistic representation of two-bay cracking scenario, it will be examined under what condition a two-bay crack can be arrested. By this new design, the stiffened panel was found to be more damage tolerant compared to the earlier one.

Keywords Damage tolerance · Crack · Fracture · Bulkhead · Tear strap
Finite element analysis · Residual strength

G. Akshitha · A. Shailesh Rao
Department of Mechanical Engineering, K.S. School of Engineering and Management,
Bangalore 560062, India

N. Srinivasan · M. Mohan Kumar (✉)
Fatigue and Structural Integrity Group, Structural Technological Division, CSIR-National
Aerospace Laboratories, Bangalore 560017, India
e-mail: mmk@nal.res.in

1 Introduction

Aircraft structure is the most obvious example where structural efficiency results in light weight and high operating stresses. An efficient structure must have three primary attributes, namely the ability to perform its intended function, adequate service life, and the capability of being produced at a reasonable cost. The major part of the aircraft structure consists of built-up panels of sheets and stringers, e.g., wing and fuselage skin panels, spar webs, and stiffeners. Despite all precautions, cracks have arisen in many of these structural elements. These cracks reduce the stiffness and the total load-carrying capacity of the structure. The fuselage is the main structure in the aircraft with the basic functions is to transmit and resist the applied loads; to provide an aerodynamic shape and to protect passengers, payload systems, etc., from the environmental conditions encountered in flight.

These requirements, in most aircraft, result in thin shell structures where the outer surface or skin of the shell is usually supported by longitudinal stiffening members and transverse frames to enable it to resist bending, compressive, and torsion loads without buckling. Such structures are known as semi-monocoque, while thin shells which rely entirely on their skins for their capacity to resist loads are referred to as monocoque. In most modern aircrafts, the skin plays an important role in carrying loads. Sheet metals can usually only support tension. But if the sheet is folded, it suddenly does have the ability to carry compressive loads, stiffeners are used for that. A section of skin, combined with stiffeners, called stringers, is termed a thin-walled structure. An aircraft fuselage structure must be capable of withstanding many types of loads and stresses. The principal source of the stresses in this structure is the internal pressure in high altitude caused by difference of cabin pressurization and reduction of the outside pressure with increase in altitude, but the structure is subjected to other loads, as bending, torsion, and thermal loads.

Fatigue loads in a pressurized fuselage are mostly due to pressure cycles that occur with each takeoff or landing cycle during flight. The most common fatigue crack orientation in a pressurized fuselage is a longitudinal crack along the direction of maximum hoop stress. Damage-tolerant designs use fracture mechanics data and analysis to predict crack growth rates and critical crack lengths [1]. Cabin pressure results in radial growth of the skin and this radial growth is resisted by frames and stringers giving local bending along the fastener lines. Fuselage skin panels are curved, and these panels are under biaxial tension loading due to cabin pressure. Cabin pressurization is the main source of loading causing longitudinal skin cracks. Two types of damage most frequently associated with the structural integrity of the fuselage are longitudinal cracks under high hoop stresses induced by cabin pressurization and circumferential cracks under stresses from vertical bending of the fuselage. The objective of paper was to present a systematic investigation of the damage tolerance design capability of typical aircraft fuselage structure for longitudinal cracks using linear elastic fracture mechanics [2]. Damage-tolerant fuselage is supposed to sustain cracks safely until it is repaired or its economic service life

has expired. Strength assessment of the structures is necessary for their in-service inspection and repair. Damage tolerance analysis should provide information about the effect of cracks on the strength of the structure. Damage tolerance evaluation must include a determination of the probable locations and modes of the damage due to fatigue or accidental damage.

The crack propagation stage is studied by using stress intensity factor. There are different methods used in the numerical fracture mechanics to calculate stress intensity factors (SIF). The crack opening displacement (COD) method and the force method were popular in early applications of FE to fracture analysis. The virtual crack extension (VCE) methods proposed by Hellen [3] and Parks [4] lead to increased accuracy of stress intensity factor results. The virtual crack extension method requires only one complete analysis of a given structure to calculate SIF. Both the COD and VCE methods can be used to calculate SIF for all three fracture modes. However, additional complex numerical procedures have to be applied to get results. The equivalent domain integral method which can be applied to both linear and nonlinear problems renders mode separation possible [5]. The VCCT, originally proposed in 1977 by Rybicki and Kanninen [6], is a very attractive SIF extraction technique because of its good accuracy, a relatively easy algorithm of application capability to calculate SIF for all three fracture modes. Leski [7], the implementation of the virtual crack closure technique in engineering FE calculations. SIF was fundamental quantity that governs the stress field near the crack tip. It depends on the geometrical configuration, crack size, and the loading conditions of the body.

2 Problem Description

Stiffened panels are the most generic structural elements in an airframe. Currently, large transport airplanes are being developed with large damage tolerance capability as a design goal. An important concept in the design of the pressurized fuselage of large transport aircraft is the provision of crack stopper straps to arrest the fast fracturing of a crack. In this project, the role of the crack stopper strap in the fail-safe design of the fuselage is investigated. As a first approximation, a stiffened flat panel with a center longitudinal crack is considered. The strength of this cracked panel is investigated as a function of crack length in the absence of crack stopper straps. Crack stopper straps is then introduced at the locations of stiffeners perpendicular to the crack line, and strength of the cracked flat panel is investigated as a function of crack length in the presence of crack stopper straps. The failure criteria that are used in this study that the skin crack will have a fast fracture when the maximum stress intensity factor becomes equal to the fracture toughness of the skin material. It is assumed that there is no rivet failure, and there is no failure of the stiffener normal to the crack line.

3 Geometrical Configuration

The stiffened panel represents a most generic in fuselage structure. The stiffened panel dimensions are 1750 mm in the longitudinal direction and 990 mm in transverse direction. The thickness of the stiffened panel skin is 1.5 mm. The stiffened panel has five frames (four bays) with 400 mm spacing and seven stringers (six bays) with 140 mm spacing. The frame has Z and L cross section with 1099 mm^2 of cross-sectional area and stringer has Z cross section with 419 mm^2 of cross-sectional area. The frames and stringers are attached to the skin by row of 3 mm diameter rivet, placed at a pitch of 21 mm. Geometric modeling is carried out using MSC PATRAN software shown in Fig. 1.

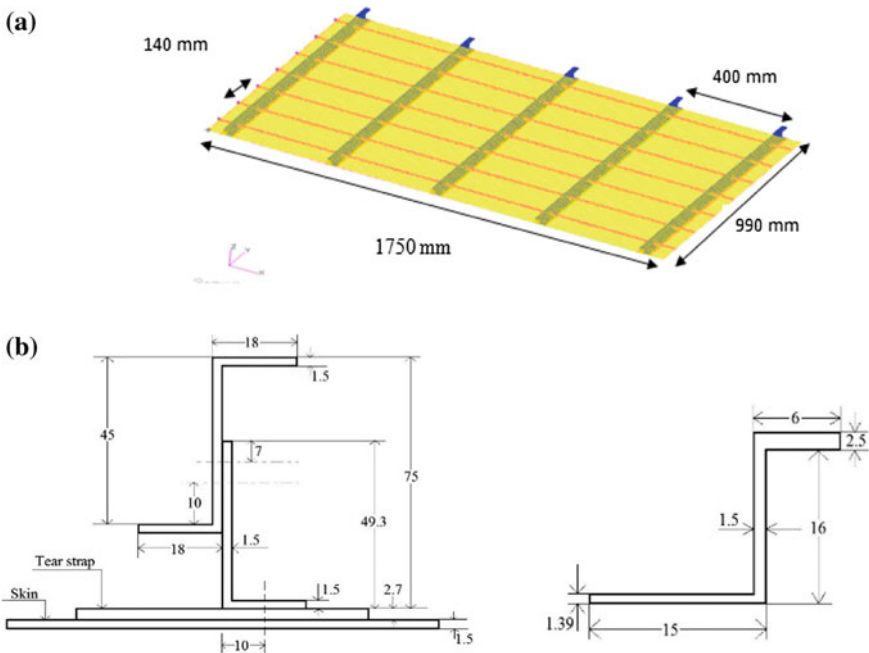


Fig. 1 a Flat stiffened panel, b details of bulkhead and stiffener

4 FE Analysis

In the present study, a segment of fuselage structure of a transport aircraft is modeled and analyzed in MSC NASTRAN/PATRAN for pressurization load case to identify the critical location on skin for the initiation of crack, and evaluating the SIF values for progressive crack lengths of a stiffened panel without and with tear strap. Fatigue life was estimated for the progressive crack lengths in the stiffened panel.

4.1 Flat Stiffened Panel

It involves modeling the different components of the flat stiffened panel such as bulkheads, stringers skin, tear strap, and rivets as shown in Fig. 2. The geometry of all the stiffened panel components in the form of models was used for the finite element modeling using MSC Patran. The modeled fuselage is a 2D integral FE model, and there are totally around 320,743 elements comprising of QUAD4, TRIA3, 1D beam elements. Various material properties for the different components that are considered in the study are shown in Table 1.

4.2 Material Properties

See Table 1.

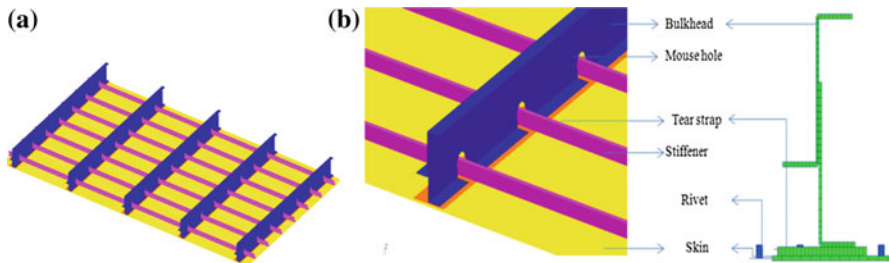


Fig. 2 a FE modeling of the stiffened panel, b parts of the stiffened panel

Table 1 Details of Material properties

Component	Material	Properties
Skin	Al-2024-T3	Young's modulus, $E = 72$ GPa
Bulkhead tear strap		Poisson's ratio, $\nu = 0.3$ Ultimate tensile strength, $\sigma_{ult} = 427$ GPa
Stiffener rivets		Fracture toughness, $K_{IC} = 31$ MPa \sqrt{m} Material constants: $C = 3.2$; $m = 3E-8$

4.3 Loads and Boundary Conditions

A differential internal pressure of 0.062 MPa is considered for the current case. The hoop stress corresponding to the internal pressure of 0.062 MPa was considered for the present stiffened panel analysis. Uniformly distributed load is applied on edges of skin and frame in the transverse direction. But, the stringers are passing in longitudinal direction in the stiffened panel. Since it is uniaxial tensile loading, the stringers are not subjected to loading. At other end, all the edge nodes of stiffened panel are constrained in all six degree of freedom (three translations and three rotations) shown in Fig. 3.

4.4 SIF Calculation

Modified virtual crack closure integral (MVCCI) method is used to determine stress intensity factor for different crack lengths in the stiffened panel. MVCCI method is based on the energy balance. Stresses at the crack tip and the nodal displacements are noted for calculating the strain energy release rate, G , and hence SIF by MVCCI method [7–9]. In this technique, SIF is obtained for fracture mode from Eqs. (1) and (2).

4.5 Calculation of Stress Intensity Factor by MVCCI Method

See Fig. 4.

$$\text{Stress intensity factor, } K_I = \sqrt{GE} \quad (1)$$

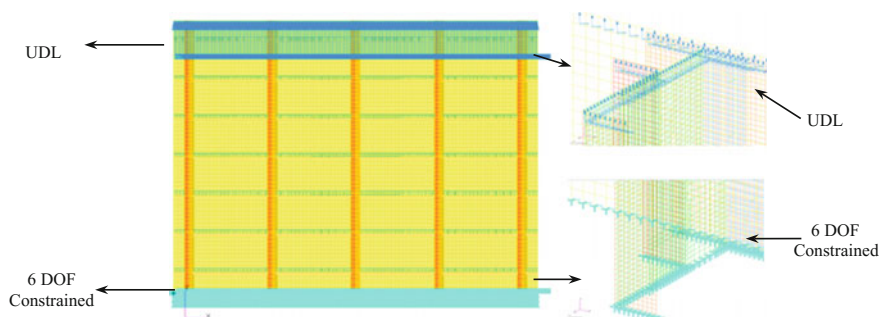
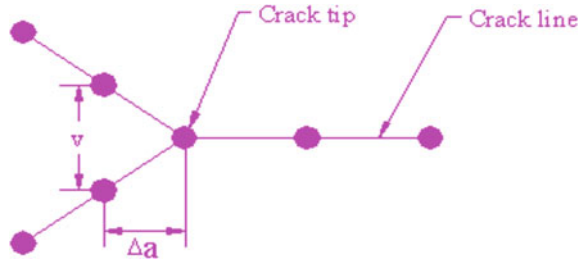


Fig. 3 Loads and boundary conditions of the stiffened panel

Fig. 4 MVCCI method



$$\text{Energy release rate, } G = \frac{(F * \Delta v)}{(2 * \Delta a * t)} \tag{2}$$

4.6 Fatigue Life Calculation

Fatigue life calculation for an initial crack length a_f to a_i .

From Paris' law we have,

$$\frac{da}{dn} = C(\Delta K^m) \tag{3}$$

Integration of above equation will give the following simple expression for the number of cycles, N_f .

$$N_f = \frac{a_f^{1-m/2} - a_i^{1-m/2}}{C(F\Delta\sigma\sqrt{\Pi})^m (1 - \frac{m}{2})} \tag{4}$$

5 Results and Discussion

The linear static stress analysis of the flat stiffened panel was carried out. Pressure of 0.062 MPa was considered as a load case for the present problem. Effect of tear strap on the stress distribution was studied; effect of tear strap on SIF values under progressive crack lengths was analyzed. Residual strength was evaluated for the considered configuration. Finally, fatigue life was estimated for the flat stiffened panel from an initial crack length of 5 mm to a final crack length of 450 mm.

5.1 Stress Analysis of a Flat Stiffened Panel

A linear static analysis of a flat stiffened panel was conducted and an overall structural response was analyzed to determine the maximum tensile stress location which was on the skin at the rivet location where the rivets are used to fasten the frames and stringer on the skin. The maximum stress distribution in the skin was 86 and 55 MPa in a flat stiffened panel without and with tear strap, respectively (Fig. 5).

5.2 Design of Tear Strap

Tear strap is principally designed for arresting longitudinal skin cracks. Tear strap is designed with thickness 1.2 mm and width 50 mm and inserted in between bottom flange of frame and skin. Selection of tear strap was based on the optimization criteria.

5.2.1 Optimization of Tear Strap Thickness

In this case, the thickness of the tear strap was varied to 1.5, 2.5, 2.7, 3, and 5 mm. Iterations are carried for a crack length of 5–500 mm, and the corresponding stress intensity factor was calculated for the corresponding crack lengths. The values of SIF for the progressive crack lengths obtained from the stiffened panel analysis by MVCCI method are plotted to obtain the characteristic curve shown in Fig. 6. From this, it is clear that for a tear strap thickness of 2.5, 2.7, and 3 mm, there is a close matching in SIF values between them. For a thickness of 1.5 and 5 mm, the SIF values are correspondingly high compared with that of 2.7 mm. Hence, tear strap of 2.7 mm thickness is considered for the present work.

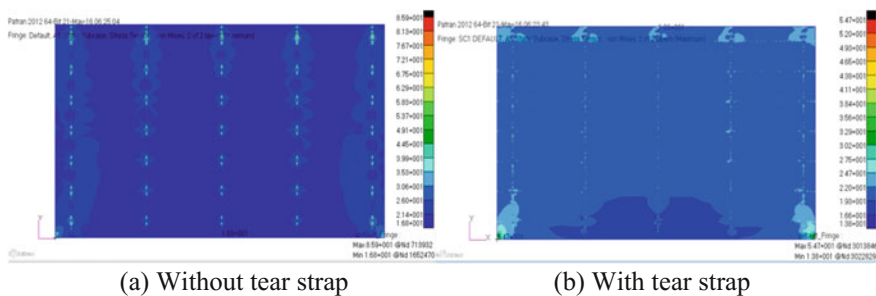


Fig. 5 Stress plots of flat stiffened panel skin

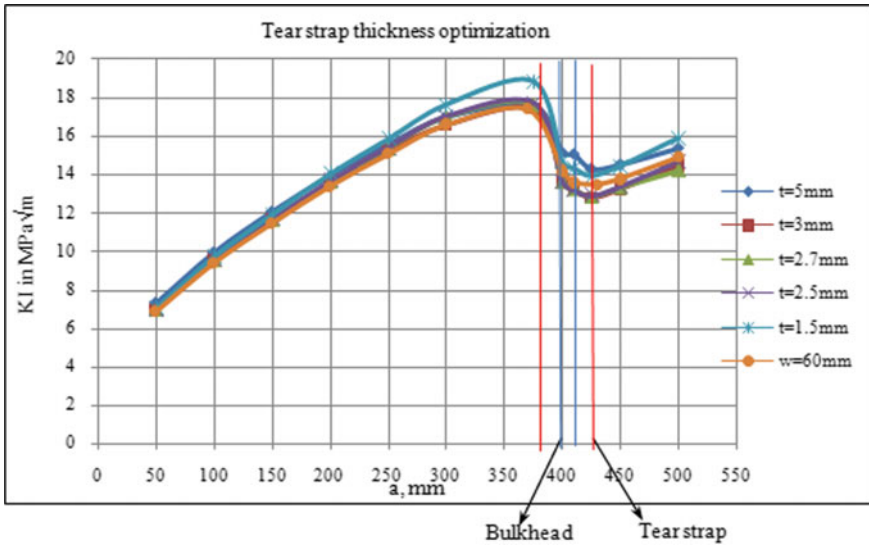


Fig. 6 Tear strap thickness optimization

5.2.2 Optimization of Tear Strap Width

In order to optimize the width of a tear strap, various iterations were carried out for a crack lengths ranging from 50 to 500 mm, and graph of SIF versus crack length was plotted shown in Fig. 7. From the graph, it was observed that the width had no effect on the SIF variation for increasing crack length.

5.3 Effect of Tear Strap on SIF

The values of SIF for the progressive crack lengths are obtained from the flat stiffened panel analysis by MVCCI method without and with tear strap and are plotted to obtain the characteristic curve shown in Fig. 8. It can be observed from the curve that the stress intensity factor (SIF) of the panel varies linearly till it reaches the stiffener position. As the crack reaches the stiffener position, the load is transferred to the stiffener through rivets, thus reducing the SIF near the stiffener, which ensures in arresting the crack from propagating further. When the crack is propagated beyond the stiffener position, there will be an increase in SIF because the load shared by the skin increases gradually. The increasing trend in the curve is observed as the crack moves away from the stiffener position.

SIF values for the progressive crack lengths were plotted for without and with tear strap were plotted. For a same crack length stiffened panel without tear strap was having higher SIF values compared to that of stiffened panel with tear

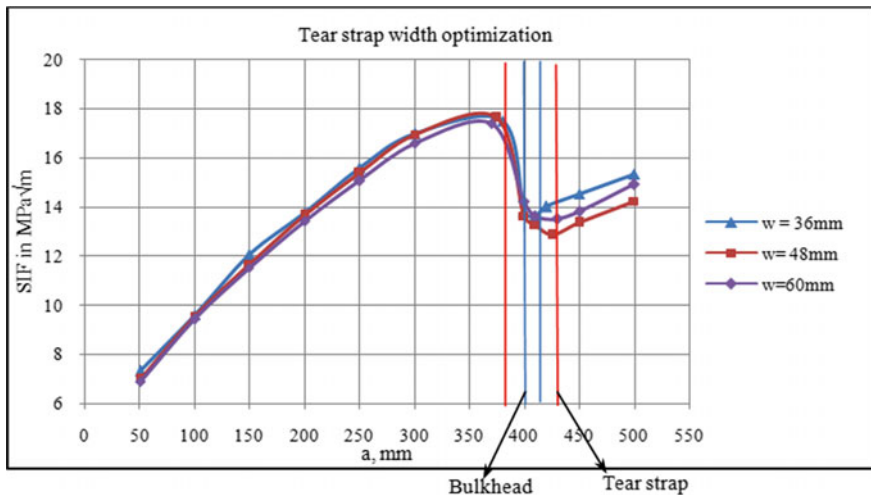


Fig. 7 Tear strap width optimization

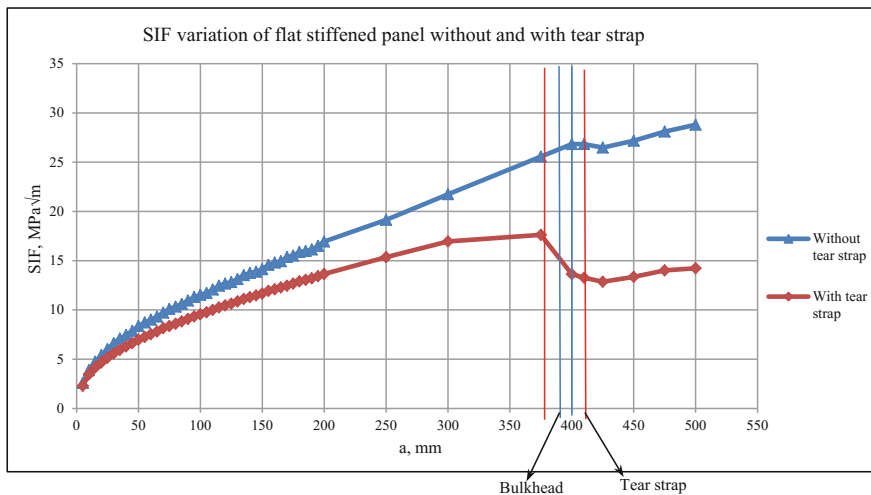


Fig. 8 SIF variation of flat stiffened panel without and with tear strap

strap. The SIF values decreased by 20% for the initial crack lengths and once the crack reaches the tear strap position the SIF values got decreased by 50% compared to the panel without tear strap. Once it crosses the tear strap, the SIF value incremental for the further crack lengths was also less compared to that of initial incremental SIF values.

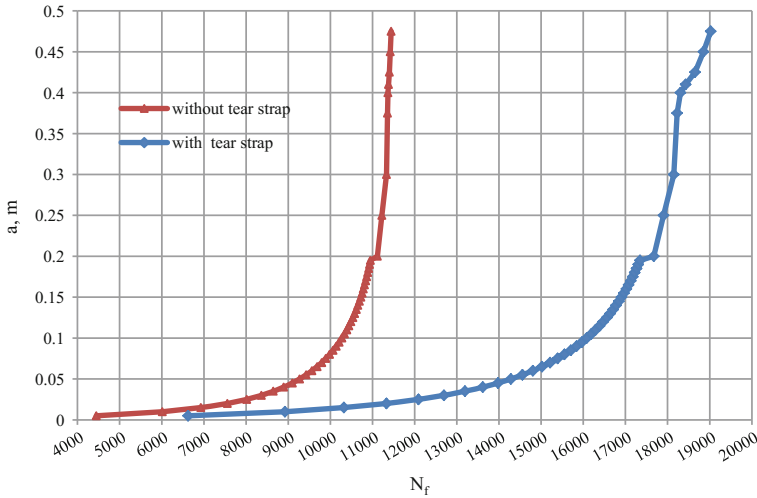


Fig. 9 Fatigue failure plot for a flat stiffened panel without and with tear strap

5.4 Fatigue Life Calculation for Progressive Crack Lengths

Fatigue life was estimated for crack lengths ranging from 5 to 450 mm. Number of life cycles required to reach the corresponding crack length were calculated for a stiffened panel without and with tear strap. A plot of number of cycles required to attain various crack lengths was plotted as shown in Fig. 9 for a flat stiffened panel without and with tear strap. In case of a flat stiffened panel without tear strap curve is varying linearly, once it crosses the bulkhead there is a small increment in the number of cycles required to attain the further crack lengths. In case of a flat stiffened panel with tear strap, once the crack reaches the tear strap position, there is an increment in the life of a panel which is indicated from the graph. The life of a panel with tear strap is almost 50% higher than that of a panel without tear strap.

6 Conclusion

In the present work, a detailed study of a flat stiffened panel was carried out in order to make the structure to be damage tolerant. Initially, a flat stiffened panel was subjected to tensile load corresponding to pressure of 0.062 MPa to identify the maximum stress location region in the panel. Effect of tear strap was studied, and SIF values are estimated for the flat stiffened panel without and with tear strap for progressive crack lengths. In the later stage, fatigue life estimation was carried out

with both the configurations of the panel to demonstrate the effect of tear strap in slowing down the crack growth of the panel.

- Stress analysis of the stiffened panel was carried out and maximum tensile stress was identified at the rivet hole of skin. Center longitudinal crack was initiated from rivet location of skin.
- Fatigue crack propagation was estimated by using stress intensity factor approach. Stress intensity factor calculations were carried out for various incremental cracks from 5 to 500 mm. The maximum value of stress intensity factor $28.67 \text{ MPa}\sqrt{m}$ was observed at crack length of 500 mm. After introducing tear strap, the value of SIF was $2.3 \text{ MPa}\sqrt{m}$ at crack length of 50 mm and increased to $18 \text{ MPa}\sqrt{m}$ at crack length of 500 mm and finally decreases to $13 \text{ MPa}\sqrt{m}$ at frame location. This SIF value is much less than the fracture toughness of material. Using tear strap, the crack propagation in the stiffened panel was found to be reduced by 50%.
- The fatigue life without the tear strap showed 11,440 cycles at the crack length of 475 mm, whereas the life for the same crack length with the tear strap showed 19,024 cycles. An increase in the fatigue life of 7584 cycles was observed by providing the tear strap in the bulkhead region. From this, it is conclude that the tear strap is used to slow down the fast fracturing longitudinal crack much effectively.

Acknowledgements The authors thank Director, NAL, and the Head, STTD, NAL, Bangalore for their support and encouragement during this work. The Principal and Head, Department of Mechanical Engineering, K.S. School of Engineering and Management, is thanked for their support and guidance during the course of this work.

References

1. G. Bibel, Fuselage metal fatigue in large commercial aircraft. *Int. J. Forensic Eng.* **1**(1), 47–57 (2012)
2. P.M. Toor, On damage tolerance design of fuselage structure (longitudinal cracks). *Eng. Fract. Mech.* **24**(6), 915–927 (1986)
3. T.K. Hellen, The finite element calculations of stress intensity factors using energy techniques, in *2nd International Conference on Structural Mechanics in Reactor Technology*, Paper G5/3 (Berlin, 1973)
4. D.M. Parks, A stiffness derivative finite element technique for determination of crack tip stress intensity factors. *Int. J. Fract.* **10**, 487–501 (1974)
5. K.N. Shivakumar, I.S. Raju, An equivalent domain integral method for three-dimensional mixed-mode fracture problems. *Eng. Fract. Mech.* **42**(6), 935–959 (1992)
6. E.F. Rybicki, M.F. Kanninen, A finite element calculation of stress intensity factors by a modified crack closure integral. *Eng. Fract. Mech.* **9**, 931–938 (1977)
7. A. Leski, Implementation of the virtual crack closure technique in engineering FE calculations. *Finite Elem. Anal. Des. (Polish Air Force Institute of Technology, Poland)* **43**(6), 261–268 (2006)

8. N. Muthu, B.G. Falzon, S.K. Maiti, S. Khoddam, Modified crack closure integral technique for extraction of SIFs in mesh free methods. *Finite Elem. Anal. Des.* **78**, 25–39 (2014)
9. D. Xie, S.B. Biggersjr, Progressive crack growth analysis using inter face element based on the virtual crack closure technique. *Finite Elem. Anal. Des.* **42**, 977–984 (2006)

Failure Analysis of a Squirrel Cage Bearing of a Gas Turbine Engine

Swati Biswas, Jivan Kumar, V. N. Satishkumar
and S. N. Narendra Babu

Abstract Premature failure of a squirrel cage bearing of a developmental aero-engine was encountered during its structural test. Four ribs (out of 12) in the cage were fractured from both ends, and the rear flange was completely separated from the cage. One of the support bearings was also found fractured, and the other was damaged to a lesser extent. There were secondary damages to the other components in the test assembly. Fractographic analysis established fatigue failure of the ribs. Two crack fronts were originated from the diagonally opposite corners of the ribs indicating failure of the bearing cage under reverse bending fatigue loading condition. No metallurgical anomalies were present at the crack origin. The rear flange was separated from the bearing cage in shear mode of failure, whereas the support bearing outer race failure was by instantaneous overloads. Design modifications were introduced after thorough stress analysis of the component. Subsequently, no such failure incidents were encountered, and the modified design has been put into service.

Keywords Gas turbine engine · Bearings · Fatigue · Beach marks
Striations · Dimples

1 Introduction

Bearings are important components of an aircraft propulsion system that allows free rotation of shafts, discs and aerofoils [1]. Key characteristics required for the bearings [2] of jet engine main shaft are (i) suitability for high-speed rotation, (ii) operability in high temperature and (iii) high reliability. The bearing types for jet engine main shafts are mainly three-point contact ball bearings and cylindrical roller bearings. The three-point contact ball bearings support load in the axial and

S. Biswas (✉) · J. Kumar · V. N. Satishkumar · S. N. Narendra Babu
Gas Turbine Research Establishment, Defence Research & Development Organization,
Bengaluru 560093, India
e-mail: swati@gtre.drdo.in

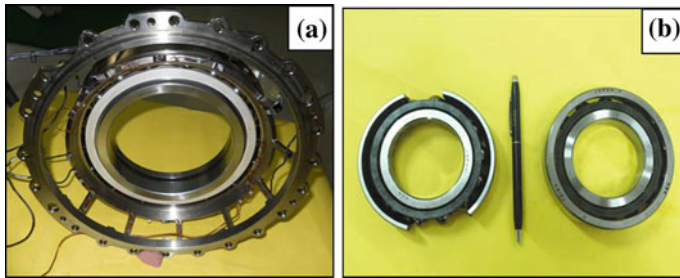


Fig. 1 Photograph showing **a** failed squirrel cage bearing; **b** two support bearings

radial directions. Different bearing manufacturers and agencies have documented the varied nature of bearing damage and failure of its various assemblies [3, 4]. Wear, fretting, pitting and corrosion are most commonly encountered problem for the inner and outer races and the rolling elements [5].

The present article describes analysis carried out on a failed roller bearing on a developmental engine. The squirrel cage bearing that supports the high pressure (HP) rotor in the aero-gas turbine propulsion system encountered failure during the structural integrity test (Fig. 1a). The component experiences high cyclic loads during operation, which comes from the unbalance loads on the structure. In order to validate the design of the component with respect to the structural integrity, the squirrel cage bearing was subjected to high-cycle fatigue test. However, the rear flange of the cage was separated from the ribs during the test. There were secondary damages to the other components of the test assembly. During dismantling, it was found that the one of the support bearings in the testing assembly has also fractured into three pieces along the outer race region, while the other support bearing was found to be slightly damaged at the inner circumference of the outer race (Fig. 1b). The material of the bearings was M50 NiL (AMS-6278A).

2 Observations

2.1 *Squirrel Cage Bearing*

2.1.1 Visual Observation

The bearing consisted of the inner race (IR), outer race (OR), front flange (FF), balls and rear flange (RF). The rear flange is connected to the main bearing by means of ribs. From the visual observation, it was found that out of total twelve ribs, all have failed from rear flange side. The mating fractured surfaces of both the ribs and corresponding region of the rear flange were severely damaged. It appeared most probable that the dislodgement of the rear flange from the squirrel cage was associated with the relative shear movement with respect to the connecting ribs

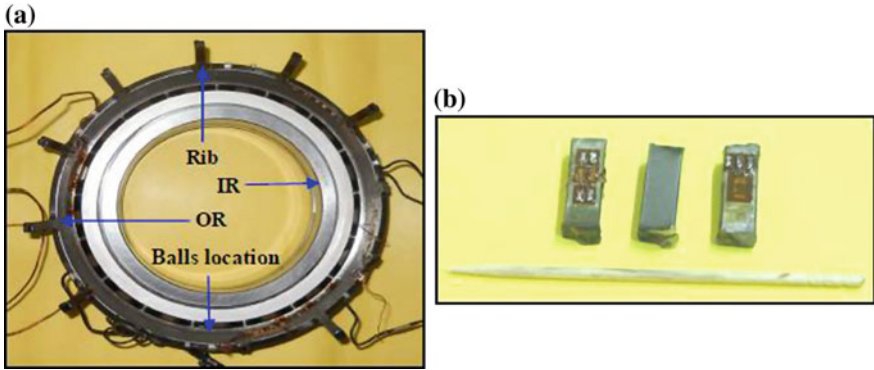


Fig. 2 Photograph showing **a** rib, inner race, outer race along with balls intact of the failed bearing cage; **b** the separated ribs

which would have caused the damage on mating fractured surfaces of the ribs and the flange. Four of the ribs failed from both the flange side and bearing side (Fig. 2b). However, three of them could be traced from the test assembly after the failure. The fractured surface of the ribs which failed from the bearing side was well preserved. Half of the inner race showed indication of overheating (Fig. 3).

2.1.2 XRF Analysis

Semi-quantitative chemical analysis was carried out on the bearing by using Portable XRF analyzer. The nominal composition details of the component are

Fig. 3 Photograph showing presence of overheated region (arrows) on the inner race surface

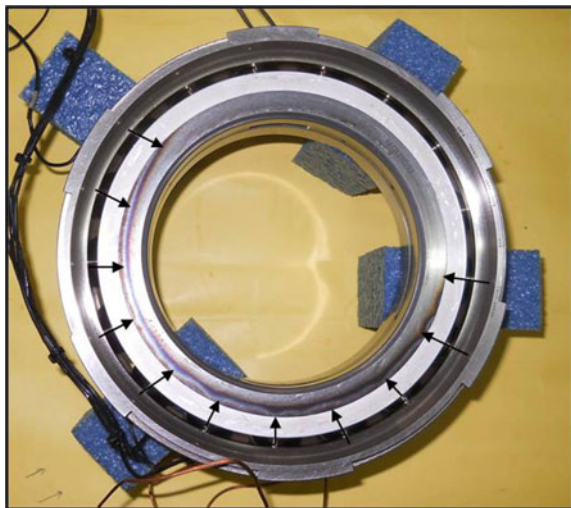


Table 1 Chemical composition of the component as per XRF

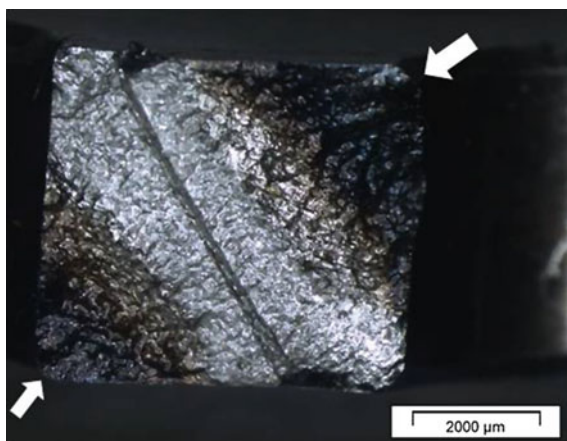
S. No.	Element	Wt (%) of #3 bearing	M50 NiL (ASTM standard)
1	Molybdenum	4.15	4
2	Vanadium	1.17	1
3	Nickel	3.42	3.5
4	Chromium	4.44	4
5	Carbon	–	0.15
6	Iron	Balance	Balance

presented in Table 1. The chemical composition of M50 NiL as per ASM Handbook [6] is listed in Table 1. Based on analysis, it was found that the material of the squirrel cage bearing showed a match with M50 NiL.

2.1.3 Stereo Zoom Microscopy

The fractured surface of one of the ribs (Fig. 4) of #3 bearing was observed under Stereo Zoom Microscope. The fractured surface revealed the presence of beach marks [7] (Fig. 4) indicating that the failure of the rib was in progressive mode. Tracing the orientation of the beach marks, two crack origins were identified; which were located at the two diagonally opposite corners of the rib (Fig. 4). Similar features were also observed on other two ribs fractured surfaces. It may be noted that failure of all the ribs was from same position, i.e. rib joint region to the bearing where chamfer is provided to avoid stress concentration. Macroscopic examination at the failure locations of the ribs was carried out on the bearing cage. Two other ribs indicated presence of crack near the rib-bearing joint (Fig. 5).

Fig. 4 Macrograph showing location of crack origins (arrows) and beach marks



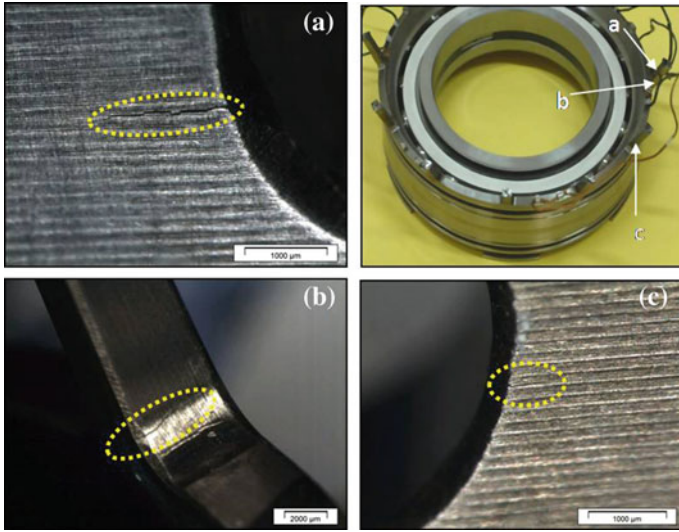


Fig. 5 Macrographs showing cracks (encircled) at two other ribs

2.1.4 Scanning Electron Microscopy for #3 Bearing Cage

A suitable piece was cut from the separated rib and was subjected to ultrasonic cleaning with acetone before the scanning electron microscope (SEM) examination on the fractured surface. Striations [7] (Fig. 6) were observed at higher magnification confirming that the failure of the rib was by fatigue crack initiation and propagation. Two independent fatigue crack fronts from two diagonally opposite corners were found to propagate towards each other. These two crack fronts were separated by a thin region (approximately 0.2 mm width) where dimples were observed (Fig. 7). This observation indicated that as the two fatigue crack fronts propagated from two diagonally opposite corners, the remaining cross section in between the two crack fronts kept on reducing and finally when the remaining area was unable to carry the load, it failed by overload. Distinct striations could be observed on the fractured surface covering almost 90–95% fractured surface. No metallurgical abnormalities (i.e. inclusions) were observed at the fatigue crack origin.

2.2 Support Bearings

2.2.1 Visual Observation

The outer race inner circumference surface of the failed support bearing showed presence of deformed and overheated region, as if the rollers have rubbed against

Fig. 6 Striations at higher magnification on the fractured surface of the rib

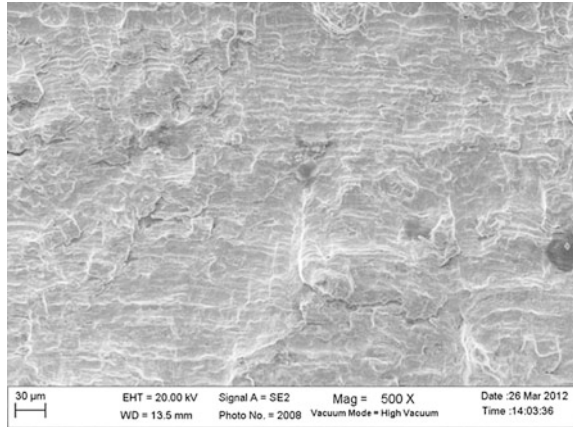
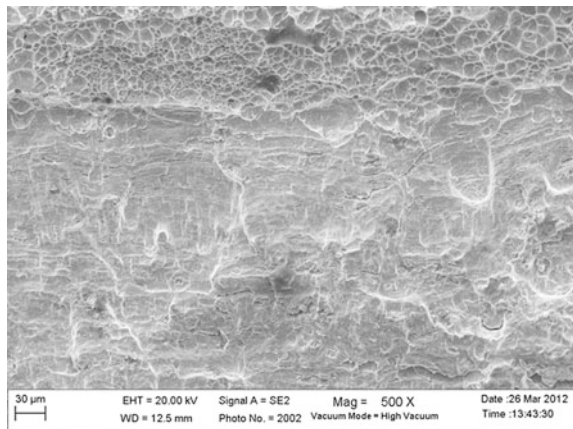


Fig. 7 Dimples (at the top of the frame) observed in between the two opposite fatigue crack fronts



the mating surface (Fig. 8a). Similar features were observed on the inner race as well (Fig. 8b). The cage supporting the ball bearings was crushed and separated into two pieces (Fig. 8c). A small deformed region was also observed on the inner circumference of the outer race of the other support bearing (Fig. 8d). Further, discolorations of the balls were observed in the failed support bearings (Fig. 9).

2.2.2 Scanning Electron Microscopy for Support Bearing

The fractured surface of the failed support bearing, as observed under scanning electron microscope, showed presence of dimples [8], indicating overload failure (Fig. 10).

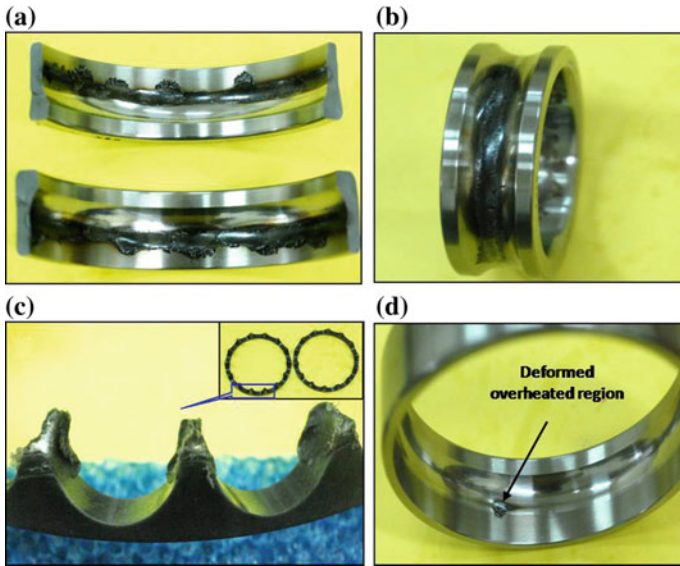


Fig. 8 **a** Photograph showing the deformed region in the inner circumferential region of outer race of failed support bearing; **b** overheated and deformed region on the outer circumference of inner race of failed support bearing; **c** fractured surface of the failed cage (inset) of support bearing; **d** deformed overheated region in the other support bearing

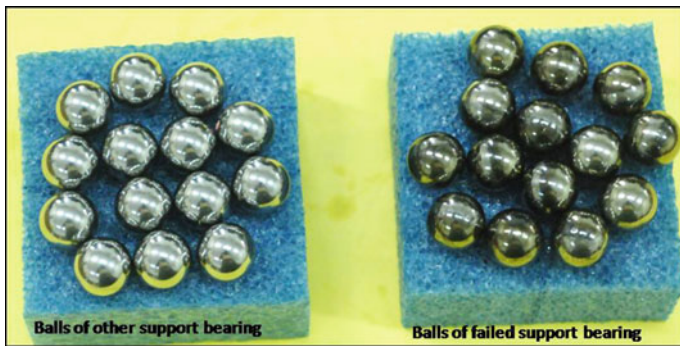
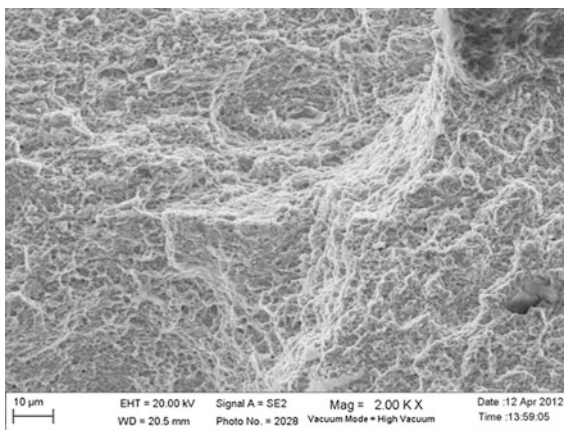


Fig. 9 Photograph showing discoloration in the balls of failed support bearing

Fig. 10 Fractured surface of the failed support bearing outer race showing presence of dimples



3 Analysis

Fractographic studies confirmed that three of the twelve ribs of the bearing cage have failed in progressive mode, i.e. by fatigue crack initiation and propagation from the bearing side. Cracks have originated from diagonally opposite corners of the rib and have propagated inward towards the centre of the surface. 90–95% of the fractured surface of the ribs showed a smooth region of fatigue crack propagation followed by final fracture due to overload. The overload region was confined to thin strip region of approximately 0.2 mm width. Cracks were also identified at the similar location of two more ribs connecting the flange with the bearing. The locations had sharp corners which are associated with stress concentration regions and are normally prone to develop fatigue crack initiation sites. Existence of fatigue crack origins at two opposite corners indicated that the bearing cage was subjected to reverse bending fatigue loading during testing [7–9]. Such operating condition may arise in two situations, (i) misalignment in the assembly and (ii) design deficiency. The roller bearing in the present case experiences high axial load during operation, while the centrifugal loads due to high rotational speed contribute to the radial loads. Under such operating condition, a slight misalignment is expected to introduce reverse bending fatigue loading [10] on the structural element of the bearing, which is the cage in the present case. However, health monitoring parameter like vibration did not indicate any abnormality in the signal. Therefore, possibility of the misalignment leading to failure was ruled out. Stress analysis on the component at a later stage revealed higher than expected imbalance load at the failure location. Overload failure of the outer race of one of the support bearings and the crushed cage indicates possible application of sudden load leading to the failure of this part.

4 Conclusion and Recommendations

Based on the analysis, it is concluded that the few of the ribs in the squirrel cage bearing failed by fatigue crack initiation and propagation. The failure of the ribs occurred under the reverse bending fatigue loads. The failure of the ribs resulted in instantaneous redistribution of the applied load causing the flange to dislodge from the bearing as well as failure of the outer race of the support bearing.

Design modifications were introduced after thorough stress analysis of the component. Subsequently, no such failure incidents were encountered, and the modified design has been put into service.

Acknowledgements The authors express their gratitude to DRDO and Director, GTRE, for supporting the work and granting permission to publish the data. The support and guidance provided by the Technical and Associate Directors and the help extended by the Structural Mechanics Group and NDT-Quality Assurance Group in completing the analysis also gratefully acknowledged.

References

1. R. Rzadkowski et al., Analysis of middle bearing failure in rotor jet engine using tip-timing and tip-clearance techniques. *Mech. Syst. Signal Process.* **76–77**, 213–227 (2016)
2. T. Nishikawa, N. Hayashi, A. Hayakawa, Technical trend of aircraft bearings. *NTN Tech. Rev.* **82**, 83–87 (2014)
3. *Bearing Failure: Causes and Cures, Technical Brochure, Barden Precision Bearings* (2007) pp. 1–15
4. *Ball & Roller Bearings: Failures, Causes and Countermeasures*, CAT. NO. B300 1 E (2009) pp. 1–20
5. *ASM Handbook, Properties and Selection: Irons, Steels, and High Performance Alloys*, vol. 1 (2005)
6. *Aircraft Turbine Engine Reliability and Inspection Investigations*, AD-A274 860, DOT/FAA/CT-92/29 (U.S. Department of Transportation, Federal Aviation Administration, 1993)
7. *ASM Handbook, Failure Analysis and Prevention*, vol. 11 (2002)
8. *ASM Handbook, Fractography*, vol. 12 (1987)
9. *ASM Handbook, Fatigue and Fracture*, vol. 19 (1996)
10. P.P. Milella, *Fatigue and Corrosion in Metals* (Springer-Verlag Italia, 2013). doi:https://doi.org/10.1007/978-88-470-2336-9_2

Part II
Civil Structures

On-line Deformation Monitoring of Building Estate Above Mining

R. Tsvetkov, Igor Shardakov, A. Shestakov and V. Yepin

Abstract Mineral extraction and mine flooding cause rock deformation and subsidence of ground surface. Also it causes deformation and damage to structures and buildings located on this surface. The paper presents deformation monitoring of estate above mining. This system monitors vertical displacement (settlement) of building foundations by the method of hydrostatic leveling. The monitoring data allow to estimate the deformation of buildings and to evaluate changes in the tilt of the ground surface at the location of the buildings. The article presents the results of settlements of the buildings and the tilt of the ground surface over the 2 years of observations. The obtained data are the basis for the analysis of the evolution of deformation parameters, forecast implementation and correction of rock mass behavior models.

Keywords Deformation monitoring · Ground surface subsidence
Hydrostatic level

Nomenclature

S Settlement or vertical displacement
 $\delta S_{i,j}$ Differential settlement between points i and j
 β Angular distortion
 ω Tilt
 k Curvature

R. Tsvetkov (✉) · I. Shardakov · A. Shestakov · V. Yepin
Institute of Continuous Media Mechanics UB RAS, 1, Korolev Street, 614013 Perm, Russia
e-mail: flower@icmm.ru

© Springer Nature Singapore Pte Ltd. 2018
R. Prakash et al. (eds.), *Advances in Structural Integrity*,
https://doi.org/10.1007/978-981-10-7197-3_11

1 Introduction

The world economy constantly requires new natural resources which have led to increases in mineral extraction, such as oil, coal or potash. Sometimes, mines are located under building estate. Mineral extraction causes rock deformation and ground surface subsidence. Also it causes deformation and damage to structures and buildings located on this surface. Mine flooding increases these deformation processes, and sinkholes may appear on the ground surface. For example, this problem is described for the Verkhnekamsk salt deposit in [1]. To control geomechanical processes of rock massif, different monitoring methods are required: geomechanical [2], microseismic [3], and geochemical [4]. Monitoring of ground surface subsidence is very important. Monitoring of ground surface can be done by instrumental observations with extensometers [5]; by GPS (GNSS) [6, 7], by satellite radar interferometry [8]. GPS detect quasi-static displacements of several numbers of points with an accuracy of 3–4-mm GPS and instrumental observations provide low-spatial resolution. Satellite radar interferometry (SAR) allows controlling a large area, but it is less often (one time per two weeks). The accuracy of the observations depends on the trajectory of the satellite in orbit and atmospheric precipitation (snow). Therefore, SAR is not applicable for monitoring in the winter time. Some buildings and structures that are located on land surface are equipped with continuous deformation monitoring systems. This monitoring systems work at any time of the year.

The aim of this work is the assessment of ground surface and rock massif based on deformation monitoring data of building groups. This method of land surface monitoring can be carried out continuously at any time of the year. This information allows to verify monitoring data of rock massif monitoring, obtained by other methods and to forecast a ground surface tilt.

2 Deformation Monitoring of Buildings

2.1 Measurement System

The foundation movement is the main reason of building damage. The measurement system has to control the foundation displacement. Vertical displacement of the foundation (or settlement) can be measured by the hydrostatic leveling method [9]. This method controls the difference in vertical displacements of points where sensors are installed. To measure the field of vertical displacements, it is possible to use a multipoint hydrostatic leveling system with a necessary number of sensors. The paper [10] describes the main aspects of using measurement systems for controlling the differential settlements and estimates of the accuracy of this measurement technique as (± 0.5 mm).

Considering the design features of each building, positions of the sensors were chosen. Installation of monitoring system components is carried out in the interior basements that reduced the influence of environmental conditions. These systems have been installed in more than 30 buildings that were located at several parts of the massif.

2.2 *The Approach of Estimation of a Deformation State of the Building*

The assessment of the safe operation of the building can be carried out based on various criteria: estimating differential settlement $\delta S_{i,j}$ or angular distortion $\beta_{i,j}$. Differential (non-uniform) settlement is defined as the difference between vertical displacements of two points where sensors are located. Angular distortion between i and j sensors, having distance $L_{i,j}$, is determined by the formula:

$$\beta_{i,j} = \frac{\delta S_{i,j}}{L_{i,j}} \quad (1)$$

According to reference [11], the greatest tolerable differential settlement is 45 mm for a clayey soil and maximum angular distortion for buildings is 1/300.

The deformation assessment is also possible by calculating the change of curvature of foundation section between three foundation points where sensors are installed. The curvature of the building foundation between sensors $i-1$, i , and $i+1$ is:

$$k = \frac{2 \cdot \delta S_{i-1}}{L_{i-1,i} \cdot L_{i+1,i-1}} - \frac{2 \cdot \delta S_i}{L_{i-1,i} \cdot L_{i,i+1}} + \frac{2 \cdot \delta S_{i+1}}{L_{i+1,i-1} \cdot L_{i,i+1}} \quad (2)$$

where δS —vertical displacements (settlements) of the sensors; L —distance between the sensors.

In addition, based on the finite element modeling, it is possible to estimate the change in the stress–strain state of building elements, using the measured values of vertical displacements at the sensor location points.

2.3 *Results of Deformation Monitoring of the Building*

Several buildings have deformation monitoring systems. For example, consider a typical 3-story brick building (length—30 m, width—12 m). The position of this building on the terrain is shown in Fig. 1a marked as number 1. The location of the sensors in the building foundation is shown in Fig. 1b. The sensors are placed on

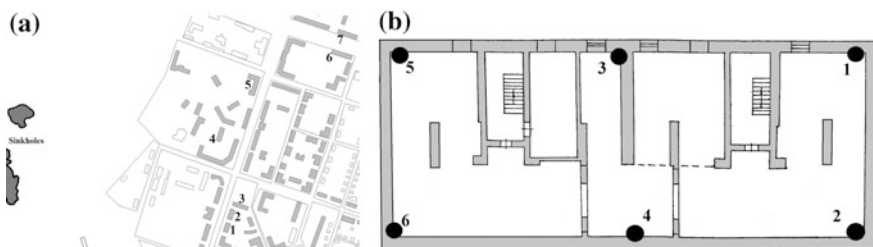


Fig. 1 The position of the buildings on map (a), the location of the sensors (b)

the building perimeter, including basement corners where ground movements may potentially represent danger.

The continuous monitoring of building started in 2014 and continues today. Evolutions of vertical displacements (or differential settlements) at the sensors are shown in Fig. 2a. The maximal settlement difference is about 14 mm for 2 years. The diagrams show that the settlements occur at constant rates. Maximal differential settlement rate (between sensor No. 5 and No. 2) is 0.5 mm per month.

Figure 2b shows changes in angular distortion of the foundation part between the sensors, and Fig. 3 shows change of the line curvature of the foundation, between the 3 sensors (1–3–5 and 2–4–6).

The submitted data demonstrate that differential settlements and angular distortions of the building foundation are increasing. However, the curvature of the building foundation changes slightly. A certain number of buildings observed exhibit similar behavior.

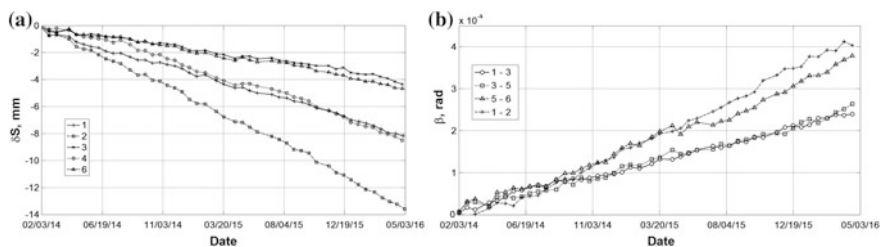


Fig. 2 Differential settlements at the sensor location points (a), changes in angular distortion of the foundation (b)

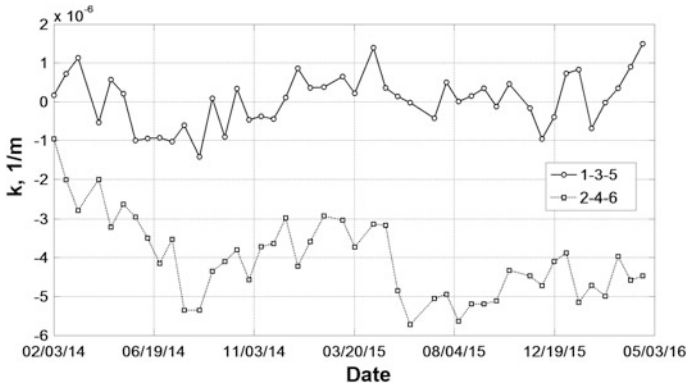


Fig. 3 Change of the curvature of the building foundation

3 Rock Massif Monitoring

3.1 Estimation of Change in the Tilt of the Ground Surface

Local hydrostatic level systems are unable to give absolute values of vertical displacements of buildings and give only the differential settlement of foundations, which are localized in certain parts on the surface of the rock massif. Since the size of buildings is less than a massif and magnitudes of curvature change slightly, let us consider each building as a rigid element. According to this approximation, we estimate the tilt of the building foundation, which is equal to the tilt of the part of the ground surface under the foundation.

On the basis of the sensor positions in the building foundation (x_i, y_i) and changes in vertical displacements for the appropriate time interval, calculation of coefficients of the plane equation characterizing a building tilt was made by the ordinary least squares method.

$$a \cdot x + b \cdot y + c \cdot z + d = 0 \tag{2}$$

Using the calculated coefficients $(a, b, \text{ and } c)$, tilt angle ω between the calculated plane and the reference plane $(0, x, \text{ and } y)$ was estimated:

$$\cos \omega = \frac{1}{\sqrt{(a/c)^2 + (b/c)^2 + 1}} \tag{3}$$

Also, the angle α characterizing the tilt direction in the coordinates system associated with the building was calculated:

$$\operatorname{tg} \alpha = \frac{b}{a} \quad (4)$$

Accuracy of the surface tilt measurement depends on accuracy of the hydrostatic leveling system, number of sensors and building size. For this case, accuracy is about 0.00002 rad.

3.2 Results

The calculation of the tilt change was made for each building with a monitoring system. Figure 4a presents the map of building estate with monitored buildings marked with numbers 1–7. The arrows associated with buildings represent the projection of the normal to the ground surface under the building onto the horizontal plane. The arrow direction corresponds to the direction of a tilt of a normal, and the arrow length is proportional to the tilt value. The change in the tilt for 1-year observation is shown in Fig. 4a.

On this part of the massif, the tilt of the buildings and ground in the direction of existing sinkholes which are in the left part of the figure is observed. The closer the building to a sinkhole is located on the surface tilt is observed more intensively. The obtained results show that it is also possible to estimate tilts of the constructions located close to the buildings equipped with monitoring systems.

Figure 4b presents the evolution of the change in the ground surface tilt at locations corresponding to the location of the buildings. The diagram shows that the building tilt rate varies slightly with time. It is possible to notice some increase rates of a tilt of the buildings located closer to sinkholes. Observation of a stable tilt rate and direction angle for several years allows us to make a several month forecast.

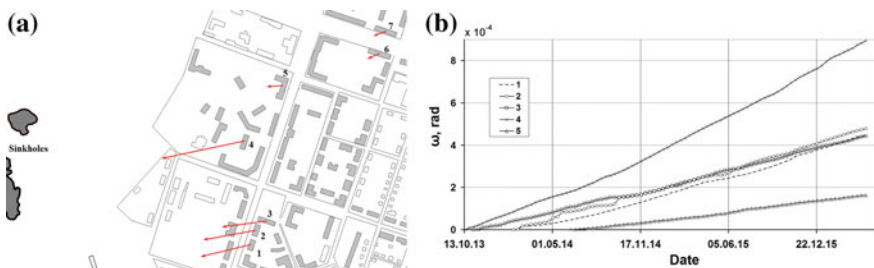


Fig. 4 The change in the tilt of the buildings for 1 year (a) and evolution of the building tilts (b)

4 Conclusion

The presented results show that it is possible to monitor the ground surface above mining using deformation monitoring data of buildings. This procedure is done all year round, as well as deformation monitoring of buildings. The estimate of the accuracy of slope measuring is about 0.00002 rad. This experimental results can supplement the measurements obtained by other geodetic measuring systems and can also be used to verify models that describe ground subsidence above mining [1].

Acknowledgements This research was performed under the grant of the Russian Science Foundation (grant № 14-29-00172).

References

1. A.A. Baryakh, SYu. Devyatkov, N.A. Samodelkina, Theoretical explanation of conditions for sinkholes after emergency flooding of potash mines. *J. Min. Sci.* **52**, 36–45 (2016)
2. Z. Kalab, Lednicka long-term geomechanical observation in the Jeronym Mine. *M. Acta Geophys.* **64**, 1513–1524 (2016)
3. D. Amitrano et al., Microseismic activity analysis for the study of the rupture mechanism in unstable rock masses. *Nat. Hazard Earth. Syst. Sci.* **10**, 831–841 (2010)
4. B.A. Bachurin, A.A. Borisov, Gas-geochemistry approach to monitoring mining-induced genesis processes in the geological environment of the Upper Kama Potassium Salt Deposit. *J. Min. Sci.* **47**, 861–866 (2011)
5. J.M. Pardo et al., Instrumental monitoring of the subsidence due to groundwater withdrawal in the city of Murcia (Spain). *Environ. Earth Sci.* **70**, 1957–1963 (2013)
6. F. Mancini et al., Monitoring ground subsidence induced by salt mining in the city of Tuzla (Bosnia and Herzegovina). *Environ. Geol.* **58**, 381–389 (2009)
7. H. Zhao, F. Ma, Y. Zhang, J. Guo, Monitoring and mechanisms of ground deformation and ground fissures induced by cut-and-fill mining in the Jinchuan Mine 2. *Environ. Earth Sci.* **68**, 1903–1911 (2013)
8. D. Walter et al., in Radar interferometric monitoring of sinkhole formations above a flooded potash mine in Berezniki Russia. *Proceedings XV International ISM Congress, (Clausthal-Zellerfeld 2013)*, pp. 136–153
9. E. Meier et al., Hydrostatic levelling system: measuring at the system limits. *J. App. Geodesy.* **4**, 91–102 (2010)
10. I.N. Shardakov, A.P. Shestakov, R.V. Tsvetkov, V.V. Yepin, The hydrostatic level method for continuous monitoring of building foundations. *SSP* **243**, 105–111 (2016)
11. J.E. Bowles, *Foundation analysis and design* (McGraw-Hill Companies, Singapore, 1997)

Mechanical Properties of Nano Concrete

Ajaysinh R. Vaghela and Gaurang R. Vesmawala

Abstract Nano materials have recently been introduced as an advanced pozzolana to improve the microstructure and stability of the cement-based system. This paper presents the effect of the addition of nano materials on the mechanical properties of concrete. To compare the different nano materials total three nano materials were taken along with polypropylene fiber. Nano silica and nano alumina were taken as 1, 2, 3, 4, and 5%; carbon nanotube was taken as 0.1, 0.2, 0.3, 0.4, and 0.5% of cementitious material. Further, nano silica and nano alumina were mixed with polypropylene fiber to check the combination of powder and fiber material. Mechanical tests such as compression test, indirect tensile test, and flexure test were performed to find mechanical properties. Results show an increase in compressive, tensile, and flexural strength with the addition of nano materials.

Keywords Carbon nanotubes · Cement composite · Concrete · Fiber reinforcement · Mechanical properties · Fracture mechanics

1 Introduction

Nanotechnology in the construction industry is a new area where the majority of research interest is focused. Nanotechnology is the most modern technology which has its roots of origin and growth in last decades.

Due to increasing demand of concrete (about 2 billion tons per year), total production of cement is also increasing which has very high amount of carbon dioxide emission. It is expected that this value would go even higher and will go up

A. R. Vaghela (✉) · G. R. Vesmawala
Department of Applied Mechanics, Sardar Vallabhbhai National Institute of Technology,
Ichhanath, Surat 395007, Gujarat, India
e-mail: vaghelaajay11111@gmail.com

A. R. Vaghela
G H Patel College of Engineering and Technology, Vallabh Vidya Nagar 388120,
Gujarat, India

to 4 times than what was in 1990 [1]. One possibility of reducing the emission of CO_2 is manufacturing of strong concrete which allows to use less amount of concrete for construction. To increase, the strength researchers have tried different supplementary materials to cement. It is considered that nanotechnology is one of the main research areas which can improve the concrete properties, i.e., strength and durability.

Nanoparticles quicken C–S–H gel creation as an aftereffect for expanded crystalline $\text{Ca}(\text{OH})_2$ amount particularly at the initial period of hydration and increase the strength of the concrete [2]. Researchers have shown that among largely available materials, SiO_2 and Al_2O_3 exhibit more effect on mechanical properties of concrete [3]. Nano silica and nano Alumina increase compressive strength and decrease water absorption with different % of nanoparticles [4]. Nano Silica (5% by weight of cementitious materials) improves durability parameters of concrete more as compared to nano alumina (3% by weight of cementitious materials), i.e., compressive strength and frost resistance increased up to 30 and 83%, respectively, for nano Silica as compared to 8 and 81%, respectively, for Nano Alumina [5]. Nano Silica, nano alumina, and their combination increase surface hardness as well as abrasion and fracture resistance [6] which prove their applicability for improving the fracture toughness of concrete. Nano Silica also increases electrical resistivity of concrete about 100–150% [7].

Apart from widely famous nano materials carbon nanotubes (CNT) also gained popularity due to their unique properties. CNTs have very high Young's modulus, high strength, and high electrical and thermal conductivity. CNTs allow the development of materials with enhanced performance characteristics. Researchers have found that addition of nanotubes affected the structure of cement hydration products, both the initial C_3A and C_3S hydration products. They also observed that CNTs accelerate the rate of hydration process by acting as a matrix for the development of C–S–H and $\text{Ca}(\text{OH})_2$ produced during the hydration [8]. Presence of oxygen-containing groups on the surface of CNTs makes possible chemical reaction between CNTs and the cement matrix [9]. CNTs go about as nucleating agent in cement hydration which increases the possibilities of reaction to occur and increases the formation of reaction products [10]. It is important to increase the flexure strength of concrete since the same would result in increased fracture toughness of the material.

In this paper, the compressive strength, tensile strength, and flexure strength of concrete containing various proportions of nano Silica (NS), nano Alumina (NA) and carbon nanotubes (CNT) are presented. Moreover, combination of NS and NA with polypropylene fiber is also checked.

2 Experimental Program

2.1 Material Used

Ordinary Portland Cement of 53 grade was used in the study. Sand from river having fineness modulus of 2.82 was used as fine aggregate. Coarse aggregate of maximum size 20 mm was used. Multiwall carbon nanotubes (MWCNTs) purchased from Cheap Tubes (USA), nano Alumina purchased from Advanced Technology Materials (Mumbai, India), and nano Silica purchased from Adinath Industries (Ajmer, Rajasthan, India) having properties as shown in Table 1 were used in the work. The transmission electron microscope image of the MWCNT and nano Alumina is also presented in Fig. 1.

Table 1 Properties of MWCNTs, nano silica, and nano alumina

Property	MWCNTs	Nano silica	Nano alumina
Appearance form	Powder	Powder	Powder
Purity	90%	98%	>99.8%
Outer diameter	20–40 nm	15–30 nm	40–75 nm
Inner diameter	5–10 nm	–	–
Length	10–30 μm	–	–
Specific surface area	>110 m^2/g	–	20–30 m^2/g
Bulk density	0.07 g/cm^3	–	–
True density	$\sim 2.1 \text{ g}/\text{cm}^3$	–	–

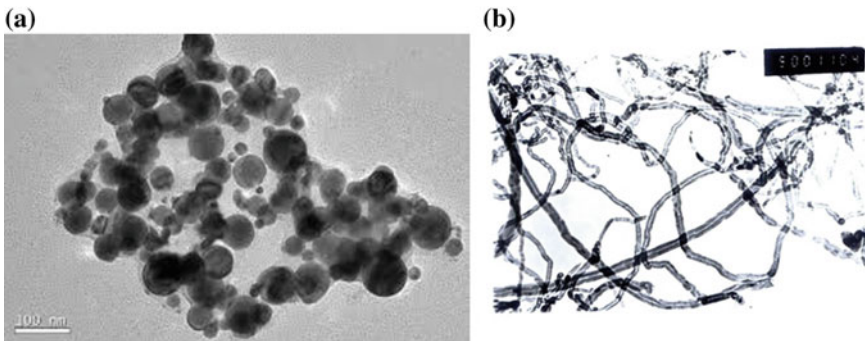


Fig. 1 a TEM image of nano alumina and b TEM image of CNT (by the manufacturer data sheet)

Table 2 Mix proportions

Material	Quantity
Cement	450
Water	180
Coarse aggregate	1121.208
Fine aggregate	659.604
Admixture	0

2.2 Mix Proportions

Mix proportion of ordinary concrete was done by IS: 10262-2009, and the quantities of different materials were obtained as shown in Table 2. Nano materials were taken as % by weight of cement. Totally 17 different mixes were taken into consideration. Nano Silica and nano Alumina were taken in 5 different proportions, i.e., 1, 2, 3, 4, and 5% by weight of total cementitious materials. CNTs were taken as 0.1, 0.2, 0.3, 0.4, and 0.5% by weight of total cementitious materials. The higher percentage of CNTs were taken to check the behavior of concrete with increased pozzolana. Moreover, combinations of nano silica and nano alumina with polypropylene fiber were also taken. Nano silica and nano alumina were taken as 3 and 2% of total cementitious material with 0.2% of polypropylene fiber.

2.3 Testing Procedure

For compression test of concrete, cubes were prepared for each mix with dimension 15 cm × 15 cm × 15 cm according to IS:516-1959. Three cubes were prepared for each test day and for each mix. Cubes were tested at 7, 14, and 28 days. Indirect tensile test specimens were prepared for each mix having a cylindrical shape with dimension 15 cm diameter × 30 cm length according to IS:5816-1999. Cylinders were tested at 28 days for tensile strength. For flexure, beams were prepared for all mix having dimensions 10 cm × 10 cm cross section with a 50 cm length according to IS:516-1959.

Calculation based on peak load for indirect tensile strength and flexure strength was done with following Eqs. (1) and (2), respectively.

$$f_{ct} = \frac{2P}{\pi ld} \quad (1)$$

where,

P Maximum load applied in N,

d Cross-sectional dimension of the specimen in mm, and

l Length of the specimen in mm.

$$f_b = \frac{P \times l}{b \times d^2} \tag{2}$$

where,

P Maximum load applied in kg,

b Measured width of the specimen in cm,

d Measured depth of the specimen at failure point in cm, and

l Length or span on which the specimen is supported in cm.

3 Result and Discussion

3.1 Compressive Strength

Compressive strength of nano concrete at 7, 14, and 28 days is shown in Table 3. The values are the average of 3 cube strength at each testing day. It can be found that the compressive strength of nano concrete increases in almost all cases as compared to ordinary concrete.

Table 3 Compressive strength of specimen (*f_c*) in MPa

Mix	Compressive strength at 7 days in MPa		Compressive strength at 14 days in MPa		Compressive strength at 28 days in MPa	
	<i>f_c</i>	Enhanced extent (%)	<i>f_c</i>	Enhanced extent (%)	<i>f_c</i>	Enhanced extent (%)
PC	36.7	0.00	43.5	0.00	49.2	0.00
NS1	37.2	1.36	41.8	1.61	51.2	4.07
NS2	39.2	6.81	44	1.15	53.8	9.35
NS3	40.3	9.81	49.2	13.10	58.7	19.30
NS4	36.4	0.27	44.2	1.61	52.6	6.91
NS5	38	3.54	46.6	7.13	53.8	9.35
NA1	35.2	0.54	44.8	2.99	50.6	2.85
NA2	38.8	5.72	49.6	14.02	56.5	14.84
NA3	36.6	0.27	48.6	11.72	53.8	9.35
NA4	37.3	1.63	46.2	6.21	52.4	6.50
NA5	36.8	0.27	49.3	13.33	54.7	11.18
CNT0.1	36.6	0.54	45.3	4.14	52.7	7.11
CNT0.2	36.9	0.54	48.2	10.80	54.3	10.37
CNT0.3	38.2	4.09	47.5	9.20	56.3	14.43
CNT0.4	37.8	3.00	49.2	13.10	57.2	16.26
CNT0.5	38.3	4.36	48.2	10.80	58.5	18.90
NS3PF0.2	37.8	3.00	46.9	7.82	53.2	8.13
NA2PF0.2	36.7	0.00	45.8	5.29	52.6	6.91

Concrete-containing nano silica increases the strength up to 9.81 and 19.30% for 7 and 28 days, respectively. The reason for increased strength is pozzolanic reaction of nano silica. Nano materials react with calcium hydroxide $\text{Ca}(\text{OH})_2$ crystals which form C–S–H gel. Nano materials also act as a filler of voids in concrete which makes concrete denser. It can be seen from the Table 3 that the optimum dose of nano silica in concrete is 3% by weight of all cementitious materials as results beyond 3% decrease with further increase in nano silica content. Decrease in strength may be due to increase in weak zones in concrete with increased nano silica content as it imparts negative effects on hydration process. Nano alumina also shows same behavior as nano silica with maximum dosage of nano Alumina found as 2%.

Addition of MWCNTs increases the formation of C–S–H gel resulting in stronger material. The reason for increased strength could be possession of voids by MWCNTs particles which resist loading. Moreover, it makes concrete denser which increases its crack resistivity. For MWCNTs, increases in the strength were reported as 18.90% as compared to ordinary concrete.

3.2 Tensile Strength

Table 4 shows values of tensile strength for nano concrete with all mixes, and result increases in all cases. MWCNTs addition is found to be suitable as far as tensile strength is concerned. The increase in tensile strength as compared to ordinary concrete is up to 69.57%. This is mainly because of the large modulus of elasticity of MWCNTs which increases stress carrying capacity of concrete. Similar results have been reported by other researcher [3]. For other nano materials, the increase in tensile strength is not as higher as MWCNTS but an increase in tensile strength can be seen up to an extent. For combination of nano silica and nano alumina with polypropylene fibers stand beneficial as compression as well tensile strength also increase with combination.

3.3 Flexural Strength

Flexural test results of all specimens at 28 days are shown in Table 5. Results show same behavior of nano material in flexure as in compression. Nano silica and nano alumina show same optimum dosage of 3 and 2%, respectively, for flexure as well.

Table 4 Tensile strength of specimen (f_{ct}) in Mpa

Mix	Tensile strength in MPa	
	f_{ct}	Enhanced extent (%)
PC	2.3	0.00
NS1	2.5	8.70
NS2	2.6	13.04
NS3	3.1	34.78
NS4	2.7	17.39
NS5	2.2	-4.35
NA1	2.4	4.35
NA2	2.8	21.74
NA3	3.0	30.43
NA4	2.9	26.09
NA5	2.5	8.70
CNT0.1	2.9	26.09
CNT0.2	3.2	39.13
CNT0.3	3.5	52.17
CNT0.4	3.9	69.57
CNT0.5	4.2	82.61
NS3PF0.2	3.4	47.83
NA2PF0.2	3.2	39.13

Table 5 Flexural strength of concrete (f_b) in MPa

Mix	Flexure strength in MPa	
	f_b	Enhanced extent (%)
PC	5.8	0.00
NS1	6.1	5.17
NS2	6.5	12.07
NS3	7.2	24.14
NS4	7.0	20.69
NS5	6.9	18.97
NA1	5.9	1.72
NA2	6.6	13.79
NA3	6.4	10.34
NA4	6.2	6.90
NA5	6.3	8.62
CNT0.1	7.8	34.48
CNT0.2	8.6	48.28
CNT0.3	9	55.17
CNT0.4	9.3	60.34
CNT0.5	9.4	62.07
NS3PF0.2	8.2	41.38
NA2PF0.2	7.9	36.21

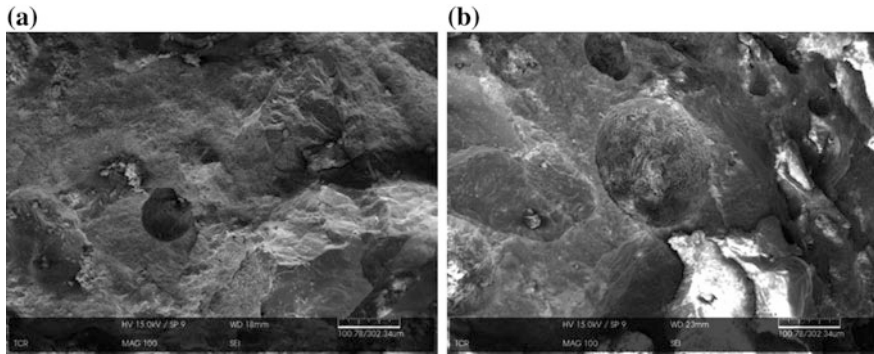


Fig. 2 a and b SEM images of MWCNTs

4 Conclusions

1. Content of nano silica increases compressive and flexural strength up to 3% by weight of cementitious material, and after further addition, strength decreases which give optimum dosage of nano silica as 3%.
2. Nano Alumina exhibits better compression, tensile, and flexural behavior as compared to ordinary concrete, but takes a back step in comparison with other nano material studied. The optimum dosage is found out to be 2% in compression only for nano alumina.
3. MWCNTs due to their high modulus of elasticity can withstand stresses more as compared to other nano materials studied. For improvement of tensile strength and Flexural strength, MWCNTs are the best available nano material.
4. Combination of nano silica and nano alumina with polypropylene fibers holds good as nano materials increase compressive strength and fibers increase tensile strength of concrete.
5. Increased flexural strength opens up a new scope for increasing fracture toughness of nano concrete using Nano silica, Nano Alumina, and MWCNTS.

References

1. The Concrete Conundrum, Chemistry World, March (2016). www.chemistryworld.org
2. A. Nazari, S. Riahi, The effects of SiO₂ nanoparticles on physical and mechanical properties of high strength compacting concrete. *Compos. B* **42**, 570–578 (2011)
3. K. Behfarnia, N. Salemi, The effects of nano-silica and nano alumina on frost resistance of normal concrete. *Constr. Build. Mater.* **48**, 580–584 (2013)
4. M. Oltulu, R. Sahin, Effect of nano-SiO₂ nano-Al₂O₃ and nano-Fe₂O₃ powders on compressive strengths and capillary water absorption of cement mortar containing fly ash. *Energy Build.* **58**, 292–301 (2013)

5. N. Salemi, K. Behfarnia, Effect of nano-particles on durability of fiber-reinforced concrete pavement. *Constr. Build. Mater.* **48**, 934–941 (2013)
6. N. Leon, Effect of nano-SiO₂ and nano-Al₂O₃ on cement mortars for use in agriculture and livestock production. *Biosystem engineering* **123**, 1–11 (2014)
7. H. Madami, A. Bagheri, T. Parhizkar, A. Raisghasemi, Chloride penetration and electrical resistivity of concretes containing nanosilica hydrosols with different specific surface areas. *Cem. Conc. Compos* **53**, 18–24 (2014)
8. T. Manzur, N. Yazdani, M.A.B. Emon, Effect of carbon nanotube size on compressive strengths of nanotube reinforced cementitious composites. *J. Mat.* **2014** (2014)
9. N. Zohadi, Functionalized graphitic nanoreinforcement for cement composites (University of South Carolina 2014)
10. S.G. Shah, S.G. Shah, Q.I. Barodawala, Nano modification of self compacting concrete. CTMC (2016)
11. Concrete Mix Design Revised, Ambuja technical literature series no. 79
12. *Design of High strength Concrete Mixes, Proceeding of a Symposium on Mix Design and Quality control of concrete.* (Cement and Concrete Association, London)
13. *Design of Normal Concrete Mixes.* (Department of the Environment, Building research Establishment, Walford, U.K. 1988)
14. IS: 10262, Concrete mix proportioning—guidelines (2009)
15. IS: 383, Specification for coarse and fine aggregates from natural sources for concrete (second revision) (1970), (reaffirmation, 1997)
16. IS: 516, Indian standard methods of tests for strength of concrete (1959), (reaffirmation, 1999)
17. IS: 5816, Splitting tensile strength of concrete—method of test (1999), (reaffirmation 2004)
18. M.S. Shetty, *Concrete Technology Theory and Practice.* (S. Chand publication 2009)

Estimation of Critical Microcrack Length in Concrete by Considering Interfacial Properties

Keerthy M. Simon and J. M. Chandra Kishen

Abstract Concrete is considered as a homogeneous material from a design perspective. However, on a close examination, it is observed that concrete is heterogeneous, which consist of coarse aggregate and fine aggregate embedded in cement paste. Further, there exists an interfacial region, which bonds the aggregate with the cement paste. The strength of this interfacial transition zone (ITZ) depends on its microstructural characteristics. This interfacial region neither possesses the properties of aggregate nor of the cement paste. Interface being the weakest zone, the microcracks are likely to initiate here when the local major principal stress exceeds the initial tensile strength of the interface. When these microcracks reach certain critical length, it propagates and coalesces with the existing macrocrack to form a major crack resulting in the failure of the bond. The microstructural character of the interfacial zone governs the mode I crack propagation in conventional concrete. The material behavior of concrete is influenced by the geometry, the spatial distribution, and the material property of the individual constituents and their interactions. This study aims at estimating the critical microcrack length using the principles of linear elastic fracture mechanics (LEFM) by analyzing the crack opening displacement at different scales. Also, a procedure to determine the material properties such as the elastic modulus and fracture toughness at the interface by knowing the concrete mix proportion is explained.

Keywords Concrete · Critical microcrack · Interfacial transition zone

1 Introduction

During mixing of concrete, the shearing stress exerted on the cement paste by the aggregates tends to separate water from cement particles and results in a small region around the aggregate particles with fewer cement particles termed as the ITZ

K. M. Simon · J. M. Chandra Kishen (✉)
Indian Institute of Science, Bangalore 560012, India
e-mail: chandrak@iisc.ac.in

© Springer Nature Singapore Pte Ltd. 2018
R. Prakash et al. (eds.), *Advances in Structural Integrity*,
https://doi.org/10.1007/978-981-10-7197-3_13

147

[1]. The composition of this zone was found to be different from that of cement paste as the density of cement particles was lesser than that of its surroundings. Although several techniques such as X-ray diffraction, X-ray photoelectron spectroscopy, secondary ion mass spectroscopy, mercury intrusion porosimetry, optical microscope, and electron microscope have been employed to study the ITZ, the complete characterization of the distinctive features of this zone has still not been achieved. The interface acts as a bridge between aggregate and the cement paste, which neither possesses the properties of aggregate nor the cement paste.

Upon loading, microcracking initiates in the ITZ when the local major principal stress exceeds the initial tensile strength of the interface [2]. Ansari [3] reported that the macrocrack would occur only when the microcrack reaches a critical length. This critical microcrack propagates and coalesces with existing macrocrack thereby resulting in the failure of the bond. The stiffness of the interface decreases although the individual components on either side of the interface possess high stiffness. This is due to the presence of voids and microcracks in this region, which do not allow the transfer of stress.

The packing and density of the cement particle around the aggregates define the strength of the interfacial zone. The strength of an interface decides whether a crack should grow around an aggregate particle or through the aggregate. Also, the fracture energy of the interface is found to be less than that of the cement paste and aggregate. The microstructural character of the interfacial zone governs the mode I crack propagation in concrete [4]. Thus, the material behavior of concrete is influenced by the geometry, the spatial distribution, and the material property of the individual material constituents and their mutual interaction. Hence, the failure of concrete structure can be viewed as a multiscale phenomenon, wherein the information of the material properties at a microlevel can be used to determine the system behavior at the macrolevel.

In this paper, the critical length of the microcrack present in the ITZ is estimated using the principles of linear elastic fracture mechanics. This is achieved by relating the crack opening displacements at two different scales, namely micro and macro. A procedure to determine the material properties at the ITZ including the elastic modulus and the fracture toughness by knowing the mix proportions of the ingredients in concrete is explained. The critical microcrack length thus determined can be treated as a material property and can be used further in predicting the macroscopic behavior of concrete.

2 Critical Microcrack Length

The initiation and propagation of microcrack at the interface between the cement paste and the aggregates are attributed to the toughness of the interface. In this study, the critical microcrack length is a parameter, which is used to characterize the interface. As the critical microcrack length increases, the toughness of the interface increases. Thus, it influences the overall strength of concrete. The existence of

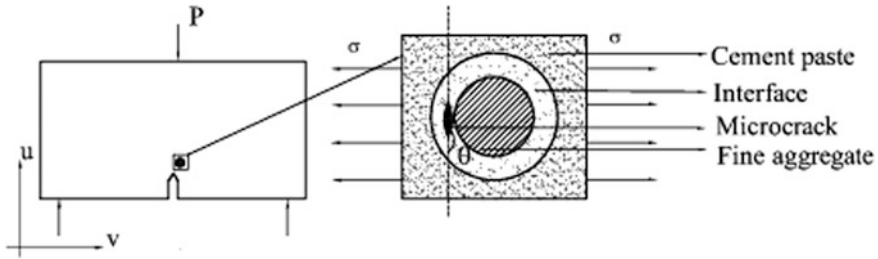


Fig. 1 Representation of microcrack at interface

microcrack and restraining stress at the macrocrack tip is a well-known fact. Upon loading, the microcrack will initiate at the interface and later coalesce with the existing macrocrack resulting in the crack increment. In this study, the critical length of the microcrack is determined by analyzing a small element near the macrocrack tip and along the interface between the cement paste and aggregate, as depicted in Fig. 1.

The following assumptions are made in the derivation of the critical microcrack length: (1) The microcrack grows in a direction perpendicular to the maximum principal stress. (2) The initial microcrack length is assumed to be much smaller than the size of the element considered. (3) The microcrack tip is sharp for linear elastic fracture mechanics to be applied.

The stresses and displacement along the crack tip for this two-dimensional crack problem are determined through an inverse method by making use of an Airy stress function (Φ), which satisfies the biharmonic equation ($\nabla^2 \nabla^2 \Phi = 0$). The stresses and strains in the polar coordinate system are further determined. Using these strains, the displacements in the polar coordinate system are obtained as

$$V_r = \frac{1}{2\mu_{\text{micro}}} \sum_{n=0}^{\infty} r^{\lambda_n} \left[-(\lambda_n + 1)B_n \cos(\lambda_n + 1)\theta + D_n \cos(\lambda_n - 1)\theta \left\{ \frac{4}{1 + \nu_{\text{micro}}} - (\lambda_n + 1) \right\} \right] \tag{1}$$

$$V_\theta = \frac{1}{2\mu_{\text{micro}}} \sum_{n=0}^{\infty} r^{\lambda_n} \left[-(\lambda_n + 1)B_n \sin(\lambda_n + 1)\theta + D_n \sin(\lambda_n - 1)\theta \left\{ \frac{4}{1 + \nu_{\text{micro}}} + (\lambda_n - 1) \right\} \right] \tag{2}$$

In the above equations, μ_{micro} and ν_{micro} are the shear modulus and the Poisson's ratio of the interface, respectively, where the microcrack is likely to occur. The microcrack present in the interface is assumed to be sharp in order to initiate the crack propagation. The crack surface of the microcrack is considered as stress free, and the corresponding boundary conditions along the upper surface denoted by (+) and lower surface denoted by (-) are given by

$$\sigma_{\theta\theta} = \sigma_{r\theta} = 0, \quad \theta = \pm\pi \quad (3)$$

Assuming the microcrack to be very sharp, the microcrack angle attains a value of π , and the characteristic equation reduces to $\sin(2\lambda_n\pi) = 0$. The roots of this characteristic equation give the eigenvalues ($\lambda_n = n/2$; $n = 0, \pm 1, \pm 2, \dots$). The crack-tip singularity is observed when the eigenvalue becomes 0.5. The displacement field near the microcrack tip reduces to the following form

$$V_r = \frac{r^{1/2}}{2\mu_{\text{micro}}} \left[-\left(\frac{1}{2} + 1\right)B_1 \cos\left(\frac{1}{2} + 1\right)\theta - \left(\frac{1}{2} + 1\right)D_1 \cos\left(\frac{1}{2} - 1\right)\theta \right. \\ \left. + \left(\frac{4}{1 + \nu_{\text{micro}}}\right)D_1 \cos\left(\frac{1}{2} - 1\right)\theta \right] \quad (4)$$

$$V_r = \frac{r^{1/2}}{2\mu_{\text{micro}}} \left[-\left(\frac{1}{2} + 1\right)B_1 \sin\left(\frac{1}{2} + 1\right)\theta + \left(\frac{1}{2} - 1\right)D_1 \sin\left(\frac{1}{2} - 1\right)\theta \right. \\ \left. + \left(\frac{4}{1 + \nu_{\text{micro}}}\right)D_1 \sin\left(\frac{1}{2} - 1\right)\theta \right] \quad (5)$$

A relationship between B_1 and D_1 is obtained by substituting the eigenvalue into the boundary condition ($B_1 = D_1/3$). This reduces the displacement field in terms of one unknown parameter D_1 . Further, by defining $D_1 = K_1/\sqrt{2\pi}$, the displacement field becomes a function of stress intensity factor (K). The crack opening displacement corresponding to the microcrack is determined by transforming the displacement component perpendicular to the loading direction (V) into rectangular coordinates by making use of the following transformation

$$V^\pm = V_r \sin(\theta) + V_\theta \cos \theta \quad (6)$$

By substituting $\theta = +\beta^*$ and $\theta = -\beta^*$, the displacement field along the upper (V^+) and the lower (V^-) surface of the crack is obtained. The corresponding displacement fields are given by

$$V^+ = V_r \sin(\theta) + V_\theta \cos(\theta)|_{\theta=+\beta^*} \quad (7)$$

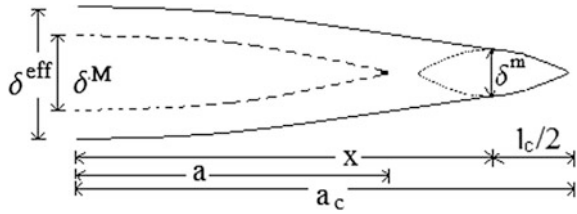
$$V^- = V_r \sin(\theta) + V_\theta \cos(\theta)|_{\theta=-\beta^*} \quad (8)$$

The following equation provides the corresponding microcrack opening displacement (δ^{micro}):

$$\delta^{\text{micro}} = V^+ - V^- \quad (9)$$

$$\delta^{\text{micro}} = 8\sqrt{\frac{r}{2\pi}} \frac{K}{E} \quad (10)$$

Fig. 2 Representation of microcrack an macrocrack at peak load



As the microcrack initiates in the interfacial region, the stress intensity factor (K), elasticity modulus (E), and r are replaced with $K^{Interface}$, $E^{Interface}$, and $l/2$ (as the total length of microcrack is assumed to be l as in Fig. 2). When the microcrack reaches a critical length (i.e., $l = l_c$), the corresponding fracture toughness and crack opening displacement reach their critical value ($K_{IC}^{Interface}$, δ_c) and are given by,

$$\delta^{micro} = 4\sqrt{\frac{l_c}{\pi}} \frac{K_{IC}^{Interface}}{E^{Interface}} \tag{11}$$

Microcracks are nucleated in concrete structure when the applied load reaches 80% of peak load. When the applied load reaches the peak load, the microcrack becomes critical, and it coalesces with the macrocrack. Figure 2 represents the existence of the microcrack at the macrocrack tip considered in this study.

The macrocrack length and the stress corresponding to the peak load (P_{peak}) are represented as the critical macrocrack length (a_c) and peak stress (σ_p). The crack length corresponding to the peak load is determined by knowing the crack mouth opening displacement (δ_p) at the peak load. The following equation provides the crack opening displacement at any point (x) along the macrocrack:

$$\delta^{macro} = \frac{4\sigma_p a_c}{E} g_2\left(\frac{a_c}{D}\right) g_3\left(\frac{a_c}{D}, \frac{x}{a_c}\right) \tag{12}$$

where E is the elastic modulus of concrete, D is the depth of the specimen, and the geometric factors $g_2(a_c/D)$ and $g_3(x/a_c, a_c/D)$ for beam specimen are taken from standard reference [5]. From Fig. 2, it is clear that the crack opening displacement due to the macrocrack at ($x = a_c - l_c/2$) will be equal to the crack opening displacement due to the microcrack at $r = l_c/2$. The critical microcrack length is determined by equating both the crack opening displacements that are given by Eqs. (11) and (12). The solution of the following equation gives the critical microcrack length.

$$\delta^{macro} \Big|_{x=(a_c - \frac{l_c}{2})} = \delta^{micro} \Big|_{r=\frac{l_c}{2}} \tag{13}$$

$$\frac{4\sigma_p a_c}{E} g_2\left(\frac{a_c}{D}\right) g_3\left(\frac{a_c}{D}, \frac{x}{a_c}\right) = 4\sqrt{\frac{l_c}{\pi}} \frac{K_{IC}^{Interface}}{E^{Interface}} \tag{14}$$

As seen from the above equation, the critical microcrack length can be obtained by knowing the fracture toughness and elastic modulus of the interfacial zone. The procedure for estimating the interfacial properties is explained in the following section.

3 Estimation of Interfacial Properties

3.1 Interfacial Fracture Toughness

The lower density of cement particles around the aggregates makes the interface weaker. The initiation and propagation of a microcrack depend on the toughness of the interface. Hillemier and Hilsdorf [6] conducted experiments and analytical investigations to determine the fracture properties of hardened cement paste, aggregate, and cement-paste interface. Huang and Li [7] considered the nucleation of a crack along the interface of aggregate and mortar and derived a relation between the effective toughness of the material and the mortar in terms of volume fractions by considering the crack deflection and interfacial cracking effects, which is

$$\frac{K_{IC}}{K_{IC}^m} = \sqrt{1 + 0.87(V_f(ca))} \sqrt{\frac{1}{1 - \frac{\pi^2}{16} V_f(ca)(1 - v_{\text{eff}}^2)}} \quad (15)$$

where K_{IC} is the fracture toughness of concrete, K_{IC}^m is the fracture toughness of mortar, $V_f(ca)$ is the volume fraction of coarse aggregate, and v_{eff} is the Poisson's ratio of concrete. In this work, a relation between the toughness of matrix and cement paste is derived by suitably modifying and replacing the fracture toughness of concrete and mortar with those of mortar and cement paste. Also, the volume fraction of coarse aggregate and Poisson's ratio of concrete is replaced with that of fine aggregate and Poisson's ratio of mortar, which takes the form

$$\frac{K_{IC}^m}{K_{IC}^{cp}} = \sqrt{1 + 0.87(V_f(fa))} \sqrt{\frac{1}{1 - \frac{\pi^2}{16} V_f(fa)(1 - v_m^2)}} \quad (16)$$

The fracture toughness of cement paste–aggregate interface is much lower than that of cement paste. Hillemier and Hilsdorf [6] conducted experiments to determine the fracture toughness of the interface and the cement paste and observed the toughness of the interface to be 0.4 times of the cement paste (i.e., $K_{IC}^{\text{Interface}} = 0.4 K_{IC}^{cp}$), which is used in the present study.

3.2 Interfacial Elastic Modulus

The elastic modulus of the interface is another major parameter used to define the critical microcrack length (l_c) and is reported to be 0.7 times the elastic modulus of cement paste (E_{cp}) [8] and is used in this study. Hashin [9] obtained a relation between the elastic modulus of homogeneous material with and without inclusion, based on volume fraction and modulus of the inclusion by considering the change in the strain energy of a loaded homogeneous body due to the insertion of inhomogeneities using the variational theorems in the theory of elasticity. Accordingly, the relation between the elastic modulus of concrete and mortar is expressed as,

$$\frac{E}{E_m} = \frac{V_f(m)E_m + (1 + V_f(ca))E_{ca}}{(1 + V_f(ca))E_m + V_f(m)E_{ca}} \quad (17)$$

where $V_f(m)$ and $V_f(ca)$ are the volume fraction of mortar and coarse aggregate, and E , E_m , and E_{ca} are the elastic modulus of concrete, mortar, and coarse aggregate, respectively. The above equation can be simplified to the form,

$$V_f(m)E_m^2 + [1 + V_f(ca)]E_m[E_{ca} - E] - V_f(m)E_{ca}E = 0 \quad (18)$$

The elastic modulus of the mortar is obtained by solving the above quadratic equation. The relationship between the modulus of elasticity of mortar and cement paste is obtained in a similar manner by replacing the material properties of concrete and mortar with the properties of mortar and cement paste. Also, the volume fraction of coarse aggregate and mortar is replaced with those of fine aggregate and cement paste. The modulus of elasticity of cement paste is determined by solving the following quadratic equation.

$$V_f(cp)E_{cp}^2 + [1 + V_f(fa)]E_{cp}[E_{fa} - E_m] - V_f(cp)E_{fa}E_m = 0 \quad (19)$$

where $V_f(cp)$ and $V_f(fa)$ are the volume fraction of cement paste and fine aggregate, and E_m , E_{cp} , and E_{fa} are the elastic modulus of mortar, cement paste, and fine aggregate, respectively.

4 Analysis of Experimental Data

The interfacial properties, such as the modulus of elasticity and fracture toughness and the critical microcrack length as discussed in the previous section, are evaluated for normal strength concrete used by researchers in their experimental program. The following experimental data are considered in this analysis: Bazant and Xu [10] and Shah and Chandra Kishen [11]. In both research works mentioned above, tests have been carried out on beams of three different sizes (designated as small, medium, and

large), which are geometrically similar under three-point bending. Table 1 shows the dimensions of the beams, the peak stress, and the crack mouth opening displacement (CMOD) at peak load. The material properties, including the fracture toughness and elastic modulus as reported in these experimental works, are given in Table 2. The mix proportion used in the experiments conducted by Bazant and Xu [10] and Shah and Chandra Kishen [11] are 1:1.86:2.61:0.54 and 1:2:2:0.6, respectively.

As discussed in the previous sections, the interfacial properties of concrete depend on the volume fraction of each of its constituents. The interfacial fracture toughness, the interfacial elastic modulus, and the critical microcrack length, calculated using the above-mentioned procedure, are tabulated in Tables 2 and 3. It is seen that the interface is the weaker region and is therefore more prone to cracking and that justifies the analysis of the interfacial region. Furthermore, as reported in the literature [5], if the interface is weaker than the coarse aggregates, the crack propagates around the aggregate. In Table 2, it is also observed that for a particular concrete mix, the computed interfacial properties remain constant.

As reported in Table 3, the critical microcrack length is found to be dependent on the properties of the interface as well as the geometry of the specimen. Also, it is found to be increasing with the size of the specimen, even though the interfacial properties remain the same. Also, Mobasher et al. [12] have reported that 80% of microcracks are smaller than 1.5 mm in length. The critical length of microcrack is found to be comparable with the size of the fine aggregate and cement particles. Further, the critical microcrack length is normalized with the depth of beam as shown in Table 3. It is seen that this normalized value remains almost constant for a given mix of concrete and could be treated as a material property.

Table 1 Geometry and material properties of specimens

Specimen designation	Depth	Span	Thickness	Stress at peak load	CMOD at peak load
	D (mm)	S (mm)	B (mm)	σ_u (MPa)	δ_p (mm)
Small [11]	76	190	50	4.476	0.0567
Medium [11]	152	380	50	3.589	0.0743
Large [11]	304	760	50	3.338	0.0483
Small [10]	38.1	95	38.1	4.750	0.0270
Medium [10]	76.2	191	38.1	3.833	0.0354
Large [10]	152.4	381	38.1	3.364	0.0436

Table 2 Material properties of concrete and interfaces

Fracture toughness (MPa $\sqrt{\text{mm}}$)		Elastic modulus (N/mm 2)		References
Concrete	Interface	Concrete	Interface	
K_{IC}	$K_{IC}^{\text{Interface}}$	E	$E^{\text{Interface}}$	
44.6	16.76	30,000	5413.5	[11]
32.0	12.45	27,120	5488.7	[10]

Table 3 Critical microcrack length

Specimen designation	Critical microcrack length (l_c) (mm)	l_c/D 10^{-2}
Small [11]	0.3659	0.39
Medium [11]	0.5717	0.38
Large [11]	0.9238	0.37
Small [10]	0.2370	0.62
Medium [10]	0.4540	0.60
Large [10]	0.9167	0.60

5 Conclusions

In this study, a critical microcrack length parameter is defined, and an expression is derived by analyzing the crack opening displacement at micro- and macroscales. The critical microcrack length is found to be dependent on the specimen size. Also, it is observed that, for a particular mix of concrete, the ratio of critical microcrack length to the specimen depth is found to be constant and can be used as a material property. The critical microcrack thus determined can be further used in predicting the macroscopic behavior of concrete.

References

1. J.C. Maso, *Interfacial transition zone in concrete, RILEM report*, vol. 11 (CRC Press, UK, 2004)
2. Iulia Carmen Mihai and Anthony Duncan Jefferson, A material model for cementitious composite materials with an exterior point eshelby microcrack initiation criterion. *Int. J. Solids Struct.* **48**, 3312–3325 (2011)
3. Farhad Ansari, Mechanism of microcrack formation in concrete. *ACI Mat. J.* **86**, 459–464 (1989)
4. J.G.M. Van Mier, A. Vervuurt, Numerical analysis of interface fracture in concrete using a lattice-type fracture model. *Int. J. Damage Mech* **6**, 408–432 (1997)
5. S.P. Shah, S.E. Swartz, C. Ouyang, Fracture mechanics of concrete: applications of fracture mechanics to concrete, rock and other quasibrittle materials. (Wiley, NY, 1995)
6. B. Hillemeier, H.K. Hilsdorf, Fracture mechanics studies on concrete compounds. *Cem. Concr. Res.* **7**, 523–535 (1977)
7. J. Huang, V.C. Li, A meso-mechanical model of the tensile behavior of concrete. Part II: modelling of post-peak tension softening behavior. *Composites* **20**, 370–378 (1989)
8. C.C. Yang, Effect of the transition zone on the elastic moduli of mortar. *Cem. Concr. Res.* **28**, 727–736 (1998)
9. Izvi Hashin, The elastic moduli of heterogeneous materials. *J. Appl. Mech.* **29**, 143–150 (1962)
10. Z.P. Bazant, K. Xu, Size effect in fatigue fracture of concrete. *ACI Mat. J.* **88**, 390–399 (1991)
11. S.G. Shah, J.M. Chandra Kishen, Fracture properties of concrete–concrete interfaces using digital image correlation. *Exp. Mech.* **51**, 303–313 (2011)
12. B. Mobasher, H. Stang, S.P. Shah, Microcracking in fiber reinforced concrete. *Cem. Concr. Res.* **20**, 665–676 (1990)

Fracture Analysis and Remaining Life Assessment of Ultra High Strength Concrete Beams

A. Ramachandra Murthy, N. R. Iyer and B. K. Raghu Prasad

Abstract This paper presents the details of crack growth study and remaining life assessment of concrete specimens made up of ultra-high-strength concrete (UHSC). Flexural fatigue tests have been conducted on UHSC beams under constant amplitude loading with a stress ratio of 0.2. A “Net K ” model has been proposed by using nonlinear fracture mechanics principles for crack growth analysis and remaining life prediction. SIF (K) has been computed by using the principle of superposition. Bilinear tension softening obtained through inverse analysis corresponding to size-independent fracture energy. Remaining life values have been predicted and compared with the corresponding experimental values and observed that they are in good agreement with each other.

Keywords Ultra-high-strength concrete · Characterization · Fatigue loading
Tension softening · Fracture energy · Stress intensity factor · Crack growth
Remaining life

1 Introduction

Concrete has been one of the most commonly used construction materials in the world. One of the major problems civil engineers face today is concerned with preservation, maintenance, and retrofitting of structures. The historical development

A. Ramachandra Murthy (✉)
CSIR–Structural Engineering Research Centre, Taramani, Chennai 600113, India
e-mail: murthyarc@serc.res.in

N. R. Iyer
Academy of Scientific & Innovative Research (AcSIR), New Delhi, India
e-mail: nageshiyer@acsir.res.in

B. K. Raghu Prasad
Civil Engineering Department, Indian Institute of Science, Bengaluru, India
e-mail: bkr@civil.iisc.ernet

of concrete material may be marked and divided into several stages. The first is the traditional normal strength concrete (NSC) where only four kinds of ingredients, namely cement, water, fine aggregates, and coarse aggregates are used. With the increasing development in physical infrastructure, such as high-rise buildings, long-span bridges, flyovers, power plant structures, and higher compressive strength, concrete is preferred in most cases. When the compressive strength of concrete is generally higher than 50 MPa, it is usually defined as high-strength concrete (HSC). The easiest way to reach high compressive strength is to reduce the water–cement ratio. However, sometimes the compressive strength is not as important and necessary as some other properties, such as low penetrability, high durability, and excellent workability. Thus, high-performance concrete (HPC) was proposed and widely studied at the end of the last century. Currently, an ultra-high-strength concrete (UHSC) with axial compressive strength more than 100 MPa and also with a high tensile strength (more than 10% of the compressive strength) was successfully developed [1–4]. Since UHSC is a relatively new material, its characterization and fracture behavior are yet to be understood. Concrete contains numerous flaws, such as holes or air pockets, precracked aggregates, lack of bond between aggregate and matrix, etc. from which cracks may originate. Cracks generally propagate in a direction, which is perpendicular to the maximum tensile stress. The fracture behavior of concrete is greatly influenced by the fracture process zone (FPZ). The variation of FPZ along the structure thickness or width is usually neglected. The inelastic fracture response due to the presence of FPZ may then be taken into account by cohesive pressure acting on the crack faces.

A few experimental investigations on fatigue crack propagation in concrete were reported [3, 5–8].

In the present study, fracture mechanics-based remaining life has been predicted for high-strength concrete (HSC) and ultra-high-strength concrete (UHSC) and compared with the corresponding experimental observations. A “Net K ” model has been proposed by using principle of superposition. Bilinear tension softening relationship corresponding to size-independent fracture energy has been used to consider the cohesive stresses acting ahead of the crack tip.

2 Experimental Investigations

Two mixes designated as high-strength concrete (HSC) and Ultra-high-strength concrete (UHSC) are characterized, and their mix proportions have been arrived at using appropriate method and several trials. For HSC, the materials are Portland cement, silica fume, quartz sand, high-range water reducer, water, and steel fibers. for UHSC, the materials are Portland cement, silica fume, quartz sand, quartz powder, high range water reducer, water, and steel fibers. The main difference between HSC and UHSC is the absence of quartz powder in the case of HSC mix. Several trials had to be tried before a final mix design. The final mix proportions and ratio obtained are given in Table 1.

Table 1 Mix ratio of HSC and UHSC

Mix ratio	Cement	Fine aggregate	Coarse aggregate	Silica fume	Quartz sand	Quartz powder	Steel fiber (%)	Water	SP (%)
HSC	1	–	–	0.25	1.5	–	2	0.33	2.5
UHSC	1	–	–	0.25	1.1	0.4	2	0.23	3.5

2.1 Mechanical Properties

Various mechanical properties such as compressive strength, split tensile strength of HSC and UHSC mix at 28 days are shown in Table 2. Table 2 also shows the size-independent fracture energy [9].

2.2 Casting of Beams

Details of the specimens prepared for experimental study and notch depth details are given in Table 3. The experimental setup consists of a MTS 2500 kN capacity servo-hydraulic UTM with online data acquisition system. Flexural fatigue tests have been conducted on HSC and UHSC specimens. Three specimens for each notch depth have been tested under load control. A stress ratio of 0.2 is maintained for all the specimens. Frequency of loading is varied for HSC and UHSC specimens. At regular intervals, crack depth versus number of cycles has been monitored for HSC and UHSC specimens. Table 3 shows the maximum load (P_{\max}), minimum load (P_{\min}), frequency of loading, and no. of cycles to failure. P_{\max} has been arrived at based on the failure load obtained from the static test. Paris crack growth constants have been evaluated from the experimental data of da/dN and ΔK . The values of C and m for various cases are shown in Table 3.

Table 2 Mechanical properties of HSC and UHSC

Mix ID	Compressive strength (MPa)	Split tensile strength (MPa)	Modulus of elasticity (MPa)	Fracture energy (N/m)
HSC	87.71	15.38	37,890	6393
UHSC	122.52	20.65	42,987	14,184

Table 3 Remaining life predicted by net K model

Beam dimensions (mm)	Notch depth	Max. load (kN)	Min load (kN)	Paris crack growth constants		Remaining life, cycles	
				log C	m	Exptl	Analytical
250 * 50 * 50 (UHSC)	5	8.0	1.6	-17.24	5.31	2112	1876
	10	6.5	1.3	-16.99	5.23	1464	1280
	15	4.9	0.9	-16.54	5.13	1172	1035
	20	3.3	0.7	-16.35	5.01	820	745
400 * 50 * 80 (UHSC)	8	11.3	2.3	-18.78	6.17	5621	5223
	16	8	1.6	-18.52	6.02	4159	3845
	24	6.1	1.2	-18.23	5.86	3215	2876
	32	4.4	0.8	-17.45	5.32	2432	2230
600 * 50 * 130 (UHSC)	13	17.5	3.5	-19.99	6.76	7654	6801
	26	11.4	2.3	-19.34	6.33	4302	3910
	39	8.1	1.6	-18.98	5.96	3214	2810
	52	5.84	1.2	-18.54	5.69	2483	2231
250 * 50 * 50 (HSC)	5	3.36	0.673	-15.46	5.12	2012	1812
	10	2.69	0.54	-14.76	5.34	1617	1503
	15	2.27	0.45	-15.21	5.01	1234	1134
	20	1.682	0.34	-14.79	5.11	1032	890
500 * 50 * 100 (HSC)	10	6.67	1.335	-17.23	6.01	4356	4089
	20	4.081	0.816	-16.89	6.11	3219	2820
	30	3.193	0.64	-16.78	5.99	2489	2178
	40	2.55	0.51	-16.56	5.67	1876	1694

3 Net K Model Considering Tension Softening

In the Net K model, nonlinear fracture mechanics principles have been used for crack growth analysis and remaining life prediction. The merits of the model are two-fold: (i) it is possible to get SIF variation from crack initiation to unstable crack propagation, and (ii) it is possible to model the fatigue behavior. SIF (K) has been computed by using the principle of superposition.

To incorporate the tension softening behavior, based on the principle of superposition, SIF has to be modified as (Fig. 1),

$$K_I = K_I^P + K_I^q \quad (1)$$

where K_I is called net K , and K_I^q is negative where K_I^P is SIF for the concentrated load P on a three-point bend specimen, and K_I^q is SIF due to the closing force applied on the effective crack face inside the process zone, which can be obtained through Green's function approach by knowing the appropriate softening relation.

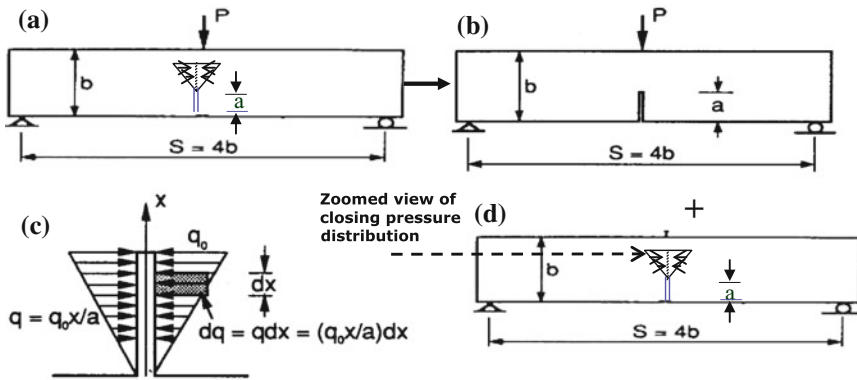


Fig. 1 Illustration of superposition principle

3.1 Computation of K_I^P

SIF due to the concentrated load P can be calculated by using LEFM principles. A three-point bending beam is shown in Fig. 1. The SIF for the beam can be expressed as

$$K_I^P = \sigma \sqrt{\pi a} g_1 \left(\frac{a}{b} \right) \quad \text{where, } \sigma = \frac{3PS}{2b^2t} \tag{2}$$

where P = applied load, a = crack length, b = depth of the beam, t = thickness and $g_1(a/b)$ = geometry factor, which depends on the ratio of span to depth of the beam and is given below for $S/b = 2.5$ [10]

$$g_1 \left(\frac{a}{b} \right) = \frac{1.0 - 2.5a/b + 4.49(a/b)^2 - 3.98(a/b)^3 + 1.33(a/b)^4}{(1 - a/b)^{3/2}} \tag{3}$$

3.2 Computation of K_I^q

The incremental SIF due to the closing force dq can be written as [11].

$$dK_I^q = \frac{2}{\sqrt{\pi \Delta a}} dq g \left(\frac{a}{D}, \frac{x}{a} \right) \tag{4}$$

where dq can be expressed as a function of softening stress distribution over the crack length Δa , the function ‘ g ’ represents the geometry factor.

3.3 Calculation of ‘dq’

By using the above concept (Fig. 1d), cohesive crack can be modeled in the following manner (Fig. 2)

The crack opening displacement w at any point x is assumed to follow linear relationship (Fig. 2) and can be expressed as,

$$w = \delta \left(\frac{a_0 - x}{\Delta a} + 1 \right) \quad a_0 \leq x \leq a_{\text{eff}} \tag{5}$$

where δ is the crack tip opening displacement, and a_0 is initial crack length.

As an example, let us consider linear softening law

$$\sigma = f_t (1 - w/w_c) \tag{6}$$

where f_t = tensile strength of concrete and w_c = critical crack opening displacement.

Substituting for w from Eq. (5) in the linear softening law given by Eq. (6), one can obtain,

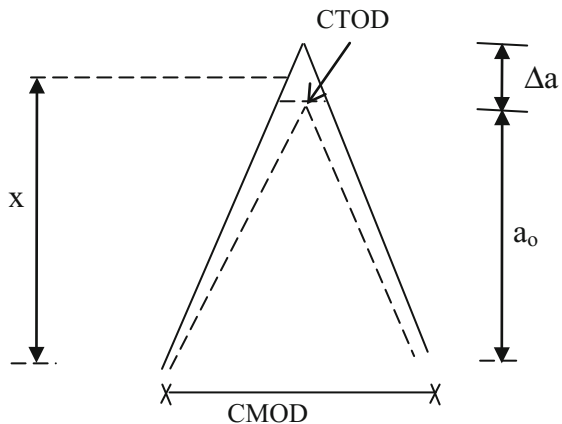
$$dq = \sigma = f_t \left\{ 1 - \frac{\delta}{w_c} \left(\frac{a_0 - x}{\Delta a} + 1 \right) \right\} \tag{7}$$

The crack opening displacement at any point $\delta(x)$ can be calculated using the following equation

$$\delta(x) = \text{CMOD } g_3 \left(\frac{a}{b}, \frac{x}{a} \right) \text{ where} \tag{8}$$

$$g_3 \left(\frac{a}{b}, \frac{x}{a} \right) = \left\{ \left(1 - \frac{x}{a} \right)^2 + \left(1.081 - 1.149 \frac{a}{b} \right) \left[\frac{x}{a} - \left(\frac{x}{a} \right)^2 \right] \right\}^{1/2}$$

Fig. 2 Cohesive crack modeling-schematic diagram of crack opening displacement



where CMOD is crack mouth opening displacement and is calculated using the following formula.

$$\text{CMOD} = \frac{4\sigma a}{E} g_2\left(\frac{a}{b}\right) \quad (9)$$

where $g_2(a/b)$ is geometric factor, depends on the ratio of span to depth of the beam and is given below for $S = 2.5b$

$$g_2(a/b) = \frac{1.73 - 8.56a/b + 31.2(a/b)^2 - 46.3(a/b)^3 + 25.1(a/b)^4}{(1 - a/b)^{3/2}} \quad (10)$$

Hence, replacing dq in Eq. (4) and integrating over length Δa , K_I^q can be obtained as,

$$K_I^q = \int_{a_0}^{a_{\text{eff}}} \frac{2f_t}{\sqrt{\pi\Delta a}} \left\{ 1 - \frac{\delta}{w_c} \left(\frac{a_0 - x}{\Delta a} + 1 \right) \right\} g\left(\frac{a}{b}, \frac{x}{a}\right) dx \quad (11)$$

where

$$g\left(\frac{a}{b}, \frac{x}{a}\right) = \frac{3.52(1 - x/a)}{(1 - a/b)^{3/2}} - \frac{4.35 - 5.28x/a}{(1 - a/b)^{1/2}} + \left[\frac{1.30 - 0.30(x/a)^{3/2}}{\sqrt{1 - (x/a)^2}} + 0.83 - 1.76\frac{x}{a} \right] \left[1 - \left(1 - \frac{x}{a} \right) \frac{a}{b} \right] \quad (12)$$

Similar expressions can be obtained for other models such as bilinear, trilinear, exponential, and power law.

3.4 Remaining Life Prediction

Analysis of fatigue crack growth and remaining life prediction requires data regarding loading conditions, type of material and crack geometry, among others. Then, a suitable crack growth law must be selected. One general expression for such a law is

$$\frac{da}{dN} = f(\Delta K, R, \dots) \quad (13)$$

The number of loading cycles required to extend the crack from an initial length a_0 to the final critical crack length a_f is given by

$$N = \int_{a_0}^{a_f} \frac{da}{f(\Delta K, R, \dots)} \quad (14)$$

Using the Paris law, the number of cycles to failure can be obtained

$$\frac{da}{dN} = C(\Delta K)^m \quad (15)$$

Here, ΔK can be computed by using the following expression

$$\Delta K = K_{\max} - K_{\min}, \text{ where } K_{\max} = K^p - K^q.$$

4 Numerical Studies and Discussion of Results

Crack growth studies and remaining life prediction have been carried out for three-point bending UHSC and HSC beams by using the above methodologies. Bilinear tension softening model developed by using inverse analysis has been used to account for tension softening. Bilinear tension softening model obtained from inverse analysis corresponding to size-independent fracture energy has been employed for crack growth analysis and remaining life prediction (Fig. 3) [12]. Paris crack growth constants (C , m), maximum load, minimum load, and predicted remaining life are shown in Table 3. From Table, it can be observed that the predicted remaining life is in good agreement with the corresponding experimental observations. A significant advantage of net K model is that it is possible to obtain ΔK as an increment in the value of K at every step.

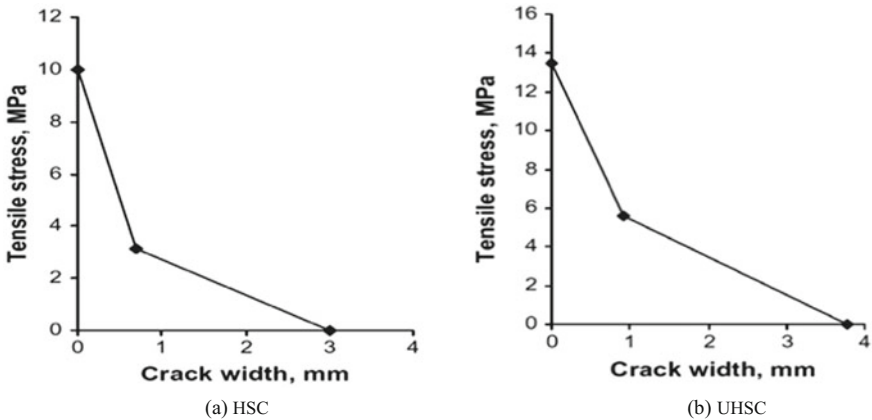


Fig. 3 Bilinear stress-crack opening relationship for HSC and UHSC corresponding to their G_F

5 Summary

A “Net K ” model has been proposed by using nonlinear fracture mechanics principles for crack growth analysis and remaining life prediction. SIF (K) has been computed by using the principle of superposition. Bilinear tension softening relationship obtained from the inverse analysis has been used to consider the cohesive stresses acting ahead of the crack tip. Numerical studies have been conducted on three-point bending concrete structural component under constant amplitude loading. The predicted remaining life values have been compared with the corresponding experimental observations and it is noted that they are in good agreement with each other.

Acknowledgements We acknowledge with thanks the valuable technical suggestions and support provided by our colleagues of Computational Structural Mechanics Group, CSIR-SERC.

References

1. P. Richard, M.H. Cheyrezy, Reactive powder concretes with high ductility and 200–800 MPa compressive strength, *ACI SP144*, 24 (1994) 507–518
2. P. Richard, M. Cheyrezy, Composition of reactive powder concretes. *Cem. Concr. Res.* **25**, 1501–1511 (1995)
3. A.N. Mingzhe, Y.U. Ziruo, M. Sun, S. Zheng, L. Liang, Fatigue properties of RPC under cyclic loads of single-stage and multi-level amplitude. *J. Wuhan Univ. Technol. Mat. Sci. Ed.* **25**, 167–173 (2010)
4. P. Goltermann, V. Johansen, L. Palbol, Packing of aggregates: an alternate tool to determine the optimal aggregate mix. *ACI Mat. J.* **94**, 435–443 (1997)
5. A.R. Ingraffea, Discrete fracture propagation in rock: laboratory tests and finite element analysis, Ph.D. Dissertation, (University of Colorado, Boulder, 1977)
6. M.V.K.V. Prasad, C.S. Krishnamoorthy, Computational model for discrete crack growth in plain and reinforced concrete. *Comput. Methods Appl. Mech. Engg.* **191**, 2699–2725 (2002)
7. Z. Wu, S. Yang, X. Hu, J. Zheng, An analytical model to predict the effective fracture toughness of concrete for three-point bending notched beams. *Engg. Fract. Mech.* **73**, 2166–2191 (2006)
8. V. Slowik, B. Beate Villmann, N. Bretschneider, T. Villmann, Computational aspects of inverse analyses for determining softening curves of concrete. *Comput. Methods Appl. Mech. Engg.* **195**, 7223–7236 (2006)
9. A.R. Murthy, B.L. Karihaloo, N.R. Iyer, B.K. Raghu Prasad, Determination of size— independent specific fracture energy of concrete mixes by two methods. *Cem. Concr. Res.* **50**, 19–25 (2013)
10. H. Tada, P.C. Paris, G.R. Irwin, *The Stress Analysis of Cracks Handbook*, 2nd edn. (St. Louis. MO, Paris Productions, 1985)
11. S.P. Shah, S.E. Swartz, *Fracture Mechanics of Concrete: Applications of Fracture Mechanics to Concrete, Rock and other Quasi-brittle Material* (Wiley, New York, 1995)
12. A.R. Murthy, B.L. Karihaloo, N.R. Iyer, B.K. Raghu Prasad, B.K. Raghu Prasad, Bilinear tension diagrams of concrete mixes corresponding to their size-independent specific fracture energy. *Constr. Build. Mater.* **47**, 1160–1166 (2013)

Part III

Composites

Rupture in Abdominal Aortic Aneurysm

Qusay Alfaori, Ashok Saxena, Hanna Jensen and Morten Jensen

Abstract Ability to predict the growth of abdominal aortic aneurysm and the rupture event is important for prognostics and treatment for this life-threatening cardiovascular disease. Uniaxial stress–strain testing of healthy and collagen-degraded aortic specimens from pigs was performed in order to study the biomechanical properties of the aortic tissue. A mathematical model for the stress–strain relationship suitable for describing the behaviour of abdominal aortic tissue was used to derive tissue properties as a function of specimen orientation and collagen degradation. The resultant properties varied significantly between healthy tissue and collagen-degraded tissue and were found to be orientation dependent. Maximum stress, maximum strain and critical strain values were significantly higher for healthy tissue group than for collagen-degraded tissue group. Finite element modelling of healthy and collagen-degraded abdominal aortas was performed using the measured properties. It is shown that this approach can potentially lead to the development of an analytical tool for assisting in prognostics and treatment of the disease.

Keywords Aneurysm · Aorta · Collagen degradation · Rupture

Nomenclature

σ	Stress
ε	Strain
$A = \varepsilon_c$	Critical strain for rupture
K	Inverse of the elastic modulus in Region 3 of the stress–strain behaviour
B	Regression constant characteristic of the stress–strain behaviour in Region 1
ε_{\max}	Maximum strain sustained prior to rupture
σ_u	Ultimate strength or maximum stress at rupture

Q. Alfaori · A. Saxena (✉) · H. Jensen · M. Jensen
Department of Biomedical Engineering, University of Arkansas, Fayetteville,
AR 72701, USA
e-mail: asaxena@uark.edu

1 Introduction

In spite of the advances in medical sciences, cardiovascular diseases remain the leading cause of death [1, 2]. Abdominal aortic aneurysm (AAA) is an irregular expansion of the abdominal aorta due to the weakening of abdominal aortic wall and is considered a form of cardiovascular disease. A patient is said to have AAA when the abdominal aortic diameter increases by 50% of the healthy original diameter [3]. Every year, 500,000 new patients are diagnosed with AAA throughout the world, 150,000 of those in the USA alone. AAA is present in about 2% of the elderly (60 years and older), a population group that is rapidly increasing in the developed countries [4, 5]. Abdominal aortic aneurysms are one of the most lethal aneurysms that can develop in the human body, with a mortality rate approaching 90% in the case of rupture [1]. Every year in the USA, a country for which accurate numbers are available, approximately 15,000–20,000 people die from AAA, and it is listed as the 13th most common cause of death and the 10th among men that are 55 years of age and older [4].

Aneurysm development is a complex process related to variability of molecular mediators and matrix-degrading proteases often related to ageing [6]. The process causes the connective tissue of the aorta to degrade, caused by destruction of important structural proteins such as elastin and collagen [6]. AAA is diagnosed using expensive medical imaging techniques such as ultrasonography, computed tomography (CT) scanning or MRI scanning that are not performed routinely during physical examinations. AAA is often being asymptomatic, making it difficult for the patients to seek critical, timely help and treatment.

Once AAA is detected, assessment of the rupture risk is important. The most common method for rupture risk assessment is measurement of the diameter of the dilated aorta using CT scan. If the aneurysm exceeds 1.5 times the healthy aorta diameter (20–30 mm), the risk of rupture is considered high at a mortality rate of 95% [3]. While not all aneurysms with diameters greater than 1.5 times the healthy diameter rupture, some aneurysms do rupture at diameters less than 1.5 times the original diameter, and thus, regular monitoring is highly recommended in order to assess growth of the aneurysm and to treat it in time to avoid catastrophic rupture. Thus, a prognostic analytical tool to assist in determining the frequency of such examinations will be very useful.

Over the past 15 years, other factors that have been identified as relevant to rupture risk assessment are wall stress distribution, wall strength and formation of intraluminal thrombus (ILT) on AAA wall [1, 7, 8]. Engineering tools such as finite element analysis (FEA) are now frequently used to model hypothetical and patient-specific aneurysms. Based on work done using FEA, factors such as expansion rate, degree of symmetry and geometrical parameters of AAA can be used as additional parameters for assessing potential risk of rupture [1].

This study was designed to address the following questions: (a) How does collagen degradation contribute to the development of AAA and (b) what is the effect of collagen degradation on the tissue's elastic modulus and other tensile

properties? It is likely that abnormal collagen degradation overtime accelerates the development of the aneurysm. Thus, quantification of the growth kinetics and rupture criteria involving collagen degradation is important.

2 Experimental Methods

An Instron 5944 (Instron, Norwood, MA, USA) universal testing machine was used for the tensile tests conducted in this study. The set-up included a Bioplus bath in which testing could be performed under environmental conditions that resemble the in vivo environment of soft tissue, as shown in Fig. 1 along with a picture of a ruptured specimen.

A total of 50 abdominal aortic specimens were obtained from pigs (5 months old weighing 80 kg). Certain sections of the abdominal aorta were cut along the sagittal plane to obtain a longitudinal orientation, and some sections were cut along the transverse plane to obtain a circumferential orientation. Each specimen had a length of 5–7 cm, a width of 2–2.5 cm and a thickness of approximately 1.5–2 mm. Specimens were frozen at a temperature of -80°C to protect them from degradation, and prior to mechanical testing and to eliminate most artefacts in measured mechanical properties, they were removed from the freezer to thaw at room temperature for 24 h. Next, the specimens were mounted on the stress–strain apparatus and were immersed in the Bioplus bath, containing a phosphate-buffered saline solution ($1 \times \text{PBS}$), at 37°C for 30 min before performing the mechanical tests. The abdominal aortic specimens marked as Type-I collagen degraded were immersed in Type-I collagenase solution for 24 h prior to mechanical testing. The collagenase solution had a concentration of 0.30 g/mL and was made via mixing of Type-I collagenase powder with $1 \times \text{HBSS}$ (Hank's Balanced Salt Solution). Uniaxial stress–strain tests on healthy abdominal aorta specimens from longitudinal and circumferential orientations and Type-I

Fig. 1 Instron testing system equipped with a Bioplus bath and a picture of a tested specimen



collagen-degraded specimens from the same orientations were then performed. All specimens from both groups were preconditioned by applying five partial loading and unloading cycles in the elastic regime.

3 Experimental Results and Discussion

A three-phase mathematical model from Raghavan et al. was [9] adapted to represent the stress–strain relationship for the aortic material, Eqs. (1) and (2), respectively, below.

$$\sigma|_{\text{Region 1}} = \frac{1}{\left(K + \frac{A}{B}\right)} \varepsilon \tag{1}$$

$$\sigma|_{\text{Region 3}} = \left(\frac{1}{K}\right) \varepsilon - \frac{A}{K} \tag{2}$$

where K , A and B are model constants derived from the experimental stress–strain data. Figure 2a and b show a schematic representation of the stress–strain

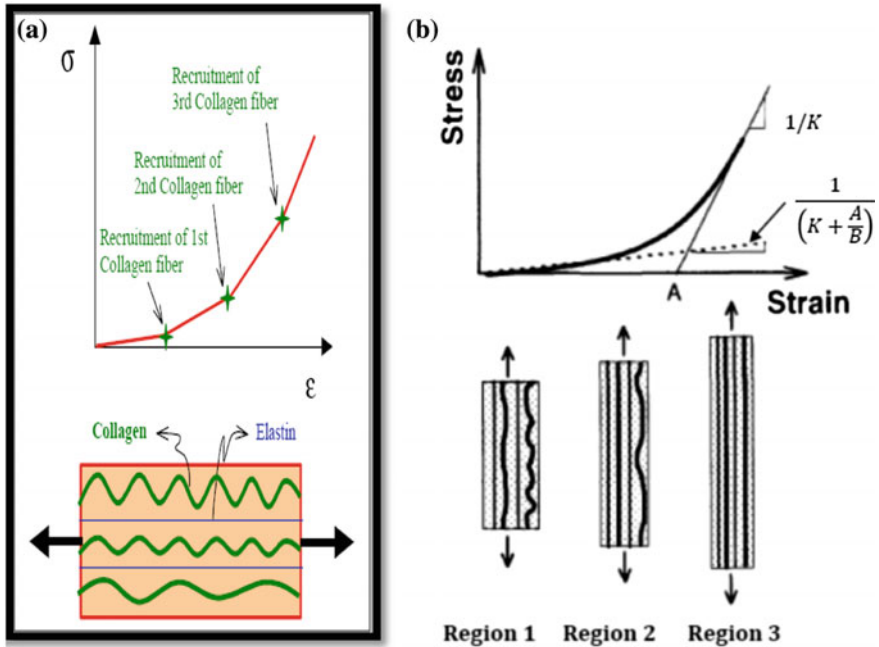


Fig. 2 Schematic representation of **a** changing stiffness the aortic material with strain due to activation of collagen fibres and **b** the three regions of stress–strain behaviour of the aortic material and parameters representing various properties [9]

relationships as described by Eqs. (1) and (2) and the physical reasoning behind the three regions. In Region 1, the stress is entirely borne by the matrix material consisting of elastin. Region 2 represents the onset of collagen fibre participation in bearing the stress and occurs sequentially as shown in Fig. 2a for three fibres, as an example. Region 2 continues until all fibres participate in bearing the stress leading to Region 3 in which complete recruitment of all collagen fibres occurs leading to greatly increased stiffness. The constant A in the above equations is the intercept of the extrapolated stress–strain trend line in Region 3 with the strain axis at zero stress. This also represents the residual strain in a ruptured specimen that can be directly measured on the tested sample and is therefore called ε_c . Equation (2) can be rewritten as Eq. (3). Similarly, the constant K can be derived from the slope of the Region 3 stress–strain behaviour. The constant K represents inverse of the stiffness of the sample. The constant B can be derived from regression of the Region 1 data using Eq. (1) and does not have a physical meaning beyond a regression constant.

$$\sigma_{\text{region 3}} = \left(\frac{1}{K}\right)\varepsilon - \frac{\varepsilon_c}{K} \quad (3)$$

While Eqs. (1)–(3) are important for understanding the physical deformation processes in the aortic material, they do not provide a single mathematical relationship between stress and strain for use in analyses. For example, no equation is available to describe the behaviour in Region 2. An exponential relationship of the type in Eq. (4) can accurately represent the relationships in all three regions and can be used to reliably extract the constants A , B and K for each of the material conditions.

$$\sigma = ae^{b\varepsilon} \quad (4)$$

where a and b are regression constants whose values were determined from the results of each test and then used to extract the value of K , A and B as listed in Table 1 along with other properties such as the maximum stress and maximum strain sustained by the aorta samples. The typical engineering stress–strain diagrams are shown in Fig. 3 for both healthy and collagen-degraded aorta samples in the longitudinal and circumferential directions. The shape of the stress–strain curves for healthy aorta is very similar to the schematic shown in Fig. 2, but they very different for the collagen-degraded samples. The properties in the longitudinal and circumferential directions in the healthy aorta are significantly different from each other. Collagen degradation results in severe degradation of strength and stiffness, and it appears that collagen fibres no longer contribute to the mechanical strength of the aorta wall in either longitudinal or circumferential direction.

Figure 4 shows some sample results from the various stress–strain diagrams and the corresponding fits using Eq. (4). The exponential form represents the entire data very well.

Table 1 Material parameters of the aortic material for healthy and collagen-degraded conditions in longitudinal and circumferential orientation

Specimen group	No of duplicate samples	B (MPa)	A = ϵ_c	ϵ_{max}	K (MPa) ⁻¹	Ultimate strength, σ_u (MPa)
Healthy, longitudinal	12	0.46 ± 0.01	0.45 ± 0.06	0.94 ± 0.11	0.15 ± 0.01	2.34 ± 0.09
Healthy, circumferential	12	0.35 ± 0.02	0.73 ± 0.08	1.19 ± 0.12	0.22 ± 0.01	2.19 ± 0.07
Degraded longitudinal	6	22.2 ± 0.4	0.02 ± 0.0	0.68 ± 0.15	9.09 ± 0.14	0.09 ± 0.00
Degraded circumferential	6	10.5 ± 0.5	0.03 ± 0.0	0.83 ± 0.10	7.14 ± 0.11	0.076 ± 0.00
Raghavan et al. values		B (N/cm ²)	A		K ($\times 10^{(cm^2/N)}$)	
AAA (longitudinal)	45	3.90 ± 0.6	0.091 ± 0.009		39 ± 5	
AAA (circumferential)	16	4.47 ± 0.9	0.103 ± 0.02		25 ± 4	

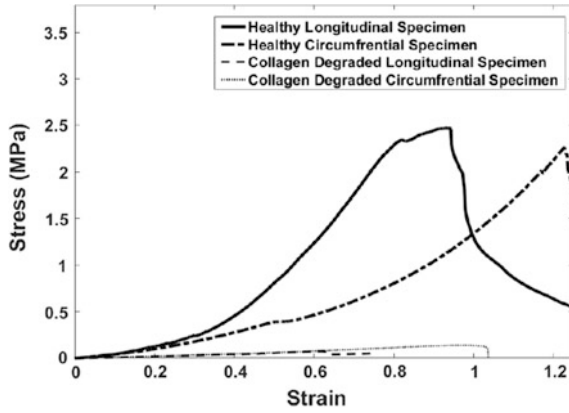


Fig. 3 Typical plot of stress and strain for healthy and collagen-degraded aorta samples in the longitudinal and circumferential orientations. The samples' values of ultimate strength stress and strain at rupture are shown in Table 1

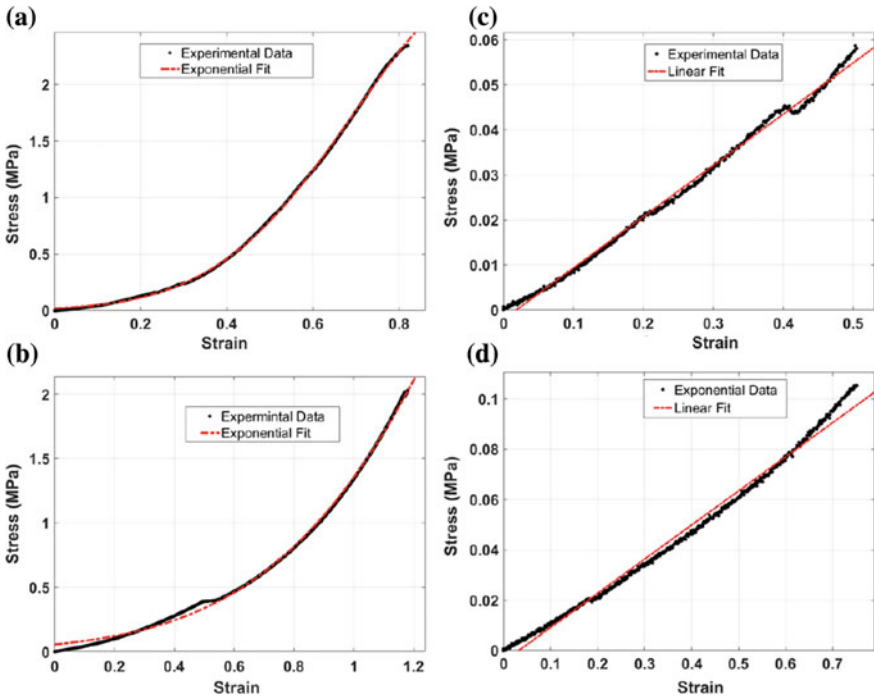


Fig. 4 Exponential fit of stress–strain data of longitudinal (a) and circumferential (b) healthy specimens and linear fit of stress–strain data of longitudinal (c) and circumferential (d) collagen-degraded specimens

The data in Table 1 and Fig. 3 strongly suggest that one of the causes of AAA could be the degradation of collagen in regions of the aorta wall that causes weakening of the aorta in those regions. The values of A in Table 1 are somewhat higher than for the values reported for humans between age 31 and 58 by Raghavan [9, 10] but comparable. Thus, samples from pigs that are much more readily available from slaughter houses than human tissue are suitable model materials for human aortas.

If the collagen degradation occurs axisymmetrically over a length of the aorta, the bulge will also be symmetric about the axis. On the other hand, if the collagen degradation occurs only on one side of the aorta wall, the bulge will be in that region only. Both types of aneurysms are lethal and whether rupture occurs or not will depend on the strain in the aneurysmal region and how close it is to the critical residual strain of ε_c , although other factors may also influence when rupture is expected to occur. This will be discussed further later in the paper. It is important to remember that collagen is not the only protein responsible for all macroscopic properties of the tissue. In fact, the cohesiveness among elastin, smooth muscle and collagen provides the tissue's ultimate structural integrity. Thus, AAA development is complex and can be related to elastin degradation, collagen fibre cross-linking and smooth muscle deterioration.

Another aspect of the deformation behaviour of aorta materials investigated was the sensitivity of the deformation properties to applied strain rate. The data in Fig. 3 were obtained from tests conducted at a strain rate of 0.1 min^{-1} . Tests were conducted at strain rates of 1, 0.01 and 0.001 min^{-1} , and it was found that the stress–strain behaviour was sensitive to strain rates indicating viscoelastic and/or viscoelastic tendencies. Thus, the long-term goal of this project includes building those capabilities in the stress–strain relationships. In this paper, only the basic relationships are used to model the aneurysm in aortas.

4 Finite Element Modelling

Finite element modelling was carried out using the commercially available ABAQUS code to explore how degradation in the wall material properties affects the development of the aneurysm. The aneurysm model included the deformation of healthy and aneurysmal aortas using the deformation constants obtained from the tested specimens. Specifically, the elastic modulus value of the healthy (in Region 3) and collagen-degraded specimens was used. Figure 5 shows the model used for the healthy and degraded aortas. In the latter, a region over which the degraded properties were used is shown in a different colour. As mentioned previously, the healthy aortic tissue properties typically display nonlinear, anisotropic, hyperelastic or viscoelastic behaviour. In this study, the analyses were conducted with simplified assumptions of isotropic, nonlinear behaviour including the characteristics of hyperelasticity using the measured value of elastic modulus ($1/K$) of 5.4 MPa for the healthy tissue (Region 3) and a value of 0.13 MPa for the collagen-degraded

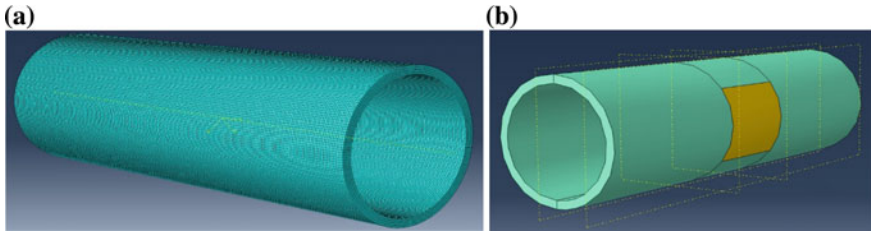


Fig. 5 Finite element model of **a** healthy and **b** aneurysmal aorta

tissue. The Poisson's ratio of 0.45 and arterial wall density of 1.2 g/cm^3 taken from the literature [11].

The structural geometry of a healthy abdominal aorta resembles that of a pipe with a circular cross section of outer radius R and inner radius r , wall thickness $w = R - r$ and Length L . The geometry of a healthy abdominal aorta was constructed with dimensions that are similar to the actual dimensions of the abdominal aorta. The outer radius of the abdominal aorta is approximately 1.5 cm, the wall thickness is approximately 2 mm, and the length ranges from 10 to 15 cm. A refined mesh was applied to the geometry which created at least 20,000 solid elements.

The boundary conditions at the edge or end of the pipe may affect the results and may cause irregular deformation behaviour in the model near the ends. Thus, the actual length of the healthy and aneurysmal abdominal aortic models was extended by 2 cm on each end so the results were not affected by the end effects. Further, the elastic modulus value of collagen-degraded aortic specimen was applied to an area to simulate the aneurysmal region in the aneurysmal aortic model. A cyclically fluctuating uniform internal pressure mimicking physiological conditions was applied to the interior wall along the entire length of the aortic models. The applied cyclic pressure is a sinusoidal wave function with a maximum amplitude of approximately 16 kPa (120 mm Hg), minimum amplitude of approximately 11 kPa (80 mm Hg) and a frequency of $60/72 \text{ s}^{-1}$ (heart's 72 beats per minute).

A cyclically varying pressure of constant amplitude with a sinusoidal waveform was applied to the internal surface of the healthy aortic model, as mentioned earlier. This was applied over a time of 10 s, and the resulting von Mises stress distributions for healthy and collagen-degraded models were calculated by applying the load and are shown in Fig. 6.

A typical element in the finite element model was chosen from the healthy aorta model and also from the collagen-degraded region of the aneurysmal aorta model to illustrate the von Mises stress and the circumferential strain magnitudes as a function of time. These results are shown in Fig. 7a and b for healthy aorta and c, d for the aneurysmal aorta. In the healthy aorta, Fig. 7a, b, the peak stress is approximately 150 kPa, and the peak strain is approximately 5.5×10^{-5} which is much below the levels required for rupture. Obviously, this can change with age as the properties of the aortic wall degrade from collagen degradation and also the wall

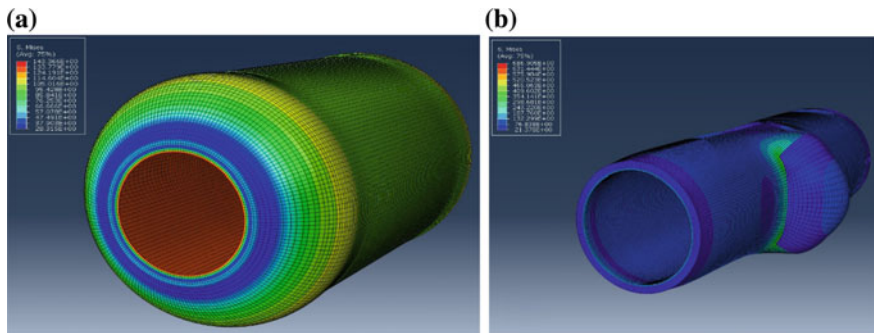


Fig. 6 Deformation of **a** a healthy aorta during systole and **b** a collagen-degraded aorta during a diastole showing the bulge in the aneurysmal region

thickness itself may decrease. By comparison, the peak stress in the collagen-degraded region is 62 kPa and the strain 0.01 that is dangerously high! With repeated cycling, the strains will accumulate each cycle making the aneurysm worse and increasing the risk of rupture. This supports the notion put forward by others that as collagen degrades, elastin is the only tissue component available to support the stress [9, 10].

Using the properties from mechanical testing in the finite element models in the modelling software clearly demonstrates that the risk of rupture will be much higher for collagen-degraded tissue. From a biological point of view, collagen degradation occurs due to the action of collagenases, which are class of proteases enzymes. Excessive collagenase activity causes weakening and destruction of the aortic wall. In fact, biomechanical studies have shown that collagen presents in media and adventitia layers of the aortic wall is responsible for maintaining tissue microstructural stability [12, 13].

The kinetics of the aneurysm growth have not been modelled in this study because a different constitutive relationship that incorporates the effects of degradation with time will be needed to model that trend. This will be the focus of future studies. Relying completely on uniaxial test data is also not optimal, and studying the stress–strain behaviour of aortic tissue under biaxial stress is needed to more accurately model the state of stress in the aorta. Conducting biaxial testing on aortic specimens will help validate the accuracy of critical strain values that were calculated in this study and to establish rupture criterion that can improve rupture prognostics for AAA patients. In addition, due to the fact that the elastic modulus in the longitudinal orientation differs from that in the circumferential orientation, orthotropic material property assumption is more appropriate in our finite element model than the isotropic material properties assumed in the calculations thus far. Also, biaxial testing will allow us to derive more tissue property constants that can be utilized in applying FEA on a viscoelastic model under the conditions of dynamic loading.

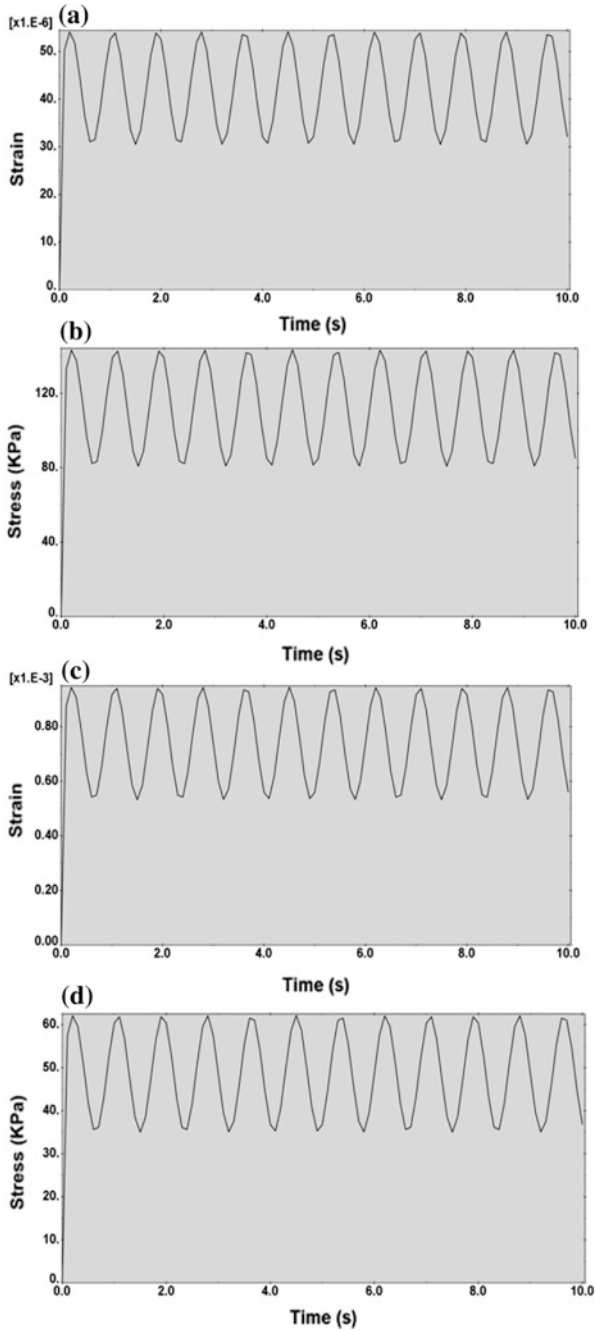


Fig. 7 **a** Circumferential strain **b** von Mises stress for a healthy aorta and **c**, **d** are the same, respectively, for collagen-degraded aortic material properties

5 Conclusions and Future Work

It has been shown that significant changes in the biomechanical properties of the aortic tissue result in the development of aneurysms. The results indicate that changes in the collagen microstructure of the tissue due to degradation greatly affect the critical strain and the maximum stress that the tissue can sustain. The critical strain to rupture and the changes that occur in its value from collagen degradation are likely will be good indicators of impending rupture in AAA patients. Also, the changes in critical strain to rupture under biaxial loading conditions are likely to be relevant but have not been investigated in this study. To our knowledge, this study is the first to examine the biomechanical behaviour of the aortic tissue after collagen degradation but lot more work must be performed to fully understand the degradation kinetics and the variables that determine its progression. More accurate data through testing of abdominal aortic tissue can improve the accuracy of the models.

Acknowledgements The animal aortic specimens were obtained from Cockrums Meat Processing and Taxidermy, Rudy, Arkansas, USA. Dr. Kartik Balachandran is thanked for his help in providing valuable insight and allowing us to use some of his laboratory space and materials.

References

1. B.J. Doyle, *3D Imaging of Abdominal Aortic Aneurysms Techniques and Applications* (Nova Science, Hauppauge, 2010)
2. The Top 10 Causes of Death, Retrieved 26 Oct 2015, from <http://www.who.int/mediacentre/factsheets/fs310/en/> (2012)
3. J.D. Humphrey, C.A. Taylor, Intracranial and abdominal aortic aneurysms: similarities, differences, and need for a new class of computational models. *Annu. Rev. Biomed. Eng.* **10** (1), 221–246 (2008)
4. D.A. Vorp, J.P. Vande Geest, Biomechanical determinants of abdominal aortic aneurysm rupture. *Arterioscler. Thromb. Vasc. Biol.* **25**(8), 1558–1566 (2005)
5. Projections of the Population by Selected Age Groups and Sex for the United States: Table 2. 2015 to 2060 (NP2012-T2), December 2012. Source: U.S. Census Bureau, Population Division at <http://www.census.gov/population/projections/files/summary/NP2012-T2.xls>
6. R.W. Thompson, J.A. Curci, T.L. Ennis, D. Mao, M.B. Pagano, C.N. Pham, Pathophysiology of abdominal aortic aneurysms: insights from the elastase-induced model in mice with different genetic backgrounds. *Ann. NY. Acad. Sci.* **1085**, 59–73 (2006)
7. J. Biasetti, P.G. Spazzini, J. Swedenborg, G.T. Christian Gasser, An integrated fluid-chemical model toward modelling the formation of intra-luminal thrombus in abdominal aortic aneurysms. *Front. Physiol.* **3**, 1–16 (2012)
8. W.R. Mower, W.J. Quiñones, S.S. Gambhir, Effect of intraluminal thrombus on abdominal aortic aneurysm wall stress. *J. Vasc. Surg.* **26**(4), 602–608 (1997)
9. M.L. Raghavan, M.W. Webster, D.A. Vorp, Ex vivo biomechanical behaviour of abdominal aortic aneurysm: assessment using a new mathematical model. *Ann. Biomed. Eng.* **24**(5), 573–582 (1996)
10. M.L. Raghavan, Cardiovascular bio-solid mechanics section, in *Biomechanics 51:050*, pp. 3–25

11. D.A. Vorp, Biomechanics of abdominal aortic aneurysm. *J. Biomech.* **40**(9), 1887–1902 (2007)
12. H. Abdul-Hussien, R.V. Soekhoe, E. Weber, J.H. von der Thüsen, A. Mulder, J.N. Lindeman, Collagen degradation in the abdominal aneurysm: a conspiracy of matrix metalloproteinase and cysteine collagenases. *Am. J. Pathol.* **170**(3), 809–817 (2007)
13. E. Choke, G. Cockerill, W.W. Wilson, S. Sayed, J. Dawson, I. Loftus, M.M. Thompson, A review of biological factors implicated in abdominal aortic aneurysm rupture. *Eur. J. Vasc. Endovasc. Surg. Off. J. Eur. Soc. Vasc. Surg.* **30**(3), 227–244 (2005)

Damage Tolerance Assessment of Laminated Composite Plates Subjected to Ballistic Impact

H. L. Vinayaka and Shivashankar R. Srivatsa

Abstract Polymer matrix composite materials in laminated plate configurations are extensively used in a wide range of fields like defense, navy, aerospace, and automotive industries due to their low weight, high-specific strength, and tailorability. However, in these applications, impact damage tolerance of laminated composite structures is a constant source of concern over the years. Ballistic impact damage tolerance assessment is a concern in many fields, besides obvious application of protective armor where the primary design objective is that of preventing projectile penetration. Soft body armors made of composites are subjected to ballistic impact from projectiles where the structure has no time to respond and could result in localized damage. Analysis of composite structures under ballistic impact, which is a transient nonlinear dynamic phenomenon, requires nonlinear finite element analysis (NLFEA). LS-DYNA, a general purpose code based on finite element method with a wide range of material models, which uses explicit time integration technique for analyzing large deformation dynamic response of solids and structures, has proven to be relevant in this respect. This paper focuses on finite element modeling of impact on composite plates subjected to ballistic impact by a fragment simulating projectile (FSP) using LS-DYNA software. Finite element modeling is defined here as analyst's choice of material models (constitutive equations and failure criteria), nonlinear finite elements, meshes, constraints, boundary conditions, analysis procedures, governing matrix equations, and their solution methods, specific pre- and post-processing options available in a chosen commercial FEA software for the intended analysis of candidate components and structures. The focus of this work is on the use of LS-DYNA software and prediction by analysis of: (1) Impact damage resistance (contact force-time history); (2) Impact response (displacement-time history, ply-by-ply strain history, ply-by-ply stresses in the

H. L. Vinayaka (✉)

Department of Mechanical Engineering, Dayananda Sagar College of Engineering,
Bengaluru 560078, India
e-mail: yoganarasimha123@gmail.com

S. R. Srivatsa

Department of Mechanical Engineering, BMS College of Engineering,
Bengaluru 560019, India

material coordinates, and contour plots of failure index); (3) Impact damage propagation (ply-by-ply failure from first ply failure to last ply failure and delamination between plies); and (4) Impact damage tolerance (stiffness, strength, life without and with damage). Significant results like energy balance, contact force-time history, displacement-time plots, and damage zone shape and size are presented. Also, a study of the failure modes and effect of failure theories on ballistic impact response of a composite structure is presented.

Keywords FEM · Nonlinear finite element analysis · Composite structure
Ballistic impact

1 Introduction

Composite materials offer many advantages compared to conventional materials, especially where high strength and stiffness to weight ratio is a concern. These properties make the composites the candidate materials in many applications such as aerospace, sports equipment, pressure vessels, and automotive parts [1]. However, structures made of composite material are susceptible to damage from impact loading as a result of their low toughness. Impact damage must be considered in the design of composite structures considering the potential impacts during fabrication, operation, and repair.

Typical damage occurring in impacted laminates consists of a combination of intralaminar damage mechanisms (such as matrix cracking or plasticity, fiber/matrix debonding and fiber fracture) and interlaminar failure, which develops at the interface between adjacent plies in the form of debonding between layers (delamination). Interface delaminations are probably the most critical and insidious failure mechanisms, since they may severely degrade the strength and the integrity of the structure, and may propagate undetected during service, leading to the unexpected collapse of the component [2].

Ballistic impact is generally a low-mass, high-velocity impact caused by a propelling source or a projectile. The velocity of the projectile varies from 300 to 2500 m/s and energy up to 20 kJ. The structure will have no time to react and may involve complete penetration of the target.

Research on the impact response of various materials including composites is available in the literature with varying ply orientations, projectile shapes, projectile velocities, etc. Literature available in the field of impact varies from the use of conventional metals and their combinations with composite materials for different applications [3, 4]. Impact experiments on composites need to be conducted with varying velocities, and associated significant failure modes can be identified [3, 5]. Analytical formulations are available for characterization of impact responses for different materials [6].

Of the methods available for evaluating the damage induced during ballistic impact (analytical, experimental, and numerical methods), numerical method is

cost-effective as well as time-saving as the other two methods are tedious and expensive in nature. Recent research includes numerical simulation as a tool for validation of experimental results and prediction of impact damage for varying conditions [1–4, 7–10]. A large number of commercial software are available for the numerical simulation of impact phenomenon.

The main objective of this work is to develop a finite element model for the analysis of impact of an impactor on a target for evaluating the damage induced during ballistic impact, using two classical lamina failure theories, namely Chang-Chang and Tsai-Wu theory using a chosen commercially available finite element analysis (FEA) software LS-DYNA. The results include prediction of ballistic limit, capture of different response plots of the structure such as force-time plots, energy balance plots, kinetic energy plots, and also damage progression contour plots for individual plies as well as for the laminate using the failure theories available in the software. However, the interlaminar failure mode (delamination) is not discussed here.

2 Finite Element Model Development

A laminated composite plate with dimensions $100 \text{ mm} \times 100 \text{ mm} \times 5.25 \text{ mm}$ is considered. The laminate is E-glass fiber reinforced polymer matrix composite with plain weave architecture having 8 laminae with $(0/90)_4$ configuration with ply thickness of 0.656 mm each. The impactor is a 0.50 caliber (12.7 mm diameter and 13.65 mm length) flat-nosed cylinder made of alloyed tool steel with a mass of $13.4 \text{ g} \pm 0.03 \text{ g}$ consistent with the mass of a NATO 0.50 caliber fragment simulating projectile (FSP), whose velocity is varied from 172 to 187.1 m/s. The material properties of the composite plate and the projectile are given in Tables 1 and 2, respectively.

Plate geometry is discretized using 4-noded quadrilateral shell elements with a mesh of 25×25 based on convergence of impact damage tolerance (force-time history). Use of a graded mesh is avoided because of the dispersion of stress waves. Use of solid elements to discretize a multilayered composite laminates subjected to ballistic impact is never used in practice. The projectile is discretized using 8-noded hexahedral solid elements with a total of 18,400 elements. The finite element model of the plate and projectile is shown in Fig. 1.

Material type *MAT_054/055—ENHANCED_COMPOSITE_DAMAGE [11, 12] is used to model the composite plate, and *MAT_03—PLASTIC_KINEMATIC [11, 12] is used to model the projectile. All the four edges of the plate are fixed with automatic surface-to-surface contact between the impactor and the plate. The analysis is carried out for a time period of 0.3 ms with a time step of 1.44×10^{-6} ms.

Table 1 Material properties of composite plate (polypropylene E-glass composite) [4]

Material property	Value
Density, ρ	1850 kg/m ³
Young's modulus, E_{11}, E_{22}	14 GPa
Young's modulus, E_{33}	5.3 GPa
Poisson's ratio, ν_{31}	0.14
Poisson's ratio, ν_{32}	0.15
Tensile strength, X_T	0.45 GPa
Tensile strength, Y_T	0.45 GPa
Tensile strength, Z_T	0.15 GPa
Compressive strength, X_C	0.25 GPa
Compressive strength, Y_C	0.25 GPa
Matrix mode shear strength, S_{12}	0.032 GPa
Matrix mode shear strength, S_{23}	0.032 GPa
Matrix mode shear strength, S_{31}	0.032 GPa
Shear modulus, G_{21}	1.8 GPa
Shear modulus, G_{31}	0.75 GPa
Shear modulus, G_{32}	0.75 GPa
Shear modulus, G_{32}	0.75 GPa

Table 2 Properties of projectile [4]

Material property	Value
Density, ρ	7800 kg/m ³
Poisson's ratio	0.28
Yield strength	1.08 GPa
Young's modulus	210 GPa

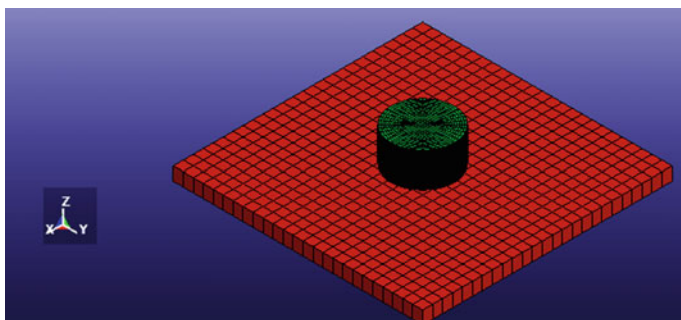


Fig. 1 Finite element model of plate and projectile

3 Results Presentation and Discussion

3.1 Ballistic Limit Prediction

For a given target-projectile combination, the ballistic limit is defined as the lowest initial velocity of the projectile that will result in complete penetration. At that impact velocity, the residual velocity of the projectile is zero. Recognizing that a certain amount of variability is always present, the ballistic limit is often defined as the velocity that will result in penetration of 50% of the samples when a large number of tests are performed. It is necessary to determine the ballistic limit and to predict the residual velocity of the projectile when the initial velocity exceeds the ballistic limit.

Here, the velocity of the projectile was initially considered at 172 m/s and increased gradually to arrive at the ballistic limit. Table 3 provides numerically predicted residual velocities for various given initial velocities, based on the two failure criteria. (Chang-Chang failure criterion identifies modes of ply-by-ply failure in addition to the failure of the ply as provided by Tsai-Wu criterion, and the two criteria is distinct and hence their predictions.)

From Table 3, it is observed that the ballistic limit velocity for an 8-ply laminate based on Chang-Chang failure criteria is 175 m/s with the projectile residual velocity of 0.856 m/s.

Significant results of impact damage resistance, impact response, and impact damage propagation are captured in the form of various response plots like energy balance plots, displacement-time plots, and contact force-time plots for the considered failure criteria along with a study of failure modes, and the effect of failure theories are presented as follows. (It is to be noted that the predictions of Chang-Chang and Tsai-Wu failure criteria is distinct and cannot be combined. Chang-Chang criterion was introduced to identify the modes of failure which is not provided by Tsai-Wu criteria.)

Table 3 Simulation results for 8-layer PP/E-glass composite material

Initial velocity (m/s)	Residual velocity (m/s)	
	Chang-Chang	Tsai-Wu
172.0	11.727	11.574
173.0	8.974	8.369
174.0	2.607	9.333
174.5	4.213	7.329
174.8	4.674	9.018
175.0	0.856	10.341
176.0	21.049	12.003
178.0	31.168	13.231
179.5	7.867	21.292
186.8	28.454	18.944
187.1	18.778	36.351

Contact Force-Time history

See Figs. 2 and 3.

Energy Balance Plot

See Figs. 4 and 5.

Displacement-Time history

See Fig. 6.

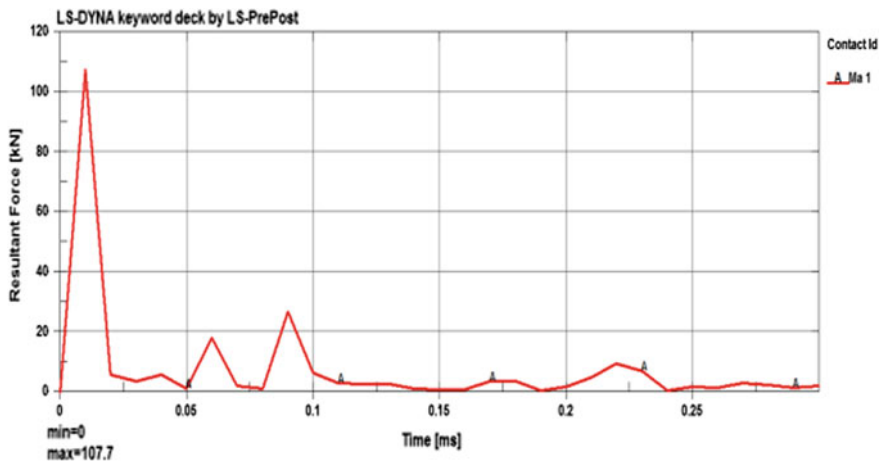


Fig. 2 Contact force (kN)—time (ms) plot Chang-Chang

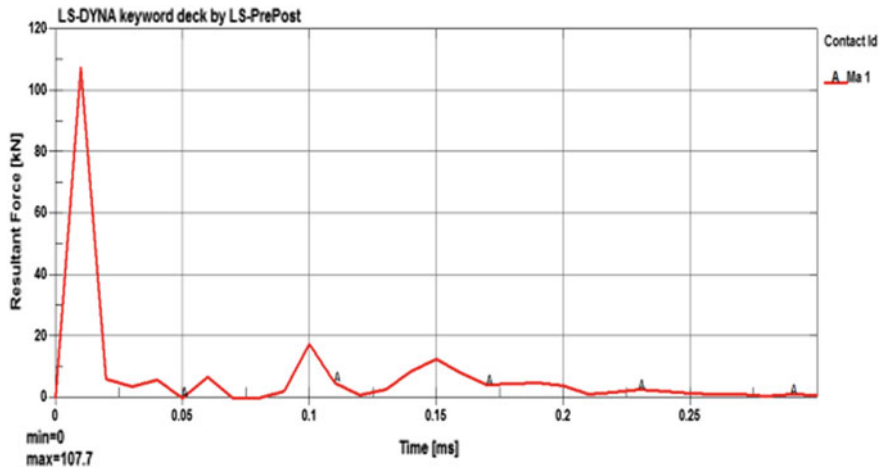


Fig. 3 Contact force (kN)—time (ms) plot Tsai-Wu

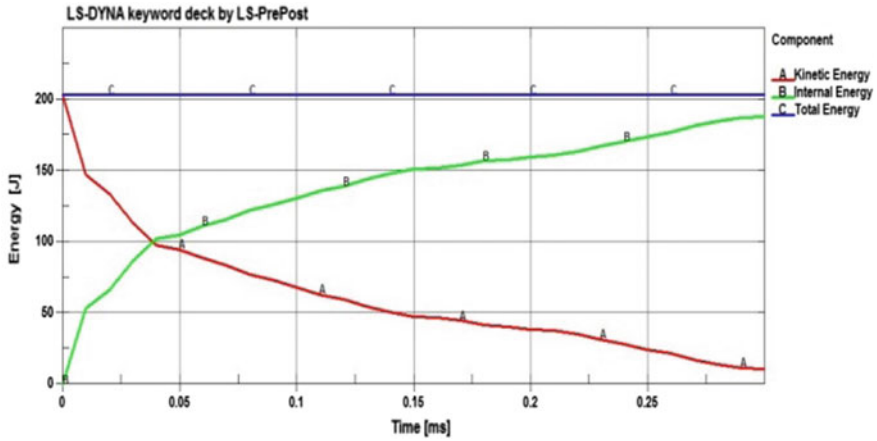


Fig. 4 Energy (J)—time (ms) plot Chang-Chang

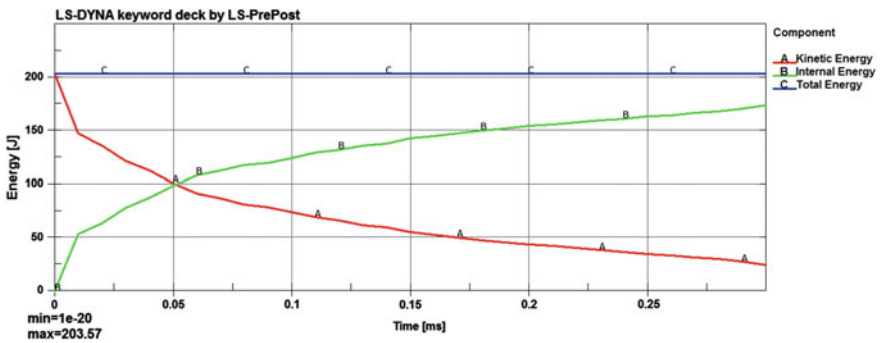


Fig. 5 Energy (J)—time (ms) plot Tsai-Wu

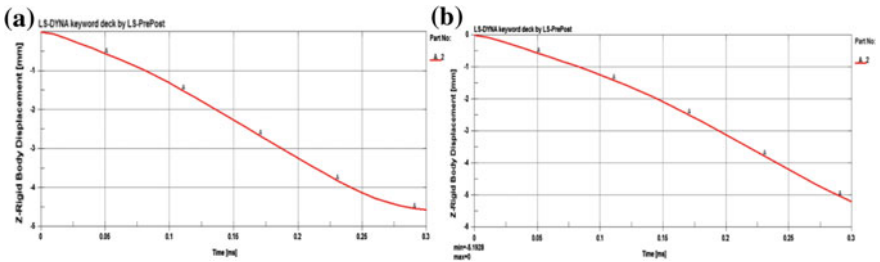


Fig. 6 Displacement (mm)—time (ms) plot, a Chang-Chang criterion; b Tsai-Wu criterion

Failure Index Contour Plots

(Failure Index Contour Plots for Tsai-Wu criterion are distinct compared to Chang-Chang criterion. They cannot be superposed.)

See Figs. 7 and 8.

Damage Propagation Failure Index Contour Plots

See Figs. 9 and 10.

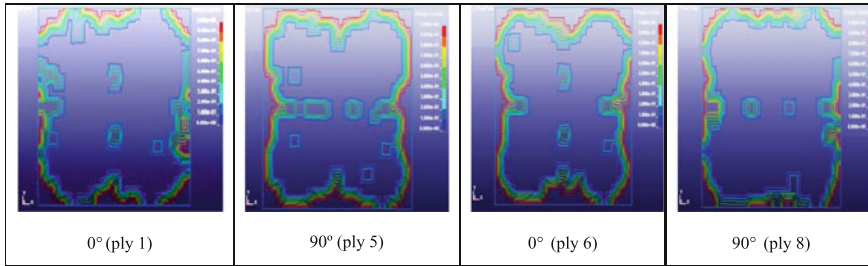


Fig. 7 Failure index line contour plots for different plies for Chang-Chang criterion at time $t = 0.3$ ms

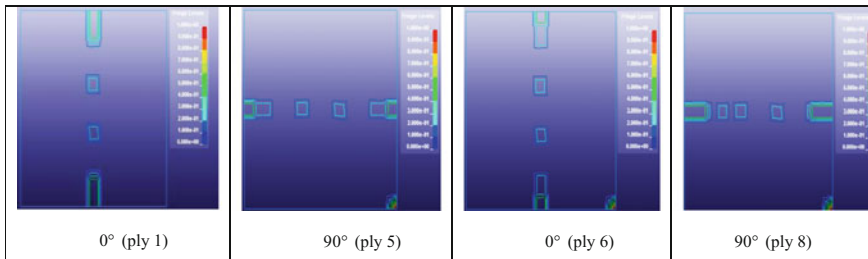


Fig. 8 Failure index line contour plots for different plies for Tsai-Wu criterion at time $t = 0.3$ ms

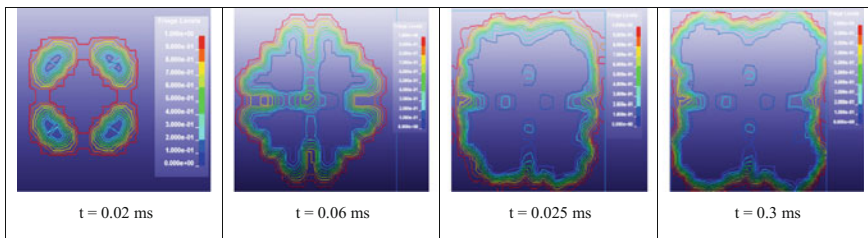


Fig. 9 Failure index line contour plots showing damage propagation at different time instants for the ensemble for Chang-Chang criterion

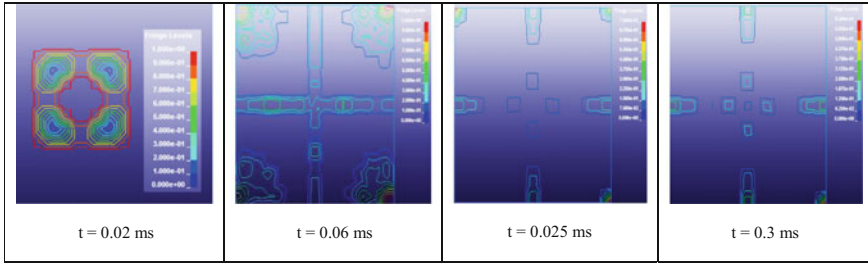


Fig. 10 Failure index line contour plots showing damage propagation at different time instants for the ensemble for Tsai-Wu criterion

Failure Index Line Contour Plots for Damage Propagation for Various Failure Mechanisms

See Figs. 11, 12, 13, 14, 15 and 16.

In this study, only a fraction of the results obtained in the modeling, analysis, and simulation of ballistic impact on a laminated composite square plate using the LS-DYNA software is given above. There is a clear need to validate the finite element model developed for the intended analysis using a benchmark with known target solutions. This work is in progress.

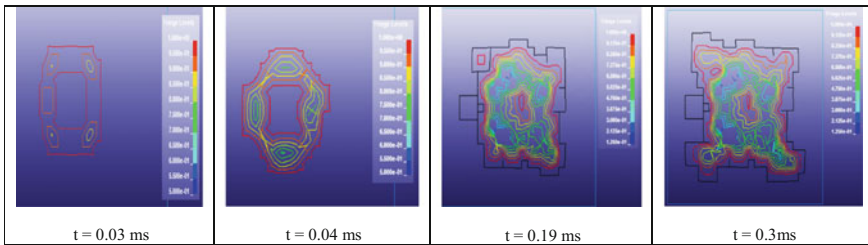


Fig. 11 Failure index line contour plots showing tensile fiber mode damage propagation at different time instants for the ensemble for Chang-Chang criterion

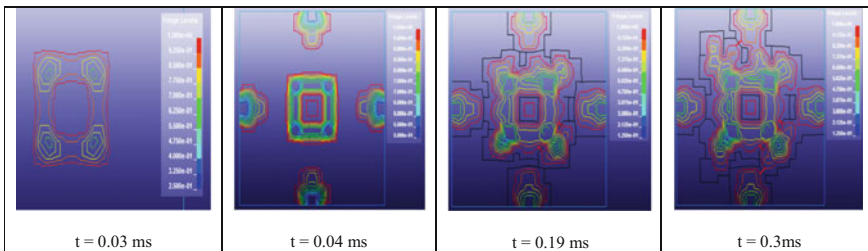


Fig. 12 Failure index line contour plots showing tensile fiber mode damage propagation at different time instants for the ensemble for Tsai-Wu criterion

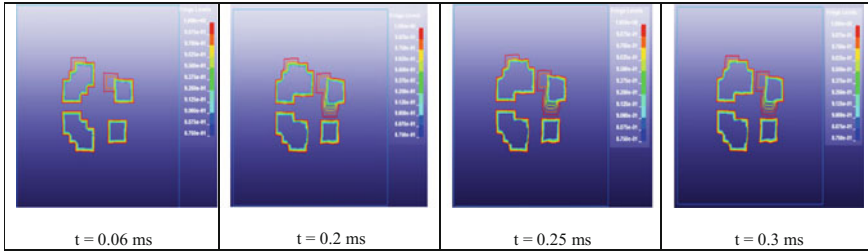


Fig. 13 Failure index line contour plots showing compressive fiber mode damage propagation at different time instants for the ensemble for Chang-Chang criterion

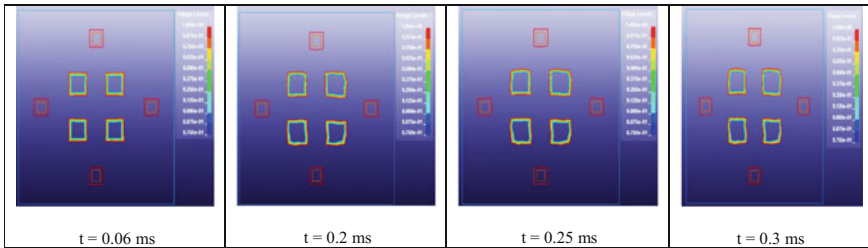


Fig. 14 Failure index line contour plots showing compressive fiber mode damage propagation at different time instants for the ensemble for Tsai-Wu criterion

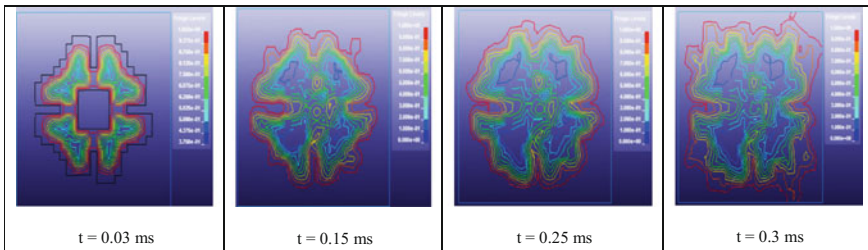


Fig. 15 Failure index line contour plots showing compressive matrix mode damage propagation at different time instants for the ensemble for Chang-Chang criterion

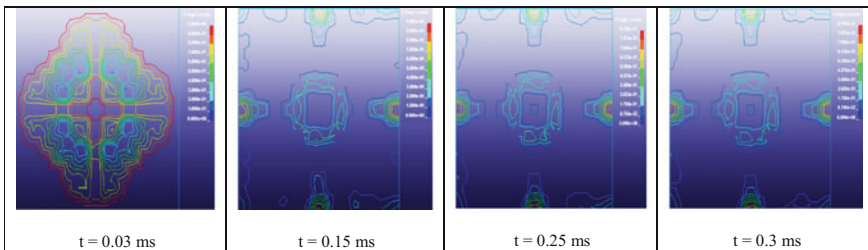


Fig. 16 Failure index line contour plots showing compressive matrix mode damage propagation at different time instants for the ensemble for Tsai-Wu criterion

The graphical post-processing capability in LS-DYNA is demonstrated in the results presented above. However, there is a need to verify these predictions through correlation studies where the numerical results are verified using experimental data. This demands the generation of experimental results which is quite tough in terms of research and test facilities. However, this work is also in progress but in an indirect route. We are on the search for experimental results in the published literature for which we will repeat the modeling analysis and simulation using LS-DYNA software.

4 Conclusions

Nonlinear finite elements for continua and structures, in general, and a commercial FEA software LS-DYNA, in particular, are used in this study for ballistic impact damage tolerance assessment of laminated composite plate-type structures. However, there is a clear need to validate finite element modeling using LS-DYNA software for simulation of ballistic impact on laminated composites components and structures. This demands benchmarks with known target solutions. Ballistic impact damage consists of ply-by-ply failure and delamination between all the plies. The ensemble of the results over all the plies and ply interfaces quantifies impact damage. However, measurement of this ensemble demands computerized ultrasonic C-scan of impact damage components, and there is also a need to exploit software capabilities to graphically display the ensemble of damage. These are topics of current research.

References

1. Y. Shi, T. Swait, C. Soutis, Modelling damage evolution in composite laminates subjected to low velocity impact. *Compos. Struct.* **94**, 2902–2913 (2012)
2. D. Feng, F. Aymerich, Finite element modelling of damage induced by low-velocity impact on composite laminates. *Compos. Struct.* **108**, 161–171 (2014)
3. M.A. Iqbal, A. Chakrabarti, S. Beniwal, N.K. Gupta, 3D numerical simulations of sharp nosed projectile impact on ductile targets. *Int. J. Impact Eng* **37**, 185–195 (2010)
4. L. J. Deka, S. D. Bartus, U. K. Vaidya, Damage evolution and energy absorption of FRP plates subjected to ballistic impact using a numerical model, in *9th International LS-DYNA Users Conference*, 2006, Dearborn, Michigan, USA
5. J. Pernas-Sánchez, J.A. Artero-Guerrero, J. Zahr Viñuela, D. Varas, J. López-Puente, Numerical analysis of high velocity impacts on unidirectional laminates. *Compos. Struct.* **107**, 629–634 (2014)
6. N.K. Naik, P. Shirao, Composite structures under ballistic impact. *Compos. Struct.* **66**, 579–590 (2004)
7. M. Loikkanen, G. Praveen, D. Powell, Simulation of ballistic impact on composite panels, in *10th International LS-DYNA Users Conference*, 2008, Dearborn, Michigan, USA
8. Sebastian Heimbs, Sven Heller, Peter Middendorf, *Simulation of low velocity impact on composite plates with compressive preload* (LS-DYNA Anwender Forum, Bamberg, 2008)

9. S.K. Chelluru, Finite element simulations of ballistic impact on metal and composite plates, M.Sc. thesis, Wichita State University, 2007
10. Costantino Menna, Domenico Asprone, Giancarlo Caprino, Valentina Lopresto, Andrea Prota, Numerical simulation of impact tests on GFRP composite laminates. *Int. J. Impact Eng* **38**, 677–685 (2011)
11. LS-DYNA Theory Manual, *Livermore Software Technology Corporation* (Livermore, CA, 2006)
12. LS-DYNA Keywords Manual, Volume I, Version 971 *Livermore Software Technology Corporation*, Livermore, CA, May 2007

Prediction of Mode II Delamination Onset Life Under Spectrum Fatigue Loads Using Equivalent Strain Energy Release Rate Concept

A. R. Anilchandra, M. Seshagirachari, Ramesh Bojja,
N. Jagannathan and C. M. Manjunatha

Abstract End notched flexure (ENF) test specimens of unidirectional IMA/M21 carbon fiber composite (CFC) were fabricated using standard autoclave process. A Teflon insert was used to simulate a delamination at the midplane. Three-point bend setup tests were conducted at an average frequency of 2 Hz using a 25 kN servo-hydraulic test machine in room temperature conditions. Constant amplitude fatigue tests were done at three different stress ratios, viz. $R = 0.0, 0.5,$ and -1.0 to construct the standard $G-N_{\text{onset}}$ diagram, similar to $S-N$ curve in its usefulness. N_{onset} was identified as 5% change in initial compliance value. Using an equivalent energy release rate parameter, G_{eq} , all the curves were collapsed into a single curve in the form of Basquin's equation. The equation was subsequently used in predicting the delamination onset-of-growth life under a standard mini-FALSTAFF spectrum load sequence. A fairly good correlation was found between the predicted and experimental mode II onset-of-growth behavior.

Keywords Composite · Delamination · Spectrum load · Onset-of-growth Compliance

Nomenclature

R	Stress ratio
N_{onset}	Number of constant amplitude (CA) fatigue cycles for onset-of-growth
G_{max}	Maximum strain energy release rate (SERR)
G_{min}	Minimum SERR
G_{eq}	Equivalent SERR
G_{IIC}	Critical mode II SERR
G'_{eq}	Basquin's coefficient
ΔG	Range SERR

A. R. Anilchandra (✉) · M. Seshagirachari · R. Bojja · N. Jagannathan · C. M. Manjunatha
Structural Technologies Division, Fatigue and Structural Integrity Group, CSIR-National
Aerospace Laboratories, Bengaluru 560017, India
e-mail: anilchandraar.mech@bmsce.ac.in

γ	Best fit parameter
N_b	Number of spectrum fatigue load blocks
D	Damage fraction

1 Introduction

Aircraft structures are increasingly being replaced with fiber reinforced plastic composites (FRPs) due to their high specific mechanical properties [1]. Delamination in such laminated FRPs possesses a serious threat to the structural integrity since these structures are highly susceptible to in-service-related events such as barely visible impact damages (BVID), assembly and service related events (over tightening, collisions), and so on [2]. While identifying such defects are quite challenging, deciding the fate of such “damaged” structure is also equally challenging [3]. The total life of a delamination under fatigue loading is the sum of number of cycles spent in onset-of-growth (N_{onset}) and subsequently the number of cycles needed for it to propagate to a critical length (N_p). The fatigue loads could be mode I (opening mode), mode II (shearing), mode III (tearing), or a mixed-mode condition. The “no-growth” philosophy of damage tolerant design presumes existence of a delamination owing to the aforementioned reasons and the energy needed in terms of load cycles for it to begin-to-grow, that is, onset-of-growth is regarded as failure of the structure/component [4]. Owing to cost and safety considerations, the aircraft industry would prefer life prediction so that catastrophic failures could be prevented and various prediction models have been proposed in the literature [5].

Life prediction under spectrum fatigue loads can be classified into three major categories, viz., empirical, phenomenological, and physics-based damage models. Empirical models are simple and rely on experimental data (stress levels, stress ratio, or frequency) without considering the inherent damage mechanisms. The Palmgren-Miner (PM) cumulative damage accumulation model is one such life prediction model and was used in our earlier work to predict the onset-of-growth under mode II spectrum loading in a carbon fiber reinforced plastic composite (CFRP) [6]. A novel constant onset life diagram (COLD), similar to constant life diagram (CLD), was proposed and used in the prediction. However, the prediction using CLD involves tedious interpolation technique and this is overcome in the present work by using the equivalent strain energy release rate (G_{eq}) concept. Attempts have been made in the past to normalize stress (S)-number of cycles to failure (N) plot in order to eliminate the effect of specimen geometry and test setup for a particular stress ratio (R) [7]. Petermann and Plumtree [8] used an energy-based approach to merge different R -ratio curves into a single curve and used it in life prediction with a good correlation between the experimental and predicted values. G_{eq} concept, similar to K_{eq} proposed by Hojo et al. [9], was shown to merge various R -ratio curves into a single curve in the G - N_{onset} plot [10].

The aim of the present work is,

- to make use of the G_{eq} concept to merge all the R -ratio curves into a single R -ratio curve in the G - N_{onset} and subsequently use it in predicting the onset-of-growth under mini-FALSTAFF spectrum load sequence and
- validate with experimental results.

2 Experiment

2.1 Material and Specimen

The unidirectional carbon fiber/epoxy IMA/M21 prepreg was obtained from M/s Hexcel in the form of 300 mm wide roll. The nominal thickness of prepreg (lamina) was about 0.18 mm. The prepreg was cut into 300 mm \times 450 mm size and laid up on a tool. Teflon sheet of 30 μ m thickness was introduced at the mid-thickness (neutral axis) to create an artificial delamination in the test specimens. The composite was then cured in an autoclave maintained at a pressure of 7 bar at 180 °C for 2 h [11]. The vacuum at 1 bar was maintained during curing process. The fiber volume fraction of the fabricated laminate was 59%. The prepared laminates of about 3.8 mm thick were ultrasonically C -scanned. End notched flexure (ENF) test specimen measuring 130 mm \times 25 mm was cut from these laminates.

2.2 Spectrum Fatigue Tests

Spectrum fatigue tests were carried out on the ENF specimen in servo-hydraulic test machine under load control mode at an average frequency of 2 Hz (four reversals per second). The photograph of the test setup is shown in Fig. 1a. The schematic, in Fig. 1b, shows the specimen dimensions and the loading arrangement. The fixture is so designed that the specimen can undergo bending either way about the neutral axis and further detailed description about the fixture could be found elsewhere [12]. A standard mini-FALSTAFF load sequence was employed for the spectrum tests. Mini-FALSTAFF is a short version of the FALSTAFF load spectrum [13], which is a standardized variable-amplitude test load sequence developed for the fatigue analysis of materials used for fighter aircraft and is shown in Fig. 2a. One block of this load sequence ($N_b = 1$) consists of 18,012 reversals at 32 different stress levels and represents loading equivalent of 200 flights. The actual load sequence for experiments and fatigue life prediction was obtained by multiplying all the peak/trough points in the entire block with a reference load. The compliance of the specimen was determined on completion of every load block. Onset-of-growth was assumed, similar to an accepted practice [14, 15] of whenever

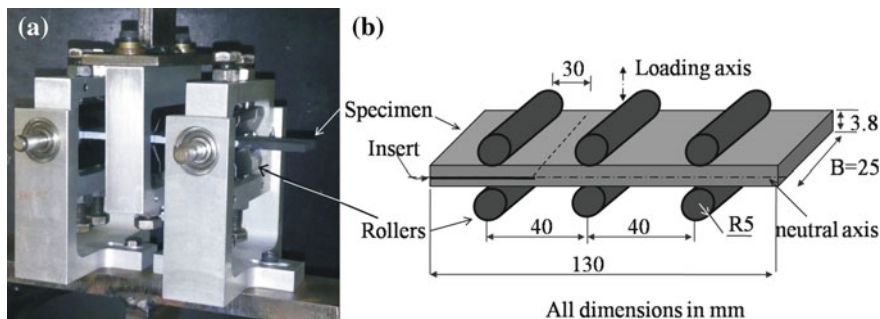


Fig. 1 **a** Photograph of the test setup highlighting the specimen and support rollers; **b** schematic of the test setup

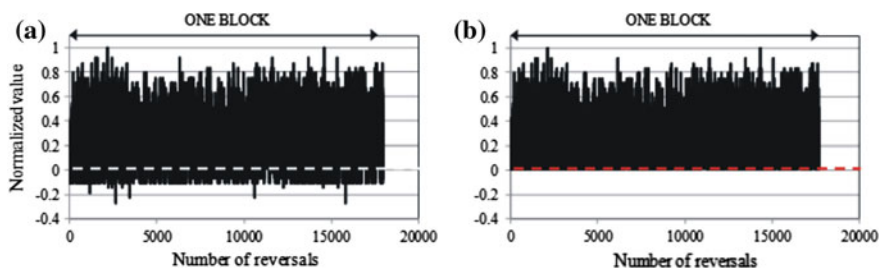


Fig. 2 **a** Mini-FALSTAFF spectrum load sequence; **b** truncated mini-FALSTAFF

5% increase in compliance from the initial value was observed. In our earlier work, a modified form of mini-FALSTAFF, called truncated mini-FALSTAFF, was used wherein all the reversals below zero level were truncated as shown in Fig. 2b [6]. Although the modified mini-FALSTAFF was not used for testing in the present work, the proposed life prediction methodology was tried on the truncated mini-FALSTAFF as well and the results were compared with the results of our earlier work.

2.3 Constant Amplitude Fatigue Tests

As a part of life prediction requirement, constant amplitude (CA) fatigue tests were conducted at three different stress ratios, $R = 0.0, 0.5,$ and -1.0 using a computer controlled 25 kN servo-hydraulic test machine under load control mode, at 2 Hz. The maximum strain energy release rate (maximum SERR or G_{max}) for each of the CA fatigue test was fixed on certain percentage of critical mode II SERR (G_{IIc}) of the material, determined in our earlier work [6]. Measuring the crack tip advance through techniques such as the microscope is extremely difficult and might lead to

erroneous results as the crack remains closed under mode II condition and hence the researchers have suggested the compliance calibration (CC) technique to monitor the crack length [16]. A 5% increase in compliance from the initial value was regarded as N_{onset} .

3 Onset-of-Growth Prediction Methodology

The N_{onset} under the mini-FALSTAFF load sequence was predicted using Palmgren-Miner (PM) empirical method and compared with the experimental results. The methodology employed was similar to the general procedure used for fatigue life prediction for composites under spectrum loads [4]. But the uniqueness in this prediction method lies in the fact that it makes use of only the G_{max} - N_{onset} data (or G - N_{onset}), similar to the S - N data. The flow chart for onset-of-growth prediction is schematically shown in Fig. 3. The procedure of prediction contains:

- Rainflow counting of the fatigue cycles [17] in the spectrum load sequence to obtain individual single cycles with specific G_{max} and G_{min} .

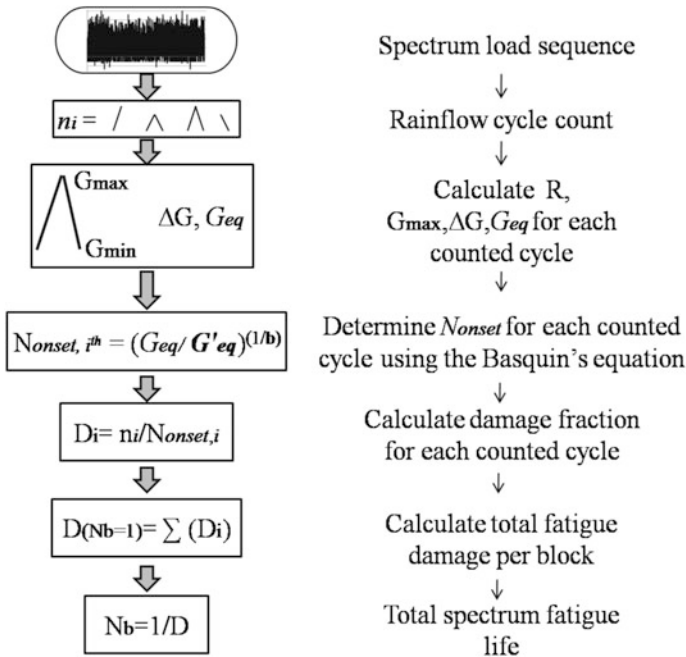


Fig. 3 Flowchart depicting the procedure used for prediction of onset-of-growth under spectrum loading

- Construction of CA $G-N_{\text{onset}}$ curves for various stress ratios. Further, the various stress ratio curves are merged using the G_{eq} concept [18] to get the $G_{\text{eq}}-N_{\text{onset}}$ plot where

$$G_{\text{eq}} = \Delta G^{(1-\gamma)} G_{\text{max}}^{\gamma} = G_{\text{max}}(1 - R)^{2(1-\gamma)} \tag{2}$$

and

$$\Delta G = G_{\text{max}}(1 - R)^2 \tag{3}$$

where γ is the best fit for the G_{eq} curve and will be discussed in subsequent section.

- Determination N_{onset} for each of the counted load cycles using the $G_{\text{eq}}-N_{\text{onset}}$ plot.
- Calculation of the damage fraction (D_i) for each of the counted load cycles, i , as the ratio of cycle count to $N_{\text{onset},i}$ obtained from the $G_{\text{eq}}-N_{\text{onset}}$ plot using the Basquin’s equation, and, finally,
- Determination of the total fatigue damage per load block (D) by summation of the damage fraction. The material is assumed to fail when the total damage fraction reaches 1.0.

4 Results and Discussion

4.1 Experimental Onset-of-Growth Under Spectrum Fatigue Tests

The onset-of-growth behavior of mode II delamination under mini-FALSTAFF load sequence determined experimentally at various reference SERR, G_{Ref} is shown in Fig. 4. Figure 4 also contains the predicted onset-of-growth life which will be

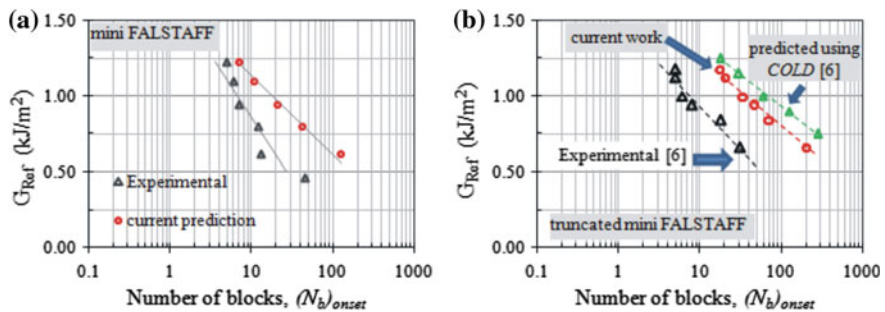


Fig. 4 Experimental and predicted $G_{\text{Ref}} - (N_b)_{\text{onset}}$ curves for mode II delamination of IMA/M21 CFC determined under, **a** mini-FALSTAFF spectrum load and **b** truncated mini-FALSTAFF

discussed in the subsequent sections. As expected, the onset-of-growth of mode II delamination increased with decrease in reference SERR, G_{Ref} . These results are in similar trend of reference stress-life curves for composites under spectrum loads [19, 20].

4.2 Prediction of Onset-of-Growth Behavior

For the purpose of prediction of onset-of-growth under spectrum loads, the fracture toughness G_{IIc} value was determined (average value is 2.2 kJ/m^2) and the procedure is elaborated in [6]. Following the procedure explained earlier (Fig. 3), the onset-of-growth life was predicted. The predicted number of blocks for onset-of-growth ($N_{\text{b}})_{\text{onset}}$ at various reference SERR (G_{Ref}) under spectrum load sequence is shown along with experimental results in Fig. 4a. Prediction appears to converge with the experimental results at higher G_{Ref} (1.25 kJ/m^2) and drift away as the G_{Ref} decreases. In our earlier work, COLD was used for prediction under modified mini-FALSTAFF load sequence and the prediction was found to be non-conservative (Fig. 4b) [6]. However, it is seen that by making use of proposed methodology ($G_{\text{eq}}\text{-}N_{\text{onset}}$) the accuracy of prediction may be improved.

4.3 Constant Amplitude Fatigue Tests and Merger of Stress Ratios

The $G\text{-}N_{\text{onset}}$ curves for IMA/M21 CFC material under mode II condition at three different stress ratios are shown in Fig. 5a. It may be clearly seen that increasing the stress ratio increases the N_{onset} . This is in agreement with similar observations made earlier in polymer composites [21, 22]. The endurance limit also increased with stress ratio, as has been observed by Bak et al. [21]. The experimental $G\text{-}N_{\text{onset}}$ curves of the IMA/M21 composite were merged into a single curve using the G_{eq} concept, explained in Sect. 3, and fit to an equation similar to Basquin's law as shown in Fig. 5b. A γ value of 0.34 was found to best fit the data points and indicates the relative contribution of ΔG and G_{max} . The Basquin's coefficient ($G'_{\text{eq}} = 5.37$) and exponent ($b = -0.24$) values were used to estimate N_{onset} and subsequently to calculate the damage fraction per rain flow counted cycle, as explained in Sect. 3. The advantage of having a single R -ratio curve in the $G\text{-}N_{\text{onset}}$ data is that the subsequent exercise of constructing COLD, used in life prediction models, is overcome and the life prediction is shown to be even better compared to the empirical model tried earlier using COLD data, shown in Fig. 4b.

Delamination studies under static and fatigue loads have been shown to exhibit some significant scatter in test results [23]. The constant amplitude data shown in Fig. 5 also shows a wide scatter. Since this data is fit to an empirical equation and

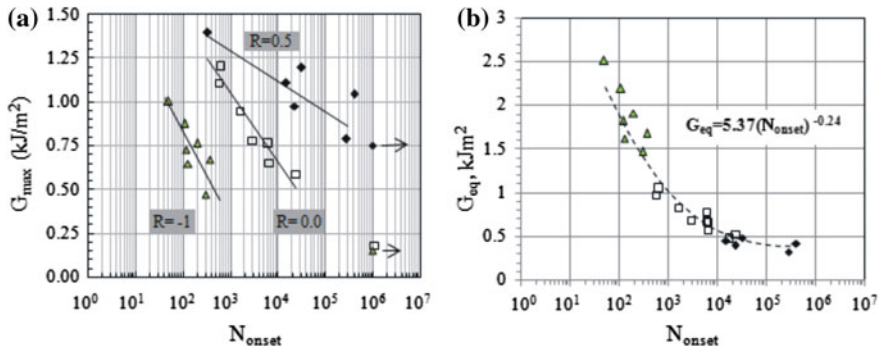


Fig. 5 **a** The constant amplitude $G-N_{onset}$ curves determined for mode II delamination in IMA/M21 CFC material, **b** the three R -ratio curves were merged into a single curve and fit to Basquin's equation

used further in prediction, the scatter may induce errors in predictions. The anomaly in the experimental and the predicted results may be attributed to the scatter in the $G-N_{onset}$ data. Hence, further work would be necessary in understanding the effect of large scatter in the $G-N_{onset}$ data and its effects on prediction.

5 Conclusions

Based on the results obtained from the present investigation, the following conclusions may be drawn:

- The three stress ratio curves of $R = 0.5, 0.0,$ and -1.0 in the $G-N_{onset}$ plot were successfully merged into a single curve using the equivalent SERR (G_{eq}) concept and fit in the form of Basquin's equation. This master plot of $G_{eq}-N_{onset}$ was subsequently used in life prediction methodology
- The predicted results are non-conservative. Nevertheless, further work is required in understanding the effect of large scatter in the $G-N_{onset}$ data on prediction, and possible the use of nonlinear damage accumulation models for onset life prediction.

Acknowledgements Authors wish to thank the AR&DB for financially supporting the project. The support and encouragement provided by Mr. Shyam Chetty, Director, Dr. Satish Chandra, Head, STTD, Dr. Ramesh Sundaram, ACD, CSIR-NAL are acknowledged. Thanks are also due to scientists and technical support staff members of FSIG-STTD and ACD, CSIR-NAL for their assistance in experimental work.

References

1. Hexcel ready to fly on the A350 XWB, *Reinf. Plast.* **57**, 25–26 (2013)
2. A.C. Garg, Delamination—a damage mode in composite structures. *Eng. Frac. Mech.* **29**, 557–584 (1988)
3. R.P. Wei, *Fracture Mechanics: Integration of Mechanics, Materials Science, and Chemistry* (Cambridge University Press, 2010)
4. FAA, Composite Aircraft Structure: Advisory Circular (AC) 20-107B, Change 1, FAA (2010)
5. N.L. Post, S.W. Case, J.J. Lesko, Modeling the variable amplitude fatigue of composite materials: a review and evaluation of the state of the art for spectrum loading. *Inter. J. Fatigue* **30**, 2064–2086 (2008)
6. N. Jagannathan, A.R. Anilchandra, C.M. Manjunatha, Onset-of-growth behavior of mode II delamination in a carbon fiber composite under spectrum fatigue load. *Compos. Struct.* **132**, 477–483 (2015)
7. M. Wisnom, M. Jones, Through thickness fatigue failure of fibre-reinforced composites. *Aeronaut. J.* **102**, 83–88 (1998)
8. J. Petermann, A. Plumtree, A unified fatigue failure criterion for unidirectional laminates. *Compos. Part A: Appl. Sci. Manuf.* **32**, 107–118 (2001)
9. M. Hojo, K. Tanaka, C.G. Gustafson, R. Hayashi, Effect of stress ratio on near-threshold propagation of delamination fatigue cracks in unidirectional CFRP. *Compos. Sci. Technol.* **29**, 273–292 (1987)
10. I. Maillet, L. Michel, F. Souric, Y. Gourinat, Mode II fatigue delamination growth characterization of a carbon/epoxy laminate at high frequency under vibration loading. *Eng. Frac. Mech.* **149**, 298–312 (2015)
11. http://www.hexcel.com/Resources/DataSheets/Prepreg-Data-Sheets/M21_global.pdf
12. A.R. Anilchandra, R. Bojja, N. Jagannathan, C.M. Manjunatha, Variable amplitude fatigue testing to characterize mode II delamination in a polymer composite. *Trans. Indian Inst. Met.* **69**, 421–424 (2016)
13. P. Heuler, H. Klätschke, Generation and use of standardised load spectra and load–time histories. *Int. J. Fatigue* **27**, 974–990 (2005)
14. W.X. Wang, M. Nakata, Y. Takao, T. Matsubara, Experimental investigation of test methods for mode II interlaminar fracture testing of carbon fiber reinforced composites. *Compos. Part A Appl. Sci. Manuf.* **40**, 1447–1455 (2009)
15. ASTM D6115, Standard test method for mode I fatigue delamination growth onset of unidirectional fiber-reinforced polymer matrix composites, vol. 15.03. Annual Book of ASTM Standards, ASTM International, West Conshohocken, PA, 2003
16. A.J. Vinciguerra, B.D. Davidson, J.R. Schaff, A.L. Smith, Determination of the mode II fatigue delamination toughness of laminated composites. *J. Reinf. Plast. Compos.* **21**, 663–677 (2002)
17. ASTM E1049, Standard practices for cycle counting in fatigue analysis. Annual Book of ASTM Standards, ASTM International, West Conshohocken, PA, 2003
18. I. Maillet, L. Michel, F. Souric, Y. Gourinat, Mode II fatigue delamination growth characterization of a carbon/epoxy laminate at high frequency under vibration loading. *Eng. Fract. Mech.* **149**, 298–312 (2015)
19. C.M. Manjunatha, R. Bojja, N. Jagannathan, Enhanced fatigue performance of a polymer nanocomposite under spectrum loads. *Mater. Perform. Charact.* **3**, 327–341 (2014)
20. C.M. Manjunatha, R. Bojja, N. Jagannathan, A.J. Kinloch, A.C. Taylor, Enhanced fatigue behavior of a glass fiber reinforced hybrid particles modified epoxy nanocomposite under WISPERX spectrum load sequence. *Int. J. Fatigue* **54**, 25–31 (2013)

21. B.L.V. Bak, C. Sarrado, A. Turon, J. Costa, Delamination under fatigue loads in composite laminates: A review on the observed phenomenology and computational methods. *Appl. Mech. Rev.* **66**, 1–24 (2014)
22. A. Argüelles, J. Viña, A.F. Canteli, M.A. Castrillo, J. Bonhomme, Interlaminar crack initiation and growth rate in a carbon-fibre epoxy composite under mode-I fatigue loading. *Compos. Sci. Technol.* **68**, 2325–2331 (2008)
23. T.K. O'Brien, W.M. Johnston, G.J. Toland, Mode II interlaminar fracture toughness and fatigue characterization of a graphite Epoxy Compos Mater, NASA/TM–2010-216838

Dependence of Crack Velocity on Stress Intensity Factor in PMMA Using Single-Edge-Notched Clamped Beams

G. R. Rahul, V. Jayaram and S. Bose

Abstract The Single-Edge-Notched Clamped Beam (SENCB) geometry, which has been used for studying fracture in graded coatings, is adapted to the study of fracture in macroscopic specimens of PMMA, a brittle, transparent polymer. Test materials were fabricated by compression molding, pre-cracked using a safety razor, and loaded at constant displacement rate at room temperature, while crack propagation was monitored with a video camera. Crack growth with time was tracked and velocity computed. The load measured from the experiment was used in FEM in conjunction with the crack length to determine the applied stress intensity factor at the different instance of crack propagation and was correlated with crack velocity. Crack grew from the interior, and a jump in crack velocity was observed as the crack spanned the width of the sample. Pre-cracking is done by physically restraining the legs and unloading as the crack propagates across the width. The average velocity of crack front was correlated with stress intensity factor (K) and was found to broadly agree with what is reported for PMMA at velocities more than 0.1 mm s^{-1} . At low velocity, the curve appears to become insensitive to K at a plateau of $\sim 0.7\text{--}0.9 \text{ MPa m}^{1/2}$.

Keywords PMMA · Single-Edge-Notched Clamped Beams · Stress intensity factor · $v(K)$ curve · Slow crack growth

Nomenclature

SENCB Single-Edge-Notched Clamped Beam
PMMA Polymethyl meta acrylate
SENB Single edge notched beam
DT Double torsion
PC Parallel cleavage
TC Tapered cleavage
DSLR Digital single lens reflex

G. R. Rahul (✉) · V. Jayaram · S. Bose
Materials Engineering Department, Indian Institute of Science, Bangalore 560012, India
e-mail: to.grrahul@gmail.com

FEM	Finite element method
K	Stress intensity factor
R	Resistance to crack extension
a/w	Crack length to width ratio
μ	Coefficient of friction

1 Introduction

The Single-Edge-Notched Clamped Beam (SENCB) has been shown to be suitable for fracture testing in microscale [1]. The test geometry is stable even under constant load because the stress gets re-distributed to the corners of the geometry as the crack propagates, whereas in most of the conventional geometries, the stress intensity factor is either constant or rises with crack extension. The microscale test specimen was made by machining out a cavity in bulk material and cutting a notch on the bottom using focused ion beam machining as shown in Fig. 1a. This configuration can be seen as a beam with connected legs to support it. In principle, the advantages observed in micron-scale should be capable of being exploited in macroscale testing. The purpose of the present work is to explore the application of this technique to a well-characterized material, i.e., polymethyl methacrylate (PMMA). Because access to the lower part of the beam for making a pre-crack would be difficult, the present work uses a modified geometry wherein two finite legs are present, shown in Fig. 1b. If the legs were physically constrained, the effective stiffness would approach that of the clamped beam; however, since the legs are free to slide sideways, the constraint is limited by the friction between the leg and the supporting substrate. The crack stability is a function of geometry, initial a/w , machine stiffness [2], and also of the initial crack front and the material's crack resistance behavior. In SENCB geometry, the driving force for crack propagation keeps decreasing with crack advance, such a geometry allows the study of slow crack growth. Thus, in comparison with the double torsion geometry [3] which employs a constant stress intensity factor, the SENCB offers the combined effect of material resistance and stress redistribution during the crack advance to produce a range of velocity and hence a range of $v(K)$ data points.

The effect of temperature on the velocity–toughness relationship in PMMA has been studied extensively [3–5]. Toughness decreases with temperature; however, at a constant temperature, the toughness increases with crack velocity in region I as shown in Fig. 2. Nonlinear behavior of energy release rate has been reported at low velocities [3, 4]. However, much of the data come from extrapolations of velocity from load relaxation. A schematic of stress intensity factor variation with velocity is given in Fig. 2 [3]. The stress intensity factor rises up to a certain velocity, and then, it drops and rises again. It has been reported that the drop is due to thermal effects (softening under conditions of adiabatic heating) at the crack tip [6]. The current

Fig. 1 **a** SENCB microbeam; **b** SENCB beam in macroscale under loading

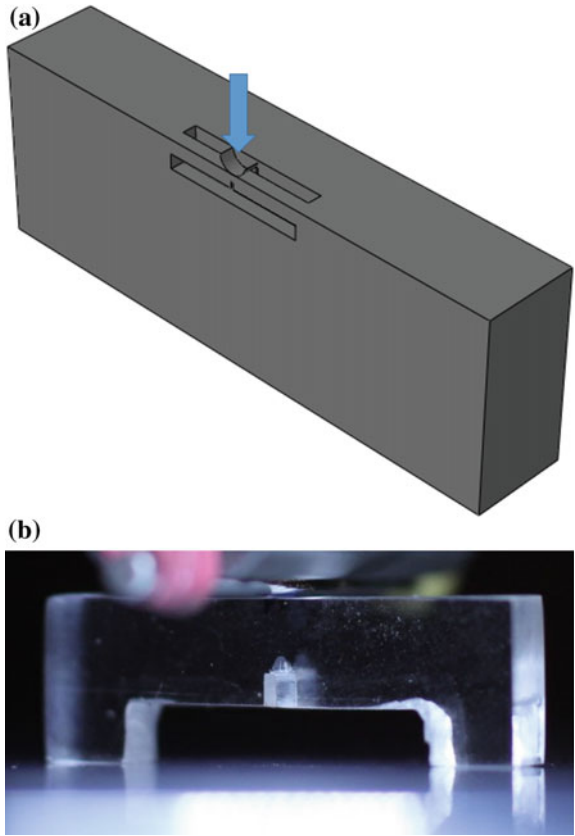
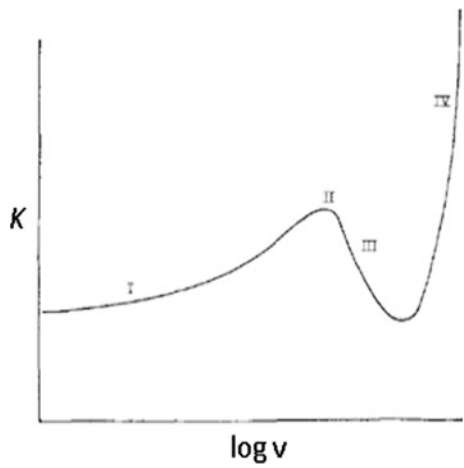


Fig. 2 Schematic of stress intensity factor versus crack velocity [3]



study is confined to the velocity region I, where stress intensity factor rises with velocity.

Applied stress intensity factor at the different instances of crack propagation was computed by Finite Element Modeling. The contour integral approach in commercial FEM package ABAQUS[®] was employed to evaluate stress intensity factor [7]. A modulus-independent method is required for computation of SIF, as crack growth is suspected to result in an effective change of modulus ahead of the crack tip in PMMA. With load as input, stress intensity factor becomes independent of the modulus. Care is taken to simulate realistic boundary conditions with respect to frictional sliding of the legs.

The experiments were done at room temperature in displacement control mode as they are inherently more stable than load control, and crack growth was recorded using a camera. Using the video of crack propagation, the crack length variation with time was tracked and correlated with load. The instantaneous crack length and the load of the geometry define the condition of the specimen. The crack is initiated in the interior of the beam and propagated across its width as it propagated. An acceleration of crack was observed when the crack front spanned the width of the beam. The stability of the geometry resulted in the drop of driving force and therefore in the reduction in crack velocity as the crack moved. A wide range of initial crack velocities was produced by varying the displacement rate and due to random variations in the initial crack profile.

2 Experimental Procedure

2.1 Sample Preparation

Polymethyl methacrylate, commonly called PMMA, is a quasi-brittle polymer. PMMA (Guzpol-P, 876G) with melt flow index of 6 g/10 min was procured from Gujarat State Fertilizers and Chemicals, India. The sample was prepared by pressure casting PMMA pellets in a Teflon mold in a compression molding machine. The machine can apply constant pressure while casting. The casting was done at 220 °C with plates preheated to 220 °C. The pellets were added in steps into the preheated mold, giving enough time for the material to flow, thus ensuring adequate supply of material in the mold cavity when the pressure is applied. The excess material is flushed out in the process. The sample is then allowed to slowly cool to room temperature under pressure inside the mold by switching off the plate heating. The surface of the specimen was polished to remove surface cracks and to obtain transparency.

2.2 Notching and Pre-cracking

A blunt notch is made on the bottom center of SENCB using a high-speed linear precision saw. The machine has a cutting disk which can transverse linearly. The cutting disk has a thickness of 0.8 mm which leads to a notch width of 0.8 ± 0.1 mm. The cutting is done on the center of the beam at 4000 rpm and at a constant feed rate of 1.2 mm/min. Care was taken to ensure that the cutting face is normal to the diameter of the cutting disk. Since PMMA is a soft material, an initial crack could be made by pressing a double-edged safety razor on the notch. However, such a crack may not be sharp and uniform across the thickness. In order to produce an ideal pre-crack, the beam's legs are clamped (to ensure maximum stability), loaded until the crack pops in and propagates across through the width, and then unloaded.

2.3 Testing

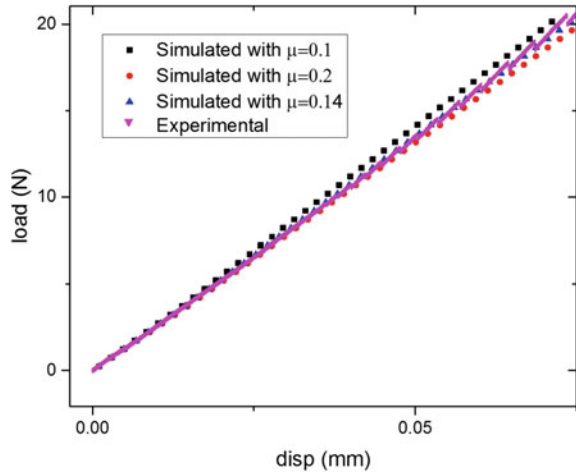
The specimen was tested in Instron make Universal Testing Machine (UTM). A load cell with a capacity of 5 KN was used for load measurement. The load cell can measure load above 0.2% of maximum capacity (i.e., 10 N). The specimen was loaded using a cylindrical indenter of 3 mm diameter. A flat plate was mounted as base. Sample was kept on the base plate, and indenter aligned above the pre-crack by visual inspection. The test was captured using a Digital Single Lens Reflex (DSLR) camera. The camera is focused on to the crack plane. Optimum illumination was provided to get a contrast between the sample and the crack. The test and the video recording are synchronized with a tolerance of ± 0.03 s. Tests were conducted in displacement control at constant crosshead velocity ranging from 5×10^{-5} to 1×10^{-2} mm/s. The test was stopped when the sample fractured completely.

3 Results and Analysis

3.1 Friction Coefficient Measurement

The friction between the bottom of the specimen leg and the base plate affects the stiffness of the beam and contributes to the redistribution of stress in the body. Physically, the role of friction may be seen as follows: when the beam is centrally loaded, the legs will tend to splay outward, thus opening the crack further. Prevention of such lateral sliding will, therefore, reduce the stress intensity factor. Therefore, friction has to be accounted for in the FEM model. The coefficient of friction was evaluated in a two-step experiment. In the first step, a beam without a

Fig. 3 Load displacement simulated with coefficient of friction 0.1, 0.14, 0.2 overlapped with experimental load displacement data in the case of beam with unconstrained legs



notch was clamped and loaded in the elastic regime. The clamping constrained the leg from sliding when the load was applied. The second step was to load the same beam without any constraint. The beam was then modeled in FEM, and stiffness of the clamped beam was matched by varying Young's modulus. By fitting in the measured modulus, the stiffness was again matched for the second experiment by varying the friction coefficient as shown in Fig. 3. By this method, a friction coefficient value of 0.14 was obtained and was used throughout the study for all beams.

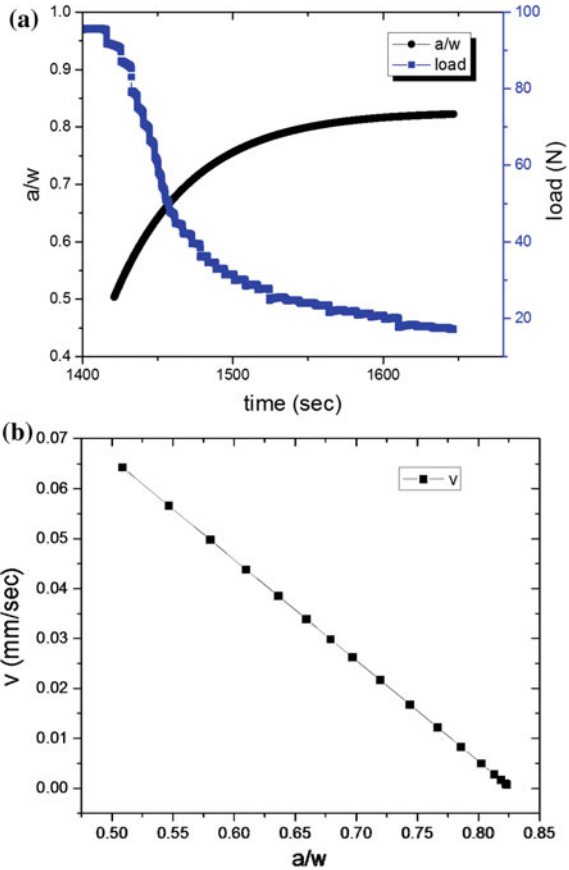
3.2 Load and Crack Length Correlation

In displacement control, as the crack propagates, the load drops in response to the drop in stiffness. Figure 4a shows the load versus time during crack growth and crack length corresponding time superimposed. The average crack length was measured by splitting the recorded video into frames and measuring the area of cracked region at various instances. Dividing the cracked area with the width of the specimen yields average crack length. And the derivative of crack length with time was taken to obtain crack velocity. Crack length and crack velocity are synchronized with experimental load values. Figure 4b shows velocity versus time for the same experiment shown in Fig. 4a. The velocity decreases steadily as crack advances. A range of velocity data is obtained from each experiment.

The factors that limit the range of analysis are as follows:

- Uncertainty in synchronizing the load displacement and crack length-time data.
- The ability to resolve crack increments much smaller than 0.1 mm.

Fig. 4 **a** Load and crack length with time. As the crack propagates, the combination of crack resistance and falling driving force retards the crack; **b** crack velocity with time for the same experiment



The load displacement and the test video can be synchronized to within ± 0.03 s. The uncertainty in load value at each point of crack increment would then vary with crack velocity. At low crack speeds, the load drops, and therefore, the uncertainty in measurement would also be low. However, at high crack velocity, a small uncertainty results in large variation of load values and hence high uncertainty in stress intensity factor. Therefore, better accuracy in experimental video synchronization is required for exploring behavior in the high-velocity regime. In the setup used a crack increment of 0.1 mm can be resolved. Therefore, in the low-velocity regime, uncertainty due to crack length measurement dominates. The uncertainty in measurement in crack length also leads to a larger error in K for long cracks, which becomes a factor even for slow cracks.

3.3 Stress Intensity Factor Using FEM

Average crack length measured at discrete instances of crack propagation from the video recorded and the load applied at corresponding instances obtained from the experimental data describes the state of the specimen during the crack advance. Applied stress intensity factor at these discrete instances is evaluated by solving the FE model of the test specimen under corresponding conditions. The friction between the specimen and the base plate, measured as shown in Sect. 3.1, is incorporated in the FE model.

The validity of the FE formulation which was tested by comparing the numerical solution of stress intensity factor to the analytical one for the ASTM three-point bend SENB geometry was modeled, and the numerical approximations closely matched with the analytical results. Contour integral method in FEM commercial was used for evaluating stress intensity factor. The contour integral method calculates J integral from displacement field and then calculates K values in each mode [7].

3.4 Crack Velocity and Profile in PMMA

The pre-crack made by the double-sided razor blade would never be uniformly through thickness. This results in lower stress intensity factor near crack tip than if it were a through crack. Hence, the crack starts moving at a higher stress intensity factor, and therefore, higher load than that needed to move a straight crack. It is observed that the initial crack develops at the interior as shown in Fig. 5a and grows simultaneously toward the indenter and the free edges, as shown in Fig. 5b. Once the crack becomes straight across the width, a sudden increase in stress intensity factor is experienced. The excess in K above equilibrium would manifest as driving force and accelerate the crack. Hence, this excess in K manifests as an initial high crack velocity even if the tests are done at quasi-static displacement rates. Subsequently, the crack stabilizes and decelerates, as shown in Fig. 5c. To achieve

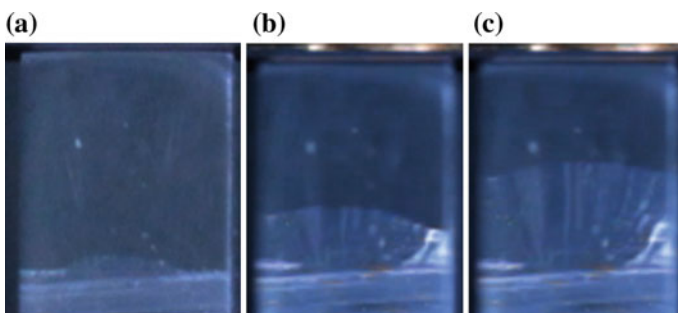


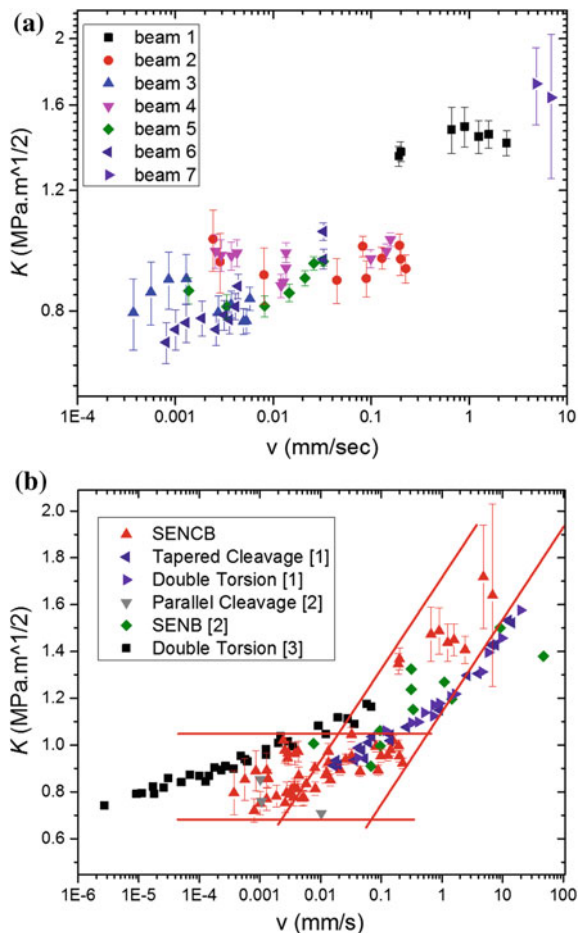
Fig. 5 a Crack initiated; b crack grown across the width; c crack face stabilized

slow crack growth, the crack was allowed to grow under loading and unloaded as the crack spreads fully across the beam width.

3.5 Crack Velocity Toughness Relation in PMMA

Average velocity of the crack front is plotted against stress intensity factor in a log-log plot, Fig. 6a. The data from earlier work on SENB, parallel cleavage, tapered cleavage, and double torsion tests are also plotted for comparison [3, 8, 9] in Fig. 6b. Unlike the double torsion and tapered cleavage beams which yield one data point per experiment, a single SENCB beam yields stress intensity factor for more than a decade of velocity values. Results from all the geometries suggest increasing velocity with stress intensity factor. Considering beams individually as given in Fig. 6a, a particular stress intensity factor yields a range of crack velocity. Tests

Fig. 6 **a** Stress intensity factor (K) versus crack velocity (v) from different SENCB beam; **b** Stress intensity factor (K) versus crack velocity (v) obtained from SENCB beams compared with the data from SENB, PC, TC, and DT geometries [3, 8, 9] in log linear plot



done on single edge notched beams and parallel cleavage geometries also yield considerable scatter. It must also be recognized that the previous double torsion data [3, 9] are not a product of direct measurements but come from models that relate load relaxation data to velocity.

Broadly speaking, the data from the present work fit in well with published results. Two bands of data points can be identified: above a velocity of around 0.1 mm/s where the stress intensity factor rises steeply and a plateau below 0.1 mm/sec where one can suggest the existence of a threshold stress intensity factor of 0.75–0.9 MPa m^{1/2} below which crack growth ceases. However, confirmation of such a threshold requires sample sizes and microscopic measurements that allow smaller crack increments to be measured than are realizable in the present optical system.

4 Conclusions

The single edged clamped beam geometry has been shown to work satisfactorily as a stable macroscopic test system to study crack propagation. Direct crack visualization coupled with load measurements allows the velocity dependence of crack growth with stress intensity factor to be mapped over four decades in crack velocity over which the toughness of PMMA varies from 0.8 to 1.6 MPa m^{1/2}.

Acknowledgements Financial support from Defense Research and Development Organization is gratefully acknowledged.

References

1. N.B. Jaya, S. Bhowmick, O.L. Warren, V. Jayaram, Optimization of clamped beam geometry for fracture toughness testing of micron scale samples. *Phil. Mag.* **95**, 1945–1966 (2015)
2. F.I. Baratta, W.A. Dunlay, Crack stability in simply supported four point and three point loaded beams of brittle material. *Mech. Mater.* **10**, 149–159 (1990)
3. G.P. Marshall, L.H. Coutts, J.G. Williams, Temperature effects in fracture of PMMA. *J. Mater. Sci.* **9**, 1409–1419 (1974)
4. A.G. Atkins, C.S. Lee, R. Caddell, Time-temperature dependent fracture toughness of PMMA. *J. Mater. Sci.* **10**, 1381–1393 (1975)
5. J.C. Pollet, S.J. Burns, An analysis of slow crack propagation data in PMMA and brittle polymers. *Int. J. Fract. Mech.* **13**, 775–786 (1977)
6. J.G. Williams, Visco-Elastic and thermal effects on crack growth in PMMA. *Int. J. Fract. Mech.* **8**, 393–401 (1972)
7. D.S. Simulia, Abaqus/CAE Users Manual version 6.7. Retrieved from egr.msu.edu: <http://www.egr.msu.edu/software/abaqus/Documentation/docs/v6.7> (2015)
8. G.P. Marshall, J.G. Williams, The correlation of fracture data for PMMA. *J. Mater. Sci.* **8**, 138–140 (1973)
9. J.Y. Robert, W.R. Beaumont, Time-dependant failure of poly(methyl methacrylate). *Polymer* **17**, 717–722 (1976)

Effect of Wrap Thickness and Ply Orientation on Cracking and Failure of FRP-Wrapped Columns

Pradeep B. Kodag and Gaurang R. Vesmawala

1 Introduction

Nowadays, retrofitting and rehabilitation of existing reinforced concrete structures are a major concern all over the world. FRP sheets are lightweight and non-corrosive, show high strength, and can be modified to satisfy performance requirements. This makes the fiber-reinforced composites a popular alternative material over the conventional materials available in the market. FRP jackets significantly increase the load carrying capacity and ductility of RC columns when used as an external reinforcement [1–3].

Most of studies showed that load carrying capacity of confined RC columns is mainly affected by parameters such as aspect ratio of specimens, FRP thickness, concrete compressive strength, modulus, and Poisson's ratio of wrapping sheet fiber orientation and type of loading [4, 5].

Some experimental studies were conducted to assess the effect of the type of loading on load carrying capacity and stiffness of confined RC columns. The results of tests conducted showed that the effectiveness of FRP-wrapped RC columns was influenced by eccentric loading. As the eccentricity increases, the effect of confining action of FRP decreases for eccentrically loaded RC columns as compared to concentrically loaded RC columns [6].

Punurai et al. studied experimental and analytical results of RC columns confined with carbon fiber-reinforced polymer (CFRP) subjected to biaxial bending. Total five RC column specimens wrapped with different layers of CFRP jackets were experimentally tested up to failure. Effect of orientation of CFRP sheets in longitudinal and transverse directions of column was studied. For all specimens, average load carrying capacity was achieved with CFRP sheets applied on all sides.

P. B. Kodag (✉) · G. R. Vesmawala
Department of Applied Mechanics, Sardar Vallabhbhai National Institute of Technology,
Ichhanath, Surat 395007, Gujarat, India
e-mail: pkodag@gmail.com

Result showed that the lateral deformation was reduced when the orientation of CFRP wrapping is along the longitudinal direction. Computational analysis done to calculate stress–strain equation for CFRP-confined concrete confirmed the behavior of tested columns. The results of experimental work and analytical program for the load versus deflections and the moment versus curvature curves were compared [7].

Rahai and Hamed carried out the experimental study on eight RC columns wrapped with carbon fiber-reinforced polymer (CFRP) under axial load and biaxial loading up to failure. This study includes variables such as CFRP sheet thickness, fiber orientations, and bi-eccentric loading. To assess the effect of these variables on the moment–curvature relationship and load–longitudinal displacement relationship, this study was carried out. Increasing longitudinal layers slightly higher than transverse layers results in a greater loading and displacement capacity of the specimens due to the overall behavior of RC wall-like columns. There was an improvement in the strength and ductility of confined RC columns [8].

Li and Hadi conducted the parametric study on FRP-wrapped columns using finite element-based software. They studied the effect of parameters like FRP thickness, stiffness, eccentric loading, and fiber orientation, comparative study of CRFP, E-glass, and steel fibers on concrete specimen wrapped with FRP. After reaching the unconfined compressive strength of columns, the mechanical properties of FRP jacket play a major role on the performance of FRP-confined columns [9].

Youcef et al. carried out an experimental work on CFRP-wrapped square RC columns under biaxial loading. For this experimentation, one to three FRP layers were wrapped to square RC columns. The load carrying capacity and deformation capacity were improved as the number of layers of FRP wrapping was increased [10].

2 Experimental Program

In this project, the experimental work was carried out for eccentrically loaded FRP-wrapped column to study the effect of change in wrap thickness and ply orientation. The experimental work was carried out by casting of 45 circular RC columns. Concrete of M20 grade was used. Experimental work was divided into two parts such as casting of unwrapped specimens and casting of GFRP-wrapped specimens. To check the consistency of the concreting, test on three cubes per batch of concreting was carried out. This experimental study was carried out to investigate the effect of following parameters on the strength of the columns reinforced with fiber composites subjected to concentric and eccentric loading.

1. Behavior of RC column due to change of loading pattern.
2. To study the effect of GFRP strengthening on the ultimate load carrying capacity of FRP-confined columns.
3. To understand the associated cracking and failure mechanism.

For the study, forty-five non-slender circular RC columns were cast; each column is having 170 mm diameter and 700 mm height. To check consistency of mix design, three cubes having size 150 mm × 150 mm × 150 mm were cast and tested, per batch of concrete. Parameters such as the GFRP thickness, fiber orientation, and the eccentricities were considered as variables. The different GFRP thickness as 0.43 and 0.86 mm (1–2 layers, respectively) and the fiber orientations as 0°, 45° and 90° were investigated. 0° referred to the orientation of fibers perpendicular to the column axis, and 90° referred to the orientation of fibers parallel to the column axis. The experimental program is summarized in Table 1.

2.1 Material Properties

All columns were cast from different batch of concrete. A concrete with a compressive strength of 20 MPa and a slump of 80–100 mm was maintained for this study. The longitudinal steel reinforcements were 4–10 mm Ø. The transverse reinforcement was provided with circular ties of 6 mm Ø stirrups 200 mm c/c. The reinforcement details for the columns are shown in Fig. 1.

2.2 Specimen Preparation and Test Setup

Column molds had to be suitably made for all the specimens with semicircular metal as shown in Fig. 2. RC cylinders were cast as per M-20 mix proportion in six batches as per dimension and after 28-day curing; the surface of cylinder was cleaned and prepared for strengthening on the next day. The GFRP fiber sheets were applied to the surface of column cylinder, saturated with epoxy. To maintain bond between GFRP sheet and concrete surface, resin was used. In transverse layer of fiber direction, 70 mm overlap was provided. The load was applied on cylinder by means of a 2000-kN load capacity universal testing machine up to failure. At top of the cylinder, eccentric load was applied with the help of special arrangement of plates of 250 mm in diameter and 25 mm thick. A steel ball of 25 mm in diameter was then placed in the relevant groove, and then, the assembly was placed under the UTM for loading.

Table 1 Experimental program

Designation	Ply orientation (°)	Number of layers of GFRP	Internal reinforcement	Number of specimens	Eccentricity (mm)	
					e_x	e_y
UE ₀	-	-	Yes	3	00	00
UE ₃₀	-	-	Yes	3	30	30
UE ₄₀	-	-	Yes	3	40	40
SWO ₀ E ₀	0	Single	Yes	3	00	00
SWO ₀ E ₃₀	0	Single	Yes	3	30	30
SWO ₀ E ₄₀	0	Single	Yes	3	40	40
SWO ₄₅ E ₀	45	Single	Yes	3	00	00
SWO ₄₅ E ₃₀	45	Single	Yes	3	30	30
SWO ₄₅ E ₄₀	45	Single	Yes	3	40	40
SWO ₉₀ E ₀	90	Single	Yes	3	00	00
SWO ₉₀ E ₃₀	90	Single	Yes	3	30	30
SWO ₉₀ E ₄₀	90	Single	Yes	3	40	40
DWO ₀ E ₀	0	Double	Yes	3	00	00
DWO ₀ E ₃₀	0	Double	Yes	3	30	30
DWO ₀ E ₄₀	0	Double	Yes	3	40	40

Note D—double wrap; E—eccentricity; e_x —eccentricity about X-axis; e_y —eccentricity about Y-axis; O—ply orientation; S—single wrap; U—unwrapped; W—wrapped

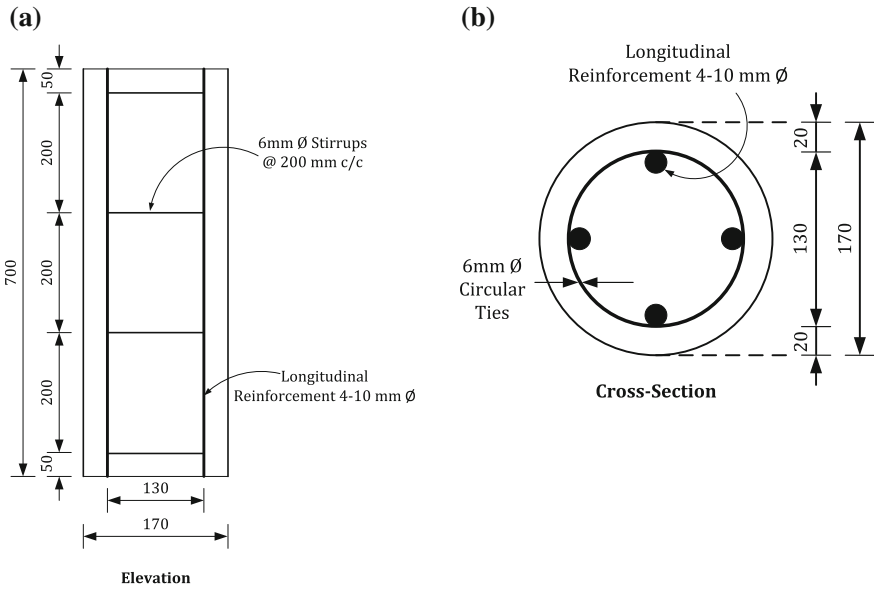


Fig. 1 Reinforcement details of circular specimen **a** elevation, **b** cross section



Fig. 2 Molds for circular columns

3 Result and Discussion

The columns were tested under load-controlled universal testing machine. The axial load was applied to the column specimen at a load rate of 1 kN/s. Figure 3 shows an experimental setup for axially and eccentrically loaded column specimens.

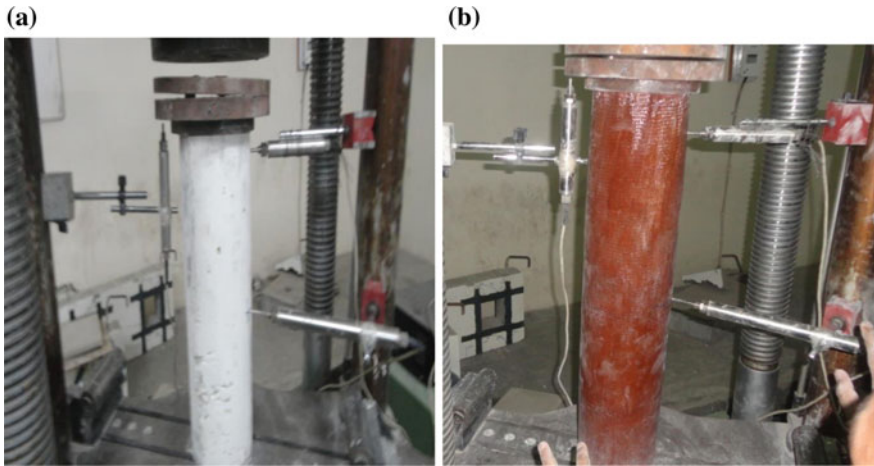


Fig. 3 Laboratory test setup for RC columns **a** unwrapped specimen, **b** wrapped specimen

3.1 *Ultimate Load Carrying Capacity*

Circular columns with 0° orientation exhibited higher axial load carrying as compared to that of other columns. As eccentricity increases, load carrying capacity of specimen decreases. 90° orientation of fiber exhibited lowest load carrying capacity. Results clearly demonstrated that variation of 0° orientations under eccentric loading plays significant role to increase load carrying capacity for RC columns. 45° orientation gives average load carrying capacity under loading. The increase in the load carrying capacity of GFRP-wrapped circular columns was 150% as compared to that of unwrapped columns. Circular shape gives full confinement and therefore has resulted in attainment of the highest compressive strength.

3.2 *Load Versus Axial Deformation*

It could be observed from Fig. 4 that GFRP-wrapped circular RC columns with ply orientation of 45° had high load carrying capacity than 90° ply orientations. Load carrying capacity decreases with increase in the eccentricity and ply angle. So as a result, 45° gives better confinement than 90° orientations.

Axial strain for columns was calculated from vertical deformation measured from LVDT. Axial stress for columns was calculated as load divided by cross-sectional area. Average axial strain was calculated from average axial deformation for the columns. Average axial stress and axial strain for unwrapped and GFRP-wrapped columns had exhibited higher axial strain as compared to that of unwrapped columns. The stress–strain specimen confinement can be considered

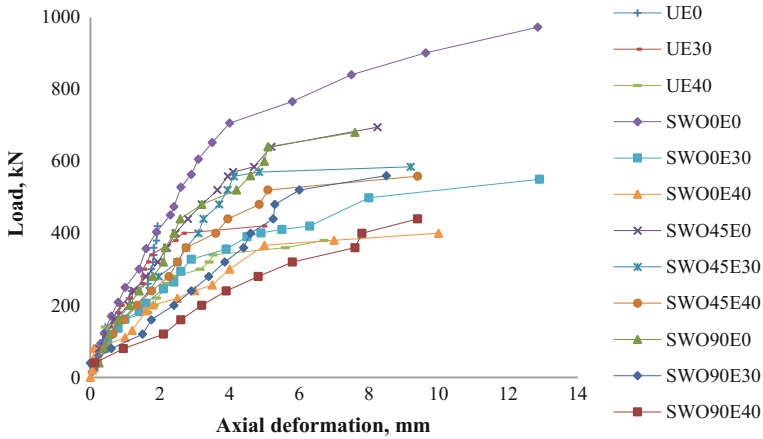


Fig. 4 Axial load versus Axial deformation

as two zones. In the first zone, stress–strain behavior of GFRP-wrapped specimen was linear, i.e., obeys Hooke’s law. In the second zone, deformation in vertical direction increases with a little increase in load and GFRP wrapping got activated, transferring the stress from dilated concrete to FRP.

3.3 Failure Modes and Crack Pattern

After reaching the ultimate strength, the failure of unwrapped RC columns was because of excessive spalling of concrete at surface and splitting of concrete between the stirrups. The governing mode of failure was shearing and spalling of the concrete in case of the unwrapped columns. Under eccentric loading, columns specimens failed mainly because of shearing. Concrete came out of the stirrups at the ultimate compressive load because of buckling of reinforcement as shown in Fig. 5.



Fig. 5 Failure pattern of unwrapped column specimen

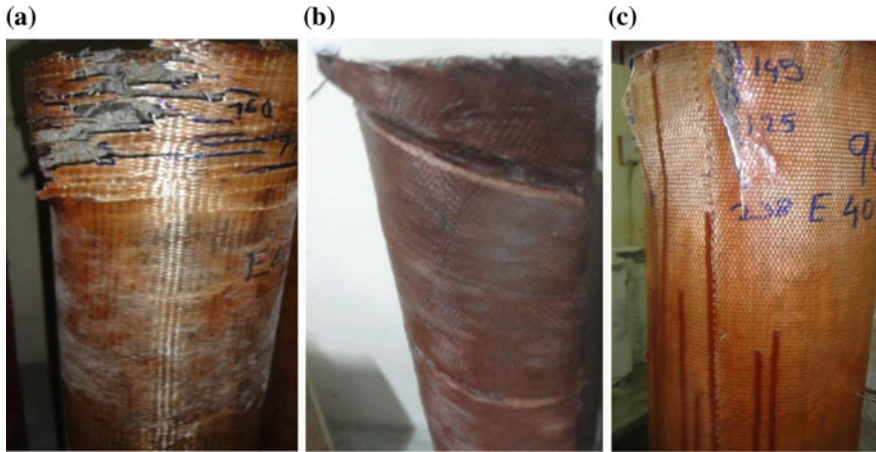


Fig. 6 Failure pattern of wrapped specimen **a** 0° wrap, **b** 45° wrap, and **c** 90° wrap

The failure of the GFRP-wrapped RC columns has been divided into three modes: (i) tensile rupture of the GFRP layer, (ii) delamination of the GFRP layer, and (iii) a combination of delamination and tensile rupture of the GFRP layer. The failure modes for the GFRP-wrapped columns are shown in Fig. 6. Most of the confined columns were failed by the rupture of the GFRP at top or bottom location. During the application of loading for the columns, typical sound was heard signifying the straining of the GFRP laminate and the cracking of the epoxy resin. Final failure for the column occurred suddenly with a significant explosive noise. Once the column reaches to the failure load, sudden rupture of GFRP wrapping was observed.

The tensile rupture of FRP composite indicates the FRP confinement has started contributing in load carrying capacity of column. Failure at top or bottom was observed for specimen wrapped with GFRP 0° and 45° orientation. The specimens were wrapped with GFRP at 90° orientation, the failure pattern observed for these specimens was vertical tearing of the GFRP sheet. Debonding failure was not observed for 0° and 90° orientation, which revealed that the overlap provided was sufficient to transfer the stress from concrete to GFRP confinement. However, for few specimens wrapped with GFRP at 45° orientation, debonding was observed.

As eccentricity increases, abrupt behavior could be seen as the result of ineffectiveness of the GFRP confinement. Thus, single layer of GFRP confinement proved to be insufficient as compared to double wrapping. In case of doubly wrapped specimens, large deformations were observed without much rupture of FRP jacket.

4 Conclusions

In order to study the behavior of FRP-confined column, total 45 reinforced concrete columns confined with GFRP sheets were cast and tested under concentric and eccentric load. The experimental work was carried out for FRP-wrapped column to access the effect of change in wrap thickness and ply orientation. From comparison and investigation between the different eccentricities, a number of conclusions were drawn:

- GFRP wrapping increased the axial load carrying capacity by providing addition confinement to the concrete without much increase in the original column size and weight of the structure.
- Effective confinement with GFRP wrapping resulted in enhancement of the compressive strength of GFRP-wrapped circular columns by 150% compared with unwrapped specimens for 0° orientation.
- All unwrapped columns failed under brittle mode with spalling effect. GFRP-wrapped circular column failed without any sign of debonding.
- Magnitude of eccentricity affects the maximum load carrying capacity of a confined column under eccentric load. As the eccentricity increases, the load carrying capacity decreases.
- GFRP-wrapped circular RC columns with 0° ply orientation showed highest load carrying capacity than 45° and 90° orientations. Load carrying capacity decreases with increase in the eccentricity. So as a result, 0° gives better confinement than 45° and 90° orientation.

References

1. S. Rocca, N. Galati, A. Nanni, Interaction diagram methodology for design of FRP confined reinforced concrete columns. *Constr. Build. Mater.* **23**(4), 1508–1520 (2009)
2. M.N.S. Hadi, Comparative study of eccentrically loaded FRP wrapped columns. *Compos. Struct.* **74**(2), 127–135 (2006)
3. M.N.S. Hadi, Behavior of FRP strengthened concrete columns under eccentric compression loading. *Compos. Struct.* **77**, 92–96 (2007)
4. M.H. Harajli, Axial stress—strain relationship for FRP confined circular and rectangular concrete columns. *Cement Concr. Compos.* **28**(10), 938–948 (2006)
5. H.J. Lin, Liao CL compressive strength of reinforced concrete column confined by composite material. *Compos. Struct.* **65**(2), 239–250 (2004)
6. El Maaddawy, Strengthening of eccentrically loaded reinforced concrete columns with fiber-reinforced polymer wrapping system: experimental investigation and analytical modeling. *J. Compos. Constr.* **13**(1), 13–24 (2009)
7. W. Punurai, C.T.T. Hsu, J. Chen, Biaxially loaded RC slender columns strengthened by CFRP composite fabrics. *Eng. Struct.* **46**, 311–321 (2012)
8. Alireza Rahai, Hamed Akbarpour, Experimental investigation on rectangular RC columns strengthened with CFRP composites under axial load and biaxial bending. *Compos. Struct.* **108**, 538–546 (2014)

9. J. Li, M.N.S. Hadi, Behavior of externally confined high strength concrete columns under eccentric loading. *Compos. Struct.* **62**(2), 145–153 (2003)
10. Youcef Y, Amziane S, Chemrouk M, The influence of CFRP on the behavior of reinforced concrete subjected to buckling, in *Proceedings of the 4th inter conf on FRP compos eng (CICE2008)* (Zurich, Switzerland, 2008)

Studies on Fracture Features and Fracture Toughness of CFRP Composites Fabricated by Resin Infusion Technique

K. Panbarasu, M. Suresh Kumar, V. R. Ranganath and R. V. Prakash

Abstract Fiber reinforced polymer matrix composite laminates are extensively employed in aerospace and other advanced applications owing to their desirable properties like high specific stiffness and specific strength. However, full weight saving potential of these composites has not been completely utilized because of their susceptibility to delamination failure. The delamination failures are usually considered as propagation of a crack between two adjacent layers, individually or in combination of Mode I and II loading conditions. Mode I fracture toughness studies were conducted on carbon fiber reinforced plastic (CFRP) composites fabricated by resin infusion technique. A small amount of fiber or other material runs in a direction perpendicular to the carbon fibers, with the main intention to hold the primary fibers in position. The unidirectional (UD) fabric employed in the present study contains 3–4 wt% of glass fibers as warp fibers. This configuration could influence the fracture toughness of the laminate. Hence, in the present study, interlaminar fracture studies were conducted under Mode I loading condition on resin infused UD fabric composites. The fracture surface characteristics were studied using scanning electron microscope (SEM). The studies reveal that Mode I fracture toughness initiation value is lower than the toughness values reported for neat resin and is ascribed to weak interface between fiber and matrix. The Mode I fracture propagation values are influenced by the use of warp glass fibers employed for holding the UD fibers intact in resin infused composites. This favors additional energy absorption mechanisms, such as crack detour, fiber displacement, and fracture in addition to fiber bridging. These and other aspects of the studies are discussed in the paper.

Keywords CFRP composites · Interlaminar fracture toughness
Resin infusion · Fractography

K. Panbarasu · M. Suresh Kumar (✉) · V. R. Ranganath
CSIR-National Aerospace Laboratories, Bangalore, India
e-mail: mskumar@nal.res.in

R. V. Prakash
Department of Mechanical Engineering, Indian Institute Technology, Chennai, India

© Springer Nature Singapore Pte Ltd. 2018
R. Prakash et al. (eds.), *Advances in Structural Integrity*,
https://doi.org/10.1007/978-981-10-7197-3_20

1 Introduction

Fiber reinforced polymer matrix composite laminates are extensively employed in aerospace and other advanced applications owing to their desirable properties like high specific stiffness and specific strength. However, full weight saving potential of these composites has not been completely utilized because of their susceptibility to delamination failure. Delaminations can significantly alter the structural properties of the composites resulting in loss of mechanical strength and stiffness, especially the compressive strength as well as fatigue life [1]. Further, delaminations can lead to exposure of the fibers to environmental conditions such as moisture and lead to failure before it can be detected or monitored.

Delaminations can be generated due to tool drop, hailstorm, and runway debris impacting on the panel surfaces and/or due to the free edge stresses arising around functional cutouts, rivet/bolt holes, etc. [2]. In general, excessive out-of-plane or interlaminar stresses could result in local delaminations [3]. Efforts are continuing to improve the delamination resistance of laminated composite materials [4–9]. The delamination failures are usually considered as propagation of a crack between two adjacent layers, individually or in combination of Mode I and or Mode II loading conditions. Some authors have studied interlaminar fracture toughness of different composite materials with emphasis on various data reduction methods for calculation of strain energy of different kinds of failure modes [10, 11]. Only a few authors have addressed this issue through fractography to understand the fracture process. Thus, Bonhomme [12] studied fracture surfaces of UD AS4/8552 carbon/epoxy prepreg composite laminate subjected to Mode I and Mode II loading conditions.

An effort was also made to correlate the fracture surface appearance with the state of stress. Recently, Greenhalgh presented an extensive study of fractography on delaminated composites [13]. However, fractographic studies on delamination failure in UD fabric carbon fiber reinforced plastic (CFRP) composites fabricated by resin infusion technique are rare in the available literature. The resin infusion technique employs UD fabric. A small amount of fiber or other material runs in a direction perpendicular to the carbon fibers, with the main intention of holding the primary fibers in position. The UD fabric employed in the present study contains 3–4 wt% of glass fibers as warp fibers [14]. This configuration could influence the fracture toughness of the laminate. Hence, in the present study, interlaminar fracture studies were conducted under Mode I loading condition on resin infused UD fabric composites. Standard ASTM recommended procedures were employed for data reduction and calculating the fracture toughness values [15]. The fracture surfaces were studied in detail to understand the mechanisms that influence the fracture toughness values.

Table 1 Resin properties

Tensile strength (MPa)	Elastic modulus (GPa)	Fracture toughness (J/m ²)
57	3.1	300 ^a

^aMean of the value arrived at from the results in Ref. [17, 18]

Table 2 Fiber properties

Tensile strength (MPa)	Elastic modulus (GPa)
4000	236

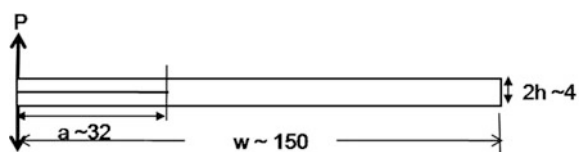
2 Materials and Methods

The laminates of UD CFRP are fabricated through resin infusion technique with epoxy resin system. The reinforcement is UD carbon fabric manufactured by M/s Hexcel composites. The resin system is Epolam 2063 supplied by M/s. Axson, France. The reinforcement/fiber constitutes 68% by weight. The properties of resin and fiber provided by the supplier [14, 16] are presented in Tables 1 and 2, respectively. A total of 26 plies, each of ~0.15 mm thick, were used to obtain a nominal laminate thickness of 4 mm. The dry fabric (reinforcement) is infused with resin-hardener mixture at 40 °C under vacuum (0.1 MPa). The infused laminates are heated to 65 °C and dwelled for 3 h. Later, it is heated to 80 °C and dwelled for 7 h. This is followed by a free-standing post-cure at 160 °C for 4 h. The UD dry fabric contains bundles of glass fibers (3–4 wt%) in a direction perpendicular to that of UD carbon fibers in order, as stated earlier on, to hold the primary fibers in position. A 12.7 μm thick Teflon foil was inserted at the midplane of the panels during layup process to define a starter delamination/crack for all the test specimens.

3 Specimen Preparation and Test Conditions

The sample geometries and test conditions used for Mode I double cantilever beam (DCB) are shown in Fig. 1. The test specimens were prepared from the fabricated laminates. The nominal dimensions of length ~152 mm, width ~25 mm, and thickness ~4 mm were employed for each case. The crack length ~32 mm was uniformly maintained in each specimen. Prior to bonding the load-hinges, the specimens were slightly abraded using 240-grade emery papers. The loading blocks

Fig. 1 DCB sample geometry and test conditions. All dimensions are in millimeter



were bonded with AralditeTM, a two-component room temperature cure adhesive. All the tests were performed on a computer-controlled test machine having a load cell maximum capacity of 5 kN. The specimens were mounted on the test fixture and tests were performed under displacement control at a cross-head displacement rate of 1 mm/min. At least five specimens were tested. Load (P) versus displacement (δ) plots were recorded during the tests. From these plots, P_{NL} [19] was obtained to calculate Mode I fracture toughness for delamination initiation ($G_{IC, ini}$). P_{NL} is the load at point of deviation from linearity of the initial P versus δ plot. The plateau values in the R -curve (G_{IC} versus delamination length) were taken as fracture toughness for delamination propagation ($G_{IC, prop}$) values. The fracture toughness values were obtained as per ASTM standards D5528-13 via modified beam theory [15] as per equation.

$$G_I = (3P\delta) / [2b(a + \Delta)] \quad (1)$$

where P is the applied load, δ is the load point displacement, b is the specimen width, a is the delamination length, and Δ is a correction term for the crack length and determined by generating a least square plot of the cube root of compliance, $C^{1/3}$ as a function of the crack length.

Specimens of suitable size for observation under LEO 440i scanning electron microscope (SEM) were prepared by sectioning the delaminated specimens with a jeweler's saw. The debris, formed on the fractured surface during sectioning, was minimized by cutting the samples before the delamination surfaces were separated. The generated debris was blown away using compressed air. The delaminated surfaces were examined in detail under SEM for fractographic characterization. The fracture surfaces were vacuum sputter coated with gold before examining under SEM.

4 Results and Discussion

Figure 2 shows typical P versus δ plot of the composite material tested for Mode I condition. Significant nonlinear behavior is observed before the maximum load is reached. The fracture toughness values obtained for delamination initiation, $G_{IC, ini}$ and propagation, $G_{IC, prop}$ are ~ 190 and 450 J/m^2 , respectively (Table 3). For the case of neat resin, a band of 210 to 390 J/m^2 has been reported in the literature [17, 18] from which if an average of 300 J/m^2 is considered for discussion, the value of $G_{IC, ini}$ for the composite considered is low. It may be noted that epoxy resins are brittle and usually exhibit relatively smaller deformation zone. Therefore, $G_{IC, ini}$ values of the composite laminate are not expected to be lower than the ones displayed by the neat resin [20]. Moreover, $G_{IC, prop}$ is higher than that of $G_{IC, ini}$. The higher value of $G_{IC, prop}$ points to greater resistance to delamination propagation. The G_{IC} variation against crack length, a , is shown in Fig. 3. G_{IC} increases monotonically in the first few millimeters

Fig. 2 P versus δ plot for resin infusion composite

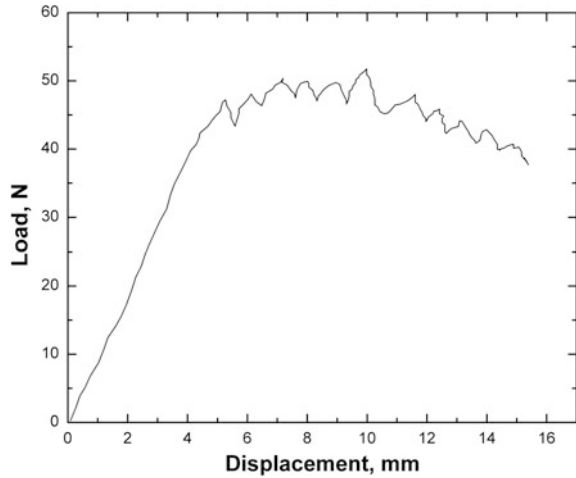
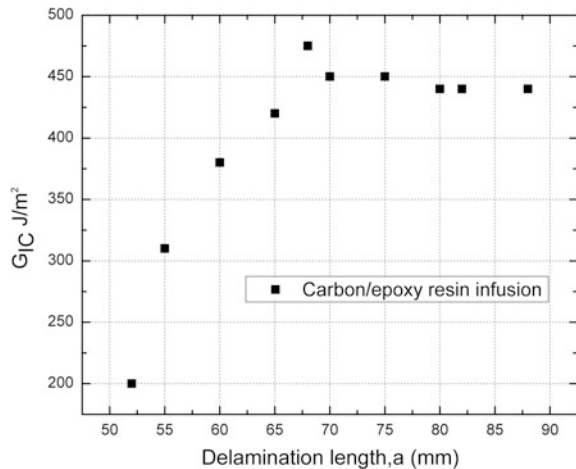


Table 3 Mode I fracture toughness values

Fracture toughness $G_C \pm$ standard deviation (J/m^2)	
Initiation	Propagation
190 ± 11	450 ± 2

Fig. 3 G_{IC} against crack length, a , for resin infusion composite



of crack propagation, and then stabilizes with further crack growth. The reasons for differing aspects of recording lower $G_{IC, ini}$ and higher $G_{IC, prop}$ values are discussed in detail through fractographic analysis on both crack initiation and propagation regions.

Typical fracture surface of resin infusion composite tested in Mode I loading is shown in Fig. 4. Detailed examination on the crack origin region revealed matrix

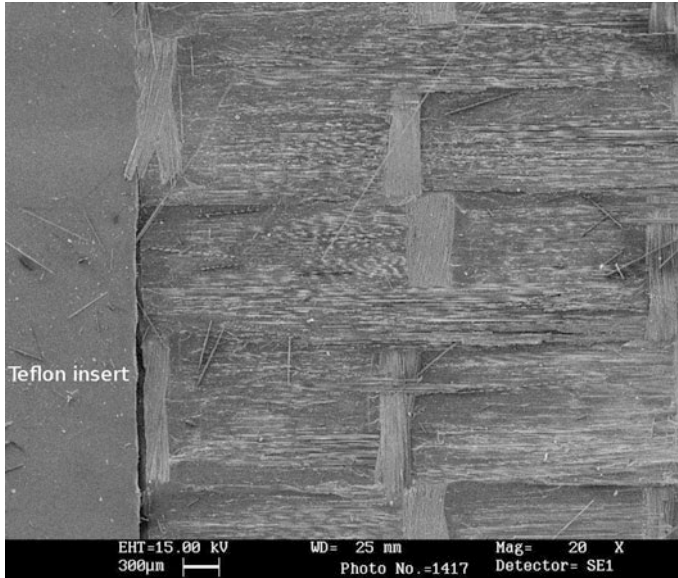


Fig. 4 Fracture surface of delaminated composite samples

cracks near fiber/matrix interface and lesser tendency for fibers to display smearing of matrix on them indicating a lesser adherence at the interface regions (Fig. 5a). This lesser adherence factor favors crack initiation and propagation along the fiber/matrix interface rather than through the matrix. Due to this, the inherent toughness of matrix could not be fully realized and leads to lower $G_{IC,ini}$ values of composite as compared to neat resin toughness.

The fracture surface in crack propagation region exhibited features of fiber breakages and lifting (Fig. 5b) which are the characteristic marks of fiber bridging phenomenon [21]. According to a report [22], fiber bridging is one of the factors responsible for increase in fracture toughness value above $G_{IC,ini}$. Therefore, fiber bridging mechanism is a factor paving way for increased $G_{IC,prop}$.

The weak interface also highlights extensive fiber bridging during crack propagation, resulting in higher $G_{IC,prop}$ as seen in the present case. Further, fracture surface also reveals an undulated surface (Fig. 6a) in the crack propagation region. Undulations are due to presence of warp glass fibers used in the fabrication of UD fabric. These warp glass fibers could favor a detour in the crack path. It has also been observed that significant amount of resin-rich regions (Fig. 6b) develop in the resin infused zones. The local resin-rich areas could act as crack detour zones owing to these regions containing less of the fibers and the associated lower adherence tendencies discussed earlier on. This situation could also lead to an increase in the propagation toughness [23]. Additionally, warp fiber pullout together with

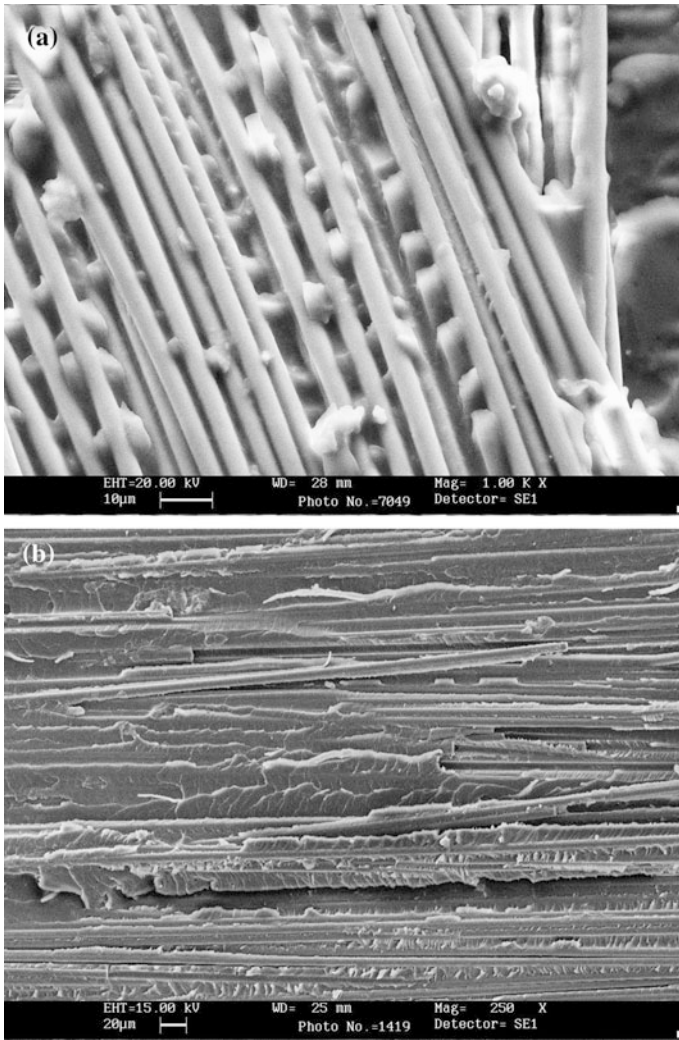


Fig. 5 a Presence of cleaner fibers with sparsely adhered matrix; b a photograph illustrating fracture and lifting of the fibers

displacement (Fig. 6c) and fracturing at a few locations (Fig. 6d) during the test could also contribute to higher energy absorption thereby resulting in increased $G_{IC, prop}$ values. Therefore, fiber bridging, crack deflection, encountering resin-rich region, fiber pullout, fiber fragmentation could all be included as the reasons for increased delamination propagation toughness in resin infused composites.

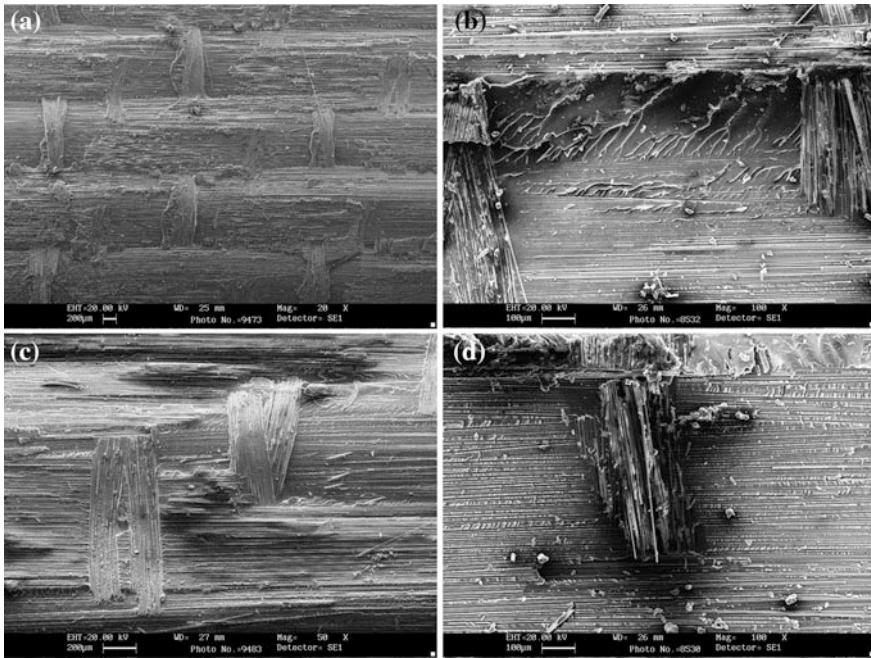


Fig. 6 Fracture surface features observed in crack propagation regions: **a** undulations; **b** typical features noticed in some resin-rich region; **c** pullout with marginal displacement of some warp fibers; and **d** fracturing of warp fibers

5 Conclusions

UD CFRP composites fabricated by resin infusion process exhibit lower $G_{IC,ini}$ and higher $G_{IC,prop}$ as compared to neat resin G_{IC} values cited in literature. Fractographic study reveals that poor interface bonding between matrix and fiber lead to such differences. Additionally, the woven glass fiber structure in resin infused composite triggers various other local energy absorption mechanisms viz., crack deflection, fiber pullout, fiber fracture, etc. that in turn lead to higher $G_{IC,prop}$ values.

Acknowledgements Authors are deeply acknowledging the staff and Head of Departments of Advanced Composite Division, Material Sciences Division and Structural Technologies Divisions of CSIR-NAL for their direct and indirect support rendered toward this work.

References

1. K. Singh, B. Dattaguru, T. Ramamurthy, P. Mangalgi, Delamination tolerance studies in laminated composite panels. *Sadhana* **25**, 409–422N (2000)
2. N.S. Choi, A. Kinloch, J. Williams, Delamination fracture of multidirectional carbon-fiber/epoxy composites under mode I, mode II and mixed-mode I/II loading. *J. Compos. Mater.* **33**, 73–100 (1999)
3. T. Nyman, Fatigue and residual strength of composite aircraft structures. Ph.D. Thesis, Institutionen för flygteknik (1999)
4. N. Sela, O. Ishai, Interlaminar fracture toughness and toughening of laminated composite materials: a review. *Composites* **20**, 423–435 (1989)
5. S. Sankaran, M. Chanda, Chemical toughening of epoxies-II. Mechanical, thermal, and microscopic studies of epoxies toughened with hydroxyl-terminated poly (butadiene-co-acrylonitrile). *J. Appl. Poly. Sci.* **39**, 1635–1647 (1990)
6. Kishore, S.M. Kulkarni, D. Sunil, S. Sharathchandra, Effect of surface treatment on the impact behaviour of fly-ash filled polymer composites. *Poly. Inter.* **51**, 1378–1384 (2002)
7. Y. Hirai, H. Hamada, J.K. Kim, Impact response of woven glass-fabric composites—I: Effect of fiber surface treatment. *Compos. Sci. Tech.* **58**, 91–104 (1998)
8. A. Peijs, R. Venderbosch, P. Lemstra, Hybrid composites based on polyethylene and carbon fibers Part 3: Impact resistant structural composites through damage management. *Composites* **21**, 522–530 (1990)
9. C. Marshall, *International encyclopedia of composite materials* (VCH Publishers, New York, 1990)
10. S.P. Blake, K.A. Berube, R.A. Lopez-Anido, Interlaminar fracture toughness of woven E-glass fabric composites. *J. Compos. Mater.* **46**(13), 1583–1592 (2012)
11. M.S. Prasad, C. Venkatesha, T. Jayaraju, Experimental methods of determining fracture toughness of fiber reinforced polymer composites under various loading conditions. *J. Miner. Mater. Charact. Eng.* **10**(13), 1263–1275 (2011)
12. J. Bonhomme, A. Argüelles, J. Vina, I. Vina, Fractography and failure mechanisms in static mode I and mode II delamination testing of unidirectional carbon reinforced composites. *Polym Test.* **28**, 612–617 (2009)
13. E.S. Greenhalgh, *Failure analysis and fractography of polymer composites* (CRC Press, Washington, DC, 2009)
14. Hexcel composites, Aerospace selector guide, USA (2010)
15. ASTM D5528–13A, Standard test method for mode I interlaminar fracture toughness of unidirectional fiber-reinforced polymer matrix composites
16. Epolam 2063 data sheet, Axson, France
17. G. Quino, J. El Yagoubi, and G. Lubineau, Characterizing the toughness of an epoxy resin after wet aging using compact tension specimens with non-uniform moisture content. *Polym. Degrad. and Stab.* **109**, 319–326 (2014)
18. Q.Q. Gustavo, Characterization of fracture toughness of epoxy resin after hygrothermal aging. M.Sc. Thesis, King Abdullah University of Science and Technology (2013)
19. K.Y. Kim, L. Ye, K.M. Phoa, Interlaminar fracture toughness of CF/PEI and GF/PEI composites at elevated temperatures. *Appl. Compos. Mater.* **1**, 173–190 (2004)
20. W.L. Bradley, R.N. Cohen, Matrix deformation and fracture in graphite-reinforced epoxies. *ASTM STP* **876**, 389–410 (1985)
21. I. Chou, I. Kimpara, K. Kageyama, I. Ohsawa, Mode I and mode II fracture toughness measured between differently oriented plies in graphite/epoxy composites. *ASTM STP* **1230**, 132–151 (1995)
22. P. Compston, P.Y. Jar, P.J. Burchill, K. Takahashi, The transfer of matrix toughness to composite mode I interlaminar fracture toughness in glass-fibre/vinyl ester composites. *Appl. Compos. Mater.* **9**(5), 291–314 (2002)
23. A.J. Brunner, B.R.K. Blackman, P. Davies, Mode I delamination. In: D.R. Moore, A. Pavan, J.G. Williams (Eds.), *Fracture Mechanics Testing Methods for Polymers, Adhesives, and Composites* (Elsevier Science Ltd, 2001), pp 277–305

Numerical and Experimental Analysis of Double-Sided Stepped Lap-Repaired CFRP Laminates Under Tensile Loading

Matta Seshadri and M. Ramji

Abstract Adhesive layer plays a critical role in the strength restoration of the scarf repaired carbon fibre-reinforced plastic (CFRP) laminates. In this work, Araldite 2015 is used. Hence, it is crucial to model the behaviour of adhesive layer accurately in case of numerical model. Modelling of adhesive layer by cohesive zone law characterises the fracture behaviour of the bonded joint accurately. In this paper, cohesive zone law parameters for mode I and mode II are determined by comparing numerical predictions to experimental observations of a double cantilever beam (DCB) for mode I and end notched flexure (ENF) for mode II fracture test. In this work, Araldite 2015 (supplied by Huntsman) is used for repair work. Strain energy release rate for both mode I and mode II is determined by performing DCB and ENF test, respectively. Traction–separation law for mode I is generated by direct method which involves differentiation of the relation between the strain energy release rate and crack tip opening displacement which is measured using digital image correlation (DIC) technique. Traction–separation law for mode II is generated by inverse method which involves fitting the numerical and experimental load–displacement curves. The obtained cohesive law is used to model the adhesive layer in numerical analysis of double-sided stepped lap joint repair of CFRP laminate subjected to tensile loading. The numerical predictions are validated by comparing the load–displacement curve obtained from the experimental study. A good agreement exists between numerical and experimental results confirming that the proposed cohesive law for mode I and mode II can be applied to model adhesive layer with CFRP as adherend.

Keywords Cohesive zone law · Strain energy release rate · Digital image correlation · Double-sided stepped lap joint

M. Seshadri · M. Ramji (✉)
Engineering Optics Lab, Department of Mechanical and Aerospace Engineering,
IIT Hyderabad, Hyderabad 502205, India
e-mail: ramji_mano@iith.ac.in

List of symbols

a	Crack length
a_e	Equivalent crack length
a_0	Initial crack length
B	Width of the specimen
C	Compliance of the specimen
C_0	Initial compliance
E_f	Flexural modulus
G_I	Mode I strain energy release rate
G_{IC}	Mode I fracture toughness
G_{II}	Mode II strain energy release rate
G_{IIC}	Mode II fracture toughness
h	Height of single adherend
L	Total specimen length
P	Applied load on the specimen
w	Crack tip opening displacement (CTOD)
δ	Displacement of the specimen
δ_0	Damage initiation relative displacement
δ_c	Ultimate relative displacement
Δ	Correction factor for root rotation effect
t_a	Adhesive thickness
σ	Normal traction

1 Introduction

In adhesive bonding, the transfer of load between panel and patch is through the adhesive layer and it constitutes as the weakest link in repaired configuration and failure initiates in the adhesive layer. Hence, adhesive layer plays a precarious role in the strength restoration of the scarf repaired carbon fibre-reinforced plastic (CFRP) laminates. It is crucial to model the behaviour of adhesive layer accurately in case of numerical model. The three approaches based on fundamental mechanics applied in finite element modelling of the adhesively layer of bonded joints are fracture mechanics, continuum mechanics, and damage mechanics. Continuum mechanics approach is based on stress and strain analysis. It is challenging to use strain- and stress-based criteria as singularity arises in the bonded joints. Energy-based parameter (joint toughness) is used in linear elastic fracture mechanics (LEFM) approach. Toughness values in opening, sliding, and mixed mode loading conditions are estimated to predict the strength of the adhesive joint. Linear elastic fracture mechanics is based on linear elastic behaviour of adhesive and the presence of initial flaws. In many cases, it can be challenging to locate flaw a priori in the composite structural component and also most of the recent adhesives

have ductile behaviour, which is the reason why LEFM approach is not suitable for practical applications. A thorough review of various analytical models on behaviour of adhesively bonded joints related to both single and double-lap joint configuration is presented in [1, 2]. In order to overcome the above difficulties, both the stress-based and the energy-based criteria are combined to model the adhesively bonded joints. Modelling of adhesive layer by cohesive zone law characterises the fracture behaviour of the bonded joint accurately. It combines both stress-based criteria and energy-based fracture mechanics criteria to simulate damage initiation and its propagation, respectively. A comprehensive review of finite element methods applied to analyse the adhesively bonded joints is presented in [3]. Advanced techniques in finite element modelling of adhesive layer are described in [4].

To obtain cohesive law of CFRP composite bonded joints, initially, strain energy release rate is measured using experimental techniques. The estimation of strain energy release rate involves measurement of crack tip progression throughout the test. It is difficult to identify the crack tip during the test which results in non-negligible errors in the estimation of strain energy release rate. A data reduction technique based on specimen compliance and beam theory is proposed in [5]. In this method, the measurement of strain energy release rate is not dependent on crack tip progression during the test, but depends wholly on the specimen compliance, which results in accurate measurement. Later, an inverse approach based on curve fitting involving curve fitting of experimental load displacement data with numerical prediction is carried to obtain the cohesive law [6]. Alternatively, in direct methods, strain energy release rate (G) is defined in terms of crack tip opening displacement (CTOD) based on the experimental behaviour [7]. The cohesive damage law is further obtained by differentiating the relation $G = f(\text{CTOD})$.

In the present work, the cohesive law for the adhesive bonding of the CFRP composite joints under Mode I and Mode II loading conditions is determined, and the obtained cohesive law is used to describe the adhesive layer behaviour in numerical model of the double-sided stepped lap-repaired CFRP laminate subjected to tensile loading. The numerical predictions are validated by comparing the load-displacement curve obtained from the experimental study.

2 Cohesive Damage Model

2.1 Pure Mode I Loading Condition

2.1.1 Estimation by Direct Method

The strain energy release rate of CFRP composite bonded joint under mode I (G_I) loading condition is determined using equivalent crack method [7]. In this method,

specimen compliance is utilised. Based on Timoshenko beam theory, the specimen compliance is given by

$$C = \frac{8a^3}{E_1 B h^3} + \frac{12a}{5BhG_{13}} \quad (1)$$

An equivalent flexural modulus is obtained from Eq. (1), which includes the effect of adhesive presence, stress concentrations, and material variability [8]. Initial crack length and compliance are considered to estimate E_f , which is given in the Eq. (2).

$$E_f = \left(C_0 - \frac{12(a_0 + h\Delta)}{5BhG_{13}} \right)^{-1} \frac{8(a_0 + h\Delta)^3}{Bh^3} \quad (2)$$

From Irwin–Kies equation, we have

$$G_I = \frac{P^2 dC}{2B da} \quad (3)$$

By substituting the value of compliance (C) from (1) in the above equation, we get

$$G_I = \frac{6P^2}{B^2 h} \left(\frac{2a^2}{E_f h^2} + \frac{1}{5G_{13}} \right) \quad (4)$$

From the above equation, to evaluate G_I experimentally crack length monitoring is required which is not easy because it is not visible clearly to identify the crack tip. Instead, equivalent crack length can be evaluated by the current compliance using the relation $a_e = f(C)$ [6]. Following this procedure is advantageous as equivalent crack length, and G_I are obtained directly from load–displacement curve.

To determine the cohesive damage law for adhesively bonded CFRP composite joint using direct method, the following relation between G_I and (CTOD) is very essential.

$$G_I = \int_0^w (\sigma) dw \quad (5)$$

The differentiation of strain energy release rate G_I with respect to the CTOD leads to cohesive law

$$\sigma = f(w) \quad (6)$$

$$\sigma(w) = \frac{dG_I}{dw} \quad (7)$$

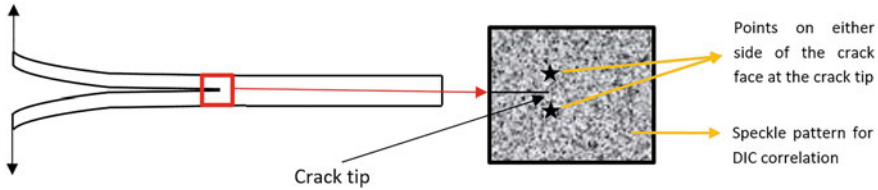


Fig. 1 Schematic of the CTOD measurement location in the DCB specimen

To obtain the CTOD in this work, DIC technique is utilised. The sensitivity analysis of digital image correlation technique is described in [9]. The CTOD is defined as the relative displacement between cracked face, measured in the normal to the crack plane, at the initial crack tip. The CTOD is estimated from the displacement field obtained from DIC, by considering displacements at the crack tip which are perpendicular to the crack surface. The schematic of the CTOD measurement location in the DCB specimen is shown in Fig. 1.

2.1.2 Experimental Test

The adherends of the DCB specimen are fabricated using carbon fibre supplied by Hindustan Technical Fabrics Ltd. India, weighing 230 gsm. The layup sequence is $[0^0]_8$. The matrix is made from epoxy resin (CY 230) and hardener (HY 951) supplied by Huntsman in 10:1 weight ratio. The weight ratio of fibre and matrix is 1:1. The CFRP composite adherends are fabricated in-house by vacuum bagging technique under room temperature with a curing time of 24 h at room temperature. The specimen dimensions are $L_c = 143$ mm, $L = 130$ mm, $B = 25$ mm, $a_0 = 50$ mm, $t_p = 2$ mm, $t_a = 0.2$ mm. An epoxy adhesive Araldite 2015 from Huntsman is used to bond the CFRP composite adherends. Initially, the bonding surfaces are roughened using emery paper and cleaned with acetone to enhance the adhesion and avoid the adhesive failure. The adhesive bond is cured at room temperature for a period of twenty-four hours, and later, piano hinges are bonded as shown in Fig. 2. The initial crack is introduced by means of Teflon tape of thickness 40 μ m. Both the CFRP adherend surfaces are applied with adhesive. A Teflon tape is placed on the adhesive layer of one of the adherend, and both the CFRP panels are joined and held in a fixture which applies equal pressure on the joint so as to maintain a constant thickness of adhesive. Teflon tape is placed in between the two adherends after applying the adhesive. Two specimens are fabricated and tested at room temperature.

The experimental set-up shown in Fig. 3 consists of computer controlled, electric motor operated Instron mechanical testing machine of 2 kN capacity. 2 mm/min displacement rate is applied, and the load–displacement ($P-\delta$) curve is captured from the test. DIC system supplied by Correlated Solution Inc. is utilised to grab images during the test procedure. On the front edge surface of the DCB

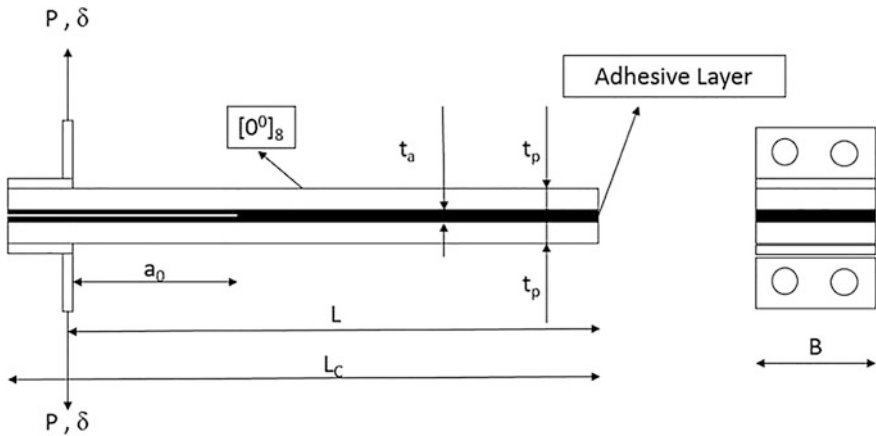


Fig. 2 Geometry of the DCB test specimen

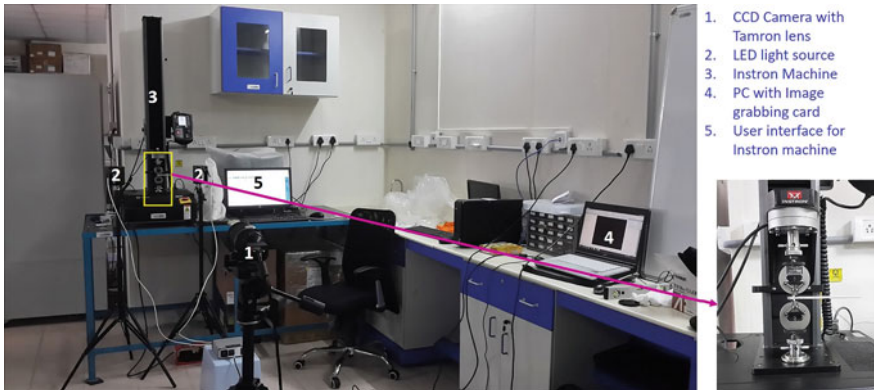


Fig. 3 Experimental set-up of DCB specimen test

specimen, a random speckle pattern is generated to perform DIC post-processing. Initially, the surface is sprayed with an acrylic white spray paint, and later, random speckle pattern is generated with carbon black colour using air gun.

To capture the speckle images, a CCD Camera manufactured by Grasshopper® (POINTGREY-GRAS-50S5M-C) with a spatial resolution of 2448×2048 pixels is used. Tamron lens (with SP AF 180 mm f/3.5 Di) is mounted on the CCD camera to capture the entire length of the specimen. Two white LED lamps of 30 W capacity are used to illuminate the surface of the specimen. Five images per second are captured and saved on a computer with Vic-Snap software from Correlated Solution Inc.

The $P-\delta$ curve generated from the Instron machine test data and $G_I-\delta$ curve evaluated using equivalent crack length method are shown in Fig. 4a, b,

respectively. The obtained G_{IC} value is closed to 0.45 N/mm which compares very well with the average G_{IC} mentioned in Ref. [5].

In order to get the cohesive law, a sixth order polynomial curve was fitted between G_I and CTOD which is shown in Fig. 5a. The polynomial is differentiated with respect to CTOD to obtain the relation $\sigma = f(w)$, which in turn gives the cohesive law of adhesively bonded CFRP composite joints under mode I loading condition. A bilinear cohesive law is adjusted over the traction–separation curve as shown in Fig. 5b. This bilinear law is then applied to model the adhesive layer in the finite element method (FEM) to validate the procedure. And the same procedure is repeated for mode II characterisation of adhesive layer in subsequent section.

2.1.3 Numerical Simulations

To validate the above method, numerical simulations are performed. A two-dimensional eight-nodded plane strain elements are selected to represent the adherends. The adhesive layer is modelled as 2D contact elements at the mid-thickness of the specimen. The lamina mechanical properties of the CFRP

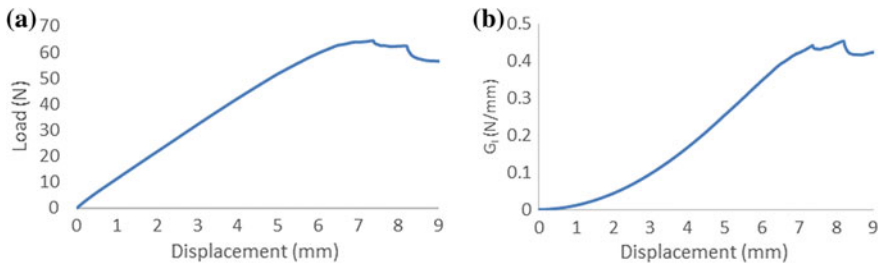


Fig. 4 Mechanical behaviour of DCB specimen. **a** P – δ curve; **b** strain energy release rate (G_I)– δ curve

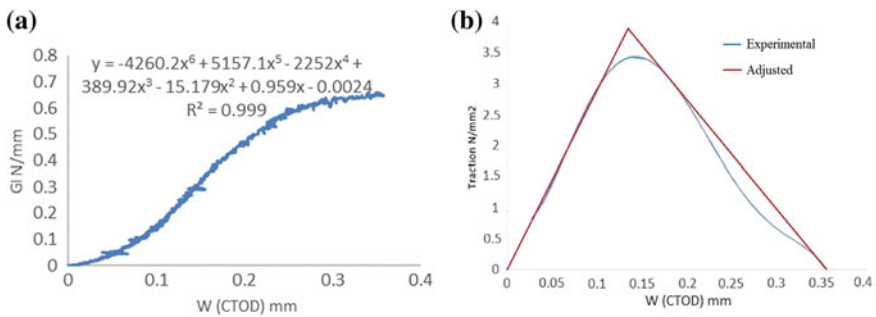
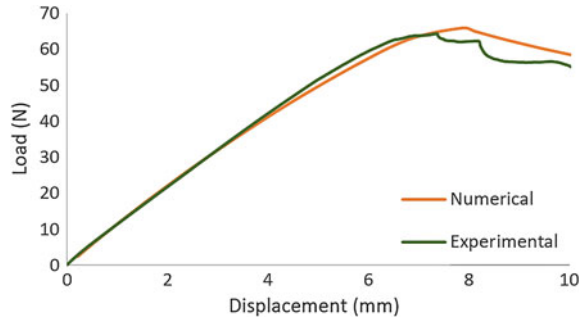


Fig. 5 Traction-separation behaviour. **a** G_I versus w curve; **b** experimental and adjusted cohesive law

Table 1 CFRP laminates and patch ply mechanical properties

Properties	Value
Longitudinal modulus, E_{11} (GPa)	82.64
Transverse modulus, $E_{22} = E_{33}$ (GPa)	7.12
In-plane Shear modulus, $G_{12} = G_{13}$ (GPa)	3.3
Out-of-plane Shear modulus, G_{23} (GPa)	2.47
In-plane Poisson's ratio, $\nu_{12} = \nu_{13}$	0.31
Out-of-plane Poisson's ratio, ν_{23}	0.43

Fig. 6 P - δ curve for comparison of experimental and numerical solution



composite are presented in Table 1. Damage initiation and progression are predicted using a pure mode I bilinear cohesive law. The P - δ curve is generated, and they are compared with the experimental one as shown in Fig. 6. There is a close match between experiment and FEM result thereby confirming the accuracy of the traction-separation law which has been arrived upon.

2.2 Pure Mode II Loading Condition

2.2.1 Estimation by Compliance-Based Beam Method

To estimate G_{II} value of CFRP composite bonded joint under mode II loading condition, compliance-based beam method (CBBM) is followed. Three different data reduction techniques to estimate the strain energy release rate under mode II loading condition are mentioned in [10]. The drawback in these methods is that in accurate measurement of crack length during propagation. Also, modern adhesives have ductile behaviour which results in the development of fracture process zone (FPZ) ahead of the crack tip. This leads to a non-negligible amount of energy dissipation, which cannot be accounted for in the standard data reduction techniques. In order to overcome these difficulties, CBBM utilises the crack equivalent concept which is experimentally determined based on the specimen compliance.

According to the beam theory, ENF specimen compliance can be written as

$$C = \frac{3a^3 + 2L^3}{8E_1Bh^3} + \frac{3L}{10G_{13}Bh} \tag{8}$$

Using initial specimen compliance as well as the initial crack length, the flexural modulus of the specimen is defined as

$$E_f = \frac{3a_0^3 + 2L^3}{8Bh^3C_{0corr}} \tag{9}$$

where C_{0corr} is given by

$$C_{0corr} = C_0 - \frac{3L}{10G_{13}Bh} \tag{10}$$

For evaluating the equivalent crack length, a correction of real crack length is measured to account for the FPZ influence. The equivalent crack length is given by

$$a_e = a + \Delta a_{FPZ} = \left[\frac{C_{corr}}{C_{0corr}} a_0^3 + \frac{2}{3} \left(\frac{C_{corr}}{C_{0corr}} - 1 \right) L^3 \right]^{1/3} \tag{11}$$

where C_{corr} is given by (10), using C instead of C_0 . Using Irwin–Kies relation, strain energy release rate under mode II (G_{II}) is given by

$$G_{IIC} = \frac{9P^2 a_e^2}{16B^2 E_f h^3} \tag{12}$$

2.2.2 Experimental Analysis

The materials and fabrication process for the adherends of the ENF specimen are similar to Sect. 2.1.2. The measurements of the specimen are $L = 100$ mm, $L_s = 50$ mm, $B = 25$ mm, $t_a = 0.2$ mm, $a_0 = 30$ mm, and $h = 2$ mm as shown in Fig. 7. The experimental set-up shown in Fig. 8 consists of a computer-controlled MTS Landmark® servo-hydraulic cyclic test machine of 100 kN capacity. A three-point bend fixture with radius of the support rollers equal to 25 mm is used.

The load–displacement curve generated from the MTS machine test data for two specimens is shown in Fig. 9. The strain energy release rate under mode II, evaluated by CBBM is given in Table 2, and its average value is found to be 3.14 N/mm.

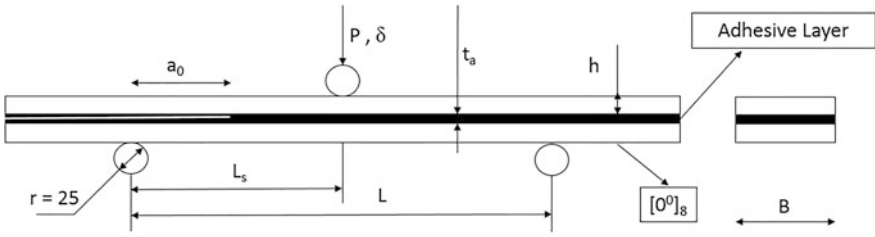


Fig. 7 Schematic presentation of the ENF test

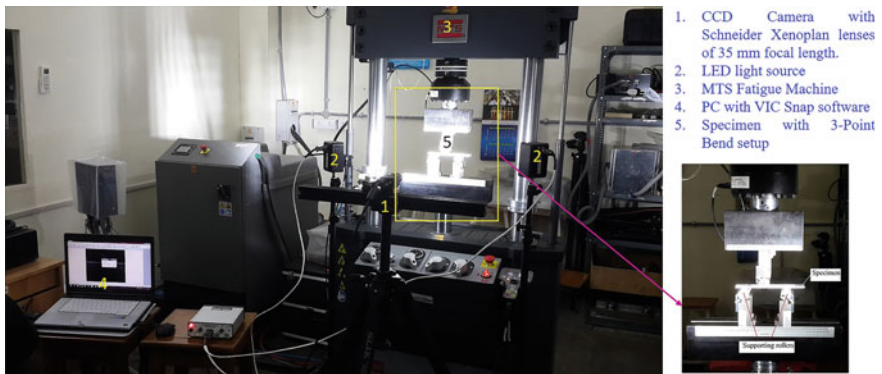


Fig. 8 Experimental set-up of ENF specimen test

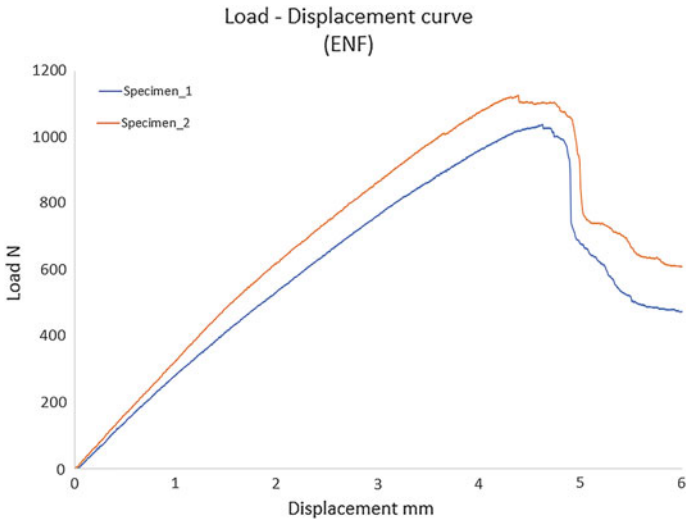


Fig. 9 Load-displacement curve of ENF test

Table 2 Fracture energies in pure mode II by CBBM

Specimen	G_{IIc} (N/mm)
1	3.21
2	3.54
3	2.69
Average	3.14

2.2.3 Numerical Simulations

The cohesive law for pure mode II loading condition is determined by inverse method, which involves fitting the experimental and numerical load–displacement curves. A two-dimensional eight-nodded plane strain elements are selected to model the adherends. The adhesive layer is modelled as 2D contact elements at the mid-thickness of the specimen. The lamina elastic properties of the CFRP composite are presented in Table 1. Damage initiation and progression are predicted using a pure mode II bilinear cohesive law. The parameters required to define the cohesive law for pure mode II are maximum tangential traction, tangential displacement jump at the completion of debonding, and critical fracture energy density for tangential slip. The cohesive parameter selection criteria are explained in [11]. The critical fracture energy density value is acquired experimentally. The traction–separation law before damage initiation is given by

$$\sigma = K\delta_r \tag{13}$$

where K is the stiffness defined as the ratio of elastic modulus of the material in tension or shear to the adhesive thickness. Assuming maximum tangential traction (σ_{IIU}) equal to the shear strength of the adhesive material, the value of tangential displacement jump at the completion of debonding (δ_U) can be estimated from the following relationship

$$G_{IIc} = \frac{\sigma_{IIU}\delta_U}{2} \tag{14}$$

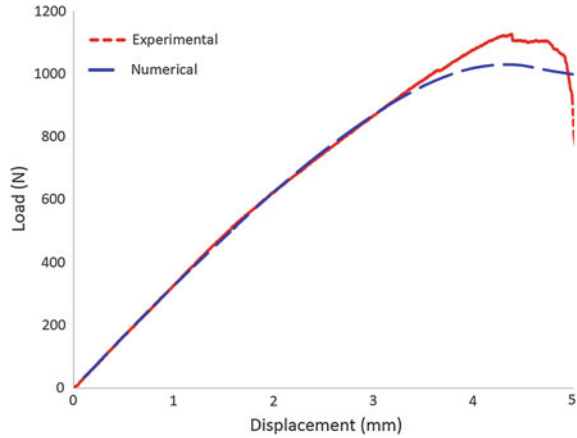
Figure 10 shows the numerical and experimental load–deformation curve for single tested specimen after the fitting procedure. From the plot, one could ascertain there is a very good coherence between experiment and FEA.

3 Double-Sided Stepped Lap Joint Repair

3.1 Numerical Analysis

A numerical analysis of double-sided stepped lap joint repair of adhesively bonded CFRP adherends subjected to tensile loading is performed. The cohesive law is

Fig. 10 P - δ curve for comparison of experimental and numerical solution



defined for modelling the adhesive layer, which was obtained from the above-prescribed methods. The CFRP laminate is modelled with a layup sequence of $[0^0]_{12}$. The geometry of the model is shown in Fig. 11. The dimensions are as follows: length of the laminate $a = 225$ mm, width $b = 45$ mm, thickness of the laminate $t = 2.4$ mm, scarf angle $\alpha = 2^\circ$, and step length = 13 mm. The elastic properties of the laminate are mentioned in Table 1. A two-dimensional eight-noded plane strain elements are assigned to the laminates, and two-dimensional interface elements are assigned to the adhesive layer. A total of three hundred interface elements are meshed along the bond length in order to have a refined mesh for the adhesive layer. The application of interface elements in modelling the adhesive layer, for progressive analysis of adhesive bond, is prescribed in [12]. The meshed model of the double-sided stepped lap joint repair including the boundary conditions is represented in Fig. 12. The geometry of the model is modelled according to the Ref. [13].

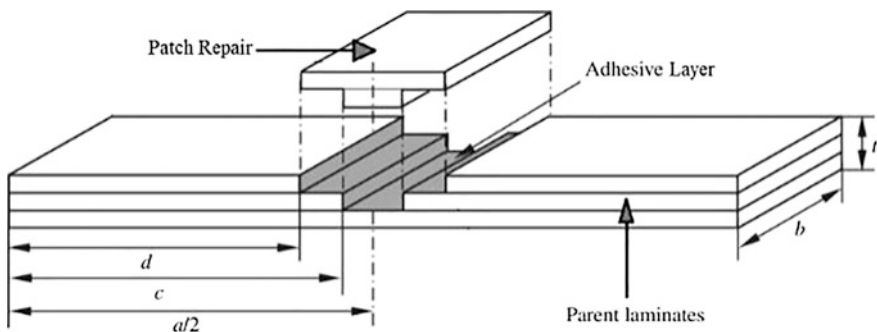


Fig. 11 Geometry of double-sided stepped lap joint repair

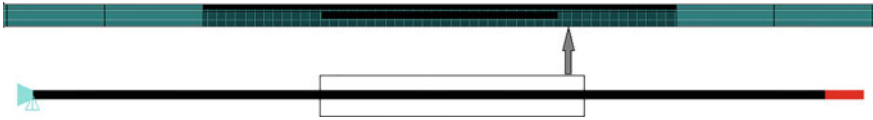


Fig. 12 FE model of double stepped lap repair

3.2 Experimental Work

To validate the numerical solution of double-sided stepped lap joint repair of CFRP laminate subjected to tensile loading, experimental work is carried out. The dimensions of the specimen are specified in Sect. 3.1. The CFRP laminates are fabricated using carbon fibre manufactured by Hindustan Technical Fabrics Ltd. India, weighing 200 gsm. The layup sequence is $[0^\circ]_{12}$. The matrix is made up of epoxy resin (CY 230) mixed in the weight ratio of 10:1 with hardener (HY 951) supplied by Huntsman. The weight ratio of fibre and matrix is maintained as 1:1. The CFRP composite laminates are fabricated in-house by vacuum bagging technique under room temperature with curing time set for 24 h.

The laminate and the patch are cut from the same casting. It is presumed that the laminate suffered damage at an intermediate section, and repair is carried out. Following, the damaged region is removed by diamond-coated milling cutter with a stepped shape as shown in the Fig. 10. Patch with the corresponding shape of the removed material is adhesively bonded over the damaged area of panel using an Araldite 2015 (Huntsman) adhesive of thickness 0.2 mm, and then, it is cured at room temperature under vacuum. Bevelled aluminium tabs of dimension $50 \text{ mm} \times 45 \text{ mm} \times 2 \text{ mm}$ are adhesively bonded at each end of the specimen for gripping purpose. The testing of the three specimens is performed on a computer-controlled MTS Landmark® servo-hydraulic cyclic test machine of 100 kN capacity. The experimental set-up for the testing of double stepped lap repaired CFRP panel is shown in Fig. 13. The P - δ curve generated from MTS data is shown in Fig. 14a. From the graph, we can infer that initially, the patch gets detached from the panel with failure of adhesive layer. Hence, there is drop in the load at point 1. This can be depicted from the Fig. 15a where the patch gets detached from the panel as a result of adhesive layer failure. But the load starts increasing because the undamaged part of the panel (unmachined part-bottom layers) starts to take the load. Finally, there is a drop in the load at point 2, as the panel fails which is the ultimate failure of the specimen. The final damaged specimen is shown in Fig. 15b, which characterise the existence of several interacting failure modes like matrix cracking, longitudinal splitting of fibres, fibre pull out, and delamination. Figure 14b displays the comparison between the load-displacement curves of experimental test and numerical simulation up to the failure point of the adhesive layer. The post-adhesive layer failure behaviour is not simulated numerically as progressive damage model is not implemented at this moment.

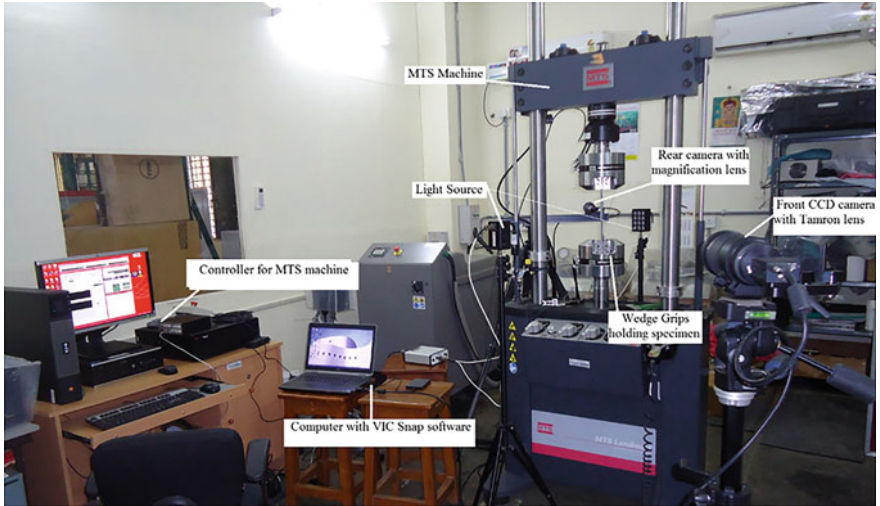


Fig. 13 Experimental set-up of DSSLJ repaired CFRP panel test

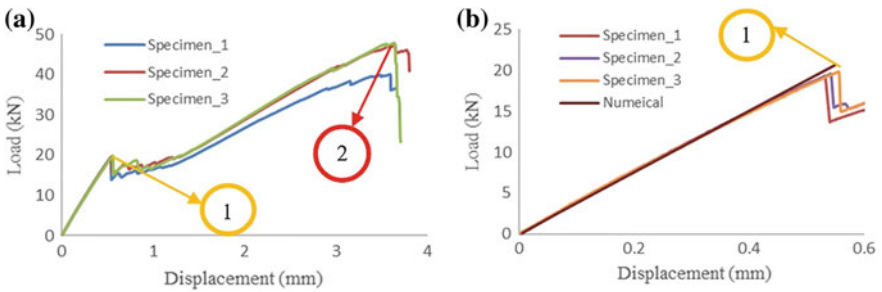


Fig. 14 a Experimental load–displacement curve, b comparison of experimental and numerical $P-\delta$ curve

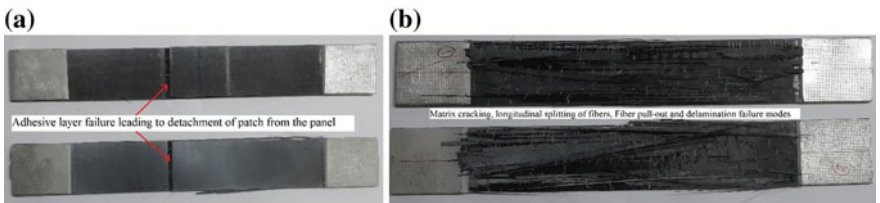


Fig. 15 Failure surface of double-sided stepped lap repaired CFRP panel. a Surface with the joint, b surface without the joint

4 Conclusion

The objective of this work is to estimate the cohesive damage law of adhesive layer (Araldite 2015) used in CFRP laminate repair under mode I and mode II loading conditions. For mode I and mode II strain energy release rate, experimental test of DCB and ENF, respectively, is performed. To obtain the cohesive law for mode I and mode II, direct method and inverse method are employed, respectively. Numerical simulation is carried out to validate the obtained cohesive law for adhesive layer by modelling it as interface elements. For mode I cohesive law, the maximum normal traction value is 3.94 MPa and critical fracture energy is 0.45 N/mm. For mode II cohesive law, the maximum tangential traction value is 25 MPa and critical fracture energy is 3 N/mm.

The obtained cohesive law for mode I and mode II is used to model the adhesive layer in numerical analysis of double-sided stepped lap joint repair of CFRP laminate subjected to tensile loading. The validation of the above-described procedure is evaluated by comparing numerical and experiments results. The initial stiffness, the maximum load until patch debonding, and the respective displacement are the parameters for comparison. Looking at the load displacement curve, a good coherence exists between experimental and numerical values corresponding to the above-mentioned parameters until adhesive layer fail. It is concluded that the procedure presented in this work can be effectively applied to predict the cohesive law for mode I and mode II loading conditions and can be used to model adhesive layer bonded with CFRP panel as adherend.

Acknowledgements The first author thank Dr. Viswanath R Chintapenta, Assistant Professor, Indian Institute of Technology Hyderabad for his guidance, lab mates in engineering optics lab and central workshop staff at Indian Institute of Technology Hyderabad.

References

1. M.D. Banea, L.F.M. da Silva, Adhesively bonded joints in composite materials: an overview. *Proc. Inst. Mech. Eng. Part L: J. Mater. Design Appl.* **223** (2009)
2. L.F.M. da Silva, P.J.C. das Neves, R.D. Adams, J.K. Spelt, Analytical models of adhesively bonded joints—Part I: Literature survey. *Int. J. Adhes. Adhes.* **29**, 319–330 (2009)
3. X. He, A review of finite element analysis of adhesively bonded joints. *Int. J. Adhes. Adhes.* **31**, 248–264 (2011)
4. L.F.M. da Silva, R.D.S.G. Campilho, *Advances in Numerical Modeling of Adhesive Joints* (Springer, Berlin, 2012)
5. M.F.S.F. de Moura, J.P.M. Gonçalves, A.G. Magalhães, A straightforward method to obtain the cohesive laws of bonded joints under mode I loading. *Int. J. Adhes. Adhes.* **39**, 54–59 (2012)
6. M.F.S.F. de Moura, J.J.L. Morais, N. Dourado, A new data reduction scheme for mode I wood fracture characterization using the double cantilever beam test. *Eng. Fract. Mech.* **75**, 3852–3865 (2008)

7. M.F.S.F. de Moura, R.D.S.G. Campilho, J.P.M. Gonçalves, Crack equivalent concept applied to the fracture characterization of bonded joints under pure mode I loading. *Compos. Sci. Technol.* **68**, 2224–2230 (2008)
8. G.F. Dias, M.F.S.F. de Moura, J.A.G. Chousal, J. Xavier, Cohesive laws of composite bonded joints under mode I loading. *J. Compos. Struct.* **106**, 646–652 (2013)
9. M. Kashfuddoja, R.G.R. Prasath, M. Ramji, Study on experimental characterization of carbon fibre reinforced polymer panel using digital image correlation: a sensitivity analysis. *J. Opt. Lasers Eng.* **62**, 17–30 (2014)
10. M.F.S.F. de Moura, R.D.S.G. Campilho, J.P.M. Gonçalves, Pure mode II fracture characterization of composite bonded joints. *Int. J. Solids Struct.* **46**, 1589–1595 (2009)
11. K. Song, C.G. Dávila, C.A. Rose, Guidelines and parameter selection for the simulation of progressive delamination, in *2008 Abaqus Users' Conference*
12. J.P.M. Gonçalves, M.F.S.F. de Moura, A.G. Magalhães, P.M.S.T. De Castro, Application of interface finite elements to the three-dimensional progressive failure analysis of adhesive joints. *Fatigue Fract. Eng. Mater. Struct.* **26**, 479–486
13. D. Li, G. Qing, Y. Liu, A three-dimensional semi-analytical model for the composite laminated plates with a stepped lap repair. *Compos. Struct.* **93**, 1673–1682 (2011)

Part IV
Computational Mechanics

Lower and Upper Bound Estimates of Material Properties of Pristine Graphene: Using Quantum Espresso

T. Chaitanya Sagar and Viswanath Chinthapenta

Abstract In this paper, the basic groundstate ($T = 0$) properties of pristine graphene are calculated using first principles with the aid of Quantum Espresso (QE). QE software suite is a tool based on ab initio quantum chemistry methods to obtain the electronic structure for materials modeling. It is an open source package built basing on the formalism of density functional theory (DFT). Using QE, the band structure, cohesive energy, and second-order elastic constants are estimated for a pristine graphene. Upper bound estimates based on the generalized gradient approximation (GGA) and lower bound estimates based on local density approximation (LDA) are obtained. The cohesive energy is found to be -7.917 eV/atom using LDA and -5.673 eV/atom using GGA. Further, the elastic properties are determined using a post-processing tool ElaStic. The second-order elastic stiffness C_{11} is found to be 491.5, and 506.7 GPa using LDA and GGA approaches, respectively.

Keywords Graphene · DFT · Quantum Espresso · Band structure
Cohesive energy and second-order elastic constants

Nomenclature

DFT Density Functional Theory
GGA Generalized Gradient Approximation
ICME Integrated Computational Materials Engineering
LDA Local Density Approximation
MD Molecular Dynamics
PP Pseudo Potentials
QE Quantum Espresso
SOEC Second-Order Elastic Constants

T. Chaitanya Sagar · V. Chinthapenta (✉)
Micro-Mechanics Lab, Indian Institute of Technology Hyderabad, Kandi, Sangareddy
502285, Telangana, India
e-mail: viswanath@iith.ac.in

1 Introduction

Conventional design of materials at the component level requires experiments to be conducted at the components scale without taking information from the entities at the underneath length and timescales. In this methodology, the choice of design is limited by the approximation that the material is homogeneous. This approximation is manifested by an arbitrarily large choice of a factor of safety. The design of materials at multiple scales accounts for the uncertainties by physically modeling the inhomogeneities at appropriate length scales and scale bridging their effect to the higher scales. The concept of design of materials at multiple scales had gained a lot of importance in the recent times [1]. The multiscale approach implemented is not limited to computations; it is also widely used in experiments, modeling, and design.

Integrated Computational Materials Engineering (ICME) [2] and predictive modeling of materials is based on multiscale modeling [3]. Wherein, the material properties are calculated with limited information from the experimental inputs [4]. Although experiments play a crucial role, the contributions of simulations performed at a lower length scales provide fundamental insights such as existence/feasibility of certain class of materials. And with the availability of high-speed computers and simulating tools, exploring new materials has become attainable. Moreover, validation of experiments with simulations has become a mandate. Hence, multiscale modeling opened a new window for computational materials science.

ICME has gained a lot of importance in the current times, and several researchers are working in this domain [5, 6]. For example, Horstemeyer [7] provides a detailed overview of a case study on the control arm of an automobile (Cadillac). In this study, the mechanical properties of the higher length scale were obtained from mesoscale simulations, mesoscale properties are obtained from the atomic-scale simulations, and atomic properties are obtained from electronic scale simulations. Different mathematical models are used at various length scales, such as FEM at continuum scale, crystal plasticity or discrete dislocations at mesoscale, molecular dynamics at atomic-scale, and DFT at electronic scale [7].

Materials can be perceived at four different levels depending on the length scales and timescales involved. These length scales range from a few angstroms to a micron to macroscopic lengths, and the timescale ranges from femtoseconds to a few seconds to years. In the top-down approach, as shown in Fig. 1, they can be classified into:

1. Continuum/Bulk scale
2. Mesoscale
3. Molecular/Atomistic scale
4. Quantum/Electronic/ab initio scale

The smallest length scale of about a few angstroms corresponds to the electronic scale. At electronic scale, the interaction of the electrons among themselves as well

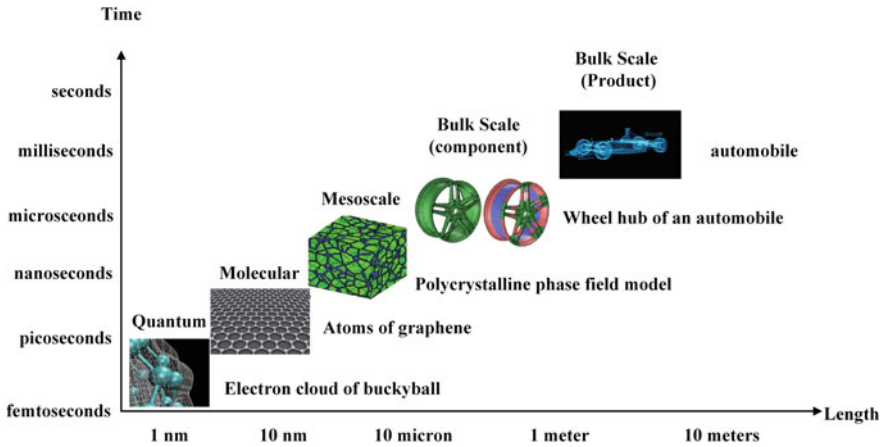


Fig. 1 Multiple scales of length and time in materials modeling

as with the nuclei is vital. Here, the total energy of the system is derived by solving computationally intensive Schrödinger equation of quantum mechanics. Hence, with the current computational architecture, systems with only a few tens of electrons can be simulated. While, with the usage of density functional theory (DFT), which can describe the properties at the ground state of a quantum mechanical system with the knowledge of the density of electrons in real space, it is possible to study systems with at least few thousands of electrons. The results from DFT calculations can provide accurate information about properties of crystalline materials. The objectives of the current study are to estimate upper and lower bounds to the electrical and also mechanical properties of pristine graphene such as electronic band structure, cohesive energy, and SOEC.

As shown in Fig. 2a, b, graphene is an allotrope of carbon having a hexagonal honeycomb structure which is one atom thick with a 0.142 nm length for the carbon-carbon bond [9]. As carbon is its source, it is abundantly available (over 95% all chemical compounds are carbon compounds). Graphene existing in three

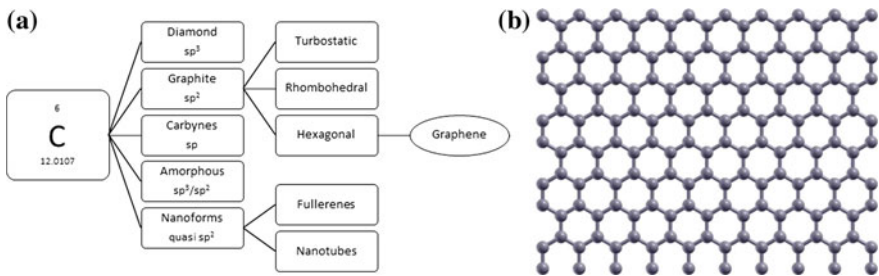


Fig. 2 a Allotropic forms of carbon depicting graphene in hexagonal form [8]; b graphene monolayer arm chair along the vertical direction

forms namely 3D-fullerenes, 2D-nanotubes, and 0D-buckyball [10] is known to show magnificent electronic [11] thermal [12–16], surface optical, and mechanical properties [17–19]. It is widely used in applications like nanoelectronics, catalysis, gas sorption, supercapacitors, and photovoltaics [20].

The manufacturability of pure graphene at an industrial scale is still a challenge compared to that of laboratory production [21]. There is tremendous variability in the values of electrical and mechanical values reported in the literature [22–27]. The factors mentioned above motivated to carry out the upper and lower bound estimates of the electrical and mechanical properties for the pristine graphene.

The paper is outlined as follows: In Sect. 2, a brief methodology of DFT-based QE is presented, followed by a procedure for generating SOEC using the ElaStic tool. In Sect. 3, the structure of graphene analyzed in the current study is presented. Using methodology listed in Sect. 2, the material properties of pristine graphene are estimated and are shown in Sect. 4. Section 4.1 illustrates the electronic properties such as Band structure, and the cohesive energies obtained using LDA and GGA approach. Similarly, Sect. 4.2 presents an upper and lower bound estimation of SOEC using LDA and GGA, determined using the ElaStic tool.

2 Methodology

2.1 *Quantum Espresso Suite*

Quantum Espresso suite is used to perform ground state calculations of total energy using and to find out the material properties of various systems. With the use of QE, a variety of models is studied to compute the behavior of materials from nanoscale and upwards. The atomic number and the pseudopotentials (PPs) for each constituent element are taken as inputs to a system. Further, QE also requires the structural input to compute the materials properties of the system. The structural input consists of details of the unit cell. The unit cell on repeating it in all direction would yield the macroscopic system to be simulated. In the lower dimension systems, the unit cell is filled with the vacuum spaces such as in a film or wire or a quantum dot. QE also supports the periodic boundary conditions which scale in all the three directions to model the infinitely large crystalline systems.

QE uses plane wave (PW) basis set to express the Kohn–Sham orbitals, while the pseudopotentials represent the interactions of the ions with only the valence electrons. These PPs are classified into ultrasoft (US) PPs, separable norm-conserving (NC) PPs, or by projector augmented wave (PAW) based on the description of atomic cores. QE is based on DFT, wherein the intermolecular interactions are taken care using the exchange and correlation functional. Generalized gradient approximation (GGA) [28] and local density approximation (LDA) [29, 30] to the exchange-correlation functional can be applied using the pseudopotentials.

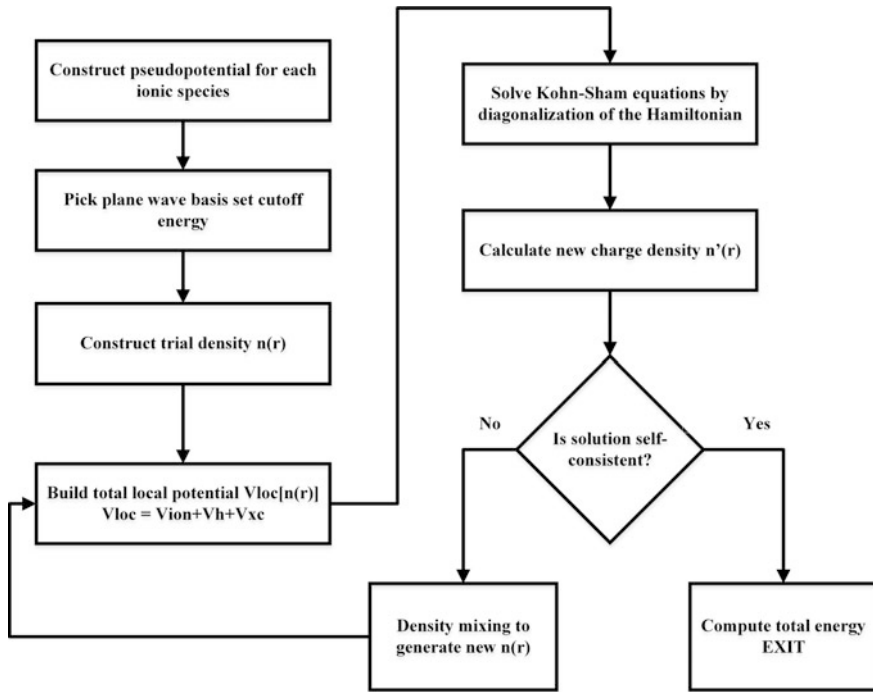


Fig. 3 DFT algorithm for implemented [31] by QE

The PWscf (the plane wave self-consistent fields based DFT) tool in QE is utilized in the current study. The algorithm of PWscf code is as shown in Fig. 3. In the first step, the pseudopotential for each element type is generated. Further, the energy cutoff for the basis set of a plane wave is determined using energy optimization. Next, the trial density for the system $n(r)$ is supplied.

Furthermore, the local potential is taken as the sum of potential contributions of ionic term (V_{ion}), Hartree term (V_H), and exchange-correlation (V_{xc}) term. This local potential is supplied to the Kohn–sham equations, and these equations are solved by diagonalization of the Hamiltonian, and a new charge density $n(r)$ is determined. This solution for the charge density is accepted to be the solution only when it satisfies the self-consistency. If the solution is not self-consistent, a new local potential is generated by giving a mixing parameter, and this solution is obtained by the iterative process.

2.2 SOEC Methodology

Elastic properties of a material quantify its resistance to various types of deformation, and hence they play a vital role in materials design. Elastic tensors can be defined as the Taylor's expansion of stress or the elastic energy in terms of the applied strain. Elastic constants of single crystals can be obtained from first principle calculations. There are two methods based on fitting total energies or stresses of appropriately deformed crystals called energy method or stress method, respectively. Different strain patterns are designed for crystals of different symmetry, and except for crystals of high symmetry, these calculations are computationally expensive. Alternative methods based on linear response theory and interatomic force constants [32] are also used in computing the elastic properties. However, these alternative methods are more computationally demanding. Moreover, due to high accuracy calculations of DFT, it is widely used in the determination of elastic constants of complex crystal structures, where experimental determination is less feasible.

In this study, ElaStic software tool is used in generating the stiffness matrix of pristine graphene. The Elastic tool functions in the following manner:

Firstly, the space group is given as input, which is determined using sgroup package [33].

- The space-group number determines the number of independent elastic constants. It then generates sets of independent deformation matrices. Then, the corresponding set of input structure files is created.
- The total energy is calculated for every set of structure data created using the DFT code QE.
- The total energies computed are plotted against the applied strain. Fitting procedure is used to determine the derivatives at zero strain.
- These derivatives help in identifying all the independent components of an elastic tensor.
- The polynomial fit and the order are decided to achieve the required accuracy of the results.

ElaStic package can be used to determine the second- and third-order elastic constants. Further, they also determine, the Voigt and Reuss averaged Young's modulus, shear modulus, bulk modulus, and Poisson ratio. The flowchart of the ElaStic tool is as shown in Fig. 4. The crystal structure of the material to be studied is provided as inputs. This crystal structure is optimized for atomic positions and cell parameters to the required accuracy to attain equilibrium configuration. Thus, the optimized structure is used as the reference system. The crystal structure is deformed to the chosen strain level, and structure is further optimized to attain the equilibrium in a deformed state. For a detailed description of evaluating SOEC, see the Refs. [34, 35].

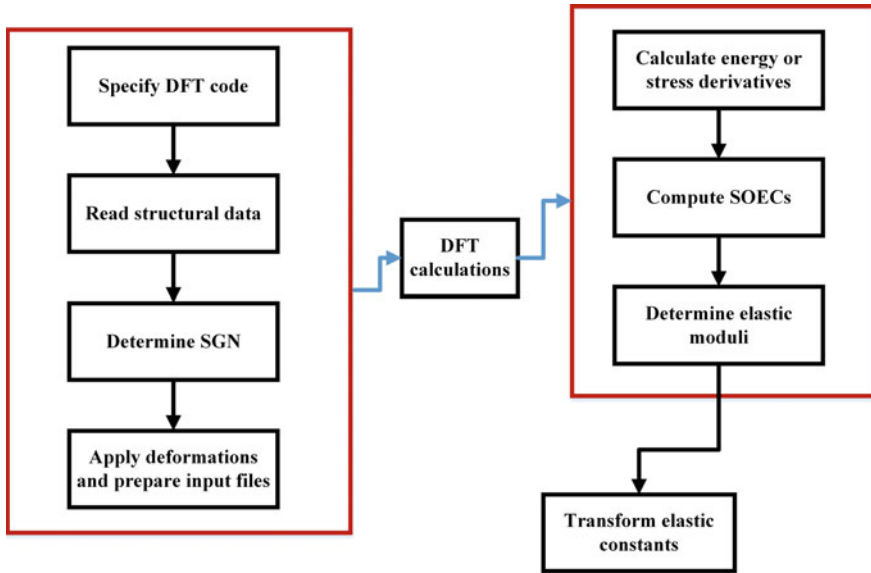


Fig. 4 Flowchart of the algorithm used for calculating SOEC using ElaStic tool [34]

3 Modeling of Graphene

The structure of graphite obtained from the experiments [36] is used in the current study, in building the graphene structure. Graphite consists of planar sheets of carbon in hexagonal form. Its intra-planar bonding is adamant, and the forces holding these sheets are weak. Hence, the structure of graphene is generated from graphite by making the inter-planar distance of parallel planes very high. Due to this, the two parallel planes of graphene remain non-interacting. Since Graphene is two dimensional in nature, only the planar properties are calculated.

Two carbon atoms are sufficient to define the primitive cell for graphene structure. As shown in Fig. 5a, the two carbon atoms are placed at $1/3$, $2/3$ positions of the lattice vector \mathbf{a} and \mathbf{b} . Conventional cells of the generated structure, indicated by 2×2 repetitions of the unit cell are shown in Fig. 5b, and $5 \times 5 \times 3$ repetitions are shown in Fig. 5c, denoting the macroscopic system is graphene structure. However, in the present analysis, the unit cell shown in Fig. 5a is used in the rest of the analysis.

Variable cell relaxation calculations are performed on the primitive cell, and equilibrated lattice parameters are determined and tabulated in Table 1. Figure 6a shows the energy variation with change in lattice parameter ' a ', while Fig. 6b shows the energy variation with change in lattice parameter ' c '. An equilibrated lattice parameter of 2.4685 \AA for ' a ' is obtained in the relaxation simulations for this study. Similarly, the minimum value of ' c ' is found to be $\sim 2.6 \text{ \AA}$. However, a sufficiently large value of ' c ' $\sim 6.928 \text{ \AA}$ is taken to ensure graphene structure.

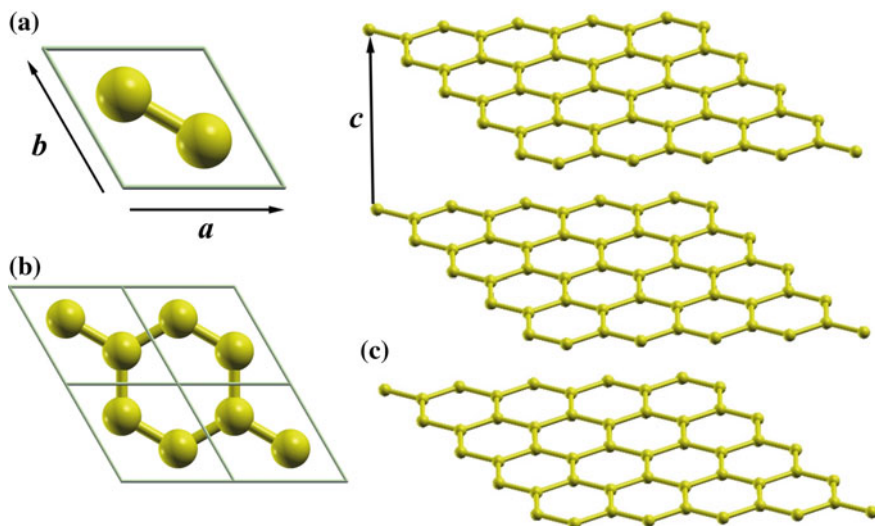


Fig. 5 **a** Primitive cell containing two carbon atoms, **b** conventional cell containing 2×2 repetitions of primitive cell in the planar direction, **c** conventional cell containing $5 \times 5 \times 3$ unit repetitions of the primitive cell

Table 1 Structural parameters of graphite and pristine graphene

Structure (hexagonal)	Space group	A (Å)	b (Å)	c (Å)	α	β	γ	Atomic positions —2 atoms (fractional)	Details
Graphite	$P6_3mc$	2.470	2.470	6.790	90	90	120	C1 (1/3 2/3 0) C2 (2/3 1/3 0)	From [36]
Graphene	$P6/mmm$ (191)	2.468	2.468	6.928	90	90	120	C1 (1/3 2/3 0) C2 (2/3 1/3 0)	Parameters after relaxing the structure in QE

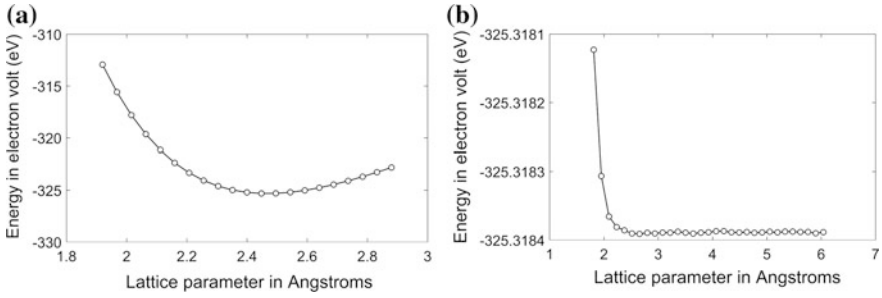


Fig. 6 **a** Convergence of lattice parameter ($a = b$) with total energy for pristine graphene, **b** convergence of lattice parameter ‘c’ with total energy (QE-GGA)

4 Results

4.1 Electronic Properties

Band Structure

Band structure calculations provide the quantum mechanical states of electrons in the crystal that are characterized by a Bloch wave vector denoted by \mathbf{k} and a band index denoted by \mathbf{n} . The Bloch wave vector considered as an element of the reciprocal space, which is limited to the first Brillouin zone. Band structure helps in explaining many magnetic, optical, and electrical properties of crystals. The location of Fermi level, the energy of the highest energy state filled at absolute zero of temperature, is of interest. If the Fermi level falls in a band gap, then the material is electrically insulating (in some cases semiconducting when the band gap is small) while in other cases it is metallic [37]. The first electronic band structure of graphene using tight binding technique was calculated more than six decades ago [38], and the study shows that it is a conductor. In our case, the band structure is

Fig. 7 Band structure of pristine graphene calculated using QE

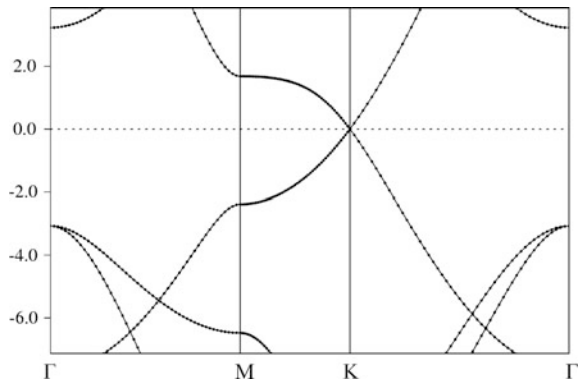


Table 2 Cohesive energies of pristine graphene

Method	Cohesive energy (eV/atom)	Reference
DFT	-7.906	[40]
Experimental	-7.600	[42]
DFT, LDA pseudopotential	-9.717	Present study
DFT, GGA pseudopotential	-5.673	Present study
Average	-7.695	Present study

calculated by choosing the K grid along selected points within the Brillouin zone which are in the reciprocal space, and the result shows no band gap along the position K of the Brillouin zone. Figure 7 indicates that it is conductive at ground state which agrees well with the result from Ref. [39].

Cohesive Energies

Cohesive energy also called as formation energy or binding energy is the gain in energy for a structure when placed in a crystalline form.

$$E_{\text{cohesive}} = E_{\text{structure}} - E_{\text{freeatoms}}$$

By the common trend in total energy calculations using DFT, it is seen that LDA under-estimates the lattice parameter due to over binding, and GGA over-estimates them due to under binding. The reported experimental values from literature fall midway between the LDA and GGA results as shown in Table 2.

4.2 Elastic Properties

In this section, the SOEC obtained by DFT calculations using ElaStic code are presented. As a first step, the structure of graphene is relaxed using ionic relaxation, and lattice parameters are updated. This updated structure is deformed using different strain patterns (deformation modes) based on the crystal symmetry. Graphene possesses hexagonal structure and therefore relates to transverse isotropy. Consequently, five independent elastic constants are sufficient to define the SOEC of graphene as shown below completely. To determine the five independent elastic constants, energy variation with strain for five different deformation modes is sufficient.

$$\begin{pmatrix} C_{11} & C_{12} & C_{13} & 0 & 0 & 0 \\ C_{12} & C_{11} & C_{13} & 0 & 0 & 0 \\ C_{13} & C_{13} & C_{33} & 0 & 0 & 0 \\ 0 & 0 & 0 & C_{44} & 0 & 0 \\ 0 & 0 & 0 & 0 & C_{44} & 0 \\ 0 & 0 & 0 & 0 & 0 & \frac{(C_{11}-C_{12})}{2} \end{pmatrix}$$

Table 3 Input parameters for SOEC calculation

Conditions	Ground state ($T = 0$)
System	Hexagonal
Material model	Transversely isotropic
No. of SOEC	5
Number of deformed structures	41
Order of the polynomial fit	6
Maximum Lagrangian strain	0.05

Table 4 Elastic properties calculated for pristine graphene

Stiffness components in (GPa)	LDA	GGA	Hills average
C_{11}	491.50	506.70	499.10
C_{33}	23.30	2.90	13.10
C_{44}	1.60	0.20	0.90
C_{12}	80.70	88.00	84.35
C_{13}	0.10	0.40	0.25
B_V	132.31	128.69	130.55
E_H	103.72	102.14	102.95
ν_H (Poisson's ratio)	0.20	0.23	0.22

In the current calculations, the energy variation for each deformation mode is calculated for 41 strain inputs. Using fitting procedure, the optimized maximum Lagrangian strain is determined to be 0.05. Hence, the strain is varied from 0 to 0.05 by 41 equal partitions. A sixth-degree polynomial is fitted to each deformation mode. The input parameters supplied in the present study are listed in Table 3.

QE procedure requires pseudopotentials (PP) to be supplied to run the calculations. The total energy obtained through LDA and GGA is the lower and upper bounds because of the formalism of exchange term in the energy functional. Hence, an averaged estimate is also obtained and presented in Table 4.

Apart from the elastic constants, the Voigt Bulk modulus (B_V), Hills shear modulus (E_H), and Hills Poisson ratio (ν_H) values are also calculated as shown in Table 4. Hills values are an average of the Voigt and Reuss values [41].

5 Summary

Using the first principle calculation through QE and ElaStic tool, the electronic and mechanical properties of graphene are obtained using two different approaches (LDA, GGA). LDA and GGA assume two distinct pseudopotentials, and hence, cohesive energy for LDA is -9.717 and GGA is -5.673 . However, the average of the LDA and GGA is in reasonable agreement with experimental results [42]. Second-order elastic stiffness is found to be 491.5, and 506.7 GPa using LDA and

GGA. The Poisson ratio of 0.215 is obtained for graphene in these calculations compared to 0.165 observed in the experiment [17, 43].

References

1. J.J. De Pablo, W.A. Curtin, J.J. de Pablo, Multiscale modeling in advanced materials research: challenges, novel methods, and emerging applications. *MRS Bull.* **32**(11), 905–911 (2011)
2. M.F. Horstemeyer, Multiscale modeling: a review, in *Practical Aspects of Computational Chemistry* (Springer Netherlands, Dordrecht, 2009), pp. 87–135
3. R.E. Miller, E.B. Tadmor, A unified framework and performance benchmark of fourteen multiscale atomistic/continuum coupling methods. *Modell. Simul. Mater. Sci. Eng.* **17**(5), 53001 (2009)
4. E.A. Carter, Challenges in modeling materials properties without experimental input. *Science* (80-) **321**(5890), 800–803 (2008)
5. R.W. Sullivan, S.M. Arnold, An annotative review of multiscale modeling and its application to scales inherent in the field of ICME, in *Models, Databases, and Simulation Tools Needed for the Realization of Integrated Computational Material Engineering* (2011), pp. 6–23
6. D.G.B. Pollock, M. Tresa, J.E. Allison, *Integrated Computational Materials Engineering: A Transformational Discipline for Improved Competitiveness and National Security* (Washington, DC: The National Academies Press, 2008)
7. M.F. Horstemeyer, *From Atoms to Autos—A new Design Paradigm Using Microstructure-Property Modeling Part 1: Monotonic Loading Conditions* (Albuquerque, NM, and Livermore, CA, 2001)
8. E.H. Falcao, F. Wudl, Carbon allotropes: beyond graphite and diamond. *J. Chem. Technol. Biotechnol.* **82**(6), 524–531 (2007)
9. J. Slonczewski, P. Weiss, Band structure of graphite. *Phys. Rev.* **109**(2), 272–279 (1958)
10. A.K. Geim, K.S. Novoselov, The rise of graphene. *Nat. Mater.* **6**(3), 183–191 (2007)
11. K.S. Novoselov, A.K. Geim, S.V. Morozov, D. Jiang, M.I. Katsnelson, I.V. Grigorieva, S.V. Dubonos, A.A. Firsov, Two-dimensional gas of massless Dirac fermions in graphene. *Nature* **438**(7065), 197–200 (2005)
12. A.A. Balandin, S. Ghosh, W. Bao, I. Calizo, D. Teweldebrhan, F. Miao, C.N. Lau, Superior thermal conductivity of single-layer graphene. *Nano Lett.* **8**(3), 902–907 (2008)
13. C. Berger, Z. Song, T. Li, X. Li, A.Y. Ogbazghi, R. Feng, Z. Dai, A.N. Marchenkov, E.H. Conrad, P.N. First, W.A. de Heer, Ultrathin epitaxial graphite: 2D electron gas properties and a route toward graphene-based nanoelectronics. *J. Phys. Chem. B* **108**(52), 19912–19916 (2004)
14. S. Ghosh, I. Calizo, D. Teweldebrhan, E.P. Pokatilov, D.L. Nika, A.A. Balandin, W. Bao, F. Miao, C.N. Lau, Extremely high thermal conductivity of graphene: prospects for thermal management applications in nanoelectronic circuits. *Appl. Phys. Lett.* **92**(15), 151911 (2008)
15. J.H. Seol, I. Jo, A.L. Moore, L. Lindsay, Z.H. Aitken, M.T. Pettes, X. Li, Z. Yao, R. Huang, D. Broido, N. Mingo, R.S. Ruoff, L. Shi, Two-dimensional phonon transport in supported graphene. *Science* (80-) **328**(5975), 213–216 (2010)
16. T. Schwamb, B.R. Burg, N.C. Schirmer, D. Poulidakos, An electrical method for the measurement of the thermal and electrical conductivity of reduced graphene oxide nanostructures. *Nanotechnology* **20**(40), 405704 (2009)
17. C. Lee, X. Wei, J.W. Kysar, J. Hone, Measurement of the elastic properties and intrinsic strength of monolayer graphene. *Science* (80-) **321**(5887), 385–388 (2008)
18. G. Tsoukleri, J. Parthenios, K. Papagelis, R. Jalil, A.C. Ferrari, A.K. Geim, K.S. Novoselov, C. Galiotis, Subjecting a graphene monolayer to tension and compression. *Small* **5**(21), 2397–2402 (2009)

19. C. Lee, X.D. Wei, Q.Y. Li, R. Carpick, J.W. Kysar, J. Hone, Elastic and frictional properties of graphene. *Phys. Status Solidi B-Basic Solid State Phys.* **246**(11–12), 2562–2567 (2009)
20. V. Singh, D. Joung, L. Zhai, S. Das, S.I. Khondaker, S. Seal, Graphene based materials: the past, present, and future. *Prog. Mater. Sci.* **56**(8), 1178–1271 (2011)
21. K.S. Novoselov, V.I. Fal’ko, L. Colombo, P.R. Gellert, M.G. Schwab, K. Kim, A roadmap for graphene. *Nature* **490**(7419), 192–200 (2012)
22. X. Wei, B. Fragneaud, C.A. Marianetti, J.W. Kysar, Nonlinear elastic behavior of graphene: Ab initio calculations to continuum description. *Phys. Rev. B Condens. Matter Mater. Phys.* **80**(20), 1–8 (2009)
23. F. Liu, P. Ming, J. Li, Ab initio calculation of ideal strength and phonon instability of graphene under tension. *Phys. Rev. B Condens. Matter Mater. Phys.* **76**(6), 1–7 (2007)
24. K.N. Kudin, G.E. Scuseria, B.I. Yakobson, C2F, BN, and C nanoshell elasticity from ab initio computations. *Phys. Rev. B* **64**(23), 235406 (2001)
25. G. Van Lier, C. Van Alsenoy, V. Van Doren, P. Geerlings, Ab initio study of the elastic properties of single-walled carbon nanotubes and graphene. *Chem. Phys. Lett.* **326**(1–2), 181–185 (2000)
26. D. Sánchez-Portal, E. Artacho, J.M. Soler, A. Rubio, P. Ordejón, Ab initio structural, elastic, and vibrational properties of carbon nanotubes. *Phys. Rev. B* **59**(19), 12678–12688 (1999)
27. E. Konstantinova, S.O. Dantas, P.M.V.B. Barone, Electronic and elastic properties of two-dimensional carbon planes. *Phys. Rev. B Condens. Matter Mater. Phys.* **74**(3), 1–6 (2006)
28. J.P. Perdew, K. Burke, M. Ernzerhof, Generalized gradient approximation made simple. *Phys. Rev. Lett.* **77**(18), 3865–3868 (1996)
29. W. Kohn, L.J. Sham, *Self-Consistent Equations Including Exchange and Correlation Effects*, vol. 385, no. 1951 (1965)
30. J.P. Perdew, J.A. Chevary, S.H. Vosko, K.A. Jackson, M.R. Pederson, D.J. Singh, C. Fiolhais, Atoms, molecules, solids, and surfaces: applications of the generalized gradient approximation for exchange and correlation. *Phys. Rev. B* **46**(11), 6671–6687 (1992)
31. Giannozzi, P., Baroni, S., Bonini, N., Calandra, M., Car, R., Cavazzoni, C., ... Wentzcovitch, R. M. . QUANTUM ESPRESSO: a modular and open-source software project for quantum simulations of materials. *J. Phys. Condens. Matter* **21**(39), 395502 (2009)
32. M. Born, Dynamical theory of crystal lattices. *Am. J. Phys.* **23**(7), 474 (1955)
33. B.Z. Yanchitsky, A.N. Timoshevskii, Determination of the space group and unit cell for a periodic solid. *Comput. Phys. Commun.* **139**(2), 235–242 (2001)
34. R. Goleseorkhtabar, P. Pavone, J. Spitaler, P. Puschnig, C. Draxl, ElaStic: a tool for calculating second-order elastic constants from first principles. *Comput. Phys. Commun.* **184**(8), 1861–1873 (2013)
35. R. Yu, J. Zhu, H.Q. Ye, Calculations of single-crystal elastic constants made simple. *Comput. Phys. Commun.* **181**(3), 671–675 (2010)
36. O. Hassel, H. Mark, Über die Kristallstruktur des Graphits. *Zeitschrift für Phys.* **25**(1), 317–337 (1924)
37. P. Hofmann, *Solid State Physics: An Introduction* (Wiley, 2015)
38. P.R. Wallace, The band theory of graphite. *Phys. Rev.* **71**(9), 622–634 (1947)
39. L.-F. Huang, Y.-L. Li, M.-Y. Ni et al., Lattice dynamics of hydrogen-substituted graphene systems. *Acta Phys. Sin.* **58**(13), S306–S312 (2009)
40. H. Shin, S. Kang, J. Koo, H. Lee, J. Kim, Y. Kwon, Cohesion energetics of carbon allotropes: quantum Monte Carlo study. *J. Chem. Phys.* **140**(11), 114702 (2014)
41. R. Hill, The elastic behaviour of a crystalline aggregate. *Proc. Phys. Soc. London, Sect. A* **65**(389), 349–354 (1952)
42. B. Aufray, A. Kara, Š. Vizzini, H. Oughaddou, C. Landri, B. Ealet, G. Le Lay, Graphene-like silicon nanoribbons on Ag(110): a possible formation of silicene. *Appl. Phys. Lett.* **96**(18), 10–12 (2010)
43. O.L. Blakslee, Elastic constants of compression-annealed pyrolytic graphite. *J. Appl. Phys.* **41**(8), 3373 (1970)

Studies on Behaviour of Steel Tubular Compression Members Subjected to Accelerated Corrosion

A. Cinitha, P. K. Umesha and G. S. Palani

Abstract The performance of steel structural components is strongly influenced by the damage due to atmospheric corrosion, whose control is a key aspect for design and maintenance of both new and existing structures. In extreme situations, it can lead to catastrophic failure of structural components. This paper presents experimental and numerical studies on corroded compression members under stressed and unstressed conditions. Experimental studies are carried out on corroded members with different percentage in thickness and weight loss. A methodology has been developed numerically to simulate three types of corrosion cases by using finite element method, namely (1) uniform corrosion, (2) pitting corrosion and (3) uniform and pitting corrosion. The failure modes and the ultimate load carrying capacity of the specimen are determined numerically and validated with experimental results. A significant reduction in load carrying capacity is observed for all corroded specimens compared to uncorroded control specimen. The failure modes and load carrying capacity of corroded members for uniform, pitting and combined effect of uniform and pitting corrosion are discussed. In the light of experimental results, it is inferred that the failure of the members is due to localised axisymmetric imperfections induced in the tubular members due to corrosion.

Keywords Corrosion · Compression member · Uniform corrosion
Pitting corrosion · Imperfections introduction

1 Introduction

Corrosion is a natural phenomenon and major cause of deterioration of steel structures which exists as part of our everyday life. In extreme situations, catastrophic failure such as collapse occurs due to reduction in the load bearing capability of a structure. Corrosion damage can also results in life threatening situations; hence, it

A. Cinitha (✉) · P. K. Umesha · G. S. Palani
CSIR-Structural Engineering Research Centre, Chennai 6000113, India
e-mail: cinitha@serc.res.in

has to be addressed for safety, environment and economic reasons. Steel structures exposed to the extreme atmosphere, especially marine and highly polluted industrial environment are subjected to corrosion. The conventional approach to evaluate residual capacity is to perform visual inspection of the corroded members and classify the members according to their level of damage. Rahgozar [1] reviewed various forms of corrosion and the effects of uniform corrosion on steel structures. They developed corrosion decay models based on the information on the locations where corrosion occurs. Beaulieu et al. [2] studied corrosion of steel structures exposed to various environmental conditions. They estimated the residual capacity of corroded members in order to decide whether to change the member, repair it or just remove corrosion and re-protect the member. Landolfo et al. [3] presented the modelling approaches of atmospheric corrosion damage of metal structures. Based on the studies conducted by Damgaard et al. [4], it was concluded that corrosion can significantly reduce the service lives/life of weathering steel girders. This paper presents the experimental and numerical studies conducted on tubular compression members subjected to accelerated corrosion of various amount. The numerical method developed to simulate uniform, pitting and combined form of uniform and pitting corrosion is discussed.

2 Experimental Set-up

2.1 *Unstressed Corrosion Set-up*

Among the accelerated corrosion techniques, Galvanostatic method is adopted to corrode the desired regions of the tubular compression members. In Galvanostatic method, constant current from a DC (direct current) source is applied, till the required amount of corrosion is achieved. Figure 1 shows the experimental set-up to induce corrosion in the tubular specimen under unstressed condition.

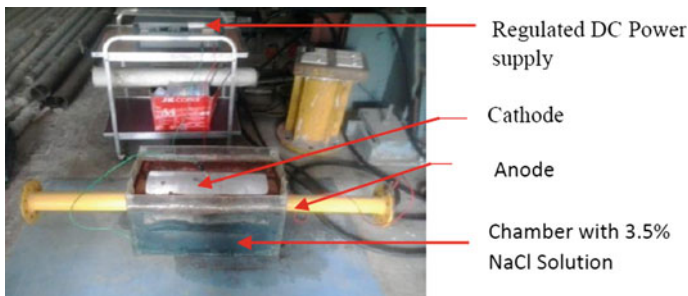


Fig. 1 Experimental set-up to induce corrosion in the tubular compression members under unstressed condition

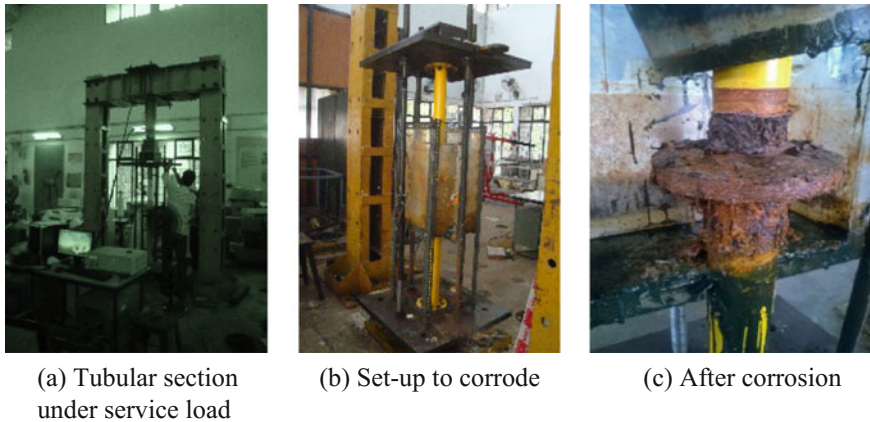


Fig. 2 Experimental set-up to induce corrosion under stressed condition

2.2 Stressed Corrosion Set-up

In order to achieve the stressed corrosion condition, a load under service condition is applied to the joint component with the help of a reaction frame. After applying the required compressive load, the load is retained by tightening the check nuts of the upper arm of the specially fabricated load retaining frame. The corrosion chamber is fixed to the region scheduled to corrode, and galvanic corrosion is carried out as per Faraday's law to achieve target % of weight loss due to corrosion, i.e. is 20%. Figure 2 shows the experimental set-up to induce corrosion under stressed condition.

3 Compression Test on Tubular Sections

The details of tubular members considered for experimental study are given in Table 1. The uncorroded specimen is named as STJC-1, corroded and unstressed specimens as STJC-2 and STJC-5, and stressed and corroded specimen as STJC-4. The specimens were subjected to static axial compression under displacement control by a hydraulically operated UTM of 250T capacity. The specimens were placed between the two heads in such a way that the centre of the flange plates of the specimen coincides with the centre of bottom platform and the top head of the compression testing machine. The experimental set-up is shown in Fig. 3. In order to measure the lateral deflection, two LVDTs are placed at mid-height of the corroded region of the specimen. Four numbers of strain gauges are glued in affected regions, i.e. two gauges along the direction of load in perpendicular to each other and other two in horizontal direction. At each load stage, deflection and strain measurements were recorded automatically using a data logger and analysed.

Table 1 Details of tubular specimens

Specimen identification	Type of pipes used	Initial thickness (mm)	Final thickness (mm)	Percentage reduction in thickness
STJC-1	80NB	3.40	3.40	0
	65NB	3.80	3.80	0
STJC-2	80NB	3.40	2.10	38.24
	65NB	3.80	2.30	39.47
STJC-4	80NB	3.40	3.14	7.65
	65NB	3.80	3.50	7.89
STJC-5	80NB	3.40	2.40	29.41
	65NB	3.80	2.70	28.94

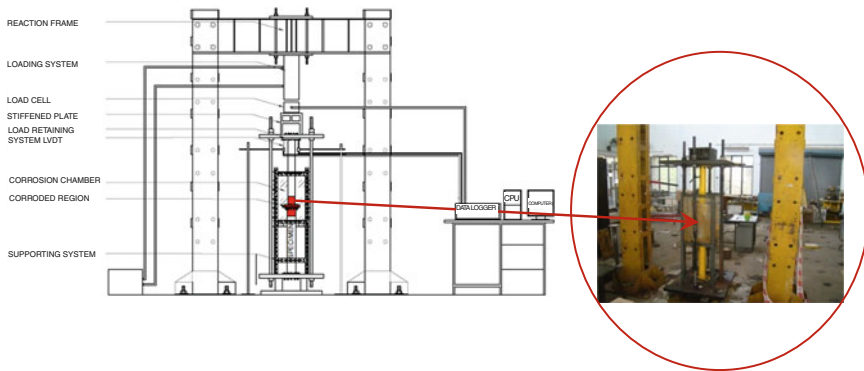


Fig. 3 Schematic sketch of experimental set-up

4 Numerical Investigation of Corroded Steel Tubular Sections

In the present study, numerical investigation is carried out on the corroded steel tubular sections by using the ABAQUS general-purpose finite element analysis software. A methodology is developed to simulate different forms of corrosion, namely uniform, pitting and combined, i.e. uniform and pitting, by varying the percentage of corrosion from 10 to 50%. The observed strength reduction of corroded tubular leg members for varying rate of corrosion is discussed.

ABAQUS software is used for the numerical simulation of behaviour of corroded steel tubular compression member (80NB and 65NB, heavy) using STATIC, RIKS procedure to account for the nonlinear effects. Young’s modulus and Poisson’s ratio of the material were taken as $2.1 \times 10^5 \text{ N/mm}^2$ and 0.3, respectively. In linear elastic bodies, the displacements are proportional to the applied loads. But in the case of buckling, even if the stress–strain relation remains linear, large deformations and the changing geometric configuration cause the structure to

behave nonlinearly. The actual behaviour can be predicted by the nonlinear analysis. The incremental plasticity model is considered and the stress–strain values corresponding to the tensile coupon test are considered. Hence, the material is modelled as elastic–perfectly plastic material. The model is discretised using the element C3D8R, i.e. 8-noded linear brick element with reduced integration. It is found that the solution converges to a unique value by using the global seed size of 50. For the ABAQUS analyses conducted for the present study, load increment size was chosen on a trial and error basis in an attempt to provide an accurate solution with reasonable computation time.

4.1 *Simulation of Boundary Conditions*

To simulate the experimental set-up in finite element analysis (FEA), the cross section centroid of the top end of the column was defined as a reference point for creating constraint, where all three translational and rotational degrees of freedom are specified. A kinematic coupling constraint was defined to constrain the motion of the top surface to that of the single reference point, where all three translational and rotational degrees of freedom were specified as shown in Fig. 4. In this case, all

Fig. 4 Coupling constraints

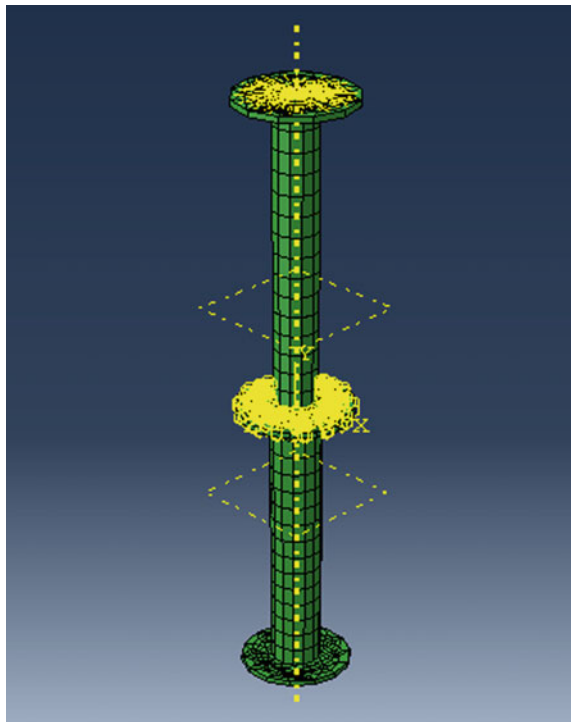
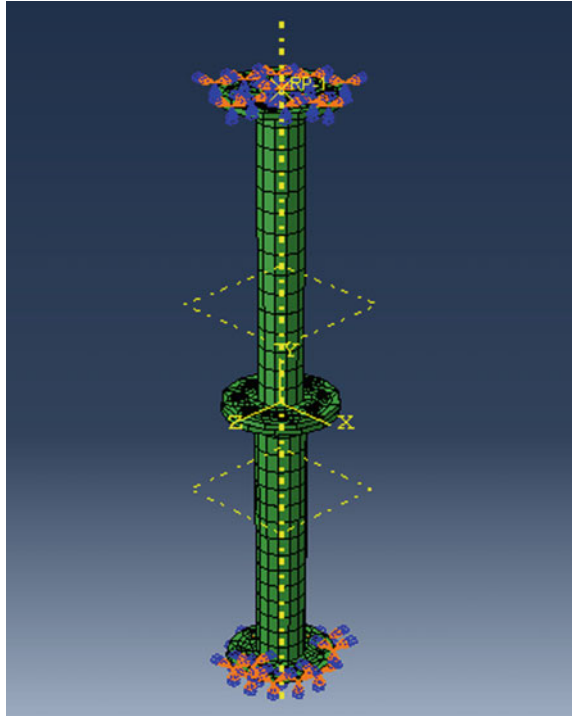


Fig. 5 Boundary conditions

coupling nodes on the top surface follow the rigid body motion of the reference point. All translational degrees of freedom of the reference point and also the nodes in the top surface were fixed, except the vertical displacement. The bottom of the member is fixed by restraining all degrees of freedom. The loading is applied at the reference point to simulate the axial loading condition. The bolts are tied to the flanges using tie constraints, and hence it will act as a rigid connection. Figure 5 shows the FE model with boundary condition.

4.2 *Simulation of Corrosion Effect*

4.2.1 **Uniform Corrosion**

The uniform corrosion effect is simulated by equal removal of thickness from the region of interest of the member. Since in tubular sections, the outer surface is most susceptible area of corrosion. A uniform corrosion effect is modelled by reducing the thickness by 10–50% of original thickness, for a region of 235 mm from either side of the mid-region of the member excluding the flanges. Figure 6 shows the modelling of uniform corrosion effect.

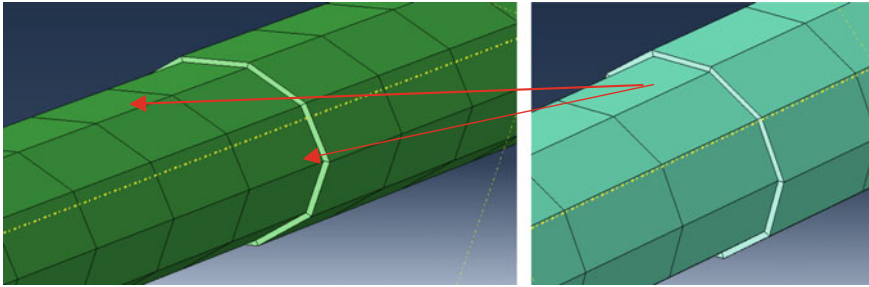


Fig. 6 FE model for simulating uniform corrosion effect

4.2.2 Pitting Corrosion

In pitting corrosion, surface of the corroded member is characterised by the formation of smaller pits resulting in the damage of the material property. Hence in the present study instead of modelling the pit holes in the geometry, the pitting corrosion is numerically modelled by reducing thickness as 1.9 mm in the pitted region of interest, as shown in Fig. 7. The thickness is removed from the randomly selected mesh elements in the centre portion of the member. The percentage of pit corrosion is assigned by the number of pitted elements to the total number of elements which is varied from 0 to 50%. The degree of pitting is defined as given in Eq. (1).

$$\text{Degree of pitting} = \frac{\text{Number of elements deleted}}{\text{Total number of elements on the surface}} \quad (1)$$

4.2.3 Uniform and Pitting Corrosion

Simulation of combined form of corrosion is carried out for a region of 235 mm from either side of the mid-region of the member. Initially, uniform corrosion is

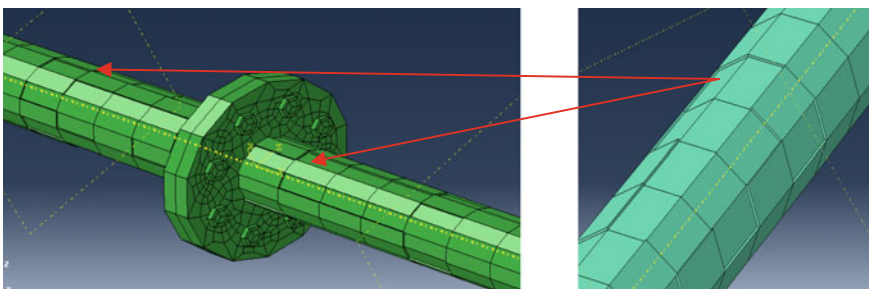


Fig. 7 FE model for simulating pitting corrosion effect

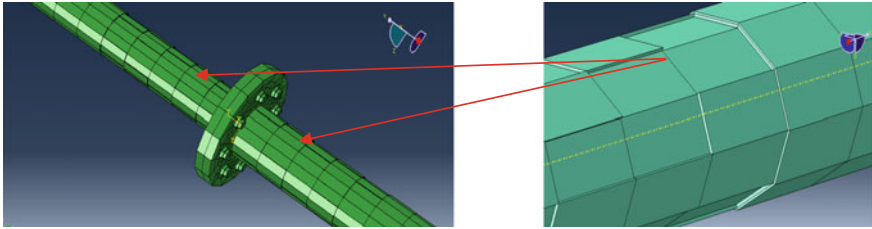


Fig. 8 FE model for simulating combined effect of uniform and pitting corrosion effect

simulated by incorporating the thickness reduction of 20% followed by the pitting corrosion effect is induced for 10–50% of the pit depth up to 30% of the original thickness. Figure 8 shows simulation of combined effect of uniform and pitting corrosion.

5 Results and Discussion

5.1 Load Bearing Capacity of Tubular Compression Members

From the results, it is observed that the load carrying capacity of corroded tubular members decreases significantly for both uniform and pitting corrosion. The mode of failure is buckling which occurs at the corroded region due to the reduction in thickness, the geometric properties such as area, moment of inertia, radius of gyration and section modulus. Table 2 gives the load carrying capacity of the tubular members studied for various types of corrosion effect. Figure 9 shows the comparison of load vs deflection behaviour.

Table 2 Load carrying capacity of the tubular sections studied numerically for various types of corrosion effect

Percentage reduction in thickness	Load (kN)		
	Uniform	Pitting	Combined
0	240.2685	240.2685	211.0608
10	231.9262	226.4492	195.9038
20	211.0608	216.6892	188.1662
30	181.7877	204.8408	181.5685
40	158.3254	201.8231	173.9538
50	132.0331	187.7304	166.8362

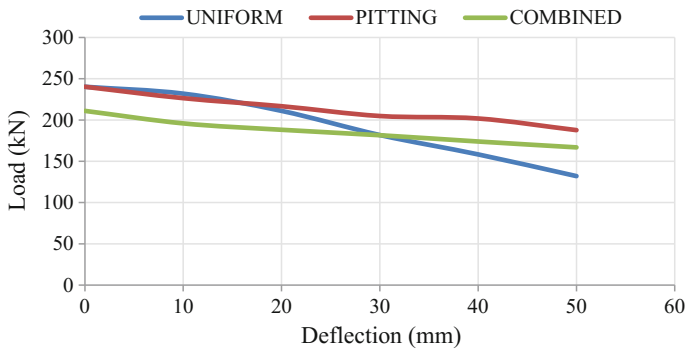


Fig. 9 Load versus deflection

5.2 Validation of Experimental Results with FEM

The experimental results are compared with FEA results and found that both the results agree well as given in Table 3. The experimentally observed deformed modes are shown in Fig. 10.

From the comparison, it is evident that the results obtained using numerical method agree well with the experimental results and the failure modes also matching well. Figure 11 shows the comparison of load vs deflection behaviour. It has been observed that the load carrying capacity decreases with the percentage increase in type and level of corrosion. And among the various foams and percentage of corrosion studied, 40% of uniformly corroded tubular members has significant reduction in strength.

It is clear that the load bearing capacity goes on reducing as the percentage of corrosion increases. Buckling is observed at the region of corrosion. This section is considered as the critical region of the tubular compression members studied. The stress concentration is more in the regions where the pits are available. Hence, there is the possibility of sudden failure. From the experimental and numerical studies, combined corrosion is more dangerous than the other forms of corrosion studied. The drastic reduction in strength may be further justified with localised axisymmetric imperfections due to corrosion along with material degradation.

Table 3 Comparison of experimental results with FEA for columns with joints

Specimen identification	Reduction in thickness	Experiment		FEM	
		P _{utest} (kN)	% Remaining capacity	P _{uFEM} (kN)	% Remaining capacity
STJC-1	0%	236.45	100.00	240.27	100.00
STJC-2	40% uniform	147.89	62.54	158.33	65.89
STJC-3	10% uniform	219.34	92.76	231.93	98.40
STJC-4	30% combined	117.65	49.75	121.24	50.46



Fig. 10 Failure modes of specimens

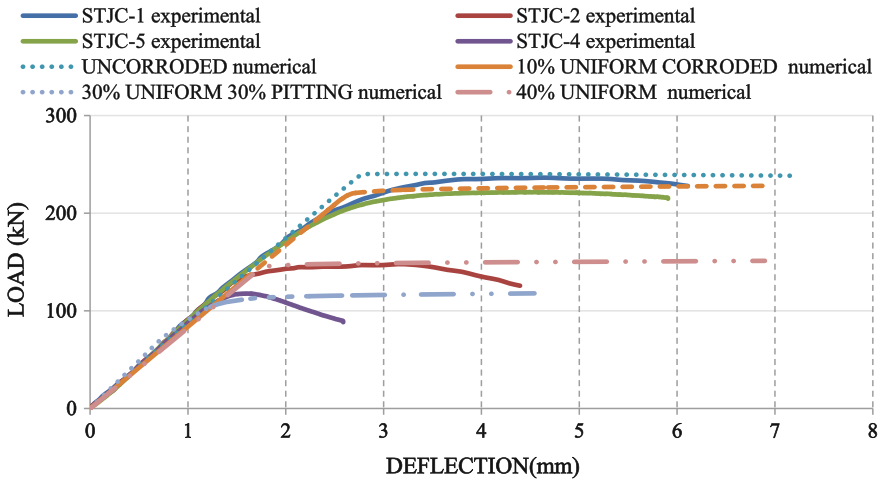


Fig. 11 Comparison of numerical and experimental results for the tubular sections studied

6 Conclusions

This paper presents experimental and numerical studies of corrosion effect on steel tubular compression members, generally used in transmission towers. The study is conducted by varying the level and type of corrosion. The level of corrosion has been varied from 10 to 50%. The various types of corrosion effect studied are uniform, pitting and combined effect of uniform and pitting. The remaining strength capacity of corroded tubular compression members for varying rate of uniform and pitting corrosion was presented and validated with experimental results.

Acknowledgements This paper is published with the permission of the Director, CSIR-Structural Engineering Research Centre, Chennai, India.

References

1. R. Rahgozar, Remaining capacity assessment of corrosion damaged beams using minimum curves. *J. Constr. Steel Res.* **65**, 299–307 (2009)
2. L.V. Beaulieu, F. Legeron, S. Langlois, Compression strength of corroded steel angle members. *J. Constr. Steel Res.* **66**, 1366–1373 (2010)
3. R. Landolfo, L. Cascini, F. Portioli, Modelling of metal structure corrosion damage: A state of the art report. *Sustainability* **2**, 2163–2175 (2010)
4. N. Damgaard, S. Walbridge, C. Hansson, J. Yeung, Corrosion protection and assessment of weathering steel highway structures. *J. Constr. Steel Res.* **66**, 1174–1185 (2010)

Effect of Delamination Defects on Buckling Behavior of Wind Turbine Blades

Vinodkumar Boniface

Abstract Blades in wind turbines are used to capture energy from wind. For MW-class wind turbines, these blades are usually composite structures. They are generally made of glass-fiber composites, while carbon-fiber composites are used selectively in large blades. Stability of these structures is one of the key design drivers. In spite of increasing focus on stringent manufacturing processes, some defects are occasionally seen in the products which lead to reduced margins and lowered life spans. These defects could be delaminations, waves, debond, etc., which can impact various design parameters such as strength, stability, and fatigue life. The specific problem of the effect of delaminations on buckling is addressed in this paper. A typical laminate stack-up is used along with different defect locations and sizes, to arrive at a comprehensive understanding and propose a new delamination model for finite element analysis. A review of recent literature is also presented.

Keywords Wind turbine blade · Composite laminate · Delamination
Buckling

1 Introduction

Blades on a wind turbine are critical for energy capture. They are typically fiber-reinforced composite structures made of monolithic laminates and sandwich panels which are either infused or bonded together. They are designed for specific environmental conditions (wind, air density, etc.) and are certified to appropriate standards. One such is the Germanischer Lloyd (GL) guideline [1], which details various aspects of wind turbine design and certification.

V. Boniface (✉)

GE Renewable Engineering, John F. Welch Technology Center,
Plot #122, EPIP Phase 2, Whitefield Road, Bangalore 560066, India
e-mail: vinodkumar.boniface@ge.com

Defects in these composite structures could occur during manufacturing or service. These defects could be delaminations, waves, debond, etc. and tend to reduce margins of safety and reduce service life of the blade. In this paper, the effect of one type of defect, i.e., delamination, on buckling margin is studied.

1.1 Wind Turbine Blade

Kim et al. [2] provided excellent information on various assessments required for a blade structure design. Though the paper deals with designing a blade having flat-back airfoils, the methodology is quite similar for other blades as well. Typically, 3D finite element analysis (FEA) is used to ensure adequate margins in fiber failure (FF), inter-fiber failure (IFF), bond stresses, and buckling stability with extreme loads. Further, fatigue loads are used for damage assessment.

Lee and Park [3] presented results from their investigation on the effect of fatigue damage on residual strength of a wind turbine blade. A 48.3 m-long-blade that had experienced initial static tests and fatigue tests in accordance with the technical specification IEC61400-23 [4] was considered. The blade had failed in negative flapwise direction during post-fatigue static test. Delaminations were one of the many failure mechanisms observed during post-failure examination.

1.2 Buckling Due to Delamination

Nilsson et al. [5] presented a numerical and computational study of delamination buckling and growth for slender composite panels, focusing on global buckling rather than thin-film buckling. Hosseini-Toudeshky et al. [6, 7] investigated delamination propagation using the softening behavior of interface elements. They showed that buckling load, delamination growth, and buckling of composite plates depended on delamination size and laminate stack-up. Batra and Xiao [8] used a layer-wise third-order shear and normal deformable plate/shell theory incorporating cohesive zone model to study initiation and growth of delamination in double cantilever beams. Butler et al. [9] developed an analytical model using thin-film assumption and cohesive zone at interface to predict the threshold value of compressive strain for buckle-driven propagation of delaminations. Lee and Park [10] studied buckling behavior of laminated composites with delamination using FEA with enhanced assumed strain (EAS) solid element.

Ovesy et al. [11] showed a considerable reduction in load-carrying capacity of the laminate in the presence of delamination using higher order shear deformation theory. Gong et al. [12, 13] investigated the effect of delamination size and shape on buckling behavior using circular and elliptical delaminations in thin beams under four-point bending. Results from stereoscopic digital image correlation and scanning electron microscopy used in experiments were compared with FEA

predictions. Wang et al. [14] studied post-local buckling-driven delamination in bilayer composite beams, by partitioning energy release rate using various partition theories. Cappello and Tumino [15] presented results from FEA of buckling and post-buckling behavior of unidirectional and cross-ply composite laminated plates with multiple delaminations. Wang et al. [16] used a cohesive element in FEA to predict delamination buckling and growth in a slender laminated composite for various parameters such as model aspect ratio and delamination parameters such as size, shape, and depth. Liu and Zheng [17] studied multiple delaminations and their interaction toward buckling and post-buckling behavior under compressive loads for symmetric and unsymmetric laminates.

Riks and Rankin [18] described implementation of a new sandwich FE model in the STAGS code that was better than models based on classical sandwich theory, with the ability to study core-to-face delaminations. Roberts et al. [19] presented experimental work on fiber-reinforced plastic sandwich panels tested in buckling in uniaxial compression for PVC foam and balsa cores. While balsa core had higher buckling loads, core bonding to face sheet was better with PVC foam core. Mahfuz et al. [20] reported experimental work, FEA, and analytical calculations showing that core density had direct influence on global buckling of a sandwich panel, while embedded delamination had minimal effect on both global as well as local buckling. Gaudenzi [21] investigated the effect of a delamination on buckling load of composite laminates under compression through two- and three-dimensional solid FEA, which were compared with existing analytical solutions. Rajendran and Song [22] used a sub-laminate approach and FEA to study delamination buckling and presented buckling loads and strain energy release rates.

2 Delaminations in Wind Turbine Blades

As seen earlier in [2], delaminations are an important mechanism in the potential failure of a wind turbine blade. Delaminations may be caused by inadequate control in manufacturing and also due to transport loads (impact) and in-service loads (progressive damage). Delaminations have been investigated from various perspectives such as buckling loads, post-buckling, delamination propagation, etc. Also, different approaches, analytical, experimental and computational, have been used to study the effect of delaminations.

This study is focused on the effect of delaminations on buckling, with particular reference to wind turbine blades. Typically, wind turbine blades are modeled using shell elements for FEA [1]. These shell elements have details of the laminae (and core in the case of sandwich panels) in the stack-up.

Here, a representative 300×300 mm laminate panel made of 11 layers of 1 mm thick carbon-fiber UD is considered for buckling analysis. Properties are shown in Table 1. A 100×100 mm delamination is considered at the center of the panel. For FEA, the model has an in-plane mesh density of 10×10 mm; for solid elements, mesh density in the thickness direction is 1 mm.

Table 1 Material properties of CFRP [13]

Property	Units	Value
E_{11}	GPa	132.0
E_{22}	GPa	10.3
E_{33}	GPa	10.3
ν_{12}		0.25
ν_{13}		0.25
ν_{23}		0.38
G_{12}	GPa	6.5
G_{13}	GPa	6.5
G_{23}	GPa	3.91

All edges of the panel are simply supported, i.e., u_y displacements are constrained. For solid elements, only the mid-layer of edge nodes is constrained. A compressive load of $F_y = 1e5N$ is applied on one edge, while the opposite edge is constrained in u_y (see Fig. 1). In Fig. 1b, delamination is shown at the center in dark blue.

For FEA, the commercial software ANSYS R15.0 is used. The panel described above is modeled using various options in FEA, resulting in the following configurations:

1. SHELL181 (one element through thickness, with 11 layers)
2. SHELL181 (11 elements through thickness, with 1 layer each)
3. SHELL181 (11 elements through thickness, with 1 layer each) + CONTA173 at delamination
4. SOLSH190 (11 elements through thickness, with 1 layer each)

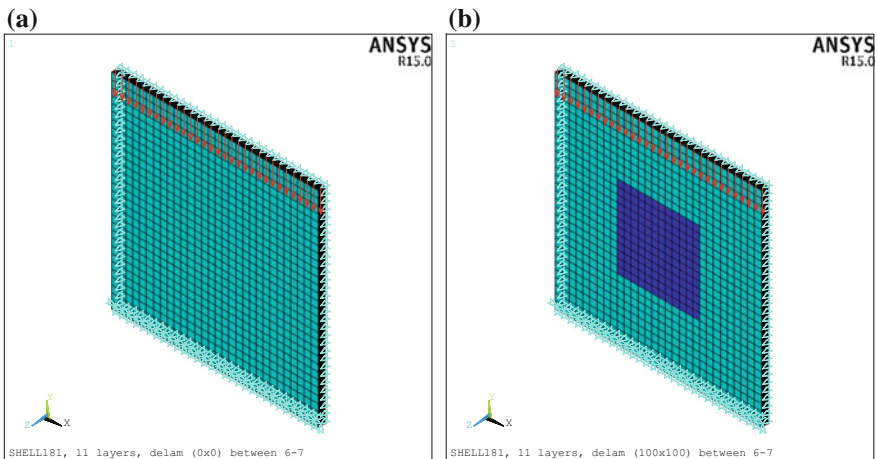


Fig. 1 Finite element model **a** without delamination, **b** with delamination at the center, shown in dark blue

- 5. SOLSH190 (11 elements through thickness, with 1 layer each) + CONTA173 at delamination
- 6. SOLID185 (11 elements through thickness, with 1 layer each)
- 7. SOLID185 (11 elements through thickness, with 1 layer each) + CONTA173 at delamination.

Note that these element types are:

- CONTA173: 3D 4-node Surface-to-Surface Contact
- SHELL181: 4-node Structural Shell
- SOLID185: 3D 8-node Structural Solid
- SOLSH190: 3D 8-node Structural Solid Shell.

2.1 Models with SHELL181 Elements

For SHELL181 elements with 11 elements through thickness (i.e., configurations 2–4), the CERIG command in ANSYS is used (which defines a rigid region using constraint equations), see Fig. 2. Each row of 11 nodes is connected using CERIG. Delaminations are modeled through a break in CERIG, i.e., using two CERIG definitions on either side of the delamination. In Fig. 2, this is shown for a delamination between layers 6 and 7.

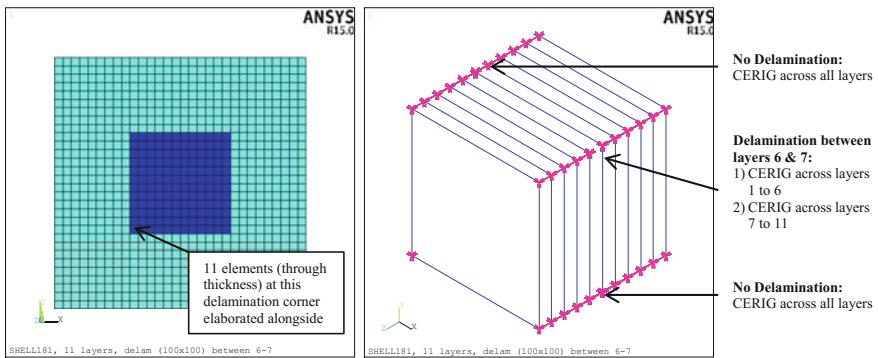


Fig. 2 Finite element model: Delamination in SHELL181 model with 11 layers

2.2 Models with Solid Elements (SOLID185 and SOLSH190)

For solid elements with 11 elements through thickness (i.e., configurations 5–7), elements are attached by merging nodes at the interface between layers. To model delamination, nodes on either side of the delamination are not merged.

3 Buckling Analysis

In this paper, the effect of delaminations on panel buckling is studied through linear eigenvalue buckling analysis. While modeling with solid elements is relatively straightforward, the CERIG approach used for shell elements needs to be validated. This is done by comparing FEA results with available analytical results.

3.1 Benchmark Problem

To establish the CERIG modeling approach mentioned in Sect. 2.1, a panel made of steel without delamination is analyzed first. This corresponds to configuration #2 with 11 elements through the thickness having 1 layer each, attached with CERIG. Properties of steel are provided in Table 2.

The first five buckling modes are shown in Fig. 3 for the steel panel of configuration #2 without delamination.

From Table 15.2 in [24], critical buckling load for a panel simply supported on all edges and subject to a compressive load is

$$P_{cr} = \left[K \frac{E}{(1 - \nu^2)} \left(\frac{t}{b} \right)^2 \right] bt \quad (1)$$

here, E is Young's Modulus, ν is Poisson's Ratio, t is thickness, b is width, a is length and K is a function of (a/b) ratio and is equal to 3.29 for $a/b = 1$. Substituting values for this steel panel, $P_{cr} = 3.368e6N$. On comparing with the applied load of $F_y = 1e5N$, it is seen that buckling load factor is 33.68. From FEA, buckling load factor is 32.34 (see Fig. 3), which matches analytical prediction within 4%. This shows that the CERIG approach used for the 11-layer shell models is acceptable. Composite panels are analyzed in the next section.

Table 2 Material properties of steel [23]

Property	Units	Value
E	GPa	210.0
ν		0.3

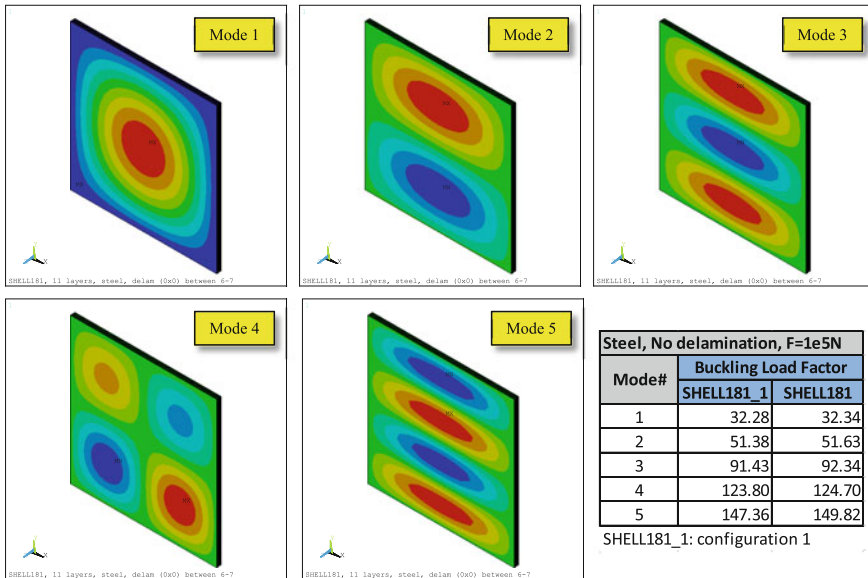


Fig. 3 First five buckling modes, steel panel without delamination, configuration 2

3.2 Composite Panels

The first five buckling modes are shown in Fig. 4 for the composite panel of configuration #2 without delamination. Note that some of the modes are similar to those in Fig. 3 for steel, though buckling load factors are quite different as seen in the table in Fig. 5.

A summary of buckling load factors from the different configurations is shown in Fig. 5. As expected, the SOLID185 model shows anomalous behavior, while SHELL181 and SOLSH190 are in agreement. Two locations with delaminations are studied:

- (a) Delamination between layers 6 and 7: In this case, the trend is similar to the panel with no delaminations, i.e., only SOLID185 model shows a different behavior. Models with and without contact elements exhibit similar behavior. This is because the delamination is at 54.5% thickness and the two parts of the delaminated laminate have approximately equal stiffness and their buckling behavior is similar.
- (b) Delamination between layers 9 and 10: In this case, however, the effect of contacts is seen. Both SHELL181 and SOLSH190 with contact elements (CONTA173) show similar results. This delamination is at 81.8% thickness, and the thinner part of the delaminated laminate has a stiffness value significantly lower than the thicker part and so approaches thin-film buckling. Unless contact elements are used, the delaminated surfaces can penetrate each other as

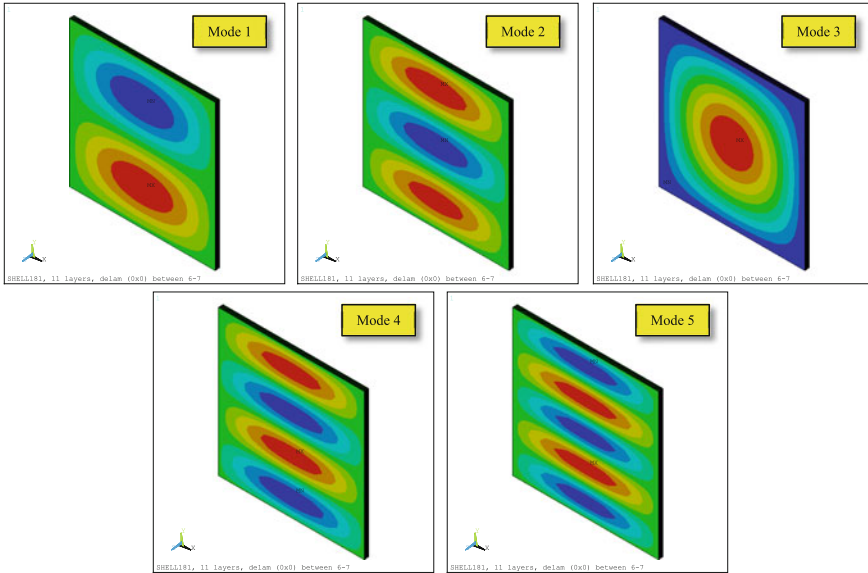


Fig. 4 First five buckling modes, composite panel without delamination, configuration 2

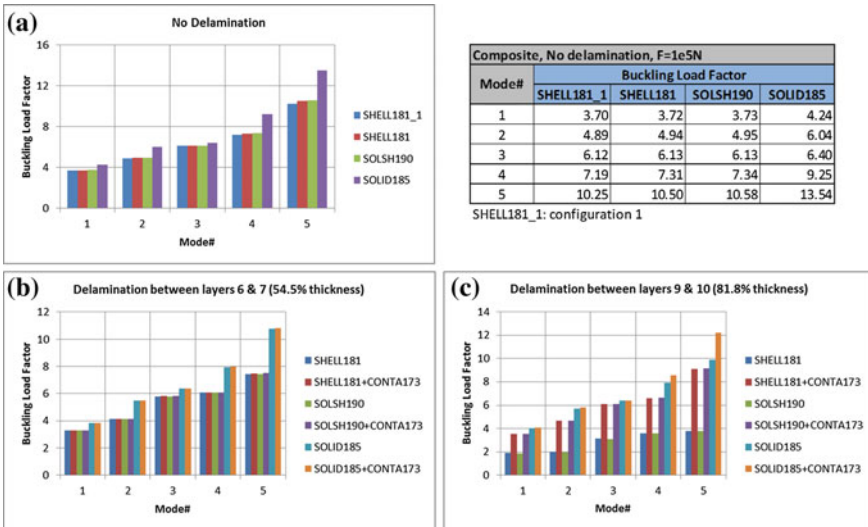


Fig. 5 Buckling Comparison a no delamination, b delamination between layers 6 and 7, c delamination between layers 9 and 10

shown next. As before, SHELL185 models show anomalous behavior, while the effect of CONTA173 in them is seen.

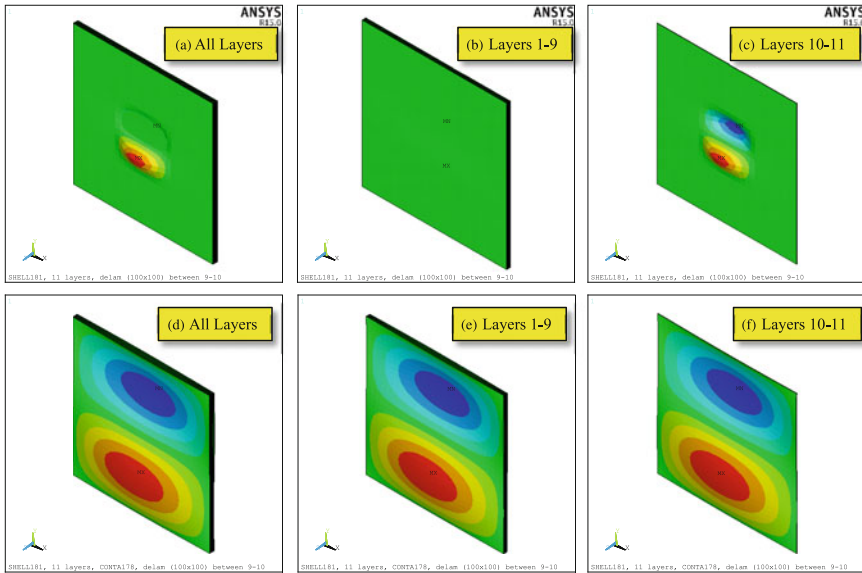


Fig. 6 Effect of contact elements on buckling for mode #1, delamination between layers 9 and 10 **a–c** without contacts, **d–f** with CONTA173

Effect of contact elements for the case of a delamination introduced between layers 9 and 10 is shown in Fig. 6. Buckling mode #1 is considered. It is seen that without contacts, Fig. 6a–c, the two surfaces of the delamination penetrate into each other. Note, however, that deformations shown here are scaled by a factor of 20. On introducing contacts, Fig. 6d–f, the surfaces do not interfere and the buckling mode is quite different.

3.3 Alternative Delamination Model

Another approach to model delamination as a soft laminate layer is investigated. In configuration #1, i.e., SHELL181 elements with one element through thickness made of 11 layers, a 12th layer is introduced at the location of delamination. This layer is modeled with negligible stiffness, $E_x = 0.001$ GPa, $\nu_{xy} = 0.3$. As before, two locations with delaminations are studied, i.e., (a) between layers 6 and 7 and (b) between layers 9 and 10. Thickness of this soft layer is varied and buckling results are compared with those from configuration #2, i.e., SHELL181 elements with 11 elements through thickness made of one layer each. Figure 7 shows this comparison for mode #1. Also shown are $\pm 5\%$ bounds from which it is seen that for a delamination thickness of around 0.02 mm, similar buckling load factors are obtained.

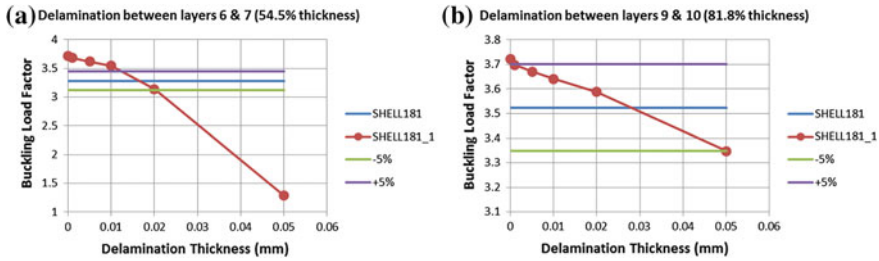


Fig. 7 Effect of introducing a thin layer of delamination in SHELL181 model with 1 element through thickness made of 11 layers **a** delamination between layers 6 and 7, **b** delamination between layers 9 and 10

This approach would be convenient for use in FEA of a Wind Turbine Blade including the effect of delaminations. However, robustness of this approach and domain of application needs to be established. A design-of-experiments (DoE) study including variables like mesh density, materials, delamination geometry, stack-up, and load is required to get a better understanding. Additionally, interaction of delaminations also needs to be studied.

4 Results and Discussion

Effect of delaminations on buckling with specific reference to wind turbine blades is addressed. Different element types are used in this study using FEA. It is seen that contacts have to be modeled in the delamination to obtain realistic buckling modes. A novel approach of using a soft layer to model delamination is investigated. Results from this approach depend on thickness of this soft layer. For the specific problem looked at here, a thickness of around 0.02 mm seems to match results from the shell model with contact elements where the 11 layers are modeled explicitly.

However, the effect of various parameters like mesh sensitivity, materials, delamination geometry (size, shape, location, etc.), stack-up, and loads need to be investigated before this approach can be used reliably. Further, experimental validation of FEA results using sub-article tests is recommended.

References

1. Guideline for Certification of Wind Turbines, Edition 2010, Germanischer Lloyd Industrial Services GmbH, Hamburg, Germany (2010)
2. S.H. Kim, H.J. Bang, H.K. Shin, M.S. Jang, Composite structural analysis of flat-back shaped blade for multi-MW class wind turbine. *Appl. Compos. Mater.* **21**, 525–539 (2014)
3. H.G. Lee, J. Park, Static test until structural collapse after fatigue testing of a full-scale wind turbine blade. *Compos. Struct.* **136**, 251–257 (2016)

4. International Electrotechnical Commission International Standard IEC 61400-23, Wind turbines—part 23: full-scale structural testing of rotor blades (2014)
5. K.-F. Nilsson, L.E. Asp, J.E. Alpmann, L. Nystedt, Delamination buckling and growth for delaminations at different depths in a slender composite panel. *Int. J. Solids Struct.* **38**, 3039–3071 (2001)
6. H. Hosseini-Toudeshky, S. Hosseini, B. Mohammadi, Delamination buckling growth in laminated composites using layerwise-interface element. *Compos. Struct.* **92**, 1846–1856 (2010)
7. H. Hosseini-Toudeshky, S. Hosseini, B. Mohammadi, Buckling and delamination growth analysis of composite laminates containing embedded delaminations. *Appl. Compos. Mater.* **17**, 96–109 (2010)
8. R.C. Batra, J. Xiao, Analysis of post-buckling and delamination in laminated composite St. Venant-Kirchhoff beams using CZM and layer-wise TSNDDT. *Compos. Struct.* **105**, 369–384 (2013)
9. R. Butler, A.T. Rhead, W. Liu, N. Kontis, Compressive strength of delaminated aerospace composites. *Philos. Trans. R. Soc. A* **370**, 1759–1779 (2012)
10. S.Y. Lee, D.Y. Park, Buckling analysis of laminated composite plates containing delaminations using the enhanced assumed strain solid element. *Int. J. Solids Struct.* **44**, 8006–8027 (2007)
11. H.R. Ovesy, M. Taghizadeh, M. Kharazi, Post-buckling analysis of composite plates containing embedded delaminations with arbitrary shape by using higher order shear deformation theory. *Compos. Struct.* **94**, 1243–1249 (2012)
12. W. Gong, J. Chen, E.A. Patterson, An experimental study of the behaviour of delaminations in composite panels subjected to bending. *Compos. Struct.* **123**, 9–18 (2015)
13. W. Gong, J. Chen, E.A. Patterson, Buckling and delamination growth behaviour of delaminated composite panels subject to four-point bending. *Compos. Struct.* **138**, 122–133 (2016)
14. S. Wang, C.M. Harvey, B. Wang, A. Watson, Post-local buckling-driven delamination in bilayer composite beams. *Compos. Struct.* **133**, 1058–1066 (2015)
15. F. Cappello, D. Tumino, Numerical analysis of composite plates with multiple delaminations subjected to uniaxial buckling load. *Compos. Sci. Technol.* **66**, 264–272 (2006)
16. R.G. Wang, L. Zhang, J. Zhang, W.B. Liu, X.D. He, Numerical analysis of delamination buckling and growth in slender laminated composite using cohesive element method. *Comput. Mater. Sci.* **50**, 20–31 (2010)
17. P.F. Liu, J.Y. Zheng, On the through-the-width multiple delamination, and buckling and postbuckling behaviors of symmetric and unsymmetric composite laminates. *Appl. Compos. Mater.* **20**, 1147–1160 (2013)
18. E. Riks, C.C. Rankin, Sandwich modeling with an application to the residual strength analysis of a damaged compression panel. *Int. J. Non-Linear Mech.* **37**, 897–908 (2002)
19. J.C. Roberts, M.P. Boyle, P.D. Wienhold, G.J. White, Buckling, collapse and failure analysis of FRP sandwich panels. *Compos. B* **33**, 315–324 (2002)
20. H. Mahfuz, S. Islam, M. Saha, L. Carlsson, S. Jeelani, Buckling of sandwich composites: effects of core-skin debonding and core density. *Appl. Compos. Mater.* **12**, 73–91 (2005)
21. P. Gaudenzi, On delamination buckling of composite laminates under compressive loading. *Compos. Struct.* **39**(1–2), 21–30 (1997)
22. S. Rajendran, D.Q. Song, Finite element modelling of delamination buckling of composite panel using ANSYS. In *Proceedings of 2nd Asian ANSYS User Conference*, Singapore, 11–13 Nov 1998
23. H.A. Kuhn, *Overview of Mechanical Properties and Testing for Design, Mechanical Testing and Evaluation*, vol. 8 (ASM International, ASM Handbook, 2000), pp. 49–69
24. Roark's Formulas for Stress and Strain, Table 15, 7th edn (McGraw Hill, New York, 2001)

Analysis of the Performance of the Cantilever-Type Piezoelectric Generator Based on Finite Element Modeling

A. N. Soloviev, I. A. Parinov, A. V. Cherpakov, V. A. Chebanenko,
E. V. Rozhkov and L. V. Duong

Abstract The paper analyzes the influence of the characteristics of proof mass on the output characteristics of cantilever-type piezoelectric generators (PEGs) with bimorph elements by using finite element modeling (FEM) in the ANSYS software. This investigation studies the effects of the geometric dimensions of proof mass and the place of its attachment. Symmetrical and asymmetrical cases of mass placement are also studied. The problems of the evaluation of influence of PEG's electromechanical characteristics on output parameters of the generators are considered. The results of the computations of output voltage and power of the PEGs are present.

Keywords Finite element method (FEM) · Piezoelectric generator (PEG) · Bimorph · Cantilever · Proof mass · Damped oscillations · Harmonics · Frequency · Voltage · Power

1 Introduction

The problem of the development of piezoelectric generators (PEGs) for different purposes has not been completely solved yet due to the low-energy efficiency of PEGs and low output power of the existing experimental models. Among the various problems arising during the development of PEGs, one can highlight the

A. N. Soloviev · I. A. Parinov (✉) · A. V. Cherpakov · V. A. Chebanenko
E. V. Rozhkov
Southern Federal University, Rostov-on-Don, Russia
e-mail: parinov_ia@mail.ru

A. N. Soloviev · A. V. Cherpakov
Don State Technical University, Rostov-on-Don, Russia

A. N. Soloviev · V. A. Chebanenko
Southern Scientific Center of RAS, Rostov-on-Don, Russia

L. V. Duong
Department of Mechanical Engineering, Le Quy Don Technical University,
Hanoi, Vietnam

most significant of them, including a choice of energy-efficient piezoceramic materials (PCMs), the development of electrical circuits of accumulation of electrical energy with minimal leakage of charge, the search of geometrical configurations, and assembly technologies of PEG's sensitive element, which induce maximum output power. Approaches used to solve these problems differ substantially, depending on the application of PEG. Previously, problems of energy harvesting systems, including PEGs, were widely discussed in the reviews [1–6]. Later, researches were focused toward the study of PEGs with low-power characteristics, where already have achieved quite tangible results [7, 8].

The finite element method (FEM) is widely used together with the analytical methods of studying PEGs (the main types of these models are present, e.g., in [9–11]). The main advantage of FEM is the capability to conduct numerical simulations of specific models of the devices. This allows one to optimize the model parameters, meet the specified performance, and achieve the maximum PEG's output characteristics. We discuss the examples of such studies below. In [12], it is investigated the material effects of various piezoelectric ceramics on energy efficiency and some resonance characteristics of a cantilever bimorph harvester. The authors concluded that PMN-32 is of greatest interest to the energy storage problems among all investigated compounds. In [13], the possibility of creating a power supply for non-destructive testing devices was investigated. Together with this, the researchers proposed a model of multimodal PEG operating from oscillations arising in the structures, where the sensors are installed usually. Previously [14, 15], we have conducted, by using the finite element modeling, the analysis of the effect of proof mass and thickness of the piezoelectric elements on the output characteristics of axial-type PEG and studied the electrical energy harvesting schemes.

2 Finite Element Modeling of PEG

2.1 *Continuous Models of Composite Elastic, Electroelastic, and Electroacoustic Medium*

Piezoelectric energy harvesting device presents itself a composite elastic and electroelastic body, oscillating with small amplitude in the moving coordinate system. The vertical displacement of the system is defined by the law $y(t)$ or, in the case of external force excitation, by $F(t)$ (or pressure $\sigma(t)$), due to the device's base moves. The initial-boundary value problem of linear electrodynamics coincides with the mathematical model, describing the operation of such a device [16].

In this paper, we use the linear theory of elasticity and electrodynamics, taking into account the dissipation of energy and realizing in the ANSYS software [17], as well as the equations of motion in the acoustic approximation [18].

The piezoelectric medium could be described by the following equations:

$$\rho \ddot{u}_i + \alpha \rho \dot{u}_i - \sigma_{ij,j} = f_i; \quad D_{i,i} = 0, \tag{1}$$

$$\sigma_{ij} = c_{ijkl}(\varepsilon_{kl} + \beta \dot{\varepsilon}_{kl}) - e_{ijk} E_k; \quad D_i + \zeta_d \dot{D}_i = e_{ikl}(\varepsilon_{kl} + \zeta_d \dot{\varepsilon}_{kl}) + \varepsilon_{ik} E_k, \tag{2}$$

$$\varepsilon_{kl} = (u_{k,l} + u_{l,k})/2; \quad E_k = -\varphi_{,k}, \tag{3}$$

where ρ is the material density; u_i are the components of the displacement vector; σ_{ij} are the components of the stress tensor; f_i are the components of the vector of the density of mass forces; D_i are the components of the electric induction vector; c_{ijkl} are the components of the fourth-rank tensor of the elastic moduli; e_{ijk} are the components of the third-rank tensor of piezoelectric coefficients; ε_{ij} are the components of strain tensor; E_i are the components of the electric field vector; φ is the electric potential; ε_{ij} are the components of the dielectric constants tensor; and α, β, ζ_d are non-negative damping coefficients (the value of $\zeta_d = 0$ is used in ANSYS software).

2.2 Modeling

The full-scale finite element model of PEG presents itself a cantilever structure with a bimorph of thin symmetric piezoelectric layers, polarized in thickness, and glued to an elastic plate. The cantilever PEG's geometrical dimensions are shown in Fig. 1a: The substrate has dimensions $l \times b \times h = 150 \times 9.8 \times 1 \text{ mm}^3$, piezoelectric elements consist of two the same piezoelectric plates, polarized in thickness with dimensions $l_p \times b_p \times h_p = 54 \times 6 \times 0.5 \text{ mm}^3$. The center of the proof mass is fixed at a distance l_m from the cantilever clamp. We varied the size of l_m in different numerical calculations into range from 65 to 150 mm. Electric scheme of compound PEG under active load is shown in Fig. 2. Parametrization of the proof mass's geometrical dimensions is shown in Fig. 3a. The length L_m and width b_m of the inertial element are constant and equal to 8 mm and 22 mm, respectively.

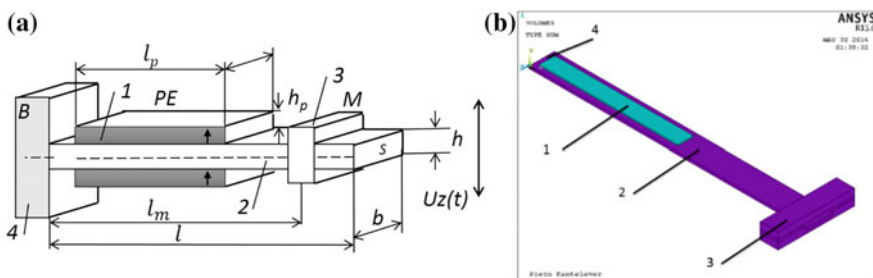


Fig. 1 Structural scheme **a** and its finite element model **b** for studied cantilever PEG: 1 piezoelectric element, 2 substrate, 3 proof mass, 4 clamp

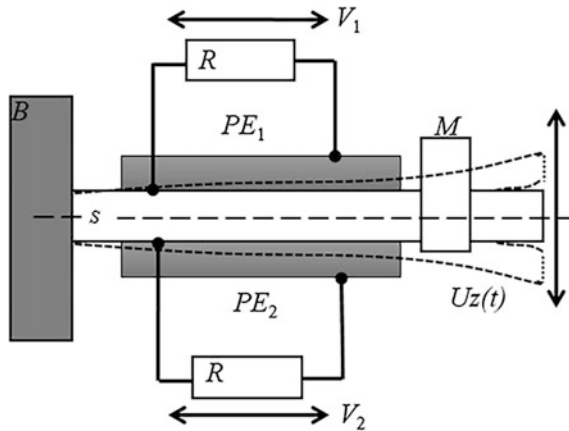


Fig. 2 Electric scheme of compound PEG under active load

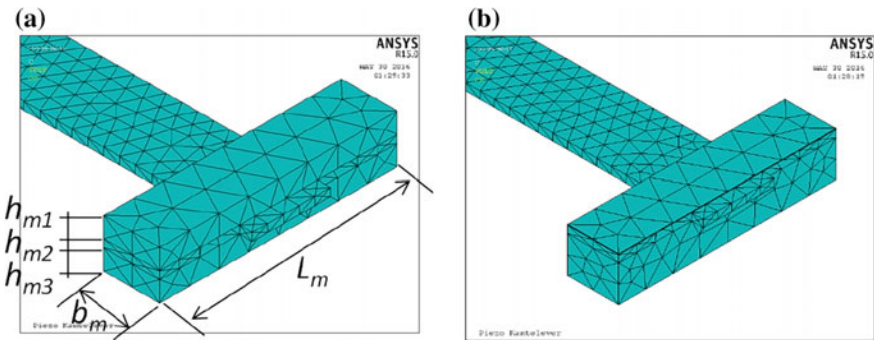


Fig. 3 Two cases of the attachment of proof mass: **a** symmetrical arrangement, **b** asymmetrical arrangement

Thickness parameters h_{m3} , h_{m1} can vary from 0.1 to 5 mm; h_{m2} is the base thickness equal to 1 mm.

The value of the proof mass was varied from 5 to 25 g, and material of piezoelectric plates was hot-pressed piezoelectric ceramic PCR-7 M, whose properties given in Table 1 [11].

As the substrate materials for PEG, we consider duralumin, steel, and fiberglass. The density values of duralumin are above density of the fiberglass, but lower than the density of steel. At the same time, the material of proof mass is a fiberglass. The properties of abovementioned materials are present in Table 2.

Figure 1b demonstrates three-dimensional finite element model of PEG. The electroelastic *FE SOLID5* with 4 degrees of freedom models piezoelectric medium 1

Table 1 Elastic moduli C_{pq}^E (10^{10} Pa), piezoelectric coefficients e_{kl} (in C/m^2) and relative permittivity $\epsilon_{kk}^E/\epsilon_0$ (at room temperature)

C_{11}^E	C_{12}^E	C_{13}^E	C_{33}^E	C_{44}^E	e_{31}	e_{33}	e_{15}	$\epsilon_{11}^E/\epsilon_0$	$\epsilon_{33}^E/\epsilon_0$
12.5	8.4	8.1	12.1	2.36	-9.0	28.3	17.9	1,430	1,350

Table 2 Mechanical properties of the used materials

Material	ρ (kg/m^3)	$E \times 10^{10}$ (Pa)	ν
Fiberglass	2,500	7.0	0.25
Steel	7,800	21.0	0.30
Duralumin	2,700	7.4	0.34

as follows: *VOLT* is the electric potential, and U_x , U_y , and U_z are the components of the displacement vector; the elastic finite element *SOLID186* models media 2 and 3.

The developed FE models based on using ANSYS software and exact formulation of the problem (1-3) allowed us to conduct modal and harmonic analysis.

2.3 Results of Calculations

The natural frequencies and their eigenforms of PEG vibrations were calculated.

Table 3 shows corresponding values, and Fig. 4 presents the eigenforms of vibrations. Modal analysis shows that the first, second, fifth, and sixth oscillation modes are transverse modes of vibration in the vertical plane *OXY*. The third oscillation mode is a transverse oscillation mode in a horizontal plane *OXZ*. The fourth mode is a torsion oscillation mode with respect to the axis *OX*. The differences of the natural vibration frequencies for first to fourth and sixth modes of vibrations are less than 1.7%, and for fifth oscillation mode, it is 6.4%.

At the first stage, it was solved the problem on the comparison of the PEG’s output parameters in symmetric and asymmetric attachments of proof mass at various values of electric resistive load on each of the piezoplates for the proof mass, located on distance $l_m = 65$ mm from the cantilever clamp. The output

Table 3 Natural frequencies of the model PEG with different symmetry of proof mass location at $l_m = 65$ mm

Mode	Proof mass geometric parameters	
	Symmetric case (Hz)	Asymmetric case (Hz)
	2.55 mm × 2.55 mm	0.1 mm × 5 mm
1	49.440	49.368
2	170.08	167.90
3	244.43	240.62
4	389.31	382.81
5	627.14	587.17
6	1184.5	1168.8

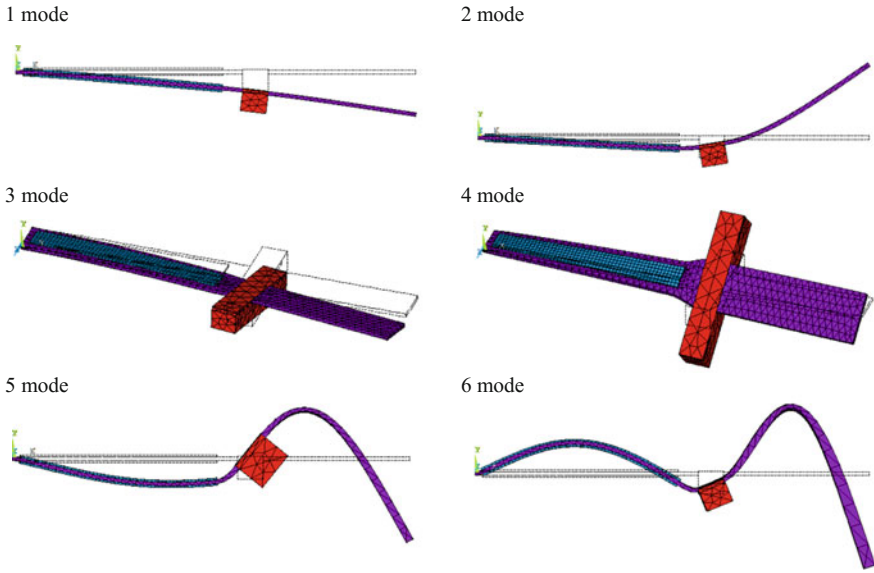


Fig. 4 First six modes of oscillation eigenforms for PEG with asymmetrical location of proof mass

Table 4 Output voltage and power for each of piezoplates at proof mass location $l_m = 65$ mm; results are shown for first oscillation mode

R_n, Ω	Asymmetric case				Symmetric case	
	U_1 (V)	U_2 (V)	P_1 (10^{-6} W)	P_2 (10^{-6} W)	$U_1 = U_2$ (V)	$P_1 = P_2$ (10^{-6} W)
1×10^6	15.17	15.19	230.00	230.70	15.11	228.30
5×10^5	14.19	14.17	402.80	401.50	14.12	398.70
2.5×10^5	12.28	12.25	602.70	599.80	12.21	596.30
1×10^5	8.18	8.17	669.60	667.30	8.15	664.20
5×10^4	5.02	5.01	503.80	502.00	5.00	500.00
1×10^4	1.17	1.17	137.10	136.70	1.17	136.00

voltage of the piezoelectric plates 1 and 2 and output power of every plate for the symmetric and asymmetric cases of proof mass attachments are present in Table 4.

Analysis of the results from Table 4 shows that the values of output voltage differ weakly for the piezoplates in the asymmetric and symmetric cases at various resistive loads. The relative voltage deviation does not exceed 0.6%. As a result, asymmetrical arrangement of the proof mass had low effect on the output parameters of PEG’s voltage in this study.

At the next stage, we analyzed output voltage on each electrode for first six vibration modes in symmetric and asymmetric attachment of the proof mass for value of distance $l_m = 65$ mm and electric load resistance equal to $R = 1 \times 10^5 \Omega$.

Table 5 shows the deviation of maximum voltage (ΔU), as well as maximum power (ΔP) on one of the electrodes at symmetric and asymmetric location of proof mass.

Analysis of the results presented in Table 5 shows that the maximum output power at the excitation of oscillations at the corresponding resonance frequency by a certain force, applied at the point on the free end of the PEG in the direction OY (Fig. 4), is achieved only at the first resonance frequency. Third and fourth oscillation modes have the least values of output power at a given vibration excitation. It is caused that the third oscillation mode excites oscillations in OXZ plane, which is perpendicular to the exciting force. The fourth oscillation mode corresponds to torsion oscillation that also affects the efficiency of the output power. The values of the output power for second, fifth, and sixth vibration modes are equal to 25.9×10^{-6} W, 33.7×10^{-6} W, and 24.9×10^{-6} W, respectively. However, they are more than 25 times less than the output power at the first vibration mode. The deviation of the output voltage on each electrode at symmetric and asymmetric location of proof mass and electric resistance load $R = 1 \times 10^5 \Omega$ is less than 1% for first, second, fifth, and sixth modes of vibrations. The difference of output power does not exceed 1.7%. For third and fourth oscillation modes, output voltage and output power on each electrode do not exceed values of 0.42 V and $1.7 \cdot 10^{-6}$ W, respectively, which is quite low compared to other modes of vibration.

At the next step of the simulation, two PEG models with different conditions of the proof mass attachment and mechanical excitation were considered (the schemes for both models are shown in Fig. 5).

Table 5 Output voltage and power for each of piezoplates at the proof mass, located on distance $l_m = 65$ mm from the cantilever clamp; results are shown for first oscillation mode at load resistance $R = 1 \times 10^5 \Omega$

Mode	Asymmetric case				Symmetric case		ΔU (%)	ΔP (%)
	U_1 (V)	U_2 (V)	P_1 (10^{-6} W)	P_2 (10^{-6} W)	$U_1 = U_2$ (V)	$P_1 = P_2$ (10^{-6} W)		
1	8.17	8.18	667.3	669.6	8.15	664.2	-0.4	-0.8
2	1.53	1.61	23.4	25.8	1.61	25.9	0.3	0.6
3	0.39	0.42	1.5	1.7	0.4	1.6	-4.0	-8.2
4	0.31	0.34	1.0	1.2	0.31	0.9	-10.4	-21.9
5	1.58	1.82	25.0	33.1	1.84	33.7	0.9	1.7
6	1.51	1.58	22.8	25.0	1.58	24.9	-0.1	-0.3

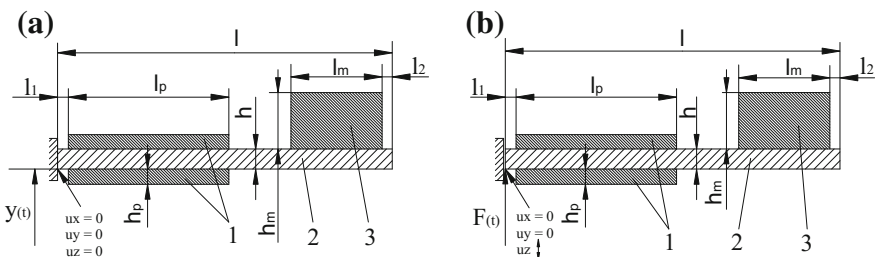


Fig. 5 Schemes for two models of cantilever PEG with proof mass (explanations are into text): 1 piezoelements; 2 substrate; 3 inertial element (proof mass)

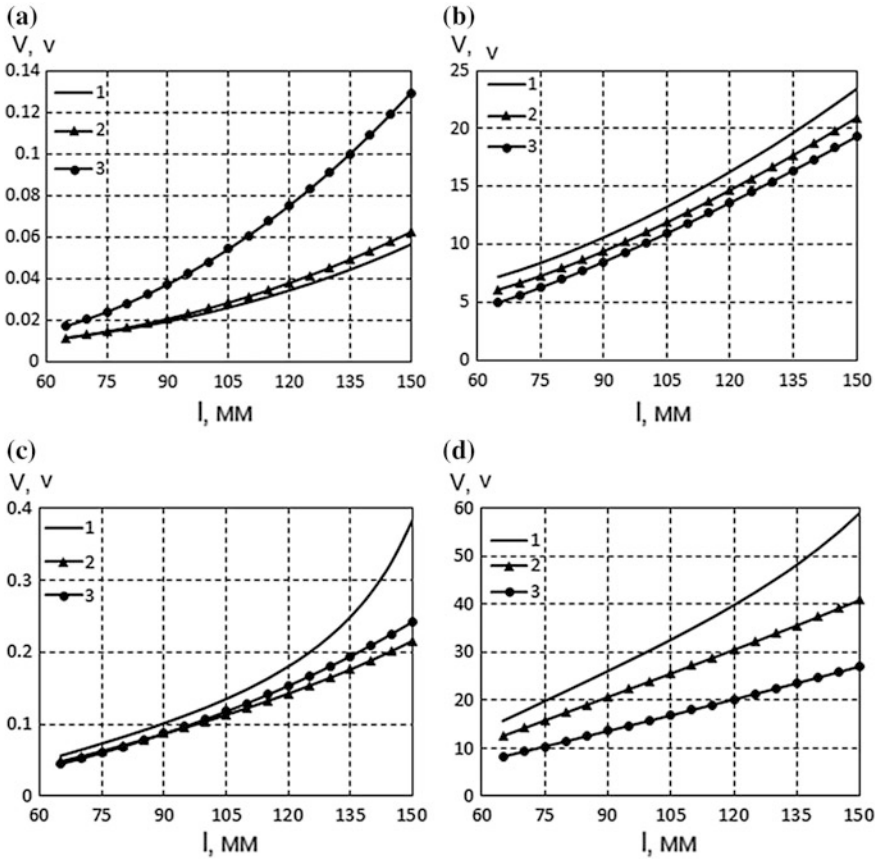


Fig. 6 Dependencies of voltage amplitude: **a** and **c** for the first model; **b** and **d** for the second model: 1 fiberglass; 2 duralumin; 3 steel

The first model performs small oscillations in the moving coordinate system, associated with the surface, which locates at the left side of the plate. The vertical vibrations of the moving system are determined by the relation:

$$y(t) = y_0 e^{-i(2\pi f)t}, \tag{4}$$

where $y_0 = 1$ mm is the oscillation amplitude, and f is the frequency of forced oscillations.

In the second model of PEG, its base can move freely only in the vertical direction, but horizontal direction is fixed. The oscillations are excited by the external force:

$$F(t) = F_0 e^{-i(2\pi f)t}, \tag{5}$$

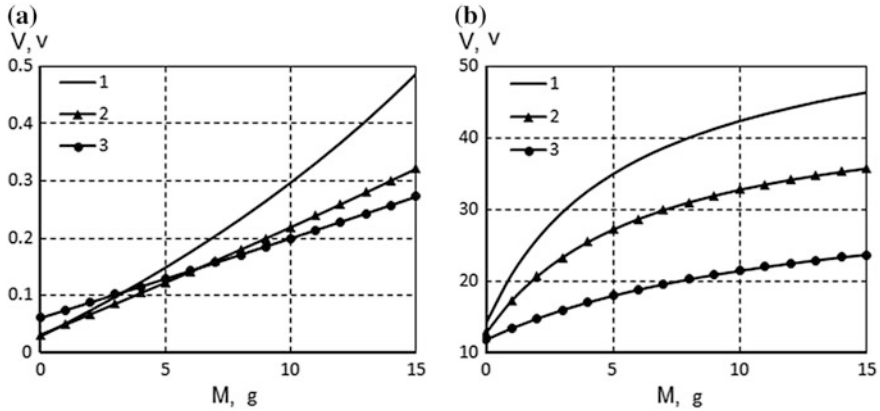


Fig. 7 Dependencies of voltage amplitude: **a** for the first model; **b** for the second model; 1 fiberglass; 2 duralumin; 3 steel

where $F_0 = 1$ N is the amplitude of exciting force, and f is the frequency of forced oscillations.

The dependencies of voltage amplitude, calculated on the free electrode, on the material properties, and on the length l of substrate, at the substrate thickness of 1.2 mm and vibrations, excited at a non-resonance frequency of 10 Hz, are demonstrated in Fig. 6. The calculation results in the case of the proof mass absence are shown in Fig. 6a, b, and the results for the inertial mass equal to 5 g are present in Fig. 6c, d.

The dependencies of the amplitude values of voltage on the upper electrode, at the non-resonance frequency of 10 Hz, on the value of the proof mass, which varies in the range of 0–15 g, are present in Fig. 7. The substrate thickness h and length l were 1.2 and 110 mm, respectively.

3 Conclusions

Based on the finite element modeling performed by using ANSYS software, the problem of influence asymmetric attachment of proof mass on the output voltage at the first resonance frequency, taking into account electric resistive load, was considered. Analysis of the parameters of PEG output voltage shows that the output voltage in the case of asymmetric location of proof mass varies no more than 0.6% compared to the value in the case of symmetric proof mass attachment.

Analysis of the results of the simulation of PEG oscillations at non-resonance frequency of 10 Hz, taking into account substrates of different materials and location of attached proof mass, shows that the elastic characteristics of the substrate directly define the output voltage of PEG. Thus, by comparing the results with

various proof mass locations, we showed that the ratio of the values of output voltage V (at $l = 65$ mm) and V (at $l = 150$ mm) can differ more than four times.

The results, presented in Figs. 6 and 7, show that the output voltage V at the non-resonance frequency 10 Hz is significantly less than the corresponding quantities in the case of resonance; however, these results allow us to choose optimal materials and geometrical dimensions of the substrate and proof mass.

Analysis of output voltage on different electrodes of PEG at asymmetric attachment of proof mass shows that a deviation of the output voltage on each electrode at symmetrical and asymmetrical fixing the attached mass and electric resistive load $R = 1 \times 10^5 \Omega$ is for first, second, fifth, and sixth modes of vibrations less than 1%. This difference of output powers does not exceed 1.7%. For third and fourth oscillation modes, the output voltage and output power on each electrode does not exceed the values of 0.42 V and 1.7×10^{-6} W, respectively, which is quite low compared to other modes of vibration.

Acknowledgements This study has been performed at partial support of Russian Foundation for Basic Research (grants Nos. 16-08-00740, 14-08-00546) and proposals Nos. 213.01-11/2014-25, 0110-11/2017-20 of the Russian Ministry of Education and Sciences (basic part). I.A. Parinov acknowledges financial support of the Russian Ministry of Education and Sciences in the framework of “Organization of Scientific Research” Government Assignment.

References

1. S.R. Anton, H. Sodano, A review of power harvesting using piezoelectric materials *Smart Mater. Struct.* **16**, K1–K21 (2007)
2. S. Priya, Advances in power harvesting using low profile piezoelectric transducers. *J. Electroceramics*. **19**, 167–184 (2007)
3. K.A. Cook-Cherault, N. Thamb, A.M. Sastry, Powering MEMS portable devices—a review of non-regenerative and regenerative power supply systems with emphasis on piezoelectric energy harvesting systems. *Smart Mater. Struct.* **17**, 043001 (2008)
4. H.S. Kim, J.H. Kim, J. Kim, A review of piezoelectric energy harvesting based on vibration. *Int. J. Precis. Eng. Manuf.* **12**(6), 1129–1141 (2011)
5. R. Caliò, U.B. Rongala, D. Camboni, M. Milazzo, C. Stefanini, G. de Petris, C.M. Oddo, Piezoelectric energy harvesting solutions. *Sensors* **14**(3), 4755–4790 (2014)
6. V.A. Chebanenko, V.A. Akopyan, I.A. Parinov, Chapter 10. Piezoelectric generators and energy harvesters: modern state of the art, pp. 243–277. in *Piezoelectrics and Nanomaterials: Fundamentals, Developments and Applications*, ed. by I.A. Parinov (Nova Science Publishers, New York, 2015), 283 pp.
7. V.A. Akopyan, Y.N. Zakharov, I.A. Parinov, E.V. Rozhkov, S.N. Shevtsov, V.A. Chebanenko, Chapter 4. Optimization of output characteristics of the bimorph power harvesters, pp. 111–131. in *Nano- and Piezoelectric Technologies, Materials and Devices*, ed. by I.A. Parinov (Nova Science Publishers, New York, 2013), 261 pp.
8. V.A. Akopyan, I.A. Parinov, Y.N. Zakharov, V.A. Chebanenko, E.V. Rozhkov, Chapter 24. Advanced investigations of energy efficiency of piezoelectric generators, pp. 417–436. in *Advanced Materials—Studies and Applications*, eds. by I.A. Parinov, S.H. Chang, S. Theerakulpisut (Nova Science Publishers, New York, 2015), 527 pp.

9. A. Erturk, P.A. Tarazaga, J.R. Farmer, D.J. Inman, Effect of strain nodes and electrode configuration on piezoelectric energy harvesting from cantilevered beams. *J. Vib. Acoust.* **131** (1), 011010 (2009)
10. N.G. Elvin, A.A. Elvin, A general equivalent circuit model for piezoelectric generators. *J. Intell. Mater. Syst. Struct.* **20**(1), 3–9 (2009)
11. Y. Liao, H.A. Sodano, Optimal parameters and power characteristics of piezoelectric energy harvesters with an RC circuit. *Smart Mater. Struct.* **18**(4), 045011 (2009)
12. A. Nechibvute, A. Chawanda, P. Luhanga, Finite element modeling of a piezoelectric composite beam and comparative performance study of piezoelectric materials for voltage generation. *ISRN Materials Science* (2012)
13. Y. Zhang, W. He, Multi-mode piezoelectric energy harvesters for wireless sensor network based structural health monitoring. in *The 15th International Symposium on Smart Structures and Materials & Nondestructive Evaluation and Health Monitoring* 2008, pp. 69340Z–69340Z
14. A.N. Soloviev, I.A. Parinov, L.V. Duong, C.C. Yang, S.H. Chang, J.C.Y. Lee, Chapter 24. Analysis of finite element models for piezoelectric devices of energy harvesting, pp. 335–352. in *Physics and Mechanics of New Materials and their Applications*, eds. by I.A. Parinov, S.H. Chang (Nova Science Publishers, New York, 2013), p. 444
15. S. Shevtsov, V. Akopyan, E. Rozhkov, V. Chebanenko, C.C. Yang, C.Y. Lee, C.X. Jenny Kuo, Chapter 24. Optimization of the electric power harvesting system based on the piezoelectric stack transducer. Advanced materials—manufacturing, pp. 639–650. in *Physics, Mechanics and Applications*, eds. by I.A. Parinov, S.H. Chang, V.Y. Topolov (Springer, Heidelberg, 2016), pp. 175, 707
16. A.V. Belokon, A.V. Nasedkin, A.N. Soloviev, New schemes of the finite element dynamic analysis of piezoelectric devices. *Appl. Math. Mech.* **66**(3), 491–501 (2002)
17. A.V. Nasedkin, The wave field in anisotropic elastic media with complicated properties and methods of finite element dynamic analysis. DrSc thesis, Rostov State University Press, Rostov-on-Don. 2001, 271 p. (In Russian)
18. V.A. Krasilnikov, V.V. Krylov, *Introduction to Physical Acoustics* (Nauka, Moscow, 1984), 403 pp. (In Russian)

Energy Absorption Characteristics of AA7075-T6 Tube Filled with Aluminum Foam

S. Vignesh, C. Lakshmana Rao and Simhachalam Bade

Abstract In this article, energy absorption and dynamic compressive stress–strain behavior of aluminum foam-filled and empty tube of aluminum alloy AA7075-T6 were investigated using a split Hopkinson pressure bar (SHPB) technique. Both quasi-static and dynamic compression tests were conducted on closed-cell aluminum foam specimens having a relative density of 0.16. The experimental results showed that the plateau stress and energy absorption of foam-filled aluminum alloy AA7075-T6 tube specimen increase with increase in strain rate. The load-deformation characteristics, failure modes, and energy absorption capacity of different structures under dynamic loading were investigated. At higher strain rates, the energy absorption capacity of foam-filled aluminum alloy tubes was found to be increased, which is useful for crashworthy applications.

Keywords SHPB · Aluminum alloy · Energy absorption · Crashworthiness ALPORAS · Crushable foam

Nomenclature

ρ^* Density of closed-cell aluminum foam
 σ_{pl} Plateau stress
 ε_D Densification strain
 W Energy absorption
 A_i Cross-sectional area of incident bar
 A_t Cross-sectional area of transmitted bar
 C_0 Longitudinal wave speed

S. Vignesh (✉) · C. Lakshmana Rao · S. Bade
Department of Applied Mechanics, Indian Institute of Technology Madras, Chennai, India
e-mail: am14m016@smail.iitm.ac.in

S. Bade
Corporate Technology Centre, Tube Investment of India Ltd., Avadi, Chennai, India

© Springer Nature Singapore Pte Ltd. 2018
R. Prakash et al. (eds.), *Advances in Structural Integrity*,
https://doi.org/10.1007/978-981-10-7197-3_26

1 Introduction

Aluminum alloys are mostly used in the automotive and aerospace industries because of their improved strength-to-weight ratios, which are a key factor for fuel economy. Aluminum alloys are also an ideal material for the energy absorption and crashworthiness application. Mostly metallic circular cylindrical aluminum alloy tubes are used as energy absorbers because of low weight and ease of manufacturing process. In recent days, aluminum foams have shown interesting properties for shock absorption and crashworthiness applications in aviation and automotive sectors. In particular, many works related to the energy absorption of foam-filled aluminum tubes have been published in the recent years [1–3]. Raj et al. [4] studied the dynamic crushing behavior of closed-cell aluminum foam and identified the energy absorbed by the aluminum foam found to be higher in dynamic compression. Mukai et al. [5] studied compression behavior of closed-cell aluminum foam at a strain rate of $2.5 \times 10^3 \text{ s}^{-1}$. He found that the energy absorption of aluminum foam at the dynamic strain rate of $2.5 \times 10^3 \text{ s}^{-1}$ is 50% greater than that at the quasi-static strain rate ($1 \times 10^{-3} \text{ s}^{-1}$). Hanssen et al. [6] investigated the energy absorption of aluminum foam-filled square aluminum extrusions subjected to a quasi-static load. It was reported that there was an increase in specific energy absorption by using foam-filled square aluminum extrusions. Hall et al. [7] compared the effects of aluminum foam in brass, aluminum, and titanium tubes and found that the energy absorption was highest in the aluminum tube. In this paper, the closed-cell aluminum foam produced by liquid melt route using titanium hydride (TiH_2) was studied for strain rate sensitivity using SHPB technique. The energy absorption of empty and foam-filled AA7075-T6 tubes was studied under dynamic compression at high strain rates using SHPB technique.

2 Materials and Measurements

Aluminum foams were prepared by melting aluminum and then adding 1–2% of TiH_2 in the form of 5–20 μm diameter particles. The viscosity of the melt was raised by adding 1.5% of calcium. As soon as TiH_2 was added in the melt, the stirring process was withdrawn, and foam was allowed to form. The melt was then cooled to solidify the foam.

The compression test specimens were cut carefully by electro-discharge machining from prepared bulk foam. The regular square prisms of size 20 mm \times 20 mm \times 40 mm were used for the quasi-static test. The quasi-static compression tests were done at a constant strain rate of $1 \times 10^{-3} \text{ s}^{-1}$ in a universal testing machine as shown in Fig. 1a. The foam specimens were compressed up to approximately 70% of their nominal strain. The six specimens were weighed accurately to determine its relative density (ρ^*/ρ_s), and the average was estimated around 0.16 (16%). The tomographic images were used to characterize the cell

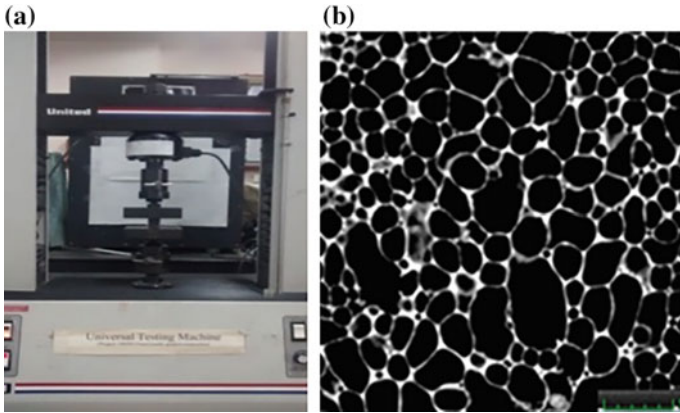


Fig. 1 a Quasi-static compression setup with the specimen. b Tomographic image of aluminum foam



Fig. 2 Empty and aluminum foam-filled AA7075-T6 tubes

shape and size. The typical tomographic image is shown in Fig. 1b. The mean cell size was found to be 3.5 mm. The regular square prisms of size 13 mm \times 13 mm \times 10 mm were used for dynamic compression of foam specimen.

Al alloy AA 7075-T6 having an inner diameter and the outer diameter of 19 and 24 mm was cut to a length of 30 mm. The inner surfaces of the tubes were wire brushed. The prepared foam was cut into cylindrical specimens by wire cut EDM process. Each tube was filled by a cylindrical foam specimen of diameter 24 mm and length 30 mm. Foam core and tubes were pasted using epoxy. Empty and foam-filled AA7075-T6 tube for dynamic compression loading is shown Fig. 2.

3 Experimental Methods

3.1 Dynamic Compression of Aluminum Foam

Kolsky [8] developed the split Hopkinson pressure bar (SHPB) technique to characterize the dynamic mechanical behavior of solid materials at high strain rates. Mostly solid bars are used as incident and transmitted bars in SHPB apparatus, and the cross-sectional areas of the incident bar (A_i) and transmitted bar (A_t) are same. When low-strength materials like aluminum foams are tested with a conventional split Hopkinson pressure bar, the transmitted pulse will have very low amplitude and is difficult to record. Chen et al. [9] reported the use of a hollow transmitted bar when testing low-strength materials like aluminum foam to amplify the strength of the transmitted pulse. In the present study, the aluminum incident bar used was 1.25 m long and 19.5 mm in diameter. The striker had a length of 350 mm and a diameter of 19.5 mm. A hollow aluminum transmitter bar of length 1.5 m with an area ratio of $A_t/A_i = 0.3$ was used. At the end of the hollow transmitted bar, an end cap was press fitted and its effect on the transmitted signal is negligible. The displacement of the incident bar–specimen interface is obtained from the incident (ε_i) and reflected (ε_r) pulse. The axial displacement u_1 is given by

$$u_1 = \int_0^t C_0(\varepsilon_i - \varepsilon_r)dt \quad (1)$$

Similarly, the displacement of the specimen-transmitted bar interface is calculated from the transmitted (ε_t) pulse. The axial displacement u_2 is given by

$$u_2 = \int_0^t C_0\varepsilon_t dt \quad (2)$$

where C_0 is the longitudinal wave speed in the bar and is given by

$$C_0 = \sqrt{\frac{E}{\rho}}$$

The compressive strain in the specimen ε_{sp} is given by

$$\varepsilon_{sp} = \frac{u_1 - u_2}{L_s} \quad (3)$$

Substituting Eqs. (1) and (2) into (3) provides

$$\epsilon_{\text{sp}} = \frac{C_0}{L_s} \int_0^t (\epsilon_i - \epsilon_r - \epsilon_t) dt \quad (4)$$

where L_s is the length of the specimen. The forces P_1 and P_2 acting at the incident bar-specimen interface and specimen-transmitted bar interface are given by

$$P_1 = EA_i(\epsilon_i + \epsilon_r)$$

and

$$P_2 = EA_t \epsilon_t$$

where A_i and A_t are the cross-sectional area of the incident and transmitted bars. The specimen is in equilibrium under the action of the above forces ($P_1 \sim P_2$), we can write

$$\epsilon_t = \frac{A_i}{A_t} (\epsilon_i + \epsilon_r) \quad (5)$$

Substituting Eq. (5) into (4) provides the expression for the compressive strain in the specimen when the hollow transmitter bar is used in SHPB apparatus as

$$\epsilon_{\text{sp}} = \frac{C_0}{L_s} \left[\left(1 - \frac{A_i}{A_t}\right) \int_0^t \epsilon_i dt - \left(1 + \frac{A_i}{A_t}\right) \int_0^t \epsilon_r dt \right] \quad (6)$$

The stress acting on the specimen (σ_{sp}) is given by

$$\sigma_{\text{sp}} = \frac{P_2}{A_{\text{sp}}} = E \epsilon_t \frac{A_t}{A_{\text{sp}}}$$

where A_{sp} is the cross-sectional area of the specimen. The specimen strain rate was obtained by evaluating the slope of the linear portion of the strain versus time plot. Modified SHPB bar set up is shown in Fig. 3.

3.2 Dynamic Compression of Foam-Filled Tubes

Dynamic compression test on empty and foam-filled AA7075 tubes were carried out using conventional split Hopkinson pressure bar as shown in Fig. 4. Maraging steels were used for striker, incident, and transmitted bar. Properties of material used in the striker and the incident and the transmitted bar are listed in Table 1.

Fig. 3 Modified split Hopkinson pressure bar set up with foam specimen

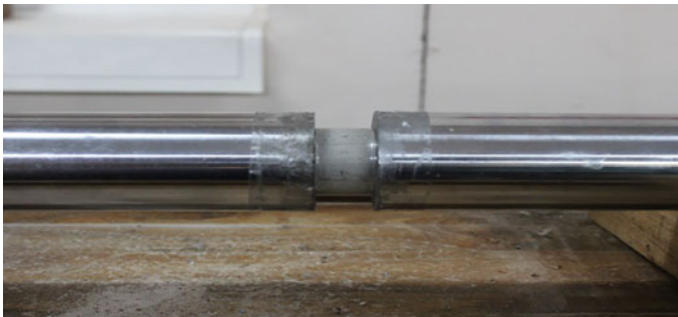
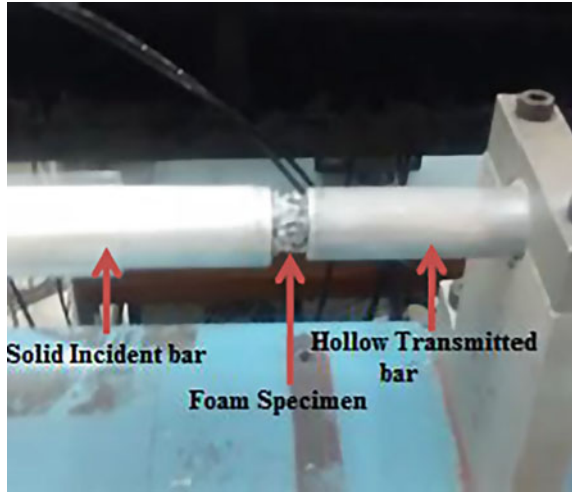


Fig. 4 Conventional Split Hopkinson pressure bar arrangement for testing foam-filled tubes

Table 1 Properties of striker, incident, and transmitter bar

Material	Bar diameter (mm)	Young’s modulus (GPa)	Poisson’s ratio	Wave speed (m/s)
Maraging steel	50	200	0.3	5000

4 Results and Discussion

Quasi-static stress–strain curve of aluminum foam showed three different modes of deformation; namely the initial elastic deformation, after which the foam cells start to buckle and finally the densification or failure mode. Densification takes place

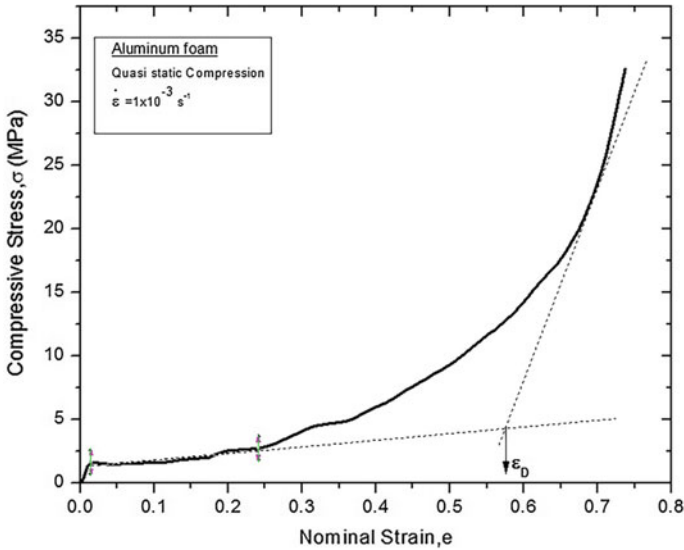


Fig. 5 Compressive stress versus nominal strain curve

when the foam was fully compressed. The compressive stress–nominal strain curve obtained for the foam is shown in Fig. 5.

The most important mechanical properties obtained from quasi-static compression tests are summarized in Table 2.

Dynamic compression experiments of aluminum foam showed that there is strain rate sensitive behavior in closed-cell aluminum foam. Factors, which cause strain rate sensitivity of closed-cell aluminum foam, are as follows,

- Cell wall material
- Micro-inertia
- Air-compressed pressure
- Localized deformation.

In aluminum foam, there is no strain rate sensitivity of cell wall material. Hence, it just needs to consider the effect of inertia, air-compressed pressure, and localized deformation. To estimate the strain rate sensitivity, the plateau stress was plotted against the strain rate in a log–log plot (see Fig. 6b). The strain rate sensitivity of closed-cell aluminum foam was found to be 0.3 from the slope of the log–log plot.

SEM photograph of a deformed cell wall is showed that the foam cell wall fractured due to tension and shear stress induced by stretching cell faces. The tensile

Table 2 Mechanical properties of aluminum foam under quasi-static compression

Foam density, ρ^* (g/cm ³)	Relative density, ρ^*/ρ_s	Young’s modulus, E (GPa)	Plateau stress, σ_{pl} (MPa)	Densification strain, ϵ_D
0.4191	0.16	0.7	2.5	0.57

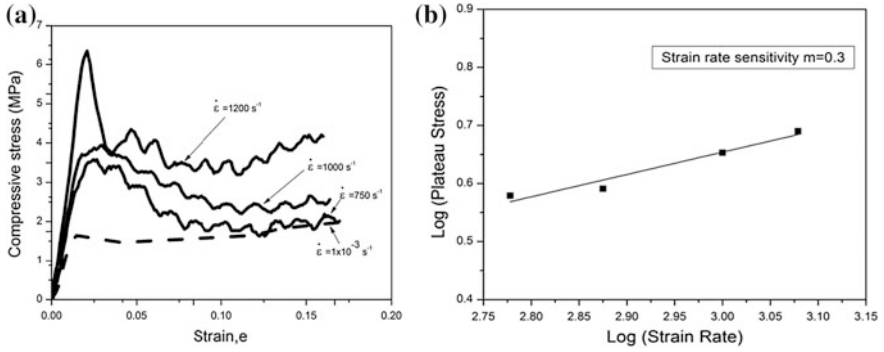


Fig. 6 a Stress–strain curve of an aluminum foam tested under dynamic and quasi-static conditions. b Strain rate sensitivity of aluminum foam

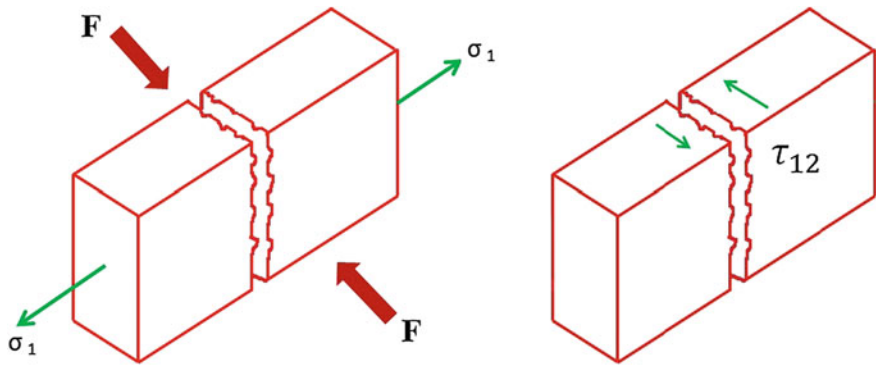


Fig. 7 Tensile and shear failure modes in aluminum foam cell wall

stress σ_1 developed is perpendicular to the compression axis. Sketch of the tension and shear failure of closed-cell aluminum foam cell wall is illustrated in Fig. 7. The fractured cell wall of deformed closed-cell aluminum foam at 20% of strain in quasi-static uniaxial compression is shown Fig. 8.

Filling foam inside AA7075 tubes significantly increases the force necessary to deform the tubes. Compressive stress–strain curve of empty and foam-filled tube at different strain rates is shown in Fig. 9. Energy absorption of foam-filled tube is higher than the empty tube, and filling foam inside the tube also increases the strain rate sensitivity of the tube. At higher strain rate, foam-filled tube showed an increase in stress, which is useful for the crashworthy application.

When the specimen is subjected to compression, the energy absorption capacity is defined as the energy necessary to deform a given specimen to a specific strain. So the absorption energy per unit volume of a sample, up to any particular strain ϵ_0 , can be evaluated by integrating the area under the stress–strain curve as given by the expression:

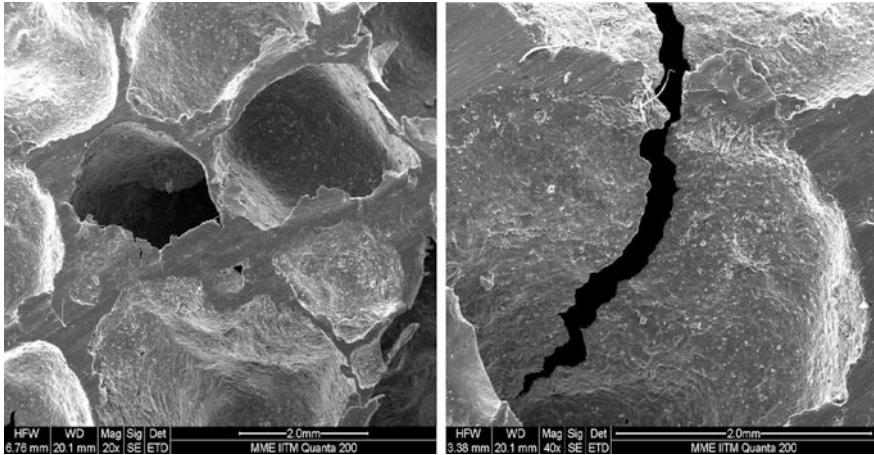
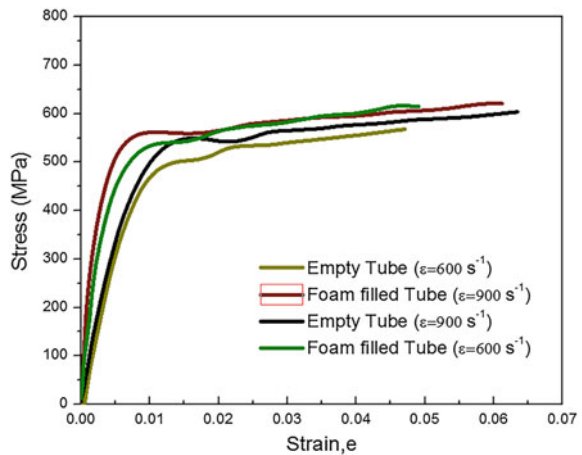


Fig. 8 SEM photograph of undeformed and deformed closed-cell aluminum foam

Fig. 9 Stress–strain response of empty and foam-filled tube at different strain rates



$$w = \int_0^{\epsilon_0} \sigma(\epsilon) d\epsilon$$

Energy absorption capacity empty and foam-filled tubes subjected to high strain rate compression up to 5% strain as shown in Figs. 10 and 11.

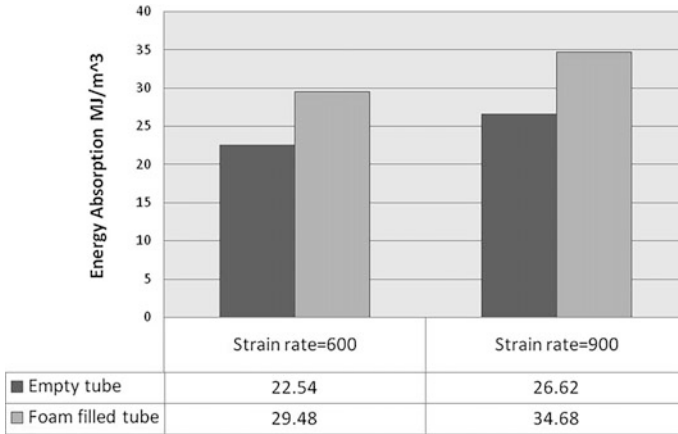


Fig. 10 Energy absorption of empty and foam-filled tube at different strain rates



Fig. 11 Deformed shape of empty and aluminum foam-filled AA7075-T6 tubes after dynamic compression

5 Conclusion

Closed-cell aluminum foams with a relative density of 0.16 were prepared by the decomposition of TiH_2 in molten metal. The behavior of foam subjected to quasi-static and dynamic compression showed that the foam with a relative density of 0.16 was sensitive to strain rate because of localized deformation and micro-inertial effect. Energy absorption of foam-filled tube is considerably higher than empty tube, and energy absorption capacity of foam-filled tubes increases with strain rates. The higher energy absorption capacity at higher strain rate is a useful property for using this material for lightweight impact energy absorption applications.

Acknowledgments The authors acknowledge Professor P. Venkitanarayanan from Indian Institute of Technology, Kanpur for valuable discussions and collaboration.

References

1. M.F. Ashby, A.G. Evans, N.A. Fleck, L.J. Gibson, J.W. Hutchinson, H.N.G. Wadley, *Making Metal Foams, Metal Foams* (2000)
2. J. Banhart, J. Baumeister, M. Weber, Damping properties of aluminium foams. *Mater. Sci. Eng., A* **205**(1–2), 221–228 (1996)
3. Aluminum Foam Technology Applied to Automotive Design, Cymat Corporation (2004)
4. R.E. Raj, V. Parameswaran, B.S.S. Daniel, Comparison of quasi-static and dynamic compression behavior of closed-cell aluminum foam. *Mater. Sci. Eng., A* **526**, 11–15 (2009)
5. T. Mukai, H. Kanahashi, T. Miyoshi, M. Mabuchi, T.G. Nieh, K. Higashi, Experimental study of energy absorption in a close-celled aluminum foam under dynamic loading. *ScriptaMaterialia* **40**(8), 921–927 (1999)
6. A.G. Hanssen, O.S. Hopperstand, M. Langseth, Validation of constitutive models applicable to aluminium foams. *Int. J. Mech. Sci.* **44**(2), 359–406 (2002)
7. I.W. Hall, M. Guden, C.J. Yu, Crushing of aluminum closed cell foams: density and strain rate effects. *ScriptaMaterialia* **43**(6), 515–521 (2000)
8. H. Kolsky, An Investigation of the Mechanical Properties of Materials at very High Rates of Loading. *Proceedings of the Physical Society. Section B* **62**(11), 676–700 (1949)
9. W. Chen, B. Zhang, M.J. Forrester, A split Hopkinson bar technique for low-impedance materials. *Experimental Mechanics* **39**(2), 81–85 (1999)

Strain Intensity Factor and Interaction of Parallel Rigid Line Inclusion in Elastic Matrix Using FEA

Prataprao Patil, S. N. Khaderi and M. Ramji

Abstract When a rigid line inclusion embedded in an elastic matrix is subjected to an external load, stress singularity is generated at the tips. The magnitude of this singularity can be quantified in terms of a strain intensity factor rather than a stress intensity factor. The principal reason is that the strain intensity factor is independent of the material properties of the matrix. The strain intensity factor can be analytically calculated for the case of single inclusion. However, for two parallel rigid line inclusions, the strain intensity factor analytical expression is not readily available. Numerical calculation of the strain intensity factor for two parallel rigid line inclusions embedded in an infinite elastic matrix and the effect of distance between rigid line inclusions on the strain intensity factor is the objective of this paper. To this end, first the stress and displacement fields near the inclusions are calculated using the finite element method (FEM). Then, we use a numerical method based on the reciprocal theorem to calculate the strain intensity factor. It is found that the strain intensity factor is equal to that of the single rigid line inclusion case when the distance between the two parallel rigid inclusions is more than twice their length.

Keywords Strain intensity factor · Rigid line inclusion · FEM Singularity

Nomenclature

E	Young's modulus of the matrix material
l	Length of rigid line inclusion
$2w$	Width of the matrix containing rigid line inclusions
$2h$	Height of the matrix containing rigid line inclusions

P. Patil · S. N. Khaderi · M. Ramji (✉)
Engineering Optics Lab, Department of Mechanical and Aerospace Engineering, IIT
Hyderabad, Kandi 502205, Telangana, India
e-mail: ramji_mano@iith.ac.in

n_j	Unit vector normal to contour
x_i	Coordinates in the i th direction, $i = 1, 2$
r, θ	Variables defining cylindrical coordinate reference system at an inclusion tip
λ	Order of singularity
ν	Poisson's ratio of the matrix material
σ_{ij}, u_i	Components of the stress tensor and displacement vector
σ_{ij}^*, u_i^*	Components of the auxiliary stress tensor and displacement vector
L_{cr}	Critical buckling load

1 Introduction

Nowadays, composite materials find wide application in aerospace, marine, automobile, and packing sectors. Both continuous and short fiber composites are used for structural applications. Short fiber composites usually use discontinuous or short fibers as reinforcing elements. They are used instead of plain polymeric components in electrical, packaging, and automobile applications. These composites are developed to fill the property gap between continuous fiber laminate and unreinforced polymer. The short fiber composites are used in secondary load-bearing structures. The load transfer mechanism is attributed to the interfacial shear stresses at the fiber/matrix interface. The fibers in short fiber composites have random orientation and spacing. The spacing in between fibers influences the structure performance in terms of damage and load-bearing capacity. As a step toward understanding the interaction between the fibers, the problem of two parallel rigid line inclusions embedded in an elastic matrix is studied. The fiber is modeled as a rigid line inclusion. This is a reasonable assumption since the elastic modulus of fiber is much larger than that of the matrix material.

The elastic field near a rigid line inclusion, subjected to a remote load, is known for isotropic and anisotropic matrix materials [1–5]. Few studies exist on characterizing fracture parameter for rigid line inclusion using analytical and experimental approach [6]. The objective of this paper is numerical estimation of the strain intensity factor near the tip of an inclusion (inclusion 1), embedded in an isotropic elastic matrix, when another similar inclusion (inclusion 2) is placed parallel to it, see Fig. 1. Now, the strain intensity factor near the tip of the inclusion 1 is influenced by the remote load as well as the distance between the inclusions.

The article is organized as follows. In Sect. 2, we detail the boundary value problem to be solved. In Sect. 3, we describe the numerical method used to calculate the strain intensity factor. In Sects. 4 and 5, we present the results and concluding remarks, respectively.

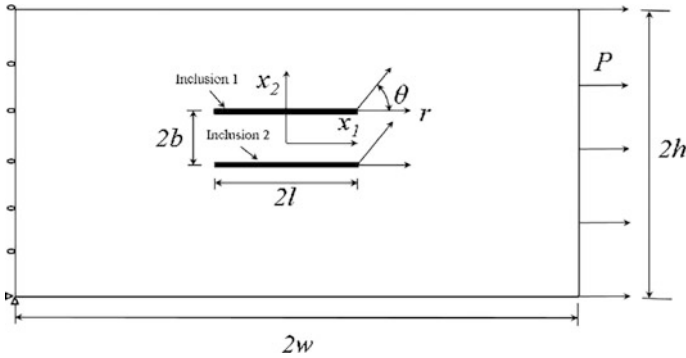


Fig. 1 General configuration of two parallel rigid line inclusions in an elastic matrix subjected to traction

2 Problem Definition

Two parallel rigid line inclusions embedded in an elastic isotropic matrix are considered, see Fig. 1. The length and width of specimen are $2w$ and $2h$, respectively. The rigid line inclusions have length $2l$ and are separated by a distance $2b$. The isotropic matrix material has Young’s modulus (E) and Poisson’s ratio (ν). The boundary conditions applied are as follows:

$$\begin{aligned} t_x(w, x_2) &= P, \\ u_1(-w, x_2) &= 0, \\ u_2(-w, -h) &= 0, \end{aligned} \tag{1}$$

where t_x is the traction along the x_1 direction, and $u_i (i = 1, 2)$ is the displacement along the i direction.

An elastic analysis of the rigid line inclusion embedded in an elastic matrix reveals that the stress and strain fields are singular at the tip of inclusion. In fracture mechanics, such a singularity is quantified in terms of stress intensity factor. In our previous work [7], we have shown that it is appropriate to quantify the singularity in terms of a strain intensity factor defined as

$$K_I^{\varepsilon} = \lim_{r \rightarrow 0} \varepsilon_{rr}(\theta = 0^0) \sqrt{r}, \tag{2}$$

where r and θ are the coordinate system shown in Fig. 1, K_I^{ε} is the strain intensity factor, and ε_{rr} is the radial strain. It was noted that the strain intensity factor is independent of matrix material property [8].

3 Numerical Method for Estimating the Strain Intensity Factor

In this section, the method for strain intensity factor estimation is discussed. The strain intensity factor is calculated by using the elastic full-field solution and an auxiliary asymptotic solution in the reciprocal theorem. The elastic full-field solution is obtained from finite element method. To proceed further, we discuss the asymptotic solution below.

The asymptotic field near the tip is of the form

$$\begin{aligned} \sigma_{ij} &= K_I^e r^{\lambda-1} f_{ij}(\lambda, \theta), \\ u_i &= K_I^e r^\lambda g_i(\lambda, \theta), \end{aligned} \tag{3}$$

where $(i, j) = (r, \theta)$, f_{ij} and g_i are functions of λ and θ , r is the distance from tip of inclusion, and K_I^e is the intensity of singularity, i.e., the strain intensity factor, and λ is the order of singularity.

The strain intensity factor for arbitrary geometry is estimated using reciprocal theorem. The reciprocal theorem can be stated as

$$\oint_C (\sigma_{ij} u_i^* - \sigma_{ij}^* u_i) n_j dS = 0, \tag{4}$$

where n_j is the unit normal to the contour C , (σ_{ij}, u_i) are the actual stress and displacement fields, and (σ_{ij}^*, u_i^*) are suitably chosen auxiliary asymptotic fields (with a unit strain intensity factor) that satisfy boundary conditions. The contour C can be subdivided into four parts. Equation 4 vanishes over C_1 and C_3 because of displacement boundary conditions (See Fig. 2). Equation 4 can be rewritten as,

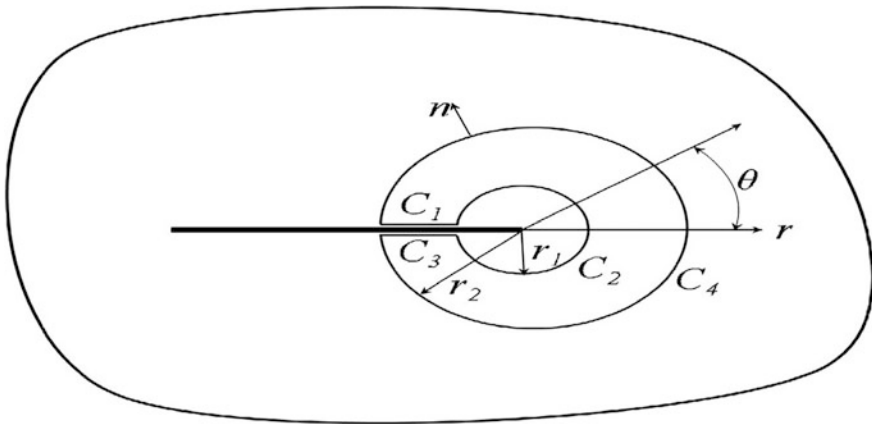


Fig. 2 Contour surrounding the tip of inclusion to evaluate strain intensity factor

$$\int_{C_2} (\sigma_{ij}u_i^* - \sigma_{ij}^*u_i) n_j dS = - \int_{C_4} (\sigma_{ij}u_i^* - \sigma_{ij}^*u_i) n_j dS \quad (5)$$

Substituting the actual elastic fields (in which K_I^e is unknown) and auxiliary fields in left-hand side of Eq. 5, we get

$$K_I^e = \frac{1}{c} \int_{C_4} (\sigma_{ij}u_i^* - \sigma_{ij}^*u_i) n_j dS, \quad (6)$$

where

$$c = \int_{-\pi}^{+\pi} (f_{ij}(\lambda)g_i(\lambda^*) - f_{ij}(\lambda^*)g_i(\lambda)) n_j d\theta. \quad (7)$$

The value of c can be calculated by numerical integration. To calculate K_I^e from Eq. 6, we need to know the actual stress fields. These are obtained by performing a finite element analysis. For more details on the implementation of numerical method, the reader is referred to [7, 9].

4 Numerical Analysis

As mentioned above, the finite element model is used to obtain stress and displacement field that will be used to estimate the strain intensity factor. The finite element (FE) model consists of two parallel rigid line inclusions in an elastic matrix (see Fig. 3). The FE simulations are performed using ABAQUS (version-6.9) in a plane strain setting. The analysis is done with 8-nodded plane strain elements. The dimensions for model are $a = 10$ mm, $w = 100$ mm, and $h = 100$ mm. The mesh pattern around inclusion tip is fine enough to capture the high stress gradients near the inclusion tip. Quarter point elements are used to capture square root singularity surrounding the tip of inclusion. A mesh convergence study has been performed to arrive at the number of element surrounding the tip of inclusion. In the simulations reported, we use 75 elements in circumferential and 60 in radial direction as shown in Fig. 3. The rigid inclusion is modeled as line using constraint equations. The boundary conditions applied are shown in Fig. 1. The magnitude of the applied traction is 0.1 MPa. The elastic properties of the matrix are taken to be $E = 7.95$ MPa and $\nu = 0.45$.

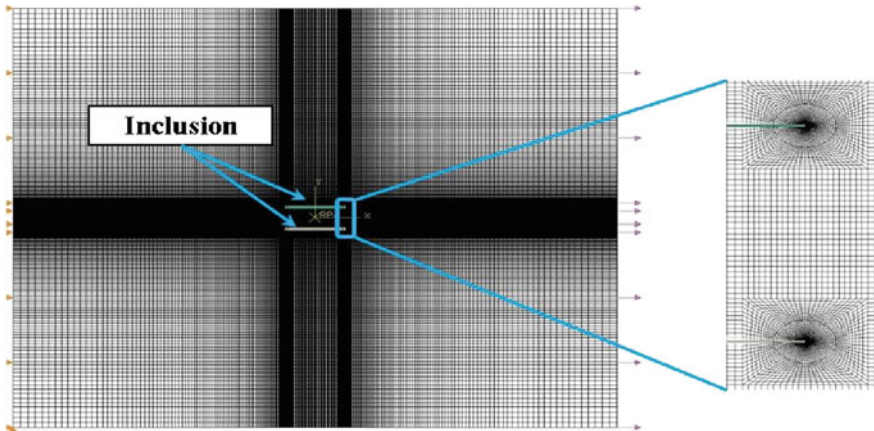


Fig. 3 Finite element mesh used for simulations

5 Results and Discussion

To qualitatively understand the interaction of two parallel line inclusions, we compare the contours of maximum shear stress for two inclusion spacing: $2b = 20$ mm and $2b = 5$ mm. The results are shown in Fig. 4. Comparison of the contour plots reveals the following aspects. The inclusion spacing has an effect on the stress distribution due to interaction between the elastic of the individual inclusions. However, the maximum stress always occurs at inclusions tip despite the spacing between the successive inclusions. This is obvious because of the stress singularity at inclusion tip.

Photoelasticity experiments are performed to qualitatively verify the stress distribution obtained from FE simulations. For experiment, a specimen of epoxy matrix with two parallel rigid line inclusions of length 20 mm and spaced 5 mm apart is fabricated. The conventional photoelastic experiment is carried out.

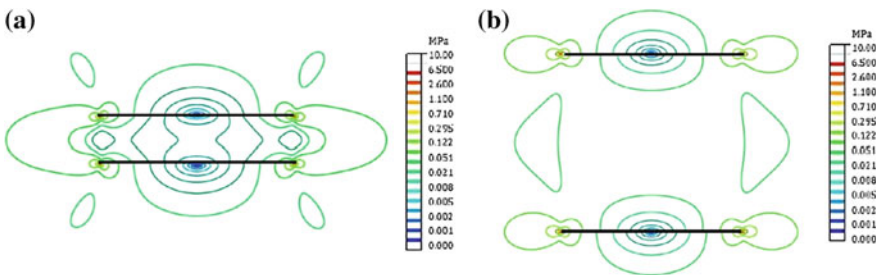


Fig. 4 Maximum shear stress distribution surrounding the rigid line inclusion from FEM for different spacing in line inclusions **a** $2b = 5$ mm, **b** $2b = 20$ mm

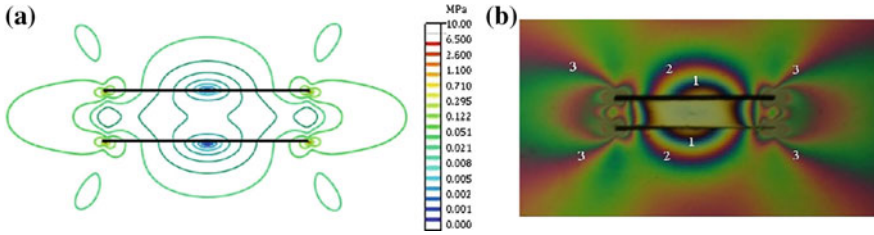


Fig. 5 Comparison of maximum shear stress contour for rigid line inclusion of spacing $2b = 5$ mm between **a** FEM and **b** photoelastic fringes

Fig. 6 Ratio of strain intensity factor considering interaction effect for two parallel rigid line inclusions

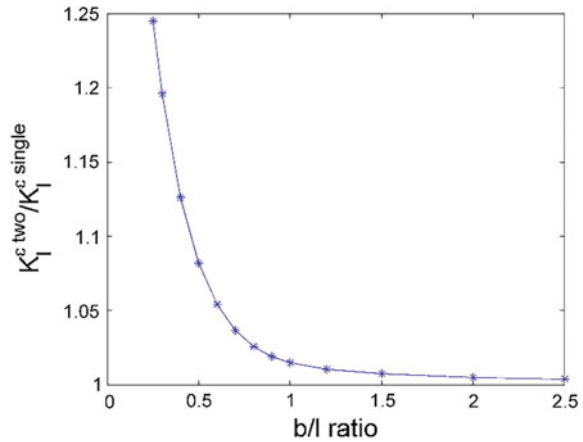


Figure 5b shows the isochromatic fringe contours surrounding rigid line inclusion. The isochromatic contours correspond to the principle stress difference, i.e., maximum shear stress. From Fig. 5, we see that the qualitative features of the maximum shear stress distribution are nicely captured by FE simulations.

The strain intensity factors for different values of inclusion spacing are estimated. The strain intensity factor of two parallel inclusions is normalized with respect to single rigid line inclusion. The normalized strain intensity factor with respect to b/l ratio for parallel rigid line inclusion in an elastic matrix is shown in Fig. 6.

The magnitude of the strain intensity factor increases with decreasing distance between the line inclusions. Strain intensity factor seems to asymptotically approach that of the single rigid line inclusion when distance between the two parallel rigid inclusions is more than their length.

6 Conclusion

We have numerically estimated the strain intensity factor when two parallel rigid line inclusions are subjected to external loading. It is found that the strain intensity factor is equal to that of the single rigid line inclusion case when the distance between the two parallel rigid inclusions is more than their length. For small values of inclusion spacing ($b = 0.25l$), the strain intensity factor is amplified by 25%.

References

1. C. Atkinson, Some ribbon-like inclusion problems. *Int. J. Eng. Sci.* **11**(2), 243–266 (1973)
2. L. Ni, N.S. Nasser, A general duality principle in elasticity. *Mech. Mater.* **24**, 87–123 (1996)
3. Z.Y. Wang, H.T. Zhang, Y.T. Chou, Characteristics of the elastic field of a rigid line inhomogeneity. *J. Appl. Mech.* **52**, 818–822 (1985)
4. D. Radaj, S. Zhang, Loading modes and stress intensity factors at rigid layer edges. *Eng. Fract. Mech.* **46**(2), 199–208 (1993)
5. P. Pingle, J. Sherwood, L. Gorbatikh, Properties of rigid-line inclusions as building blocks of naturally occurring composites. *Compos. Sci. Technol.* **68**, 2267–2272 (2008)
6. G. Noselli, F.D. Corso, D. Biboni, The stress intensity near a stiffener disclosed by photoelasticity. *Int. J. Fract.* **166**, 91–103 (2010)
7. P. Patil, S.N. Khaderi, M. Ramji, Numerical estimation of strain intensity factors at the tip of a rigid line inclusion embedded in a finite matrix. *Eng. Fract. Mech.* **172**, 215–230 (2017) (Online Available)
8. A. Akisanya, N. Fleck, Interfacial cracking from the free edge of a long bi-material strip. *Int. J. Solids Struct.* **34**(13), 1645–1665 (1997)
9. P. Patil, S.N. Khaderi, M. Ramji, Finite geometry correction factor for stress singularities of rigid line inclusion, in *International Conference on Computer Aided Engineering (CAE-2015)*, pp. 269–272 (2015)

Part V
Creep-Fatigue

Creep-Fatigue Damage Assessment of Reactor Hot Pool Components During Crash Cooling

Rosy Sarkar, S. Jaladeen and K. Velusamy

Abstract In the prototype fast breeder reactor (PFBR), when there is a reactor SCRAM, the shutdown takes place in two phases. First, there is hot shutdown, i.e. the hot pool sodium temperature is rapidly brought down from 820 to 623 K in 25 min, and the II phase is to proceed to the cold shutdown (453 K isothermal) condition gradually by deploying operating grade decay heat removal system (OGDHR). The controlled cooling involving high and varying operating mode of suction pressure of the pump makes the pump design complex. In view of this, the requirement of controlled cooling has been relooked in the commercial breeder reactor (CBR), and it is proposed to deploy the OGDHR only after reaching cold shutdown. Thermo-mechanical analysis of the reactor components, i.e. control plug (CP), inner vessel (IV) and intermediate heat exchanger (IHX) has been carried out using a finite element (FE) code. The approach followed for writing the program (imposing the fall in sodium level (~ 16 mm/min) at the free surface along with the drop in temperature (~ 7 K/min) and the creep-fatigue damage assessment for each case has been discussed in this paper.

Keywords OGDHR · Crash cooling · CBR · Control plug · Inner vessel
Intermediate heat exchanger

Nomenclature

T_{Na} Sodium temperature
 T_{Ar} Argon cover gas temperature
 l_{ti} Inner surface top length
 l_{bi} Inner surface bottom length
 l_{to} Outer surface top length
 l_{bo} Outer surface bottom length
 ΔL Level change
 L Sodium level

R. Sarkar (✉) · S. Jaladeen · K. Velusamy
Indira Gandhi Center for Atomic Research, Kalpakkam 603102, Tamil Nadu, India
e-mail: roslysarkar@gmail.com

1 Introduction

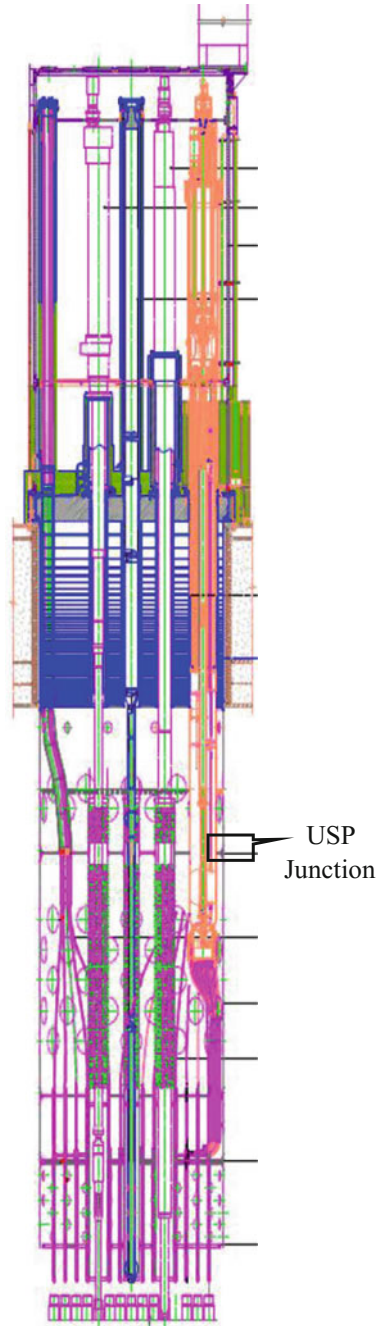
In the prototype fast breeder reactor (PFBR), the hot pool sodium is maintained at 820 K during normal operating condition. When there is a reactor SCRAM, the shutdown takes place in two phases. In the I phase, the hot pool sodium is rapidly cooled from 820 to 623 K within 25 min by operating the main condensers. The II phase is to cool down the sodium systems from 623 to 453 K at a controlled rate of 20 K/h by deploying the operating grade decay heat removal system (OGDHR). When there is controlled cooling, the pumps incorporated in the OGDHR system face the high suction pressure of the order of 170 bars and vary up to about 15 bars. The high and varying operating mode of suction pressure of the pump makes the pump design complex, mainly from the point of view of sealing arrangement. In view of this, the requirement of controlled cooling rate from 623 to 453 K has been relooked in the commercial breeder reactor (CBR) and it is proposed to deploy the OGDHR only after reaching cold shutdown condition [1].

In CBR, the need for an alternate system having a lower capacity for decay heat removal (DHR) during shutdown state is envisaged. The simplified scheme for DHR through steam generators has been proposed [1]. During the phase when the reactor systems are at high temperature (820 K), the cool down takes place at a high rate (~ 400 K/h), and subsequently, when the reactor systems are at low temperature (623 K), the cool down is performed at lower rate (100 K/h), when main condenser is used for cool down. The thermo-mechanical analysis of the reactor components in primary sodium has been carried out using a finite element (FE) code. The approach followed for writing the program [imposing the fall in sodium level (~ 16 mm/min) at the free surface along with the drop in temperature (~ 7 K/min)] and the creep-fatigue damage assessment for each case has been discussed in the subsequent sections.

2 Reactor Components in the Hot Pool

During crash cooling, the sudden change in the hot and cold pool sodium temperatures induce stresses in the reactor components like control plug (CP), inner vessel (IV) and intermediate heat exchanger (IHX), which are immersed in the primary sodium. This results in creep and fatigue damage of the components. Hence, detailed investigation of the hot pool components has been carried out to estimate the damage. The critical region in CP, IV and IHX is the sodium-free level because of the continuous change in the sodium level and sodium temperature. The geometrical details of the CP, IV and IHX are given in Fig. 1 [2], Fig. 2 [3] and Fig. 3 [4], respectively.

Fig. 1 Vertical section of CP



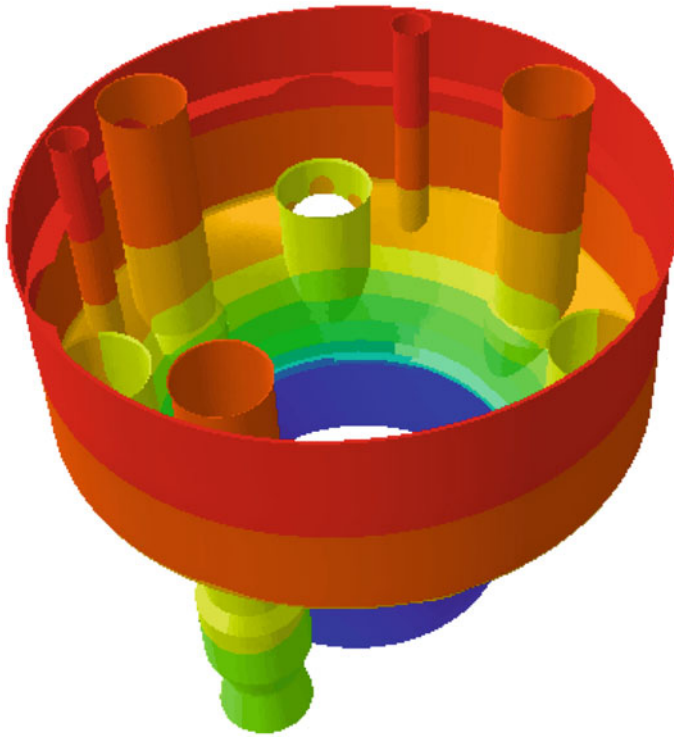


Fig. 2 3D details of IV

3 Loading Conditions

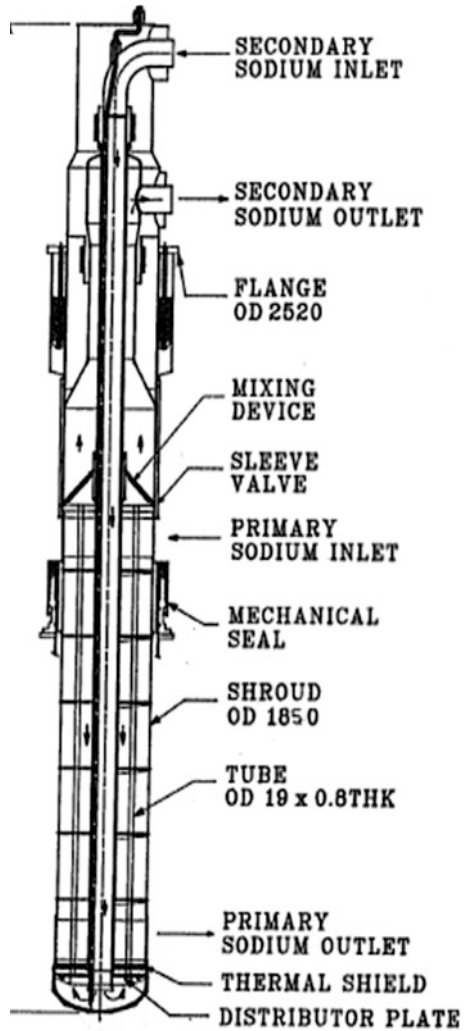
Following SCRAM, the sodium temperature is brought down by operating the main condensers. With a decrease in sodium temperature, the density of sodium increases and thereby the volume decreases, resulting in continuous fall in sodium level with fall in sodium temperature.

3.1 Change in Sodium Level

Following SCRAM, the initial sodium level (at 820 K) is at 27,400 mm. During the I phase, when the sodium is cooled to 623 K in 25 min, the sodium level reaches to 27,000 mm. Thus, the average rate of change in the sodium level is 16 mm/min.

During the II phase when the sodium at hot shutdown condition (623 K) is cooled to the cold shutdown condition (453 K), the sodium level falls from 27,000

Fig. 3 Vertical section of IHX



to 26,700 mm at 100 K/h (1.67 K/min). Thus, the average rate of change in sodium level is 3 mm/min.

The sodium level change is same for all the hot pool components.

3.2 *Change in Sodium Temperature*

The evolution of hot and cold pool temperature, following SCRAM, in the case without the deployment of OGDHRS is shown in Fig. 4 [5]. The hot pool

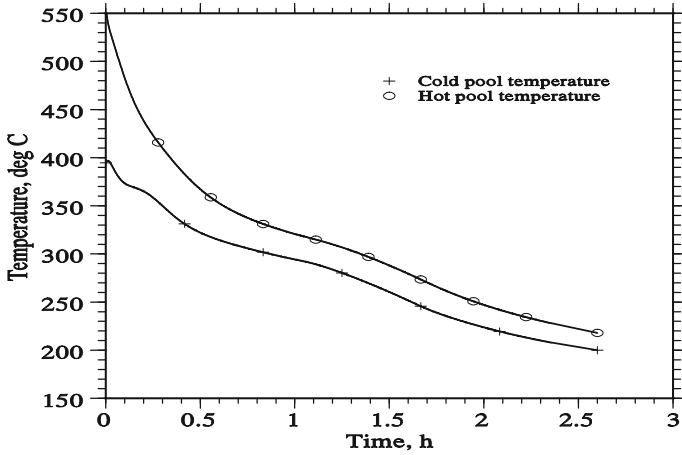


Fig. 4 Evolution of hot and cold pool temperature following SCRAM, without deployment of OGDHR

temperatures given in Fig. 4 are the input for both inside and outside the CP (12 mm thick). The hot pool and cold pool sodium temperatures, shown in Fig. 4, are given as input for the inside and outside surfaces of the inner vessel (15 mm thick), respectively.

The IHX shell (16 mm thick) is filled in with secondary sodium, and the sleeve valve (5 mm thick) is surrounded by primary sodium inside (annulus—50 mm) and outside. There is argon cover gas above the primary sodium in the annulus and outside the sleeve. Following SCRAM, the temperatures at each surface during hot shutdown (I phase) are as shown in Fig. 5. The temperature drop during cold shutdown (II phase) is 100 K/h.

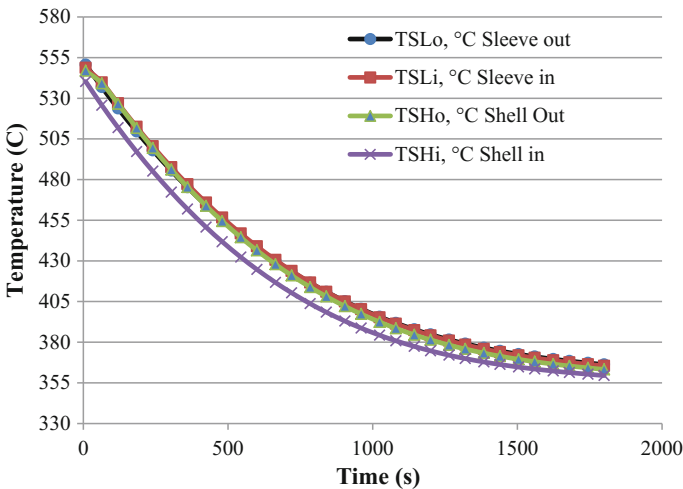


Fig. 5 Temperatures at shell and sleeve in IHX

4 Flow Chart for Writing FE Program

The generalized approach followed to obtain the stresses and temperature distribution at every minute, at the transient with varying sodium level and sodium temperature is shown in the flow chart in Fig. 6.

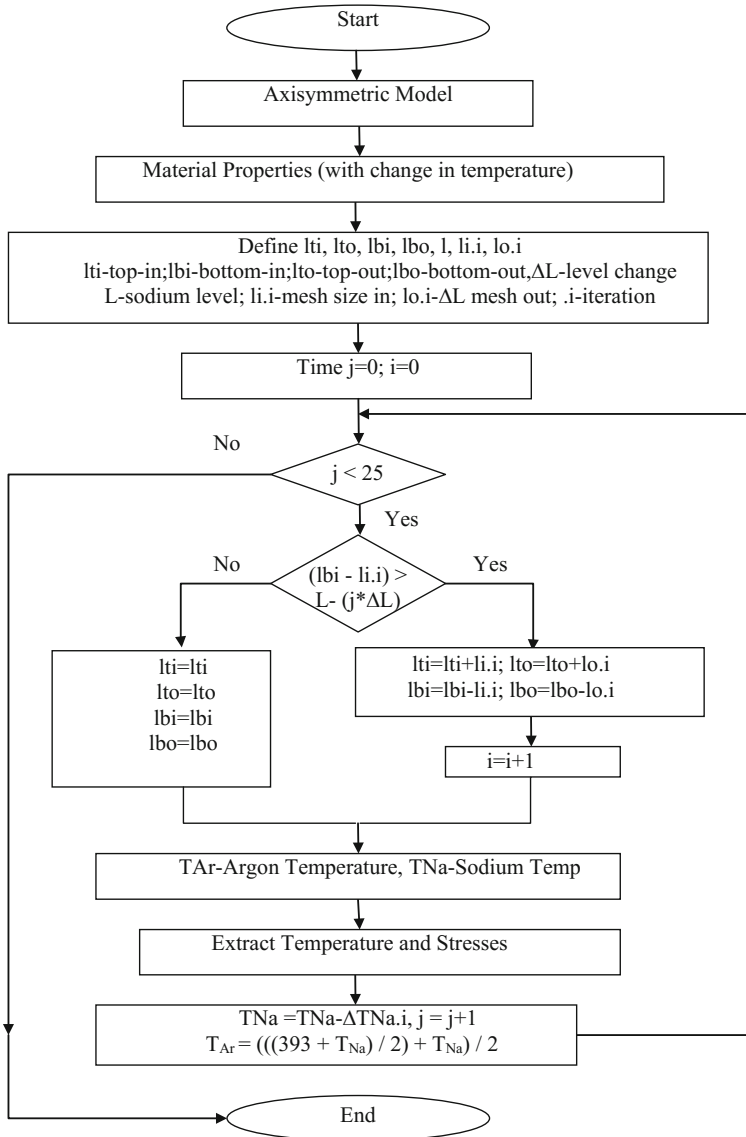


Fig. 6 Flow chart for writing a finite element program to simulate the change in length and temperature of primary sodium

An axisymmetric solid element model for each component has been modelled, and the radial components have been arrested for simulating the boundary conditions. The material for the construction of CP, IV and IHX is SS 316 LN. Density has been conservatively taken at 423 K, and all the other material properties (except conductivity) have been taken at 823 K. The change in the conductivity values with a change in temperature has been incorporated.

The length of the component that is immersed in sodium is categorized as bottom (lbi and lbo), and the rest is the top region (lti and lto), where 'i' and 'o' are inner and outer surfaces. ' L ' is the initial sodium level, and ΔL is the change in sodium level at each iteration.

Convection heat transfer is considered, with $h = 10 \text{ W/m}^2 \text{ K}$ at the top region of the component that is surrounded by argon cover gas. Conduction heat transfer is considered for the bottom portion which is surrounded by sodium, which has a very high heat transfer coefficient.

5 Control Plug (CP)

5.1 Methodology

During the I phase (i.e. to reach the hot shutdown condition), there is ~ 400 mm fall in sodium level and the maximum stresses are expected at this region (shown in blue in Fig. 7a).

During the II phase, there is ~ 300 mm fall in sodium level and this is the region of interest as shown in Fig. 7b (in pink). The zones A, B, C in I phase and A', B', C' in II phase are shown in Fig. 7a, b, respectively. Both the phases are modelled separately, and the stresses are evaluated separately (because of different loading conditions), and the creep-fatigue damages at each location are added to get the final creep-fatigue damages.

5.2 I Phase (To Reach Hot Shutdown Condition)

Transient analysis of the CP with the above-mentioned loading and boundary conditions has been carried out. The length considered for this analysis is from elevation 27,500 to 26,900 mm. The whole length is divided into 10 sub-zones namely 1S, 2S, 3S, 4S, 5S, 6S, 7S, 8S, 9S, 10S, where 1S is the bottom-most sub-zone and 10S is the topmost sub-zone. The evolution of temperature and stress is shown in Fig. 8a, b, respectively. The stress and temperature distribution curves for each sub-zone are extracted. The temperature distribution curve and the stress distribution curve at the maximum damaged sub-zone (in zone-B) are shown in Fig. 9a, b, respectively.

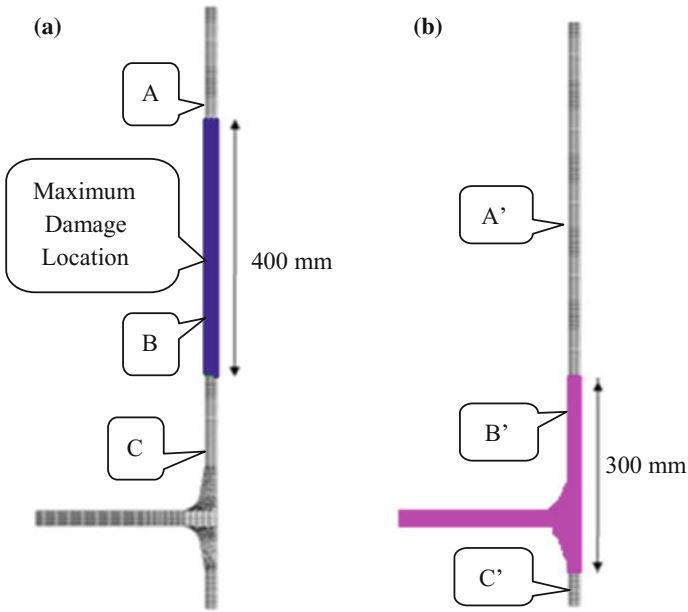


Fig. 7 a Categorization of zones in I phase, b categorization of zones in II phase

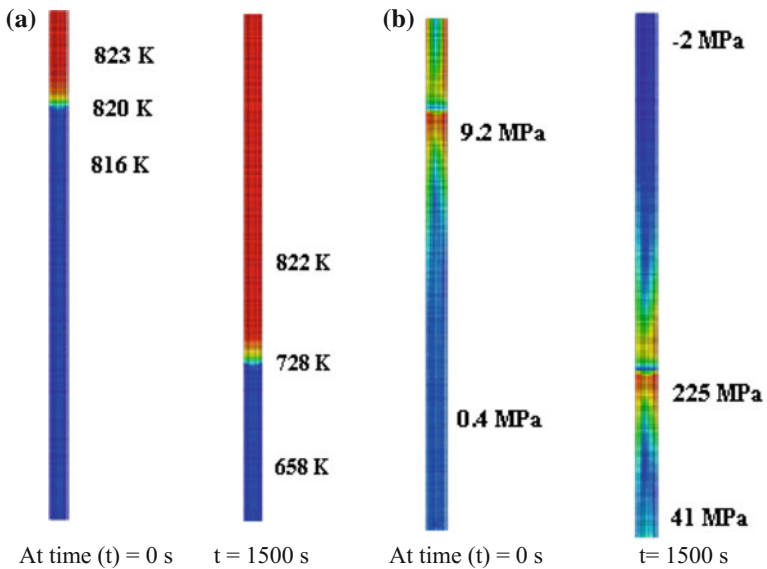


Fig. 8 a Temperature evolution in CP during I phase shutdown, b stress evolution in CP during I phase shutdown

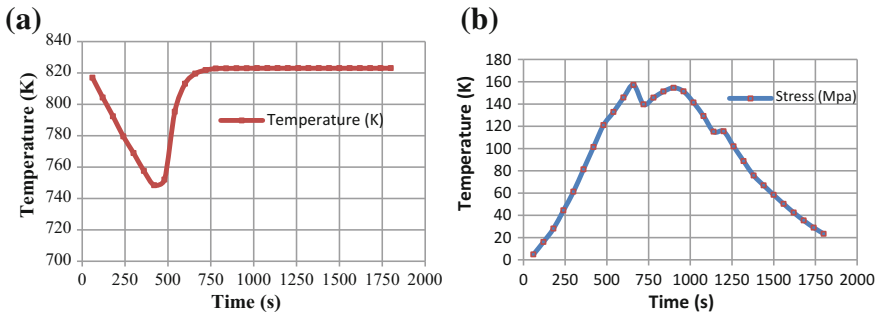


Fig. 9 a Temperature versus time (CP, I phase), b stress versus time (CP, I phase)

Table 1 Creep-fatigue damage for CP during I phase shutdown

Zone (sub-zone)	Creep effect	Fatigue damage	Creep damage
A (10S)	Significant	6.32E-19	2.88E-06
B (7S)	Significant	1.71E-07	6.0E-04
C (1S)	Negligible	1.26E-08	–

The zones which are under significant creep and negligible creep are identified, and the creep and fatigue damages are calculated accordingly. The creep and fatigue damages for significant creep zones are calculated by taking the maximum stress at each grid (Fig. 9a) at the corresponding temperature at the corresponding grid (Fig. 9b), and the cumulative damage is determined. For the negligible creep zones, the stress range at the maximum temperature is considered and the fatigue damage for the cycle is calculated directly. The creep and fatigue damage calculations are done as per RCC MR-RB [6]. Table 1 gives the creep and fatigue damages at the maximum damaged sub-zones 10S, 7S, 1S at the zones A, B, C, respectively.

5.3 II Phase (From Hot Shutdown Condition to Cold Shutdown Condition)

Transient analysis has been carried out for the length considered from elevation 27,100 to 26,500 mm. The whole length is divided into 10 sub-zones namely 1S', 2S', 3S', 4S', 5S', 6S', 7S', 8S', 9S', 10S', where 1S' is the bottom-most sub-zone and 10S' is the topmost sub-zone. The stress distribution curve and the temperature distribution curve at every location have been extracted. The evolution of temperature and stress in II phase is similar to that of I phase.

As the maximum temperature 623 K is below the creep regime, only fatigue damage is calculated, taking the maximum stress range at the maximum

Table 2 Creep-fatigue damage for CP during II phase shutdown

Zone (sub-zone)	Creep effect	Fatigue damage	Creep damage
A' (10S')	Negligible	1.14E-33	1.14E-33
B' (4S')	Negligible	1.7E-11	1.7E-11
C' (1S')	Negligible	1.76E-28	1.76E-28

Table 3 Combined creep-fatigue damage for CP during shutdown

Zone (sub-zone)	Fatigue damage	Creep damage
A + A'	6.32E-19	2.88E-06
B + A'	1.17E-07	6E-04
C + B'	1.262E-08	–
C + C'	1.26E-08	–

temperature. Table 2 gives the creep and fatigue damages at the maximum damaged sub-zones 10S', 4S', 1S' at the zones A', B', C', respectively.

5.4 Combined Damage for the I and II Phases

From Fig. 7a, b, it can be observed that, on combining the zones of the two phases, we get four zones, i.e. A + A', B + A', C + B' and C + C'. The creep and fatigue damages for these zones are added as shown in Table 3.

Thus, the maximum fatigue and creep damages are found to be at B + A', with the values, 1.17E-07 and 6E-04, respectively, for 861 cycles. The maximum damage location is shown in Fig. 7a.

6 Inner Vessel (IV)

The methodology followed is same as that in CP. The zones categorized in I phase and II phase are shown in Fig. 10a, b, respectively. The IV, which separates the hot pool sodium from the cold pool, has 2.25 m height difference between hot and cold pool sodium during normal operating condition (in CBR). Following SCRAM, the height difference between hot (lbi) and cold pool (lbo) sodium reduces to 75 mm. This difference in sodium height has been modelled in the analysis. The temperature evolution and the difference in hot and cold pool sodium level can be observed in Fig. 10c.

From Fig. 10a, b, it can be observed that, on combining the zones of the two phases, we get four zones, i.e. D + D', E + D', F + E' and F + F'. The creep and fatigue damages for these zones are added and are given in Table 4.

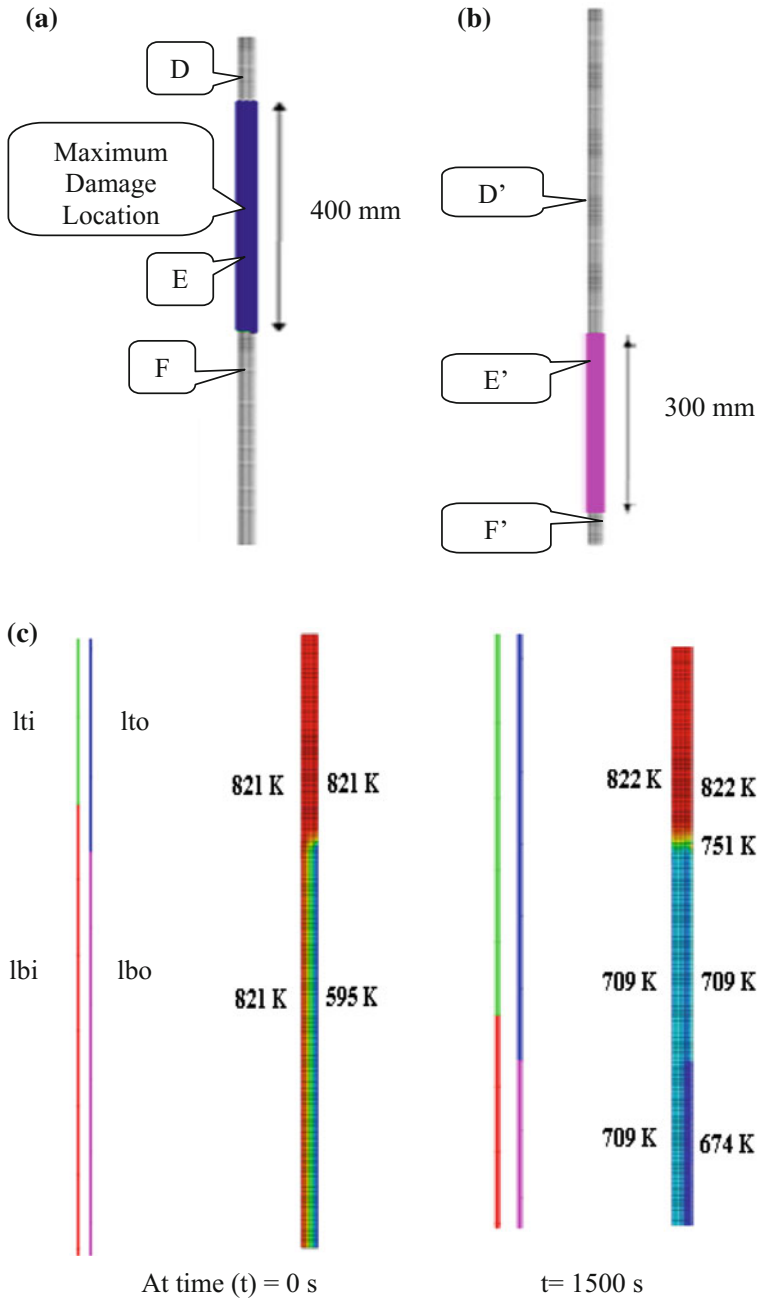


Fig. 10 a Zones in I phase in IV, b zones in II phase in IV, c temperature evolution in IV during I phase shutdown

Table 4 Combined creep-fatigue damage for IV during shutdown

Zone	Fatigue damage	Creep damage
D + D'	6.16E-04	2.21E-03
E + D'	0.0057	0.0019
C + B'	2.61E-07	-
C + C'	2.4E-07	-

7 Intermediate Heat Exchanger (IHX)

The intermediate heat exchanger (IHX) transfers thermal power from the primary sodium which is radioactive to the non-radioactive secondary sodium circuit. There are four IHX per secondary loop. The methodology followed is same as that in CP. The zones categorized in I phase and II phase are shown in Fig. 11a, b, respectively. During the I phase of the shutdown, there is ~400 mm fall in primary sodium level, and during the II phase, there is ~300 mm fall in primary sodium, but the secondary sodium level in IHX shell is always constant. There is no level change inside the shell. There is only temperature change in secondary sodium. For primary sodium, both level change and temperature changes are considered.

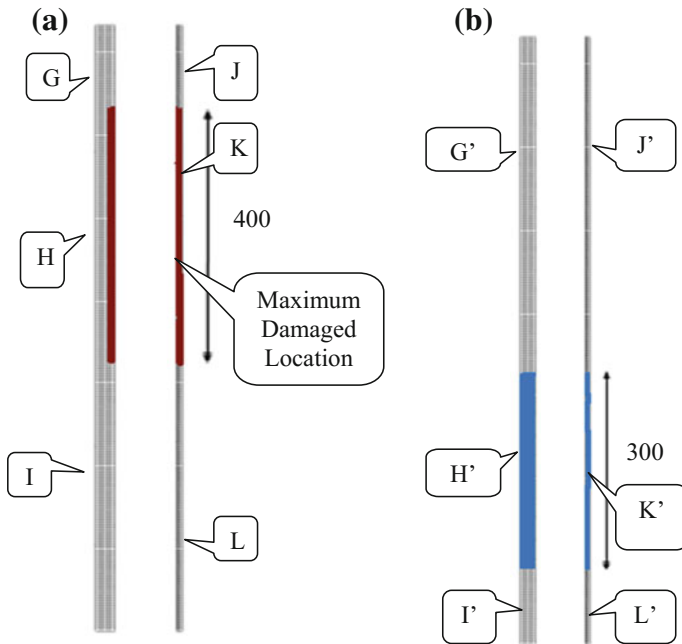
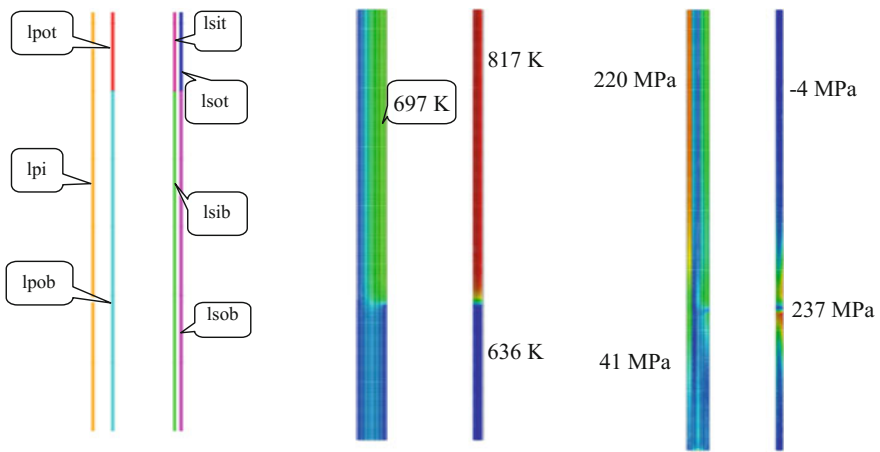


Fig. 11 a Zones in I phase in IHX, b zones in II phase in IHX

Table 5 Combined creep-fatigue damage for IV during shutdown

Zone	Fatigue damage	Creep damage
G + G'	7.04E-08	–
H + G'	1.1E-07	–
I + H'	8.22E-14	–
I + I'	8.22E-14	–
J + J'	9.13E-16	1.94E-05
K + J'	7.58E-04	1.01E-03
L + K'	6.78E-07	–
L + L'	6.78E-07	–



Where, lpot-Shell out top, lpi-Shell in, lpob- Shell out bottom,
 lsit- Sleeve in top, lsot- Sleeve out top, lsib- Sleeve in bottom, lsob- Sleeve out bottom

Fig. 12 Temperature evolution in IHX during I phase shutdown

From Fig. 11a, b, it can be observed that, on combining the zones of the two phases, we get eight zones, i.e. G + G', H + G', I + H', I + I', J + J', K + J', L + K' and L + L'. The creep and fatigue damages for these zones are added and are given in Table 5.

The evolution of temperature for IHX is shown in Fig. 12.

8 Conclusion

In the future fast breeder reactor, the requirement of controlled cooling rate from 350 to 180 °C has been relooked to avoid various complexities and it is proposed to deploy the OGDHR only after reaching cold shutdown condition. Hence, the main

condenser is used to cool down the hot pool sodium from 550 to 350 °C (I phase) at an average rate of 400 K/h and from 350 to 180 °C (II phase) at the rate of 100 K/h. The thermo-mechanical design of the shutdown systems, i.e. control plug (CP), inner vessel (IV) and intermediate heat exchanger (IHX), has been carried out for the shutdown involving two phases, and the combined creep-fatigue damage at each location has been estimated. It is found that the maximum fatigue damage values are $1.17\text{E}-07$, 0.0057 , $7.58\text{E}-04$ and the maximum creep damage values are $6.0\text{E}-04$, 0.0019 and 0.001 for CP, IV and IHX, respectively. As the values are negligible, the simplified scheme for DHR through steam generators is recommended.

Acknowledgements The authors thank Mr. K. Natesan, Mr. Juby Abraham and Mr. U. Parthasarathy of Thermal Hydraulics Section, IGCAR, for providing the temperature input for the reactor components.

References

1. K. Natesan et al., Simplified scheme for DHR through steam generators, Internal Report (2015)
2. R. Sarkar et al., Dependence of control plug life on primary sodium heating rate during power raising, Internal Report (2015)
3. R. Sarkar et al., Design and life assessment of inner vessel for FBR-1&2. *Trans. Indian Inst. Met.* **69**(2), 543–547 (2016)
4. R. Srinivasan et al., Conceptual design of intermediate heat exchanger, Internal Report
5. K. Natesan, Integrated plant operations, Internal Report
6. RCC-MR Section I, Subsection B, design and construction rules for class-1 components of FBR nuclear islands (2010)

The Influence of Prior Plasticity on the Creep Resistance of Two Elevated Temperature Power Plant Steels

Valliappa Kalyanasundaram and Stuart R. Holdsworth

Abstract Analysis of the risk of creep–fatigue (C-F) cracking is an integral part of the condition assessment of elevated temperature structural components operating in modern power plants. The advanced martensitic steels used in such applications tend to exhibit a high degree of C-F deformation interaction relative to low-alloy bainitic steels. Of particular interest to this work is characterising the influence of plasticity on the creep resistance of two power plant steels from both a qualitative and quantitative perspective. Uniaxial strain-controlled cyclic/hold C-F tests, with a hold period at peak tensile strain, have been performed in this context on 1%Cr and 10% Cr steels at their respective peak operating temperatures of 550 and 600 °C. In addition to C-F tests, monotonic stress relaxation tests have also been conducted on both the steels at different elastic/inelastic strains (strain amplitudes). With this information the influence of *magnitude* of the loading transients, both monotonic and cyclic, on the subsequent creep behaviour is systematically studied. Experimental results indicate that the creep deformation resistance of these steels is clearly modified as a consequence of prior, but not exclusively cyclic, plasticity. In particular, creep deformation kinetics are found to be influenced by the magnitude of the first inelastic loading transient for both the monotonic and cyclic loading histories under consideration. This effect is therefore not limited to the stress relaxation response during the midlife cycle hold, but also to the creep strain accumulated during the first cycle hold when preceded by an inelastic loading transient. This work also examines the determination of forward creep properties from the obtained stress relaxation data (and *vice versa*) without and with prior monotonic or cyclic inelastic loading.

Keywords Creep–fatigue interaction · Prior fatigue · Creep strength degradation
Creep curve prediction · Stress relaxation · Cyclic softening

V. Kalyanasundaram (✉) · S. R. Holdsworth
ICMI, Inspire AG c/o. EMPA, Überlandstrasse 129, 8600 Dübendorf, Switzerland
e-mail: kalyanasundaram@inspire.ethz.ch

S. R. Holdsworth
Swiss Federal Laboratories for Materials Science and Technology (EMPA),
Überlandstrasse 129, 8600 Dübendorf, Switzerland

1 Introduction

The thermomechanical loading profile of metallic structural components operating at elevated temperature typically includes cyclic transients (during start-up and shut-down) and steady-state operating periods during service. Under such operating conditions, fatigue, creep and their synergistic interaction become the predominant modes of material deformation and damage accumulation [1, 2]. As operating conditions become increasingly flexible, frequent power transients induce enhanced cyclic plasticity in the material especially in critical locations involving multiaxial stress concentrations. There is mounting evidence to indicate the significant effects of prior plasticity on the subsequent creep deformation resistance of several elevated temperature materials [2]. As a consequence, the influence of plasticity and its magnitude on creep needs to be systematically characterised for more effective remnant life assessments and for improved design protocols in the future. Since the temperature and stress handling capability of fossil-fired turbomachinery, for example, is expected to gradually increase over time so as to minimise environmental pollution and to maximise operating efficiency and flexibility, the requirement for such fundamental knowledge becomes more important [3, 4]. The major objective of the current study is therefore to characterise the effect of plasticity, both monotonic and cyclic, on creep in two commonly adopted power plant steels that exhibit cyclic softening at/near their respective peak operating temperatures. Equal focus is given to obtaining qualitative and quantitative information in this context, with the aid of experimental data from cyclic/hold, monotonic stress relaxation and forward creep tests. In particular, the importance of the first loading transient and its magnitude is analysed with reference to recent observations that implicitly suggest accelerated creep kinetics as a consequence of the initial few cycles of plastic deformation in sequential [5, 6] or simultaneous test schemes [7, 8].

The detrimental influence of synergistic creep–fatigue (C-F) interactions from a damage perspective has been well documented in the literature for various steels within the broad class of cyclic softening materials [7–13]. However, relatively few literature exists focussed specifically on obtaining a systematic understanding of the effect of cyclic plasticity on creep resistance at elevated temperatures [5, 6, 14–17]. These studies clearly show the creep resistance to be significantly reduced as a consequence of plasticity as evidenced by higher minimum creep-rates in comparison with those under pure creep. Other researchers suggest the degree of creep softening due to plasticity to be much less significant if cycling is responsible for predominantly elastic deformation [6, 8, 9]. All these experimental observations thus highlight the need for a better understanding of the influence of prior plasticity and its magnitude on subsequent creep from a deformation viewpoint for cyclic softening steels. The experiments conducted in this study explicitly offer clear qualitative insights into this regard for two materials (1%Cr and 10%Cr steels) that have been preferred for critical applications in power plants in recent years.

Besides qualitative analyses, quantitative comparisons further facilitate a complete characterisation of the experimentally observed material response under different deformation histories. Differences in the nature of stress relaxation during a tensile hold after elastic/inelastic loading transients either under monotonic or cyclic plasticity therefore need to be systematically evaluated. Since degradation in observed creep resistance needs to be compared with that under pure creep, the amount of stress relaxation evaluated under the different deformation histories should be converted to equivalent creep curves. In summary, $\sigma(t)$ stress relaxation curves obtained during the strain-controlled tensile holds under varying stress need to be converted to equivalent $\varepsilon(t)$ creep curves under a nominally constant stress. Conversely, it should also be possible to convert conventional forward creep curves to equivalent stress relaxation curves to address the same issue. The applicability of both these approaches will be explored in this work for experimental results obtained with the 10%Cr steel alone.

Among the existing analytical methodologies [18–22], commonly employed approaches are those based on the Norton-Bailey (NB) equation either assuming time- or strain-hardening as appropriate for the application under consideration. More often than not, the strain-hardening assumption is judged to more closely simulate material response in practical applications than time-hardening (e.g. [23]), although concerns exist regarding its adequacy under variable loading conditions [24].

A brief discussion of the experimental details is provided next followed by a detailed description of the NB model assuming strain-hardening chosen for study in this work. The obtained experimental and analytical results are comprehensively discussed in the section thereafter followed by a summary of the major conclusions.

2 Experimental Details

2.1 Test Materials

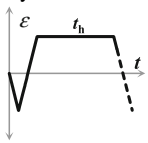
A low-alloy 1%Cr steel and an advanced martensitic 10%Cr steel were the test materials chosen for this study, both exhibiting cyclic softening at/near their respective peak operating temperatures of 550 and 600 °C. The former had a tempered bainitic microstructure while the latter a tempered martensitic structure after quenching and tempering heat treatments. The 10%Cr steels generally exhibit a ≥ 50 °C temperature advantage relative to 1%Cr steels [15], primarily due to enhanced strengthening against elevated temperature deformation imparted by chromium-rich carbide and carbonitride precipitates.

2.2 Test Matrix

Standard 8 mm diameter specimens with parallel gauge lengths of 50 mm (creep) and 20 mm (monotonic and cyclic/hold) were used for the conducted isothermal tests. Conventional creep tests were performed only on the 10%Cr steel for three different stress levels (75, 130 and 170 MPa) at 600 °C in accordance with [25] until the accumulation of 1% inelastic strain.

Uniaxial strain-controlled cyclic/hold tests and monotonic stress relaxation tests were conducted in ambient environment in an induction heating based servo-hydraulic test system of 100 kN capacity. The middle (control) thermocouple was kept to within ± 1 °C of the target temperature during the course of the entire test. A Class 0.5 side-entry extensometer, with a datum leg spacing of 15 mm, was used for the measurement and control of axial strain. Loading started compression-going for the cyclic/hold tests following a trapezoidal waveform under fully reversed conditions (strain ratio, $R_\varepsilon = -1$) with a hold at the peak tensile strain. The cyclic/hold tests were stopped after macroscopic crack initiation within the gauge length as per the 2% load-drop criterion. In the stress relaxation tests, the specimens were strained monotonically in tension to a prescribed strain, held therein for a few hours and unloaded thereafter to zero strain. A detailed summary of the monotonic and cyclic/hold C-F tests conducted on both the steels is provided in Table 1. When multiple stress relaxation routines were performed on a single specimen, only the last loading transient was responsible for macroscopic yielding while the earlier one(s) were only responsible for elastic deformation.

Table 1 Summary of the experimental test matrix for both the test materials considered in this work

Loading type	Test material	T (°C)	$\dot{\varepsilon}$ (%/s)	Test ID	Strain amplitude (%)	Hold time, t_h
	10%Cr steel	600	0.1	1	± 0.39	15 min
				2	± 0.51	15 min
				3	± 0.50	30 min
				4	± 0.50	60 min
	1%Cr steel	550	0.1	5	± 0.50	30 min
				6	± 0.50	60 min
Monotonic stress relaxation	10%Cr steel	600	0.01	7	+0.075	3 h
					+0.15	3 h
					+0.40	4 h
	1%Cr steel	550	0.1	9	+0.075	2 h
					+0.15	2 h
					+0.40	3 h

3 Analytical Method

3.1 NB Strain-Hardening Formulation

One of the most commonly used analytical formulations to represent material deformation during primary creep is the Norton-Bailey (NB) equation, i.e.

$$\epsilon_{cr} = A_{NB} \sigma^n t^p \tag{1}$$

where ϵ_{cr} is the creep strain (in %), A_{NB} is a temperature-dependent constant, n is the exponent for stress, σ and p is the exponent for time, t . To predict forward creep behaviour from stress relaxation data (and *vice versa*), a formulation derived from Eq. (1) assuming strain-hardening is employed in this study. Following this approach, the instantaneous creep-rate in the material ($\dot{\epsilon}_{cr}$) is assumed to depend on the current stress and strain irrespective of the current time [26]. A closed-form expression for the NB strain-hardening formulation is possible only for specific values of n and p . Hence, n is left as a variable for optimisation with experimental data while p is kept at 1/3 in this study. Accordingly, the predicted time ($t_{pred.}$) for stress to relax from σ_i to that at σ_t can be expressed as shown in Eq. (2):

$$t_{pred.} = \frac{1}{p} \left(\frac{1}{A_{NB} E} \right)^{\frac{1}{p}} \frac{1}{\sigma_t^{\frac{n-1}{p}}} \left[\begin{array}{l} - \left\{ \frac{p}{3p-n} \left(1 - \left(\frac{\sigma_t}{\sigma_i} \right)^{\frac{n}{p}-3} \right) \right\} \\ + \left\{ \frac{2p}{2p-n} \left(1 - \left(\frac{\sigma_t}{\sigma_i} \right)^{\frac{n}{p}-2} \right) \right\} \\ - \left\{ \frac{p}{p-n} \left(1 - \left(\frac{\sigma_t}{\sigma_i} \right)^{\frac{n}{p}-1} \right) \right\} \end{array} \right] \quad \text{when } p = \frac{1}{3} \tag{2}$$

where σ_i is the stress at the onset of hold ($t = 0$), σ_t is the stress at time t and E is the elastic modulus. To ensure robust fits, the assessment involved both the prediction of time required for stress to relax from its peak value to that at t and the stress expected at a given time t . The optimised NB model parameters (A_{NB} , n and p) assessed from stress relaxation data were then substituted in Eq. (1) for forward creep curve construction. Similarly, NB parameters assessed from experimental primary creep data as per Eq. (1) were used in Eq. (2) to obtain stress relaxation curves at 0.075 and 0.50%.

3.2 Model Parameter Optimisation

The root-mean-square (RMS) error calculated between experimental and corresponding predicted values was minimised using Z , the scatter factor, formulated as [27]:

$$Z = 10^{(2.5 \cdot \text{RMS})} \quad (3)$$

While a Z value of unity implies a perfect fit, values slightly above this are not unusual as a consequence of data measurement errors and/or to testing uncertainties, especially at elevated temperatures. Parameter optimisation was carried out in Microsoft Excel[®] using the SOLVER routine, and a systematic protocol ensured that the best-fit values were not arbitrarily influenced by the chosen starting values.

4 Results and Discussion

4.1 Creep Relaxation Data Comparisons

Figure 1 shows creep relaxation curves obtained for both test materials that have been stress-normalised to account for the different peak stress values at the onset of tensile hold periods in monotonic and cyclic/hold tests. The creep response for the different deformation histories can be qualitatively appreciated from these profiles by realising that increasing amounts of stress relaxation indicate the propensity of the material to accumulate more creep strain (i.e. to creep soften) during the hold times of such tests. The figures clearly indicate the detrimental influence of increasing strain (strain amplitude), and initial peak stress, on subsequent creep deformation resistance for both the steels after monotonic and cyclic (*cycle-1*) loading. The larger the strain (strain amplitude), and initial peak stress preceding the hold period, the more the steels creep soften at their respective test temperatures, with the effect tending to saturate progressively after macroscopic yielding. Comparison of the stress relaxation profiles obtained for the 10%Cr steel corresponding to +0.50% under monotonic and cyclic (*cycle-1*) straining to $\pm 0.50\%$ also clearly shows further creep softening due to reduced flow stresses after strain reversal. Although not shown here, the existence of such material response due to the Bauschinger effect is also observed for the 1%Cr steel.

Figure 2 shows stress relaxation profiles obtained during cycle-1 and midlife cycle tensile holds (60 min) for specimens strained to $\pm 0.50\%$ strain. For both steels, the component figures also compare observed midlife cycle stress relaxation responses with those predicted using the appropriate cycle-1 NB parameters, assuming strain-hardening. For both the steels, the plastic strain accumulated between cycle-1 and the midlife cycle is apparently responsible for further creep softening. Hence, the consideration of plasticity effects on creep in both the steels is critical and detailed microscopy studies are required to systematically understand the microstructural reasons for the observed material response.

Strain rates observed as a function of instantaneous stress during the cycle-1 and midlife cycle hold periods of the cyclic/hold creep-fatigue tests are compared with forward creep test minimum creep-rates for the two steels in Fig. 3. These indicate the effect of plastic strain accumulated between cycle-1 and the midlife cycle on

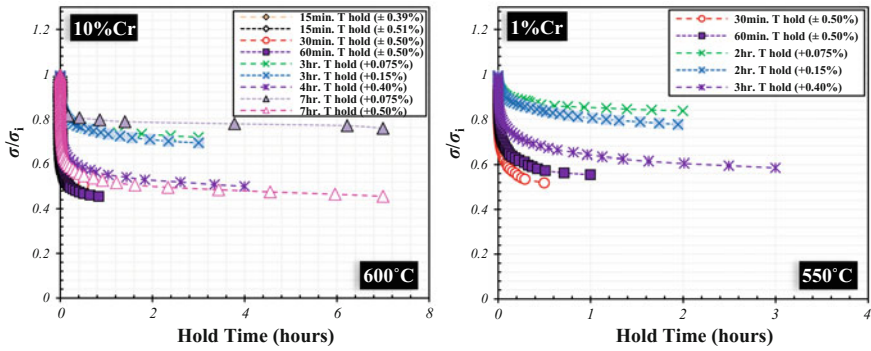


Fig. 1 Normalised stress relaxation response during tensile hold for 10%Cr steel at 600 °C and 1%Cr steel at 550 °C after monotonic and cyclic (*cycle-1*) straining to different strain amplitudes ('+' represents a tensile-going ramp directly to the indicated strain value at tensile hold, whereas '±' represents compressive-going and tensile-going ramps to the indicated strain value prior to the tensile hold)

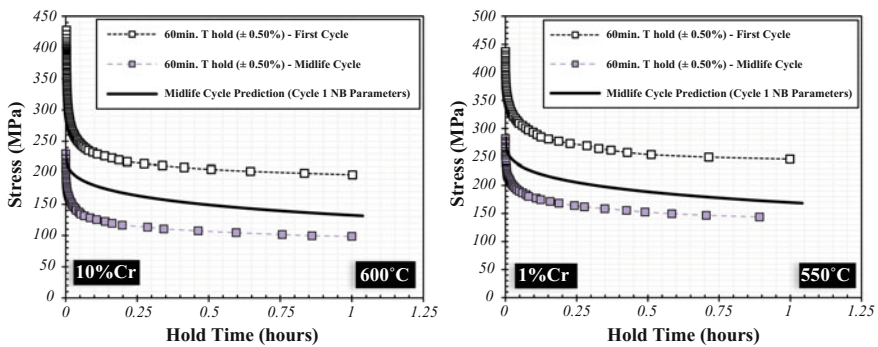


Fig. 2 Experimentally observed stress relaxation responses for 10%Cr steel at 600 °C and 1%Cr steel at 550 °C during first- and midlife cycle tensile hold times for a cyclic strain range of 1% (the predicted midlife cycle relaxation profiles were determined using cycle-1 NB parameters to illustrate the influence of plasticity on creep in both the cyclic softening steels)

primary creep rates, and how the influence is greater for the 10%Cr steel (Fig. 3a) than for the 1%Cr steel (Fig. 3b).

Defining a short-form terminology for the different deformation histories under consideration is necessary for brevity in the following text concerned with the quantitative comparison of the discussed results. The isothermal assessment of stress relaxation profiles obtained from 10%Cr specimens that were strained monotonically to either +0.075% or +0.15% preceding the tensile hold is termed NPP (no prior plasticity), while those strained to either +0.40% or +0.50% are termed 1PT-M (1 plastic transient—monotonic). Similarly, the isothermal assessment of stress relaxation profiles obtained from 10%Cr specimens that were strained cyclically first in compression and then to either +0.39%, +0.50% or +0.51% immediately

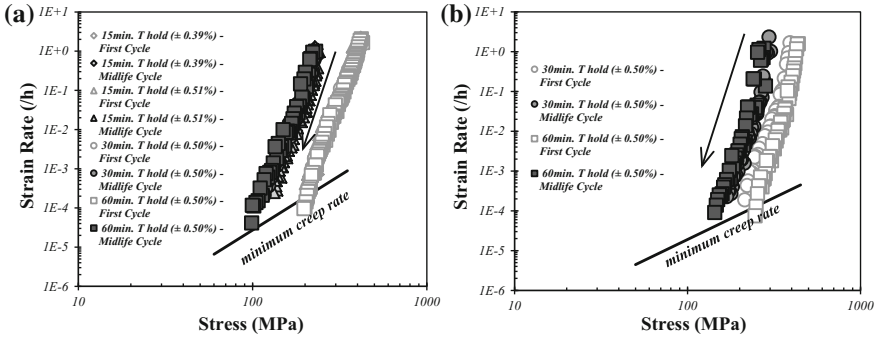


Fig. 3 Comparison of cycle-1 and midlife cycle hold time strain rates (mainly due to primary creep) with minimum creep-rates from forward creep tests of **a** 10%Cr steel at 600 °C and **b** 1%Cr steel at 550 °C

preceding the tensile hold is termed 2PTC (2 plastic transients—cyclic), with this terminology being adopted with reference to both cycle-1 and midlife cycle response. Figure 4 shows creep curves constructed from stress relaxation data using the NB model, assuming strain-hardening, for the 10%Cr steel at (a) 75 and (b) 170 MPa. The figures for the two stress levels, at least qualitatively, illustrate a systematic influence of the plastic strain accumulated by the different cycle types on creep response. It is acknowledged that any uncertainty in these creep response predictions would be minimised by the informed consideration of anelastic recovery (e.g. [23]). In particular, the amount of creep accumulation is observed to be higher at midlife (2PTC—Midlife curves) than that at cycle-1 (2PTC—Cycle-1 curves), possibly as a consequence of the steel’s pronounced cyclic softening over time. The NB model fit parameters for some of these profiles are given elsewhere [28]. In summary, increasing the strain (strain amplitude) above the limit of proportionality reduces the creep deformation resistance of cyclic softening steels.

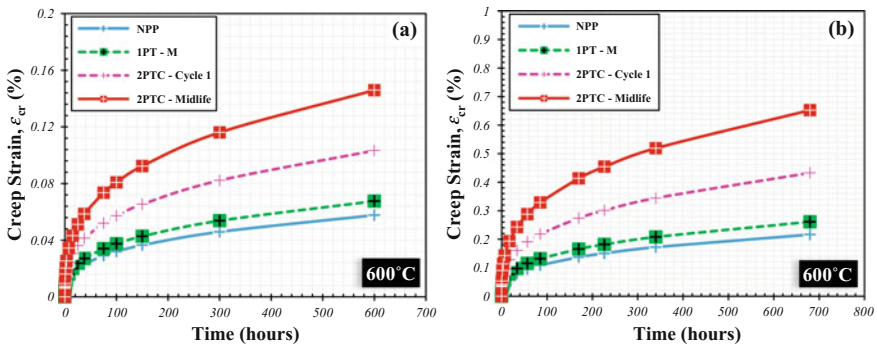


Fig. 4 Primary creep curves constructed from stress relaxation data for 10%Cr steel at 600 °C using the NB model, assuming strain-hardening, for stress levels of **a** 75 MPa and **b** 170 MPa

4.2 Forward Creep Data Comparisons

Primary creep data generated using the NB model, assuming strain-hardening, for the 75 and 170 MPa stress levels can also be presented in the form of creep-rate versus time plots to further illustrate relative differences between the various prior deformation histories (Fig. 5). Predictably, NB modelled creep-rates drop rapidly at the start of the hold period, with the rate of drop being higher for cases where the material had yielded macroscopically before the start of the tensile hold and lower when the peak strain was below the limit of proportionality, i.e. when the deformation preceding the hold time was elastic. The enhancement of creep-rates due to prior plastic deformation, as reported in [6, 14–17], can also be observed at both the creep stress levels. Moreover, the increase in creep-rates, at any point in the time range considered, as a consequence of macroscopic yielding can be clearly observed for both the stress levels.

The experimentally observed forward creep lines in the log–log representations in Fig. 5 are essentially linear in the primary creep regime. Since they originate from tests conducted on the same heat of 10%Cr steel, it is not surprising that the agreement is good with the NPP-based NB model predicted behaviour at the lower stress level (Fig. 5a). At the higher stress (Fig. 5b), the NPP model predictions underestimate the experimentally observed forward creep-rates largely due to the greater influence of anelastic recovery under these conditions.

Results obtained using the NB model, assuming strain-hardening, to predict stress relaxation curves from forward creep data for the 10%Cr steel at 600 °C are presented in Fig. 6. While application of the NB model assuming strain-hardening approximates the experimentally observed stress relaxation behaviour well at lower strains (below the limit of proportionality, Fig. 6a), this is not the case for strains (strain amplitudes) and initial stresses in excess of yield (Fig. 6b). Once again, the

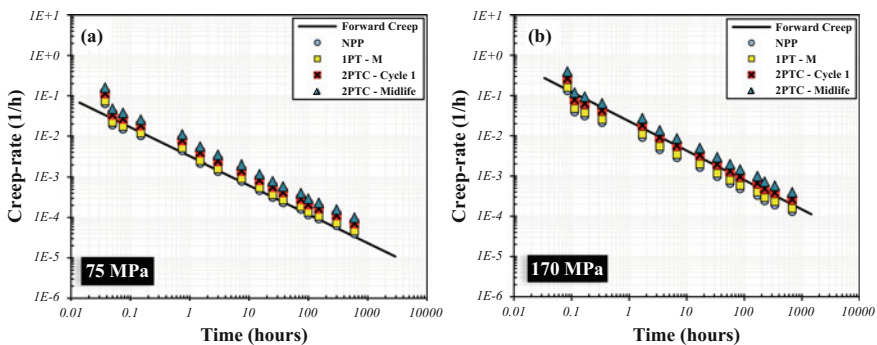


Fig. 5 Creep-rate versus time plots for 10%Cr steel at 600°C obtained using data predicted by the NB model assuming strain-hardening for the different deformation histories at **a** 75 MPa and **b** 170 MPa

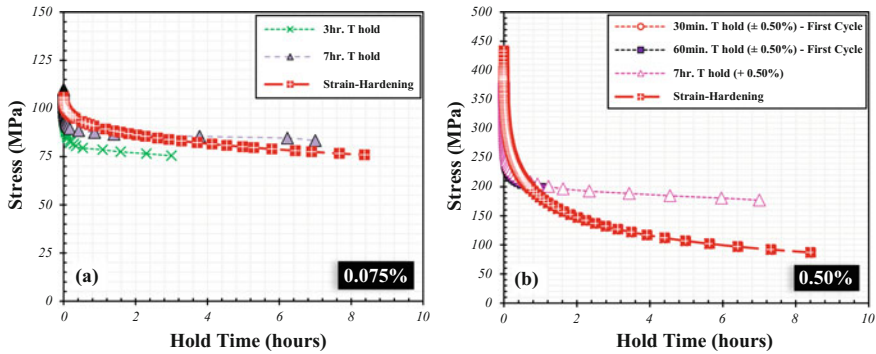


Fig. 6 Stress relaxation curves predicted using the NB model determined from forward creep data for 10%Cr steel at 600 °C for strain levels of **a** 0.075% and **b** 0.50% (assuming strain-hardening)

discrepancy in creep relaxation responses is attributed to the greater influence of anelastic recovery in the high stress regime, which is currently not formally considered in the present model.

5 Concluding Remarks

The major focus of this study has been a systematic evaluation of the influences of monotonic and cyclic plasticity and their extent on the creep deformation response of a 10%Cr steel at 600 °C and a 1%Cr steel at 550 °C. The obtained results indicate the degree of creep softening to increase with the accumulated plastic strain associated with increasing prior strain (strain amplitude) and initial stress at the start of the relaxation period.

The evidence indicates that for hold times of up to 60 min in strain-controlled creep–fatigue tests on the two power plant steels at their respective maximum application temperatures, stress relaxation is due to primary creep deformation.

The effectiveness of the NB model fitting approach applied to the stress relaxation data to examine the influence of prior plasticity on forward creep on 10%Cr steel at 600 °C is examined by using forward creep determined NB parameters to predict stress relaxation behaviour for the same heat of 10%Cr steel. It is concluded that adoption of the NB model, assuming strain-hardening, can effectively transform forward creep to stress relaxation and *vice versa* in the low stress regime, but not at higher stresses when the consequences of anelastic recovery are more influential.

Acknowledgements The authors would like to acknowledge the assistance offered by Mr. Freddy Bürki during creep testing and by other members of the High Temperature Integrity Group at EMPA during the course of this work.

References

1. D.A. Miller, R.H. Priest, Materials response to thermal-mechanical strain cycling, in *High Temperature Fatigue: Properties and Prediction*, ed. by R.P. Skelton (Elsevier Applied Science Publication, Dordrecht, 1987), pp. 113–175
2. S.R. Holdsworth, E. Mazza, L. Binda, L. Ripamonti, Development of thermal fatigue damage in 1CrMoV rotor steel. *Nucl. Eng. Des.* **237**, 2292–2301 (2007)
3. R.L. Klueh, Elevated temperature ferritic and martensitic steels and their application to future nuclear reactors. *Int. Mater. Rev.* **50**, 287–310 (2005)
4. F. Abe, T.U. Kern, R. Viswanathan, *Creep-resistant Steels* (CRC Press, Cambridge, 2008)
5. C. Vorpahl, A. Möslang, M. Rieth, Creep-fatigue interaction and related structure property correlations of EUROFER97 steel at 550 °C by decoupling creep and fatigue load. *J. Nucl. Mater.* **417**, 16–19 (2011)
6. A. Sarkar, V.D. Vijayanand, P. Parameswaran, V. Shankar, R. Sandhya, K. Laha, M.D. Mathew, T. Jayakumar, E. Rajendra Kumar, Influence of prior fatigue cycling on creep behavior of reduced activation ferritic-martensitic steel. *Metall. Mater. Trans. A* **45**, 3023–3035 (2014)
7. J.S. Dubey, H. Chilukuru, J.K. Chakravarty, M. Schwienheer, A. Scholz, W. Blum, Effects of cyclic deformation on subgrain evolution and creep in 9–12% Cr-steels. *Mater. Sci. Eng. A* **406**, 152–159 (2005)
8. B. Fournier, M. Sauzay, C. Caës, M. Noblecourt, M. Mottot, L. Allais, I. Tournie, A. Pineau, Creep-fatigue interactions in a 9 pct Cr-1 pct Mo martensitic steel: Part I. Mechanical test results. *Metall. Mater. Trans. A* **40**, 321–329 (2009)
9. E.G. Ellison, A.J.F. Paterson, Creep fatigue interactions in a 1 CrMoV steel. *Proc. Inst. Mech. Eng.* **190**, 319–330 (1976)
10. D. Sidey, Creep-fatigue interactions in a low alloy steel. Part III—Fatigue: Micromechanisms, in *Fracture 1977, ICF4, Waterloo*, vol. 2 (1977), pp. 813–819
11. S.R. Holdsworth, Prediction of creep-fatigue behaviour at stress concentrations in 1CrMoV rotor steel, in *Proceedings of Conference on Life Assessment and Life Extension of Engineering Plant, Structures and Components*, Cambridge (1996), pp. 137–146
12. S.R. Holdsworth, Component assessment data requirements from creep-fatigue tests, ASTM STP1539. *J. ASTM Int.* **8**, 1–14 (2011)
13. V. Kalyanasundaram, Creep, fatigue and creep-fatigue interactions in modified 9% Chromium-1%Molybdenum (P91) steels, Ph.D. Dissertation, University of Arkansas, Fayetteville, 2013
14. L. Binda, S.R. Holdsworth, E. Mazza, Influence of prior cyclic deformation on creep properties of 1CrMoV. *Mater. High Temp.* **27**, 21–27 (2010)
15. S.R. Holdsworth, Creep-fatigue in steam turbine materials, in *Proceedings of the 6th International Conference on Advances in Materials Technology for Fossil Power Plants* (EPRI, Sante Fe, USA, 2010), pp. 487–503
16. S.R. Holdsworth, Influence of prior fatigue on creep properties, in *Proceedings of the 12th International Conference on Creep and Fracture of Engineering Materials and Structures* (CREEP 2012), Kyoto (2012)
17. A. Sarkar, V.D. Vijayanand, V. Shankar, P. Parameswaran, R. Sandhya, K. Laha, M.D. Mathew, T. Jayakumar, E. Rajendra Kumar, Cyclic softening as a parameter for prediction of remnant creep rupture life of a Indian reduced activation ferritic-martensitic (IN-RAFM) steel subjected to fatigue exposures. *Fus. Eng. Des.* **89**, 3159–3163 (2014)
18. J.H. Laflen, C.E. Jaske, Cyclic relaxation response under creep-fatigue conditions, in *Stress Relaxation Testing* ed. by A. Fox (ASTM STP676, 1979), pp. 182–206
19. N.K. Sinha, Limitations of stress relaxation tests for determining stress dependence of strain rate at high temperatures. *Scr. Mater.* **48**, 731–736 (2003)
20. H. Altenbach, K. Naumenko, Y. Gorash, Creep analysis for a wide stress range based on stress relaxation experiments. *Int. J. Mod. Phys. B* **22**, 5413–5418 (2008)

21. G.G. Grzywinski, D.A. Woodford, Design data for polycarbonate from stress-relaxation tests. *Mater. Des.* **14**, 279–284 (1993)
22. D.A. Woodford, *Accelerated Testing for High-Temperature Materials Performance and Remaining Life Assessment, Report TR-114045* (EPRI, Palo Alto, USA, 1999)
23. J. Bolton, A “characteristic-strain” model for creep. *Mater. High Temp.* **25**, 197–204 (2008)
24. E. Krempl, *Cyclic Creep: An Interpretive Literature Survey, Bulletin 195* (Welding Research Council, New York, 1974), pp. 63–123
25. BS EN ISO 204, Metallic materials—Uniaxial creep testing in tension—Method of test (2009)
26. C.C. Davenport, Correlation of creep and relaxation properties of copper. *Trans. ASME J. Appl. Mech.* **60** A55–A60 (1938)
27. S.R. Holdsworth, G. Merckling, ECCC developments in the assessment of creep-rupture properties, in *Proceedings of the 6th International Charles Parsons Turbine Conference* (IOM, Dublin, 2003), pp. 411–426
28. V. Kalyanasundaram, S.R. Holdsworth, Prediction of forward creep behaviour from stress relaxation data for a 10% Cr steel at 600 °C. *Trans. Indian Inst. Met.* **69**, 573–578 (2016)

Structural Integrity Mechanics and Creep Life Prediction of 304HCu Austenitic Stainless Steel Under Multiaxial State of Stress

Kanhu Charan Sahoo, Sunil Goyal, P. Parameswaran, S. Ravi
and K. Laha

Abstract For increasing the efficiency of fossil power plants, the boiler tube material has to withstand higher temperature and pressure which calls for extensive research for identifying materials having high-temperature strength, good corrosion resistance and adequate mechanical properties. The 304HCu stainless steel 9304HCu SS is one of the candidate materials for boiler tubes employed in advanced ultra-super critical power plants. However, under above circumstances, material will subject to multiaxial state of stress that arises from internal pressure, weld joint, inhomogeneous structure, sudden change in dimension and change in cross section of the tube. Present study aims to introduce multiaxial state of stress through notches of different root radius on creep samples. Notch of different root radii, e.g. 0.25, 0.5, 2.5 was creep tested by keeping notch throat diameter 5 mm. Both plain and notch specimen had creep tested at same stress level at a particular temperature. Notch specimen possesses higher rupture life as compared to plain specimen. Based on these observations, the material is found to be 'notch strengthening'. Then both SEM and optical micrograph were carried out on the unfailed notch which revealed that cavity density was decreased from notch root towards centre for relatively sharper notch, while random distribution of cavity for shallow notch. FE analysis has been carried out to understand the contribution of different components of stresses, i.e. von-Mises, maximum principal and hydrostatic stresses. Different models given by Cane, Hayhurst and Nix were examined for creep life prediction under multiaxial state of stress. The average hardness near to notch root was more in comparison with regions away from the notch root and shallow notch was found exhibit more hardness in comparison with sharper notch.

Keywords AUSC · Multiaxial creep · Finite element analysis
Life prediction · Hardness measurement

K. C. Sahoo (✉) · S. Goyal · P. Parameswaran · S. Ravi · K. Laha
Metallurgy and Materials Group, Indira Gandhi Centre for Atomic Research,
Kalpakkam 603102, Tamil Nadu, India
e-mail: kanhu2011.sahoo@gmail.com

1 Introduction

Fossil-fired power plant contributes nearly half of the total amount of electrical energy production made all over the world. This is true for both developing and developed countries as far as producing electricity is concerned. However, the main problem associated with the coal-fired power plants is the poor efficiency and generation of green house gas. Increasing efficiency of electricity generation is related to steam line temperature and pressure. For increasing efficiency, the steam line temperature of the plant should be above 60–70 K in comparison with conventional power plant. This essentially calls for materials that withstand higher temperature and pressure. Therefore, the structural components operating under this harsh condition causes creep damage which results from the nucleation, growth and coalescence of cavities and enhanced microstructural degradation resulting from coarsening of precipitates and production of dislocation sub-structural network [1]. Advanced ultra-super critical power plant (AUSC) is conceived specifically for increasing efficiency and decreasing carbon emission. In this respect, 304HCu SS is a candidate material for advanced ultra-super critical power plant [2]. While designing components, generally the designers use the uniaxial data with factor of safety. However, the structural components experience multiaxial state of stress due to internal pressure, change in geometry, inhomogeneous microstructure as in a weld joint and possible changes in the mode of loading during service [3, 4]. Thus, the failure of the material will be decided based on the multiaxial conditions that prevail upon the components. The life and damage prediction of such components could be assessed by using notched specimen testing to simulate the multiaxial state of stress. The notched specimens are the most convenient and widely used ones to generate multiaxial state of stress in laboratory scale [5]. Presence of notch introduces some constraints which depend on the notch geometry, material chosen and stress level. Notched specimens are designed to simulate the behaviour of various stress-raising features in components, and, generally they fall into two categories— (i) those which exhibit a high degree of constraints where deformation of the locally high-stressed region is limited by the low value of the second stress invariant and corresponds to a region of high-stress triaxiality and (ii) situations of low constraint where the stress peak is usually less pronounced and a lower degree of triaxiality is observed [6]. Different types of notch root radius, specimens are used to investigate the range of behaviour associated from high degree to low degree of constraints [7]. The contribution of different components of stresses, i.e. von-Mises, maximum principal and hydrostatic stresses which can be used to study the effect of multiaxial state of stress on creep rupture life. A concept of representative stress which accounts the relative contribution of von-Mises and maximum principal stresses have been introduced to estimate the rupture life under multiaxial state [8–11]. According to Hayhurst et al. [9], the representative stress is the algebraic sum of maximum principal stress and von-Mises stress. Cane [10] proposed that the

representative stress is the multiplication of the maximum principal stress and von-Mises stress by incorporating material-dependent parameter which influences the relative contribution of each stress.

In the present study, three notches were machined in the steel to establish a relationship between the creep rupture life of uniaxial and multiaxial data. While the specimen would fail from one of the notches, the other two notches will serve for post-creep microstructural studies. Among the different notches employed, variation of root radius of notch from 0.25, 0.5 and 2.5 mm was employed, keeping a fixed depth of notch. In addition, smooth specimen was also tested under the same conditions of stress and temperature (973 K). Further, for predicating the rupture life by simulation, finite element analysis was carried out. Subsequently, scanning electron microscopy (SEM) studies were carried out on unfailed notch to know the propagation of crack and distribution of cavities and wedge cracks from the root of the notch to the centre of the specimen. The hardness distribution as a function of distance from the notch root was measured along the notch plane.

2 Experiment

Effect of multiaxial state of stress has been studied by carrying out creep test on both notch and smooth specimen in the stress range 140–220 MPa at 973 K. The effect of notch sharpness has been studied by carrying out test on notch root radii of 0.25–5 mm (r) by keeping notch throat diameter as 5.00 mm (d). These notches resulted notch acuity ratio (d/r) of 1–20. The geometry of notched specimen is illustrated in Fig. 1. Creep tests were systematically carried out in smooth specimen to know the coefficients in Norton's creep law ($\epsilon_s = A\sigma^n$).

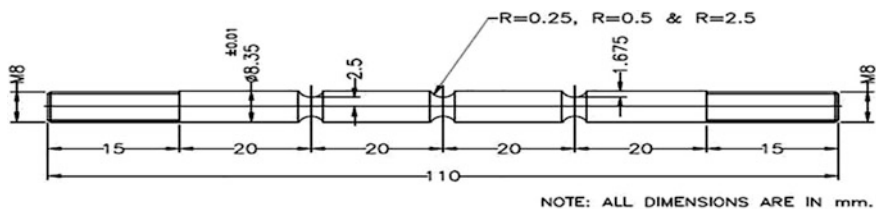


Fig. 1 Schematic representation of notch specimen of different root radius

3 FE Analysis of Stress Distribution

Finite element analysis of stress distribution has been carried out in notch plane to know the distribution of different components of stresses, viz. von-misses, maximum principal and hydrostatic components of stresses during creep exposure [12]. The 2D axisymmetric analysis was carried out using 4 noded quadrilateral elements with ABAQUS 6.10 finite element solver [13]. In the analysis, the elastic modulus was assumed to be 189 GPa. The value of the parameters A and n obtained from smooth specimen data was 1.74×10^{-24} and 8.84, respectively. The stress concentration factor of the notched specimen is 1.4, 2.46 and 3.4 for notch acuity 2, 10 and 20, respectively. Initially, the deformation of the material was assumed to behave elastically followed by creep deformation [14]. Then element size was reduced closer to the notch root by structured mesh configuration and elastic analysis was used to assure that the mesh configuration was sufficiently refined near the notch root for the theoretical stress concentration factor. The stress redistribution was generally considered to attain stationary state condition when the total strain at the notch throat plane reached the elastic strain in the material as stated by Calladine [15].

4 Results and Discussion

Figure 2 shows the variation of (a) rupture life with net applied stress, (b) rupture life with notch acuity ratio and (c) creep ductility (%RA) with notch acuity ratio. Creep rupture life of 304HCu SS increases in the presence of notch, exhibiting the ability of the material to ‘notch strengthen’. The ‘notch strengthening’ in the presence of notch with notch acuity ratio of 2, 10 and 20 when creep tested at 973 K is found to exhibit a trend in the strengthening effect as it increases with notch acuity ratio and, it tends to saturate for higher notch acuity ratio. This is similar to what was observed in P91 steel and 2.25Cr–1Mo steel earlier similar studies [12, 13, 16]. On the other hand, creep rupture ductility decreased in the

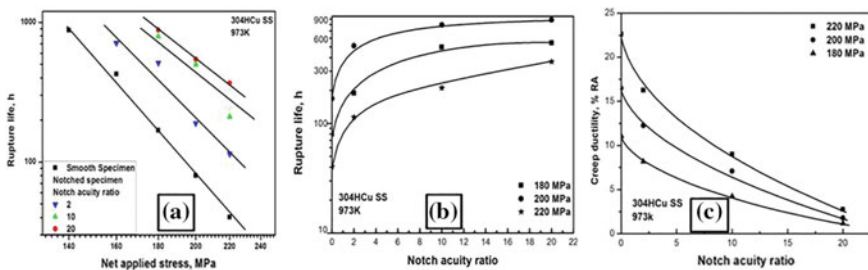


Fig. 2 Variation of (a) creep rupture life with net applied stress (b) creep rupture life with notch acuity ratio (c) creep rupture ductility (reduction in area %) of both smooth and notch specimens of the steel at 973 K

presence of notch, and the decrement was more profound for higher notch acuity. The fracture behaviour of the steel for shallow and sharper notches [2, 12] was also found to be varied in nature.

4.1 Creep Cavitation and Deformation Study Through SEM

Generally, it is known that the austenitic stainless steels are more prone to cavitation and deformation. Shallow notches are more prone to cavitation while sharper notches are more prone to crack. Sharper notches form crack easily than shallow notches because of higher stress concentration factor. Therefore, scanning electron microscopy (SEM) studies were carried out on the unfailed notch region of the creep tested specimen. The specimens were grounded and polished up to half of their diameter and then systematically SEM studies were carried out. Figure 3 shows the progressive increase in wedge crack and voids (r -type) from notch centre to the root region.

Generally, the cavities nucleate, on locations specifically where three-dimensional defects, namely precipitates occupy on the grain boundaries perpendicular to the tensile axis. It has been observed that the creep fracture can occur by 'w' or wedge-type cracking at grain boundary triple points. The wedge cracking develops as a consequence of grain boundary sliding, i.e. grain boundary sliding is not accommodated which arises at higher stresses (low temperature) and larger

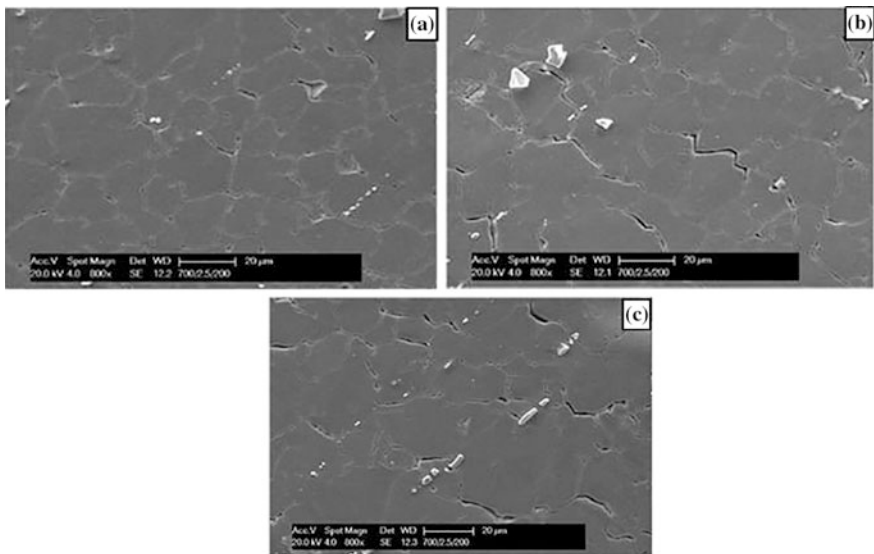


Fig. 3 SEM micrographs from notch root to centre of unfailed notch creep specimen of notch root radius 2.5 mm creep tested at 200MPa, 973K

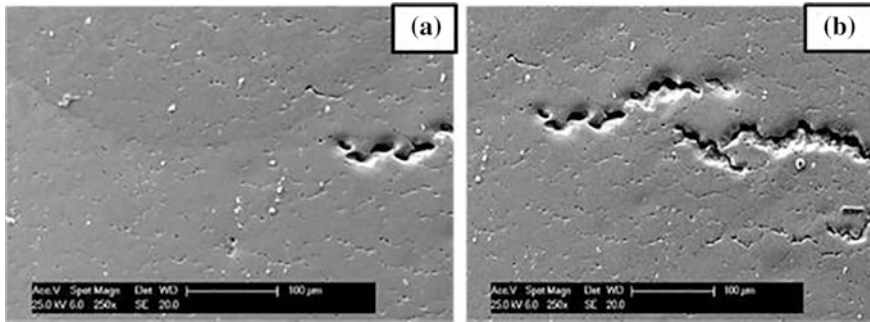


Fig. 4 SEM micrographs from notch root to centre of unfailed notch creep specimen of notch root radius 0.25 mm, creep tested at 200 MPa and 973 K

grain sizes. These wedge cracks are propagated by the formation of r -type voids as well. The wedge cracks are simply accumulation of r -type voids and small cavities. The presence of voids, microcracks, wedge cracks and their accumulation and propagation is shown in Fig. 4. It suggests that because of high-stress concentration factor, crack has nucleated at the notch root and propagated towards centre. The generation of lots of cavities and wedge crack during creep exposure is attributed to the high strength and limited ductility of the material. Figure 4a, b distinctly shows the migration and coalescence of voids into wedge-type cracks and then into cracks which lead to final failure in sharper notch specimen.

4.2 Effect of Notch Sharpness on Creep Rupture Behaviour

To understand the effect of multiaxial stress on creep strengthening, FE analysis was carried out on notch throat plane. Effect of plastic behaviour of the material in the stress distribution across the notch throat plane was also assessed considering the material's elasto-plastic deformation behaviour. Shallow notch has less plastic deformation at notch root than sharper notch because of less stress concentration at the notch plane. The plastic deformation and plastic zone increase with notch acuity ratio and tend to saturate at higher notch acuity ratio. FE analysis of stress distribution across the notch throat plane in 304HCu SS steel during creep deformation has been carried out by incorporating material's time-independent (plastic) and time-dependent (creep) behaviour in the model [17].

In the FE analysis, the material was considered to undergo elastic/elasto-plastic deformation followed by creep deformation. Under creep condition, the distribution of stress was found to change with creep exposure and attain a stationary state. The variations of von-Mises, maximum principal and hydrostatic state of stress across the notch in the steel for notch acuity ratio 20 and 2 are shown in Fig. 5. von-Mises

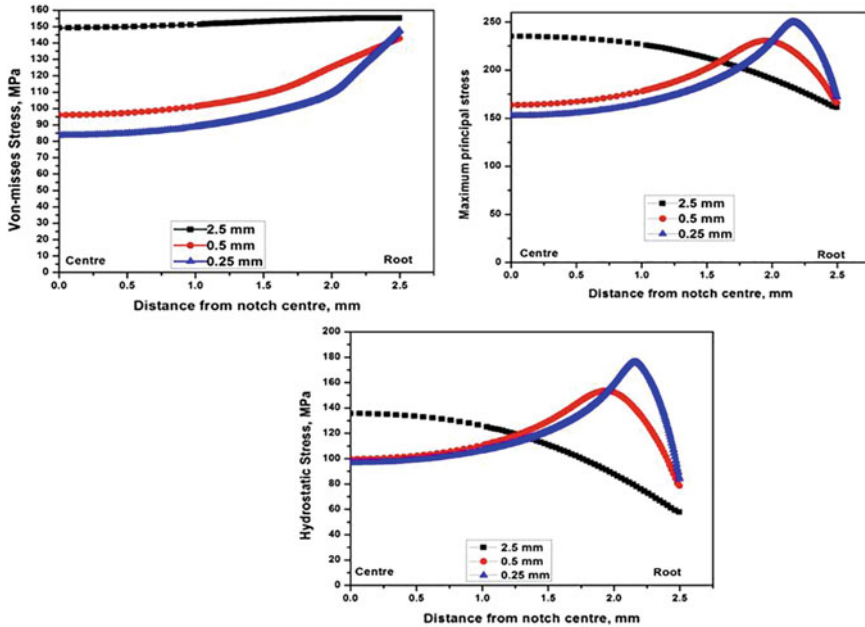


Fig. 5 Distributions of (a) von-Mises, (b) Maximum principal and (c) Hydrostatic stresses across the notch throat plane for different notch acuity ratio (creep tested at 200 MPa, 973 K)

stress increases with increase in distance from centre to root which is more significant in case of sharper notch. For shallow notch, the Von-mises stress was uniform at notch root while it is more concentrated for sharper notch. Maximum principal stress decreases at the notch root in case of shallow notch while it is increasing in its trend as observed in case of sharper notch. Hydrostatic stress exhibited similar behaviour as that of the maximum principal stress. The contour plots of von-Mises and maximum principal stress are shown in Figs. 6 and 7 for notch acuity ratio (a) 2 and (b) 20 at 200 MPa, 973 K, respectively. For shallow notch, the Von-mises stress was uniform at notch root (Fig. 6a) while it is more concentrated for sharper notch (Fig. 6b). In case of maximum principal stress, it was not uniform across the notch and found to be concentrated at the central region of notch for relatively shallow notches (Fig. 7a) and close to notch root for sharper notches (Fig. 7b).

4.3 Creep Life Prediction Based on the Representative Stress

The creep rupture life under uniaxial loading is expressed in terms of the applied stress as

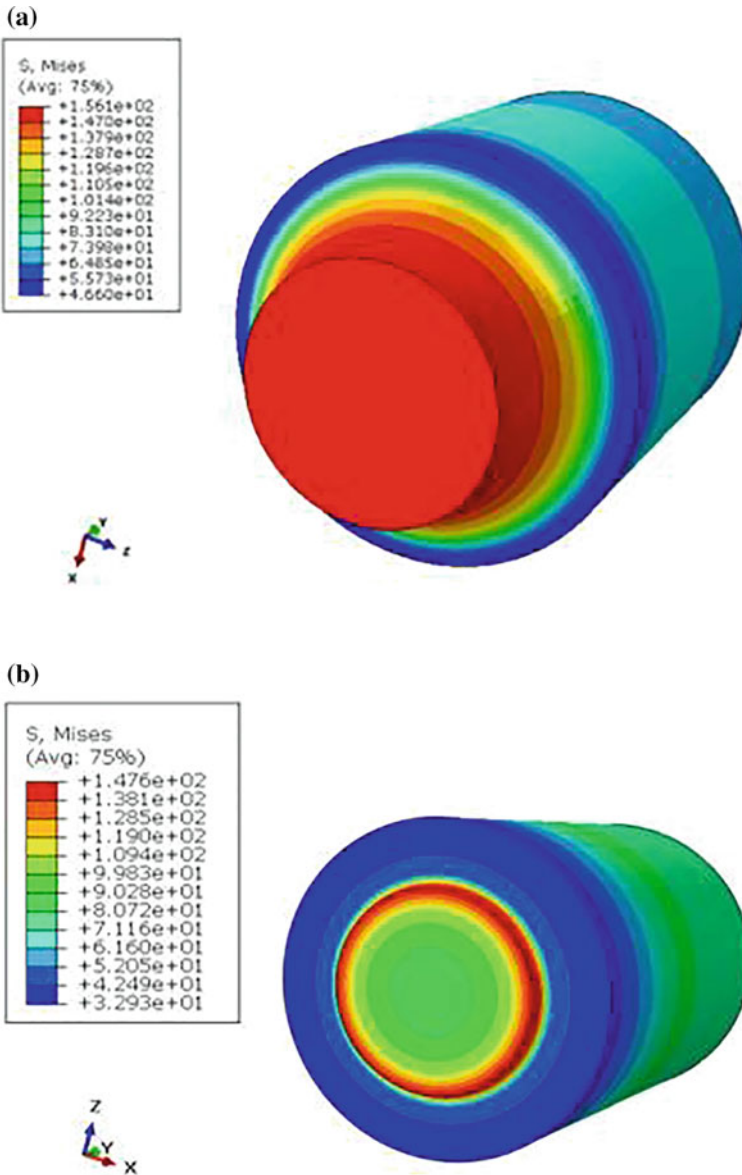


Fig. 6 The variation of von-Mises stress for notch acuity ratio (a) 2 and (b) 20, for creep tested at 200 MPa, 973 K

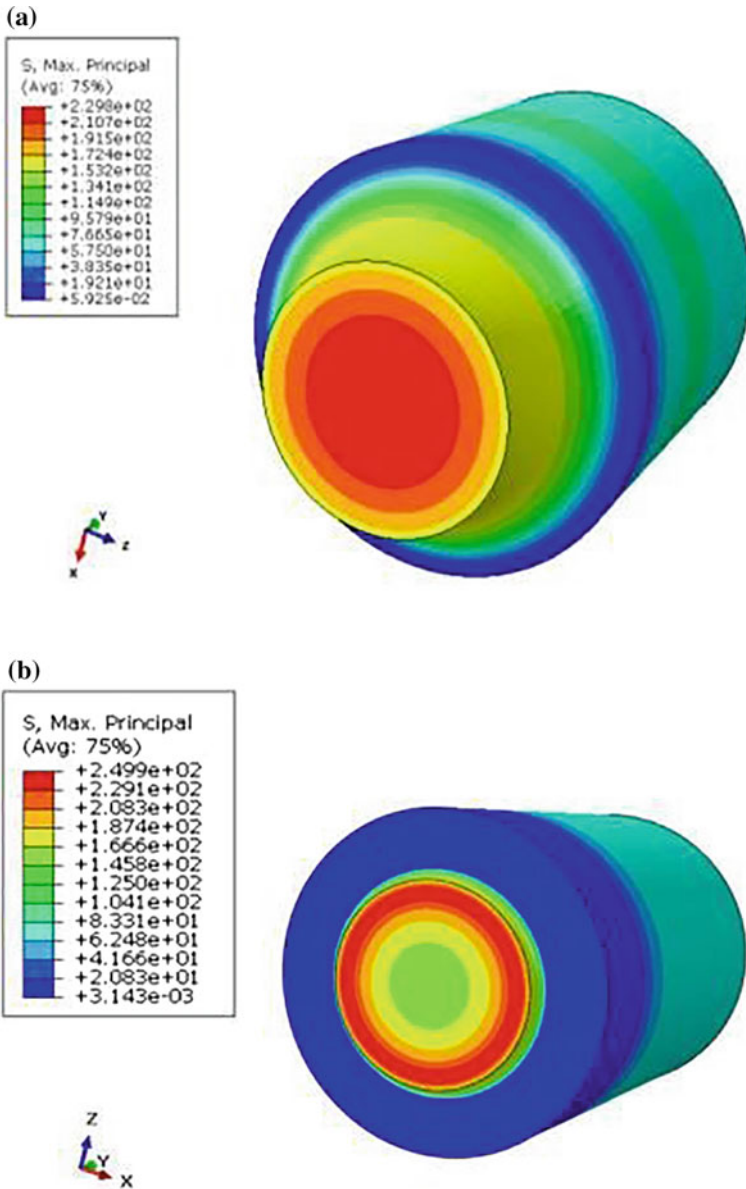


Fig. 7 The variation of Maximum principal stress for notch acuity ratio (a) 2 and (b) 20, for creep tested at 200 MPa, 973 K

$$t_r = M\sigma^{-m} \quad (1)$$

where ‘ m ’ is the slope of uniaxial creep plot.

Creep rupture life under multiaxial state of stress can also be described by similar equation in which σ_{rep} is the representative stress calculated through notched specimen data by incorporating suitable factor from different models, viz. Hayhurst, Cane and Nix model.

$$t_r = M\sigma_{\text{rep}}^{-m} \quad (2)$$

The representative stress (σ_{rep}) is applied to the uniaxial specimen which will result in the same rupture life as that of notched specimen. If at a particular temperature $\sigma_{\text{rep}} > \sigma_{\text{net}}$ (net stress applied to the notched specimen), then the presence of notch weakens the material, i.e. ability of the material to ‘notch weaken’. If $\sigma_{\text{rep}} < \sigma_{\text{net}}$, then the presence of notch strengthens the material, i.e. material exhibits ‘notch strengthening’. As already discussed, creep deformation and cavitation depends upon three components of stress, viz. maximum principal stress, hydrostatic stress and von-Mises stress in governing the creep deformation and cavitation [2, 12]. The von-Mises stress controls the deformation and creep cavity nucleation processes, the maximum principal and hydrostatic stress control the continuum cavity growth whereas the maximum principal stress controls the stress directed diffusion controlled intergranular cavity growth [12, 13].

In this paper, creep life prediction has been done by the relationships provided by Hayhurst et al. [9], Cane [10] and Nix et al. [11]. The prediction obtained from these three methods compared and based on the close fitting by least square method, their applicability has decided.

Hayhurst’s model

$$\sigma_{\text{rep}} = \alpha\sigma_1 + (1 - \alpha)\sigma_{\text{vm}} \quad (3)$$

Cane’s model

$$\sigma_{\text{rep}} = \sigma_1^{\gamma/m} \sigma_{\text{vm}}^{(m-\gamma)/m} \quad (4)$$

Nix’s model

$$\sigma_{\text{rep}} = 2.24 \sigma_1 - 0.62(\sigma_2 + \sigma_3) \quad (5)$$

where m , γ and α are material constants and ‘ σ_1 ’ is the maximum principal stress and ‘ σ_{vm} ’ is the von-misses stress, σ_2 is the intermediate principal stress and ‘ σ_3 ’ is the minimum principal stress, respectively.

For $\alpha = 0$ and $\gamma = 0$, $\sigma_{\text{rep}} = \sigma_{\text{vm}}$, i.e. representative stress fully depends on the von-misses stress.

For $\alpha = 1$ and $\gamma = m$, $\sigma_{\text{rep}} = \sigma_1$, i.e. representative stress fully depends on the maximum principal stress.

During creep exposure the stresses vary across the notch throat plane but at skeletal point is attained on reaching a stationary state. But it is difficult to identify the location in notch plane at which the stress can be considered as representative stress. Hayhurst et al. [9], Goyal et al. [12] based on FE analysis have introduced the skeletal point concept in determining the representative stress.

4.4 Skeletal Point Concept

The skeletal point is the location in notch throat plane for a given notch geometry, where the variation of stress across the notch throat plane for different stress exponent ' n ' in Norton's law intersects. FE analysis has been carried out for several values of ' n ' ranging from 1 to 10 to obtain the skeletal point at a particular stress 200 MPa. The value of coefficient ' A ' was obtained based on the creep strain of 10^{-5} h^{-1} . Similar works were reported by Webster [8, 13] and Goyal et al. [12] The details regarding the variation of skeletal point with notch acuity ratio have been discussed in detail by Goyal [12] where the authors show that the maximum principal and hydrostatic stresses at skeletal point were found to increase with notch acuity ratio and tend to saturate at higher notch acuity ratio; whereas, von-Mises stress decreased with increase in notch acuity ratio.

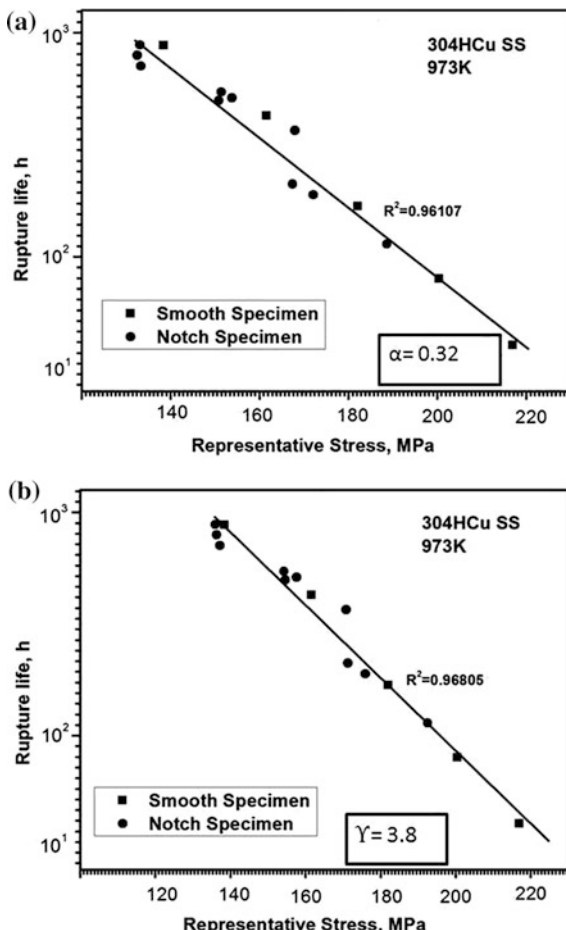
From Hayhurst Eq. (1), the value of ' α ' was decided by carrying out the regression analysis for the representative stress based on the skeletal point stress for each notch geometry. The best fit value of ' α ' is 0.32 with high correlation coefficient (0.96107) for this steel. So creep rupture life is mainly depended by von-Mises stress to an extent of contribution of 68% while the rest is from maximum principal stress.

Cane's model also used for prediction of rupture life which incorporates ' γ ' as a material parameter. By carrying out systematic regression analysis, the best value of ' γ ' was found to be 3.8 with high correlation coefficient (0.968). Figure 8 shows the presentation of multiaxial creep rupture data based on the calculation of representative stress based on the models proposed by (a) Hayhurst, (b) Cane.

4.5 Effect of Notch in Change in Hardness Due to Creep

The creep tested samples failed in one of the three notches. Other two notches of steel were used to generate the information regarding change in microstructural and mechanical property like hardness. In order to judge the change in hardness at notch plane due to creep exposure, the steel was chopped from both sides of notch and ground and polished up to half of their length. Systematically Vickers hardness was measured with distance for sharper (0.5 mm) notch case and shallow notch

Fig. 8 Multiaxial creep life prediction based on representative stress calculated based on the models proposed by (a) Hayhurst, (b) Cane at 973K



(2.5 mm) case across the notch plane. Figure 9 shows the hardness profile of creep tested and failed specimen of two cases, viz. (a) one with a notch of 0.5 mm root radius and (b) another with a notch of 2.5 mm root radius, traversing from notch root to another side. The above figure suggests that in both the cases, the average Vickers hardness at notch root region was more than at the central region. Since the specimen exhibits more stress concentration at the notch root, it is more strained during creep testing. The change in hardness could be attributed to grain boundary strengthening caused by grain size changes, dislocation density produced by creep deformation and sub-structure development, the precipitation hardening derived from fine precipitation of nano-precipitates and other phases or creep damage accumulation. So any of the above phenomena can cause significant amount of change in hardness [18]. But as compared to sharper notch shallow, notch showed significant increase in hardness in both notch root and centre. In sharper notch, the decrease in hardness is due to long rupture time, softening phenomena is more due

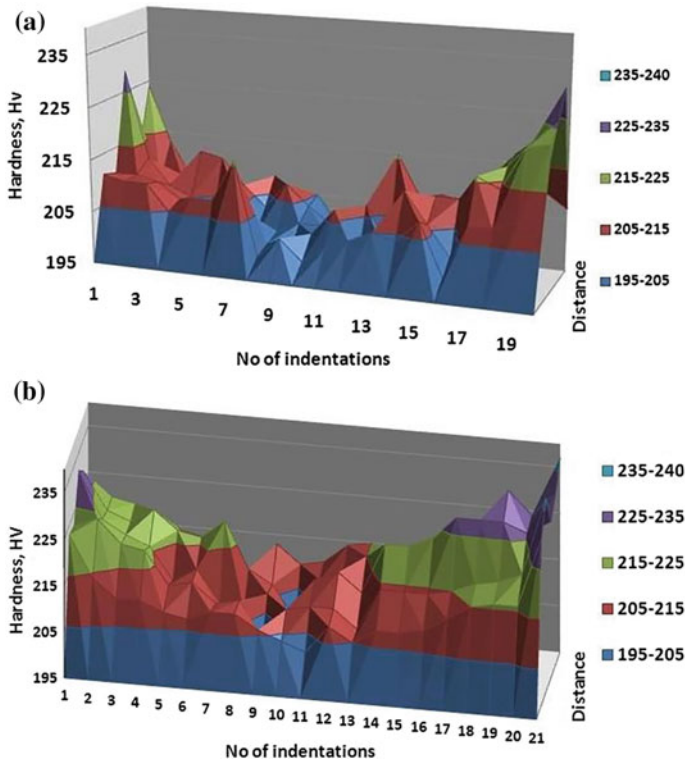


Fig. 9 3-D Hardness variation across the notch throat plane (un-failed notch) (a) shallow notch (notch root radius 0.5 mm) (b) sharp notch (notch root radius 2.5 mm), creep tested at 200 MPa, 973 K

to predominance in tertiary creep while in shallow notch, increase in hardness is due to the phenomena of strain hardening and lack of recovery due to creep exposure [19].

5 Conclusions

1. Presence of circumferential-U notch increases the creep rupture life of 304HCu SS material in comparison with material taken in the form of smooth specimen.
2. SEM investigations reveal that the random distribution of wedge crack and cavities was distinct in the case of shallow notch material compared to uniform distribution of void, wedge crack and sub-crack in the case of sharper notch one.
3. Effect of notch sharpness shows von-misses stress was uniform at notch root in shallow notch while it is more concentrated for sharper notch. The maximum principal stresses were found to concentrate at the central region of notch for relatively shallow notches and close to notch root for sharper notches.

4. The creep life prediction by means of representative stress through skeletal point method was done by both Hayhurst and Cane's model. Cane's model represented well for the multiaxial creep data with uniaxial creep data.
5. The average Vickers hardness at notch root region was more than the central region for sharper notch, and the average hardness of shallow notch both at centre and root was more due to the absence of recovery phenomena in tertiary creep.

Acknowledgements The authors gratefully acknowledge the encouragement and continuous support received from Dr. A. K. Bhaduri, Director, IGCAR, Kalpakkam. The authors also wish to record their sincere thanks to V. D. Vijayanand, SO/D, IGCAR, Kalpakkam for his help and support during analysis.

References

1. W.D. Nix, Mechanisms and controlling factors in creep fracture. *Mater. Sci. Eng. A* **103**, 103–110 (1988)
2. K.C. Sahoo, S. Ravi, S. Goyal, P. Parameswaran, K. Laha, Creep ruptures behavior and microscopy analysis of 304 HCu austenitic stainless steel under multiaxial state of stresses at 973 K. *Trans. Indian Inst. Met.* **69**(2), 451–455 (2016)
3. S. Goyal, K. Laha, K.S. Chandravathi, P. Parameswaran, M.D. Mathew, Finite element analysis of Type IV cracking in 2.25Cr-1Mo steel weld joint based on micro-mechanistic approach. *Phil. Mag.* **91**, 3128–3154 (2011)
4. T.H. Hyde, W. Sun, A.A. Becker, Failure prediction for multi-material creep test specimens using a steady-state creep rupture stress. *Int. J. Mech. Sci.* **42**, 401–423 (2000)
5. A. Forghani, M. Shahbazi, N. Zobeiry, A. Poursartip, R. Vaziri, An overview of continuum damage models used to simulate intralaminar failure mechanisms in advanced composite materials. in *Composites Science and Engineering* (A volume in Woodhead Publishing Series) (2015), pp. 151–173
6. P.S. Westera, C. Pickard Rolls-Royce plc, Derby Rolls-Royce plc, Derby the prediction of stress rupture life of notched specimens in the Ti5331s beta-processed titanium alloy
7. W. Li, F. Liao, T. Zhou, H. Askes, Ductile fracture of Q460 steel: effects of stress triaxiality and lode angle. *J. Construct. Steel Res.* **123**, 1–17 (2016)
8. G.A. Webster, S.R. Holdsworth, M.S. Loveday, K. Nikbin, I.J. Perrin, H. Purper, R. P. Skelton, M.W. Spindler, *Fatigue Fract. Eng. Mater. Struct.* **27**, 319–342 (2004)
9. D.R. Hayhurst, *J. Mech. Phys. Solids* **20**, 381–390 (1972)
10. B.J. Cane, in *Proceedings of the International Conference on Mechanical behavior of Materials*, ed. by K.J. Miller, R.F. Smith (Pergamon Press, Oxford, 1979), pp. 173–182
11. W.D. Nix, J.C. Earthman, G. Eggeler, B. Ilschner, *Acta Metall.* **37**, 1067–1077 (1989)
12. S. Goyal, K. Laha, Creep life prediction of 9Cr-1Mo steel under multiaxial state of stress. *Mater. Sci. Eng. A* **615**, 348–360 (2014)
13. S. Goyal, K. Laha, M.D. Mathew, Creep life prediction of modified 9Cr-1Mo steel under multiaxial state of stress. *Procedia Eng.* **86**, 150–157 (2014)
14. S. Goyal, K. Laha, C.R. Das, S. Panneerselvi, M.D. Mathew, Effect of constraint on creep behavior of 9Cr-1Mo steel. *Metall. Mater. Trans. A* **45**(2), 619–632 (2014)
15. C.R. Calladine, *Proc. R. Soc. Lond. A* **309**, 363 (1969)
16. S. Goyal, K. Laha, C.R. Das, S. Panneerselvi, M.D. Mathew, Finite element analysis of effect of triaxial state of stress on creep cavitation and rupture behaviour of 2.25Cr-1Mo steel. *Int. J. Mech. Sci.* **75**, 233–243 (2013)

17. S. Goyal, K. Laha, A.K. Bhaduri, Response of triaxial state of stress to creep rupture life and ductility of 316 LN austenitic stainless steel. *J. Mater. Eng. Perform.* **26**(2), 752–763 (2017)
18. Z. Yan, Z. Jie, L.I. Xiaona, Microstructural evolution and change in hardness during creep of NF709 austenitic stainless steel. *Acta Metall. Sin. (Engl. Lett.)* **24**(3), 220–224 (2011)
19. H. Tanaka, M. Murata, F. Abe, H. Irie, Microstructural evolution and change in hardness in type 304H stainless steel during long-term creep. *Mater. Sci. Eng. A* **319**, 788–791 (2001)

Stress Analysis for Integrity Assessment of High-Energy Hot Reheat Pipe Bends of 210 MW Coal-Fired Unit

Rajesh Daga and Mahendra Kumar Samal

Abstract The critical high-energy piping components of thermal power plant are predominantly subjected to damage mechanisms of creep, fatigue, and their interactions during their service. These pipings at high temperature and transient loadings under sustained loadings and thermal movements are designed as per the piping code. The creep damage mechanism causes irreversible thermal expansion in the piping inducing thermal stresses. The pipings under altered state of stresses due to thermal expansion are supported by suitable hangers and supports for ensuring stresses to be within the permissible design limits. The present paper discusses the layout of hot reheat piping of a coal-fired 210 MW_e unit. The piping material as per specification ASTM A335 P22 with hot reheat steam temperature 540 °C and hot reheat steam pressure of 4.7 MPa pressure operates under creep domain. The piping under these pressure and temperature loadings is subjected to load ramps during the start-ups, shutdowns, and load fluctuations and the steady loading during the sustained load operations. The scope of the study includes hot reheat pressure and low-pressure bypass pipelines. The piping layout with respect to the designed stresses, stress ratios, support loads, element forces, and displacements at each node has been considered for the present ongoing assessment. The design of the piping layout is accomplished to ensure that the structural integrity of the piping doesn't exert excessive load to the nozzles of the connecting equipment. The stress analysis of the piping and support system should be carried out to ensure that the stresses are within the allowable values as per the applicable design code during the service. The

R. Daga (✉)
NTPC Energy Technology Research Alliance, NTPC Ltd,
Greater Noida 201306, India
e-mail: daga.raj@gmail.com

M. K. Samal
Division of Engineering Sciences, Homi Bhabha National Institute,
Mumbai 400094, India
e-mail: mksamal@yahoo.com; mksamal@barc.gov.in

M. K. Samal
Reactor Safety Division, Bhabha Atomic Research Centre, Trombay,
Mumbai 400085, India

stress analysis data were utilized in modeling the pipe bend before control valve of the intermediate pressure turbine for online creep fatigue damage monitoring.

Keywords Stress analysis · High-energy piping · Hanger and support
Piping code · Creep · Thermal movement · Creep fatigue damage assessment

1 Introduction

Main stream, hot and cold reheat, and high-pressure and low-pressure bypass piping are the critical high-energy pipings of thermal power plants at high pressure and temperature subjected to a number of damage mechanisms like creep, fatigue, thermal fatigue, microstructural instability, and flow-accelerated corrosion fatigue during their service [1]. These high-energy pipings under the effect of service-induced stresses experience damage which lead to cracking at base metal locations and weldments. Such damages under high stresses during the service cause cracking, steam leak, or failure. Thus, it is imperative to predict and prevent failures under the effect of in-service damage mechanisms in such high-energy critical pipings. With an understanding of the damage mechanism, extent of damage is evaluated on applying rules of damage accumulation and remaining life of the component is assessed. Globally, considerable work is being done for integrity of such critical structures in service at elevated temperatures [2]. The life assessment of a hot reheat pipe bend of a 200 MW subcritical unit on real-time basis is discussed elsewhere [3]. The stress analysis of the hot reheat piping loop including low-pressure bypass piping was performed to evaluate the piping load. The stresses were computed induced due to piping loads in hot reheat pipe bend for the fluid temperature and pressure.

To prevent stresses beyond the code permissible values in piping systems, major aspect of a thermal power plant is to have an effective inspection program [4]. For a safe and reliable operation of the power plant, condition assessments of the critical components are essential. For maintaining the system stresses during the online and offline conditions, the pipe support systems are to be monitored during their service. The present paper discusses on the guidelines and its importance for ensuring the integrity of the piping structure.

2 Overview: Stress Analysis of Design Layout of the Hot Reheat Piping

High-energy piping generally refers to main steam, hot and cold reheat, feedwater, and extraction steam piping. High-energy piping has no expected design life. When in service, the piping undergoes continuous damage. The fabrication codes have built up design margins to ensure that the anticipated damage rate would not result in failure of major components during the economic life of a unit. The failure occurs

normally due to inadequate design, overestimation of material strength, an incomplete understanding of the metallurgical impact of fabrication variables, and significant change in operating practices. The stress analysis of the design layout of 210 MW unit of high-energy piping of hot reheat and low-pressure bypass piping was carried out as per design code ASME B31.1. The stresses within the piping system are limited within the code allowable limit under the defined load cases expected to occur in service conditions. The forces and moments expected to pass on to the equipment nozzles through the connected piping under the defined loading conditions are limited to the equipment manufacturer’s allowable limit. The objective of the stress computations carried out for flexibility analysis was to ensure structural integrity of the piping system.

3 Piping System Surveys

The high-energy piping system designed and fabricated as per Power Piping Code B31.1 experiences different loading types, namely sustained, thermal, and occasional loads. The system stresses of the piping are to be maintained, while the hangers are in the online (hot) and offline (cold) positions. The pipe support system which primarily accomplishes the task of maintaining the stresses in the piping within the code allowable limits is also the vital component. The hanger and support system supports the dead weight of the piping, the insulation, the contained fluid, and the weight of other attached components, which allows for thermal

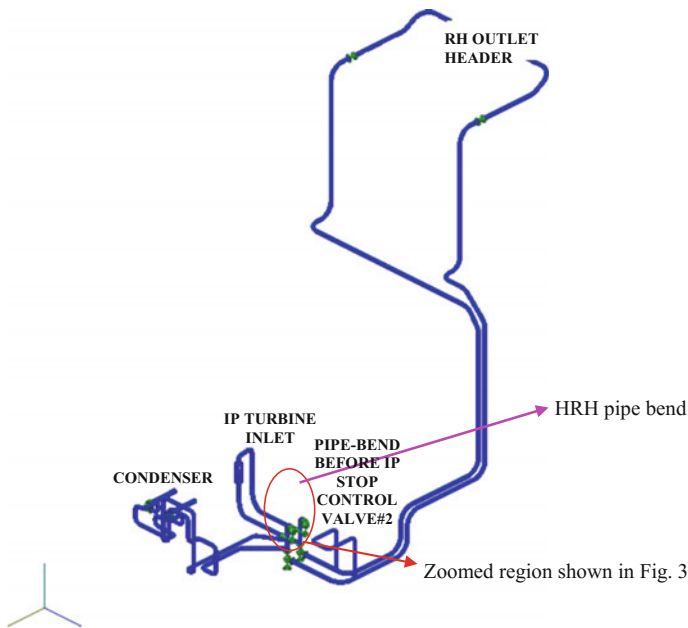


Fig. 1 Piping layout of the reheat pipe line where the bend is located

<u>Loads on the elbow at 540 deg. C</u> <u>(thermal load)</u>	<u>Loads on the elbow at 540 deg. C</u> <u>(dead weight)</u>
$F_{x1} = -14489.37 \text{ N}$, $F_{x2} = 14489.37 \text{ N}$ $F_{y1} = 5709.42 \text{ N}$, $F_{y2} = -5709.42 \text{ N}$ $F_{z1} = -9496.08 \text{ N}$, $F_{z2} = 9496.08 \text{ N}$	$F_{x1} = 35541.63 \text{ N}$, $F_{x2} = -26388.9 \text{ N}$ $F_{y1} = 559.17 \text{ N}$, $F_{y2} = -559.17 \text{ N}$ $F_{z1} = 1657.89 \text{ N}$, $F_{z2} = -1657.89 \text{ N}$
$M_{x1} = 16765476.39 \text{ N-mm}$ $M_{x2} = -25331431.05 \text{ N-mm}$ $M_{y1} = 75101955.93 \text{ N-mm}$ $M_{y2} = -39126527.73 \text{ N-mm}$ $M_{z1} = -43734049.29 \text{ N-mm}$ $M_{z2} = 35168212.35 \text{ N-mm}$	$M_{x1} = -487890.54 \text{ N-mm}$ $M_{x2} = 1320141.51 \text{ N-mm}$ $M_{y1} = -61513349.94 \text{ N-mm}$ $M_{y2} = 14451709.41 \text{ N-mm}$ $M_{z1} = -3389786.64 \text{ N-mm}$ $M_{z2} = 4221998.37 \text{ N-mm}$ Gravity acts in negative x-direction and specific weight $= \rho g = -8.7897e-5 \text{ N/mm}^3$

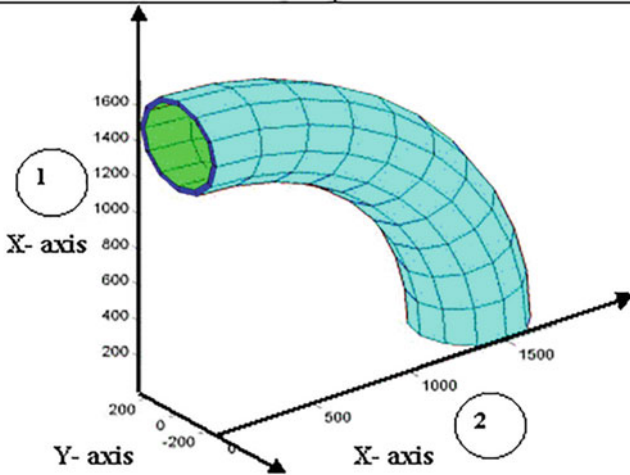


Fig. 2 Piping loads on HRH pipe bend used in the online creep-fatigue monitoring

expansion of the piping while minimizing the load transfer at the terminal points of boiler header and turbine connections. Additionally, the support systems are designed to withstand dynamic loadings, namely vibration, water, and steam hammer. For an improperly designed support system, considerable stresses are imposed in the piping if the thermal expansion differences are not accommodated and hanger support malfunction. The elevated stresses under improper design cause distortion of the steam piping or premature failure of girth or attachment welds.

The walkdown inspections of the piping system during the cold and hot conditions are carried out to ensure the proper operation of the hanger in accordance with its designed capacity. Figure 1 shows the piping layout of the hot reheat pipeline where the bend is located. The piping system supported by the hangers

should not get stressed beyond the allowable stresses as per the applicable piping design codes. Survey of condition of piping and support system is performed to identify broken or bottomed out hangers and trend the hanger readings. Such monitoring of the support system helps in identifying the potential problems with the critical piping and their support systems which may become significant. The timely corrective measures for the repair are initiated when hanger failure is identified. The effect of hanger failure on the piping system under service loadings is to be assessed by stress analysis of the piping system. The cause of the hanger failure is to be ascertained. A reason for the hanger failure may be attributed to the hanger load exceeding its designed load capacity. The consequential damage to the piping system in the event of hanger failure causes system stresses to exceed beyond allowable code stresses leading to premature creep failure and fatigue cracks. The stress analysis of the piping system is carried out to determine the location of the damage in the piping. The piping loads acting on the pipe bend are shown in Fig. 2.

4 Effect of Damage Mechanisms on the Piping and Life Assessment

Primarily, a comprehensive understanding of the potential damage mechanisms affecting the piping component is essential in predicting a component's effective life span and preventing failures. The damage depends on factors, namely design, operating modes, water chemistry, and fuel characteristics which are unit-specific. The piping components must be considered individually to obtain realistic life assessments. The life span of any high-energy piping component is primarily a function of factors such as operating conditions, namely stresses and temperatures; geometry, namely piping layout, support placement, and wall thickness; material; and type of damage. The presence of uncertainties like material properties, fabrication tolerances, and stress states makes the life assessment of the piping component difficult. Thus, life assessment is focused on setting inspection intervals to obtain inputs for taking decisions to whether repair or replace the component. Several researchers have stressed the need to develop a life prediction methodology to address various aspects of failure mechanisms [5–12].

5 Analysis of Hot Reheat Pipe Bend as a Part of Piping Loop

In order to carry out thermo-mechanical analysis of pipe bend of hot reheat loop of the coal-fired thermal power plant, the geometrical and boundary condition details of the piping loop are required. As shown in Fig. 1, the entire loop considering

different anchor points, support, and hangers has been modeled using finite element code. 3D piping elements have been used for the analysis. Both straight and bend pipe elements have been included in the loop in order to realistically calculate the stresses and loading coming in the loop due to dead weight as well as thermal loads. As the hot reheat pipings have been designed to operate at 540 °C and 4.63 MPa, the same has been considered in the analysis. The segment of pipe bend for which detailed thermo-mechanical analysis has been carried out is shown in Fig. 2. The actual geometry has been modeled using 3D 20-nodded solid brick elements. The loads and moments coming from the connected pipings are applied as boundary loads in the finite element model of the 3D pipe bend. The online damage monitoring system incorporates this piping bend as a module in the system, and entire information regarding geometry, loading, and boundary conditions is fed into the system through necessary input files. The input contains information regarding the discretization of the component, material data, and associated loading and boundary conditions. Piping forces in three Cartesian coordinate systems and moments (two bending and one torsional) about three axes are also considered. The above procedure ensures that the thermo-mechanical behavior of the pipe bend is simulated as accurately as possible. In the next section, the details of thermal analysis, stress analysis, and damage evaluation (due to creep and fatigue) of the hot reheat pipe bend as carried out by the online damage monitoring system are described in detail.

6 A 3-D FE Model Hot Reheat Pipe Bend and Damage Calculation

A detailed 3-D finite element (FE) model of the pipe bend was made using 20-noded brick elements. The element information for the FE mesh is stored as element–node relationship and nodal coordinates in a static file specific to the component. Similarly, all the loadings and boundary conditions at specific nodes and element surfaces are stored in the same file. During run-time, the software computes the element stiffness matrices and load vectors, assembles, and then solves for metal temperature distribution (in thermal module) and metal stress information (in the structural module). The element loading information is for unit internal pressure rise, dead weight, and associated piping loadings due to temperature rise (from room temperature to design temperature condition). Actual loading is calculated at run-time once the fluid pressure and temperature information are known from the data acquisition system. The bending moments, end pull, and shear forces at the ends of the pipe bends are converted into equivalent loading information in the element surfaces covering the two ends. The 3-D FE model along with material parameters and loading (due to internal pressure, dead weight, thermal gradient, and piping expansion loads) is used by the system BARC Online Structural Safety Evaluation System (BOSSSES) for online monitoring of damage due to creep, fatigue, and creep–fatigue crack growth. The nodal temperature data

of the FE mesh (obtained by thermal or transient temperature module of BOSSES) are used to calculate the load due to temperature transients seen by the component. Thermal load due to temperature gradient, internal pressure, associated piping loads, etc., is then used in a stress analysis module to calculate stresses at different gauss points of the pipe bend. In our analysis, the pipe bend is in equilibrium under the action of all the forces and bending moments. For prevention of rigid body motion, some soft springs are provided at the two ends of the bend.

The metal temperature information is stored in file (as restart files) to be used for heat conduction analysis in the next time step. All the stress information at the Gauss points is stored for a specific time interval (one hour) so that rain-flow cycle counting algorithm can be used to know the number of stress cycles. The stress cycles are used further to calculate fatigue damage at the Gauss points using Minor's cycle summation rule. The stress and temperature information at each time step is used to calculate creep damage using Robinson's life fraction rule. For the above purpose, the appropriate creep and fatigue properties of the material are used. The temperatures and stresses at different time are also used to compute crack growth of different postulated cracks due to creep and fatigue at various locations of the pipe bend in the fracture mechanics module. The life consumed by the component is predicted by extrapolating the damage and crack growth information to the previous operating hours. The contour information of stress intensities, metal temperature, creep, and fatigue damage, etc., at the last time step is written into specific dynamic plot files. The history of stress intensity, temperature, creep, and fatigue damage at different critical locations is also stored in plot files for visualization. All the information is upgraded, and restart files are saved for successive computation. The system also keeps automatic backup of contour and history information of different parameters of the component at user-specified intervals. The real-time process data of the pipe bend are made available to the researcher's desk through client-server network.

For the components operating at high temperature and subjected to plant transients and cyclic loads during plant start-up and shutdown, creep-fatigue interaction is an important damage mechanism. Due to cyclic loads, fatigue micro-cracks initiate at the metal surface which can join with the grain boundary cavitation sites (due to creep damage and grain boundary sliding, there is progressive cavitation and micro-crack formation), and the micro-cracks can grow along the grain boundaries. Hence, computation of crack growth due to creep-fatigue interaction is an important aspect of life assessment which has been carried out here using fracture mechanics methods. For fatigue crack growth calculation, modified Paris law has been used in this analysis which uses effective stress intensity factor range for the given loading cycle in the pre-cracked geometry. For creep crack growth calculation, the C^* parameter is used as a crack tip loading parameter and the universal creep crack growth law is used. The evaluation of C^* integral requires calculation of reference stress and stress intensity factor for the given crack configuration in the component.

For selection of components for online monitoring, one must make an assessment of the potential risk associated in case of failure of the component in terms of

plant unavailability, economic loss, consequences to environment and human life, etc. The risk of damage depends upon the local stress concentration due to abrupt change in geometry (such as shell–nozzle junctions and tee joints) as creep damage accumulation depends upon the effective stress and temperature. Definitely, the headers (especially the shell–nozzle junctions) are potential creep damage-prone areas. Again, the shell–nozzle junctions contain welded regions where there can be further complications due to in-homogeneities in the mechanical and creep properties, microstructures of the material, residual stresses, etc. The pipe bends are also subjected to stress in-homogeneity due to their geometry (which depends upon the bend radius, bend radius to thickness ratio, diameter to thickness ratio, etc.). However, the particular pipe bend under consideration is important for online monitoring because of the prior bulge observed (which may be because of some prior imperfection). The consideration of existing local imperfection such as ‘bulges’ as mentioned above is very important from the point of view of stress analysis and damage prediction. As we discretize the actual 3D geometry using 3D continuum finite elements, it will be possible to incorporate the bend ovality easily if we know the details of it (i.e., the location, profile, and amount of ovality). The information has to come from actual measurement in the plant. In this work, the ovality details are not measured, and hence, the same is not considered here. However, incorporation of this information is crucial to life prediction, and it will be carried out in future.

As the damage monitoring system was implemented recently and has accumulated data for roughly 25,937 h, it is necessary to extrapolate the results of creep and fatigue damage for the actual service life (e.g., 78,251 + 25,937 h.) of the HRH pipe bend by the system during online calculations. The remaining life assessment is performed on the basis of cumulated material damage and crack growth. The consumed life of the pipe bend is very small (i.e., of the order of 5%) when the creep and fatigue usage factor (the limiting factor being unity for crack initiation at a material point) is considered. However, when crack growth is considered as the lime-limiting mechanism, the predicted life consumed is still less (smaller than 1%), when the crack of 1.5 mm depth was considered and the most severe crack was found to be the longitudinal semi-elliptical surface crack at the outer surface of the intrados of the pipe bend. Hence, the pipe bend is found to be very safe, and the usual annual inspection during shutdown of the plant is not necessary for this component. However, the above prediction can be fine-tuned once more, and more data are available from the previous operation and inspection history, which can be used to suitable schedule the future inspection interval. The fluctuation of steam pressure, temperature, and boiler load index (tones/hour) for the hot reheat pipe bend is shown in Fig. 3, and the computed metal temperature, stress intensity, and damage index in the pipe bend are shown in Fig. 4. The contour for maximum stress intensity and accumulated creep and fatigue damage in the pipe bend is shown in Figs. 5 and 6, respectively.

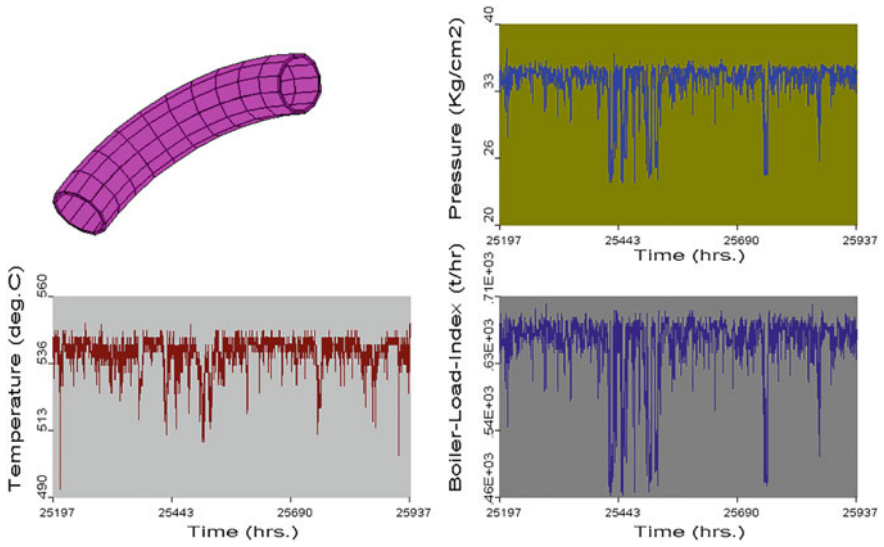


Fig. 3 Recorded thermal hydraulic parameters (pressure, temperature, and flow of steam through the bend)

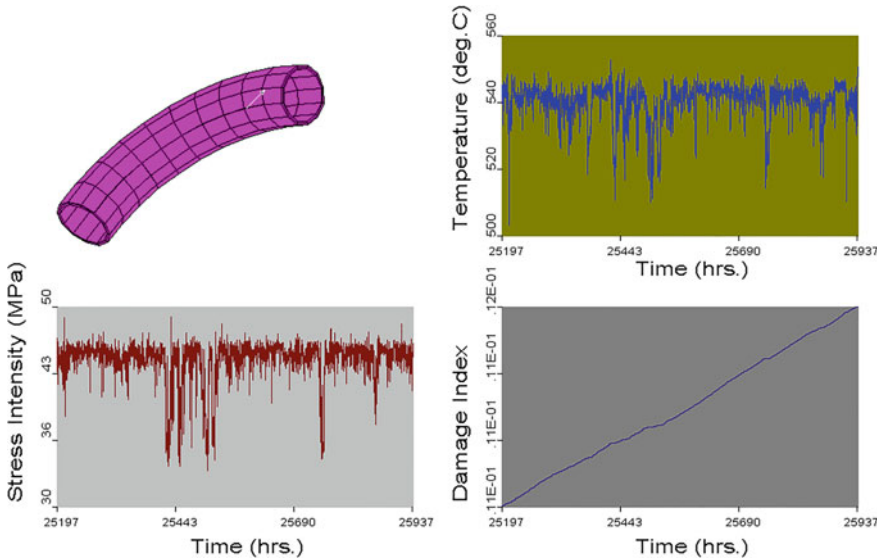


Fig. 4 Computed temperature, stresses, and damage factor (due to creep and fatigue) at a material point in the HRH pipe bend

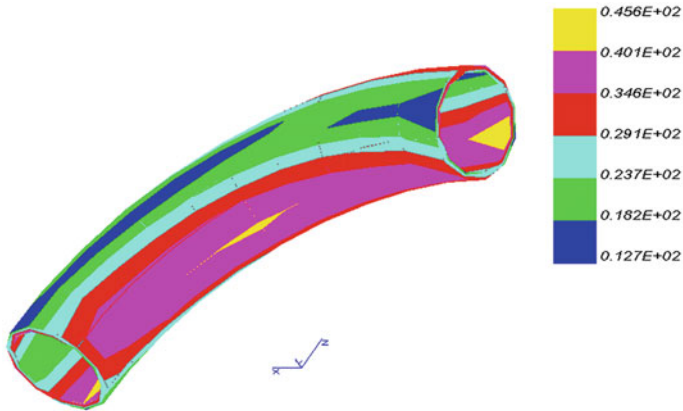


Fig. 5 Contour of maximum stress intensity in MPa (due to mechanical, thermal, and piping loads) over HRH pipe bend at 25,937 h of monitoring

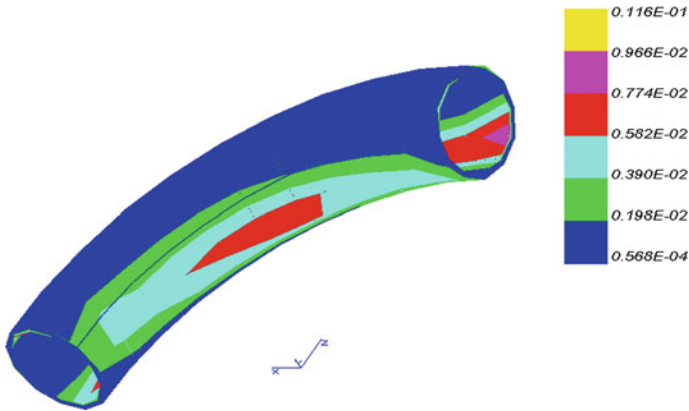


Fig. 6 Contour of accumulated damage (due to creep and fatigue) over HRH pipe bend at the end of 25,937 h of monitoring

7 Discussion and Recommendation

A properly operating high-energy piping system essentially requires the weight, thermal, and pressure stresses to be kept at acceptable levels as per the piping codes. The stress analysis of the piping involves calculation of piping code stresses, loads, and deflections under static and dynamic loading conditions. The piping should be well supported and should have controlled deflections under its weight, thermal, and other loads. Thus, stress analysis of the piping system ensures the piping layout conforms to allowable code values of weight, thermal, and pressure stresses during its service loads.

The hanger and support system are the vital and critical components which properly maintain high-energy piping system. They maintain the stresses of the piping system in online (hot) and offline (cold) conditions. This primary function is achieved by supporting the dead weights (piping, insulation, fluid, and other components), allowing thermal expansion of piping and supporting dynamic loads (vibration, water, and steam hammer). Summarily, the piping system with hangers and supports should be code compliant for both sustained and thermal load cases.

To properly maintain the high-energy piping system, performance of hangers and supports has to be evaluated. A thorough hot and cold walkdown of the piping and support system is required to ensure its healthiness. A hanger inspection should be carried out for maintaining the hanger operation properly. The failure of hanger causes damage to the piping. The increased piping load due to hanger failure causes deformation in the piping, accelerated creep and fatigue damage, and thus eventually reduces the piping life.

Piping code ASME B31.1 recommends that the hangers should be periodically examined to look for changes both in the piping and in the hangers. Hangers can become inoperable as a result of creep deformation of the piping, a dynamic event in the line such as a water or steam hammer, or deterioration of the spring and other components. For constant-support and variable-load hangers, the code recommends that hanger readings should be obtained both in the fully hot position and when the unit is offline in the cold position. The hanger readings should be recorded and permanently stored. The temperature of the pipe at the time of observations should also be noted.

The issue of validity of damage predictions versus actual observed plant damage is very crucial and needs to be discussed here. One needs to measure the actual damage in specific critical locations of the plant components in order to validate the assessment approach and have a better understanding of the models used. The measurements are usually in terms of change in microstructure, hardness, carbide precipitation, grain boundary cavitation, grain boundary micro-cracks, etc. There exists quantification techniques in literature, like measurement of cavity density and A-parameter. The authors are actually in the process of quantifying the damage due to creep and fatigue in the above pipe bend. Replicas at some critical locations of the pipe bend have been taken and are currently being analyzed. However, this aspect will be addressed in the future work. Apart from creep and fatigue damage in high-temperature components, flow-assisted or erosion corrosion, corrosion pitting, corrosion fatigue, stress corrosion cracking, etc., are of major concern in low-temperature pipework systems. However, laboratory experiments are now carried out by researchers worldwide to address specific cases, to have an in-depth understanding and to generate experimental data from which some empirical or analytical models can be derived. For flow-assisted corrosion in nuclear pipings, some popular models exist. Once we generate such models for the thermal power plant feedwater line conditions, it may be possible to deal with it analytically. Otherwise, one has to resort to periodic inspections based on plant-specific and component-specific experience for dealing with life assessment of components subjected such dominant mechanisms.

The accuracy of predictions of the above online system is based on the level of modeling used in the analysis and use of proper material properties. However, if there is some prior imperfection which is not known and not considered explicitly in the modeling, the results may not be very accurate. For these reasons, site investigations are required. However, the extent of site investigation and the associated maintenance and inspection costs can be minimized if such a system is used as a guiding tool as it provides online information on status of the damage in critical components which is based on available data and actual loading conditions seen by them. The above system actually guides the plant maintenance engineer to decide inspection and maintenance intervals of critical plant components and hence fits into a comprehensive risk assessment program. The correlations between predictions and actual damage can be improved by conducting metallurgical investigations at certain intervals for the critical locations to provide better material properties so that the system gets more accurate information for prediction. Though component inspections cannot be ruled out, these can be minimized by adopting a risk-based in-service inspection program in which online monitoring is an integral part.

The prevailing approach/practice of the utilities to estimate the need for inspection is on the basis of offline inspection and the past operation and maintenance (O&M) experience. These result in frequent inspections of problem-free equipment by the utilities and also often cause unexpected failures. Presently, the system uses only one deterministic value, i.e., mean value of the material properties for calculation of damage and crack growth due to creep and fatigue. However, a probabilistic analysis module is currently being developed where the effect of type of distribution, coefficient of variation, etc., of the material properties can be accommodated to calculate the band of variation of the predicted damage parameters (i.e., 5 and 95% percentile values) instead of a single value. The system is capable of monitoring welds as well. One needs to specify the mechanical, creep, and fatigue properties of the weld in the weld region. In the finite element model, the material properties are associated with a material number which is in turn allocated to the corresponding elements falling in the respective regions of the materials. In the present analysis, the bend does not have weld regions and hence weld material properties are not used.

The issue of prior system loading, i.e., the pull-up stresses that will be applied during original plant construction, is also an important consideration in the prediction of damage due to creep and fatigue in high-temperature components. If the system pull-up stresses are known, it can be easily incorporated in the finite element model as an initial stress problem. However, when the above information is not known (especially for older plants), the assessment may be done with applications of some initial pull-up stresses in the FE model according to certain codal guidelines. The assessment of damage due to creep-fatigue interaction is an important aspect of life assessment and remaining life prediction exercise. In ASME, the rules for damage accumulation due to creep-fatigue interaction are different for different materials (e.g., low alloy steel and stainless steel). The effective damage depends upon the relative damage of creep and fatigue damages (the locus of effective

damage curve is not a straight line, but sometimes a bilinear or nonlinear curve). Again, because of many sources of uncertainties such as system initial stresses and local in-homogeneities, usually the predictions are done based on codal guidelines which are conservative in nature. However, given sufficient laboratory database for a given material under wide range of loading conditions for the above effects, it may be better to use own database (specific to the material of the component under monitoring) which can remove the conservatism to some extent.

Use of non-destructive and metallurgical investigations for the critical bulged location of the pipe bend under monitoring will provide a method of validation of the predicted results of the current online monitoring system. The damage prediction due to creep depends upon the constitutive equations used. However, the selection of creep constitutive equation depends upon the particular material under consideration. It has been shown in literature that no single creep constitutive law can fit well for all the materials for all temperature and stress ranges. Of course, creep laws based on continuum damage mechanics theories (e.g., Kachanov's and Hayhurst's) are more promising as they consider the coupled effect of stress and damage in the material. In the current analysis, Only Robinson's life fraction rule has been used for creep damage prediction. More advanced theories such as continuum damage mechanics will be considered in future work of the authors.

The authors envisage covering more number of critical components in an unit as well as covering many further coal- and gas-based thermal power plants of NTPC Ltd in near future so that the integrity of these components can be assessed in the real time and this shall help in decision making by the concerned plant engineers as well as maintenance staff regarding minimization of cost and overall downtime of the plants. The presence of online damage monitoring system shall also generate the necessary information which shall help in future design and material improvements.

Acknowledgements Dr. M.K. Samal acknowledges the support from Dr. D.N. Badodkar, Director RD&DG, Mr. V. Bhasin, Associate Director, NFG, BARC for carrying out this R&D activity regarding online damage monitoring of plant components. Mr. R. Daga acknowledges the support from Dr. P. Jain, General Manager, NETRA, NTPC and engineers from NTPC thermal power plants at different locations.

References

1. EPRI Report 1012201, *Fossil Plant High-Energy Piping Damage*, vol. 1. (June 2007)
2. R. Viswanathan, *Damage Mechanisms and Life Assessment of High Temperature Components* (Ohio, ASM International, 1989), pp. 182–263
3. R. Daga, G. Bandyopadhyay, M.K. Samal, B.K. Dutta, J. of power plant operation. *Maintenance Mater. Issues* **5**(1), 1–19 (2008)
4. C. Basavaraju, W.S. Sun, *Piping handbook*, “Stress analysis of piping systems” (The McGraw-Hill Companies, NY, 2004)
5. R. Daga, M.K. Samal, *Real-Time Monitoring of High Temperature Components*, 6th International Conference on Creep, Fatigue and Creep-Fatigue Interaction (CF-6), (23–25 January 2012, Chennai, India)

6. M.K. Samal, B.K. Dutta, H.S. Kushwaha, R. Daga, G. Bandyopadhyay, Creep damage evaluation of a power plant header using combined FEM analysis and quantitative metallography. *Trans. Indian Inst. Met.* **63**(2–3), 411–416 (2010)
7. Assessment of components operating in the creep regime, Section 10 of API-579 document (June 2001)
8. R. Daga, G. Bandyopadhyay, M.K. Samal, B.K. Dutta, A.K. Mohindru, Combined creep life fraction assessment of critical locations of an in-service superheater outlet header under surveillance programme. *Trans. Indian Inst. Met.* **63**(2–3), 423–429 (2010)
9. R. Daga, M.K. Samal, Structural integrity assessment of superheater header through FE analysis and in-situ metallography (Global Energy Technology Summit (GETS), 2014, India, 7–9 November 2014)
10. R. Daga, M.K. Samal, Creep Fatigue Damage Assessment of an In-service Superheater Outlet Header. International Conference on Fatigue Durability and Fracture Mechanics, (Bangalore, India, 28–30 May 2015)
11. Power Piping Code, ASME B31.1
12. R. Daga, M.K. Samal, Remote monitoring of health of critical high temperature components by real-time finite element technique, (Global Energy Technology Summit (GETS) 2015, India, 7–9 November 2015)

Part VI
Energy and Transportation

Structural Integrity Study for Additional Piles on an Existing Jacket Structure in Western Indian Offshore

Praveen Bhat and Bakul Master

Abstract Oil and Natural Gas Corporation (ONGC) operates more than 265 steel jacket-supported platforms installed in water depths ranging from 25 to 90 mts. and secured to the seabed using steel piles. Quite large number of platforms have either exceeded their design lives and/or undergone modifications/mitigation/strengthening due to change in design premises and/or revamping projects executed for enhanced oil recovery. This calls for requalification studies for their extended “fit for use purpose.” This paper describes the structural integrity assessment of an existing platform found to have highly overstressed piles and failing members and joints based on design-level analysis. A pushover analysis has been carried out to assess the reserve strength ratio (RSR) for checking the structural adequacy of the jacket structure, and suitable mitigation measures have been suggested for the particular platform as a combination of additional retrofit members/piles, removal of redundant facilities, and strengthening of members/joints, etc.

Keywords Jacket structure · Design in-place analysis · Ultimate strength analysis RSR

1 Introduction

The hunt for Black Gold started in the Indian offshore region when Oil and Natural Gas Corporation Limited (ONGC) started its operations in the western offshore region of India in the year 1976. Since then, more than 265 well, process, and living quarter platforms have been installed and operated by ONGC. By now, quite a large number of platforms have either exceeded their design lives or undergone/undergoing modification/mitigation measures due to change in design premises and/or revamping projects executed for enhanced oil recovery. Re-assessment of

P. Bhat (✉) · B. Master
Institute of Engineering and Ocean Technology, ONGC-Panvel, Panvel 410221,
Maharashtra, India
e-mail: bhat_praveen@ongc.co.in

these offshore platforms involves structural integrity check after taking due consideration of change in design premises along with new loads and structural damages, if any.

This paper describes the summary of the work carried out at the Institute of Engineering and Ocean Technology (IEOT), ONGC, on the project of global static in-place structural integrity check of an existing platform and consequential mitigation measures. The mitigation measures suggested for the particular platform are in combination with the removal of redundant equipment and appurtenances, restriction on marine growth, strengthening of members/joints, and additional retrofit members/piles. The paper highlights the main findings of the study with special emphasis on the jacket and pile structure.

2 Structural Analysis

2.1 Design-Level Analysis

The study for this typical jacket structure, located in western offshore, for the structural integrity check on specific requirements from the asset/platform operator in the context of its design life has been outlined. The salient features of the platform have been listed in Table 1 and Fig. 1.

An initial global static in-place design level analysis of the platform has been carried out for 100-year extreme storm condition with 85% environmental loading considering all lateral loads, i.e., Wave, Current, and Wind, with a load factor 0.85 (reduced environmental criteria¹) in combination with other design loads including gravity loads due to self-weight and production facilities installed on the platform topside. A marine growth thickness of 100 mm from EL (+) 6 m to EL (-) 30 m and 50 mm from EL (-) 30 m to mud line has been considered in the analysis.

The primary structural members have been checked for yield, stability, and nominal joint strength assessment for 100-year extreme storm condition [1]. In the

Table 1 Platform details

Water depth	77.455 m
No. of main piles	4
No. of skirt piles	2
Diameter of main piles	1.372 m
Diameter of skirt piles	1.372 m
Piles vertical penetration for main piles	95.555 m
Piles vertical penetration for skirt piles	77.724 m
<i>Production details</i>	
No. of conductors	12 (9 inside + 3 clamp on)
No. of risers	6 (1 * 4" + 2 * 6" + 1 * 10" + 1 * 12" + 1 * 14")

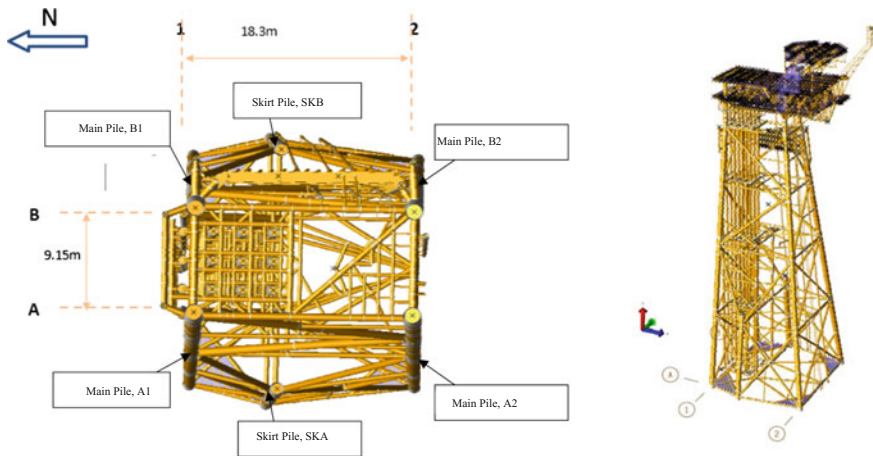


Fig. 1 Key plan and 3-D view of the jacket structure

design-level analysis, all the piles have been checked for axial load carrying capacity and the pile head stresses.

The results of the design-level analysis revealed that for 100-year extreme storm condition with 85% environmental loading and associated design loads, the factor of safety (FOS) against axial capacity for all the piles is more than 1.50 under various load cases in both compression and pull out. In pile head stress utility ratio check, all the piles were found to have material utilization higher than the maximum permissible limit of 1.0. Hence, re-analysis was performed after incorporating load reduction measures. The load reduction measures comprised of removal of redundant sump and pump caisson, non-consideration of future riser protector, and restriction of marine growth thickness to 50 mm throughout. The results of the re-analysis showed that still some of the piles were highly overstressed with a UC value higher than the permissible limit of 1.00 (refer Table 2).

Member strength assessment revealed that six structural members were having capacity utilization more than the API (RP-2A-WSD) specified limit value of 1.0 with a maximum capacity overutilization by 24%. In joint strength check, three structural joints were showing high capacity utilization with UC ratios exceeding the acceptable limit of UC ratio of 1.0 with a maximum capacity overutilization by 28%.

2.2 Simplified (Linear) Ultimate Strength Analysis

Subsequently, simplified (linear) ultimate strength in-place analysis with 100% environmental loading was performed, and few primary structural members and joints were found to be having utility ratio higher than the acceptable value of 1.2781. Hence, few structural members and joints were not passing the assessment

Table 2 Pile FOS and pile UC values for original condition (with 85% environmental loading) with suggested load reduction measures

Pile No.	Location	Axial force in comp. (MN)	Pile capacity in comp. (MN)	Min. FOS in compression	Axial force in pull out (MN)	Pile capacity in pullout (MN)	Min. FOS in pull out	Max. pile UC
1	A1	14.334	38.781	2.71	10.225	30.020	2.94	0.948
2	B1	17.057	38.781	2.27	8.984	30.020	3.34	1.006
3	A2	19.475	38.781	1.99	13.539	30.029	2.22	1.300
4	B2	20.452	38.781	1.90	12.521	30.029	2.40	1.382
5	SKA	10.695	23.152	2.16	4.268	23.759	5.57	0.945
6	SKB	13.189	23.152	1.76	3.544	23.759	6.70	1.063

requirement even as per the simplified ultimate strength analysis check (Linear global analyses check as per API-RP-2A (WSD)).

Member Check Results:

S. No.	Member	UC ratio ^a	UC ratio ^b
1	203L-0743	1.034	1.278
2	201L-0004	1.099	1.352
3	202L-0005	1.043	1.255
4	203L-0006	1.243	1.530
5	204L-0007	1.119	1.347
6	0001-404L	1.008	1.181

Joint Check Results:

S. No.	Brace member	Location	UC ratio ^a	UC ratio ^b
1	0007	Row-A, X-brace joint, b/w EL (-) 52.76 m and EL (-) 77.455 m	1.280	1.538
2	0253	Horizontal level, EL (-) 52.760 m	1.232	1.426
3	0005	Row-B, X-brace joint, b/w EL (-) 52.76 m and EL (-) 77.455 m	1.225	1.466

Note ^aDepicts design-level analysis with 85% environmental loading

^bDepicts simplified ultimate strength analysis with 100% environmental loading

2.3 Nonlinear Ultimate Strength Analysis

As the results of the design-level analysis and simplified ultimate strength analysis revealed that some of the primary structural members, joints, and piles do not meet the assessment requirement, a higher level nonlinear ultimate strength analysis was carried out for eight directions of environmental loading. In this paper, results of nonlinear plastic collapse analysis [2] using USFOS [3] software have been discussed for assessing the ultimate strength of the jacket platform, and reserve strength ratio (RSR) values for the structure have been presented. The RSR is defined as

$$RSR = \frac{\text{Ultimate lateral load carrying capacity}}{100 \text{ year environmental condition lateral loading}}$$

The results of the ultimate strength analysis revealed that the structure is not able to withstand the environmental forces up to the target RSR [4] level of 1.323 for all the considered directions, primarily due to failure of Row-2 piles (refer Fig. 3) and X-brace joints present on Row-A and Row-B of the jacket structure, around a load level of 1.05 (refer Fig. 2).

Thereafter, a re-analysis for nonlinear ultimate strength check was carried out after considering conductors as piles for providing the lateral support [5]. The re-analysis results revealed that the structural adequacy of the jacket structure of platform still could not be documented for all the wave approach directions even after considering the conductors as piles.

The analysis results (both design-level and ultimate strength) revealed that the structure was having overstressed piles (predominantly Row-2 piles) and X-brace joints. The main reason for that is the change in the design regime (design hydrodynamic coefficients, hydrodynamic marine growth thickness, etc.) and installation of additional facilities on the platform over a period of time. All these factors have contributed to an increase in the hydrodynamic loading by more than 45%.

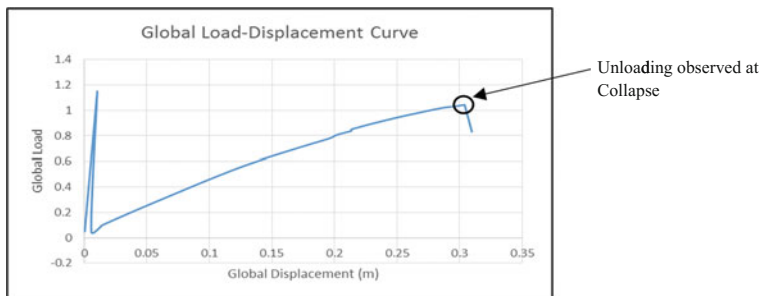
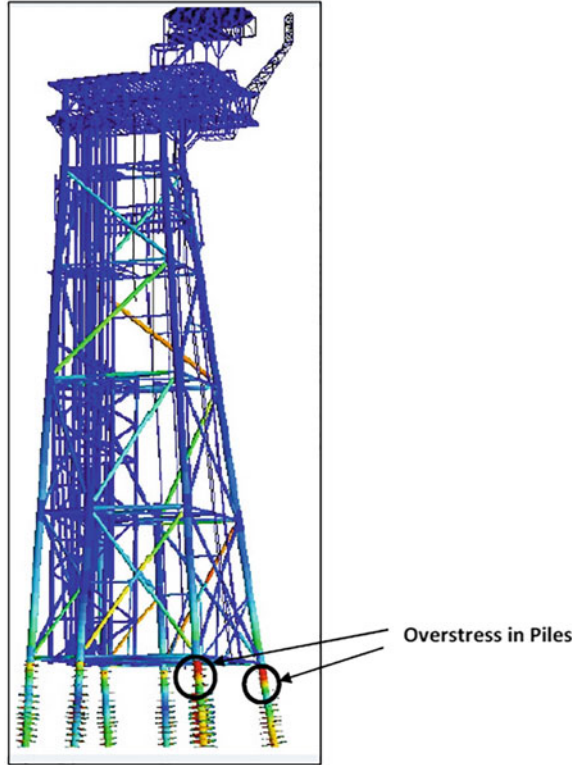


Fig. 2 Jacket structural collapse around a load level of 1.05

Fig. 3 Failure of row-2 piles, depicting plastic utilization



3 Additional Piles/Strengthening Requirement

3.1 Load Transfer and Load Distribution Mechanism for Additional Pile Arrangement

In view of the insufficient capacity of the jacket structure to withstand the design loading, an analysis study for installation of additional piles along with grouting of overstressed joints and members is contemplated.

The existing piles on Row-2 of the platform are found to be highly overstressed, and hence, additional piles have been contemplated to be installed near them. For ensuring proper load transfer, adequate strength pile connection needs to be designed, fabricated, and installed. The load distribution pattern needs to consider the fact that the vertical loads due to self-weight of the structure and topside (deck) loading would have already mobilized the pile-soil resistances for the existing piles, and the additional piles will only be contributing toward sharing the incident environmental loading. To assess the structural adequacy of the additional piles for sharing the environmental loading on the jacket structure, two separate analysis studies (with 100% loading) have been carried out:

1. In-place design-level analysis with only existing piles considering only gravity loads (100%)
2. In-place design-level analysis with all piles (incl. additional piles) considering only environmental loads (100%)

The effects on the support system (pile-soil system) were then combined to achieve the pile head loads for ascertaining the pile material utilization and soil capacity utilization (refer Table 3). It is important to note that pile material utilization is of utmost concern as the jacket structure was having highly overstressed piles in its original condition. An iterative procedure was adopted for the selection of adequate pile size for providing sufficient support capacity, and therefore, pile sizes ranging from 60 in. up to 84 in. were checked for. Following this procedure, it was finally proposed to install four 84 in. (2.134 m) additional piles on Row-2 of the platform (two additional piles each at pile location A2 and B2); thereby all the piles been found to meet the requisite strength requirements.

Additionally, the exact new pile intra-spacing and distance from existing piles on Row-2 (refer Fig. 4) will have to be ascertained for assessing the load distribution and pile group effects. The proximity to which the installation barge could approach the platform and the obstruction posed due to the structure deck needs to be duly considered.

Table 3 Factor of safety for extreme storm condition for both compression and pull out for well platform

Pile No.	Location	Min. FOS in compression ^a	Min. FOS in pull out ^a	Max. pile UC ^a
1	A1	2.46	3.51	0.408
2	B1	2.08	4.08	0.683
3	A2	2.88	7.51	0.647
4	B2	2.63	20.58	0.925
5	SKA	1.93	5.05	0.246
6	SKB	1.55	5.83	0.532
7	A2 (NP1)	2.56	1.95	0.302
8	A2 (NP2)	3.24	2.29	0.262
9	B2 (NP1)	3.18	2.25	0.276
10	B2 (NP2)	2.23	2.23	0.303

^aSump-pump caisson and future riser protector considered to be removed

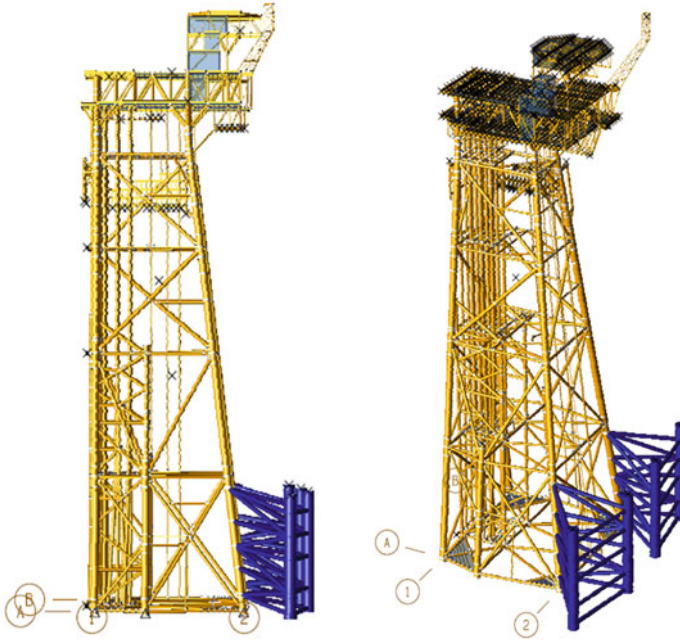


Fig. 4 Structural model with additional piles

3.2 Proposed Additional Pile Details

Number: 4

Size: 2.134 m (84 in. outer diameter) \times 0.065 m (Thickness)

Vertical Penetration below mud line: 45.5 m

It is to be noted that after carrying out the strengthening of the jacket structure with additional four piles on Row-2 of the structure, the load redistribution has effectively resulted in the reduction of stresses in some of the adjacent members and joints, e.g., the Row-A and Row-B primary X-brace joints (b/w EL (-) 52.76 m and EL (-) 77.455 m) were now found to be stressed within permissible limits.

3.3 Grouting Scheme

One of the primary structural members and two primary structural joints were found to be overstressed after carrying out the analysis with additional piles; so, strengthening of these components has been proposed. The analysis has been carried out after considering the strengthening of the member 0001-404L with adequate strength grout [6] (Fig. 5), the results of which reveal that the member is stressed within the permissible limits. The results of the re-analysis performed after

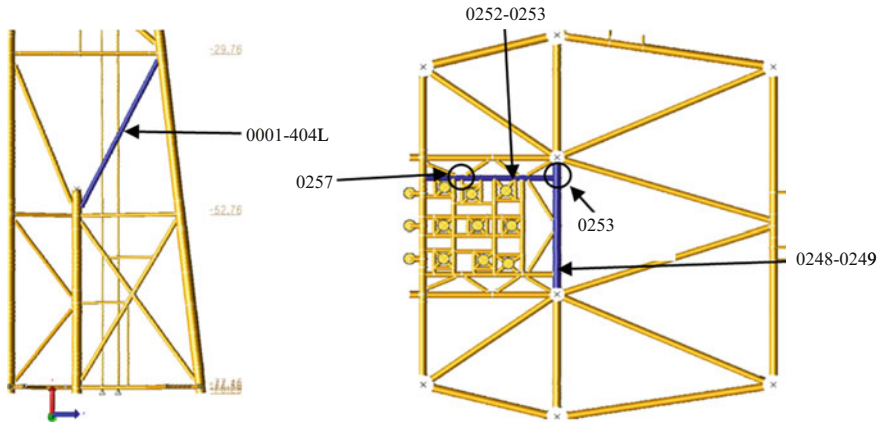


Fig. 5 Structural components proposed for grouting (as highlighted)

considering the strengthening of the respective chords for joints 0253 and 0257 with adequate strength grout (Fig. 5) reveal that the structural joints 0253 and 0257 are stressed within the permissible limits.

4 Conclusion and Recommendations

The results of the structural analysis show that in the original condition, even after incorporating the suggested mitigation measures, the jacket structure of the platform did not meet the structural adequacy requirements primarily due to overstressed Row-2 piles and X-brace joints.

In view of the same, it has been contemplated to install four additional piles near Row-2 of the platform. A design-level analysis has been carried out with additional piles proposed to be installed on the platform. The structural adequacy of the platform could be documented for all the considered environmental directions subject to the following mitigation/strengthening measures:

1. Removal of sump and pump casing,
2. Non-consideration of future riser protector on Row-2 of the structure,
3. Installation of additional four 84" (2.134 m) piles on row-2 of the platform (two each at A2 and B2), and
4. Grouting of primary structural member 0001-404L and primary joints 0253 (Joint Chord member 0248-0249 to be grouted) and 0257 (Joint Chord member 0252-0253 to be grouted)

The additional pile-jacket connection details along with final additional pile penetration below mud line, and members grout properties will be required to be designed while carrying out the detailed engineering. From above, it can be

concluded that old-age platforms can be re-qualified with the implementation of appropriate mitigation measures adopted after carrying out detailed nonlinear assessment of the structure. These structures can continue production of hydrocarbons without pressing the need of platform abandonment process or installation of new platforms.

Acknowledgements We acknowledge the support and resources provided by ONGC required for carrying out this study. The study has been immensely beneficial in understanding the pertinent issues relevant to the structural behavior of jacket structures and is of vital importance in purview of ONGC's operational requirements to carry out life extension studies of existing platforms. We extend our sincere thanks to Shri C. Tandi, ED-HoI, IEOT-ONGC for his generous support and encouragement. We are also immensely grateful for the continuous motivation received from Shri Dinesh Kumar, GGM (Civil)-Head of Structures Section, IEOT-ONGC.

References

1. IEOT—ONGC: re-qualification methodology for fixed offshore platforms in west coast of India, IEOT-LIFE-001, rev. 4, 2012-06-05
2. J. Chakrabarty, *Theory of Plasticity* (McGraw-Hill International, New York, 1987), p. 1987
3. ULTIGUIDE—guidelines for ultimate strength analyses of fixed offshore structures, DNV—SINTEF—BOMEL (1999)
4. DNV-OS-C101, Design of offshore steel structures, general (LRFD method) (April 2011)
5. API RP-2A WSD, Recommended practice for planning, design and constructing fixed offshore platforms—working stress design. API Recommended practice 2A-WSD, 21st ed. Supplement 3 (2007)
6. Assessment of repair techniques for ageing or damaged structures, doc. ref. C357R001 Rev 1, MSL Engineering Limited

Structural Integrity Assessment of a Reactor Pressure Vessel Using State-of-the-Art Methodologies—A Case Study

V. Chaudhry, S. M. Ingole, A. K. Balasubrahmanian and U. C. Muktibodh

Abstract Structural integrity assessment of reactor pressure vessel (RPV) has been carried out for design life of the reactor using state-of-the-art methodologies. Irradiation damage is the governing material degradation for core belt region of RPV, and it is quantified based on the surveillance program. Structural integrity assessment has been carried out for the postulated flaw at the core belt region to demonstrate the protection of the vessel against catastrophic failure, plastic collapse, and tearing instability. Protection against catastrophic failure has been demonstrated based on the linear elastic fracture mechanics (LEFM) approach. Stable crack extension and flaw stability due to ductile tearing have been demonstrated based on J -integral and failure assessment diagram (FAD). Limiting values of flaw depth and flaw length have been evaluated to demonstrate the protection against all failure modes. Further, leak-before-break (LBB) criterion has been adopted to demonstrate the defense in depth philosophy. Limiting flaw length to depth ratio has been quantified in order to demonstrate leak-before-break criterion. The assessment has demonstrated the healthiness of the vessel for safe operation.

Keywords Irradiation damage · Catastrophic failure · Plastic collapse · Tearing instability · Leak-before-break

1 Introduction

Reactor pressure vessels (RPVs) are designed and fabricated in accordance with consensus codes and are considered as life-limiting component for light water reactors (LWRs). Selection of the material for RPVs is generally based on the special considerations pertaining to high strength, good hardenability, and excellent fracture properties. Commonly used materials in the construction of vessels for LWRs are ASTM SA 302Gr B (plates)/SA 508 class 2 in the USA, 20MnMoNi55

V. Chaudhry (✉) · S. M. Ingole · A. K. Balasubrahmanian · U. C. Muktibodh
Nuclear Power Corporation of India Limited, Mumbai 400094, India
e-mail: vchaudhry@npcil.co.in

in Germany, 16MnD5 in France, and 15X2HMΦA in Russia. Although many other materials are acceptable for reactor vessels, the choice is limited due to consideration of fracture toughness and radiation-induced material degradation.

A typical RPV of boiling water reactor has been considered to demonstrate its structural integrity for its design life, say 40 years. The life-limiting region of RPV is the core belt region where the irradiation damage is the governing material degradation. Large efforts have been made in many countries to characterize the irradiation-induced damage in RPV steels as well as to understand and model the mechanism governing the damage through experimental studies in research reactor and through surveillance programs. The results obtained can be used to forecast the behavior of RPV material under irradiation environment. Now, it is well understood that the susceptibility of RPV steel to radiation damage is strongly affected by the presence of copper, nickel, phosphorus, and manganese [1]. The correlations for predicting the irradiation damage to the material are available in US Nuclear Regulatory Commission (USNRC) Guide RG 1.99 Revision 2 [2], ASTM E 900-02 [3], and ASME Section XI Appendix G [4].

Structural integrity assessment of RPV has been carried out to rule out the typical failure modes of RPV for the design life of the reactor, and also to demonstrate the protection against the instability for the postulated defect in the core belt region. Typical failure modes are non-ductile failure, plastic collapse, and tearing instability. ASME codes provide the guidelines for integrity assessment considering these failure modes [4]. The assessment is made based on postulating a defect in core belt region having a depth of quarter thickness and length of one-and-half the thickness. Limiting flaw length to depth ratio has been quantified in order to demonstrate leak-before-break criterion.

2 Design Details of RPV

RPV considered in the present study is a cylindrical shell of ASTM SA 302Gr B (plates) with an inside diameter of around 4000 mm, length of 20,000 mm, and thickness of 124 mm having hemispherical top and bottom heads with thickness of 102 mm. The inside surface of the vessel is clad with stainless steel of 5 mm thickness. Figure 1 shows the schematic of a typical BWR pressure vessel [5]. The loading conditions considered for the assessment of the vessel are:

- *Design condition*: Design pressure of 8.75 MPa and design temperature of 300 °C.
- *Normal operating condition (NOC)*: Normal operating pressure of 7.0 MPa, operating temperature of 286 °C, and heating and cooling rate of 55 °C/h.
- *Upset condition*: Normal operating pressure of 7.0 MPa, operating temperature of 286 °C, and cooling rate of 150 °C/h.
- *Test condition*: Hydro test at 7.7 MPa with heating rate of 55 °C/h (the heating rate are much less than 55 °C/h in test condition).

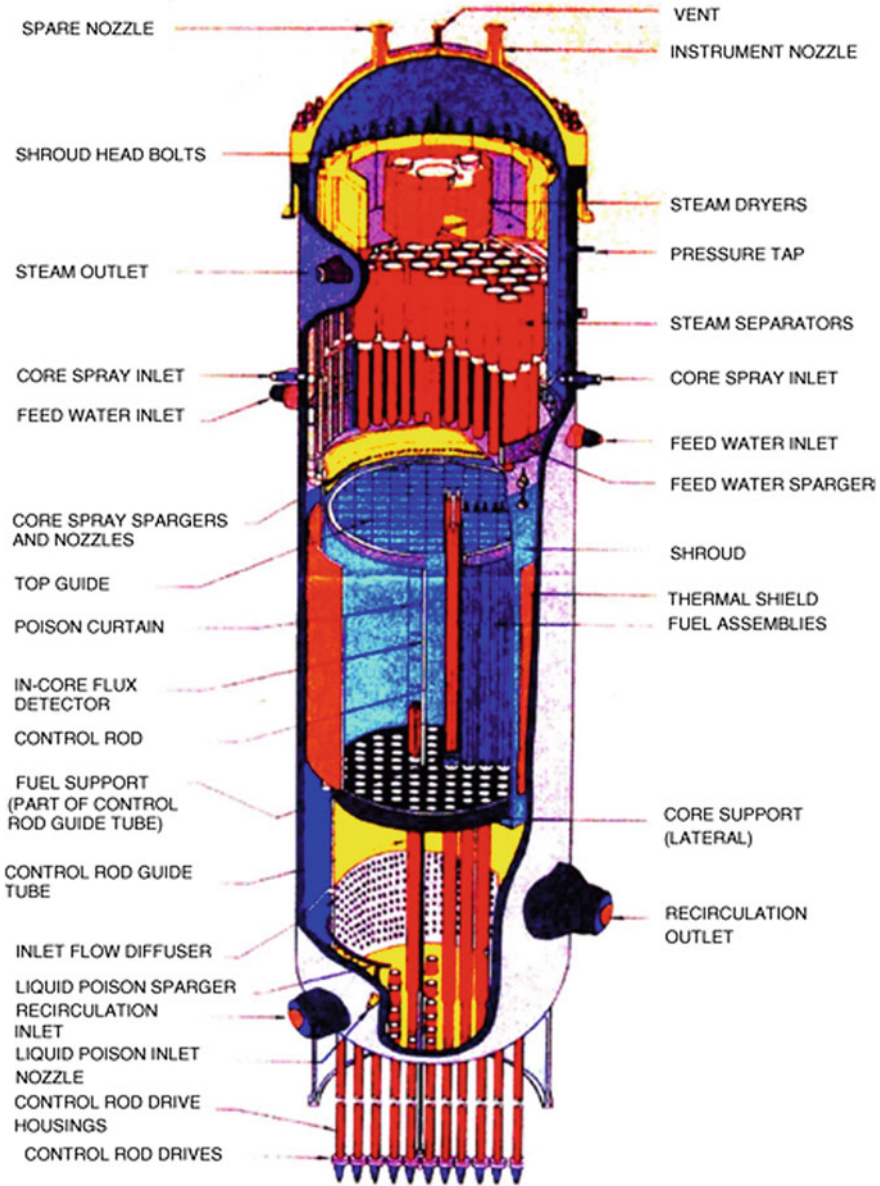


Fig. 1 Typical boiling water reactor vessel [5]

The most severe transient for light water reactors comes from the combination of thermal stresses (resulting from rapid cooling) and stresses due to internal pressure. BWR vessels operate with a large inventory of water at saturation condition so that

any cooling transient would result in steam condensation, and results in system depressurization, preventing the coupling of high thermal and pressure stresses.

Structural integrity assessment for different failure modes has been carried out based on postulating an elliptical defect in vessel wall core belt region having a depth of quarter wall thickness and length of one-and-half thickness.

3 Irradiation Damage Quantification

As discussed earlier, the correlations for prediction of shift in ductile-to-brittle transition temperature are available in US Nuclear Regulatory Commission (USNRC) Guide RG 1.99 Revision 2, ASTM E 900-02, and ASME Section XI Appendix G. These correlations can be used to evaluate the shift in ductile-to-brittle transition temperature due to irradiation damage in a material under operating condition and neutron fluence. These correlations were developed from large number of surveillance data from pressurized water reactors (PWRs) and boiling water reactors (BWRs). Over a period of time, understanding of the damage mechanisms was developed such that the correlations are mechanistically driven rather than being purely statistical in nature. This aspect is of great importance when the correlations are extrapolated beyond the maximum value of the database, for example, deciding the design life of a reactor.

In the USA, the radiation embrittlement of RPV beltline material is assessed by RG1.99 Revision 2 and 10CFR 50.61. The 41 J temperature is used as the index for transition temperature shift based upon ASTM specified Charpy V-notch (CVN) impact test. The guide RG1.99 gives a method for estimating the shift in the ductile-to-brittle transition temperature (DBTT) and the drop in the Charpy upper-shelf energy (USE). The correlations specified in RG1.99 were derived statistically from a database containing fewer than 170 surveillance data points. Later, significant data has been generated and published from material test, a program which has enhanced the mechanistic understanding of the microstructural changes in the material leading to embrittlement. ASTM E 900-87, a standard guide for predicting neutron radiation damage to reactor vessel materials, was issued based on 216 CVN surveillance data points. Later, Electric Power Research Institute (EPRI) sponsored to evaluate independently the mechanistic and statistical bases from the data consisting of 752 measurements (80–90 were from BWR surveillance) and new correlation was developed, details of which are provided in EPRI technical report [6]. The EPRI correlation was accepted by ASTM E 900-02. Further, additional 62 data points from BWR surveillance program were produced. The assessments showed that the BWR data points were not predicted well by the correlations based on PWR dominated data. In particular, the embrittlement shift for BWR material tends to underpredicted by ASTM E 900-02. As a result, additional work was carried out to generic improved correlations for both PWR and BWR. One of the correlations proposed by Oak Ridge National Laboratory (ORNL) [7]

with additional 24 BWR data values is presently adopted by ASME Section XI Appendix G [4].

4 Assessment Details

4.1 Protection Against Catastrophic Failure

To demonstrate the protection against catastrophic failure of vessel, structural integrity assessment has been carried out as per ASME Section XI Appendix G [4]. The criteria for the protection against catastrophic failure is given by,

$$2K_{1m} + K_{1t} < K_{1c} \quad (1)$$

where K_{1m} and K_{1t} are the stress intensity factors (SIF) under pressure and thermal loadings and are evaluated using the methodology given in ASME Section XI Appendix G [4]. The defect is postulated in axial and circumferential direction at inside and outside surface of the vessel. Equation (1) needs to be satisfied for startup/shutdown condition for the postulated flaw in axial and circumferential direction for different operating conditions. Table 1 provides the SIFs for different operating conditions and its comparison with the critical stress intensity (K_{1c}). The K_{1c} value has been evaluated according to ASME Section XI Appendix G depending on the operating temperature and the shift in DBTT (discussed in Sect. 3). The K_{1c} value is considered here as 240 MPa√m (upper bound value).

It is evident from Table 1 that the maximum SIF is observed to be for an axial flaw on inside surface under shutdown condition. This is from the fact that under shutdown condition, the thermal gradient produces significant tensile stress at inside surface of the vessel.

Table 1 SIF for postulated flaw under different operating conditions

S. No.	Operating conditions	Postulated flaw location	$2K_{1m} + K_{1t}$ (MPa√m)				K_{1c} (MPa√m)
			Hydro test	Design condition	NOC	Upset condition	
1	Startup	Axial flaw on inside surface	74.15	84.26	67.40	67.4	240
2	Startup	Axial flaw on outside surface	75.66	85.39	69.17	69.17	240
3	Startup	Circumferential flaw on outside surface	39.73	44.56	36.5	36.5	240
4	Shutdown	Axial flaw on inside surface	79.58	89.69	72.8	82.23	240
5	Shutdown	Circumferential flaw on inside surface	40.87	45.69	37.64	47.03	240

4.2 Protection Against Plastic Collapse

The limiting values of flaw depth and flaw length have been evaluated as per ASME Section XI Appendix C [4] presuming that plastic collapse is the dominant mode of failure.

The allowable flaw length (L_f) for end-of-evaluation period is given by,

$$L_f = 1.58 (R_m t)^{0.5} \left[\frac{\sigma_f^2}{\sigma_h^2} - 1 \right]^{1/2} \quad (2)$$

where σ_f is the flow stress, σ_h is the hoop stress, R_m is the mean radius of vessel, and t is the vessel thickness.

The allowable flaw lengths for hydro test pressure (7.7 MPa) and design pressure (8.75 MPa) are 2874.8 and 2501.57 mm, respectively. The allowable flaw depth at the end-of-evaluation period flaw length L_f is given by,

$$a/t = \frac{M_2(1 - S)}{M_2 - S} \quad (3)$$

where $M_2 = \left[1 + L_f^2 \left(\frac{1.61}{4tR_m} \right) \right]^{1/2}$ and $S = SF_m \sigma_h / \sigma_f$, SF_m is the structural factor taken as 2.7 and 2.4 for normal and upset operating conditions, respectively.

The allowable flaw depths of cylindrical shell for hydro test condition and design pressure are 119.61 and 119.75 mm, respectively. The applicability of Eq. (3) is limited to a flaw depth of 93 mm ($0.75t$). Thus, protection against plastic collapse for a flaw of depth 93 mm and length 2501.57 mm has been demonstrated.

4.3 Protection Against Tearing Instability

The evaluation procedure and acceptance criteria used to demonstrate structural integrity of RPV are specified in ASME Section XI Appendix K [4]. The approach is used to check the effect of low upper-shelf energy on the plastic zone at the crack tip which dictates the tearing stability. The original purpose of appendix K was to demonstrate the structural integrity of RPV with low upper-shelf energy (USE). The technical basis for Appendix K is described in WRC bulletin 413 [8]. The approach is equally applicable to any region of the reactor vessel where the fracture toughness can be described with elastic plastic parameters.

In order to demonstrate the flaw stability, there are two acceptable methods as per ASME Appendix K, for a vessel with wall thickness lesser than 150 mm.

Method-1

Criteria-1: This criteria state that a crack starts growing when the applied J_I equals the material resistance to crack initiation J_{IC} ($J_{0.1}$).

$$J_I \leq J_{0.1} \tag{4}$$

where J_I is the applied J -integral considering a structural factor of 1.15 on maximum pressure (overpressure) and 1.0 on thermal loading, and $J_{0.1}$ is J -integral resistance of a ductile flaw extension of 2.5 mm.

The material properties used in the assessment are taken from EPRI report [9]. To be on a conservative side, the sulfur content of the vessel is assumed to be more than 0.018%. The estimated mean minus two standard deviation bilinear J - R curve of the material (200–287 °C) is shown in Fig. 2, having $J = J_{IC}$ at $da = 0$ to $J = 1.31J_{IC}$ at $da = 2.54$ mm, and $J = 1.31J_{IC}$ for all crack extensions greater than 2.54 mm.

Applied J -integral for axial flaw, $J_{app} = 18.16$ kJ/m²

Applied J -integral for circumferential flaw, $J_{app} = 5.0145$ kJ/m²

$J_{0.1} = 92.7$ kJ/m² (Fig. 2)

Thus, $J_I \leq J_{0.1}$

Criteria-2: This criterion demonstrate flaw stability due to ductile tearing,

$$\frac{\partial J}{\partial a} \leq \frac{\partial J_R}{\partial a} \quad \text{at } J_{app} = J_{mat} \tag{5}$$

The structural factor considered are 1.25 on pressure and 1.0 on thermal loading.

Figure 3 shows the comparison of the slopes of the applied J -integral curve and the material J - R curve for axial and circumferential flaws, respectively. The slopes of applied J -integral curve are lower than the J - R curve for the material, and thus,

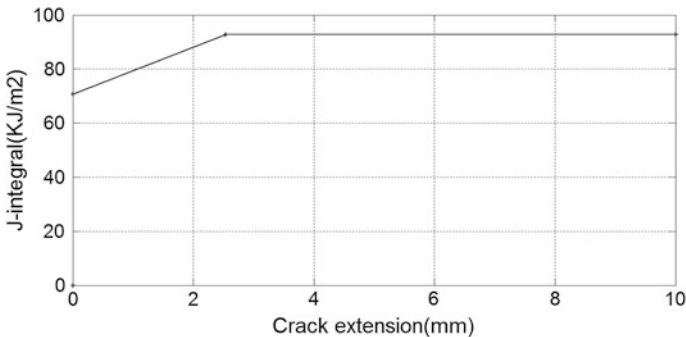


Fig. 2 Bi-linear J - R curve for low-alloy steel material [9]

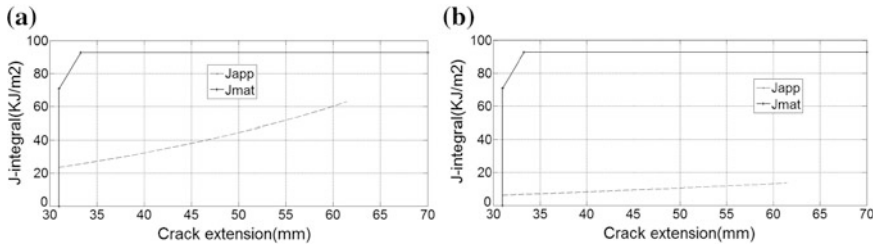


Fig. 3 Comparison of the slopes of the applied J -integral curve and the J - R curve for **a** axial flaws **b** circumferential flaws

demonstrate the stability against the ductile tearing for a flaw depth equal to half the vessel wall thickness.

Thus, the Method-1 demonstrated the stability against crack growth for a postulated flaw of quarter thickness depth and stability against ductile tearing for a flaw depth equal to half the vessel wall thickness.

Method-II

This method uses failure assessment diagram (FAD) curve for checking the stability of postulated axial and circumferential cracks. Using this method, crack initiation or tearing instability can be determined by plotting the calculated assessment points on FAD. For crack initiation, the assessment point must fall inside the curve. The curves provided in ASME Appendix K [] are based on material properties which are characteristics of reactor pressure vessel steels, which includes SA 302Gr A and B, SA 533 Gr B class 1, and SA 508 classes 2 and 3 steels. The FAD curves for axial and circumferential flaws are reproduced in Fig. 4. Figure 4 shows that all the assessment points for a flaw having depth ranging from $0.25t$ to $0.35t$ lie inside the failure assessment curve. Thus, the acceptance criteria based on J -integral approach (method-1) are validated using alternative FAD approach, which accounts the interaction effect of fracture and plastic instability.

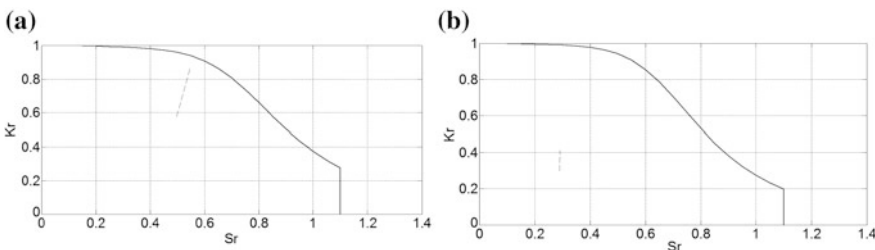


Fig. 4 FAD along with failure assessment points for the postulated **a** axial flaws **b** circumferential flaws for depth varying from $0.25t$ to $0.35t$

4.4 Leak-Before-Break (LBB)—A Conceptual Approach

A part through crack in pressure vessel may grow by fatigue or stress corrosion until it reaches the outer surface. This possibility exists if there is a crack at vessel inside surface and it starts growing. If this crack once become through wall, the vessel starts leaking, and there is sufficient time (time available between the detection and the crack reaches a critical size or become unstable) available for corrective action, then the criterion of leak-before-break is applicable. In order to demonstrate the LBB criterion, it is essential to evaluate the limiting flaw length to depth ratio which provides leak indication prior to break.

A simplified leak-before-break criterion was purposed by Irwin [10]. The criteria were based on the fact that a surface flaw will be semicircular when it pops through the vessel wall, implying that it develops a through-wall crack of length equal to twice the vessel thickness. This approach is oversimplified approach and does not give a solution for surface flaws longer than twice the thickness. A more general LBB criterion can be derived on the basis of fracture mechanics principles in order to evaluate the limiting flaw length to depth ratio.

The fracture condition of a surface flaw, after accounting the correction for back free surface, plastic zone, and the proximity of the free surface in front of the crack (Fig. 5), is given by [11]

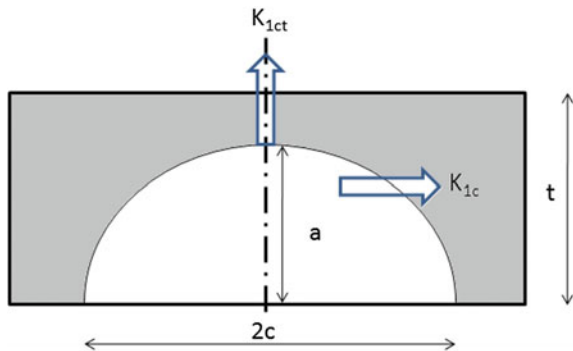
$$K_{1ct} = 1.12M_k(p_1/\Phi)(1 + R/t)\sqrt{\pi a} \tag{6}$$

where M_k is the Kobayashi stress intensity magnification factor, R is the mean radius of vessel, p_1 is the internal pressure for unstable propagation of surface flaw, a is the flaw depth, and Φ can be approximated as,

$$\Phi = (\pi/8)(3 + a^2/c^2) \tag{7}$$

where c is the half crack length.

Fig. 5 Schematic representation of the crack



Consider a surface flaw which will grow to become a through-wall crack of size $2c$. The fracture condition is given by [11],

$$K_{1c} = M_F p_2 (R/t) \sqrt{\pi c} \tag{8}$$

where M_F is the Folias correction factor and is equal to 1 for large R/t ratio, p_2 is the unstable propagation of the through-wall crack, and c is the half crack length.

Crack will be arrested when the pressure to propagate a through-wall crack of length ‘ $2c$ ’ is greater than the pressure for instability of a flaw having a depth ‘ a .’ Hence, the LBB criterion follows from $p_2 > p_1$ and is given by,

$$\frac{K_{1c}}{K_{1ct}} > \frac{\Phi M_F (R/t)}{1.12 M_K \left(1 + \frac{R}{t}\right) \sqrt{a/c}} \tag{9}$$

Assuming that the vessel is made of rolled plates and possess anisotropy in mechanical properties, specifically, in CVN or fracture toughness. The CVN or fracture toughness in the transverse direction is around 65% of the longitudinal values [12]. Further, it has been assumed that fracture toughness in transverse and normal direction is same. This implies that the ratio K_{1c}/K_{1ct} for pressure vessel will be 1.54.

Figure 6 shows the variation of the ratio K_{1c}/K_{1ct} versus $a/2c$ for different a/t ratio. The variation of limiting flaw length with flaw depth is shown in Fig. 7. It is evident that for demonstration of LBB, the limiting length of flaw is around 4–6 times the flaw depth.

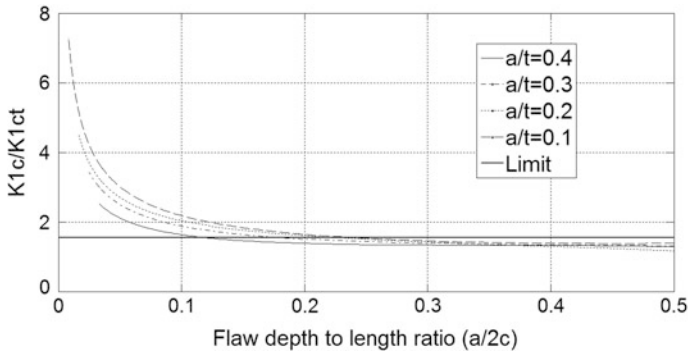
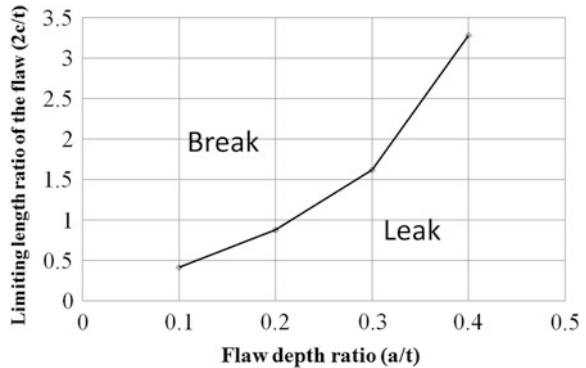


Fig. 6 Variation of the ratio (K_{1c}/K_{1ct}) versus $a/2c$ for different a/t ratio

Fig. 7 Limiting flaw length and flaw depth based on LBB criterion



5 Conclusion

Structural integrity assessment of reactor pressure vessel of a typical BWR has been carried out to demonstrate the protection of vessel against catastrophic failure, plastic collapse, and tearing instability using state-of-the-art methodologies. As a defense in depth, the vessel has been qualified for LBB criterion and limiting flaw length to depth ratio has been quantified. The assessment has demonstrated the healthiness of the vessel for its design life.

References

1. IAEA Nuclear Energy Series, No NT-T-3.11 (2009)
2. USNRC Regulatory Guide 1.99 Rev 2 (1988)
3. ASTM E 900-02, Standard guide for predicting radiation-induced transition temperature shift in reactor pressure materials, E706, Reapproved-2007
4. ASME Section XI, 2015
5. S.C. Katiyar, S.S. Bajaj, Tarapur atomic power station units-1 and 2: design features, operating experience, and license renewal. *Nucl Energy Des* **236**(7–8), 881–893 (2006)
6. EPRI technical report, BWR Pressure Vessel Embrittlement correlation studies, 1019056 (2009)
7. E. Eason, G.R. Odette, R.K. Naustad, T. Yamamoto, A physically based correlation of irradiation-induced transition temperature shifts for RPV steels, ORNL report, ORNL/TM-2006/530 (2007)
8. WRC bulletin 413, Development of criteria for assessment of reactor vessels with low upper shelf fracture toughness (Welding Research Council, New York, 1996)
9. EPRI report, Evaluation of the toughness properties and ASME service A/B upper shelf toughness criteria for A 302B vessel steel, report no. TR-103434 (1994)
10. G.R. Irwin, *Fracture of Pressure Vessels*, McGraw-Hill (1963)
11. D. Broek, *Elementary Engineering Fracture Mechanics* (1978)
12. USNRC RG 1.161, Evaluation of Reactor Pressure vessel with Charpy upper-shelf energy less than 50ft-lb (1995)

Sodium-Free Level Fluctuations: Concern on Structural Integrity for the Pool-Type Sodium-Cooled Fast Breeder Reactor

V. R. Chandan Reddy, R. Suresh Kumar, Anil Kumar Sharma,
K. Velusamy and P. Selvaraj

Abstract In the case of sodium-cooled pool-type fast breeder reactor, the weight of the entire reactor assembly along with sodium coolant is carried by a large-sized cylindrical vessel called the main vessel. Since main vessel is one of the primary boundaries from the radiation shielding point of view, the structural integrity of the main vessel is an essential safety feature to be ensured under all operating conditions. The inner surface of the main vessel is partly filled with high-temperature sodium coolant, and the remaining part is in contact with relatively low-temperature argon cover gas. Due to large surface area of the main vessel pool, the free surface level of the sodium oscillates. This environment creates drastic temperature cycling in the main vessel wall at the sodium-free level interface. This transient temperature cycling imposed on the main vessel with negligible attenuation can lead to high-cycle thermal fatigue damage in the vicinity of sodium-free level. This high-cycle thermal fatigue can be detrimental in ensuring the structural integrity of the main vessel considering the number of cycles (approximately 9.5×10^8 cycles) applied in the plant's lifetime. This paper presents the numerical studies carried out towards assessing the structural integrity of the main vessel by considering the effect of sodium-free level fluctuations. The magnitudes of level fluctuations of 100 and 30 mm with a frequency range of 0.1–10 Hz with different increment of frequencies are considered as a parametric study. In this study, the critical portion due to level fluctuation has been identified from the thermal stress cycling point of view, and the effect of level fluctuation frequency on the structural integrity of the main vessel has been quantified.

Keywords Level fluctuation · Fast breeder reactor · High-cycle fatigue
Structural integrity

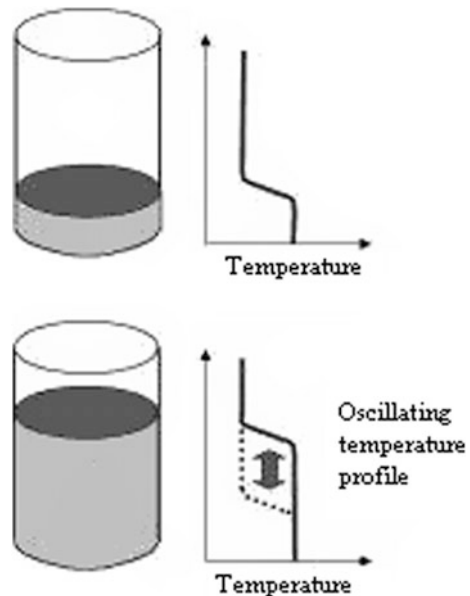
V. R. Chandan Reddy (✉)
Homi Bhabha National Institute, Anushaktinagar, Mumbai 400094, India
e-mail: chandanreddy.vr@gmail.com

V. R. Chandan Reddy · R. Suresh Kumar · A. K. Sharma · K. Velusamy · P. Selvaraj
Reactor Design Group, Indira Gandhi Centre for Atomic Research, Kalpakkam 603102,
Tamil Nadu, India

1 Introduction

Prototype fast breeder reactor (PFBR) is a 500-MWe-pool-type reactor, with sodium as a coolant, which is contained within the main vessel of diameter 12,900 and 12,700 mm height. The total surface area of the main vessel is around 700 m² and the volume is 1500 m³. Liquid sodium coolant with its excellent heat transfer properties provides better natural heat removal capability in the pool-type reactor. However, from the structural mechanics point of view, there are certain critical problems, associated with sodium particularly during thermal transients that occur under various operating conditions [1]. The structural material 316LN austenitic stainless steel (SS 316LN) has low thermal conductivity and high thermal expansion coefficient. The critical combination of SS 316LN and sodium induces high thermal stress even for a small change in temperature. The main vessel is filled with hot liquid sodium, and it is covered with inert argon cover gas to prevent it from interacting with atmospheric gases. The heat transfer properties of argon are weak. The thin walled vessel in the vicinity of sodium free level experience high temperature fluctuations just below the free level, and the portion above the free level experience low-temperature argon cover gas. This induces a large temperature gradient in the vicinity of sodium-free level as shown in Fig. 1. Further, due to large sodium pool surface area, the sodium-free level oscillates. So the temperature gradient at the sodium-free level also oscillates inducing transient temperature cycling in the main vessel-free level portion. These thermal fluctuations can lead to high-cycle thermal fatigue of the immersed components.

Fig. 1 Temperature profile oscillation due to sodium level fluctuation in a reactor vessel



Due to good heat transfer properties of sodium, the wetted surface of the structure attains the temperature of sodium immediately. But the depth of penetration of temperature depends on the amplitude and frequency of surface temperature oscillations. In the present study, detailed transient thermal stress analysis has been performed using the idealised model of the reactor vessel as depicted in Fig. 2a to study the characteristics of thermal stress fluctuation in the main vessel structural wall.

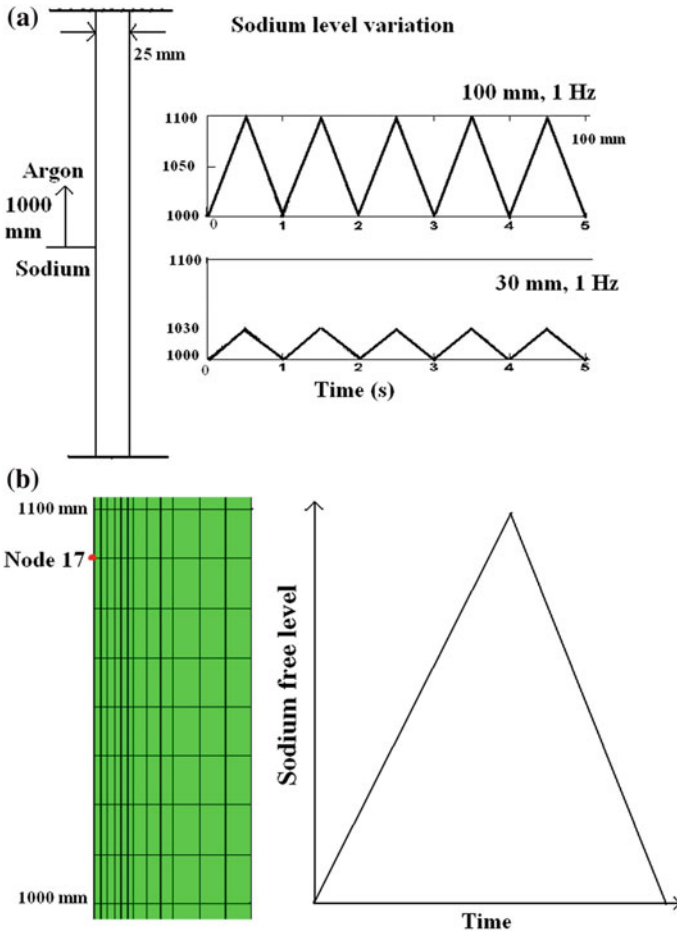


Fig. 2 a Mathematical model of reactor vessel, b finite element mesh

2 Frequency and Amplitude of Level Fluctuations

The typical main vessel geometry considered for studying the level fluctuation is 12,900-mm-diameter and 25-mm-thick vessel. The experiments conducted by Laxman et al. [2] on the $\frac{1}{4}$ -scaled model of reactor assembly described the amplitude and frequency of level fluctuations in the reactor pool. The amplitude of level fluctuation varies from 38 to 92 mm after applying the proper scaling laws. The frequency of oscillations during the normal operating condition is in the range of 0.1–2.0 Hz. This paper also presents the study carried out for the reactor vessel for the amplitude of level fluctuations of 100 and 30 mm for a frequency range of 0.1–10 Hz using finite element simulation. The loading cycle for the level fluctuation is shown in Fig. 2a.

3 Transient Heat Transfer Analysis

The reactor vessel is modelled as an axisymmetric shell structure. Since the effect of variation is confined within 1000 mm above and 1000 mm below the vicinity of sodium-free level the main vessel is analysed for 2100 and 2030 mm for 100 and 30 mm of level fluctuation, respectively. It is analysed for a temperature difference of 100 K between sodium (675 K) and argon (575 K). An additional subroutine is formulated in the numerical tool ABAQUS [3] to create cyclic temperature variation at the curved surface of the cylinder by imposing moving temperature profile along the axis of the cylinder. The temperature profile was generated by varying the film coefficient along the axis of the cylinder [4]. Film coefficients considered for sodium is 25,000 W/m² K while that of argon is 10 W/m² K. The rate of change of the film coefficient with respect to the surface temperature is kept equal to zero. Temperature-dependent properties of SS 316LN used for the analysis are shown in Table 1. The reactor vessel is analysed for 1000 s for a frequency range of 0.1–10 Hz for both 100 and 30 mm level fluctuations.

The finite element mesh for the analysis is shown in Fig. 2b. The outcome of the analysis is the transient temperature variation at each node of the finite element model. The variation of temperature for the node 17 (node corresponding to the maximum amplitude of temperature fluctuation on the surface of the main vessel wall) and other nodes along the thickness of the reactor vessel wall at 1 Hz frequency for 100 s is shown in Fig. 3a. Initially, the amplitude of temperature variation is about 60 K on the wall surface for a temperature difference of 100 K between argon and sodium. This temperature amplitude decays with time, and steady temperature amplitude of about 20 K is achieved after about 200 cycles of level variation, and it remains same further. The temperature amplitude decay trend remains similar for all other frequencies.

Table 1 Temperature-dependent properties of SS 316 LN

Temperature (K)	Density (kg/m ³)	Thermal conductivity (W/m K)	Specific heat capacity (J/kg K)	Coefficient of thermal expansion (10 ⁻⁶ /K)	Young's modulus (GPa)
293	7966	13.94	470	15.9	192
323	7949	14.37	476	16.1	190
373	7932	15.08	486	16.4	186
423	7910	15.80	497	16.7	182
473	7889	16.52	508	17.0	178
523	7867	17.24	518	17.2	174
573	7846	17.95	529	17.5	170
623	7824	18.67	539	17.7	166
673	7803	19.39	550	17.9	161
723	7781	20.10	560	18.1	157

3.1 Temperature Variation Along the Length of the Reactor Vessel

The amplitude of temperature fluctuation on the surface of the reactor vessel wall is a function of the frequency of level oscillation and the plots for 100 and 30 mm level fluctuations at 1000 s are shown in Fig. 4a, b respectively. The maximum temperature amplitude is for 0.1 Hz frequency in both the cases, as the reactor vessel wall will be in contact with hot sodium for more time at 0.1 Hz frequency compared to other higher frequencies. The amplitude of temperature fluctuation on the surface varies along the length of the cylinder and is highest at approximately 90 and 27 mm from the bottom most point of sodium-free level for 100 and 30 mm level variations, respectively. These are the points which will be in contact with low-temperature argon cover gas for major part of the cycle. Figure 4a, b depict the amplitude of temperature fluctuations with height of reactor vessel in the vicinity of sodium-free level. From these figures, it is clear that the amplitude of temperature variation on the surface of reactor vessel wall depends only on the frequency of level variation and not a function of its amplitude.

3.2 Temperature Variation Along the Thickness of the Reactor Vessel Wall

The amplitude of temperature fluctuation in the wall decays with the increasing depth from the surface of reactor vessel wall. The temperature amplitude along the thickness of the cylinder at node 17 for 100 mm level fluctuation at 1000 s is shown in Fig. 6a. The temperature amplitude reduces to a very low value with in

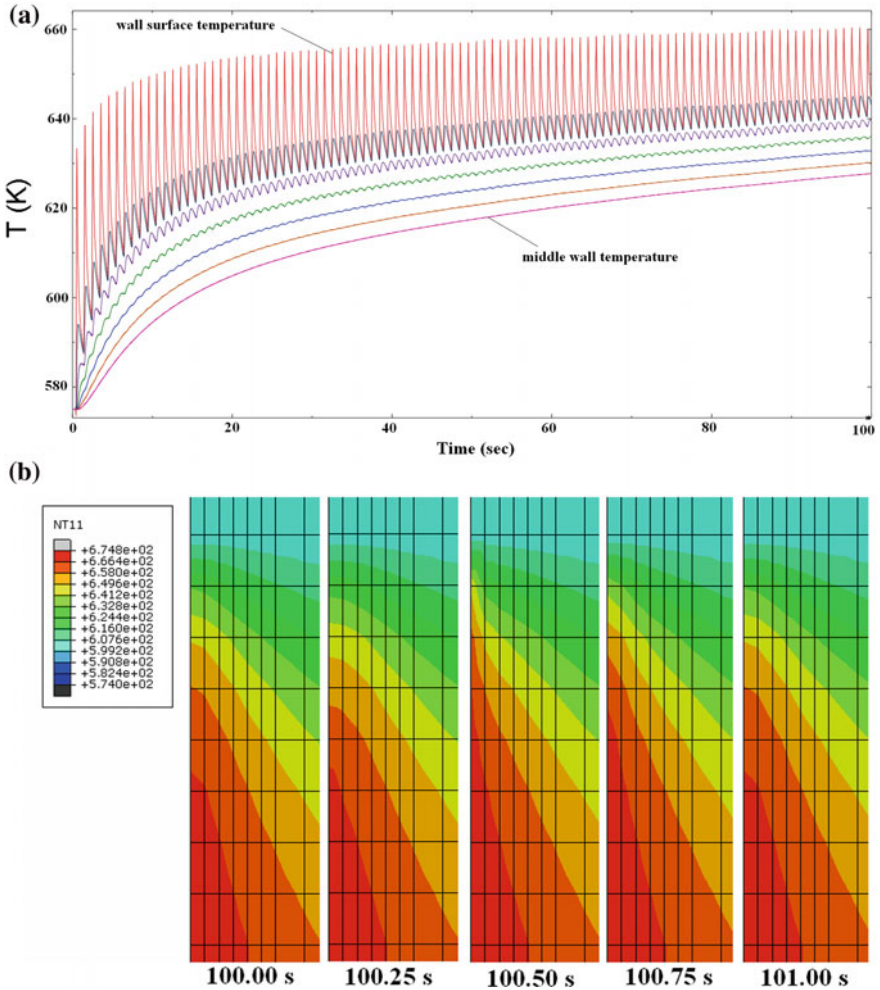


Fig. 3 a Temperature variation at node 17 and other nodes across wall thickness, b temperature contour plot at node 17 at 100 s

half the thickness of the reactor wall. And hence, the point on the inner surface of the reactor vessel wall is the location with maximum temperature amplitude at any point along the length of the cylinder, and the temperature amplitude is negligible beyond half the thickness of reactor vessel wall.

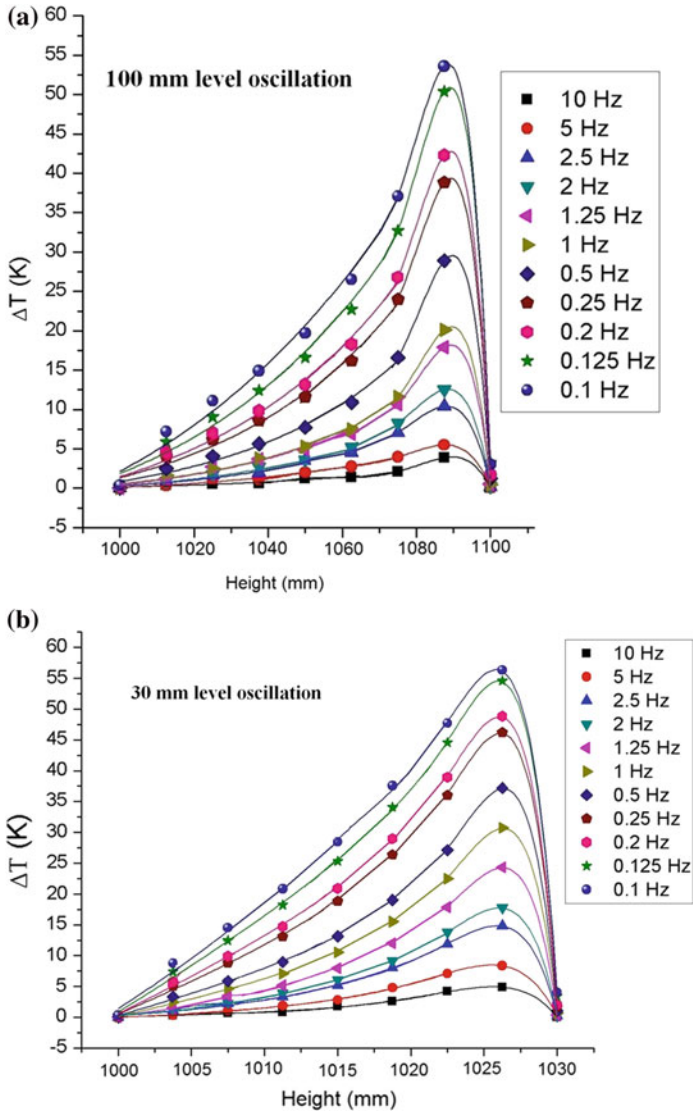


Fig. 4 **a** Amplitude of temperature fluctuation along the length of the reactor vessel for 100 mm level fluctuation, **b** amplitude of temperature fluctuation along the length of the reactor vessel for 30 mm level fluctuation

4 Transient Thermal Stress Analysis

The results of the transient heat transfer analysis are used as input for the transient linear elastic stress analysis. The same mesh of heat transfer analysis as shown in Fig. 2b is used for the stress analysis. The thermal expansion coefficient for the SS 316LN is defined as a temperature dependent property and the nodal stress components field outputs are requested. The stress variation with time for node 17 and other nodes along the thickness of the reactor vessel wall are shown in Fig. 5a. It shows that initially the amplitude of stress is high and decays with time. Steady stress amplitude is achieved after about 200 cycles of level variation. This initial transient stress region appears whenever the reactor is restarted. Since 100 reactor scrams are assumed in the design during the plant life of 40 years, this transient

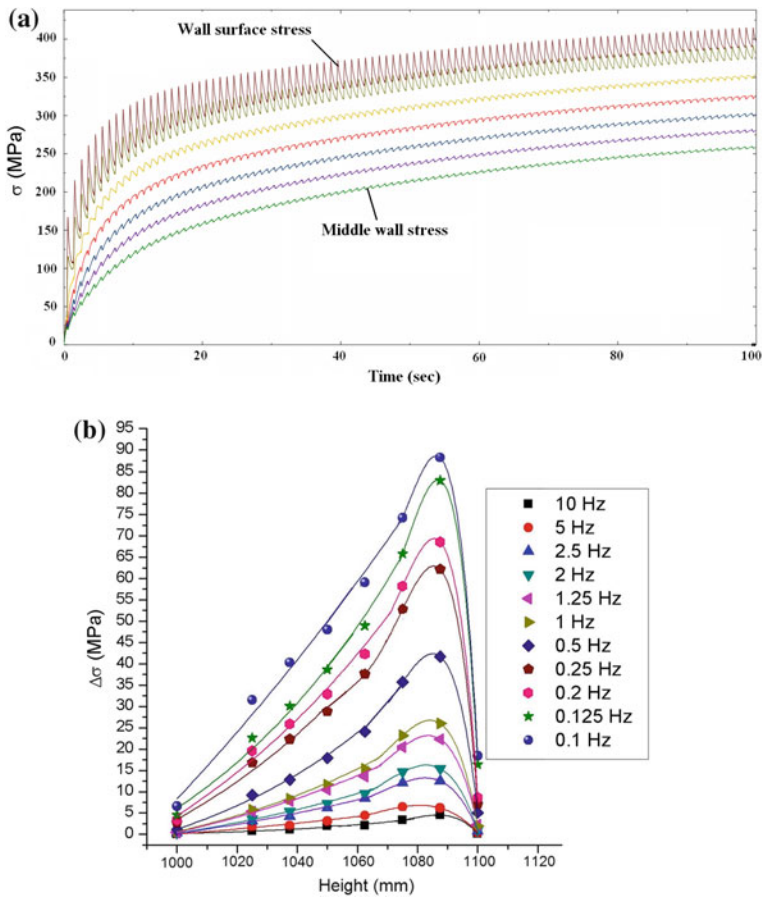


Fig. 5 a Stress across wall thickness at node 17, b stress fluctuation amplitude along the length of the reactor vessel

region is getting repeated accordingly. The damage fraction for this initial transient region is higher than the damage caused during steady-state stress amplitude. Thus depending on the number of scrams in a reactor life time, this transient stress needs to be converted to equivalent steady-state stress amplitude for accurate damage prediction.

Stress amplitude along the length of the reactor vessel increases with the amplitude of level fluctuation similar to temperature amplitude and is shown in Fig. 5b. It shows that the stress amplitude is a function of frequency of the level fluctuation and it increases with the decrease in frequency thus maximum stress amplitude is for a frequency of 0.1 Hz. The location with the maximum amplitude of stress variation is at about 90 and 27 mm from the bottom most point of sodium-free level for 100 and 30-mm-level variation, respectively. This is equivalent to 0.9 times the amplitude of level variation. Hence, the location of maximum stress amplitude is at about 0.9 times the amplitude of level variation from the bottom most point of sodium-free level irrespective of the amplitude of level variation.

The stress amplitude variation along the thickness of the reactor vessel is a function of the frequency of level fluctuation and is shown in Fig. 6b. The stress amplitude decays exponentially along the thickness and the stress variation beyond half the thickness of reactor vessel wall can be neglected. This indicates that the stress in the reactor vessel wall due to sodium level fluctuation acts like skin stresses with a large temperature gradient along the thickness of the wall. These skin stresses are critical in structural integrity point of view as the cracks are mostly initiated at the surface of the metal walls.

It can be seen from Fig. 7 that the maximum stress amplitude induced in the reactor vessel wall subjected to sodium-free level fluctuation is a function of the frequency of level fluctuation and independent of amplitude of level variation. Even though the difference between the two amplitudes of level variations is about 70 mm, there is no significant change in the maximum stress amplitude induced in the reactor vessel wall.

5 Conclusion

The analysis carried out in the present study deals with the numerical studies carried out to assess the effect on the structural integrity of the main vessel subjected to sodium-free level fluctuations in a typical 500-MWe-sodium-cooled fast breeder reactor. The magnitude of level fluctuation of 100 and 30 mm for different frequencies in the range of 0.1–10 Hz are considered in the numerical analysis. It is found that the critical location of maximum stress amplitude is independent of amplitude of sodium-free level fluctuation and is predominant particularly at lower frequency range of 0.1–2 Hz which is also the frequency range of interest of present study.

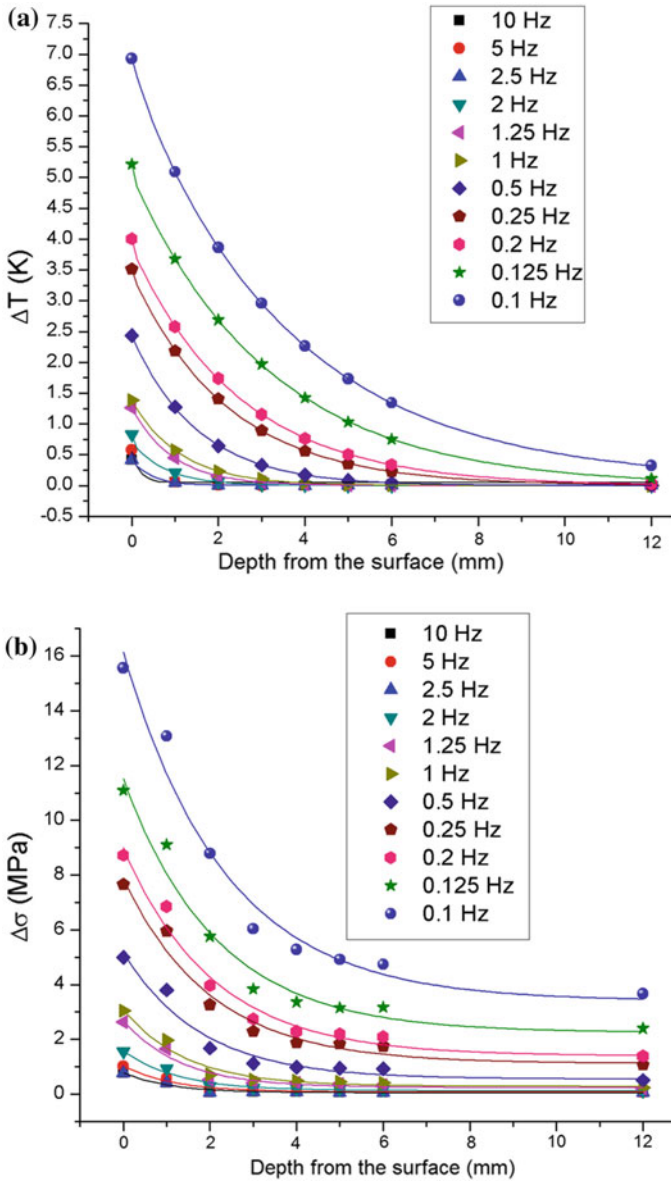
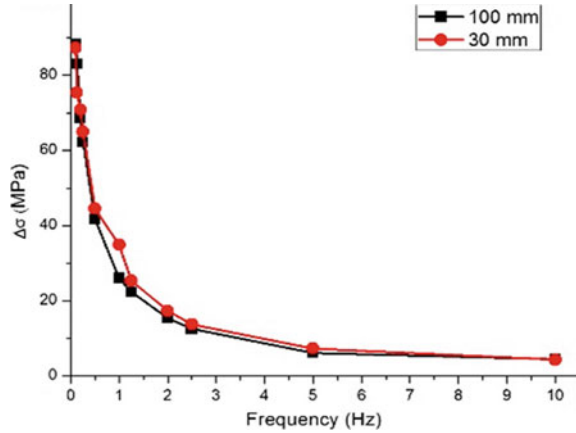


Fig. 6 a Amplitude of temperature fluctuation along the thickness of the reactor vessel at node 17, b amplitude of stress fluctuation along the thickness of the reactor vessel at node 17

Fig. 7 Maximum amplitude of stress variation induced in the reactor vessel wall due to sodium-free level fluctuation



Apart from the aforementioned high-cycle thermal fatigue (HCF), the sodium-free level zone is further subjected to low-cycle fatigue (LCF) due to reactor scram and restart cycles. As the zone is subjected to both LCF and HCF simultaneously the cumulative damage will be higher than the individual damages. At present, matured design rules are not available to calculate damage due to this complex LCF–HCF interaction phenomenon. Considering the importance of the main vessel in maintaining the structural integrity of the plant, this paper is the first step in accurate prediction of damage due to this complex phenomenon.

Acknowledgements The authors are thankful for the support and motivation by Dr. S.A.V. Satya Murthy, Director, IGCAR and Shri P. Puthiyavinayagam, Director, RDG. The Authors gratefully acknowledge the grant of the research fellowship from Indira Gandhi Centre for Atomic Research, Department of Atomic Energy, India.

References

1. K. Velusamy, P. Chellapandi, S.C. Chetal, B. Raj, Overview of pool hydraulic design of Indian prototype fast breeder reactor. *Sadhana-Acad. Proc. Eng. Sci.* **35**(2), 97–128 (2010)
2. D. Laxman, P.K. Gupta, C. Asokane, J. VenkataRamanan, C.A. Gopal, K. Rajesh, G. Padmakumar, V. Prakash, G. Vaidyanathan, Experimental study of free level fluctuations in 1/4 scale reactor assembly model of PFBR, NUTHOS-6 (Nara, Japan, 2004)
3. ABAQUS 6.10, Dassault Systèmes Simulia Corp (Providence, RI, USA, 2010)
4. A. Mishra, R.S. Kumar, P. Chellapandi, Progressive deformation behaviour of thin cylindrical shell under cyclic temperature variation using Combined Hardening Chaboche Model. *Lat. Am. J. Solids Struct.* **11**(6), 980–992 (2014)

Monotonic Fracture Studies on Bi-metallic Pipe Weld Joints Having Circumferential Through-Wall Crack

G. Raghava, S. Vishnuvardhan, M. Saravanan, P. Gandhi,
Suranjit Kumar, P. K. Singh, I. A. Khan and V. Bhasin

Abstract Bi-metallic welded joints are necessary in pressurized and boiling water reactors where heavy section low alloy carbon steel components are connected to stainless steel primary piping systems. The behaviour of such bi-metallic weld joints is very difficult to understand, and very limited experimental data are available in the literature on the fracture behaviour of such joints. It is essential to develop fracture assessment methodologies for these joints and validate them experimentally to ensure safe operation of power plants. In this background, fracture studies were carried out under monotonic bending on seven numbers of bi-metallic pipe weld joints of 324 mm nominal outer diameter having circumferential through-wall crack. The specimens were made of SA 508 Gr.3 Cl-1 low alloy steel (ferritic) pipe on one half and SA312 Type 304LN stainless steel (austenitic) pipe on the other half. The initial through thickness notch was located in the different regions of the weld joints such as weld centre, buttering, heat-affected zones and base metals (low alloys steel and stainless steel). Initial notch angle was either 60° or 90°. Prior to the fracture tests, fatigue pre-cracking was carried out to create sharp crack front. Subsequently, fracture tests were conducted under four-point bending and displacement control. The collapse load of the weld joint having crack in the buttering layer is 12% less compared to that having crack in the heat-affected zone. Increase in the crack angle present in the heat-affected zone from 60° to 90° reduced the collapse load of the weld joint by 19%.

Keywords Bi-metallic pipe weld joints · Monotonic fracture · Heat-affected zone
Buttering · Through-wall notch · Four-point bending

G. Raghava (✉) · S. Vishnuvardhan · M. Saravanan · P. Gandhi
CSIR-Structural Engineering Research Centre, Chennai 600113, India
e-mail: raghavag@serc.res.in

S. Kumar · P. K. Singh · I. A. Khan · V. Bhasin
Bhabha Atomic Research Centre, Mumbai 400085, India

© Springer Nature Singapore Pte Ltd. 2018
R. Prakash et al. (eds.), *Advances in Structural Integrity*,
https://doi.org/10.1007/978-981-10-7197-3_35

Nomenclature

$2C$	Initial notch length
D	Diameter of the pipe
l	Length of the pipe
L	Inner span
R_m	Mean radius of the pipe
t	Thickness of the pipe
W	Width of the notch
Z	Outer span
θ	Half notch angle
σ_y	Yield strength
σ_u	Ultimate tensile strength
σ_f	Flow stress of the material

1 Introduction

Bi-metallic weld joints are used in the primary heat transport system of light water cooled reactors of nuclear power plants. These weld joints are used to join pressure vessel nozzle (low alloy steel) to stainless steel piping. Large difference in physical, chemical and mechanical properties of low alloy steel and stainless steel calls for a deposit of material (buttering) on ferritic steel with intermediate properties. This helps in minimizing the residual stresses and distortion during welding. The buttering material is generally nickel-rich Inconel alloy. The bi-metallic weld joints have varying metallurgical, mechanical and fracture toughness properties across the joint, which affects the integrity of the joints. The behaviour of such bi-metallic weld joints is very difficult to understand, and very limited experimental data are available in the literature on the fracture behaviour of such joints. Therefore, it is essential to develop fracture assessment methodologies for these joints and validate them experimentally to ensure safe operation of power plants.

Brocks et al. [1] conducted two large-scale four-point bend tests on a piping assembly containing a SA 508 ferritic steel to AISI 304 L stainless steel weld with a notch at the interface between the ferritic steel and the buttering layer. Crack growth analyses were also carried out at material level, and the results were compared with the results of finite element analysis. A crack tip opening displacement (CTOD) criterion was applied to predict crack initiation and growth. CTOD appeared to be better suited for welded structures than J as CTOD is a near-field quantity which

does not suffer from problems like path dependence, material gradients, etc., and CTOD-based resistance curves can be easily determined experimentally even for welded structures. Faidy et al. [2, 3] studied performance of two benchmark four-point bend pipe tests, conducted on a nominal 6-inch piping assembly, containing a ferritic to stainless steel (A508-308/309SS-304SS) bi-metallic weld (BMW). The weld was notched at the ferritic steel/buttering layer interface, to simulate plant experiences of the cracking behaviour of such components. A range of analysis methodologies including conventional flaw assessment methods, J approaches and local approach methods were applied to predict the critical load for initiation of the defect, the extent of crack growth and the path followed by the crack through the weld up to the maximum load.

Guozhen et al. [4] conducted fracture tests and microscopic observations on an Alloy 52 M dissimilar metal welded joint (DMWJ) between A508 ferritic steel and 316L stainless steel in nuclear power systems. The results showed that the crack growth always deviates to the materials with lower strength, and the crack path deviations are mainly controlled by the local strength mismatch. If the local fracture resistance properties could not be obtained and used for cracks in heat-affected zone (HAZ), interface and near interface zone, the use of the J -resistance curves of base metals or weld metals following present codes will unavoidably produce non-conservative (unsafe) or excessive conservative assessment results.

Very limited experimental data are available in the literature on fracture behaviour of bi-metallic pipe weld joints. Hence, a systematic study was carried out by the authors on the fracture behaviour of straight pipe weld joints having circumferential through-wall crack.

2 Material Properties

The bi-metallic pipe weld specimens were made of base materials SA 508 Gr. 3 Cl-1 low alloy steel and SA 312 Type 304LN stainless steel, and buttering material was nickel-rich Inconel alloy (ENiCrFe-3) conforming to AWS A5.11/A 5.11M-2010 [5]. The SA 508 Gr. 3 Cl-1 material conformed to ASTM A508/A508M-14 [6], and the SA 312 Type 304LN stainless steel conformed to ASTM A312/A312M-14b [7]. The chemical composition and the mechanical properties of steels used in bi-metallic pipe weld joints are given in Tables 1 and 2.

Table 1 Chemical composition of steels used in bi-metallic pipe weld joints

Elements	Chemical compositions (%)					
	Low alloy carbon steel			Stainless steel		
	Tested values [8]	ASTM A508/A508M-14 Grade 3 Class 1 [6]	Tested values [8]	ASTM A312/A312M-14b [7]	Tested values [8]	ENiCrFe-3
Carbon	0.190	0.250 (max)	0.023	0.035	0.038	AWS A5.11/A5.11M-2010 [5]
Manganese	1.300	1.200–1.500	0.820	2.000	6.750	0.100 (max)
Phosphorous	0.018	0.250 (max)	0.024	0.045	0.014	5.000–9.500
Sulfur	0.002	0.250 (max)	0.001	0.030	0.015	0.030 (max)
Silicon	0.230	0.400 (max)	0.460	1.000	0.870	0.015 (max)
Nickel	0.700	0.400–1.000	8.17	8.000–12.000	66.000	1.000 (max)
Chromium	0.170	0.250 (max)	18.13	18.000–20.000	16.590	59.000 (min)
Molybdenum	0.440	0.450–0.600	0.260	–	0.800	13.000–17.000
Copper	0.130	0.200 (max)	1.070	–	0.080	–
Titanium	–	0.015 (max)	–	–	0.029	0.500 (max)
Aluminum	0.020	0.025 (max)	0.027	–	0.062	1.000 (max)
Niobium	–	–	–	–	2.100	–
Tantalum	–	–	–	–	–	1.000–2.500
Iron	96.8	–	71.015	–	6.240	10.000 (max)

Table 2 Mechanical properties of steels used in bi-metallic pipe weld joints

Properties	Carbon steel		Stainless steel	
	Tested values [8]	ASTM A508/A508M-14 Grade 3 Class 1 [6]	Tested values [8]	ASTM A312/A312M-14b [7]
Yield strength, σ_y (MPa)	570	450	208	205 MPa
Ultimate tensile strength, σ_u (MPa)	694	620–795	549	515 MPa
Percentage elongation	23	16	81	35 (L)
	–	–	–	25 (T)

L Longitudinal; T Transverse

3 Experimental Investigations

3.1 Details of Bi-metallic Pipe Weld Joints

The bi-metallic pipe weld joints were of 324 mm nominal outer diameter having circumferential through-wall crack. The specimens were made of SA 508 Gr.3 Cl-1 low alloy steel (ferritic) pipe on one half and SA312 Type 304LN stainless steel (austenitic) pipe on the other half. The length of the specimens was 4000 mm, and the average thickness was 24 mm. Initial notch angle was either 60° or 90°; the corresponding notch length was 170 or 254 mm. Table 3 gives details of the bi-metallic pipe weld joints.

3.2 Details of Fatigue Pre-cracking

Prior to the fracture tests, fatigue pre-cracking of the bi-metallic pipe weld specimens was carried out under four-point bending, under load control, using a ±1000 kN capacity servo-hydraulic actuator. The inner and outer spans during fatigue pre-cracking of the pipes were 972 and 3500 mm, respectively. The load ratio was 0.1, and the frequency was maintained in the range of 0.5–1.8 Hz. The maximum cyclic load was around 20% of the Theoretical Plastic Collapse Load (TPCL) of the pipe weld specimen. The TPCL was calculated using the following Eq. (1):

$$P_L = \frac{16\sigma_f R_m^2 t}{Z - L} \left(\cos \frac{\theta}{4} - \frac{1}{2} \sin \frac{\theta}{2} \right) \tag{1}$$

Flow stress (σ_f) is defined as the mean of yield strength and ultimate tensile strength. Minimum yield strength and tensile strength were considered for calculation of collapse load. Fatigue pre-cracking was carried out till the crack growth in the circumferential direction reached approximately 2 mm at both the notch tips. Table 4 gives details of inner and outer spans, frequency and magnitude of cyclic

Table 3 Details of bi-metallic pipe weld joints

Specimen ID	Carbon steel		Stainless steel		l (mm)	Details of notch		
	D (mm)	t (mm)	D (mm)	t (mm)		$2C$ (mm)	W (mm)	2θ (°)
QMSP-1-60TWC-Fe	325	24.09	323	23.96	4000	169	2.12	59.77
QMSP-2-60TWC-CW	325	24.72	324	24.01	4013	174	2.35	61.44
QMSP-3-90TWC-CW	325	24.14	324	23.72	4007	254	2.37	89.69
QMSP-4-60TWC-CB	325	23.99	324	23.37	4008	175	3.25	61.79
QMSP-5-60TWC-CHAZ	326	25.13	325	24.50	4011	172	3.00	60.55
QMSP-6-60TWC-Au	326	24.21	326	23.77	4012	170	2.38	59.75
QMSP-7-90TWC-CHAZ	325	24.37	324	23.99	4012	255	3.00	90.05

Type of notch Through-wall; *Fe* Crack is located at ferritic region; *CW* Crack is located at centre of weld; *CB* Crack is located at centre of buttering; *CHAZ* Crack is located at centre of heat-affected zone; and *Au* Crack is located at austenite region

Table 4 Details of fatigue pre-cracking of bi-metallic pipe weld joints

Specimen ID	Span (mm)		Frequency (Hz)	Cyclic load (kN)		Number of cycles	Crack length* (mm)		Crack angle*, 2θ (°)
	Inner span	Outer span		Min.	Max.		Tip A	Tip B	
QMSP-1-60TWC-Fe	972	3500	0.5	16	160	17,500	2.92	2.95	61.85
QMSP-2-60TWC-CW	972	3500	0.5	16	160	29,500	2.85	2.18	63.22
QMSP-3-90TWC-CW	972	3500	0.5	12	120	24,000	2.67	3.21	91.77
QMSP-4-60TWC-CB	972	3500	0.5	16	160	45,000	1.71	0.85	62.70
QMSP-5-60TWC-CHAZ	972	3500	0.5	16	160	17,500	2.83	2.27	62.35
QMSP-6-60TWC-Au	972	3500	0.5-1.5	12	120	105,250	2.91	7.13	63.29
QMSP-7-90TWC-CHAZ	972	3500	0.5	12	120	21,000	0.75	2.00	90.74

*After fatigue pre-cracking

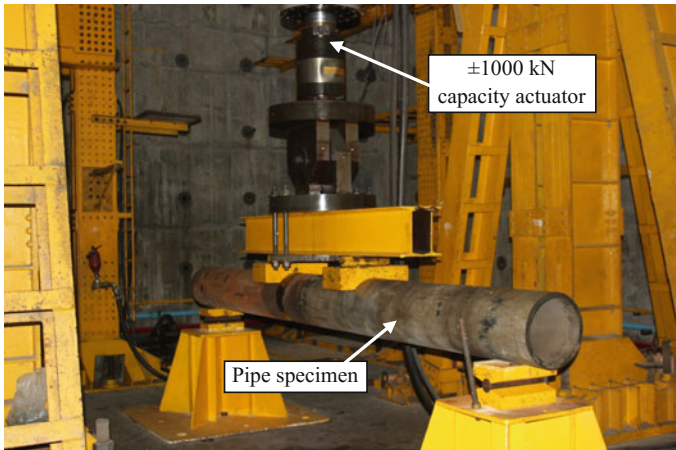


Fig. 1 A view of fatigue pre-cracking of a bi-metallic pipe weld joint

loading during fatigue pre-cracking of bi-metallic pipe weld joints. The pipes were simply supported with hinge support at one end and roller support at the other end. A steel distribution beam was used to apply cyclic load at two points along the span to simulate four-point bending with constant bending moment between the two loading points. Figure 1 shows a view of fatigue pre-cracking of a bi-metallic pipe weld joint. Digital camera was used to monitor surface crack growth during fatigue pre-cracking.

3.3 Fracture Tests

3.3.1 Test Set-up Arrangement

After fatigue pre-cracking, the welded pipe specimens were subjected to monotonic loading with intermittent unloading to carry out fracture test. The experimental set-up used for carrying out fracture tests was the same as that used for carrying out fatigue pre-cracking. A view of fracture test set-up for a bi-metallic pipe weld joint is shown in Fig. 2. Fracture tests were carried out using ± 1000 kN/ ± 2000 kN capacity servo-hydraulic actuator. The servo-hydraulic actuator was fixed to a steel reaction frame, which was connected to the strong floor of the laboratory. The actuator system consists of an inbuilt LVDT for measuring displacement and a load cell for measuring the applied load. Figure 3 shows close-up view of a bi-metallic pipe weld joint and fracture test set-up.

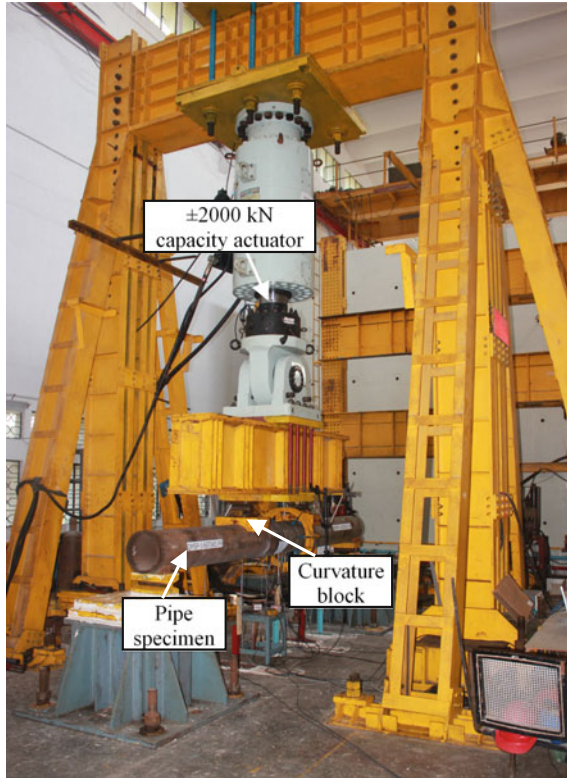


Fig. 2 Fracture test set-up for bi-metallic pipe weld specimen QMSP-1-60TWC-Fe

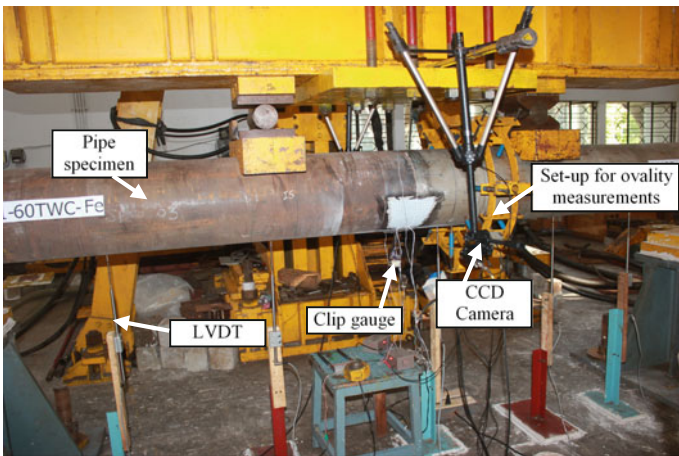


Fig. 3 Close-up view of the bi-metallic pipe weld specimen and fracture test set-up

3.3.2 Instrumentation and Data Acquisition

During the fracture tests, the pipe weld specimens were instrumented to obtain the following data:

- Applied load from inbuilt load cell in servo-hydraulic actuator
- Load-line displacement (LLD) from inbuilt LVDT in servo-hydraulic actuator
- Crack mouth opening displacement (CMOD) using Clip gauge
- Surface crack growth using Image Processing Technique
- Deflection of bi-metallic welded pipe specimen using LVDT
- Angular rotation of pipe using inclinometer
- Circumferential deformation (ovality) using ovality ring with LVDTs.

The applied load and load-line displacement were measured directly using strain gauge-based load cell and inbuilt LVDT of the actuator. Crack mouth opening displacement was measured using specially fabricated clip gauges. Strain gauge-based clip gauges with opening of 5–30 and 15–60 mm range were used, and these were calibrated prior to the tests to the required range of displacement. The clip gauges were connected to the data acquisition system, and the data were continuously acquired. Circumferential deformation (ovality) measurements were also made at the stainless steel portion of the pipe using an ovality set-up. The ovality set-up consisted of an ovality ring and four LVDTs. IPT was used to measure surface crack growth at both the crack tips. The IPT consisted of three CCD cameras interfaced to a computer system with image analysis software. Two CCD cameras were focused towards the crack tips. A grid of 5 mm spacing was made on the welded pipe specimen near the crack tips to obtain the crack growth data. The third CCD camera was focused towards the control console of the actuator to record the images of load and displacement corresponding to the crack growth at various stages of loading. The images at the two crack tips gave the surface crack growth. The deflection of the pipe weld specimen was measured by means of ± 100 mm range LVDTs kept along the span. The LVDTs were connected to MGC Plus data logger interfaced to a computer. Totally, five post-yield strain gauges were mounted on the pipe specimen to measure the strains during the fracture tests. Out of the five strain gauges, four strain gauges were mounted adjacent to the two notch tips, and the remaining one strain gauge was mounted on the opposite side of the notch.

3.3.3 Details of Loading

The bi-metallic welded pipe specimens were subjected to monotonic loading with intermittent unloading. The static monotonic load was applied in displacement control at the rate of 0.04 mm/s initially till the displacement value reached 20 mm.

Then, the specimen was unloaded in displacement control at the rate of 0.04 mm/s till the displacement value dropped by 2 mm. Subsequently, the specimen was loaded till the increment in displacement value reached 10 mm (i.e. 30 mm from beginning). The procedure was continued in this manner till the end of the test. During the fracture tests, load, load-line displacement, crack mouth opening displacement, ovality in the austenitic steel pipe at 245 mm from notch plane and deflection of the specimens (at five locations) were continuously monitored. Surface crack growth was monitored using Image Processing Technique (IPT). Additionally, angular rotation at both the loading supports was also recorded with respect to load and load-line displacement.

4 Results and Discussion

Table 5 gives the results of fracture tests on bi-metallic pipe weld joints [9–12]. Figure 4a–c shows the load versus load-line displacement curves for the joints.

Figure 5a–c shows the load versus crack mouth opening displacement curves. Presence of initial notch of length 254 mm reduced the collapse load of the specimen by 30% when compared with the specimen having initial notch of length 174 mm at the centre of the weld. The collapse load of the weld joint having crack in the buttering layer is 12% less compared to that with crack in the heat-affected zone. Increase in the angle of crack in the heat-affected zone from 60° to 90° reduced the collapse load of the weld joint by 19%. In the case of specimen having initial crack in the HAZ towards ferritic region, crack grew towards the fusion line between buttering and ferritic region. In the case of specimen having initial crack in the austenitic region, crack growth was in the plane of the notch till the end of the test. In the remaining specimens, i.e. specimens having initial crack in the centre of the weld, centre of the heat-affected zone and centre of the buttering, propagation of the crack was towards the stainless steel region. Figure 6 shows deflected shape of the specimen QMSP-6-60TWC-Au at the end of fracture test, and Fig. 7 shows close-up views of crack tip locations at the end of fracture test. Final crack lengths (including initial notch length) for the specimens at the end of fracture test varied from 247 to 455 mm. Results of the studies will be useful in developing fracture assessment methodologies which are required to ensure structural integrity of bi-metallic pipe weld joints.

Table 5 Results of fracture tests on bi-metallic pipe weld joints

Specimen ID	Span (mm)		MML ^a (kN)	Load-line displacement ^b (mm)	CMOD ^b (mm)	Crack length ^c (mm)		Final crack angle, 2θ (°)
	Inner span	Outer span				Tip A	Tip B	
QMSP-1-60TWC-Fe	1134	3700	1001.02	210.50	17.10	45.21	30.15	86.42
QMSP-2-60TWC-CW	972	3700	804.97	96.24	14.02	92.28	87.50	126.71
QMSP-3-90TWC-CW	972	3700	562.60	58.70	13.30	96.13	89.70	157.39
QMSP-4-60TWC-CB	972	3700	753.40	91.90	12.10	81.91	83.18	120.10
QMSP-5-60TWC-CHAZ	972	3700	854.70	140.00	17.90	46.22	55.37	96.32
QMSP-6-60TWC-Au	1134	3700	758.40	124.20	25.10	106.53	108.69	135.41
QMSP-7-90TWC-CHAZ	972	3700	691.40	95.90	16.40	120.17	80.29	160.34

MML: Maximum Measured Load; ^aAs recorded in data logger; ^bValues corresponding to MML; ^cAs obtained from IPT

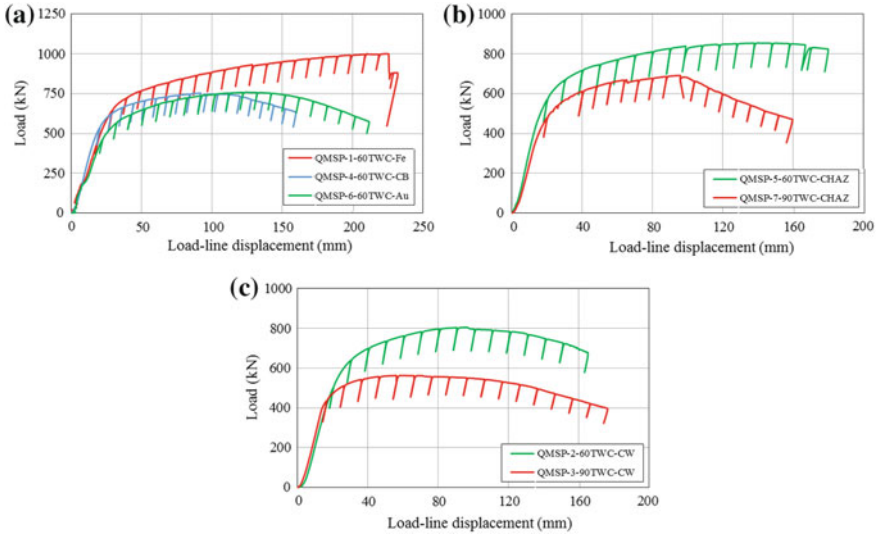


Fig. 4 Load versus load-line displacement curves for the bi-metallic pipe weld joints

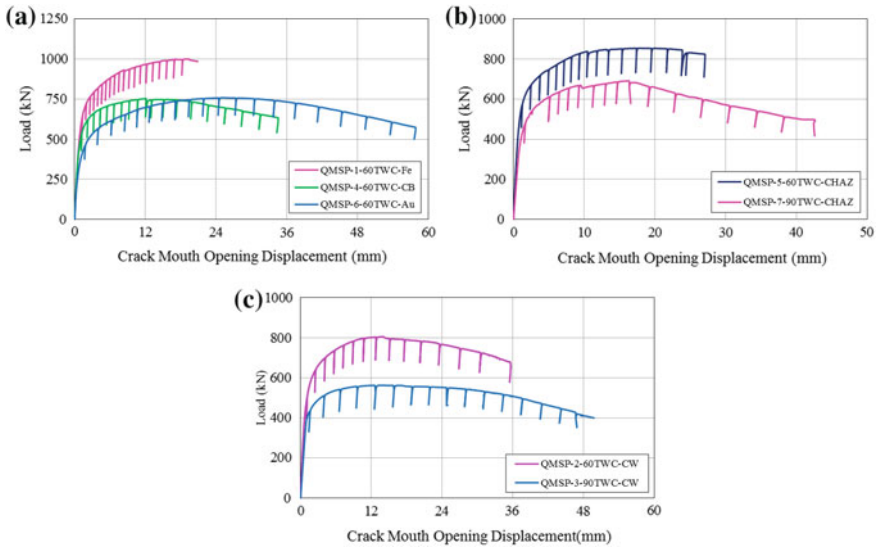
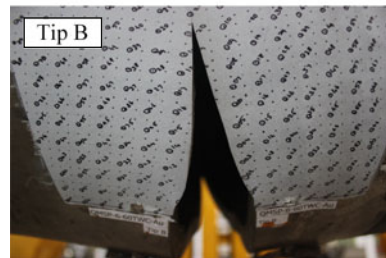


Fig. 5 Load versus CMOD curves for the bi-metallic pipe weld joints

Fig. 6 Deflected shape of the specimen QMSP-6-60TWC-Au at the end of fracture test



Fig. 7 Close-up views of crack tip locations at the end of fracture test for the specimen QMSP-6-60TWC-Au



5 Summary and Conclusions

Fracture studies were carried out under monotonic bending on seven numbers of bi-metallic pipe weld joints of 324 mm nominal outer diameter having circumferential through-wall crack. The specimens were made of SA 508 Gr.3 Cl-1 low alloy steel (ferritic) pipe on one half and SA312 Type 304LN stainless steel (austenitic) pipe on the other half. The initial through thickness notch was located in the different regions of the weld joints such as weld centre, buttering, heat-affected zones and base metals (low alloy steel and stainless steel). Based on the results of the studies, the following conclusions are made:

- In the case of specimens having notch at the weld centre, collapse load of the specimen with initial notch length of 254 mm reduced by 30% in comparison with that of the specimen with initial notch length of 174 mm.
- The collapse load of the weld joint having crack in the buttering layer is 12% less in comparison to that with similar crack in the heat-affected zone, the initial notch length being approximately 175 mm in both the cases. Increase in the initial notch angle in the heat-affected zone from 60° to 90° reduced the collapse load of the weld joint by 19%.
- In the case of specimen having initial crack in the HAZ towards ferritic region, crack grew towards the fusion line between buttering and ferritic region.
- In the case of specimen having initial crack in the austenitic region, crack growth was in the plane of the notch till the end of fracture test.
- The specimens having initial crack in the centre of the weld, centre of the heat-affected zone and centre of the buttering, propagation of the crack was towards the stainless steel region.
- Results of these studies will be useful in developing fracture assessment methodologies which are required to ensure structural integrity of bi-metallic pipe weld joints.

Acknowledgements The authors from CSIR-SERC thank Prof. Santosh Kapuria, Director and Dr. K. Balaji Rao, Advisor (Management), CSIR-SERC, Chennai, for their valuable guidance, encouragement and support in the R&D activities. The assistance rendered by the technical staff of the Fatigue and Fracture Laboratory, CSIR-SERC in conducting the experimental investigations is gratefully acknowledged. This paper is published with the permission of the Director, CSIR-SERC, Chennai.

References

1. W. Brocks, A. Cornec, W. Schönfeld, Fracture mechanics assessment of a bi-metallic welded joint, in *Proceedings of the 14th European Conference on Fracture Mechanics (ECF 14)*, Krakow, Poland, 2002
2. C. Faigy, G. Chas, S. Bhandari, M.P. Valeta, R. Hurst, A. Youtsas, P. Nevasmaa, W. Brocks, D. Lidbury, C. Weisner, Structural integrity of bi-metallic components BIMET, Brite-Euram Final Project Report, 2001
3. C. Faigy, G. Chas, S. Bhandari, M.P. Valeta, R. Hurst, A. Youtsas, P. Nevasmaa, W. Brocks, D. Lidbury, C. Weisner, BIMET: structural integrity of bi-metallic components. *Nucl. Engg. Desig.* **209**(1–3), 79–85 (2001)
4. G. Wang, H. Wang, F. Xuan, S. Tu, Local fracture behavior and integrity assessment of a dissimilar metal welded joint in nuclear power systems, in: *Proceedings of 13th International Conference on Fracture*, Beijing, China, 6–21 June 2013
5. AWS A5.11/A 5.11M—2010, Specification for nickel and nickel-alloy welding electrodes for shielded metal arc welding, American Welding Society. An American National Standard (2010)
6. ASTM A 508/A 508M—14, Standard specification for quenched and tempered vacuum-treated carbon and alloy steel forgings for pressure vessels. ASTM International (2014)

7. ASTM A 312/A 312M—14b, Standard specification for seamless, welded, and heavily cold worked austenitic stainless steel pipes. ASTM International (2014)
8. S. Kumar, P.K. Singh, I.A. Khan, V. Bhasin, R.K. Singh, K.K. Vaze, K.N. Karn, J. Derose, S. P. Srivastava, A.K. Sinha, Evaluation of tensile and fracture properties of dissimilar metal pipe weld: low alloy ferritic steel and austenitic stainless steel. Technical Report, BARC/2014/E/2014, Bhabha Atomic Research Centre, Mumbai (2014)
9. M. Saravanan, S. Vishnuvardhan, G. Raghava, P. Gandhi, Monotonic and cyclic fracture studies on bi-metallic pipe weld joints. Sponsored research report no. R&D 03-SSP 14541-SR-1, Jan 2015 (CSIR—Structural Engineering Research Centre, Chennai)
10. M. Saravanan, S. Vishnuvardhan, G. Raghava, P. Gandhi, Monotonic and cyclic fracture studies on bi-metallic pipe weld joints. Sponsored research report no. R&D 03-SSP 14541-SR-2, June 2015 (CSIR—Structural Engineering Research Centre, Chennai)
11. M. Saravanan, S. Vishnuvardhan, G. Raghava, P. Gandhi, 'Monotonic and cyclic fracture studies on bi-metallic pipe weld joints. Sponsored research report no. R&D 03-SSP 14541-SR-3, Sept 2015 (CSIR—Structural Engineering Research Centre, Chennai)
12. M. Saravanan, S. Vishnuvardhan, G. Raghava, P. Gandhi, Monotonic and cyclic fracture studies on bi-metallic pipe weld joints. Sponsored research report no. R&D 03-SSP 14541-SR-4 and Final, Dec 2015 (CSIR—Structural Engineering Research Centre, Chennai)

Part VII
Experimental Techniques

Assessment of Strain in a Corrosive Environment of Structural Steel

A. Cinitha, P. K. Umesha and K. Kesavan

Abstract Corrosion damage not only causes structural failure, but also leads to maintenance and repair costs. Improving the effective sensor technology for corrosion detection can reduce the economic loss and provide safe structures with longer service. This paper presents an evaluation technique developed to assess the progressive strain in a corrosive environment using fiber Bragg grating (FBG) sensors. The progress in corrosion process of structural steel coupons under stressed and unstressed condition in a laboratory environment is studied. The strains are measured with electrical resistance strain gauges and FBG sensors and are compared. Strain in coupons under stressed and unstressed condition is measured, and distinct strain behavior is brought out along with reliability of measurements in adverse environment. The central wavelength shift and peak power of FBG are analyzed with interrogator, and the capability of FBG sensor to monitor the progress in corrosion is brought out.

Keywords Corrosion · Fiber Bragg grating sensor · Electrolyte
Electrical resistance strain gauge

Nomenclature

n	Effective refractive index of the core
p_e	Effective photo-elastic coefficient
$P_{i,j}$	Coefficients are the Pockel's coefficients of the stress-optic tensor
ΔT	Incremental increase in temperature
ΔM	Incremental increase in mass loss
ΔR	Resistance change in the gauge in ohms
R_o	Original or unstrained gauge resistance
α_T	Coefficient of thermal expansion
ε	Unit engineering strain in the specimen surface
ν	Poisson's ratio

A. Cinitha (✉) · P. K. Umesha · K. Kesavan
CSIR-Structural Engineering Research Centre, Chennai 600113, India
e-mail: cinitha@serc.res.in

Λ	Grating pitch
$\Delta\varepsilon$	Incremental increase in strain
α, β, γ	Constant coefficients
λ_B	Bragg wavelength

1 Introduction

Fiber optic-based sensing technology has shown remarkable progress and accuracy level in structural health monitoring of bridges, towers, industrial plants, silos, offshore platforms, etc. These optical sensors, which are superior in durability, corrosion resistance, waterproof, and explosion proof, provide numerous advantages over conventional electrical resistance sensors such as their small size, their low weight, or their immunity to electromagnetic interference. Fiber Bragg grating (FBG) sensors are one of the advanced devices in this technology, especially to measure strain and deformations in severe environments. FBG-based sensors are capable to measure the physical parameters such as strain, pressure, and temperature [1–3] and had reviewed advances in fiber Bragg sensor technologies. Although the conventional electric resistance-based sensors were well established and are still under continuous development, fiber grating sensors have exhibited their distinct advantages and competitiveness in developing, e.g., sensor array multiplexed in serial, remote sensors for harsh environment monitoring, and ultrasensitive miniature optical sensors, besides their well-known merits including electrically passive operation, immunity to electromagnetic interference, self-referencing, and high sensitivity [4], demonstrated simultaneous measurement of strain and temperature using FBG sensors. The corrosion phenomena of structural steel involve mainly two elements: the material and its environment. In particular, corrosion is defined as the deterioration of a material, usually a metal, which results from a reaction with its environment, causing the degradation of both. The local pH and temperature influence corroding chemical reactions and affect the rate of corrosion. In the present study, comparative measures of laboratory simulated corroded coupons bonded with FBG and conventional electrical resistance sensors are carried out. Corrosion is induced by galvanostatic method on structural steel coupons. The variation in temperature and pH of electrolyte is monitored with WTW probes. Initially, the response of the FBG sensor is validated with electrical resistance strain gauge under ambient condition, for two sets of tension coupon test. Further to the validation, four sets of experiments are carried out in a corrosive condition by two different methods, case 1: unstressed and case 2: stressed and the results are discussed.

2 Fiber Bragg Grating (FBG) Sensors

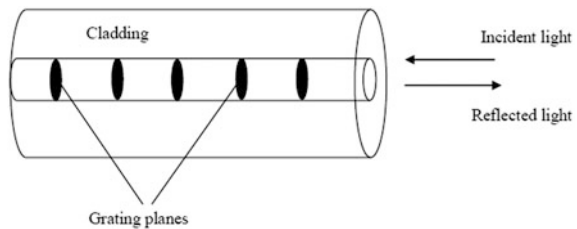
The FBGs used are fabricated by creating a periodic modulation of the refractive index along a photosensitive silica fiber, reflectivity of more than 95%, and a bandwidth of 0.2 nm. Fiber Bragg gratings are used as strain or temperature, pH sensors in which variations of those parameters are transformed to a shift of the Bragg wavelength reflected back as a Gaussian profile signal. In general, fiber Bragg gratings are periodic structures that are imprinted directly into the core of glass optical fiber by powerful ultraviolet radiation. Such structure consists of a periodically varying refractive index over typically several millimeters of the fiber core. The specific characteristic of FBG for sensing applications is that their periodicity causes them to act as wavelength-sensitive reflectors. During imprinting process, the intensity of the ultraviolet illumination is made to occur in a periodic fashion along the fiber core. At a sufficiently high power level, local defects are created within the core, which then give rise to a periodic change in the local refractive index. This change in refractive index (RI) created is permanent and sensitive to a number of physical parameters, such as pressure, temperature, strain, and vibration. Thus, by monitoring the resultant changes in reflected wavelength, FBG can be used for sensing applications to measure various physical quantities. Fiber Bragg grating sensor the response arises from two sources, namely the induced change in pitch length (Λ) of the grating and the perturbation of the effective core refractive index (n). The wavelength of the reflected spectrum band is defined by the Bragg condition [5], given by the expression

$$\lambda_B = 2n\Lambda \tag{1}$$

where n is effective refractive index of the core and Λ is the grating pitch.

Λ fiber Bragg grating consists of a longitudinal, periodic variation in the refractive index of the core of an optical fiber as shown in Fig. 1.

Fig. 1 Schematic of the in-fiber grating structure of a fiber bragg sensor



3 Fiber Bragg Grating Sensing Technique

Fiber Bragg grating (FBG) is a passive optical component obtained by recording a local, longitudinal period modulation of the refractive index in the optical fiber core, as depicted in Fig. 2a. Due to the local change of the refractive index, any light propagating along the fiber core suffers partial reflection at each of the grating layers. As a consequence of the periodicity of the index modulation, constructive interference of the reflected light takes place for those wave vectors that satisfy the Bragg condition given in Eq. 1. This implies that part of the incident spectrum is not transmitted, but reflected, by grating as shown in Fig. 2a. The technical details of the FBG used for the present study are given in Table 1. Since the wavelength reflected by the grating is a function of n and Λ , variations of the temperature and variations of the strain due to loss of metal (i.e., subsequent change in geometry of corroded surface) attributed by change in pH, i.e., or of the strain to which the grating is submitted, give rise to appreciable wavelength change, which can be considered as indicated in Fig. 2b. Where α, β, γ constant coefficients and $\Delta T, \Delta M, \Delta \epsilon$ are incremental increase in temperature, metal loss factor, and strain, respectively. The principle of operation of FBG sensing consists of monitoring the Bragg wavelength and correlating wavelength change, B , to the variations in the measured value.

The length of the FBG, which is an integral part of the fiber, is normally few millimeters. When light from a broadband source is launched in the fiber, the FBG reflects wavelength intensity that satisfies Eq. 1 while the rest of the wavelengths

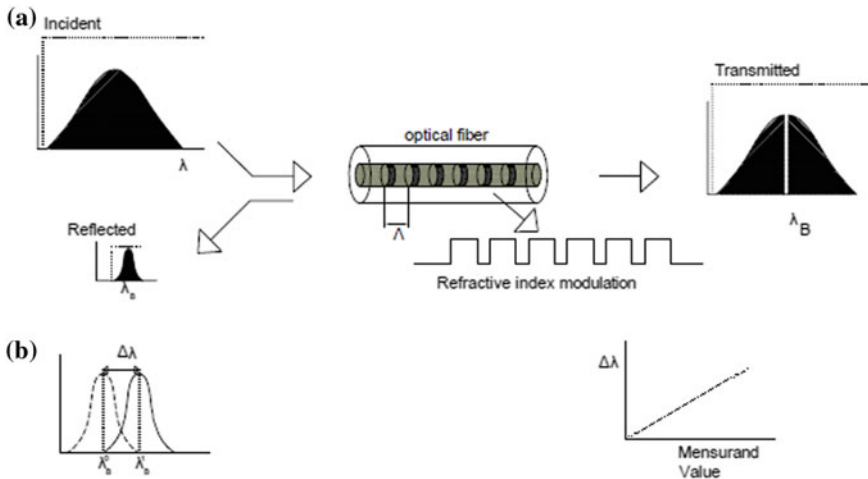


Fig. 2 Scheme of fiber Bragg grating operation

Table 1 Technical details of FBG

Center wavelength	CW tolerance	Reflectivity	3 dB band width	Fiber type	Grating length
1540 nm	±1 nm	0.70%	0.25 ± 0.05 nm	SMF28-C Polymide	10 mm

get transmitted. The reflected wavelength λ_B is called Bragg wavelength and is determined by the period of the grating (Λ). The Bragg wavelength is sensitive to changes in either the fiber-core refractive index or the period of the grating. This makes it an excellent sensor for measurement of mechanical or thermal perturbations. Unlike intensity-modulated sensors which need a very stable light source and interferometric sensors which need a highly coherent laser, fiber Bragg grating-based sensors generally require a broadband source and a high-resolution wavelength shift detection system. Fiber Bragg gratings have been reported for the measurements of strain temperature, dynamic magnetic field, etc. The sensing principle is that the Bragg wavelength will vary with the change of these parameters experienced by the fiber. In the case of load-induced strain, both physical elongation of the optical fiber (and the corresponding change in the grating pitch) and the change in the refractive index of the fiber due to photo-elastic effects take place. As a result, the shift in Bragg wavelength occurs. The shift in Bragg wavelength with strain can be expressed as

$$\Delta\lambda_B = (1 - p_e)\lambda_B \varepsilon \tag{2}$$

where ε is the applied strain and p_e is an effective photo-elastic coefficient term, for the present study it has been taken as 0.2.

The sensing of strain and temperature due to physical elongation of the sensor and change in fiber index due to photo-elastic effect is expressed [1], as

$$\Delta\lambda_B = 2n\Lambda \left(\left\{ 1 - \left(\frac{n^2}{2}\right)[P_{12} - \nu(P_{11} + P_{12})] \right\} \varepsilon + \left[\alpha_T + \frac{\left(\frac{dn}{dT}\right)}{n} \right] \Delta T \right) \tag{3}$$

where ε is the applied strain, $P_{i,j}$ coefficients are the Pockel's coefficients of the stress-optic tensor, ν is Poisson's ratio, and α_T is the coefficient of thermal expansion of the fiber material and is the temperature change. The factor $\left(\frac{n^2}{2}\right)[P_{12} - \nu(P_{11} + P_{12})]$ has a numerical value of ≈ 0.2 . However, there is not much studies are carried out to sense the change in fiber index due to combined effect of change in strain, temperature, and pH in a corrosive environment.

4 Electrical Resistance Strain Gauge

The electrical resistance strain gauge is a physically simple device, which can be easily applied in a straightforward manner for elementary measurements of surface strains. In the present study, electrical foil strain gauge of gauge length 2 mm is fixed to the coupon using cyanoacrylate adhesive. The foil gauge, Fig. 3, is essentially a small printed circuit on photographic plate. The details of the foil gauge used for the present study are shown in Table 2. The gauge factor is 2.0. In order to use such a gauge for detecting a strain of $1 \mu\epsilon$ (which corresponds to that produced by a 206.84 kN/m^2 stress in steel for a simple uniaxial loading), a change of resistance ΔR of $240 \mu\Omega$ needs to be measured with an indicator.

The relative change in resistance is given by

$$R = \rho \frac{L}{A} \quad (4)$$

The strain sensitivity can be defined as a basic bulk property of the strain-sensitive alloy used in a strain gauge. When this metal is formed into a grid and provided with attachment points for lead wires, the gauge will exhibit a different relationship between resistance change and applied strain. The term ‘gauge factor’ (GF) [6] is used to quantify this relationship and is defined as

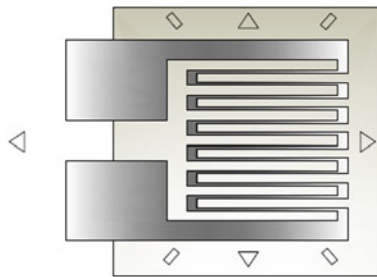


Fig. 3 Typical foil strain gauge

Table 2 Details of foil strain gauge

Gauge length (mm)	Gauge width (mm)	Backing length (mm)	Backing width (mm)	Resistance (Ω)
2	1.5	6.5	3	120

Note The present gauge backing is made of epoxy resin with thickness 0.03 mm which exhibits excellent electrical insulation performance. The backing has self-temperature compensation for steel ranging from 0 to $80 \text{ }^\circ\text{C}$

$$GF = \frac{\Delta R/R_o}{\Delta L/L_o} = \frac{\Delta R/R_o}{\epsilon} \tag{5}$$

where ΔR is resistance change in the gauge in ohms, R_o is original or unstrained gauge resistance, and ϵ is unit engineering strain in the specimen surface under the gauge grid $\Delta L/L_o$.

However, the use of electric strain gauges in harsh environment is not advisable due to their low sensitivity to respond against variation in temperature and pH.

5 Experimental Set-up

Experiments are carried out with fiber Bragg grating-based sensors and conventional electrical resistance strain gauges to monitor strains induced during simulated corrosion of unstressed and stressed coupons under galvanic method. The tension coupons are cut from tubes of diameter 76.1 mm and are corroded by using accelerated corrosion process. The corrosion process is carried out by keeping the test specimen as anode and steel plate cut from the same parent metal as cathode. They are placed in the electrolyte of 3.5% NaCl solution. The specimen (coupons are 250 mm long with a mid-gauge length of 60 mm and width as 12.5 mm, as per ASTM E8 M [7] specifications, Fig. 4) to be corroded is treated as anode, and a structural steel specimen of slightly large area of exposure than anode (80 mm 75 mm) is considered as cathode. Anode is connected to the +ve terminal. A specimen cut from the same parent metal was used as cathode and connected to the -ve terminal. Calomel electrode is used to measure the initial and final potential under zero current condition. The width of the gripping edge is 75 mm, and width of the gauge length area is 12.5 mm. The galvanic corrosion of the gauge portion is completely achieved by passing current of 3.4 A for duration of 300 min. The gauge length of the coupon is bonded with FBG sensor of center wavelength 1540 nm and grating length 10 mm and conventional electrical resistance strain gauge of 2 mm gauge length on the opposite face of corrosion. Initially, the response of FBG sensors is validated with electrical strain gauge (ESG) under ambient condition through a series of tensile test, namely FBG-TT-01, FBG-TT-02, ESG-TT-01, and ESG-TT-02 as shown in Fig. 5. The corrosion is carried out by

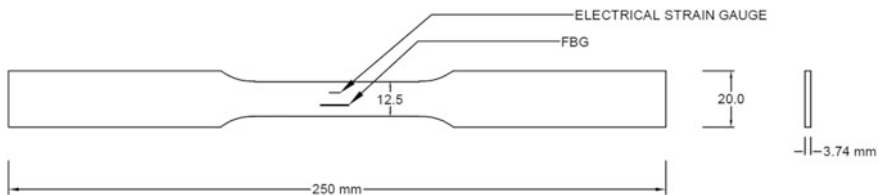


Fig. 4 Structural steel coupons glued with FBG and Electrical resistance strain gauge

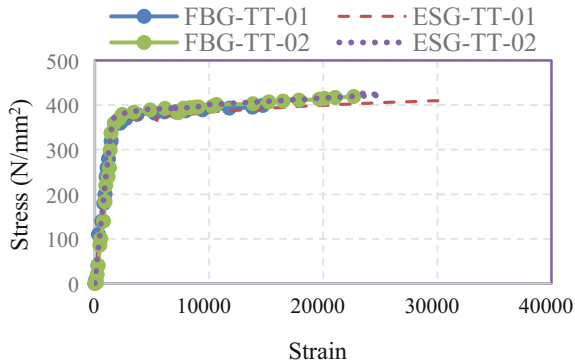


Fig. 5 Comparison of strain measurements of FBG and ESG

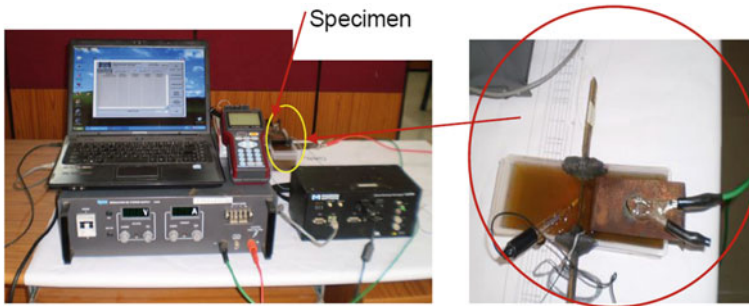


Fig. 6 Experimental set-up for unstressed condition

two methods: case 1 is unstressed condition, Fig. 6, and case 2 is stressed condition, Fig. 7. Four sets of coupons, namely FBG-ST-01, FBG-ST-02, FBG-ST-03, and FBG-ST-04, are the specimens used for unstressed condition, and FBG-SST-05, FBG-SST-06, FBG-SST-07, and FBG-SST-08 are the respective specimens used for stressed condition. Under stressed condition, the tension coupon specimen is gripped in a 25-ton UTM and applied 10% of the ultimate load to generate stress under the test condition.

An optical sensor for steel corrosion monitoring based on etched FBG sputtered with iron film showed intrinsically sensing capability as their resonant wavelengths vary with the perturbation induced change of the grating period and the fiber effective index [8]. In the present study, the strains measured by FBG sensor glued to steel coupons in a progressive corrosive environment are considered as the sum total of low strains generated due to metal loss followed by irregular changes on the exposed surface and due to variation in temperature. While the performance of ordinary strain gauge used is guaranteed till 23 °C with 50% relative humidity, the apparent strain is guaranteed for a range of 0–80 °C. And variation in pH is having

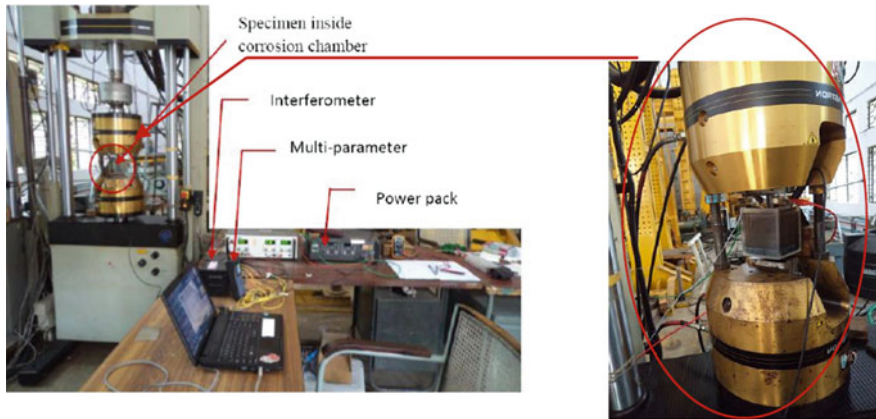


Fig. 7 Experimental set-up for stressed condition

influence on rate of corrosion. During the accelerated corrosion process, it is observed that temperature as well as pH of the electrolyte varies. The temperature and pH characteristics of the electrolyte during corrosion process are also measured with WTW probes.

6 Results and Discussion

The observed strain versus time behavior of FBG sensors and electrical resistance strain gauge under induced corrosion process under stressed and unstressed condition are shown in Figs. 8, 9 and 10. From the experimental investigations, it is observed that the strain sensed by the electrical resistance strain gauge varies from -28 to $500 \mu\epsilon$, and strain sensed by FBG sensors varies from 0 to $800 \mu\epsilon$ for duration of 5 h. The observed strain measurements confirm that there is no physical damage due to applied load to the specimen. The detected strains in all cases by sensors are due to metal loss from the corroding surface along with variation in pH and temperature. The entire gauge region of the specimen is expected to be completely corroded within 5 h (i.e., 300 min). Initially, under unstressed condition, both FBG and electrical resistance strain gauge were initialized, whereas under stressed condition, both FBG and electrical resistance strain gauge show initially a strain value of $283 \mu\epsilon$ due to applied load and initialized. As the corrosion process progresses, the electrical resistance strain gauge shows apparent strain, i.e., compensation for temperature component during unstressed condition (case 1), whereas under stressed condition, it is capable to sense strain induced due to combined effect of abrupt reduction in cross-sectional area and temperature. Compared to electrical resistance strain gauges, FBG sensors show its versatility to sense strains induced due to abrupt changes in cross-sectional area and chemical changes due to variation

Fig. 8 Strain versus time from FBG sensor under unstressed condition

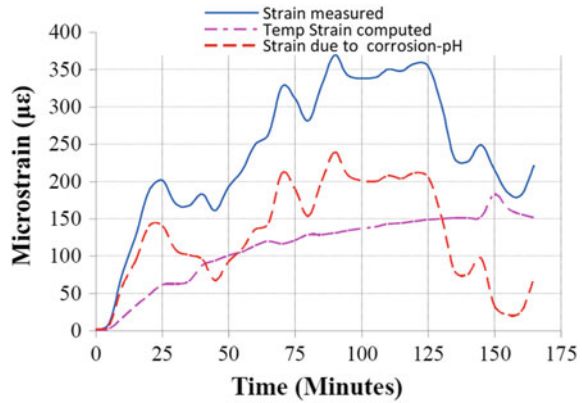
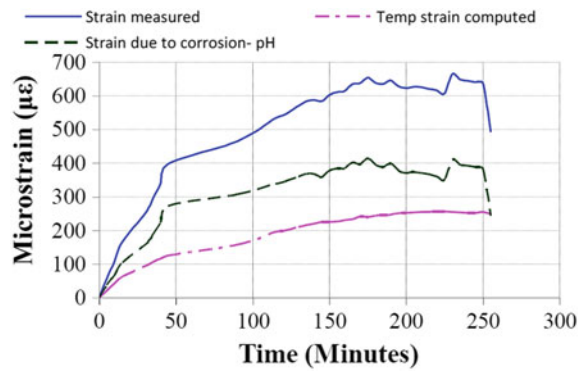


Fig. 9 Strain versus time from FBG sensor under stressed condition



in pH and temperature in a severe corrosive environment. The strain sensed by FBG sensor consists of three components, the induced strain due to stress (i.e., strain induced due to abrupt change in cross-sectional area under stressed condition), the strain induced due to change in temperature, and the low strain induced due to metal loss (in a varying pH and temperature environment). Under unstressed condition, the strain sensed by FBG is due to change in temperature and metal loss due to corrosion (in a varying pH and temperature environment). The sensed strain by FBG sensor for stressed condition (case 2), Fig. 12, is found to be higher than unstressed condition (case 1), Fig. 11, and this may be due to higher rate of corrosion in a stressed condition. After 130 min (2.17 h) of test, FBG sensors under case 1 show dropping behavior under unstressed condition, and this indicates the depletion of sensor from surface of the specimen. Almost 50% of the initial weight of the metal from the surface of anode is expected to be removed due to electrochemical process within 2.5 h. Then the formation of irregularities on the surface of anode observed to be high, and this may be correctly sensed by the FBG. The typical variation in temperature and pH observed during the test is shown in Figs. 13 and 14, respectively.

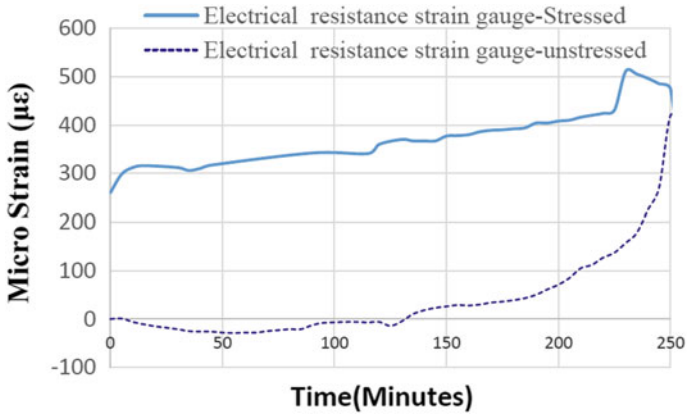


Fig. 10 Strain versus time electrical strain gauge under stressed and unstressed condition

Fig. 11 Comparison of unstressed FBG strain measurements

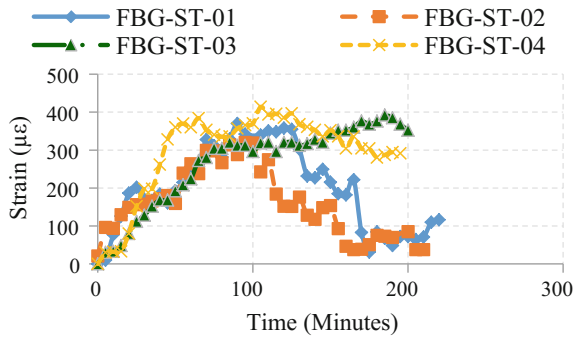


Fig. 12 Comparison of stressed FBG strain measurements

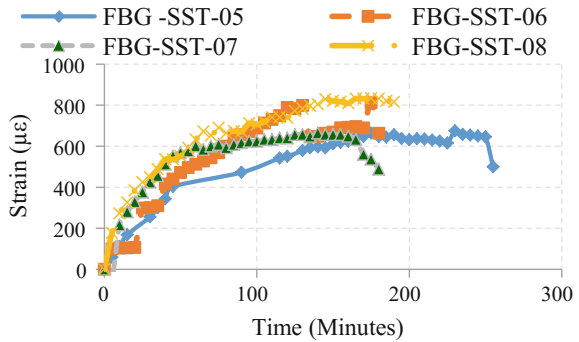


Fig. 13 Typical temperature versus time

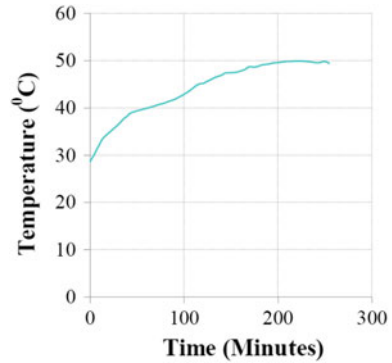
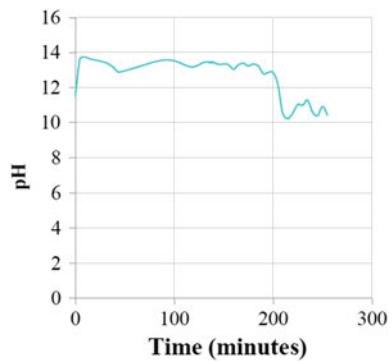


Fig. 14 Typical pH versus time



7 Conclusion

In the present study, experiments are carried out by inducing galvanic corrosion on structural steel coupons. The coupons are corroded under two conditions, viz., unstressed (case 1) and stressed (case 2). The strain measurements in coupons under stressed and unstressed conditions are monitored with FBG sensors and electrical resistance strain gauges. From the studies, it is concluded that FBG is suitable to measure strain due to corrosion, since it is capable to measure strains due to temperature (0–50 °C) and other interference (variation in pH from 11.4 to 14). The electrical resistance strain gauge is incapable to sense the induced strain on a metal surface exposed to corrosive environment with varying temperature and pH. From the FBG, it is concluded that the strain induced during unstressed condition is combined effect of temperature and variation in corrosion rate due to change in pH. Resultant strain in stressed condition is combined effect of strain due to stress, temperature strain, and variation in corrosion rate due to change in pH. Thus, FBG-based sensors are reliable than other conventional electrical resistance-based strain gauges. FBGs can be used to assess the onset of the corrosion before major impairment in the surface of the metal specimen.

Acknowledgements This paper is published with the permission of the Director, CSIR-Structural Engineering Research Centre, Chennai, India.

References

1. A.D. Kersey, M.A. Davis, H.J. Patrick, M. LeBlanc, K.P. Koo, C.G. Askins, M.A. Putnam, E. J. Friebele, Fiber grating sensors. *J. Lightwave Technol.* **15**(8), 1442–1463 (1997)
2. L. Suzhen, Z. Wu, L. Zhou, Health monitoring of flexural steel structures based on distributed fiber optic sensors. *Struct. infrastruct. Eng.* **6**(3), 303–315 (2010)
3. A.P. Zhang, S. Gao, G. Yan, Y. Bai, Advances in optical fiber Bragg grating sensor technologies. *Photonic Sens.* **2**(1), 1–13 (2012)
4. C. Fernandez-Valdivielso, I.R. Matias, F.J. Arregui, Simultaneous measurement of strain and temperature using a fiber Bragg grating and a thermochromic material. *Sens. Actuators*, 107–116 (2002)
5. B.D. Gupta, *Fiber Optic Sensors Principles and Applications* (New India Publishing Agency, New Delhi, 2006)
6. R.L. Hannah, S.E. Reed, *Strain Gage User's Handbook* (Elsevier Applied Science, New York, 1997)
7. ASTM E8/E8M-11, *Standard Test Methods for Tension Testing of Metallic Materials*. ASTM International, 100 Barr Harbor Drive, PO Box C700, West Conshohocken, PA, 19428–2959 US
8. Zhang Ning, Wei Chen, Xing Zheng, Hu Wenbin, Min Gao, Optical sensor for steel corrosion monitoring based on etched fiber Bragg grating sputtered with iron film. *IEEE Sens. J.* **15**(6), 3551–3556 (2015)

A Test Stand for Studying Subcritical and Critical States of Full-Size Reinforced Concrete Structures

Igor Shardakov, Irina Glot, Aleksey Shestakov, R. Tsvetkov and V. Yepin

Abstract Reinforced concrete is one of the basic building materials. Therefore, it is essential to study the behavior of reinforced concrete structures in subcritical and critical states. In this paper, we discuss the performance of a test stand designed to study deformation processes in the elements of full-size models of reinforced concrete structures subjected to quasi-static and dynamic loadings. The design of the stand and its main technical characteristics have been developed based on the results of numerical simulations of the evolution of deformation processes in the tested structure in going from elastic to inelastic state, which finally leads to its destruction. These simulations allowed us to design the foundation and load frame of the stand, to define the parameters of loading devices able to provide a wide range of deformations, to choose apparatus for recording the successive stages of damage accumulation and macroscopic fracture occurrence.

Keywords Experimental stand · Reinforced concrete · Fracture mechanics
Full-scale testing

1 Introduction

The operation safety of reinforced concrete (RC) buildings and constructions is of great practical importance. For such constructions, the elaboration of models, which can properly describe the deformation processes in subcritical and critical states, is still an open question. This is due to the fact that the critical states in structures develop according to a rather complex spatial–temporal scenario. Normally, a deformed structure consists of a great number of inhomogeneous elements, interrelations between these elements are rather complex, and the structural characteristics of reinforced concrete can vary widely. The deformation processes taking

I. Shardakov (✉) · I. Glot · A. Shestakov · R. Tsvetkov · V. Yepin
Institute of Continuous Media Mechanics UB RAS, Korolev Street, 1,
614013 Perm, Russia
e-mail: shardakov@icmm.ru

place in separate structural elements, for example in beams, are extensively investigated in the literature [1, 2]. However, the available information on testing separate structural elements is not sufficient to create a model, which can adequately describe the behavior of the entire structure. To do this would require experiments based on the full-scale model, which is a reinforced concrete structure consisting of structural units (several stories and several typical units disposed in a horizontal plane). For such experiments, it is essential to design a test stand of a scale suitable for generating, visualizing, and identifying subcritical and critical strain states. Worldwide, there are only few laboratories, where full-scale structural testing experiments can be conducted. For example, the European Laboratory for Structural Assessment (ELSA) in Italy carries out research in the area of improving safety of constructions [3]. Studies of the seismic characteristics of multi-story concentrically braced frames described in [4–6] are of immediate interest to experimentalists. This interest has arisen in connection with the problems of using structures in the regions of high seismic activity. The description of static full-scale structure tests is rarely found in the literature. A series of loading tests performed on a 1:2 scale replica of a Cypriot single-story structure are described in [7].

Creation of an experimental stand for testing full-scale constructions will make it possible to generate subcritical and critical strain processes in structures and their components under various quasi-static loading scenarios. Registration of these processes will enable adjustment of the existing mathematical models describing the deformation behavior of precast and cast-in-situ reinforced concrete constructions.

In this paper, we present the results of mathematical simulation of the deformation behavior of a RC structure and its components affected by the external force and kinematic factors. The RC structure is a physical model, which will be tested on a stand, which is currently under development. The proposed mathematical model considers the process of deformation from the initial elastic state to the state of complete failure. Analysis of the results of numerical simulation allows us to develop one of the possible variants of the structural scheme of the test stand and to estimate its parameters.

2 The Model of the Concrete Structure

In our investigation, we have studied the fragment of a 1:2 scale four-story building (Fig. 1e). The model object comprises 24 typical structural cells combined into four levels. The total height of the structure is 6 m, and base proportions are 6×9 m. A multi-element factor is assumed for all three directions (height, length, and width). By considering this factor, we can determine a true character of the spatial distribution of deformation, especially at the stage of subcritical and critical states of the RC structure. Note that the chosen scale (1:2) allows us to use standard

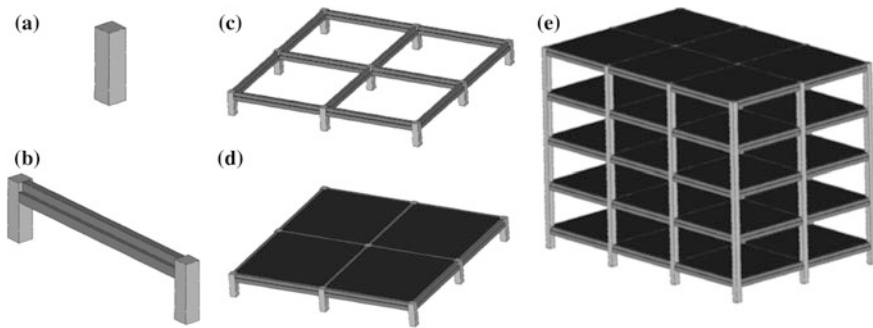


Fig. 1 Scheme of the RC structure (e) and its main elements: **a** “one column”; **b** “2 columns–beam”; **c** “9 columns–12 beams”; **d** “9 columns–12 beams–4 floor slabs”

concrete with a known mass fraction ratio to manufacture model structural units. Using of smaller-scale models made of this material can not guarantee that the deformation process occurring in them be identical to the processes in the original object.

Figure 1 presents the fragments of the tested model structure from the simplest to the most complex from the viewpoint of their design. For each fragment and the structure as the whole, we have simulated the process of deformation from the initial elastic state to the state of complete failure and loss of bearing capacity. Quasi-static loading was realized kinematically (due to the prescribed displacement of separate fragments of the structure).

Mathematical modeling of the deformation process, including the cracking stage, was performed within the framework of solid mechanics. Cracking in concrete was described as a sharp reduction in the material stiffness in a localized region. Based on the governing tensor relations, we determined the direction of propagation of the localized, reduced-stiffness region, the location of this region, and the mechanisms responsible for reducing material stiffness. The main theoretical principles underlying this approach were described in [8]. A jump-wise reduction of material stiffness represents a peculiar feature of cracking in concrete. The deformation process in the metal reinforcement was modeled in the context of the elastoplastic theory [9]. The numerical implementation of the model was carried out using the finite-element method in the framework of the ANSYS package.

3 The Results of Numerical Analysis

3.1 Uniaxial Tension—Compression of One Column

We have modeled the deformation process in a RC column by the relative displacement (ε) of the column ends along its axis. Two diagrams ($F-\varepsilon$) were obtained,

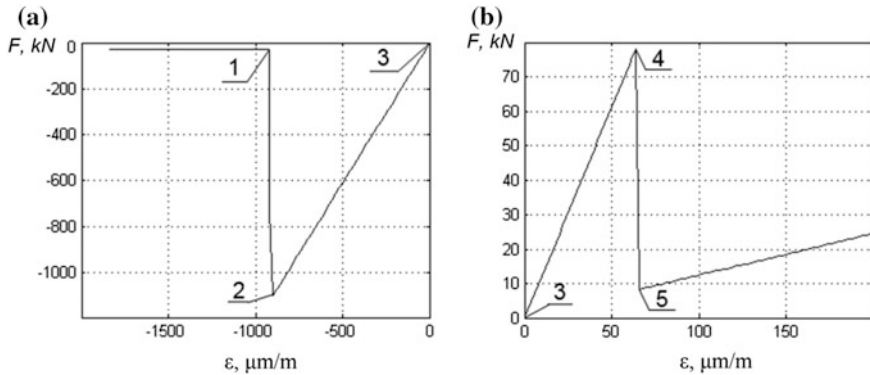


Fig. 2 Calculation results: **a** (F - ε) compression diagram for the column; **b** tension diagram

respectively, for compression (Fig. 2a) and tension (Fig. 2b). Here, F is the resultant response of the column to the relative displacement of its ends. On compression of the sample (Fig. 2a) from its initial state, point 3 ($\varepsilon = 0, F = 0$), the force increases linearly up to point 2 ($\varepsilon = -900 \times 10^{-6}, F = -1100$ kN). After the force passes point 2, the concrete destroys and the total force is exerted upon the reinforcement, which thus loses its stability and is unable to withstand extra loads—point 1 ($\varepsilon = -920 \times 10^{-6}, F = -31$ kN).

The process of tension (Fig. 2b) proceeds linearly to point 4 ($\varepsilon = 64 \times 10^{-6}, F = 78$ kN); then, the concrete destroys, and the entire force is exerted upon the reinforcement—point 5 ($\varepsilon = 66 \times 10^{-6}, F = 8$ kN). With increasing deformation, the force increases until the reinforcement material enters into the plastic strain zone. After the plastic deformation, the reinforcement experiences rupture.

3.2 Deformation of the System “2 Columns–Beam”

The beams and columns are connected in such a way as to form the frame of the building. Due to uneven settlement of columns, the beam experiences a bending moment. This gives rise to tension zones, where the fracture in the form of cracks is realized. In these zones, the tension force is exerted upon the reinforcement only. A further increase in uneven settling leads either to reinforcement rupture, or to failure of the concrete in its compressed region. This strongly reduces the stiffness of the material and even may cause its full failure. The simplest system representing this mechanism consists of 2 columns and 1 beam (Fig. 1b). The loading test involves vertical displacement (U) of the foundation of the first column, while the second column remains fixed.

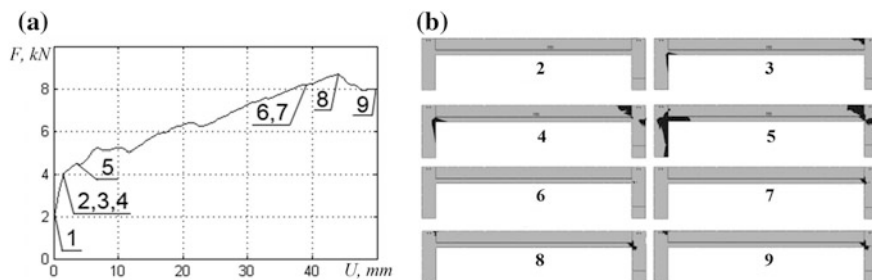


Fig. 3 Calculation results obtained for the system “2 column–beam” under differential settlement conditions: **a** diagram showing how the force exerted on the column changes at given displacement (numbers—key deformation points); **b** fracture due to tension (points 3–5), and fracture due to compression (points 6–9)

Based on the results of numerical simulation, we have plotted the curve ($F-U$) (Fig. 3a). Here, the force F is the resultant response of the end of the right-hand column directed along its axis. The numbers at this curve show key deformation points. Rupture areas corresponding to these deformation stages are shown in black in Fig. 3b. At points 3–5 on the curve ($F-U$), fracture is caused by tension and at points 6–9 by compression. Before applying displacements, the structure is under its proper weight—point 1 ($U = 0, F = 1.9$ kN). Linear increase in the displacements up to point 2 ($U = 1.2$ mm, $F = 3.7$ kN) proceeds without ruptures. However, the subsequent points 3 ($U = 1.6$ mm, $F = 4.0$ kN) and 4 ($U = 2.0$ mm, $F = 4.1$ kN) are associated with the generation and propagation of cracks in the extended zones, which increase essentially at point 5 ($U = 3.6$ mm, $F = 4.5$ kN). At point 6 ($U = 38.9$ mm, $F = 8.2$ kN), the compressed region becomes the site of nucleation of the fracture zone (right-hand low part of the beam), which on approaching point 7 ($U = 38.9$ mm, $F = 8.2$ kN) becomes more pronounced. The concrete in the second compressed zone located in the left-hand upper part of the beam destroys at point 8 ($U = 44.4$ mm, $F = 8.6$ kN). After that, the force exerted on the column decreases until point 9 ($U = 49.7$ mm, $F = 7.8$ kN) is reached. Further increase in the displacement leads to complete loss of load-bearing capacity.

3.3 Deformation of the System “9 Columns–12 Beams”

The next fragment of higher complexity is the system consisting of 9 columns and 12 beams (Fig. 1c). It indicates a combined action of beams and columns of the first story at vertical displacement U of the central column foundation (Fig. 4a). As in

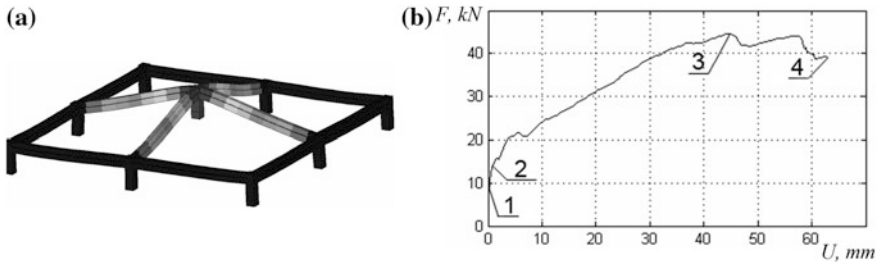


Fig. 4 Calculation results obtained for the system “9 columns–12 beams”: **a** deformed shape of the system at relative vertical displacement of the central column; **b** diagram force (F) versus displacement (U)

the previous calculation, a plot of force F generated in the column versus the given displacement of its foundation is constructed (Fig. 4b).

The fracture of beams is similar to that observed in the system “2 columns–beam.” The key deformation points are shown in Fig. 4b: 1 ($U = 0$, $F = 6.0$ kN)—system under its proper weight; 2 ($U = 0.8$ mm, $F = 10.7$ kN)—fracture initiation in the extended zones of beams; 3 ($U = 45.0$ mm, $F = 44.6$ kN)—maximum force and initiation of fracture in the compressed zones of beams; 4 ($U = 62.9$ mm, $F = 39.2$ kN)—loss of bearing capacity.

3.4 Deformation of the System “9 Columns–12 Beams–4 Floor Slabs”

A contribution of floor slabs to the operation of the examined structure is considered by studying the behavior of the system “9 columns–12 beams–4 floor slabs” (Fig. 1d). This system differs from the previous one by the presence of four floor slabs. The deformed shape of the system due to relative vertical displacement of the central column foundation is presented in Fig. 5.

Figure 6a presents the plot of force F applied to the central column versus the prescribed displacement U . The key deformation points marked on the graph are as follows: 1 ($U = 0$, $F = 34.1$ kN)—system is under its proper weight; 2 ($U = 0.5$ mm, $F = 69.5$ kN)—splitting of joints between the floor slabs accompanied by simultaneous fracture of the concrete in the extended zone; 3 ($U = 3.1$ mm, $F = 126.8$ kN)—maximum force achievement, initiation of fracture in beams; 4 ($U = 4.7$ mm, $F = 110.5$ kN)—complete fracture of floor slabs; 5 ($U = 13.3$ mm, $F = 107.8$ kN)—fracture of the concrete in the compressed zone and loss of bearing capacity. In Fig. 8b, the areas of destroyed concrete in the slabs formed at the loading stages corresponding to points 2, 3, and 4 are shown in black. In contrast to the same system but without floor slabs, the maximum force exerted

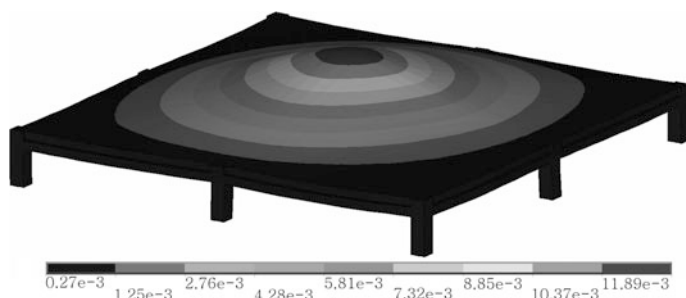


Fig. 5 Deformed shape of the system “9 columns–12 beams–4 floor slabs” at relative vertical displacement of the central column

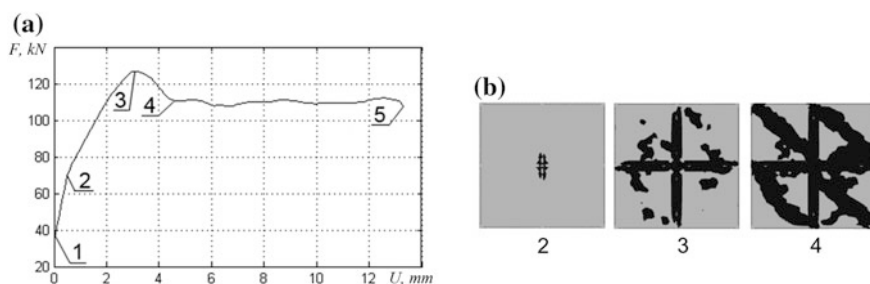


Fig. 6 Calculation results for the system “9 columns–12 beams–4 floor slabs”: **a** diagram force versus displacement (numbers—key deformation points); **b** fracture areas (black color—top view) in compliance with points on the plot ($F-U$)

on the column increases by a factor of 2.8, and the displacement of columns at the moment when the force reaches a maximum decreases by 14 times. Hence, it can be concluded that the floor slabs have a strong impact on deformation and fracture of the structure.

3.5 Deformation of the Four-Level Structure

The structure is deformed due to the vertical displacement of the foundation of one internal column with respect to other fixed ones (Fig. 7a). Analysis of the results of numerical simulation yields the plot ($F-U$), Fig. 7b. Here, the force F is the axial force in the foundation of the internal column, for which the displacement U is specified. The key deformation points marked on the curve are as follows: 1 ($U = 0$, $F = 147$ kN)—system at its proper weight; 2 ($U = 0.5$ mm, $F = 260$ kN)—appearance of first

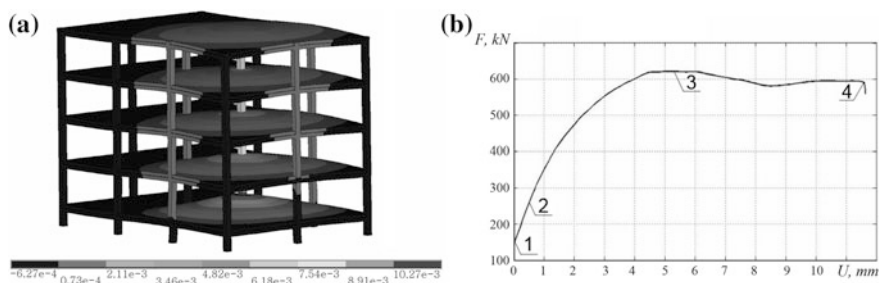


Fig. 7 Results of modeling of the deformation process in the four-story structure: **a** deformed shape of the structure, **b** diagram force versus displacement

cracks in the extended zones of beams; 3 ($U = 5.2$ mm, $F = 621$ kN)—generation of cracks in floor slabs corresponds to the maximum force in the column; 4 ($U = 11.6$ mm, $F = 590$ kN)—fracture of the compressed zones of beams.

4 The Structure Diagram of the Test Stand and Its Parameters

Numerical simulations of deformation of the model reinforced concrete structure subjected to subsequent loading up to its destruction allowed us to develop the structure of the test stand for physical experiments with large-scale structures. Figure 8 presents the structure diagram of the test stand with a model construction inside it. The dimensions of the model construction are $6 \times 6 \times 9$ m. Overall dimensions for the force loop of the test stand and the reinforced concrete foundation are given in figure.

Based on the results of numerical experiments, we have evaluated parameters for the loading units of the stand. It has been established that the range of force generated by the loading unit in order to reliably reach the critical state of the model should be 0–1000 kN. Table 1 gives the values of estimated critical loads (forces and displacements) applied to the components of the model construction at different loading stages. To provide a controlled transition of the model from elastic to subcritical and critical states, it is necessary to ensure accurate dosing of loading. Simulations showed that the accuracy of prescribing the displacement of separate elements of the model construction should be as high as 0.1 mm.

The analysis of the sites of fracture initiation found from numerical experiments of the construction allowed us to determine the appropriate locations of strain sensors and to fit the parameters of the registration apparatus (sensor types, measurement accuracy). This information will be used to perform physical experiments on studying the evolution of critical states in the model reinforced concrete construction.

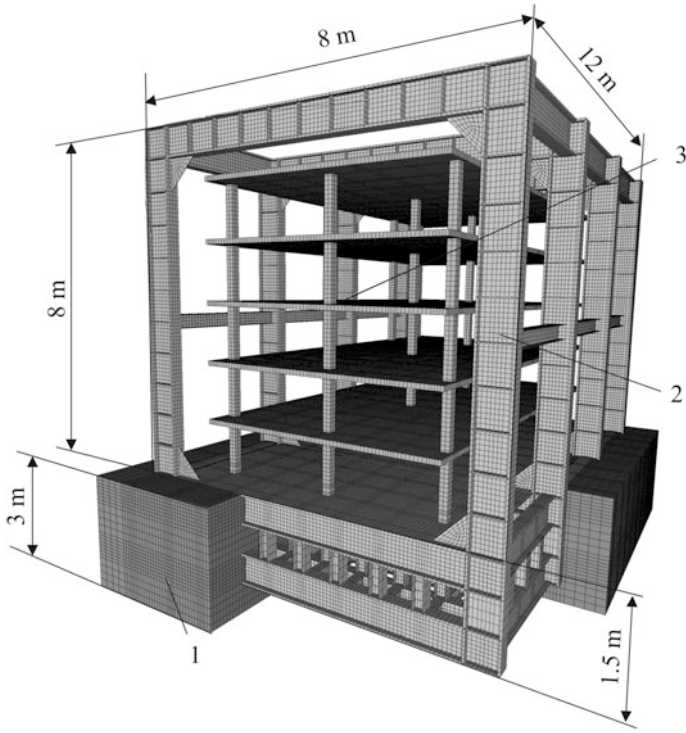


Fig. 8 Test stand with scale model of the structure: 1—reinforced concrete foundation, 2—force loop, 3—scale model of building

Table 1 Forces and displacements at various deformation stages in the assembled structure and its fragments

Structure element	Limiting values of elastic deformation F (kN)	Limiting values of elastic deformation U (mm)	Max. force at all deformation process F (kN)
“2 column–beam”	3.7	1.2	8.6
“9 column–12 beams”	10.7	0.8	44.6
“9 column–12 beams–4 floor slabs”	69.5	0.5	126.8
Four-story structure	260	0.5	621.0

5 Conclusion

Based on the mathematical simulation of quasi-static deformation processes taking place in the model RC structure and its fragments, we determined the following:

- linear dimensions of the scale model;
- specific forces, deformations, and displacements at which one can realize sub-critical and critical deformation processes in the assembled RC structure and its components;
- scenarios for spatial distribution of fracture in the assembled RC structure and its components;
- required accuracy of the prescribed kinematic loadings.

The obtained preliminary estimates served as a basis for the development of the structural stand for investigating deformation processes in reinforced structures. A set of loading units able to provide a controlled transition of the model construction to the critical state were proposed. The strain registration system was designed.

Acknowledgements The work is supported by Russian Science Foundation (project No. 14–29–00172).

References

1. C. Casandjian, N. Challamel, C. Lanos, J. Helleland, *Reinforced Concrete Beams, Columns and Frames: Mechanics and Design* (ISTE and Wiley, 2013)
2. Ł. Skarżyński, J. Tejchman, Experimental investigations of fracture process in concrete by means of X-ray micro-computed tomography. *Strain* **52**, 26–45 (2016)
3. P. Negro, D.A. Bournas, F.J. Molina, Pseudodynamic test on a full-scale 3-storey precast concrete building: global response. *Eng. Str.* **57**, 594–608 (2013)
4. D.P. McCrum, B.M. Broderick, An experimental and numerical investigation into the seismic performance of a multi-storey concentrically braced plan irregular structure. *Bull. Earthq. Eng.* **11**, 2363–2385 (2013)
5. K.C. Tsai, P.C. Hsiao et al., Pseudo-dynamic tests of full-scale CFT/BRB frame—part 1: specimen design, experiment and analysis. *Earthq. Eng. Struct. D* **37**, 1081–1098 (2008)
6. K.C. Tsai, P.C. Hsiao et al., Pseudo-dynamic tests of full-scale CFT/BRB frame—part 2: seismic performance of buckling-restrained braces and connections. *Earthq. Eng. Struct. D* **37**, 1099–1115 (2008)
7. R. Illampas, D.C. Charmpis, I. Ioannou, Finite element simulation of the structural response of adobe masonry buildings subjected to lateral loading, in *Proceedings SAHC* (Mexico, 2014), 12 p
8. K.J. William, E.P. Warnke, Constitutive model for the triaxial behavior of concrete. *Proc. Int. Assoc. Bridge Struct. Eng.* **19**, 1–30 (1974)
9. L.M. Kachanov, *Foundations of Theory of Plasticity* (North-Holland, Amsterdam, 1971)

Mode I SIF Determination of Orthotropic Laminates with Double-Ended Cracks Using a Single-Strain Gage

Debaleena Chakraborty, D. Chakraborty and K. S. R. K. Murthy

Abstract The experimental determination of mode I SIF (K_I) in orthotropic composites is significant, and strain gage-based approaches for SIF determination are quite economic and easy to use. Strain gage techniques that have been developed for measurement of K_I of orthotropic laminates are based on the solutions of single-ended crack theories. The present investigation aims at demonstrating the application of a single-strain gage technique (based on single-ended crack theory) recently proposed by the authors to double-ended cracked configurations for accurate measurement of KI. Finite element-based numerical analyses have been conducted on carbon-epoxy orthotropic laminates having center-cracked configurations. The existence and determination of optimal gage locations for accurate measurement of K_I have also been shown through numerical studies. Numerical results show that accurate values of K_I for double-ended cracked orthotropic laminates can be obtained with the help of a single-strain gage, when placed within the optimal zone.

Keywords Orthotropic laminate · Strain gage · Mode I SIF · Double ended cracks

Nomenclature

a_{11}, a_{12}	Material properties depending on Young's modulus, Poisson's ratio, and shear modulus
a_{22}, a_{21}	Material properties depending on Young's modulus, Poisson's ratio, and shear modulus
α, β	Parameters dependent on material properties
E_i	Young's modulus along i th direction ($i = L, T$)
G_{LT}	Shear modulus in L - T plane
L, T	Principle material directions (longitudinal and transverse)

D. Chakraborty (✉) · D. Chakraborty · K. S. R. K. Murthy
Department of Mechanical Engineering, IIT Guwahati, Guwahati 781039, India
e-mail: debaleena@iitg.ernet.in

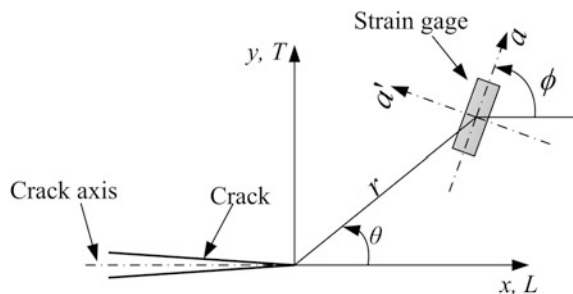
1 Introduction

A substantial amount of work has been reported in the field of fracture mechanics of composite materials in the last few decades. Irwin [1] and Wu et al. [2] reported on the feasibility of applying the concepts of linear elastic fracture mechanics (LEFM) to homogenous, isotropic materials to composites following appropriation to account for the directional properties of these materials. This leads to the examination of crack instability of these materials using stress intensity factor (SIF) as a criteria to measure the strength of a cracked body.

The experimental determination of SIF using strain gages is quite popular due to its cost-effectiveness and feasibility in handling. The Dally and Sanford [3] single-strain gage technique is the first of its kind for homogeneous isotropic materials which enables the determination of mode I SIF (K_I) using a single-strain gage and necessitates a single-strain gage to be placed along a line (decided by angle, θ and called gage line) and oriented along ϕ as shown in Fig. 1.

A significant emphasis has been laid on the experimental determination of SIFs of cracked composite panels since they are of great utility not only in complex configurations but also in validating the numerical and experimental results [4–9]. Cerniglia et al. [6] formulated an over deterministic method for estimation of K_I in orthotropic materials by employing large number of strain gages. Shukla and coworkers [7] were the first to propose a single-strain gage technique for the determination of K_I for orthotropic laminates. However, instead of a three-parameter series like Dally and Sanford, they used a two-parameter series representation of the strain field around the crack tip thereby limiting the allowable radial distance for pasting the strain gage. Khanna and Shukla [8] employed the technique proposed by Shukla et al. [7] in fracture analysis of a dynamic crack in orthotropic composites. A straightforward extension of the Dally and Sanford technique to orthotropic materials has been developed by Chakraborty et al. [9], where the benefits of using a three-parameter series can be availed and the gage could be placed at such a distance from the crack tip that not only the singular solution remains valid in that zone but the strain readings are also unaffected by strain gradients and 3-D effects.

Fig. 1 Crack tip local coordinate system and location of strain gage



It may be pointed out that till date single-ended crack theories have been employed to develop experimental methods for measurement of mode I SIF of orthotropic materials using strain gages [6–9] and tested only on single-ended cracked configurations. However, these single-ended crack theories, can be successfully applied to double-ended crack configurations when the distance between the neighboring crack tips is such that their stress fields don't interact with each other [10].

Only recently Chakraborty et al. [11] extended the strain gage technique by Chakraborty et al. [9] (which is based on single-ended crack theory) to the double-ended cracks for the accurate estimation of K_I in laminated orthotropic composites having internal cracks. Using the same technique, an attempt has been made in the present work to determine K_I of a $[90_2/0]_{10S}$ carbon-epoxy laminate having a center-cracked configuration. Numerical simulations have been presented using the laminate properties of $[90_2/0]_{10S}$ carbon-epoxy laminates.

2 Theoretical Formulations

In this section, the extension of the Dally and Sanford technique [3] to orthotropic materials and a theoretical basis for ascertaining the limit of the maximum radial distance for possible positioning of a strain gage has been laid out. Using three-parameter strain series, the normal strain component ε_{aa} at an angle ϕ with the crack axis at a point P (Fig. 1) located by r and θ within the singularity dominated zone can be obtained as

$$\varepsilon_{aa} = \frac{A_0}{\sqrt{r}} f_1(r, \theta, \phi) + A_1 \sqrt{r} f_2(r, \theta, \phi) + B_0 f_3(\theta, \phi) \tag{1}$$

where f_1, f_2 , and f_3 , the coefficients of A_0, A_1 , and B_0 , are functions of θ, ϕ and material properties of the orthotropic laminate (E_L, E_T, G_{LT} and ν_{LT}) and is given by

$$f_1(\theta, \phi) = \sqrt{4}(\cos^2 \theta + (\beta + \alpha) \sin^2 \theta) \left\{ \begin{aligned} & \left[\frac{1}{E_T} \left(\frac{1 - \nu_{LT} \nu_{TL}}{1 + \nu_{LT}} \right) \frac{\alpha - \beta}{2\alpha} \cos \left(\frac{1}{2} (\tan^{-1}((\beta + \alpha) \tan \theta)) \right) \right] \\ & - \left[\frac{1}{G_{LT}} \left(\frac{\nu_{LT}}{(1 + \nu_{LT}) \sqrt{\nu_{TL}}} \right) \frac{1}{2\alpha} \sin \left(\frac{1}{2} (\tan^{-1}((\beta + \alpha) \tan \theta)) \right) \right] \end{aligned} \right\} \\ + \sqrt{4}(\cos^2 \theta + (\beta - \alpha) \sin^2 \theta) \left\{ \begin{aligned} & \left[\frac{1}{E_T} \left(\frac{1 - \nu_{LT} \nu_{TL}}{1 + \nu_{LT}} \right) \frac{\alpha + \beta}{2\alpha} \cos \left(\frac{1}{2} (\tan^{-1}((\beta - \alpha) \tan \theta)) \right) \right] \\ & + \left[\frac{1}{G_{LT}} \left(\frac{\nu_{LT}}{(1 + \nu_{LT}) \sqrt{\nu_{TL}}} \right) \frac{1}{2\alpha} \sin \left(\frac{1}{2} (\tan^{-1}((\beta - \alpha) \tan \theta)) \right) \right] \end{aligned} \right\} \tag{2}$$

$$f_2(\theta, \phi) = \frac{1}{E_T} \left(\frac{1 - \nu_{LT}\nu_{TL}}{1 + \nu_{LT}} \right) \frac{1}{2\alpha} \left\{ \begin{array}{l} \frac{\cos\left(\frac{1}{2}\tan^{-1}((\beta + \alpha)\tan\theta)\right)}{\sqrt{4(\cos^2\theta + (\beta + \alpha)^2\sin^2\theta)}} (\alpha - \beta) \\ + \frac{\cos\left(\frac{1}{2}\tan^{-1}((\beta - \alpha)\tan\theta)\right)}{\sqrt{4(\cos^2\theta + (\beta - \alpha)^2\sin^2\theta)}} (\alpha + \beta) \end{array} \right\} \quad (3)$$

$$+ \frac{1}{G_{LT}} \left(\frac{\nu_{LT}}{(1 + \nu_{LT})\sqrt{\nu_{TL}}} \right) \frac{1}{2\alpha} \left\{ \begin{array}{l} \frac{\sin\left[\frac{1}{2}\tan^{-1}((\beta + \alpha)\tan\theta)\right]}{\sqrt{4(\cos^2\theta + (\beta + \alpha)^2\sin^2\theta)}} \\ - \frac{\sin\left[\frac{1}{2}\tan^{-1}((\beta - \alpha)\tan\theta)\right]}{\sqrt{4(\cos^2\theta + (\beta - \alpha)^2\sin^2\theta)}} \end{array} \right\}$$

and

$$f_3(\theta, \phi) = \left\{ \frac{\beta}{2\alpha} [(\alpha + \beta)^2 - (\beta - \alpha)^2] (a_{11} \cos^2\phi + a_{12} \sin^2\phi) \right\} \quad (4)$$

It could be shown that there are specific values of θ and ϕ for which the coefficients of A_1 and B_0 could be made zero. Putting those values in Eq. (1), we get

$$\varepsilon_{aa} = \frac{1}{\sqrt{r}} \times A_0 \left\{ \begin{array}{l} \frac{1}{E_2} \left(\frac{1 - \nu_{LT}\nu_{TL}}{1 + \nu_{LT}} \right) \frac{1}{2\alpha} \left[\begin{array}{l} \frac{\cos\left(\frac{1}{2}\tan^{-1}((\beta + \alpha)\tan\theta)\right)}{\sqrt{4(\cos^2\theta + (\beta + \alpha)^2\sin^2\theta)}} (\alpha - \beta) \\ + \frac{\cos\left(\frac{1}{2}\tan^{-1}((\beta - \alpha)\tan\theta)\right)}{\sqrt{4(\cos^2\theta + (\beta - \alpha)^2\sin^2\theta)}} (\alpha + \beta) \end{array} \right] \\ + \frac{1}{G_{12}} \left[\frac{\nu_{LT}}{(1 + \nu_{LT})\sqrt{\nu_{TL}}} \right] \frac{1}{2\alpha} \left[\begin{array}{l} \frac{\sin\left(\frac{1}{2}\tan^{-1}((\beta + \alpha)\tan\theta)\right)}{\sqrt{4(\cos^2\theta + (\beta + \alpha)^2\sin^2\theta)}} \\ - \frac{\sin\left(\frac{1}{2}\tan^{-1}((\beta - \alpha)\tan\theta)\right)}{\sqrt{4(\cos^2\theta + (\beta - \alpha)^2\sin^2\theta)}} \end{array} \right] \end{array} \right\} \quad (5)$$

$$\Rightarrow \varepsilon_{aa} = \frac{A_0}{\sqrt{r}} C$$

where C is a constant for a given value of θ, ϕ and material properties. Taking logarithm on both sides of Eq. (5), we get

$$\ln(\varepsilon_{aa}) = -\frac{1}{2}\ln(r) + \ln(C') \quad (6)$$

A plot of Eq. (6) between $\ln(\varepsilon_{aa})$ and $\ln(r)$ leads to a straight line of slope equal to -0.5 with an intercept of $\ln(C')$. If r_{\max} is the extent of valid three-parameter zone, theoretically, the straight line property should break beyond $r > r_{\max}$ as more than three parameters will be needed in Eq. (1) to estimate the ε_{aa} . Thus, by placing a single-strain gage as shown in Fig. 1 at a radial distance r within r_{\max} from the crack tip along the line at an angle of θ and oriented at an angle of ϕ , the measured

strain ϵ_{aa} can be equated to Eq. (5) to obtain the value of unknown coefficient A_0 . By applying the standard definition of mode I SIF, K_I , it can be easily shown that A_0 is related to the SIF by the relation

$$K_I = \sqrt{2\pi}A_0 \tag{7}$$

3 Numerical Simulation

A center-cracked orthotropic $[90_2/0]_{10S}$ carbon-epoxy laminate configuration subjected to uniform tensile stress with the material properties as $E_L = 67.77$ GPa; $E_T = 142.7$ GPa; $\nu_{LT} = 0.01$; $G_{LT} = 4.304$ GPa is considered (Fig. 2a). Following the procedure described in Sect. 2, the values of ϕ and θ for which the coefficients B_0 and A_1 become zero are found to be 84° and 61° , respectively.

Finite element analysis is carried out using ANSYS[®]. Figure 2b shows the analysis domain with boundary conditions used for the numerical analysis, and Fig. 2c shows the typical finite element mesh considered after proper convergence study. Eight-noded isoparametric elements (PLANE 183) have been used for finite element discretization of the plate, and quarter point elements (QPE) have been

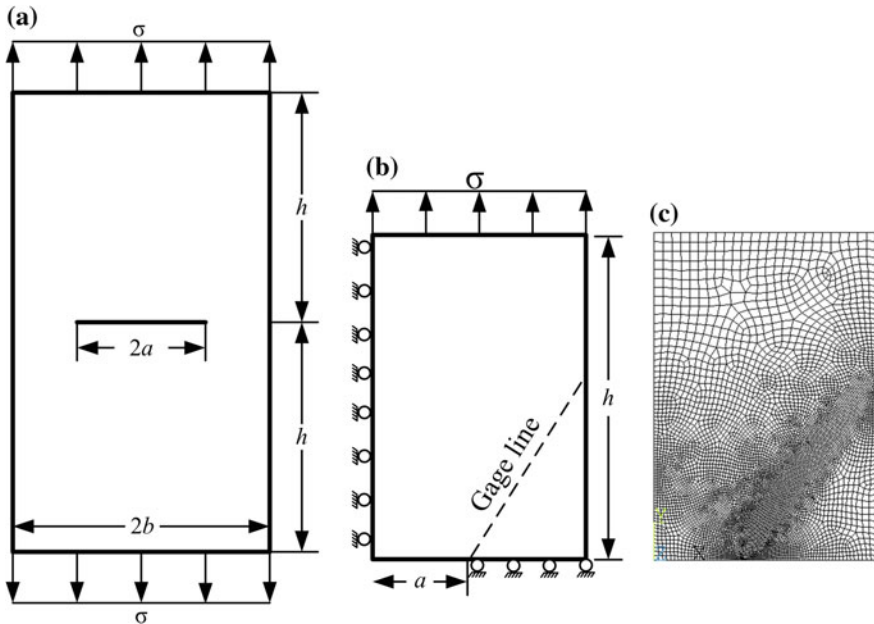


Fig. 2 a Orthotropic center-cracked plate, b analysis domain, c FE mesh of the model

used around the crack tip. The mesh has been designed such that the nodes of several elements are made to lie along the gage line. According to the present technique, a single-strain gage is to be placed at an appropriate location along the gage line and oriented along ϕ in order to measure the linear strain ϵ_{aa} .

From the finite element results, the linear strain (ϵ_{aa}) and radial distance (r) are computed for all the nodes along the gage line. Figure 3 shows the plot of $\ln(\epsilon_{aa})$ versus $\ln(r)$ for all the nodal values along the gage line. Crack tip point is not plotted as the radius of this point is zero. It can be seen that the plot consists of a linear plot followed by a nonlinear one as predicted by the theory. The radial distance till which the plot is linear and beyond which the plot changes from a linear one to a nonlinear one is r_{max} or the extent of the three-parameter zone or the optimal radial location for pasting the strain gage. A line of slope -0.5 is superposed on the plot of $\ln(\epsilon_{aa})$ versus $\ln(r)$. Considering this line to be the exact solution, absolute percentage relative error at all values of radius is being calculated. Finally, r_{max} is estimated as the radius at which the error is less than 1% (as one goes from right to left in Fig. 3). The analytical value of mode I SIF of this configuration is given by [7]

$$K_I = Y_I(a/b)\sigma\sqrt{a} \tag{8}$$

where σ is the applied stress, a is the crack length, and Y_I is the specimen geometric factor given by [12]

$$Y_I = 1.77 + 0.227(a/b) - 0.510(a/b)^2 + 2.699(a/b)^3 \tag{9}$$

For this configuration with crack length to width ratio (a/b) of 0.4 and loaded at $\sigma = 100$ MPa, the reference value of mode I SIF determined using Eq. (8) is $K_I = 27.6$ MPa \sqrt{m} and r_{max} is found to be 22.42 mm. Radial locations are selected within and outside the simulated r_{max} to establish the importance of radial positioning of the strain gage. The percent relative errors in measured K_I determined

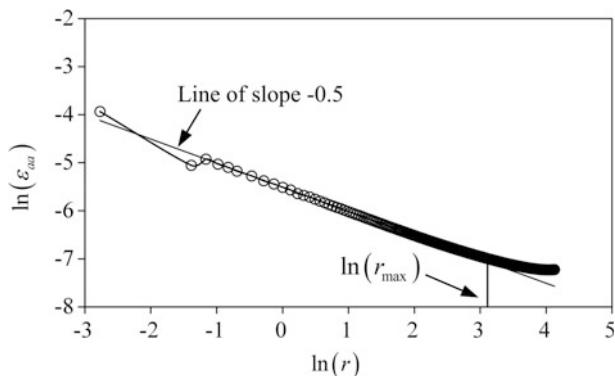


Fig. 3 Linear and nonlinear variation of $\ln(\epsilon_{aa})$ with $\ln(r)$ for the nodes along the gage line

Table 1 Simulated mode I SIF of the orthotropic panel at optimal and nonoptimal positions

r (mm)	ϵ_{aa}	K_I (MPa \sqrt{m})	% Relative error
10.04	1.29E-03	28.11	1.8
16.06	1.05E-03	28.2	2.1
25.01	8.82E-04	33.25	20.47
30.06	8.28E-04	34.22	23.98

using Eq. (7) from the strain readings at those locations obtained from the finite element analysis are shown in Table 1. The percentage relative error in K_I measured at those locations is computed as

$$\%Rel. \text{ error} = \frac{K_{\text{Referencesolution}} - K_{\text{measuredorsimulated}}}{K_{\text{Referencesolution}}} \times 100 \tag{10}$$

Results in Table 1 clearly show that it is possible to accurately determine K_I (order of error 2%) for center-cracked orthotropic laminates using a single-strain gage if the gage is placed within r_{max} . On the other hand, placing a strain gage outside r_{max} leads to highly inaccurate values of K_I of about 24%. These results substantiate that the present technique of determination of K_I using a single-strain gage can be used for accurate determination of K_I even for double-ended cracked orthotropic composite specimens if the gages are placed within the optimal locations.

4 Conclusion

The single-strain gage technique for determination of mode I SIF of cracked orthotropic materials has been numerically verified for carbon-epoxy laminates with a double-ended cracked configuration thereby establishing the successful implementation of the single-ended crack theory to double-ended cracks for orthotropic materials. Numerical results show that accurate estimation of K_I of the center-cracked carbon-epoxy laminate is possible for strain gages well within the optimal locations. On the other hand, high errors of the order of around 24% could be observed if the gages are placed outside the estimated r_{max} for that configuration. These observations establish the fact that proper positioning of strain gages as per the predetermined optimal locations is essential for accurate estimation of SIFs.

References

1. G.R. Irwin, Analytical aspects of crack stress field problems. T&AM Report No. 213, University of Illinois, Urbana (1962)
2. E.M. Wu, On the application of fracture mechanics to orthotropic plates. T&AM Report No. 248, University of Illinois, Urbana (1963)

3. J.W. Dally, R.J. Sanford, Strain gage methods for measuring the opening mode stress intensity factor. *Exp. Mech.* **27**, 381–388 (1987)
4. M.C. Baik, S.H. Choi, J.S. Hawong, J.D. Kwon, Determination of stress intensity factors by the method of caustics in anisotropic materials. *Exp. Mech.* **35**, 137–143 (1995)
5. M. Mojtahed, L.W. Zachary, Use of photoelasticity to determine orthotropic stress-intensity factor. *Exp. Mech.* **27**, 184–189 (1987)
6. D. Cerniglia, V. Nigrelli, A. Pasta, Experimental and numerical determination of stress intensity factor in composite material, in *Conference Proceedings ICCM-12, Paper 932, Europe* (1999)
7. A. Shukla, B.D. Agarwal, B. Bhusan, Determination of stress intensity factor in orthotropic composite materials using strain gages. *Eng. Fract. Mech.* **32**, 469–477 (1989)
8. S.K. Khanna, A. Shukla, Development of stress field equations and determination of stress intensity factor during dynamic fracture of orthotropic composite materials. *Eng. Fract. Mech.* **47**, 345–359 (1994)
9. D. Chakraborty, K.S.R.K. Murthy, D. Chakraborty, A new single strain gage technique for determination of mode I stress intensity factor in orthotropic composite materials. *Eng. Fract. Mech.* **124–125**, 142–154 (2014)
10. K. Bearden, J.W. Dally, R.J. Sanford, Experimental determination of for short internal cracks. *J. App. Mech.* **68**, 937–943 (2001)
11. D. Chakraborty, K.S.R.K. Murthy, D. Chakraborty, Determination of in orthotropic laminates with double ended cracks using a single strain gage technique. *Theory Appl. Frac. Mech.* **82**, 96–106 (2016)
12. H. Tada, P.C. Paris, G.R. Irwin, *The Stress Analysis of Cracks handbook* (ASME, New York, 2000)

Mechanical Testing of Elevated Temperature PMC, Metallic, and CMC Coupons

Erik A. Schwarzkopf and Michael J. Shepard

Abstract A cornerstone of structural integrity is the proper use and characterization of structural materials. Improper materials characterization or use of a material system outside its designed use range (intentionally or unintentionally) can have perilous results for structural integrity. As gas turbine engines and other applications drive toward higher operating temperatures for structural elements, the materials characterization and design allowable generation activities become increasingly difficult. We discuss elevated temperature testing requirements and the development of testing solutions aligned with these requirements. Mechanical testing systems for elevated temperature testing for polymeric matrix composites (PMCs), metallics, and ceramic matrix composites (CMCs) were developed. Test capability for temperatures as high as 1500 °C was demonstrated. The development of these systems will be briefly reviewed with particular focus on design aspects, system performance, and general usability of a system targeting testing of cylindrical metallic specimens at temperatures up to 1200 °C.

Keywords High temperature · PMC · CMC · Metals · Mechanical testing

1 Introduction

The global marketplace is driving toward transportation and energy products and systems that are increasingly efficient. In this drive toward increasing efficiency, two principle themes are dominant with regard to material selection. The first theme is the utilization of alternative materials that are superior in terms of their mechanical properties on a density normalized (specific) basis. The second theme is increasingly high operational temperatures for energy conversion processes where this will improve efficiency (combustion). These material selection themes can

E. A. Schwarzkopf (✉) · M. J. Shepard
MTS Systems Inc., 14000 Technology Drive, Eden Prairie, MN 55344, USA
e-mail: Erik.Schwarzkopf@MTS.com

often involve substitutions of materials of entirely different classes. Relevant examples of such substitutions from an aerospace context include ceramic matrix composites (CMCs) for nickel alloys, titanium alloys for nickel alloys, and polymer matrix composites (PMCs) for titanium or aluminum alloys.

The ramifications of these material selection decisions with respect to materials testing requirements at a wide range of temperatures have been discussed and summarized previously [1–7]. Mechanical testing systems must be capable of achieving appropriate testing temperatures and mechanical loading conditions. The temperature requirements tend to be a primary consideration due to the complexity that elevated temperatures bring for general system function and durability. Summarizing briefly, for PMCs, titanium alloys, and aluminum alloys, a nominal use temperature range of 23–425 °C is appropriate. For high-temperature metals, a temperature range of nominally 800–1200 °C covers a useful range of service and processing temperatures. And finally for CMCs in structural applications, testing at temperatures between 800 and 1500 °C are required.

For each of these temperature ranges and families of materials, appropriate systems for mechanical testing are required. In addition to a load frame, a mechanical testing system will require a method of holding and applying load to test specimens (grips), a method for getting the test specimen to appropriate temperature (furnaces or environmental chambers, induction heating), and often some method of characterizing strain (extensometry, strain gages, etc.). Each of these elements contributes to the proper execution of the mechanical test and the accuracy of the collected data. The performance of these individual components can be interrelated, so a systems approach is appropriate.

This paper will focus on experimental system evaluation results for a testing system designed for testing cylindrical, metallic specimens at temperatures up to 1200 °C.

1.1 High-Temperature Grips

To understand how interrelated component issues manifest during test setup, consider a typical specimen and a typical loading history. Metallic parts used in turbine engines often have duty cycles that include “through-zero” loading. Accurate elevated temperature and property measurement of these materials require minimal thermal gradient in the specimen gage section and the ability to maintain positive specimen contact with the grip while maintaining good specimen alignment during the entire loading history [8, 9]. Traditionally, this means that both the grips and specimen are controlled to the desired test temperature to minimize temperature gradients. For cylindrical metallic specimens, traditional grip end designs are threaded or “button-head” to allow sufficient compressive preloading of the grip end to allow through-zero testing of the gage section. These “hot” grips become problematic when the application temperature for metallic specimens exceeds about

1000 °C [10]. At these highest temperatures, the stresses in the grips exceed the strength of commonly available materials and also leave the grip structures susceptible to creep distortion or microstructural instability.

“Cold” grips, where the specimen is gripped outside of the furnace, are often used in these more aggressive temperatures, but require a long specimen to extend outside of the furnace, and result in significant temperature gradient in the specimen. Experimental economy, especially with costly developmental materials, does not generally allow these longer specimens, and the thermal gradients can become significant, adding experimental scatter and potentially reducing test yield due to failures outside the gage section.

“Warm grips” are a compromise. Multi-zone furnaces are used to keep the specimen gage length at the desired test temperature while the grip and specimen ends are heated as close as possible to the test temperature while still maintaining the strength of the grips. These grips also allow significantly shorter specimen dimensions and greatly reduced thermal gradients. The trade-off, essentially, is an increase in grip and furnace complexity in exchange for an increase in test quality. Three zone furnaces for materials testing are common, but “warm grips” usually require special integrated cooling of the grip, since the grip is so close to the very hot center zone of a furnace.

The advantage of “warm grips” becomes more apparent when testing CMC specimens at the highest application temperatures approaching 1500 °C [11]. CMCs, like PMCs, typically are tested as flat specimens. Unlike the metallic specimens, these flat, “dog-bone” specimens do not have threaded ends or buttons for end preloading. The most common solution is to load the specimen faces in shear using wedges. A very effective solution is to use hydraulically actuated wedges to grip the flat faces of these specimens. CMC and PMC specimens often have very poor through-thickness (short transverse) strength so uniformly applied pressure from hydraulic wedge faces on the gripped region minimizes specimen damage during gripping. often lack compressive strength across their thinnest cross section, and the evenly applied pressure from the hydraulic wedges protects the fibers in the polymer or ceramic matrix. In addition to preventing specimen damage, hydraulic grips also maintain constant gripping pressure as the specimen reaches testing temperature. Other solutions exist for gripping flat specimen, but many of the other solutions are limited to tensile only loading, or apply even displacement, rather than even pressure, which changes as both the grip and coupon changes their shape during heating.

The wedges used for flat composite specimen are retained by a wedge chamber, and at temperatures above 1000 °C, no commonly available material can easily withstand the hoop stress caused by the wedges in the chamber. As a result, “warm grips” are used for CMC testing at test temperatures between 1000 and 1500 °C. “Hot grips,” with the grips at the same temperature as the specimen, are used for PMC testing at temperatures below 425 °C.

1.2 *Furnaces and Chambers*

Furnaces and chambers must be paired with gripping technology to optimize elevated temperature testing results and minimize data variability. For the highest temperatures, where “warm grips” are required, furnaces typically have a special central zone with special elements providing the energy density to reach these highest 1200–1500 °C temperatures. For these highest temperatures, MoSi₂ heating elements are typical. These elements require slightly more complex controlling electronics for laboratory furnaces, but provide higher energy densities and higher temperatures than more traditional silicon carbide or resistive alloy heating elements used in most laboratory furnaces.

The high power density of MoSi₂ furnace elements allow the heated zone of the furnace to be smaller, allowing testing professionals to use smaller specimens. The hot, center zone of these very high-temperature furnaces is typically about 50 mm allowing for a 25 mm gage length. The outer zones of these 1200 °C plus furnaces typically use resistive alloy elements due to their cost-effective and robust nature.

Elevated temperature testing of PMCs uses “hot grips,” since the test temperature is typically much less than 371 °C, the highest T_g temperatures for the composite resins. These MTS model 647 All-Temperature grips are general purpose wedge grips designed for working temperatures up to about 540 °C. As general purpose grips, they can accommodate a wide range of specimen geometries, with a concomitant increase in size of the wedge chamber. The preferred heating subsystems used for these PMC tests are referred to as an environmental chamber and are usually comprised of a large heated box chamber (1/4 cubic meter heated space) to accommodate the hydraulic wedge grips and provide ample volume for various fixtures associated with PMC testing. Environmental chambers offer a capability to include test effects such as humidity and allow for controlled venting of noxious gasses that can be given off by composites during elevated temperature testing. The chamber for these PMC tests is often larger than the furnaces required for higher temperature metal or CMC tests. Although larger equipment usually is less efficient, the thermal mass of the grips and chamber leads to very stable test environments.

1.3 *Contact and Optical Extensometry*

The most common methods for accurate strain measurement during mechanical testing are contact extensometry and strain gages. Contact extensometry works well for testing with more conventional furnaces. With a smaller furnace, extensometers can be situated outside the chamber with their rods extending through furnace penetrations to contact the specimen [12–14]. With environmental chambers used for PMC testing, the larger chamber makes using contact extensometers more difficult. Due to the size of the environmental chamber, the extensometer rods become too long and cause additional measurement variability. A more compact

extensometer could be used inside the chamber but the high temperatures needed for some experiments would not be compatible with most available extensometers. Strain gages are available that can perform at elevated temperatures, but the inconvenience and expense of strain gage application is not particularly desirable, especially for high volume testing.

Increasing use is being made of video extensometry/digital image correlation. These methods are generally available are non-contact and can be situated outside the chamber if an optical quality window of sufficient size is available. The method requires a specimen with significant surface texture or user-applied targets or patterns. Uniform lighting is particularly important. At higher temperatures, the glow from heated specimens can reduce contrast and interfere with the video quality needed for precision measurements. For the PMC system discussed, a custom blue LED lighting solution was utilized in conjunction with filters to minimize any loss of contrast due to specimen heating.

2 Results

Representative, preliminary results are reported for the testing system capable of testing cylindrical, metallic specimens at temperatures up to 1200 °C. This system is depicted in Fig. 1 after over 1000 h of elevated temperature use. Similar characterizations are complete or in-process for the previously discussed systems operating at 425 and 1500 °C.

2.1 System Alignment

Proper system/grip alignment is critical to ensure excessive bending strains are not induced in the test specimen, reducing test accuracy. The relevant specifications for alignment are ASTM E1012 and ISO 23788. The alignment of the MTS 1200 °C test system, installed on a custom fabricated servo-hydraulic load frame, was assessed using the MTS 709 alignment system, as per ASTM E1012. The system was found to be alignable to better than ASTM E1012 Class 5, the best available classification. This level of alignability has been demonstrated with both a button-head and threaded specimen end configuration.

Figure 2 depicts one relevant experiment from this alignment exercise. In this figure, the bending strains associated with three banks (upper, middle, and lower) of four strain gages on the gage section of an alignment specimen are plotted. For compliance with ASTM E1012 Class 5 alignment requirements, all data must fall under the bending strain limits indicated by the dotted lines. The system was found

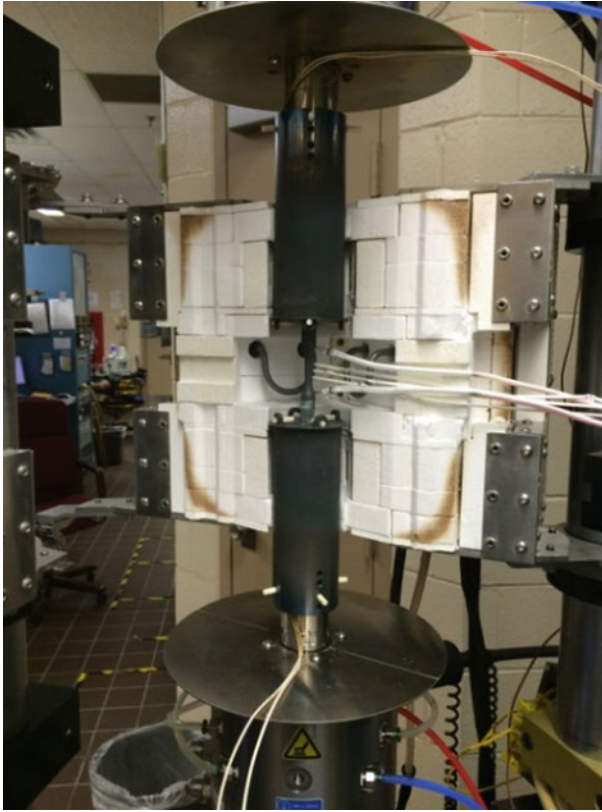


Fig. 1 1200 °C test system (grips and furnace) installed on servo-hydraulic load frame

compliant with E1012 Class 5, as indicated in Fig. 2, as well with repeated removal and rotation of the specimen, as required by ASTM E1012.

2.2 Thermal Gradients in Specimen Gage Section

To evaluate thermal gradients achievable in typical specimen gage sections at 1200 °C, representative cylindrical dog-bone specimens were fabricated in three different total specimen lengths, all as per the recommendations of ASTM E606—Standard Test Method for Strain-Controlled Fatigue. The specimens were thermocoupled to allow for an assessment of the thermal gradient achievable in the specimen gage section. Figure 3 depicts the thermal gradients achieved over the specimen gage sections as a function of time for the longest specimen (152.4 mm total length). Table 1 depicts the thermal gradients achieved for all specimen

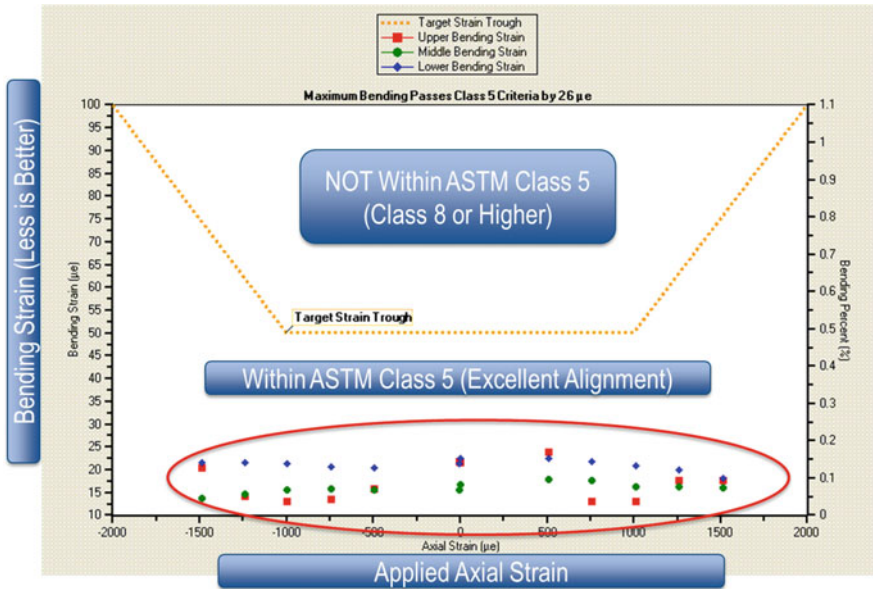


Fig. 2 Bending strain versus applied axial strain for ASTM E1012 1200 °C system alignment

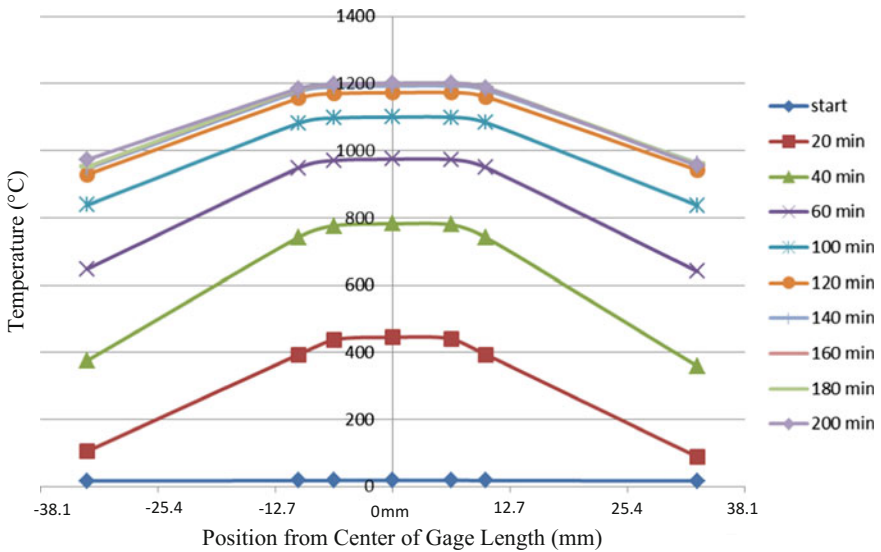


Fig. 3 Thermal gradients over time for 152.4 mm specimen

Table 1 Gage section thermal gradients achieved for three representative specimen lengths at 1200 °C

Total specimen length (mm)	Gage length (mm)	Gage gradient (°C)	ASTM E606 target (°C)
101.6	25.4	7	14.7
127	19.0	3–5	14.7
152.4	12.7	2–3	14.7

lengths. The gradients are significantly better than the $\pm 1\%$ recommended in E606, demonstrating excellent thermal gradient performance.

2.3 Grip Durability

Since the load-bearing elements of the grip are operating at significantly elevated temperatures, durability needs to be thoroughly evaluated. No failures were experienced through 990 h of elevated temperature operation. Historically, in grips operating for extended periods at elevated temperatures, gross creep distortion had been observed in structural elements subjected to the most aggressive combinations of temperature and stress. In the case of this grip design, the grip inserts (sometimes called grip nuts) experienced the most challenging creep exposures (highest temperatures under sustained load). Measurements were made throughout the testing campaign to document gross creep distortion (Fig. 4). No measurable creep distortion was observed, and operation of these threaded elements was routine throughout all 990+ hours of use.

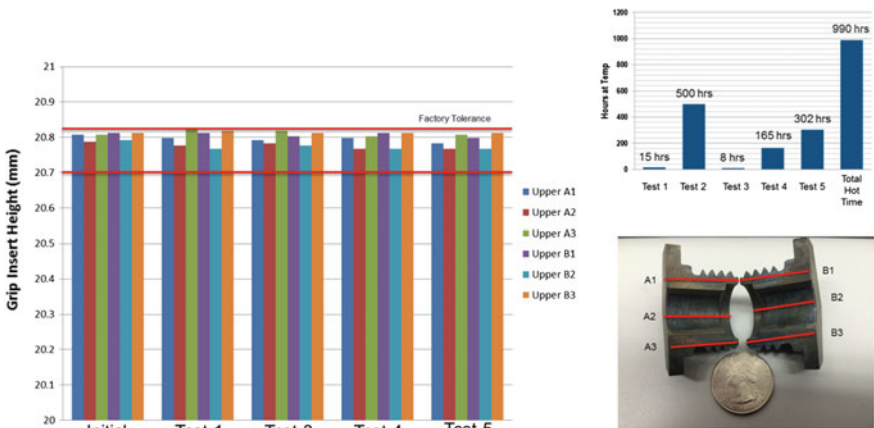


Fig. 4 Creep assessment in worst-case structural elements (no gross creep distortion indicated)

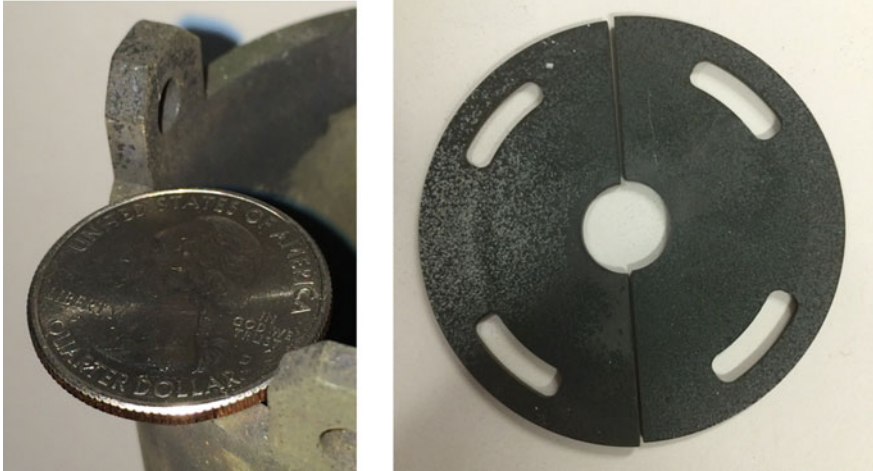


Fig. 5 Minor oxidation distress in non-structural elements

On non-structural elements, subjected to temperatures nearly as high as the gage section, some modest oxidation was observed. The observed oxidation was not sufficient to inhibit function or warrant replacement (Fig. 5).

3 Conclusions

High-temperature testing considerations for three mechanical testing systems have been discussed—a system for PMCs (up to 425 °C), a system for metals (up to 1200 °C), and a system for CMCs (up to 1500 °C). Equipment and associated trade-offs are discussed particularly with respect to alignment, thermal gradient, durability, and strain measurement, with specific examples being provided for the 1200 °C system under development.

The importance of appropriate gripping solutions was reviewed. A proper grip needs to effectively couple loads into a specimen without causing damage in the gripped section. The grip needs to align properly so that any bending moments induced in the specimen are strictly minimized. And finally, it needs to be able to survive the testing temperatures sufficiently well to provide a satisfactory service life. This may require the grip to be made of high-temperature materials and, in extreme cases, have integrated water and/or air cooling.

The selected thermal solution (furnace, chamber, etc.) needs to be sufficient to reach the targeted temperatures with the lowest possible thermal gradient across the specimen gage section. It also needs to accommodate any needed accessories such as contacting or video extensometry.

Finally, if strain measurement is required for the experiment, the system architecture, particularly the heating solution, needs to be configured to accommodate it. The strain measurement solution itself needs to be employed in a manner that will not subject it to a damaging environment or reduce its accuracy significantly.

Acknowledgements The continuing assistance of the US Air Force Research Laboratory's Materials and Manufacturing Directorate under Cooperative Research and Development Agreements 13-210-RX-01 and 13-210-RX-02 is kindly acknowledged. Particular thanks are extended to Drs. Andrew Rosenberger and Jonathan Spowart. Additional valuable support was provided by Mr. Phillip Blosser and Ms. Jennifer Pierce of the University of Dayton Research Institute, as well as Mr. Larry Zawada of Universal Technologies Corporation.

References

1. E.A. Schwarzkopf, Evaluating tradeoffs in high-temperature testing. *Adv. Mater. Process.* **174**, 16–18 (2016)
2. Z. Fawaz, Quality control and testing methods for advanced composites materials in aerospace engineering, in *Advanced Composite Materials for Aerospace Engineering: Processing, Properties, and Applications*, ed. by S. Rana, R. Fanguiero (Woodhead Publishing/Elsevier Science, 2016), pp. 429–452
3. U. Burger, L. Rochat, Aspects of damage tolerance and fatigue of CFRP structural components. *SAE Int. J. Aerosp.* **8**(2), 292–302 (2015)
4. A.L. Gyekenyesi, M.G. Castelli, J.R. Ellis, C.S. Burke, A study of elevated temperature testing techniques for the fatigue behavior of PMCS: Application to T650-35/AMB21. NASA Technical Memorandum 106927 (1995)
5. J. Mills-Brown, K. Potter, S. Foster, T. Batho, The development of a tensile testing rig for composite laminates. *Compos. A* **52**, 99–105 (2013)
6. D.C. Larsen, S.L. Stuchly, The mechanical evaluation of ceramic fiber composites, in *Fiber Reinforced Ceramic Composites*, ed. by K.S. Mazdiyasn (Noyes Park Ridge, NJ, 1990), pp 182–221
7. D.M. Dawson, R.F. Preston, A. Purser, *Fabrication and materials evaluation of high performance aligned ceramic fiber-reinforced, glass-matrix composite*, ed. by W. Smothers. 11th Annual Conference on Composites and Advanced Ceramic Materials: Ceramic Engineering and Science Proceedings, vol. 8, Issue 7/8, (Wiley, Hoboken, NJ, USA, 1987)
8. K. Staerk, High temperature axial strain-controlled LCF/TMF fatigue testing of flat-sheet specimens, in *Fatigue and Durability Assessment of Materials, Components and Structures*, ed. by M.R. Bache, P.A. Blackmore, J. Draper, J.H. Edwards, P. Roberts, J.R. Yates (Sheffield, UK, 2003), pp. 389–397
9. P.B.S. Bailey, A.D. Lafferty, Specimen gripping effects in composites fatigue testing—Concerns from initial investigation, *sXPRESS. Polym. Lett.* **9**(5), 480–488 (2015)
10. R.J. Greene, G.S. Hartman, A.H. Rosenberger, Detection of small cracks in nickel-based superalloys at elevated temperature, in *2004 SEM X International Congress & Exposition on Experimental & Applied Mechanics* (2004)
11. G.A. Hartman, L.P. Zawada, S.M. Russ, *Techniques for elevated temperature testing of advanced ceramic composite materials*, in Fifth Annual Hostile Environments and High Temperature Measurements Conference. Society for Experimental Mechanics, Costa Mesa, CA (1988)
12. J.Z. Gyekenyesi, J.H. Hemann, Optical strain measuring techniques for high temperature tensile testing. NASA Contractor Report 179637 (1987)

13. J.Z. Gyekenyesi, P.A. Bartolotta, An evaluation of strain measuring devices for ceramic composites. NASA Technical Memorandum 105337 (1991)
14. L.P. Zawada, Longitudinal and transthickness tensile behavior of several oxide/oxide composites. *Cerm. Eng. Sci. Proc.* **19**(3), 327–339 (1998)

In Situ Measurement of Deformation Under Tension of ABPBI and Its Composites

Abhijeet Dhiman, F. G. S. Wasim, M. Neergat and Krishna N. Jonnalagadda

Abstract Fuel cell devices convert chemical energy directly into electrical energy using hydrogen as fuel and are appreciated for generating clean energy, but are not yet commercially significant. Research in this area is in progress to make hydrogen fuel cells commercially feasible with good efficiency and reliability. Operating fuel cells below 100 °C temperature lead to poisoning of platinum electrodes due to small traces of carbon mono-oxide. This effect can be reduced significantly at temperatures above 150 °C. However, the commonly used Nafion membrane cannot be used at such temperatures due to the degradation in conductivity as a result of dehydration. One solution to this problem is to substitute commonly used Nafion membrane by other polymer electrolytic membrane, which can be operated at high temperatures. Recently, Poly (2,5-benzimidazole) (ABPBI) has been developed as a potential polymer electrolyte membrane (PEM) for fuel cell applications. ABPBI membrane doped with strong acids like phosphoric acid enhances conductivity at high temperatures. Furthermore, operating at high temperatures poses challenges to mechanical integrity and durability of the membrane. The mechanical endurance is one of the limiting factors for the long-term durability of PEM-based fuel cells. The degradation in performance of membrane is believed to be the result of mechanical and chemical effects acting together. Taking mechanical effects in brief, variation in temperature and humidity during the operation of fuel cell produces strains in membrane. Also, high strains are generated while starting fuel cell from cold state to operating temperature of 150 °C. In this work, the mechanical response of ABPBI polymer, ABPBI polymer doped with PWAZrO₂ inorganic filler, and phosphoric acid-doped ABPBI polymers was characterized. Mechanical behavior was extracted via in situ tensile experiments on 20–40 μm polymer specimens. It was found that the addition of filler increased the stiffness of

A. Dhiman (✉) · M. Neergat · K. N. Jonnalagadda
Indian Institute of Technology Bombay, Powai, Mumbai 400076, India
e-mail: abhi.dhiman.iitb@gmail.com

K. N. Jonnalagadda
e-mail: krishnajn@iitb.ac.in

F. G. S. Wasim
IITB-Monash Research Academy, Powai, Mumbai 400076, India

the membrane while acid-doped membranes with and without fillers showed a significant decrease in the stiffness and an increase in ductility.

Keywords Fuel cell · Polymer electrolytic membrane · Poly (2,5-benzimidazole) Digital image correlation · In situ tensile testing

1 Introduction

Fuel cell devices convert chemical energy directly into electrical energy using hydrogen as fuel. Polymer electrolyte fuel cells are constructed using polymer electrolytic membrane (PEM) as the proton conductor which separates the anode and the cathode. Three main functions of PEM include acting as medium for ion conductivity, providing barrier for separating reactant gases, and support structure for electrode catalysts [1]. Over the years, several membranes materials have been developed, of which Nafion is the most commonly used polymer electrolytic membrane or proton exchange membrane. For effective conduction of protons, Nafion has to be hydrated with water, which limits its use up to the temperature of 80 °C [2]. Above this temperature, conductivity of Nafion reduces drastically as the result of dehydration. Furthermore, platinum electrodes used in PEMFCs are very sensitive to corrosion in the presence of even small traces of carbon mono-dioxide, which are present along with reactant gases or fuel. This poisoning of platinum electrodes can be reduced by operating at higher temperatures in range of 150–200 °C [3]. Also, operating at higher temperatures improves heat and thermal management of fuel cell with increase in reaction rates [4]. During the past decade, there has been extensive research on developing polymer electrolyte membranes, which could exhibit adequate proton conductivity at low humidity levels. But high cost and low durability are the two barriers for their commercial use.

Acid-doped polymer membranes are believed to be possible substitution of Nafion due to thermal stability and ionic conductivity at high temperatures. poly-benzimidazole (PBI) is a commercially available polymer, which shows appreciable conductivity up to 200 °C when doped with strong acids, such as phosphoric acid and sulfuric acid [5–7]. The family of polybenzimidazole is not limited to PBI. The base polymer studied in this work, poly (2,5-benzimidazole) (ABPBI), is the simplest among benzimidazole-type polymers since it can be prepared from single and inexpensive commercial monomer (3,4-diaminobenzoic acid) (DABA) by condensation in polyphosphoric acid (PPA) or methanesulfonic acid (MSA). Compared to PBI, the ABPBI polymer has a higher affinity toward phosphoric acid because of the absence of phenylene ring. High amounts of phosphoric acid doping are required in ABPBI to achieve high proton conductivity at high temperature same as the case of PBI. However, the mechanical properties of PBI-based membranes have been shown to deteriorate by doping with strong acids due to swelling, plasticizing nature of acid [8], and acid leaching under continuous usage. To increase resistance to deformation, ABPBI membranes have been doped with

inorganic filler like ZrO_2 [9]. Impregnation of inorganic filler shows increase in stiffness but also results in decrease in strain-to-failure due to poor adhesion between nano-fillers and polymer matrix.

The durability of membranes is affected by the combined mechanical and chemical loads acting together during the operation of the fuel cell. Variations in temperature and humidity are the main factors for deterioration in mechanical response of PEM membrane as they cause swelling and internal stresses. At the molecular scale, the fluctuation in humidity level can induce changes in morphology as well as lead to macroscopic dimensional changes, which can be quite significant. Huang et al. [10] showed that the adverse effects of relative humidity cycling on mechanical properties in Nafion. At the start of a PEM fuel cell, the acid-doped ABPBI undergoes large changes in humidity and temperature. Furthermore, RH fluctuations during operation of fuel cell can affect the overall performance and durability. Hence, it is also important to study the mechanical behavior of polymer electrolytic membrane subject to different RH conditions.

Various techniques have been developed over the past few decades to estimate the mechanical properties of polymers. The reported values for modulus of ABPBI varied depending upon the type of testing method, viz., tensile test, indentation and varied in the range of 1.19–2.4 GPa [9, 11, 12]. Tensile strength was reported in range of 69.9–121 MPa [12–14], and strain-to-failure was reported between 8 and 65% [12–14] for ABPBI polymer. Determination of the elastic modulus and fracture strength for polymeric thin films using tensile testing method has been reported to be a better technique [15, 16]. In situ tensile experiments provide accurate measurements of mechanical properties of thin films over a wide range of loading conditions. In this work, in situ optical experiments were combined with DIC to extract local deformation fields used to compute the mechanical properties of polymer at room temperature of 25 ± 0.5 °C and humidity of $55 \pm 5\%$. The advantage of this technique is its ability to measure local strains with minimally invasive specimen preparation, which is not affected by strain localization, necking, and cracks in the gauge section of the specimen. In this work, the mechanical behavior in the form of stress–strain curves has been extracted for ABPBI membranes in dry as well as wet conditions with and without PWAZrO_2 inorganic filler. All the experiments were conducted in situ, and therefore, accurate measure of strain was obtained under large extensions to failure.

2 Experiments

2.1 Materials

Phosphotungstic acid (PWA), zirconium dioxide nano-particles (ZrO_2), and 3,4-diaminobenzoic acid (DABA) 97% from Sigma-Aldrich and phosphorous pentoxide (P_2O_5), methanesulfonic acid (MSA), phosphoric acid (PA), and ammonium hydroxide (NaOH) from Merck were used without further treatment. De-ionized (DI) water was obtained from Direct-Q Millipore de-ionizer.

2.2 Synthesis of Poly (2,5-Benzimidazole) (ABPBI)

ABPBI was synthesized by following the method reported elsewhere [14]. The synthesis procedure is as follows: in a round bottom flask, 3 g of P_2O_5 was dissolved in 22 mL of MSA at a temperature of 150 °C for 1 h under nitrogen. The temperature was raised to 160 °C and 2 g of DABA was added slowly, and the reaction was carried out under nitrogen purging. After 30 min, the dark purple viscous solution was precipitated in de-ionized water and neutralized with 10% NaOH solution. The polymer was again washed several times with DI water and dried in oven at 80 °C. The obtained filaments of polymer were crushed and used for further characterization (Fig. 1).

2.3 Synthesis of Phosphotungstic Acid-Grafted Zirconium Dioxide Particles (PWA/ ZrO_2)

About 400 mg of phosphotungstic acid was dissolved in 50 mL DI water and 2 g of ZrO_2 nano-particles were added and magnetically stirred for 24 h [17]. The reaction temperature was increased to 100 °C and the dispersion was allowed to dry under continuous stirring. The dried powder was calcined at 200 °C for 2 h and stored in airtight bottle for further use.

2.4 Preparation of Membrane

The ABPBI filaments were dissolved in a known amount of MSA for 10 h on a magnetic stirrer to make a 3 wt% solution [14]. The homogeneous viscous solution was poured on a petri dish and heated to 180 °C on a hot plate under a fume hood until the solvent completely evaporated. The petri dish diameter was appropriately chosen to get the desired membrane thickness. Membranes of thickness varying

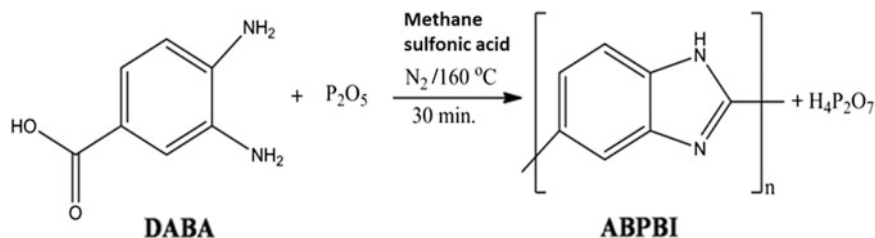


Fig. 1 Synthesis of ABPBI from DABA

between 10 and 40 μm were cast to perform different experiments. The dried membranes were immersed in DI water to remove any traces of acid. Further, membranes were dried in vacuum oven at 60 $^{\circ}\text{C}$ for 6 h.

2.5 Preparation of Composite Membranes

Composite membranes of 2 and 5 wt% PWA/ ZrO_2 nano-particles were prepared in the following way: a known amount of PWA/ ZrO_2 nano-particles were sonicated in 5 mL MSA to get a uniform dispersion of the particles and mixed with the ABPBI solution to get the desired loading. The mixture was magnetically stirred for 3 h and sonicated well before casting on the petri dishes; uniform, 10–40 μm thick membranes obtained.

2.6 Phosphoric Acid Doping of the Membranes

The ABPBI and composite ABPBI membranes dried in the oven at 80 $^{\circ}\text{C}$ for 24 h, and the dry weight of the membrane was recorded. The dry membranes were immersed in 60 wt% phosphoric acid for 3 days and the surface acid was wiped with a tissue and dried in oven at 80 $^{\circ}\text{C}$ to get the acid-doped membranes. The percentage intake of phosphoric acid doping was calculated by recording the weight change before and after phosphoric acid doping. All the membranes showed an acid uptake of $\sim 80\%$.

2.7 Specimen Preparation for Tensile Experiments

For tensile experiments, the ABPBI and ABPBI composite specimen geometry was designed for holding between two symmetric clamps, which leads to end effects near the boundaries [18]. These end effects result in non-uniform stress distribution near boundaries. To reduce the end effects, tensile test specimen was prepared in the shape of a dog bone by carefully cutting them from the membrane using a template, whose shape was patterned by EDM wire cut machining to ensure precision. Figure 2a shows the pattern and specimen prepared. The dimensions of dog bone-shape specimen used for the experiments are shown in Fig. 2b with 5 mm gauge length and 0.7 mm width. The dimensions of specimen were chosen as per the relation mentioned in literature [18]. To verify the dimensions selected, an elastic finite element (FE) Analysis was done to ensure uniform stress distribution in gauge length under uniaxial tensile loading. As observed from Fig. 2c, uniform

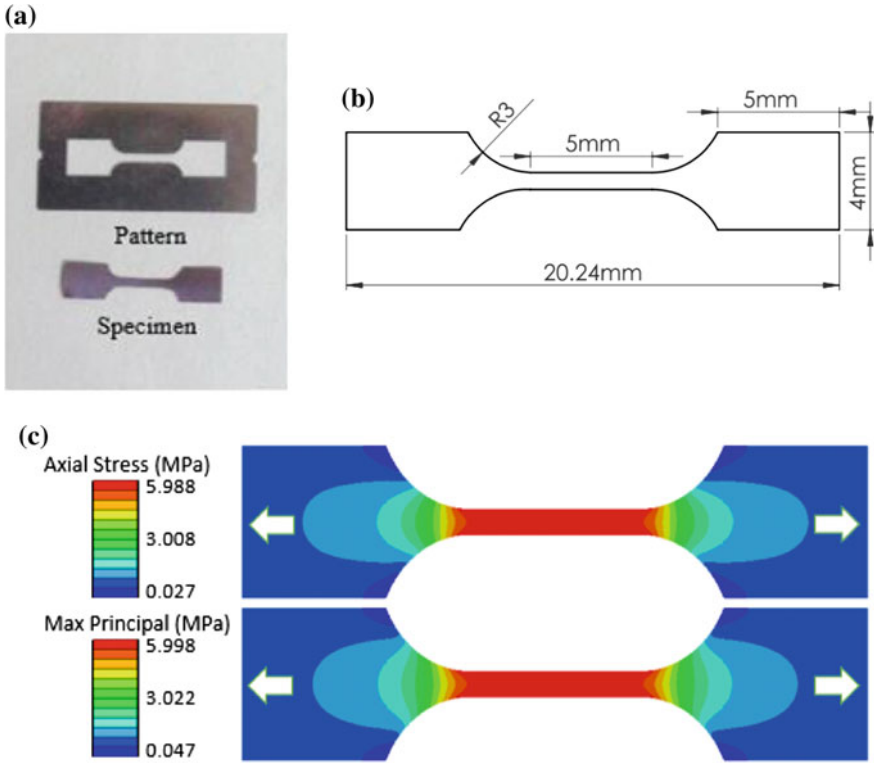


Fig. 2 **a** Template and specimen, **b** dimension of dog bone-shape specimen, and **c** axial stress and maximum principal stress distribution under uniaxial tension

stress distribution is obtained at gauge section. There were regions of stress variation at ends of gauge section, but the magnitude of stresses here is less as compared to those in the gauge section. Thus, from this analysis, the region of gauge section can be considered under uniaxial loading.

2.8 *In Situ Tensile Experiment*

The tensile tests were carried out on a modified micro-tensile setup developed in our laboratory [16]. The apparatus, shown in Fig. 3, mainly consists of an optical microscope, camera, piezoelectric actuator, load cell, positioning stages, data acquisition system (DAQ), and computer. During the experiment, optical images were captured using a microscope at 50× magnification and a Sony monochrome CCD camera with 1024 × 780 pixels. Conventional strain measurement techniques cannot be used because of small dimensions of the specimen. So, digital image



Fig. 3 In situ optical micro-tensile setup

correlation (DIC) was employed to calculate full-field deformation on the sample surface [19–21].

Digital image correlation technique requires the surface of the specimen with speckle pattern, which gives a random distribution of gray values when images are taken with a monochrome camera. The casted ABPBI and PWAZrO₂ composite polymer membrane were found to have dense and random speckle pattern Fig. 4, which was suitable for extracting deformation fields over the gauge section. However, pure ABPBI membrane has a pattern, which is quite large for quality DIC results. To get more accurate results, a small and dense pattern of silicon powder is sprayed over the surface [16]. Figure 4c shows the speckle pattern made from silicon powder. The specimen was gripped between clamps on the side of actuator and load cell. Fine adjustments were made using the translational and rotational

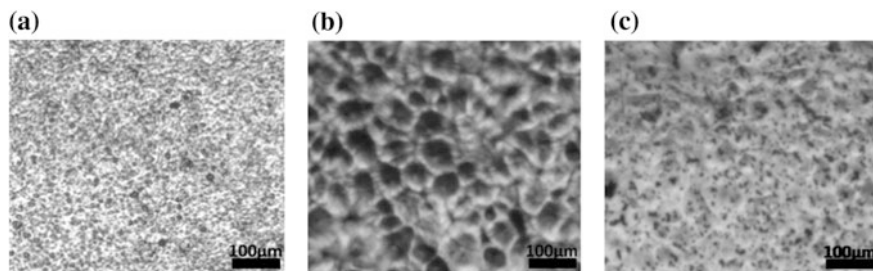


Fig. 4 Speckle pattern of **a** ABPBI, **b** ABPBI/PWAZrO₂, and **c** silicon powder over ABPBI

stages for alignment of specimen. An actuator applied the displacement at constant velocity and simultaneously the specimen is continuously imaged, which were post-processed to get strain fields and strains using VIC-2D DIC software.

3 Results and Discussion

3.1 *In Situ Tensile Testing*

The optical images of the thin film specimens obtained during the tensile experiments were analyzed with the DIC software. Figure 5 shows the full-field displacement contours calculated using DIC software for ABPBI with 2 wt% PWA-ZrO₂. Note that all the experiments in this manuscript are conducted at strain rate range of 0.0002/s. The displacement contours were aligned with the loading axis (u), and this confirmed good alignment for uniaxial experiment during the experiments.

Figure 6 shows the stress–strain response of ABPBI, ABPBI with 2 wt% PWA-ZrO₂, and ABPBI with 5 wt% PWA-ZrO₂. These results suggest that the elastic modulus and yield strength increase with increasing percentage of PWA-ZrO₂ nano-particle fillers. It can be concluded that the incorporation of PWA-ZrO₂ enhances the anti-deformation capacities and stiffness of membranes. The decrease in strain-to-failure with increasing PWA-ZrO₂ percentage might be due to weak interfacial strength between the composite particulate and membrane matrix. Table 1 summarizes the mechanical properties measured from tensile experiments, where the Young's modulus and ultimate tensile strength (UTS) increased with filler content, while the failure strain showed a monotonic decrease.

Doping of ABPBI and its composite membranes with phosphoric acid up to 80% by weight shows decrease in mechanical properties like elastic modulus and yield strength due to swelling and plasticizing nature of phosphoric acid [22]. Due to weakening of the intermolecular forces by inclusion of the acid within the membrane structure and its swelling leads to mechanical deterioration [1]. However,

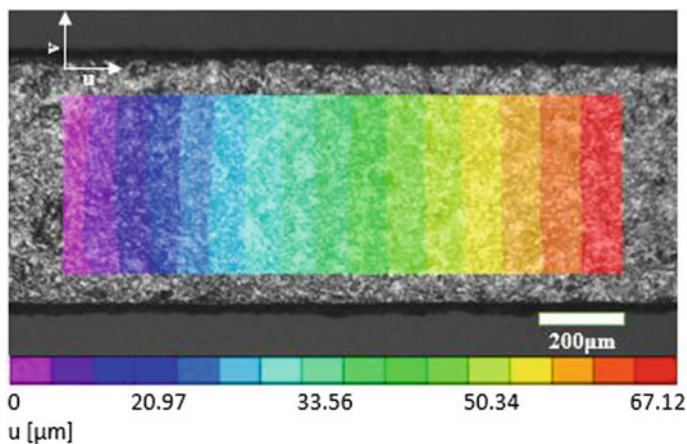
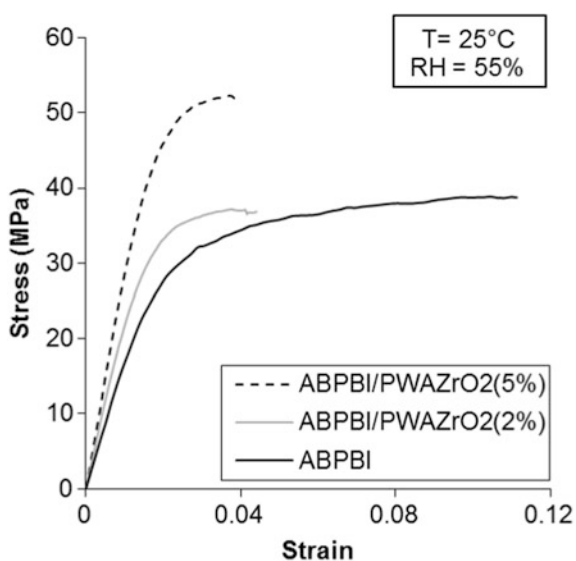


Fig. 5 Displacement contours along the loading axis (u) for ABPBI with 2 wt% PWA-ZrO₂

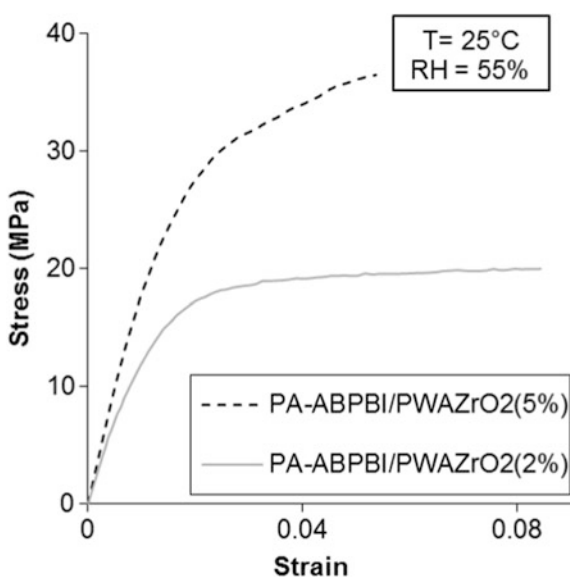
Fig. 6 Stress versus strain response of ABPBI and PWA-ZrO₂ composite ABPBI membranes



impregnation of PWA-ZrO₂ nano-particles results in increase of elastic modulus and yield strength as shown in Fig. 7. Note here that experiments on acid-doped pure ABPBI membranes were not possible as the pattern deposited externally on the samples either before or after acid doping did not adhere well to the surface and hence surface deformation using DIC could not be measured.

Table 1 Mechanical properties of ABPBI and ABPBI composites

Specimen	Young's modulus (GPa)	Ultimate tensile strength (MPa)	Strain-to-failure (%)
ABPBI	1.703 ± 0.029	31.056 ± 6.898	11.2
ABPBI/PWAZrO ₂ (2%)	2.417 ± 0.083	39.922 ± 4.647	4.2
ABPBI/PWAZrO ₂ (5%)	3.001 ± 0.088	47.679 ± 3.985	3.6
PA-ABPBI/PWAZrO ₂ (2%)	1.386 ± 0.070	26.484 ± 6.177	8.4
PA-ABPBI/PWAZrO ₂ (5%)	1.814 ± 0.052	36.916 ± 0.643	5.4

Fig. 7 Stress versus strain response of acid-doped ABPBI and PWA-ZrO₂ composite ABPBI membranes

4 Conclusion

From stress–strain curves, it can be concluded that incorporation of PWA-ZrO₂ fillers, the mechanical properties like Young's modulus and yields strength can be enhanced significantly, whereas doping with phosphoric acid degrades the properties because of swelling and plasticizing nature of acid. Hence, mechanical properties of polymer electrolytic membrane are crucial for overall performance of fuel cell.

References

1. R. He, Q. Li, A. Bach, J.O. Jensen, N.J. Bjerrum, Physicochemical properties of phosphoric acid doped polybenzimidazole membranes for fuel cells. *J. Membr. Sci.* **277**(1), 38–45 (2006)
2. Q. Li, J.O. Jensen, R.F. Savinell, N.J. Bjerrum, High temperature proton exchange membranes based on polybenzimidazoles for fuel cells. *Prog. Polym. Sci.* **34**(5), 449–477 (2009)
3. S. Gottesfeld, J. Pafford, A new approach to the problem of carbon monoxide poisoning in fuel cells operating at low temperatures. *J. Electrochem. Soc.* **135**(10), 2651–2652 (1988)
4. C. Yang, P. Costamagna, S. Srinivasan, J. Benziger, A. Bocarsly, Approaches and technical challenges to high temperature operation of proton exchange membrane fuel cells. *J. Power Sour.* **103**(1), 1–9 (2001)
5. J. Wainright, J.-T. Wang, D. Weng, R. Savinell, M. Litt, Acid-doped polybenzimidazoles: A new polymer electrolyte. *J. Electrochem. Soc.* **142**(7), L121–L123 (1995)
6. Y.-L. Ma, J. Wainright, M. Litt, R. Savinell, Conductivity of pbi membranes for high-temperature polymer electrolyte fuel cells. *J. Electrochem. Soc.* **151**(1), A8–A16 (2004)
7. R. Savinell, E. Yeager, D. Tryk, U. Landau, J. Wainright, D. Weng, K. Lux, M. Litt, C. Rogers, A polymer electrolyte for operation at temperatures up to 200 °C. *J. Electrochem. Soc.* **141**(4), L46–L48 (1994)
8. J. Lobato, P. Canizares, M. Rodrigo, J. Linares, J. Aguilar, Improved polybenzimidazole films for h₃po₄-doped pbi-based high temperature pemfc. *J. Membr. Sci.* **306**(1), 47–55 (2007)
9. H. Zheng, M. Mathe, Enhanced conductivity and stability of composite membranes based on poly (2,5-benzimidazole) and zirconium oxide nanoparticles for fuel cells. *J. Power Sour.* **196**(3), 894–898 (2011)
10. X. Huang, R. Solasi, Y. Zou, M. Feshler, K. Reifsnider, D. Condit, S. Burlatsky, T. Madden, Mechanical endurance of polymer electrolyte membrane and pem fuel cell durability. *J. Polym. Sci., Part B: Polym. Phys.* **44**(16), 2346–2357 (2006)
11. E.A. Franceschini, H.R. Corti, Elastic properties of nafion, polybenzimidazole and poly [2, 5-benzimidazole] membranes determined by afm tip nano-indentation. *J. Power Sour.* **188**(2), 379–386 (2009)
12. H. Zheng, L. Petrik, M. Mathe, Preparation and characterisation of porous poly (2, 5benzimidazole)(abpbi) membranes using surfactants as templates for polymer electrolyte membrane fuel cells. *Int. J. Hydrogen Energy* **35**(8), 3745–3750 (2010)
13. J.J. Linares, C. Sanches, V.A. Paganin, E.R. Gonzalez, Poly (2, 5-bibenzimidazole) membranes: physico-chemical characterization focused on fuel cell applications. *J. Electrochem. Soc.* **159**(7), F194–F202 (2012)
14. H.-J. Kim, S.Y. Cho, S.J. An, Y.C. Eun, J.-Y. Kim, H.-K. Yoon, H.-J. Kweon, K.H. Yew, Synthesis of poly (2, 5-benzimidazole) for use as a fuel-cell membrane. *Macromol. Rapid Commun.* **25**(8), 894–897 (2004)
15. K. Wouters, P. Gijsenbergh, R. Puers, Comparison of methods for the mechanical characterization of polymers for mems applications. *J. Micromech. Microeng.* **21**(11), 115027 (2011)
16. C. Robin, A. Vishnoi, K.N. Jonnalagadda, Mechanical behavior and anisotropy of spin-coated su-8thin films for mems. *J. Microelectromech. Syst.* **23**(1), 168–180 (2014)
17. M.A. Naik, S. Samantaray, B. Mishra, Phosphotungstic acid nanoclusters grafted onto high surface area hydrous zirconia as efficient heterogeneous catalyst for synthesis of octahydroquinazolinones and β-acetamido ketones. *J. Cluster Sci.* **22**(2), 295–307 (2011)
18. I.M. Ward, J. Sweeney, *Mechanical properties of solid polymers*, (Wiley 2012)
19. A.D. Mulliken, Low to high strain rate deformation of amorphous polymers: experiments and modeling, Ph.D. thesis, Massachusetts Institute of Technology, 2004

20. F.-P. Chiang, R.-M. Juang, Laser speckle interferometry for plate bending problems. *Appl. Opt.* **15**(9), 2199–2204 (1976)
21. M. Sutton, W. Wolters, W. Peters, W. Ranson, S. McNeill, Determination of displacements using an improved digital correlation method. *Image Vis. Comput.* **1**(3), 133–139 (1983)
22. A. Sannigrahi, D. Arunbabu, T. Jana, Thermoreversible gelation of polybenzimidazole in phosphoric acid. *Macromol. Rapid Commun.* **27**(22), 1962–1967 (2006)

Determination of Effectiveness of Viscoelastic Dampers in Controlling the Seismic Response of Piping System by Shake Table Testing

R. K. Verma, P. N. Dubey and G. R. Reddy

Abstract Piping systems are considered as lifeline of the industrial units. The earthquake load is one of the important design basis accidental loadings, considered in the design of the nuclear power plant piping systems. To meet the contradictory requirements of thermal and earthquake loads, snubbers are used. Snubbers allow free thermal expansion in case of thermal loads and act as rigid support in the case of earthquake load. However, the structure of snubber is complex, provides less damping, expensive, and requires frequent maintenance. In addition to this, mechanical snubber may pose locking problem and hydraulic snubber, if used, may leak and may not cater the intended function when required. Leakages in hydraulic snubbers and locking of mechanical snubbers have been observed in nuclear power plants (NPPs) worldwide. In view of this, passive dampers are encouraged to control the seismic response of piping in NPPs. Passive energy dissipation devices absorb and dissipate a substantial portion of the energy imparted to the piping system by earthquake shaking. Viscoelastic damper is a kind of passive energy dissipating device. To determine the effectiveness of commercially available viscoelastic dampers in controlling the seismic response of piping systems, shake table testing has been performed at CPRI, Bangalore. A 6" NB schedule 40 piping loop fitting to the 3 m × 3 m size of CPRI shake table has been designed and fabricated. Shake table testing of piping loop subjected to sinusoidal loading in the form of sine sweep with a sweep rate of 1 octave per minute to get the response of the piping with/without viscoelastic dampers has been carried out. Sweep was from 1 to 20 Hz, which was the range of interest as frequencies of the most of the piping systems lie in this range. Piping loop was also subjected to response spectra with 0.15 and 0.45 g Zero Period Acceleration (ZPA) to get the response of the piping due to earthquake loading. To determine the variation of stiffness and damping coefficient, viscoelastic damper has also been tested at different frequencies. It has been observed from the test results that the viscoelastic dampers are effective in controlling the seismic response of piping systems.

R. K. Verma (✉) · P. N. Dubey · G. R. Reddy
Reactor Safety Division, Bhabha Atomic Research Centre, Trombay,
Mumbai 400085, India
e-mail: rajeev@barc.gov.in; rajeev.ballia@gmail.com

Keywords Viscoelastic damper · Snubber · Shake table · Sine-sweep test
Site-specific ground response spectrum

1 Introduction

Chemical and nuclear power plant piping systems are generally supported on spring hangers, rod hangers, U-clamps, snubbers, and friction supports, etc. In normal operating condition, piping system is subjected to deadweight, pressure, and thermal loads. On the other hand, during an earthquake, it will also be subjected to abnormal earthquake loads in addition to the normal loads. It is well known that the requirement of piping characteristics for the thermal and the earthquake loads is not the same. In case of thermal load, piping should be flexible enough to allow thermal expansion, and for the earthquake loads, it should be rigid enough to limit the earthquake-induced displacements. Therefore, it is a good design practice to have a balance between stiffness and flexibility.

Conventional supports such as rod hangers increase the stiffness and reduce the flexibility in vertical direction. These are preferable if thermal expansion of the piping in the vertical direction is low. Spring hangers are generally called deadweight supports and have low stiffness. These supports are simple to design and require absolutely no maintenance. Snubbers are good for both the thermal and earthquake loads. Snubbers allow free thermal expansion in case of thermal loads and act as rigid support in the case of earthquake load. However, the structure of snubber is complex; it provides less damping, is expensive, and requires frequent maintenance. In addition to this, mechanical snubber may pose locking problem and hydraulic snubber, if used, may leak and may not cater the intended function when required [1].

In view of above, passive dampers are encouraged to control the seismic response of piping in newer power plants. One such energy-absorbing device discussed in the present work is viscoelastic damper.

2 Viscoelastic Damper

Viscoelastic dampers are devices for dissipating energy. They are used for reduction of vibration in piping systems and together with helical steel springs in the vibration isolation of massive industrial equipment such as presses and forging hammers. Viscoelastic damper typically consists of a moving part immersed in highly viscous fluid. The moving part is in the form of a rod (piston). The damper piston can move in all directions, and damping forces are developed as a result of shearing action and displacement in the fluid. Schematic of a viscoelastic damper has been shown in Fig. 1. The dynamic characteristics of a viscoelastic damper depend primarily on the properties of the viscous fluid and secondarily on the geometry of the device viz. shape of piston, gap between piston and cylinder. The viscoelastic damper exhibits viscoelastic behavior i.e., behavior that incorporates both elastic and viscous characteristics. Furthermore, the properties of viscoelastic dampers are strongly frequency dependent [2, 3].

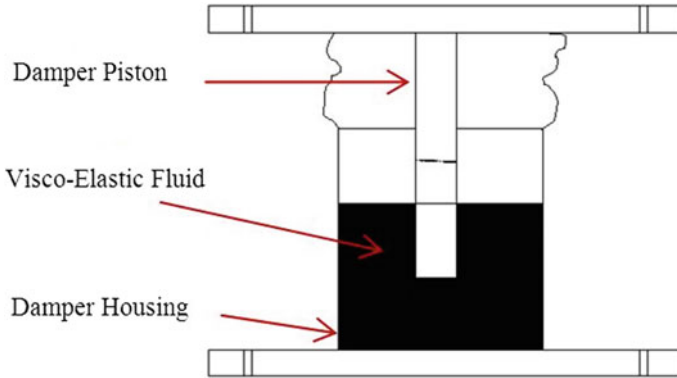


Fig. 1 Schematic of a viscoelastic damper

3 Testing of Viscoelastic Damper

To characterize the commercially available viscoelastic dampers, tests have been conducted at different frequencies to determine the variation of stiffness and damping coefficient with frequencies. Figure 2 shows the force versus displacement graphs of viscoelastic dampers at different frequencies. The stiffness and damping

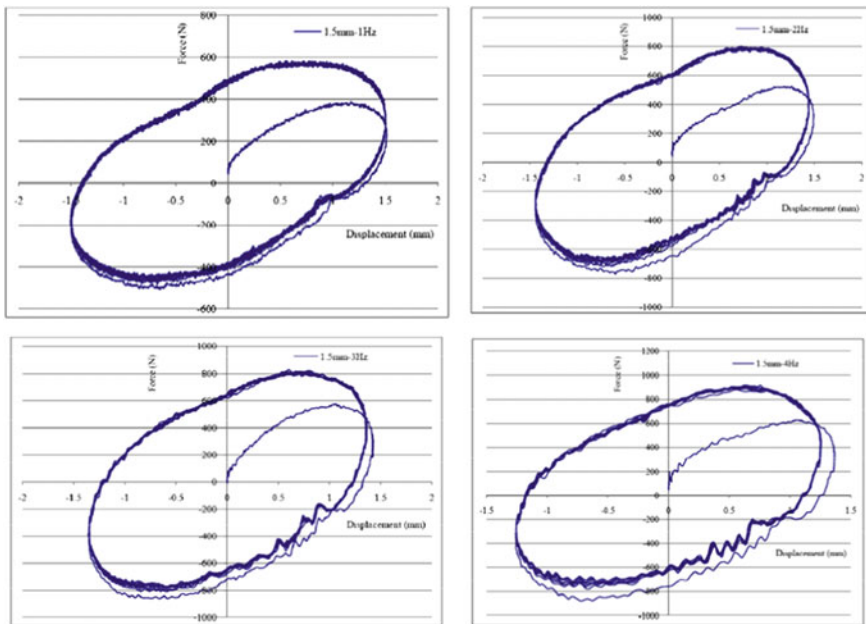


Fig. 2 Force versus displacement at frequencies 1, 2, 3, and 4 Hz

Table 1 Variation of stiffness and damping coefficient with frequencies

Frequency (Hz)	Stiffness (N/mm)	Damping coefficient (Ns/mm)
1.00	212.18	54.46
1.50	271.18	42.29
2.00	311.60	36.89
3.00	393.69	28.52
3.50	433.43	27.29
4.00	485.68	23.91

coefficient at different frequencies has been calculated from force versus displacement graphs. Variations in stiffness and damping coefficient with frequencies have been listed in Table 1. It can be observed from Table 1 that the properties of viscoelastic dampers are strongly frequency dependent.

4 Fractional-Derivative Maxwell Model for Viscoelastic Damper

Makris and Constantinou [4] observed that the frequency dependency of the mechanical properties of the high viscous dampers varied as frequency was raised to fractional rather integer powers. This suggests that differentials of fractional order could be used in modeling of such dampers.

Similar observations prompted Gemant [5] to first propose fractional-derivative models for viscoelastic materials. The shear stress–strain relationship in the fractional-derivative Maxwell model is

$$\tau + \lambda D^r[\tau] = \mu D^q[\gamma] \quad (1)$$

in which τ = shear stress; γ = shear strain; μ and λ = generalized material constants; $D^r[f(t)]$ = fractional derivative of order r of the time-dependent function f .

For motion in the vertical direction, Makris and Constantinou observed that the damper fluid is primarily subjected to shearing action. Accordingly, the force–displacement relationship in vertical motion is expressed as

$$P + \lambda D^r[P] = C_0 D^q[u] \quad (2)$$

where P = force; u = displacement; C_0 = damping coefficient at zero frequency that could be measured in an oscillatory test at very low frequency. By applying the Fourier transform to Eq. 2, the relationship between force amplitude $\tilde{P}(\omega)$ and displacement amplitude $\tilde{u}(\omega)$ is given by

Table 2 Maxwell parameters obtained from the test

Maxwell parameters	Values obtained from the test
C_0	80,000
q	1
r	0.7
λ	0.2

$$P(\omega) = [K_1(\omega) + iK_2(\omega)]u(\omega) \tag{3}$$

where i = imaginary unit; and K_1 and K_2 are storage and loss stiffness, respectively.

$$K_1 = \frac{C_0\omega^q \cos\left(\frac{q\pi}{2}\right) \left[1 + \lambda\omega^r \cos\left(\frac{r\pi}{2}\right)\right] + C_0\lambda\omega^{q+r} \sin\left(\frac{r\pi}{2}\right) \sin\left(\frac{q\pi}{2}\right)}{1 + \lambda^2\omega^{2r} + 2\lambda\omega^r \cos\left(\frac{r\pi}{2}\right)} \tag{4}$$

$$K_2 = \frac{C_0\omega^q \sin\left(\frac{q\pi}{2}\right) \left[1 + \lambda\omega^r \cos\left(\frac{r\pi}{2}\right)\right] - C_0\lambda\omega^{q+r} \sin\left(\frac{r\pi}{2}\right) \cos\left(\frac{q\pi}{2}\right)}{1 + \lambda^2\omega^{2r} + 2\lambda\omega^r \cos\left(\frac{r\pi}{2}\right)} \tag{5}$$

$$C(\omega) = \frac{K_2(\omega)}{\omega} \tag{6}$$

Here, $C(\omega)$ is the damping coefficient.

The experimental data was used to estimate the parameters r and λ of fractional-derivative Maxwell model, described by Eq. 2. This was done by setting the parameter q to unity and curve fitting of storage stiffness (K_1) and damping coefficient (C) of tested damper by fractional Maxwell model. The constant C_0 was found by projecting the damping coefficient curve to zero frequency. The values so obtained are summarized in Table 2. Figure 3 shows the variation of stiffness and damping coefficient with frequencies of viscoelastic damper.

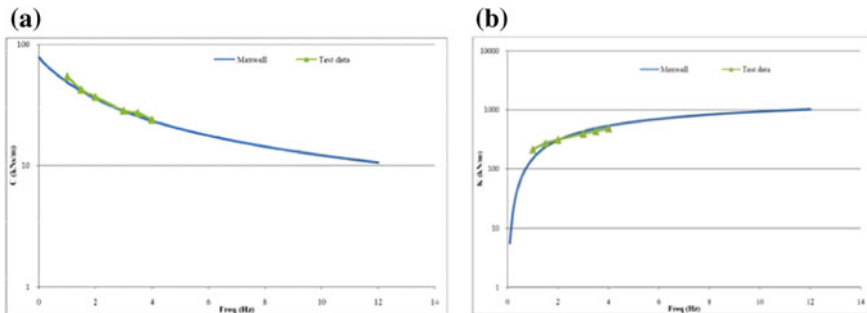


Fig. 3 a Variation of damping coefficient versus frequency; **b** variation of stiffness versus frequency

5 Shake Table Testing of Piping Loop With/Without Viscoelastic Damper

To study the effectiveness of viscoelastic dampers in controlling the seismic response of piping systems, shake table testing has been performed at CPRI, Bangalore. A 6" NB Schedule 40 piping loop has been designed to accommodate it on the shake table of 3 m \times 3 m in size. Figure 4 shows the piping layout for shake table testing at CPRI, Bangalore. Masses of 250 kg each have been attached at D and E locations to bring the frequency down to spectral peak in order to attract maximum seismic excitation. The fundamental frequency of the piping loop is 3.75 Hz obtained from the finite element analysis.

Testing of piping loop with/without viscoelastic dampers has been carried out. Piping loop was subjected to a sinusoidal loading in the form of sine sweep with a sweep rate of 1 octave per minute to get the response of the piping. Sweep was from 1 to 20 Hz, which was the range of interest as frequencies of the most of the piping systems lie in this range. Acceleration time histories (responses) have been measured at B, C, I, and J. Figure 5 shows the response of the piping loop with/without viscoelastic dampers for a sinusoidal loading of 0.2 g amplitude at C. The fundamental frequency of the piping loop obtained from the test is 3.64 Hz.

An artificial time history corresponding to Tarapur Atomic Power Station (TAPS) site-specific ground response spectrum has been generated as shown in Fig. 6. This time history has been used as an input to shake table for testing of the

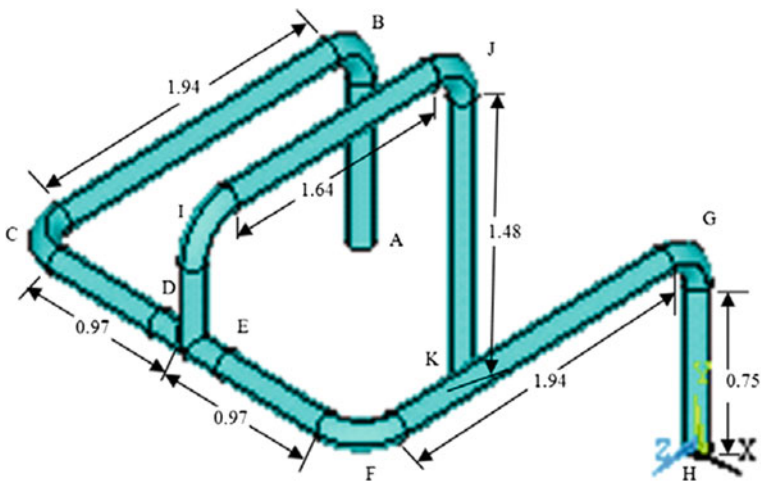


Fig. 4 Piping loop for shake table testing at CPRI, Bangalore

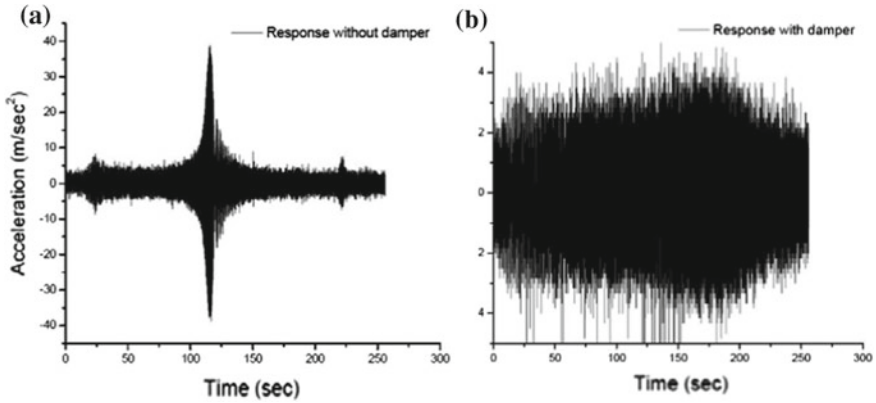


Fig. 5 Response of piping loop for a sinusoidal loading of 0.2 g amplitude at C. a Without dampers; b with dampers

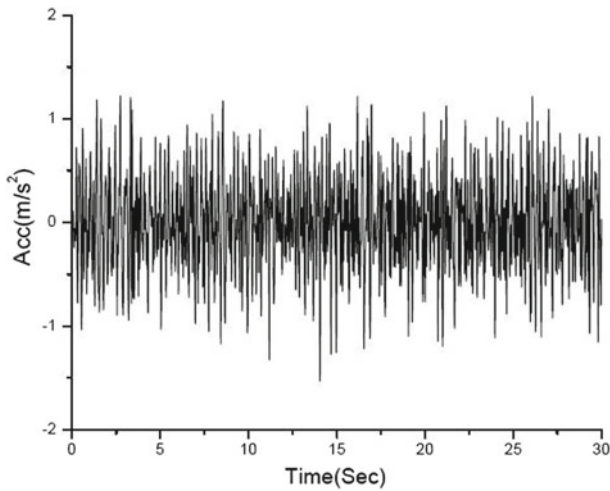


Fig. 6 Input time history (0.15g PGA)

piping loop with/without viscoelastic dampers. Testing has been done for two levels of earthquake, viz., 0.15 and 0.45g PGA, to get the response of the piping due to earthquake loading.

Figures 7 and 8 shows the response of the piping loop with/without viscoelastic dampers for an earthquake load corresponding to 0.15 and 0.45g PGA at C, respectively. piping loop with/without visco

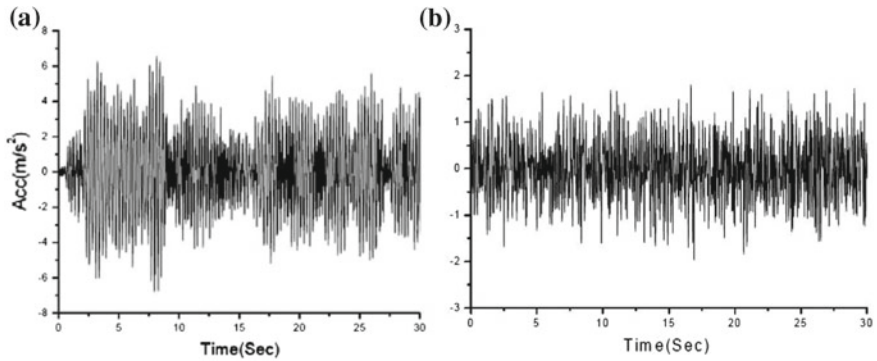


Fig. 7 Response of piping loop for an earthquake load corresponding to 0.15 g PGA at C. **a** Without dampers; **b** with dampers

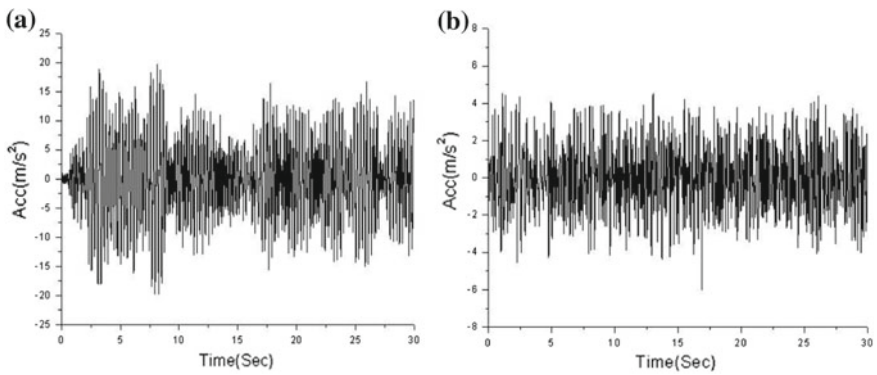


Fig. 8 Response of piping loop for an earthquake load corresponding to 0.45 g PGA at C. **a** Without dampers; **b** with dampers

6 Conclusions

Shake table testing of a commercially available viscoelastic damper has been done to study the effectiveness of the damper in controlling the seismic response of piping systems. Based on the above study, the following conclusion can be made.

1. The properties (stiffness and damping coefficient) of viscoelastic dampers are strongly frequency dependent.
2. The fractional-derivative Maxwell model may be used to model the viscoelastic damper used in the present study.
3. Viscoelastic dampers are effective in controlling the response of the piping systems subjected to sinusoidal and earthquake loadings.

References

1. J. Jonczyk, P. Gruner, Loads of piping systems due to malfunctions of snubbers. Nucl. Eng. Des. **130**, 411–433 (1991)
2. V.V. Kostarev, A.M. Berkovski, A.J. Schukin, in *Upgrading of Dynamic Reliability and Life Extension of Piping by Means of High Viscous Damper Technology*. Conference on Transactions of PVP ASME, Boston, (1999).
3. F.P. Barutzki, Extending the service life of piping systems through the application of viscous fluid dampers. GERB Vib. Control Syst. Inc (2002).
4. N. Makris, M.C. Constantinou, Fractional-derivative Maxwell model for viscous dampers. J. Struct. Eng., ASCE **117**(9), 2708–2724 (1991)
5. A. Gemant, A method of analyzing experimental results obtained from Elasto viscous bodies. Physics **7**(8), 311–317 (1936)

Experimental Study of Deformation Processes in Reinforced Concrete Beams Strengthened with a Carbon Fiber Sheet

Anton Bykov, Igor Shardakov, Aleksey Shestakov and Irina Glot

Abstract In practical terms, repair and strengthening of reinforced concrete structures with composite materials is an issue of great importance. However, how this strengthening affects the strength of reinforced structures has not been adequately justified. The specific features of the deformation behavior of strengthened structures are mainly determined by the debonding of the composite from the concrete surface. Experimental data describing the debonding process are practically absent. This paper presents the results of experimental studies of deformation processes taking place in bending reinforced beams strengthened with carbon fiber sheets. A thermography technique was used to detect the debonding in the examined structures. The results obtained made it possible to evaluate the effect of the strengthening of carbon fiber sheets on the deformation process and bearing capacity of reinforced concrete beams.

Keywords FRP · RC beams · Strengthening · IC debonding · Infrared thermography

1 Introduction

External reinforcement methods of concrete bent elements with composite materials are already widely used in the world [1–4]. It is well known that when loading a concrete beam reinforced with a composite, delamination of the composite from the concrete base occurs due to the opening of cracks [4–7]. However, the deformation behavior of beams under real loads is insufficiently investigated. In practice, the

A. Bykov

Perm National Research Polytechnic University, Komsomolski Av., 29,
614990 Perm, Russian Federation

I. Shardakov (✉) · A. Shestakov · I. Glot

Institute of Continuous Media Mechanics UB RAS, Korolev Street, 1, 614013
Perm, Russia

e-mail: shardakov@icmm.ru

© Springer Nature Singapore Pte Ltd. 2018

R. Prakash et al. (eds.), *Advances in Structural Integrity*,

https://doi.org/10.1007/978-981-10-7197-3_42

technology of restoration of the working capacity of beams is used, in which cracks have formed during loading. These include injecting of cracks with special repair materials and subsequent gluing with a carbon fiber sheet. But there are almost no experimental data describing the features of the deformation process, accompanied by delamination of the composite in the reinforced concrete beams, which have been restored in unloaded condition or directly under load. Works [8–11] are devoted to the issues concerning the use of the infrared thermography technique in order to detect defects in the area of the debonding of the external reinforcement from the concrete surface. However, the use of the infrared thermography technique to register delaminations that occur by a cohesive scenario (with a violation of the integrity of the surface layer of concrete) in these works is not mathematically justified.

This paper presents the results of a study of deformation processes in reinforced concrete beams strengthened with CFRP before load application and during loading after the appearance of the first cracks and their injection. To study temperature distribution on the beam surface, the infrared thermography technique was used. A developed mathematical model is demonstrated to describe the temperature changes in the system of “a carbon fiber sheet–epoxy resin–concrete–delamination–concrete,” which simulates the concrete base with a glued composite and voids in the surface layer of concrete. Based on this model, numerical experiments were performed which allowed us to determine the rational parameters of the infrared photography to register delamination of carbon fiber layer from the concrete base.

2 Testing Samples

Twenty-two rectangular cross-sectional sample beams of width 120 mm, height 220 mm, and a total length of 1290 mm were prepared for the study. The samples were divided into two groups: group B1 of concrete strength class B20 and group B2 of concrete strength class B35. In our investigation, the following test series were performed: the “a” series with non-strengthened beams (reference samples), the “b” series with beams strengthened in the unloaded state prior to their installation on the test bench (Fig. 1a), and the “c” series with beams strengthened under loading (Fig. 1b).

It should be noted that the test of the “c” series samples was held in two stages: stage 1—loading of the unstrengthened beam until the appearance of cracks and their opening to 1 mm in width; stage 2—additional loading of the beam after repair and strengthening until its destruction. Repairing of the cracks and strengthening of the beam with a carbon fiber sheet, without removing the load from it, took place between the first and second stages. When repairing the cracks, they were widened, grouted with a repair compound, and injected with a low-viscosity epoxy resin, as shown in Fig. 2. As the repair compound, a mixture of 0.5 mm sand fraction and the epoxy adhesive Sikadur-330 in the ratio of 1:1 were used. A carbon fiber sheet SikaWrap-230 and the epoxy resin Sikadur-330 were used for strengthening purpose. The reinforcement scheme of the beams with carbon fiber and steel is shown in Fig. 3.

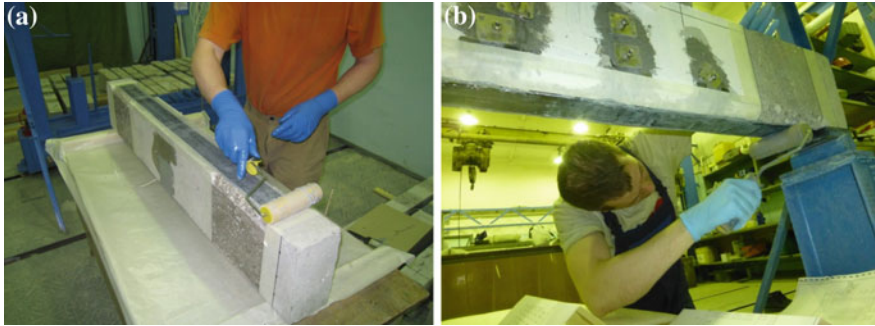


Fig. 1 **a** Bonding of the sheet onto the “b” series beams; **b** bonding of the sheet onto the “c” series beams



Fig. 2 Epoxy crack injection

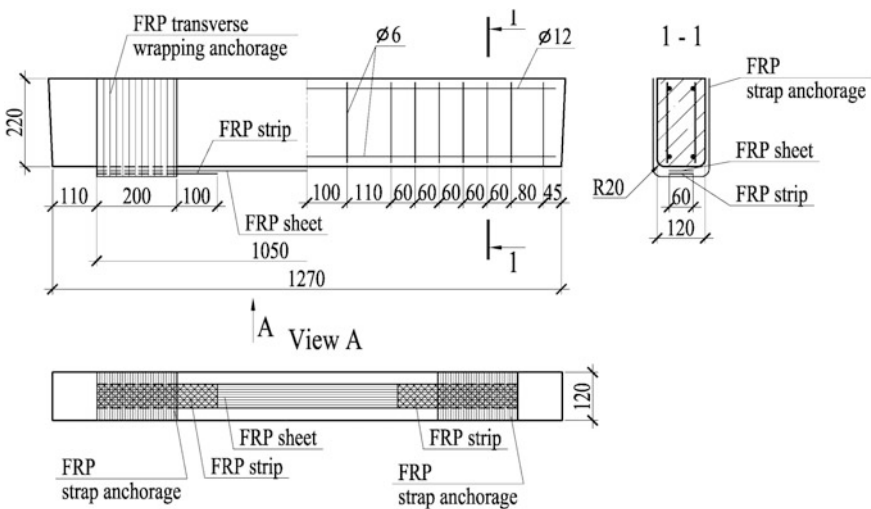


Fig. 3 Reinforcement scheme of beams with steel and a carbon fiber sheet

3 The Modeling of Heat Transfer in the System of “Carbon Sheet–Epoxy Resin–Concrete–Delamination–Concrete”

To simulate the heat transfer processes in the beam covered with a strengthening layer, an initial boundary value problem was set, describing one-dimensional non-stationary temperature field in the system of “a carbon sheet–epoxy resin–concrete–delamination–concrete,” which takes into account the specific of debonding the composite layer with a concrete fragment (cohesive scenario). The design scheme of the beam cross section is shown in Fig. 4. The mathematical formulation of the problem is described by a heat conduction equation (1), boundary (2), and initial (3) conditions.

$$\frac{\partial T_i}{\partial t} = \frac{\lambda_i}{c_i \rho_i} \frac{\partial^2 T_i}{\partial x^2}, \quad i \in (1, 5), \quad x \in (l_{i-1}, l_i), \quad l_0 = 0; \tag{1}$$

$$\lambda_1 \frac{\partial T_1}{\partial x} = \begin{cases} Q, & t = t_h \\ 0, & t = t > t_h \end{cases}; \quad \lambda_i \frac{\partial T_i}{\partial x} = \lambda_{i+1} \frac{\partial T_{i+1}}{\partial x}, \quad T_i = T_{i+1}, \quad i \in (1, 4), \quad x = l_i; \quad \lambda_5 \frac{\partial T_5}{\partial x} = 0, \quad x = l_5; \tag{2}$$

$$T_i(x, 0) = 0, \quad i = (1, 5), \quad x \in (l_{i-1}, l_i); \tag{3}$$

where the subscript i denotes the number of the layer, and in accordance with Fig. 4, $T = T(x, t)$ —temperature; t —time; x —spatial coordinate; c —specific heat; p —density; and λ —thermal conductivity coefficient.

It is possible to achieve high accuracy in simulation of temperature changes in the given multilayer system if we know the actual thermal characteristics of its materials. To determine the thermophysical parameters of the materials of the

Fig. 4 Design diagram of the problem for the beam cross section: 1 carbon sheet, 2 epoxy resin, 3 delaminated concrete, 4 delamination (air gap), 5 concrete base

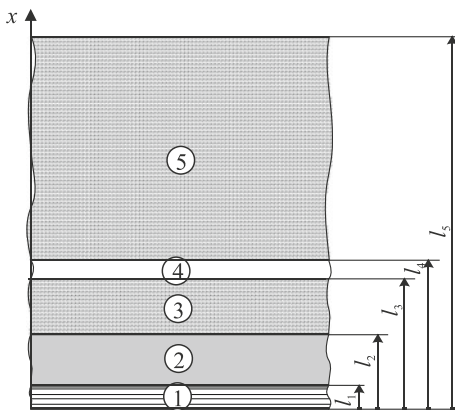
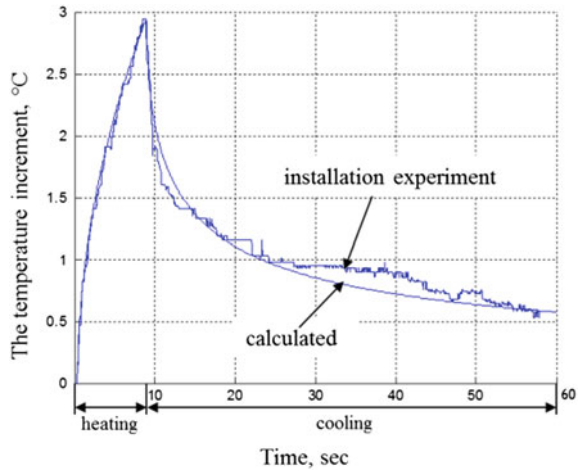


Fig. 5 Evolution of the temperature increment on the concrete surface during heating and cooling



system “a carbon sheet–epoxy resin–concrete–delamination–concrete,” a preliminary experiment was performed. Using an external heat source of the given capacity, the surface of the composite bonded onto the concrete was heated. After exposure for a certain time, the source was removed, then the multilayer system was cooled, and non-stationary temperature distribution occurred. Temperature changes on the CFRP surface were recorded using an infrared imager. As a result, the time dependence of the temperature on the CFRP surface was obtained. A similar dependence was obtained in the numerical experiment. Then, such thermal parameters of the elements were chosen, which have provided a satisfactory agreement between the results of calculation and experiment.

Figures 5 and 6 display graphs of the temperature changes on the surface of the entire concrete and of the multilayer system during heating and cooling, respectively. Each figure shows two graphs: The first one was obtained experimentally and the second one using the mathematical model. Table 1 shows the thermal parameters of the system “a carbon sheet–epoxy resin–concrete–delamination–concrete.” The values chosen during the preliminary experiment are marked with *. The other parameters, listed in the table, correspond to the reference values. The heat source capacity and heating duration, allowing to register delamination of 0.05 mm thickness at depth of 1 mm, were also determined in the simulation. They are equal to 926 W/m² and 9 s, respectively.

The subsequent numerical experiments let us establish time dependence of the temperature increment on the sample surface during heating and cooling for the samples having delamination and without it (Fig. 7). It was found that the evolution of the temperature increments of the entire sample and samples with delamination is different. We denote the difference between the temperature increments of the entire sample and the sample with a defect corresponding to a certain point of time as a temperature signal. This quantity is an informative parameter, which gives an indication of the presence of delamination. Numerical simulations have shown that

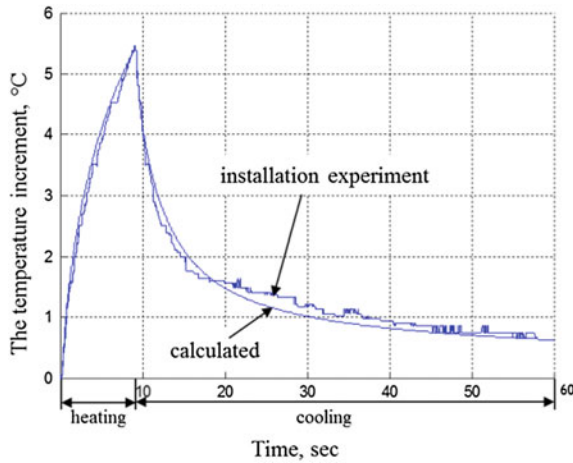


Fig. 6 Evolution of the temperature increment on the surface of the multilayer system during heating and cooling

Table 1 Parameters of the system elements

System elements	Specific heat J/(kg grad)	Thermal conductivity W/(m grad)	Density (kg m ³)	Thickness (mm)
Carbon sheet (1)	720	256	1600	0.1
Epoxy resin (2)	1300*	0.17*	1100	0.9
Delaminated concrete (3)	710*	0.63*	2400	1**
Delamination–air gap (4)	1000	0.026	1225	0.05**
Concrete base (5)	710*	0.63*	2400	13

the value of the temperature signal is not constant: It is greater in the cooling step than in the heating one, and it reaches its maximum at one point t_m (Fig. 8). As followed from the numerical simulation, for the tested samples, the temperature signal must be recorded during the cooling step after heating for 9 s. The maximum temperature signal is recorded at the 19th second from the beginning of observation (or in the 10th second from the beginning of cooling).

The maximum temperature signal characterizes the sensitivity of this method to the presence of a delamination defect. Figure 9 in the coordinates “thickness of the defect–occurrence depth of the defect” shows a family of lines, separating the area of delamination sizes that may be detected using the infrared shooting from the field of “invisible” delaminations. For every duration of heat impulse, the detectable delamination area lies below the corresponding curve as shown in Fig. 9.

As shown by numerical experiments, as the heat time increases, the area of visible defects becomes greater. However, when observing in the 19th second after

Fig. 7 Change in the temperature increment on the surface of carbon fiber during heating and cooling: 1 without delamination, 2 with delamination of thickness 0.05 mm, a depth of occurrence of 1 mm

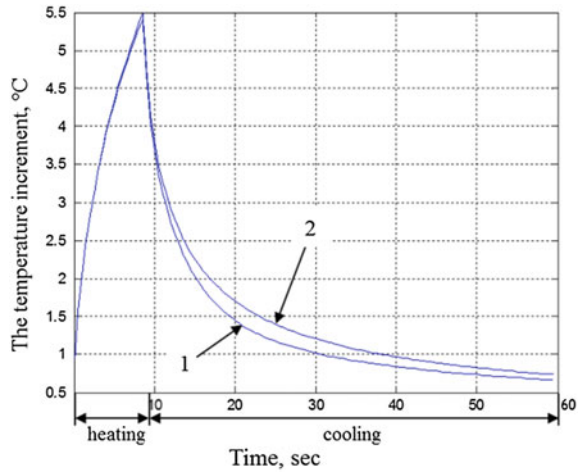


Fig. 8 Change in the difference of the increment in the temperatures shown in Fig. 4

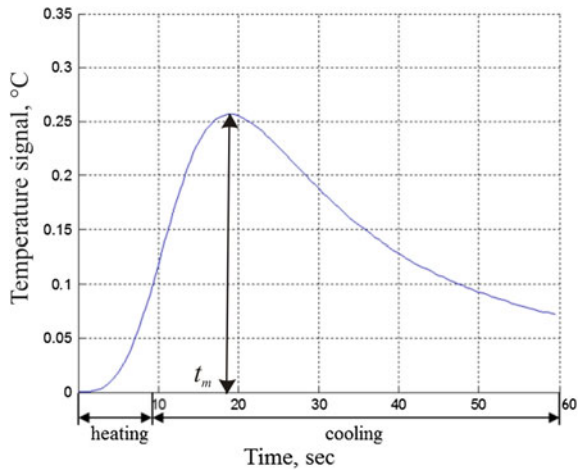
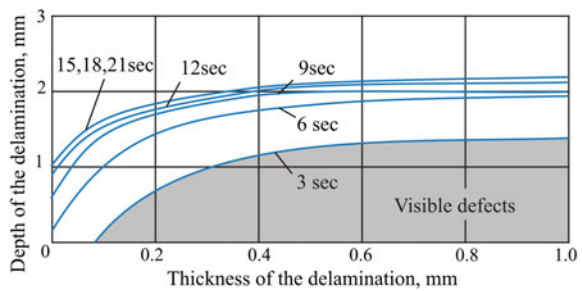


Fig. 9 Curves that determine the areas of possible delamination registration for different heating duration



the start of heating, heating longer than 15 s does not lead to further expansion of the field of defects visible for thermography. Therefore, the heating, characterized by parameters determined by the results of the mathematical modeling, allows to register delaminations more than 1 mm thick, lying at a depth less than 2 mm under the concrete surface.

4 The Technique of Testing Beams

The tests were carried out on a specially designed and manufactured test bench, as shown in Fig. 10a, according to the scheme of a four-point bending. When testing the “c” series, the beam was fixed in a bent shape at the time of repair works, including the injection of the cracks and solidification of the CFRP layer (about 10 days). Fixation was performed using a special telescopic strut which provided a constant bending moment for a long time.

The loading of the beams was performed by a successive increasing quasistatic load with a step of 2 kN, representing 4–6% of the breaking load. At each stage of loading, a 5–10-min stop was done, during which the pattern of cracks was recorded, as well as their opening width. During the stop, the stretched surface of the beam was subjected to heating of 926 W power and 9-s duration and subsequent

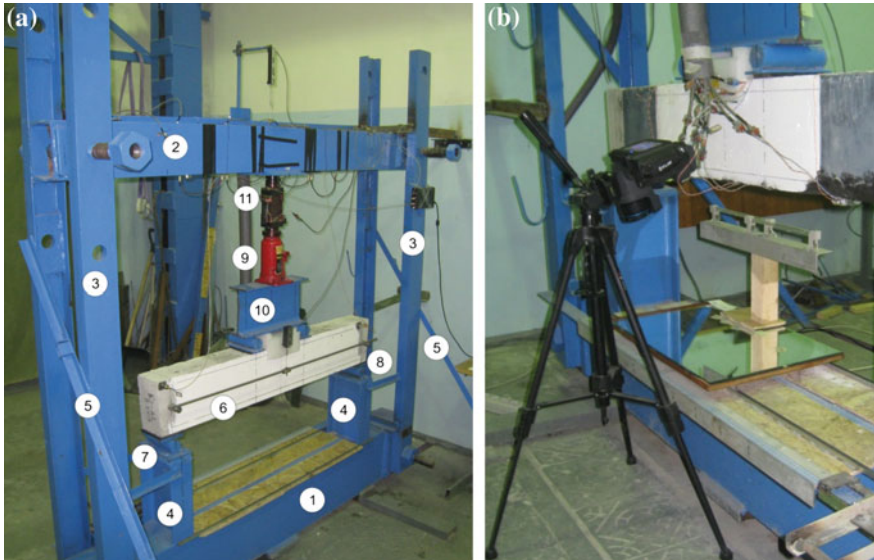


Fig. 10 **a** Test bench: 1 the bottom beam of the test bench, 2 the top beam of the test bench, 3 twin rack, 4 rack, 5 mowing, 6 a sample beam, 7 hinged movable support, 8 hinged immovable support, 9 hydraulic jack, 10 distribution bar, 11 loadmeter; **b** the scheme of the infrared photography: 12 the thermal imager FLIR T620, 13 halogen lamp, 14 mirror

cooling. The scheme of the equipment arrangement in the infrared photography is shown in Fig. 10b. Thermographic measurements were supplemented with a set of mechanical measurements. At each load step, strains in specific sections of the beam were measured by strain gauges, deflections of the beam were measured using displacement sensors, and cracks on the beam surface were recorded.

The main provisions of thermogram recording technique were as follows:

- Along the length of the beam, five locations of the infrared imager mounted on a tripod were fixed, so that five thermograms, sequentially lined up, would give a panoramic picture of the carbon fiber strip.
- Thermal markers, necessary for accurate combining of individual thermograms in a panoramic image, were attached to the lower surface of the beam.
- The shooting was made through the reflection in the mirror; thus, it ensured safety of the expensive equipment when shooting on the steps close to the beam destruction.
- Prior to loading, the beams performed the infrared shooting, which gave the image of the beam without delamination.
- The heating of the carbon fiber strip was carried out with a halogen lamp. When turned off, the lamp was put aside to ensure uniform cooling of the beam surface;
- The heating time and the observation time were monitored with the help of a stopwatch with an accuracy of 0.5 s.

The primary thermograms of the beam surface (Fig. 11a) were obtained during the tests, which were then transformed by a specially developed algorithm and implemented in the MATLAB package. Let $T(x; y)$ denote the primary temperature which for an arbitrary point (x, y) on the CFRP surface sets a difference between the temperatures at the initial moment and in the 19th second after the beginning of observation. The so-called normalized thermograms were calculated on the first step of the algorithm (Fig. 11b):

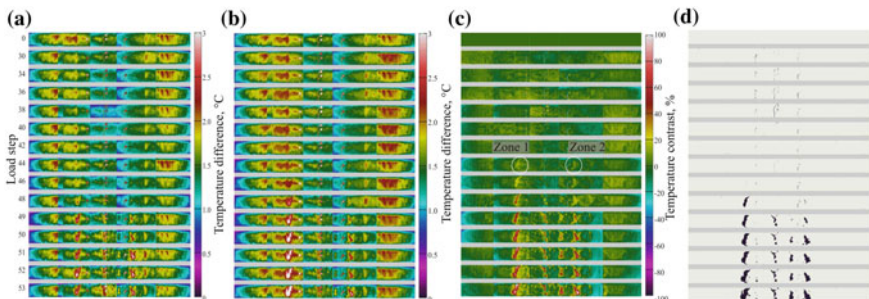


Fig. 11 **a** Primary thermograms; **b** normalized thermograms; **c** temperature contrast maps; **d** binary defect maps

$$T_j^n(x, y) = T_j(x, y) \frac{T_0(x_*, y_*)}{T_j(x_*, y_*)}, \quad (4)$$

where $T_j^n(x, y)$ and $T_j(x, y)$ are the normalized and primary temperatures at the j th stage of loading at the point with coordinates (x, y) ; $T_0(x_*, y_*)$ and $T_j(x_*, y_*)$ are the primary temperatures at the initial stage and j th stage of loading at the point (x_*, y_*) where there is no delamination until the destruction of the beam.

Then, the values of the current temperature contrast were calculated $C_j(x, y)$ (Fig. 11c), reflecting the difference of the values of the normalized temperature at arbitrary point at the j th stage of loading $T_j^n(x, y)$ and the primary temperature at the same point $T_0(x, y)$ at the initial stage:

$$C_j(x, y) = \frac{T_j^n(x, y) - T_0(x, y)}{T_0(x, y)} \cdot 100\%. \quad (5)$$

The increased values of the current temperature contrast indicate the presence of delamination in the observed area of the beam. The magnitude of the threshold values of the temperature contrast C^* , separating the defect-free regions from the defect ones, can be obtained by estimating the average contrast value \bar{C}_j and the standard deviation σ_j in those areas of the thermograms, where the presence of defects is excluded. The estimation of these values, obtained according to the data of the tests of all the tested beams with a reinforcing layer, made it possible to find the following magnitude of the threshold value: $C^* = \bar{C}_j + 3\sigma_j = 27.9\%$. The areas, where the current temperature contrast value does not exceed the threshold value, were identified as defect-free and the rest as areas with delamination. Figure 11d shows the binary defect maps corresponding to successive steps of loading.

5 Results

The “a” series samples were destroyed due to rupture of the tensile reinforcement and the fragmentation of the compression concrete area. The “b” and “c” series samples were destroyed due to rupture of the carbon fiber sheet in the middle part of the span. The average values of the limiting bending moment of the “a” series beams are 6.83 and 7.12 kNm for B1 and B2 groups, respectively. For the reinforced series “b” beams, the limiting bending moment equals to 10.47 and 10.76 kNm for B1 and B2 groups, respectively. For the reinforced series “c” beams, the limiting bending moment is 10.29 and 11.00 kNm for B1 and B2 groups, respectively.

Figure 12 shows the dependence of the maximum deflection of the beam on the bending moment obtained when testing the three series of beams: beams without

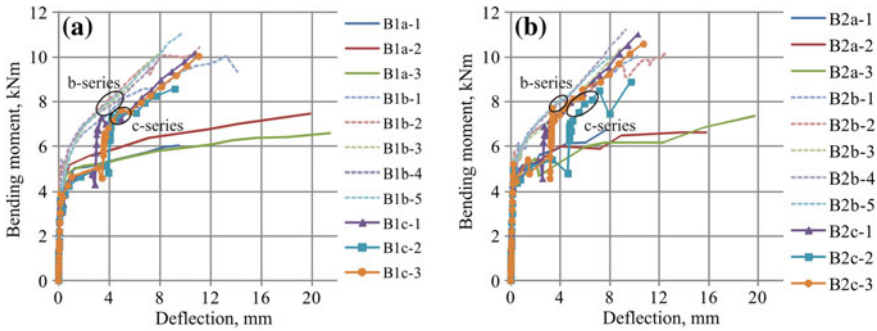


Fig. 12 **a** Bending moment–deflection relationships for group B1; **b** bending moment–deflection relationships for group B2

any reinforcement layer (the “a” series); beams that preliminary reinforced with a carbon fiber sheet (the “b” series); and beams which underwent the reinforcing procedure while testing (the “c” series). The comparison of the graphs obtained in the “a” and “c” series clearly demonstrates an increase in the bearing capacity of the beams that have undergone the preliminary reinforcement with the CFRP sheet. The maximum bending moment, which such beams can stand, has happened to be 37–39% higher than the reference samples. The graphs clearly depict the formation stage of the first cracks in the concrete: It corresponds to a sharp change in the slope angle of the curves.

It is found experimentally that on average, the first crack in reinforced beams appears when deformation in the carbon fiber reaches 170–250 $\mu\text{m}/\text{m}$. After the appearance of the first crack, the deformations of the carbon fiber rapidly increase to 1000–2500 $\mu\text{m}/\text{m}$ depending on the distance of the strain gauge from the crack. Thus, after the appearance of the first crack, the compatibility of deformations of the concrete base and carbon fiber sheet is violated. A certain area appears where the concrete can no longer perceive tensile deformation and gets destroyed, and the carbon fiber is deformed without breaking. This area, in fact, is the area of delamination, and the moment of reaching limit deformations in the concrete is the onset of delamination. However, delamination, associated with the appearance of the first crack, is not visible in the infrared photography. Delamination that is noticeable in the infrared range occurs after crack opening up to 0.3–0.5 mm. For the “b” series beams, delamination develops in the area between the principal main cracks, and for the “b” series beams, it develops between the new crack of the second generation and the old crack of the first generation (the dashed line), as shown in Fig. 13.

The set of curves showing dependencies of carbon fiber sheet deformations on the value of the relative area of delamination is given in Fig. 14.

The presented dependences are close to linear ones. When the limit state of the beam is achieved, the area of delamination in the preliminary reinforced beams (the

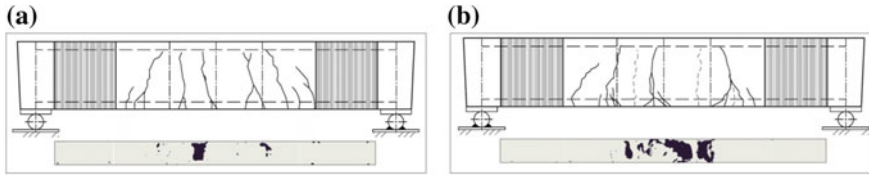


Fig. 13 a A pattern of cracks and a binary defect map for «b» series; b a pattern of cracks and a binary defect map for «c» series

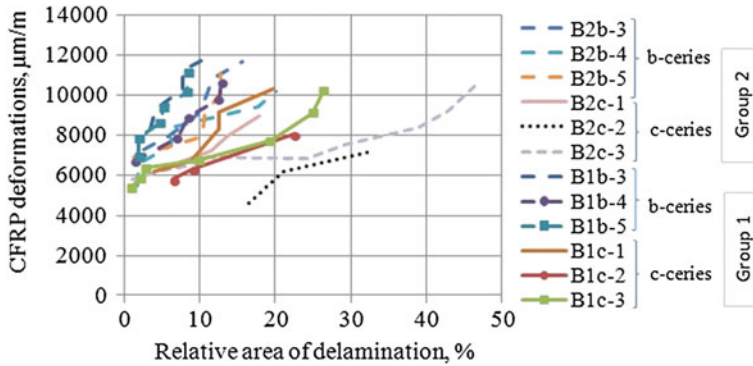


Fig. 14 Dependence of carbon fiber sheet deformations on the value of the relative area of delamination

“b”-series) is in 2.1–2.3 times less than in the reinforced under load beams (the “c” series), at the same relative deformation of the carbon fiber.

6 Conclusions

A mathematical model was developed to describe the temperature changes in the system of “a carbon sheet–epoxy resin–concrete–delamination–concrete”, which takes into account the characteristic features of cohesive delamination of the composite from the concrete base. This model allowed us to determine the parameters of the infrared shooting to register delamination of the carbon fiber of thickness 1 mm from the concrete base as follows: heating power—926 W/m²; heating duration—9 s; and the optimal observation moment—at the cooling stage after the heating in the 19th second after the start of observation. Infrared shooting in this mode makes it possible to detect delaminations of a thickness exceeding 1 mm, which lie at a depth down to 2 mm.

It is shown that for the composite strengthened beams, which are destroyed due to the rupture of CFRP, their bearing capacity does not depend on the point when

strengthening was performed. The bearing capacity of previously reinforced beams and beams reinforced during loading after the appearance of the first cracks and their grouting are higher by 37–39 and 38–49%, respectively, than the unreinforced beams.

It was found that for the beams reinforced during loading, the relative area of delamination increases in 2.1–2.3 times in comparison with the beams reinforced before load application.

Acknowledgements This research was supported by the Russian Science Foundation, project No. 14-29-00172.

References

1. J.G. Teng, Failure modes of FRP-strengthened restructures, in *26th Conference on Our World in Concrete & Structures*: 27–28 Aug 2001, Singapore, pp. 627–634
2. A.A. Bykov, A.V. Kalugin, New model for evaluation of FRP debonding strain for Russian design code. *Adv. Mater. Sci. Eng.* **2013**. <http://dx.doi.org/10.1155/2013/130162>
3. M.R. Esfahani, Flexural behaviour of reinforced concrete beams strengthened by CFRP sheets. *Eng. Struct.* **29**(10), 2428–2444 (2007)
4. H. Saadatmanesh, RC beams strengthened with GFRP plates. I: experimental study. *J. Struct. Eng.* **117**(11), 3417–3433 (1991)
5. J. Yao, J.G. Teng, J.F. Chen, Experimental study on FRP-to-concrete bonded joints. *Compos. B Eng.* **36**(2), 99–113 (2005)
6. S.K. Woo, J.J. Kim, K. Byun, Y. Song, Bond-slip parameter determination procedure of RC flexure member strengthened with prestressed CFRP plates. *KSCE J. Civ. Eng.* **17**(1), 179–191 (2013)
7. R.J. Gravina, S.A. Hadigheh, S. Setunge, Bond and force transfer of FRP materials bonded to concrete using sitecure system, in *Proceedings of the 3rd Asia-Pacific Conference on FRP in Structures*, Hokkaido, 2012
8. J. Tashan, R. Al-Mahaidi, Detection of cracks in concrete strengthened with CFRP systems. *Compos. B Eng.* **64**, 116–125 (2014)
9. J.R. Brown, H.R. Hamilton, Quantitative infrared thermography inspection for FRP applied to concrete using single pixel analysis. *Constr. Build. Mater.* **39**, 1292–1302 (2013)
10. C.W. Hu, J.K.C. Shih, R. Delpak, D.B. Tann, Detection of air blisters and crack propagation in FRP strengthened concrete elements using infrared thermography, in *Proceedings of the 3rd Annual Thermographers' Conference «InfraMation 2002»*, Orlando, 2002
11. S.A. Keo, F. Bracheleta, F. Breabana, D. Defera, Defect detection in CFRP by infrared thermography with CO₂ laser excitation compared to conventional lock-in infrared thermography. *Compos. B Eng.* **69**, 1–5 (2015)

Partial Delamination Detection and Quantification in Composite Laminates Using Laser Doppler Vibrometer

Yashdeep P. Nimje and Gangadharan Raju

Abstract Vibration-based structural health monitoring techniques are widely used for detection and quantification of delamination in composite structures. In this work, non-contact vibration measurement technique namely laser Doppler vibrometer (LDV) is used for damage characterization of partial delamination in composite beams. The modal information such as natural frequencies and mode shapes of composite beam are obtained using LDV and validated with finite element models for comparison with the obtained experimental results. Mode shape-based damage detection algorithms such as fractal dimension approach are used for quantification of delamination in composite beams. In the present work, a modified generalized fractal dimension technique is proposed to locate delamination of different sizes and shapes in the composite beam. Different types of partial delamination like C-type, I-type in composite beam specimens were fabricated and experimentally studied using LDV. The modified fractal dimension technique was then applied to the mode shapes results of the various partial delaminations to quantify the damage.

Keywords Laser Doppler vibrometer · Delamination · Composites laminates
Fractal dimension technique

1 Introduction

Over the last two decades, there is a growing need for real-time monitoring of structures made of composite materials to avoid catastrophic failures and provide confidence on the usage of these high-performance materials into aerospace, marine

Y. P. Nimje (✉) · G. Raju
Department of Mechanical & Aerospace Engineering, Indian Institute of Technology
Hyderabad, Kandi 502205, Telangana, India
e-mail: me14mtech11038@iith.ac.in

G. Raju
e-mail: gangadharanr@iith.ac.in

and wind energy sectors. Unlike metals, failure mechanisms are quite complex in composites involving fibre breakage, fibre pull-out, matrix cracks, fibre-matrix debonding and delamination. Among the various failure modes, delamination is a barely visible damage induced by transverse impact and results in significant reduction of the strength and stiffness of the composite. Delamination can alter the dynamic responses such as natural frequencies, mode shapes, and these changes can be extracted to estimate damages in the structure by modal analysis [1, 2].

Vibration-based structural health monitoring (SHM) is one of the major approaches for inspection and structural integrity evaluation. Reliable modal-based methods are essential to detect and quantify damages for implementation of robust SHM systems. The challenges are to identify the changes in the physical parameters due to delamination type of damage and correlate them with the corresponding measured modal parameters [3]. The present research work focuses on developing the relationship between the dynamic response of healthy and damaged composite specimens for damage identification and quantification. Vibration-based SHM has gradually moved from accelerometers for sensing to embedded piezo sensors, fibre optic sensors and non-contact measurements like laser Doppler vibrometer (LDV) to capture the modal response of structures. Lestari et al. [4] proposed a combined analytical and experimental modal approach to locate delamination in composite beams using curvature mode shapes. They used surface bonded piezo-electric wafers to capture the mode shape of composite structures. Qiao et al. [5] used LDV for damage detection in composite plates using modal curvature and developed algorithms based on global smoothing method fractal dimension technique to locate the damage. Shang et al. employed LDV to perform modal testing of composites and later proposed damage detection based on subset selection technique to locate the delamination. In this work, LDV measurement system is used to capture the mode shapes of the various delaminated composite structures. The acquired mode shapes were then analysed using the modified fractal dimension technique for locating the delamination and quantification of their size. Furthermore, numerical finite element analysis of partial delaminated composite structures is carried out to validate the damage detection algorithms.

2 Finite Element Modelling of Composites

Numerous works have been reported on the vibration studies on delaminated composite structures. Della and Shu [6] have presented a comprehensive review of the various analytical and numerical approaches on the vibration of delaminated composites. Most of the works rely on finite element modelling for modal analysis of delaminated composites [1, 2, 7–9]. Finite element analysis was carried out using commercial software ANSYS 12 to model the healthy and delaminated composite structures in order to extract their vibration behaviour, i.e. natural frequency and mode shapes. A three dimensional 8 noded ANSYS element SOLID185 is used to model the composite beam. To model the delamination using finite elements, the

approach proposed by Ihesiulor et al. is used. In this approach, two volumes were created above and below the delamination and meshed using brick elements. Next, the nodes situated along the interface of healthy segments were merged together by introducing contact elements, while nodes in the interface of delaminated region were not merged. Contact elements (TARGET170/CONTACT173) were introduced between the surfaces to prevent separation and inter-penetration. Reduced integration was carried out to avoid the shear locking problem when analysing thin structures. A mesh sensitivity study was conducted to determine the number of element to be employed for healthy as well as delaminated beam. For each laminae, finite element mesh density of 100, 20 and 1 elements are chosen along the length, width and thickness direction, respectively. Block Lancos method was then used to extract the modal parameters. Torsion and in-plane bending mode were discarded, and only, flexural bending modes were used in this study. Edge or partial delamination is a serious concern in helicopter blades and turbine blades. In the present work, the objective was to numerically investigate the effect of partial delamination on the modal characteristics of the composite structure. The schematic diagram of the various types of delamination numerically studied using finite element analysis is shown in Fig. 1.

For validation purpose, the numerical examples of partial delaminated composite beam given by Kumar et al. [7, 10] are investigated. For the numerical study, graphite/epoxy composite specimen with stacking sequence $[0/90]_{2s}$ and dimensions given by length = 0.127 m, width = 0.0127 m and thickness = 0.254 mm was chosen. Material properties of the laminae are given by $E_{11} = 134$ GPa, $E_{22} = 10.3$ GPa, $E_{33} = 10.3$ GPa, $G_{12} = 5$ GPa, $G_{23} = 3.59$ GPa, $G_{31} = 5$ GPa, $\gamma_{12} = 0.33$, $\gamma_{23} = 0.37$, $\gamma_{13} = 0.33$, density = 1480 kg/m^3 . Finite element modelling of C-type and I-type delamination was carried out in ANSYS by varying the size of delamination in width-wise direction and keeping the length to be constant of 50.8 mm. The nodes associated along the interface of healthy region are merged together with the help of contact elements (TARGET170/CONTACT173), and the nodes in delaminated region were set free.

From Table 1, it is inferred that natural frequency results obtained using FEA closely match with the results given by Kumar et al. [7, 8]. Next, the mode shape information is further studied using signal processing algorithms for location of the delamination in composite structure.

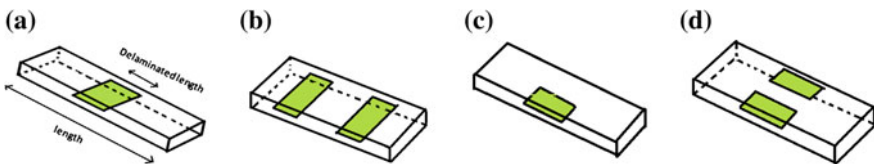


Fig. 1 Schematic diagram of beam having delamination **a** through width delamination, **b** multiple delamination, **c** C-type delamination, **d** I-type delamination

Table 1 Channel-type delamination at first interface having 50.8 mm lengthwise delamination and I-type delamination at first interface of 76.2 mm lengthwise delamination

Percentage of width-wise delamination (%)	First layer C-type delamination, natural frequency (Hz)		First layer I-type delamination, natural frequency (Hz)	
	Kumar	FEA results	Kumar	FEA results
0	81.46	81.40	81.46	81.40
30	81.32	80.93	81.51	81.34
50	80.15	80.19	81.12	81.19
70	78.01	79.09	80.31	80.94
90	76.12	78.99	80.48	80.69
100	76.04	75.43	68.24	64.69

3 Damage Detection Method—Fractal Dimension Technique

Various type of damage detection techniques are available such as damage index method [3], gapped smoothening method [3] which require the information of healthy structures for damage detection. Generalized fractal dimension technique is another widely used approach which does not require healthy structure information for damage location. Fractal dimension technique was proposed by Hadjileontiadis and Douka [11] and used for locating the crack in beams. Later, it was modified by Qiao et al. [5] and applied to locate delamination in composite plates. Delamination in the structure will affect the local stiffness of the structure, which in turn will introduce small changes in their mode shapes. Evaluating fractal dimension on mode shapes data will enhance the small localized change and will help in detecting and locating the delamination. Generalized fractal dimension was defined by Qiao et al. [5] and it is given by:

$$GFD = \frac{\log_{10}(n)}{\log_{10}\left(\frac{d_s}{l_s}\right) + \log_{10}(n)} \tag{1a}$$

$$d_s = \sqrt{(y_{i+k} - y_i)^2 + S^2(x_{i+k} - x_i)^2} \tag{1b}$$

$$l_s = \sum_{j=1}^M \sqrt{(y_{i+j} - y_i)^2 + S^2(x_{i+j} - x_i)^2} \tag{1c}$$

where n is the number of nodes used in a single window; x and y are the system coordinates, and S is the scale factor which needs to be chosen carefully in order to detect the delamination successfully. In Eq. (1b), d_s is the maximum distance in the curve; l_s is the total length of the curve; k is the size of the window. However, Qiao

et al. [5] did not give a proper explanation on choosing the scaling factor S for various mode shapes. In this work, the scaling factor was removed to compute the fractal dimension and a modified expression is given by:

$$\text{MGFD} = \frac{\log_{10}(n)}{\log_{10}\left(\frac{D_s}{L_s}\right) + \log_{10}(n)} \tag{2a}$$

$$D_s = \sqrt{(\Delta y_{i+k} - \Delta y_i)^2 + (\Delta x_{i+k} - \Delta x_i)^2} \tag{2b}$$

$$L_s = \sum_{j=1}^M \sqrt{(\Delta y_{i+j} - \Delta y_i)^2 + (\Delta x_{i+j} - \Delta x_i)^2} \tag{2c}$$

where in Eq. (2b), Δx_i is the normalized nodal displacement with respect to maximum nodal displacement in x -direction; Δy_i is the normalized nodal displacement with respect to maximum nodal displacements in y -direction. M is the number of nodes present in the single window. D_s is the difference in the normalized nodal displacement between the first and last node of the chosen window; k is size of the window; x is the out of plane deformation; y is vertical distance of the node. To locate the delamination and compute the size of the delamination, GFD and MGFD were applied to mode shapes acquired from ANSYS modelling. Firstly, through width, delamination case taken for the study and the details of the specimen are shown in Fig. 2a. GFD and MGFD were applied to the first mode shape of the

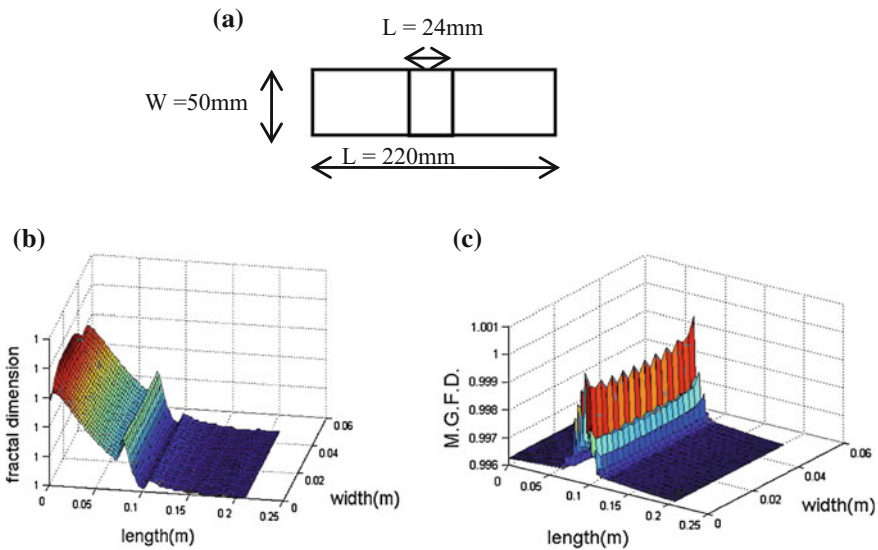


Fig. 2 a Schematic diagram of beam having delamination at the centre, b first mode by using fractal dimension, c first mode by using modified fractal dimension technique

composite beam, and the results are shown in Fig. 2b, c, respectively. Both the approaches are effectively capturing the delamination location and size as shown in Fig. 2.

Subsequently, both the approaches were applied to study the delamination at the tip of the beam. The results of GFD and MGF D are presented in Fig. 3. GFD approach is not able to identify the delamination location at the tip of the beam, whereas MGF D can capture the delamination location and size more accurately.

Next, the minimum size of the delamination that can be identified by both the approaches was investigated. Figure 4 shows that MGF D can capture delamination of size 2.2 mm, whereas GFD fails to locate it.

GFD and MGF D were then applied to study the multiple delamination case, and the results are presented for the first mode shape in Fig. 5. GFD was able to locate the delamination near the fixed end, but was not able to capture the delamination at the tip (Fig. 5b). MGF D was able to capture the delamination near the fixed end and the tip of the beam. Both the approaches were then applied to the fourth mode shape, and the results are shown in Fig. 6.

MGF D overcomes all the above limitations of GFD, and the results in this section show that it can capture location and size of delamination more accurately. Thus, the proposed MGF D was then applied to study the experimental mode shapes obtained by LDV in order to identify the delamination.

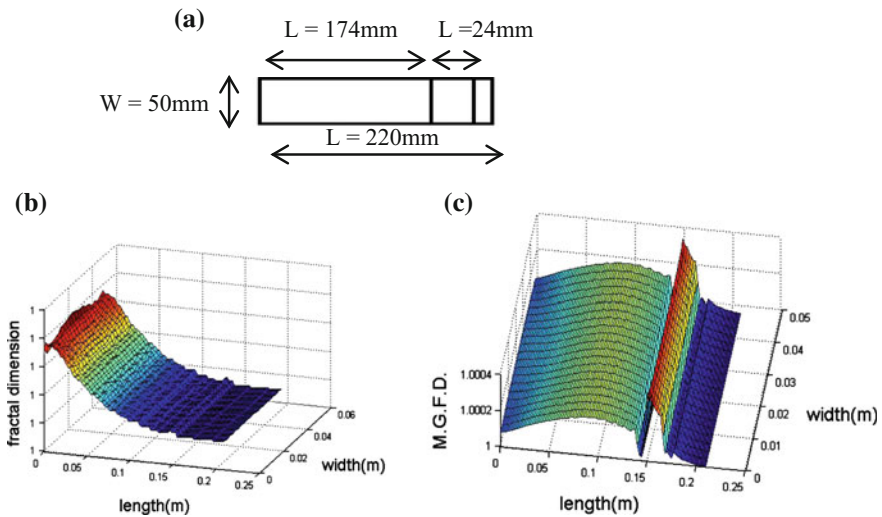


Fig. 3 a Schematic diagram of beam having delamination at the tip, b first mode by using fractal dimension, c first mode by using modified fractal dimension technique

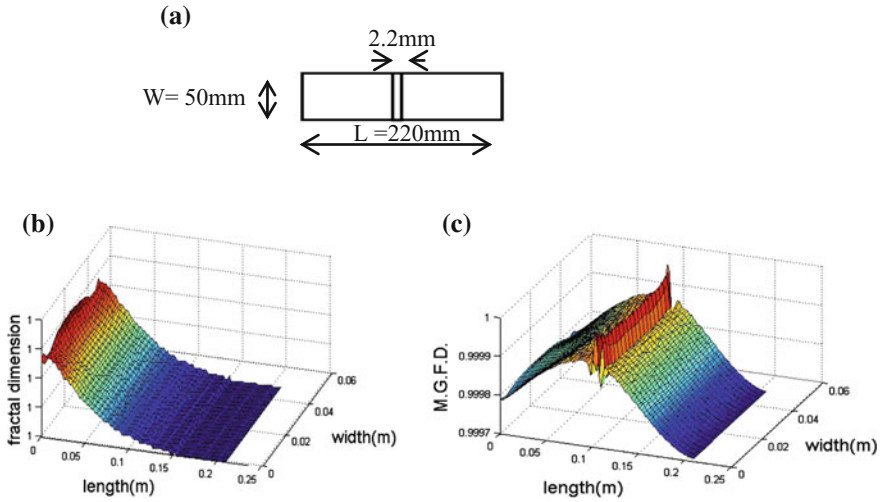


Fig. 4 a Schematic diagram of beam having delamination at the centre, b first mode by using fractal dimension, c first mode by using modified fractal dimension technique

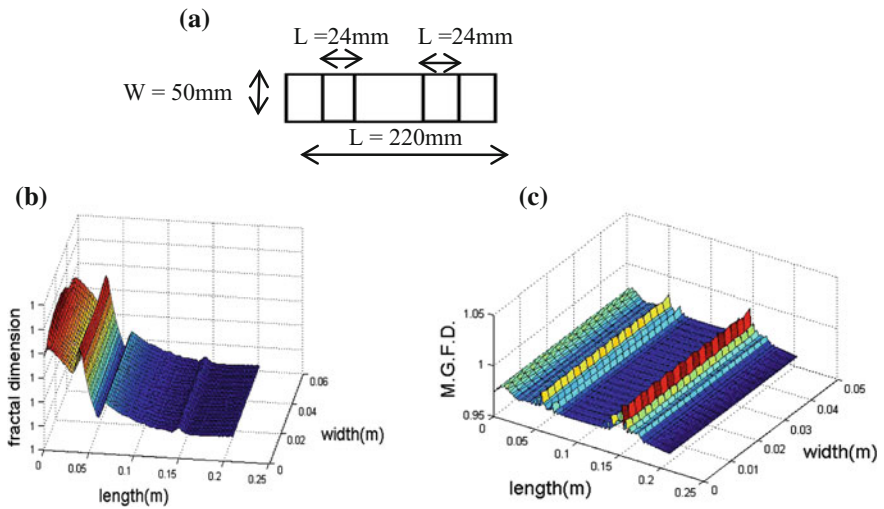


Fig. 5 a Schematic diagram of beam having multiple delamination, b first mode by using fractal dimension, c first mode by using modified fractal dimension technique

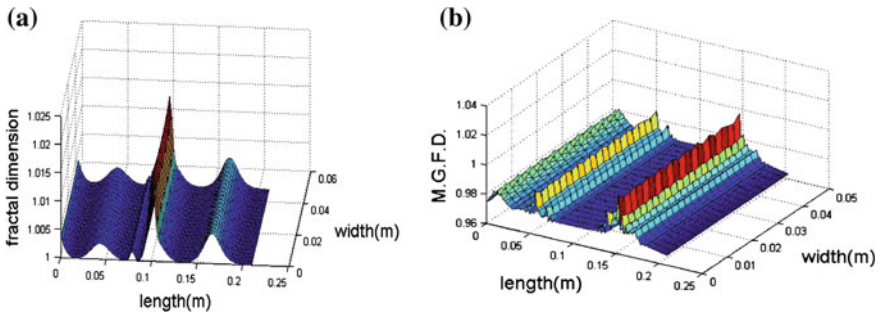


Fig. 6 **a** Fourth mode by using fractal dimension, **b** fourth mode by using modified fractal dimension technique

4 Experiment Setup

Laser Doppler vibrometer (LDV) is a non-contact vibration measurement technique capable of measuring the movements of the scanning points in Z-direction, i.e. out of plane displacement. The system works on the principle of Doppler effect and interferometry for vibration measurement. The schematic diagram of the experimental setup to capture the modal information of composite beams using LDV is shown in Fig. 7.

A periodic chirp signal in the frequency range of 10 Hz–50 kHz is used for the excitation of the composite beam. To improve the reflective ability of the composite specimen, a thin layer of reflective white spray paint was used. The beam was excited by mounting on an electronic shaker as shown in Fig. 7. In this study, glass fibre reinforced plastic (GFRP) laminates were chosen for experimental study. The GFRP specimens were fabricated using hand layup and vacuum bag technique. For the creation of delamination between layers, Teflon tape of thickness 0.09 mm was inserted between the laminas.

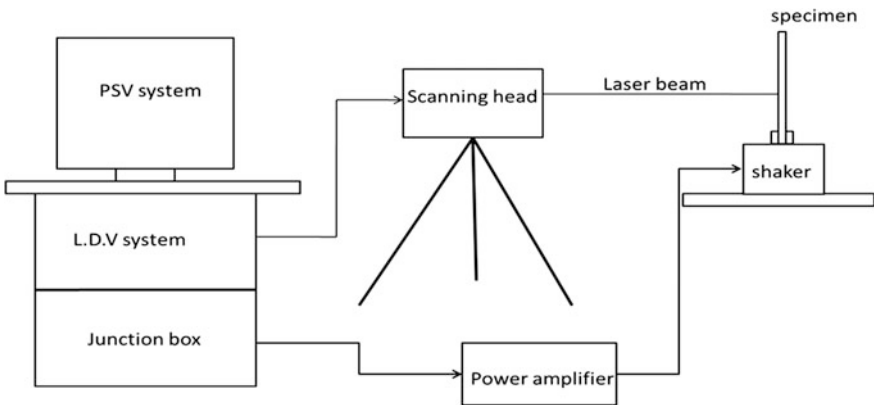


Fig. 7 Laser Doppler vibrometer

Table 2 Experimental and numerical results of various delaminated GFRP specimens

Mode No.	Healthy specimen (Hz)		Full-width delamination (Hz)		C-type delamination (Hz)		I-type delamination (Hz)		Multiple delamination (Hz)	
	FEA	Exp	FEA	Exp	FEA	Exp	FEA	Exp	FEA	Exp
First	16.84	17.18	16.82	16.60	16.83	16.60	16.83	16.06	16.79	15.625
Second	105.47	107.81	105.43	105.46	105.45	105.46	105.45	105.40	102.96	104.50
Third	295.37	287.57	284.96	279.06	291.58	283.06	291.68	–	291.62	270.50
Fourth	578.78	582.50	573.74	580.89	577.92	581.08	577.84	–	564.31	577.80

5 Experimental Results for GFRP Composite Specimen

Experimental study was carried out on the unidirectional GFRP laminate [0]₄ specimen having dimension of 220 mm × 50 mm × 1.16 mm. The material properties of GFRP laminae were obtained by ASTM standard tests and are given by $E_{11} = 42.1$ GPa, $E_{22} = E_{33} = 10.3$ GPa, $G_{12} = 3.84$ GPa, $G_{23} = 3.97$ GPa, $G_{31} = 3.84$ GPa, $\gamma_{12} = 0.27$, $\gamma_{23} = 0.37$, $\gamma_{31} = 0.27$ and density = 2100 kg/m³. The C-type and I-type delamination composite specimens were fabricated as per the information given in the reference [7, 8]. Experiments were carried out on the various delaminated specimens using LDV, and the natural frequencies obtained are given in Table 2.

The results in the table show that both the experimental and finite element modelling results of the delaminated GFRP specimen are close to each other. Subsequently, MGFDF was applied to the first mode shape of the delaminated specimen, and the results are given in Fig. 8. Thus, MGFDF technique can be effectively used for locating and quantifying the partial delamination in GFRP specimens.

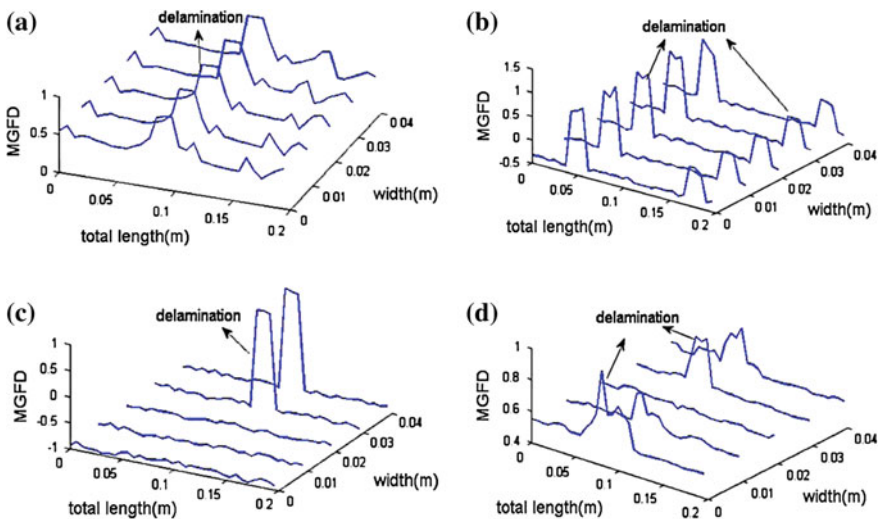


Fig. 8 a Full-width delamination specimen, b multiple delamination specimen, c C-type delamination specimen, d I-type delamination specimen

6 Conclusion

In this work, we investigated experimentally and numerically the modal properties of various partially delaminated specimens. Finite element modelling of partial delaminated specimen was successfully carried out to validate the results available in the literature. Modified fractal dimension technique was proposed and applied to various delamination cases. MGF and GFD techniques were then applied to both numerical and experimental mode shapes of various delaminated specimens. MGF technique was accurate in locating and estimating the actual size of the partial delamination in GFRP specimens. In future, we want to extend the MGF technique to locate delamination in composites plate structures.

Acknowledgements I would like to thank Dr. Ashok Pandey (SENSOR and ACTUATORS laboratory, IIT Hyderabad) for allowing to use the LDV facility and perform my experiments.

References

1. O.K. Ihesiulor, K. Shankar, Z. Zhang, T. Ray, Delamination detection with error and noise polluted natural frequencies using computational intelligence concepts. *Compos. Part B* **56**, 906–925 (2014)
2. Z. Zhang, K. Shankar, T. Ray, E.V. Morozov, M. Tahtali, Vibration-based inverse algorithms for detection of delamination in composites. *Compos. Struct.* **102**, 226–236 (2013)
3. W. Fan, P. Qiao, Vibration based damage identification methods a review and comparative study. *Struct. Health Monit.* **10**(1), 83–29
4. W. Lestari, P. Qia, S. Hanagud, Curvature mode shape based damage assessment of carbon/epoxy composite beam. *J. Intel. Mat. Syst. Struct.* **18**, 189–208 (2007)
5. P. Qiao, K. Lu, W. Lestari, J. Wang, Curvature mode shape-based damage detection in composite laminated plates. *Compos. Struct.* **80**, 409–428 (2007)
6. C.N. Della, D. Shu, Vibration of delaminated composite laminates: a review. *Appl. Mech. Rev.* **60**(1), 1–20 (2007)
7. S. Keshav Kumar, Delamination modelling and detection in composite structure, PH.D. thesis, Indian Institute of Science, Bangalore
8. S. Keshav Kumar, R. Ganguli, D. Harursampath, Partial delamination modelling in composite beams using a finite element method. *Finite Elem. Anal. Des.* **75**, 1–12
9. P. Mujumdar, S. Suryanarayan, Flexural vibration of the beams with delamination. *J. Sound Vib.* **125**(3), 441–461 (1988)
10. M.H.H. Shen, J.E. Grady, Free vibrations of delaminated beams. *AIAA J.* **30**(5), 1361
11. L.J. Hadjileontiadis, E. Doukab, A. Trochidis, Fractal dimension analysis for crack identification in beam structures. *Mech. Syst. Signal Process.* **19**, 659–674 (2005)

FEA and Experimental Analysis on Buckling and Post-buckling Behavior of CFRP Composite Panel Using Digital Image Correlation Technique

Muhammad Shuaib NK, Ramji M, Naresh Reddy Kolanu and Gangadharan Raju

Abstract Finite element and experimental study have been carried out to investigate the buckling and post-buckling behavior of carbon fiber reinforced polymer (CFRP) composite flat panels. For the experimental study, panels were manufactured using hand lay-up followed by vacuum bagging process. The composite panels were then subjected to uniaxial compression loading on an MTS test system with the specimen simply supported on all the sides using specially designed fixture. Digital image correlation technique (DIC) was used for capturing whole field strain, axial displacement, out-of-plane deflection, and mode shapes. Experimental buckling and post-buckling results are compared with the finite element analysis.

Keywords Buckling · Composites · Carbon fiber reinforced polymer (CFRP) Digital image correlation (DIC)

Nomenclature

a Length of the plate
 b Width of the plate
 t Thickness of the plate
 D_{ij} Plate bending stiffnesses
 w Out-of-plane deflection
 N Line pressure load
 L_{cr} Critical buckling load

Muhammad Shuaib NK · Ramji M (✉) · Naresh Reddy Kolanu
Engineering Optics Lab, Department of Mechanical & Aerospace Engineering,
Indian Institute of Technology Hyderabad, Hyderabad 502205, India
e-mail: ramji_mano@iith.ac.in

G. Raju
ND & E Lab, Department of Mechanical & Aerospace Engineering,
Indian Institute of Technology Hyderabad, Hyderabad 502205,
Telangana, India

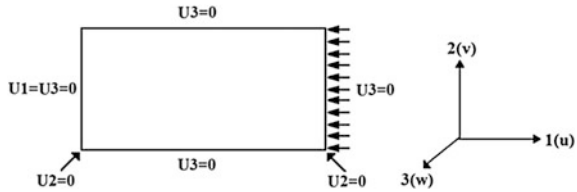
1 Introduction

Composite materials have a wide range of applications because of their high strength/stiffness to weight ratio, excellent fatigue, and possibility of tailored properties. Starting from traditional application areas such as military aircraft, use of composites has grown rapidly to impact various engineering and industrial fields including automobiles, civil structures, sports equipment, and even marine structures. As the range of application increases, it is very important to have a deep understanding of all the mechanical behaviors such as stiffness, strength, and stability behavior of the composites. As composites are commonly used in mass reduction applications, most of the structures are thin in nature, and there is a higher chance for buckling under compressive loading. Because of this thin nature of composite structures, buckling is an important design driver for their safe and reliable design.

Earlier Chen and Bert [1] have done a numerical study on optimal design of simply supported rectangular laminated plates of composite material, subjected to uniaxial compressive loading. Whitney [2] and Bao et al. [3] developed an exact solution for critical buckling of solid rectangular orthotropic plates with all edges simply supported and two edges simply supported/two edges clamped, respectively. Jana and Bhaskar [4] have done few important studies on buckling of simply supported rectangular plates under uniform and non-uniform uniaxial compression for thin-walled structures. Yeh and Fang [5] investigated laminated plates under pure bending analytically and experimentally. Later, Radu and Chattopadhyay [6] investigated dynamic instability associated with composite panels using higher order shear deformation theory. Shukla and Kreuzer [7] have done significant work on estimating the critical/buckling loads of laminated composite rectangular plates under in-plane uniaxial and biaxial loadings for different combinations of simply supported, clamped, and free boundary conditions.

Although we get critical loads using load versus displacement graph from testing machine in experiments, getting whole field strain, and out-of-plane deflection is not possible using strain gauges, noncontact laser displacement meters [8] or using linear variable displacement transducers [9] where we get the deflection of point or multiple points. Recently developed 3-D DIC technique can be used to capture the whole field deflection behavior which provides insight into the physics behind buckling of plates. Ruran [10] has used 3-DIC technique to determine the delamination buckling and growth behaviors of a cross-ply composite laminate. In this study, 3-D DIC technique has been used to analyze pre-buckling and post-buckling behavior such as, whole field strain, axial displacement, and out-of-plane deflection of composite panel.

Fig. 1 Loading and boundary condition



2 Problem Description

Finite element and experimental studies are carried out for an eight-layered carbon fiber reinforced polymer composite (CFRP) rectangular flat plate having dimensions of length (a) = 400 mm, width (b) = 200 mm, and thickness (t) = 1.8 mm. The plate is analyzed for in-plane uniaxial compressive loading, and the boundary conditions are shown in the Fig. 1. Plate with quasi-isotropic lay-up sequence [$\pm 45^\circ/90^\circ/0^\circ$]s is chosen for the study, and all the edges are assumed to be simply supported.

3 Finite Element Analysis

Finite element study has been carried out using commercial finite element software ANSYS Version 15.0. An 8-node shell element (Shell-281) having 6 degree of freedom per node is chosen for performing the buckling and post-buckling analysis of composite panels. Mesh convergence study was performed, and the element size was chosen to be 10 mm \times 10 mm, with a total number of 800 elements over the complete plate of dimension 200 mm \times 400 mm. Material properties for CFRP composites are obtained from material characterization tests conducted as per ASTM standards. Material properties obtained from characterization tests are listed in Table 1.

Block Lanczos mode extraction method was used to compute the critical buckling load of the composite plates. The results of buckling analysis were then used to perform the post-buckling analysis. An initial imperfection or a small lateral load is necessary to initiate the instability of the structure which leads to buckling.

Table 1 CFRP material properties

Material properties		Values
Longitudinal modulus	E_{11}	98.41 GPa
Transverse modulus	E_{22}	6.3 GPa
In-plane shear modulus	G_{12}	1.53 GPa
Out-plane shear modulus	G_{23}	1.91 GPa
In-plane Poisson's ratio	ν_{12}	0.23
Out-plane Poisson's ratio	ν_{23}	0.30

The first mode shape from Eigen buckling analysis has been used as the initial imperfection with a scaling factor of 10% of the thickness of the plate. In the post-buckling regime, the strain displacement relationship is nonlinear and requires nonlinear solvers to solve the resulting finite element matrix equations. Newton–Raphson method with automatic load stepping option was chosen to perform the post-buckling analysis.

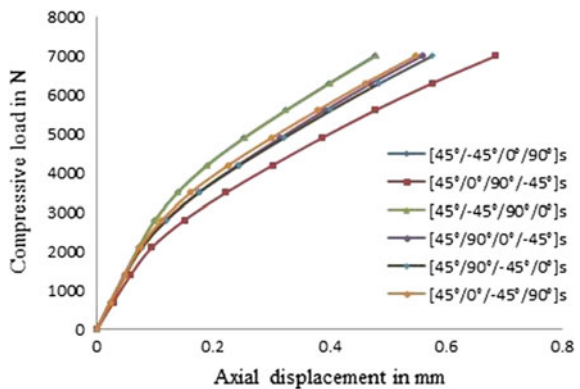
3.1 FEA Results

Initially, finite element analysis is done for CFRP composite having 8 layers with a thickness 0.25 mm for each layer and with material properties listed in Table 1. Comparison between different quasi-isotropic lay-up has been done to find out the best lay-up sequence having higher critical buckling load and maximum post-buckling stiffness.

From Fig. 2, quasi-isotropic $[45^\circ/-45^\circ/90^\circ/0^\circ]_S$ sequence is found out to be having higher critical buckling load and maximum post-buckling stiffness, and further studies have been carried out for the same lay-up sequence. The first three critical buckling loads and their corresponding mode shapes are shown in Fig. 3a–c, respectively.

Subsequently, post-buckling analysis was carried out on the composite panels to study the reduction of stiffness of the plate after buckling and also the out-of-plane displacement behavior of the panels. The results of the post-buckling analysis are shown in Fig. 4.

Fig. 2 End shortening with uniform loading for different quasi-isotropic lay-up sequences



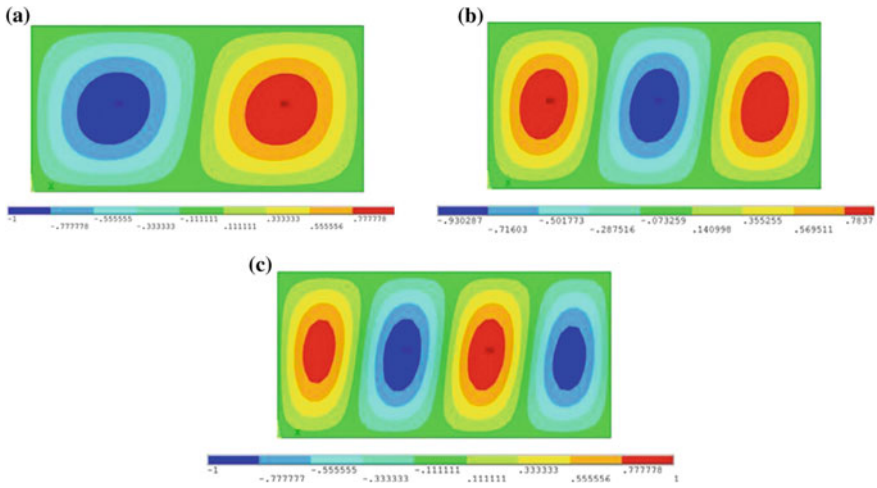


Fig. 3 Different mode shapes for buckling of quasi-isotropic panel from finite element analysis, **a** 1st buckling mode shape, critical buckling load, $N_{cr}^1 = 3550.5$ N, **b** 2nd mode shape, $N_{cr}^2 = 3779.9$ N, **c** 3rd mode shape, $N_{cr}^3 = 4499.5$ N

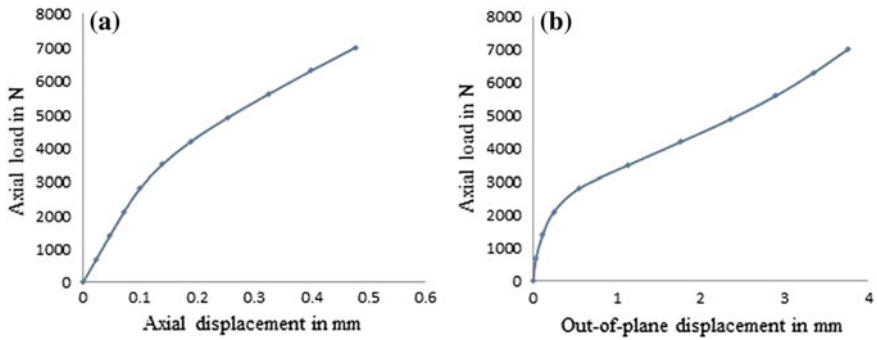


Fig. 4 Post-buckling behavior from nonlinear buckling analysis, **a** end shortening with uniform compressive loading, **b** variation in maximum out-of-plane deflection with uniform compressive loading

4 Experimental Study

Experimental studies using 3-D DIC technique have been carried out to determine the in-plane and out-of-plane deformation and variation of axial load with the applied compression load.

4.1 Specimen Fabrication

CFRP composite panels having a length of 400 mm, width 200 mm, and thickness 1.8 mm and having both unidirectional $(0^\circ)_8$ and quasi-isotropic $[45^\circ/-45^\circ/90^\circ/0^\circ]_S$ lay-up sequences were made as shown in Fig. 5, for the experimental studies. Composite panels were fabricated using hand lay-up followed by vacuum bagging technique which gives an excellent fiber volume fraction. Unidirectional carbon fiber mat having a density of 200 grams per square meter is used as the reinforcement and CY-230 Epoxy resin mixed with HY-951 hardener in a weight ratio of 10:1 is used as the matrix. Weight of resin taken is same as the weight of fiber to form laminate and then kept it under vacuum. Aluminum plate of thickness 3 mm is placed on top to get uniform thickness throughout the panel. A burn-off test has been conducted to determine the constituent content of CFRP made by vacuum bagging process, and the volume fraction of fiber in the composite is found out to be 0.53, and the weight fraction is 0.61.

4.2 Fixture Design and Fabrication

A fixture specially designed to realize the simply supported boundary condition and loading described in Fig. 1 has been fabricated using EN-08 steel to perform the experiment. Fixture consists of 4 parts, bottom plate, top plate, and 2 side supports (see Fig. 6). Side supports are bolted to bottom plate and can slide through the rectangular cutout made on top plate. 60° V-grooves are made on inner surfaces of both plates and side supports to constrain out-of-plane deflection of all the sides of testing panel.



Fig. 5 Casting of composite panel using vacuum bagging technique

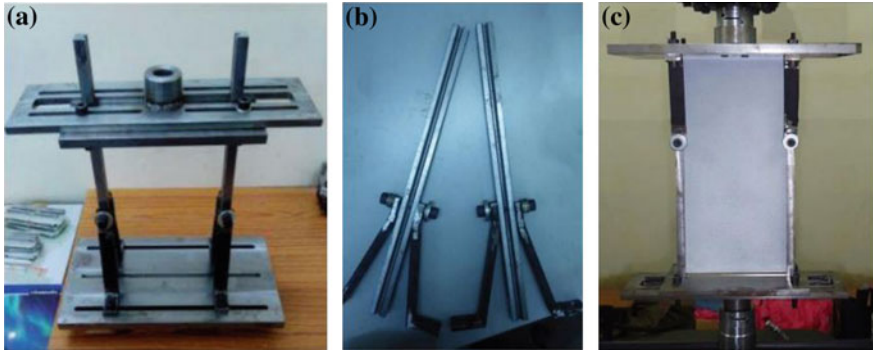
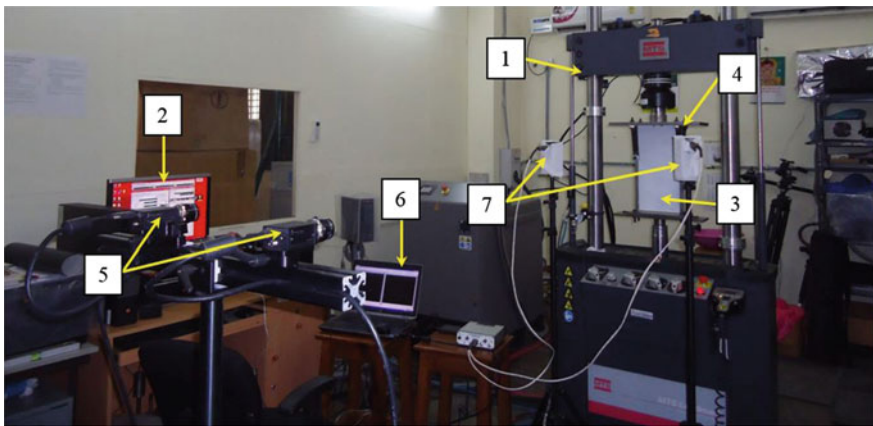


Fig. 6 a Complete assembled fixture for buckling test, b two side supports with V-grooves, c complete fixture with composite flat panel loaded

4.3 Experimental Setup

CFRP panels with zero degree unidirectional and quasi-isotropic $[45^\circ/-45^\circ/90^\circ/0^\circ]_S$ lay-up sequences were tested using MTS servo-hydraulic cyclic testing machine of 100 kN capacity. Panels were painted and speckled after vacuum bagging and machining for getting speckled images for 3-D DIC analysis during testing. Displacement controlled loading has been given to composite panels at a rate of 0.4 mm per minute, and images captured using two grasshopper CCD cameras (Point Grey-GRAS-5055 M-C) having a spatial resolution of 2448×2048 pixel at the rate of 2 images per second. Images are captured using VIC snap software and post-processed using VIC 3-D software from correlated solution. Figure 7 shows the typical experimental setup used for the present study.



(1) 100 kN MTS load frame (2) user interface (3) composite plate compression load (4) Fixture (5) CCD cameras (6) image grabbing PC (7) LED light source

Fig. 7 Experimental setup for buckling study of composite flat panels

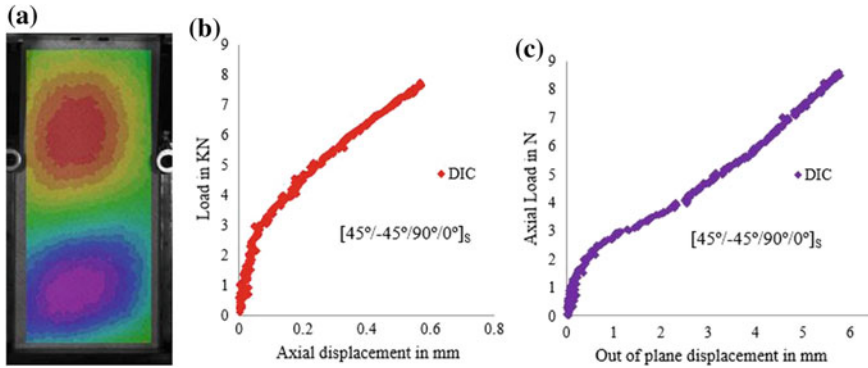


Fig. 8 Experimental results obtained for a 8-layered quasi-isotropic $[45^\circ/-45^\circ/90^\circ/0^\circ]_S$ laminate using 3-D DIC technique, **a** mode shape obtained at 4.5 kN, **b** applied load versus end shortening, and **c** applied load versus maximum out-of-plane deflection

4.4 Result

Post-processing of captured images obtained from experiment was done using VIC 3-D software. Buckling mode shape, in-plane axial displacement, and post-buckling results are extracted and shown in Fig. 8. There is a reduction in axial in-plane stiffness and a drastic increase in out-of-plane deflection at load near 3100 N, which can be taken as critical buckling load.

5 Results, Comparison, and Discussion

Mode shapes, critical buckling load, axial displacement, and post-buckling results obtained from experiments using 3-D DIC are compared with FEA.

Mode shapes are showing the same trend in both FEA and experimental analysis for UD ply as well as quasi-isotropic ply. Number of half sine waves in first mode shape for UD and quasi-isotropic lay-ups are one and two, respectively, along with the loading axis. For UD laminates at 2.0 kN load, the maximum out-of-plane deflections are matching with an error percentage of 15.2% (Fig. 9a), whereas in quasi-isotropic lay-up, both minimum and maximum deflections are matching with an error percentage less than 10% (Fig. 9b). Change in maximum out-of-plane deflection with respect to loading has been compared with both UD and quasi-isotropic lay-ups in Fig. 10.

The plot of applied compression load versus out-of-plane deflection for both UD and quasi-isotropic panels is shown in Fig. 10. For UD laminate, the post-buckling results show the out-of-plane behavior of FEA as well as experimental study that are close to each other. However, for quasi-isotropic, experimental critical buckling

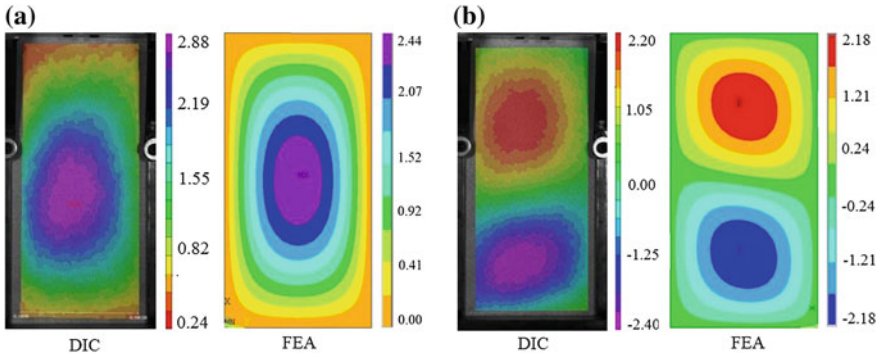


Fig. 9 Experimental (DIC) and finite element (FEA) comparison of out-of-plane deflection in mm, **a** unidirectional lay-up at 2.0 kN load, **b** quasi-isotropic lay-up at 4.5 kN load

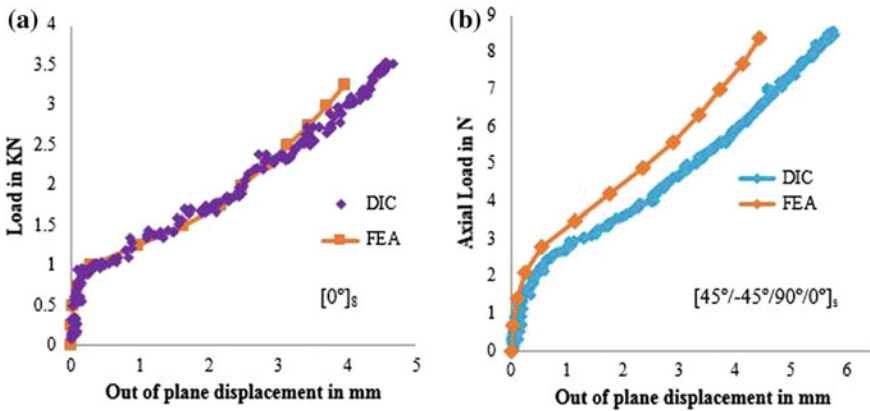


Fig. 10 Experimental (DIC) and finite element (FEA) comparison of variation of out-of-plane deflection with loading, **a** unidirectional lay-up, **b** quasi-isotropic lay-up

load is slightly less than the FEA value, though both FEA and experimental post-buckling results are showing similar trend.

End shortening of panel with compressive loading in FEA and experiment has also been compared for quasi-isotropic lay-ups. From Fig. 11a, there is a significant difference in experimental post-buckling stiffness compared to FEA for uniform compressive loading, which was later identified to be slight tilting (0.17 mm) of the testing fixture toward left side. This condition was then simulated in FEA by replacing the uniform loading with parabolic compressive loading, and the computed post-buckling stiffness is matching with the experimental results. The effect of tilting is clearly visible from Fig. 11c, where the in-plane axial displacement contours are tilted instead of straight horizontal lines.

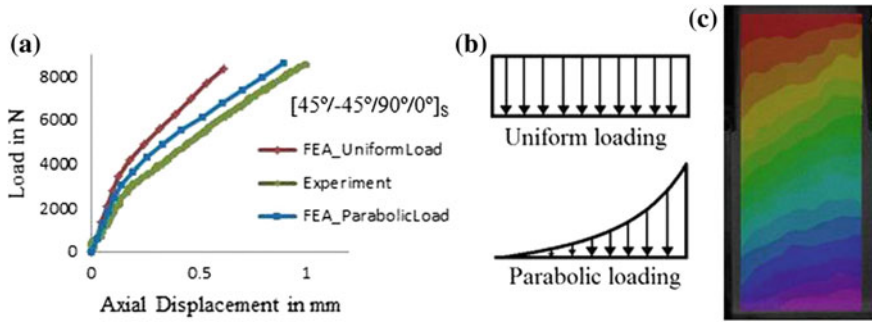


Fig. 11 a Experimental (DIC) and finite element (FEA) comparison of end shortening of quasi-isotropic lay-up, b schematic diagram of loading, c in-plane axial displacement from experiment

6 Conclusion

Study has been done for understanding the pre-buckling and post-buckling behavior of the CFRP flat panel under in-plane axial compressive loading with all the sides simply supported. Finite element study using Eigen buckling followed by nonlinear analysis has been done to obtain the buckling behavior of CFRP panel including mode shapes, critical buckling load, and axial/out-of-plane deflections, which are used to validate the experimental results obtained from 3-D DIC technique. From finite element study, $[45^\circ/-45^\circ/90^\circ/0^\circ]_S$ lay-up shows the highest post-buckling stiffness and has got a higher critical buckling load among all quasi-isotropic lay-up sequences. The composite plate fabricated for experimental study of quasi-isotropic panel is of the above sequence. From experimental and finite element study, comparing UD and quasi-isotropic lay-up sequences, even though the UD lay-up sequence is having a very high pre-buckling and post-buckling stiffness, the critical buckling load is very less compared to the quasi-isotropic lay-up. Experimentally determined mode shapes, critical buckling load, and out-of-plane deflection are to match well with finite element estimates for both UD and quasi-isotropic lay-up sequences. Although there was a noticeable reduction in experimentally determined results of plane axial stiffness in comparison with FEA, which is later resolved by exactly replicating the experimental loading condition in the finite element modeling. As the CFRP panel shows excellent stiffness toward compression, even slight non-parallelism (in range of micro meters) between top and bottom side of fixture leads to experimental errors in terms of in-plane axial stiffness. Making them parallel and perfectly aligning both the sides of the loading fixture would exert a uniform load and would generate exact stiffness in experimental studies.

References

1. T.L.C. Chen, C.W. Bert, Design of composite-material plates for maximum uniaxial compressive buckling load. *Proc. Okla. Acad. Sci.* **56**, 104–107 (1976)
2. J.M. Whitney, *Structural Analysis of Laminated Anisotropic Plates* (Technomic Publishing, Lancaster, PA, 1987)
3. G. Bao, W. Jiang, J.C. Roberts, Analytic and finite element solutions for bending and buckling of orthotropic rectangular plates. *Int. J. Solids Struct.* **34**(14), 1797–1821 (1997)
4. P. Jana, K. Bhaskar, Stability analysis of simply-supported rectangular plates under non-uniform uniaxial compression using rigorous and approximate plane stress solutions. *Thin-Walled Struct.* **44**, 507–516 (2006)
5. M.K. Yeh, L.B. Fang, Bending behavior of delaminated composite plates with contact effects. *Compos. Struct.* (1997) (Elsevier)
6. A.G. Radu, A. Chattopadhyay, Dynamic stability analysis of composite plates including delaminations using a higher order theory and transformation matrix approach. *Int. J. Solids Struct.* **39**(7), 2000
7. K.K. Shukla, Y. Nath, E. Kreuzer, K.V. Sateesh Kumar, Buckling of laminated composite rectangular plates. *J. Aerosp. Eng.* **18**, 215 (2005)
8. H. Suemasu, T. Irie, T. Ishikawa, Buckling and post buckling behavior of composite plates containing multiple delaminations. *J. Compos. Mater.* **43**(2), 191–202 (2009)
9. H. Gu, A. Chattopadhyay, An experimental investigation of delamination buckling and post buckling of composite laminates. *Compos. Sci. Technol.* **59**(6), 903–910 (1999)
10. J.T. Ruan, F. Aymerich, J.W. Tong, Z.Y. Wang, Optical evaluation on delamination buckling of composite laminate with impact damage. *Adv. Mater. Sci. Eng.* **2014**, 390965 (Hindawi Publishing Corporation)

Part VIII
Fatigue

High Cycle Fatigue Strength of Spring Steel with Small Scratches

Yoshiro Nishimura, Masahiro Endo, Keiji Yanase, Yuichi Ikeda,
Susumu Miyakawa and Nobuyuki Miyamoto

Abstract When the compression coil springs are subjected to high cyclic stress, fatigue crack sometimes initiates and propagates from small scratch or defect produced in the manufacturing process. However, there are a limited number of studies on the fatigue behavior of high-strength spring steel in the presence of small scratch. In this study, the fatigue tests were conducted to examine the uniaxial fatigue behavior of a high-strength spring steel (JIS G 3561, SWOSC-V) in the presence of small circumferential notches. Based on \sqrt{area} parameter model, the sensitivity of hard steels, including a high-strength spring steel, to small scratches was qualitatively and quantitatively examined.

Keywords Spring steel · Scratch · Notch effect · Fatigue limit · \sqrt{area}

1 Introduction

These days, a number of components in the automotive vehicles have various types of compression coil springs. Further, because of the strong demand for better performance of automotive vehicles, the use of high-strength spring steels has been increasing [1]. When the compression coil springs are subjected to high cyclic stress, fatigue crack sometimes initiates and propagates from small scratch or defect

Y. Nishimura (✉) · S. Miyakawa · N. Miyamoto
Materials Engineering R&D Division, DENSO Corporation, 1-1 Syowa-cho,
Kariya City 448-8661, Japan
e-mail: yoshirou_nishimura@denso.co.jp

M. Endo · K. Yanase · Y. Ikeda
Department of Mechanical Engineering, Fukuoka University, 8-19-1 Nanakuma Jonan-ku,
Fukuoka City 814-0180, Japan

M. Endo · K. Yanase
Institute of Materials Science and Technology, Fukuoka University, 8-19-1 Nanakuma
Jonan-ku, Fukuoka City 814-0180, Japan

produced in the manufacturing process. As well recognized, fatigue is by far the most common cause of failure for engineering components. Therefore, its prevention is a major preoccupation for a number of industries. The fatigue strength of engineering components can be significantly lowered by the presence of surface scratches, surface finish flaws, nonmetallic inclusions, casting defects, etc. Accordingly, the ability to predict the effects of those defects on fatigue life and fatigue strength is crucial in engineering design.

In this study, to gain a fundamental understanding of the fatigue behavior of a spring steel (JIS G3561, SWOSC-V) with a small scratch, the fatigue tests were conducted in the high cycle fatigue regime. The uniaxial fatigue behavior was investigated by using a rotating bending fatigue testing machine. The effect of scratch was investigated by introducing the small circumferential notch on the specimen surface. Finally, the effects of small scratches were studied by using the \sqrt{area} parameter model ([2], cf. [3–5]).

2 Experiment

The investigated material was an oil-tempered Si–Cr steel wire used for valve springs (JIS G3561, SWOSC-V). SWOSC-V is a super clean steel, especially intended for the manufacture of valve springs and other springs that require excellent fatigue properties and excellent relaxation properties at moderately high working temperature. Chemical compositions of the investigated material are listed in Table 1. The mechanical properties of the material are controlled through patenting, drawing, and oil-tempering process, and they are shown in Table 2.

Figure 1 shows the specimens manufactured from the wires with a diameter of 9 mm by turning and grinding process. The center of specimen is finished by using paper polishing, electro-polishing, and colloidal silica to reduce the roughness and the residual stress on the specimen surface. The surface roughness of the specimen was negligibly small, and it had no effect on fatigue behavior. The residual stress in the axial direction was measured with an X-ray diffraction, and the residual stress of the specimen was within ± 20 MPa on the specimen surface. By using a micro-Vickers hardness tester, the Vickers hardness, HV , was measured both in cross-sectional and longitudinal section of a specimen. As shown in Fig. 2, the anisotropy on HV was not observed, and $HV = 533$ kgf/mm² was obtained. To investigate the effect of scratch on the fatigue properties, a small 60° V-shaped circumferential notch with depth of $t = 50, 100$ μm and notch root radius of $\rho = 15 \pm 5$ μm were introduced on the specimen surface (cf. Fig. 1b).

Table 1 Chemical compositions of SWOSC-V (in % weight)

C	Si	Mn	Cr	Cu	P	S
0.51 ~ 0.59	1.20 ~ 1.60	0.50 ~ 0.80	0.50 ~ 0.80	~ 0.2	~ 0.025	~ 0.025

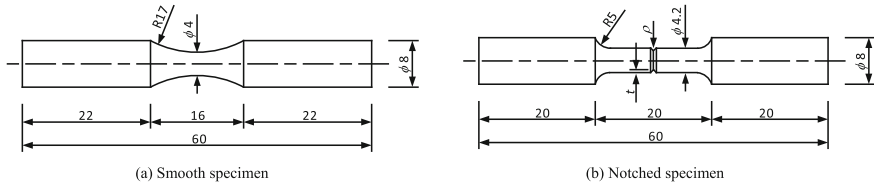


Fig. 1 Geometries and sizes of test specimens (in mm)

Fig. 2 Results of measurement for Vickers hardness

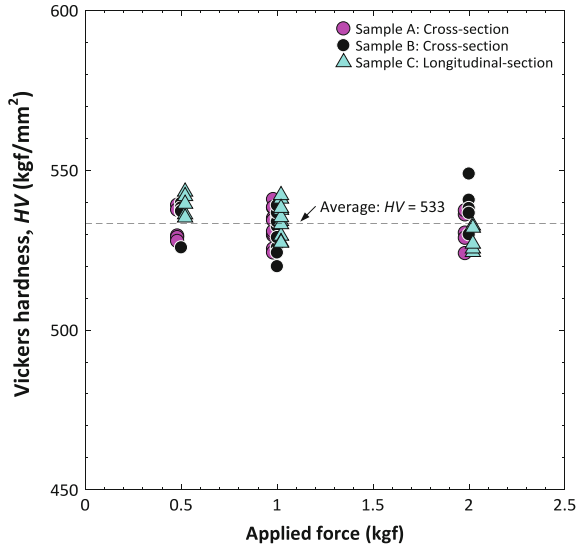


Table 2 Mechanical properties of SWOSC-V

0.2% proof stress (MPa)	Tensile strength (MPa)	Reduction of area (%)
1400 ~ 1570	1610 ~ 1760	40 ~

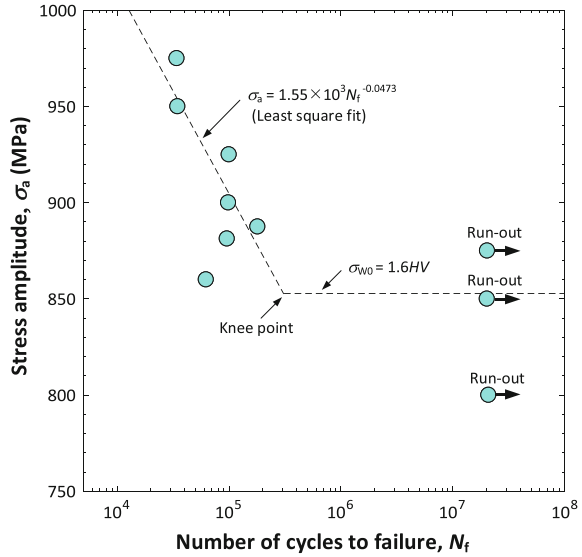
2.1 Smooth Specimen

Based on the applied bending moment, M , the nominal stress amplitude, σ_a , is defined as:

$$\sigma_a = \frac{M}{Z}, \quad \text{where } Z = \frac{\pi d^3}{32} \tag{1}$$

Here, d is the diameter of specimen. Figure 3 shows the $S-N$ data of smooth specimen at room temperature, and its fatigue limit is experimentally determined as

Fig. 3 *S-N* data of smooth specimen



$\sigma_{w0} = 850$ MPa. On the other hand, fatigue limit of smooth specimen can be predicted by the following equation [2]:

$$\sigma_{w0} = 1.6HV \pm 0.1HV \tag{2}$$

Here, σ_{w0} is in MPa and HV is in kgf/mm^2 . By substituting $HV = 533$ in Eq. (2), $\sigma_{w0} = 853$ MPa is obtained, which is nearly equal to $\sigma_{w0} = 850$ MPa that is determined by experiment. The relationship of Eq. (2) holds when fatigue crack mainly initiates from slip bands on the material surface, and Eq. (2) is usually applicable for $HV < 400$. On the other hand, when $HV > 400$, the defects and inclusions inside the materials frequently influence the initiation of fatigue crack. Namely, fatigue limit of high-strength steel becomes sensitive to the presence of defects and inclusions, and fatigue limit cannot be properly predicted with Eq. (2). In this study, however, fatigue cracks initiate from the surface despite $HV > 400$, and fatigue limit is reasonably predicted with Eq. (2). This fact indicates that the size of inclusions in SWOSC-V is significantly small, and fatigue limit is controlled by the bulk material property of SWOSC-V (i.e., HV). In the literature, Akiniwa et al. [6] reported that fatigue cracks in SWOSC-V were initiated in all specimen at the surface, and no inclusion or granular facet areas were detected at the crack initiation site. Thus, they concluded that since the resistance of SWOSC-V against crack propagation from internal inclusions is relatively large, the presence of inclusion does not decrease fatigue strength up to the giga cycle fatigue regime. Finally, as shown in Fig. 3, the knee point emerges at relatively small number of cycles, $N \approx 3.0 \times 10^5$ cycles.

2.2 Notched Specimen

Figure 4 shows a preliminary result of notched specimen, in which the effect of residual stress at the notch root is highlighted. Fatigue limit with a small circumferential notch can be predicted by the following equation [1]:

$$\sigma_w = \frac{1.43(HV + 120)}{(\sqrt{area})^{1/6}}, \quad \text{where } \sqrt{area} = \sqrt{10} \cdot t \quad (3)$$

Here, \sqrt{area} (in μm) represents the square root of the defect projected onto the plane perpendicular to the loading direction, and t (in μm) is the notch depth (Fig. 1b). As shown in Eq. (3), in the case of small circumferential notch, fatigue limit is governed by the notch depth, t , not by the notch root radius, ρ . To calculate the applied stress, the outer diameter of specimen is used for d in Eq. (1). It is noted that the accuracy of Eq. (3) is within 10% for a wide variety of steels [2]. As shown by Fig. 4, before electro-polishing, the specimens with $t = 50 \mu\text{m}$ did not fail until $N \approx 10^7$ cycles though much higher stresses (20 and 30%, respectively) than the predicted fatigue limit were applied. Interestingly, after electro-polishing, those specimens instantly failed under the same applied stresses. Figure 5 shows the non-propagating crack observed at the notch root before electro-polishing. The existence of

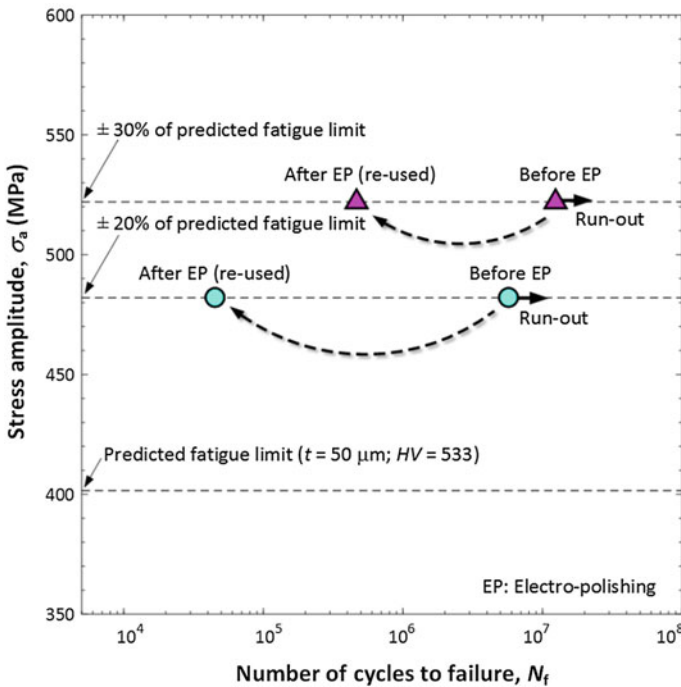
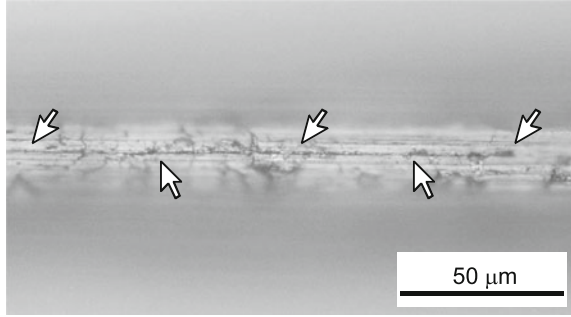


Fig. 4 Effect of electro-polishing on the fatigue strength ($t = 50 \mu\text{m}$)

Fig. 5 Non-propagating cracks observed at the notch root before electro-polishing (stress amplitude is +30% of the predicted fatigue limit, cf. Fig. 4)



non-propagating crack indicates the presence of compressive residual stress at the notch root due to machining, and the residual stress affects the fatigue crack growth behavior and fatigue limit. After a slight electro-polishing, the previously observed non-propagating crack disappeared, thus the depth of crack would be very small (2–5 μm). Accordingly, though the affected zone is small, the removal of residual stress at the notch root is essential to properly evaluate the effect of notch for the present material. Therefore, electro-polishing was applied to remove a layer of 10–15 μm thickness at the notch root, and the fatigue test was conducted accordingly.

Figure 6 shows the comparison of *S-N* data for smooth and notched specimens. When a specimen endured the load cycles of $N \geq 1.2 \times 10^7$ cycles, it is regarded

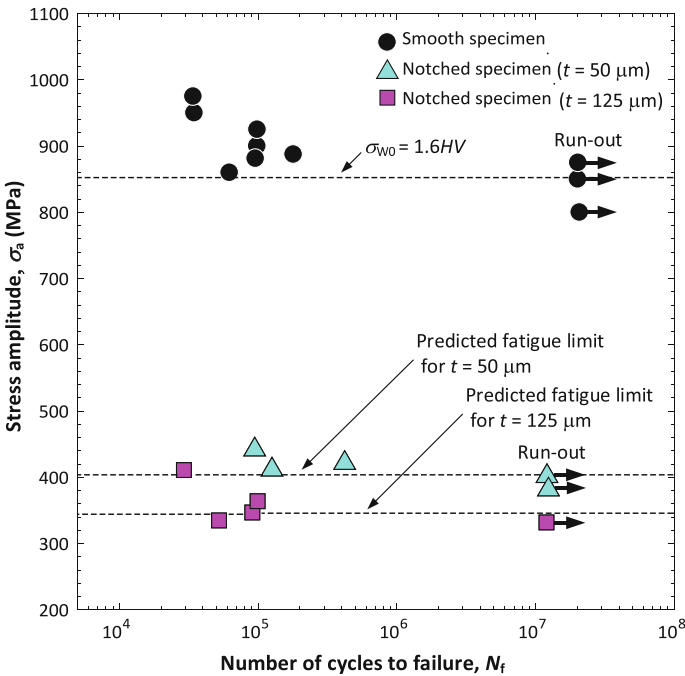
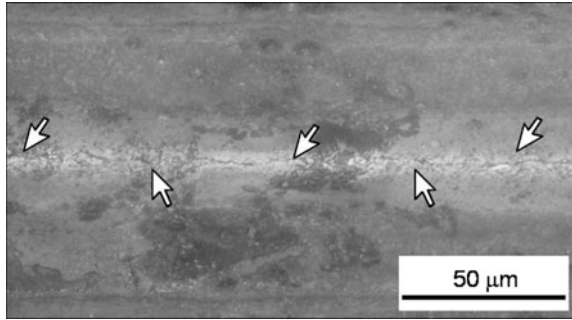


Fig. 6 Comparison of *S-N* data

Fig. 7 Non-propagating cracks observed at the notch root ($t = 50 \mu\text{m}$) (stress amplitude is $\pm 0\%$ of the predicted fatigue limit, cf. Fig. 6)



as a run-out specimen. For instance, based on Fig. 6, fatigue limit is experimentally determined as $\sigma_w = 402 \text{ MPa}$ for $t = 50 \mu\text{m}$ that is equal to the prediction with Eq. (3). It is widely recognized that fatigue limit of notched components is frequently dictated not by crack initiation, but by the critical condition for the propagation of a short crack at the root of a notch. Therefore, the boundary between propagation and non-propagation separates the safe from the potentially unsafe fatigue regime (cf. [7–9]). Figure 7 shows the non-propagating crack observed at the fatigue limit for $t = 50 \mu\text{m}$, and such a crack was not observed when the stress amplitude was reduced to $\sigma_a = 381 \text{ MPa}$ (-10% of predicted fatigue limit, cf. Fig. 6). Accordingly, $\sigma_a = 381 \text{ MPa}$ is smaller than the crack initiation threshold for $t = 50 \mu\text{m}$, and the non-propagating crack exists in the limited range of stress amplitude.

Figure 8 shows the variations of fatigue limit associated with the size of circumferential notch. In addition to SWOSC-V, the experimental data of S45C ($HV = 400$, unpublished data), S50C ($HV = 375 \sim 378$, [2]), and maraging steel

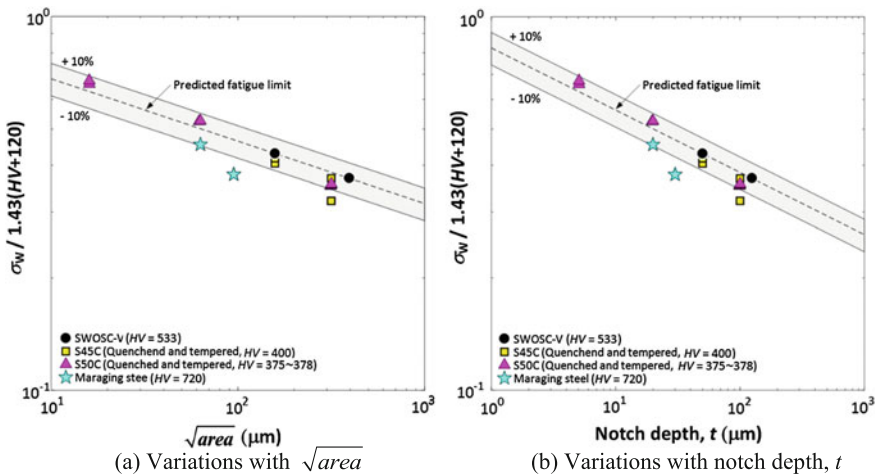


Fig. 8 Variations of fatigue limit associated with the size of circumferential notch

($HV = 720$, [2]) are plotted. As shown, the overall accuracy of $\pm 10\%$ still holds for these hard steels. However, if any, as the material hardness increases, the experimental data tend to deviate from the prediction line at smaller \sqrt{area} or t . Such a behavior is typically highlighted for maraging steel (symbol * in Fig. 8). To investigate this behavior for SWOSC-V, the fatigue tests with notched specimens will be further conducted.

3 Conclusion

In this study, the fatigue tests were conducted to examine the uniaxial fatigue behavior of high-strength spring steel, SWOSC-V. To study the effects of small scratch, the small circumferential notch was carefully introduced to the specimen surface. The present investigation confirms that the \sqrt{area} parameter model is applicable to predict the fatigue strength of SWOSC-V and other hard steels. However, the tendency of deviation of experimental data for hard steels from the prediction line is observed as the size of notch increases.

References

1. N. Ibaragi, Developments in automotive valve spring wire rods. Kobe Steel Eng. Rep. **50**, 27–30 (2000). (in Japanese)
2. Y. Murakami, *Metal Fatigue: Effects of Small Defects and Nonmetallic Inclusions* (Elsevier, New York, 2002)
3. M. Endo, K. Yanase, Effects of small defects, matrix structures and loading conditions on the fatigue strength of ductile cast irons. Theor. Appl. Fract. Mec. **69**, 34–43 (2014)
4. K. Yanase, M. Endo, Multiaxial high cycle fatigue threshold with small defects and cracks. Eng. Fract. Mech. **123**, 182–196 (2014)
5. B.M. Schönbauer, K. Yanase, M. Endo, VHCF properties and fatigue limit prediction of precipitation hardened 17-4PH stainless steel. Int. J. Fatigue **88**, 205–216 (2016)
6. Y. Akiniwa, S. Stanzl-Tschegg, H. Mayer, M. Wakita, K. Tanaka, Fatigue strength of spring steel under axial and torsional loading in the very high cycle regime. Int. J. Fatigue **30**, 2057–2063 (2008)
7. M. Endo, A.J. McEvily, Fatigue crack growth from small defects under out-of-phase combined loading. Eng. Fract. Mech. **78**, 1529–1541 (2011)
8. K. Yanase, M. Endo, Analysis of the notch effect in fatigue. J. ASTM Int. **9**, 1–13 (2012)
9. K. Yanase, K. Shojima, C. Ogata, High-cycle fatigue threshold behaviors in notched plates. Int. J. Damage Mech **22**, 1006–1022 (2013)

Estimation of Load Sequence Effect on Fatigue Crack Growth Life According to Various Prediction Models

A. N. Savkin, A. A. Sedov, A. V. Andronik and K. A. Badikov

Abstract Possible variability of endpoints on the $da/dN-\Delta K$ curve is analyzed, and its influence on crack growth life is shown. Basics of the fatigue crack growth model of material with a single crack are presented. The proposed model calculates local stress at a remoted point close to the crack tip. The model establishes a relationship between the stresses and the near-threshold range of stress intensity factor. Tests were carried out for the low crack growth rates on aluminum alloy 2024-T3 and low carbon steel with rare small overloads of different sequence, and as a result, $a-N$ and $da/dN-\Delta K$ plots were received. Fatigue predictions were done using existing Elber, Barsom, Wheeler, Willenborg models, NASGRO and FASTRAN software and the proposed model. It is shown that the proposed model of local stress calculation at the distance from crack tip is able to predict fatigue life considering load sequence of no less accurate than the best of existing models. However, application area is restricted to small overloads, high cycle ratio, and low crack growth rate at the moment.

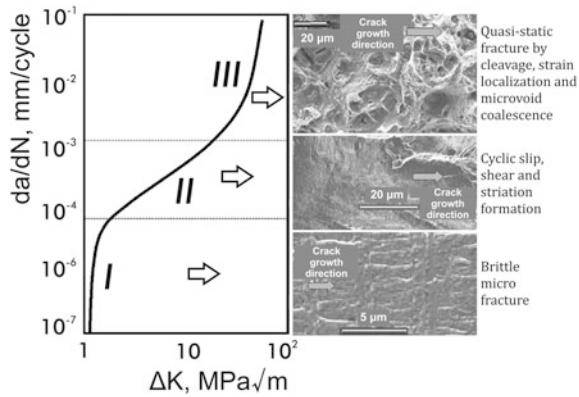
Keywords Fatigue crack growth · Load sequence · Prediction models
Local stress calculation

1 Introduction

Growth of macrocracks usually may be described by the $da/dN-\Delta K$ curve, which is a plot of the crack growth rate da/dN function of the stress intensity factor range (SIF) ΔK (Fig. 1). Three regions can be noted on the $da/dN-\Delta K$ curve [1]: (1) the region of the near-threshold crack growth rates (I); (2) the Paris regime (II); (3) the region of stable tear preceding fracture (III). Nonlinear form of the $da/dN-\Delta K$ curve is conditioned by various dominated crack growth mechanisms on the various

A. N. Savkin · A. A. Sedov (✉) · A. V. Andronik · K. A. Badikov
Department of Strength of Materials, Volgograd State Technical University,
Lenina Av., 28, Volgograd, Russian Federation 400005
e-mail: alexander.a.sedov@gmail.com

Fig. 1 da/dN - ΔK curve and corresponding fractographies for the aluminum alloy 2024-T3 [2]



regions that is affirmed by fractography analysis [2]: (1) brittle microfracture occurs on the I region; (2) cyclic slip and shear prevails on the II region; (3) quasistatic fracture by cleavage, strain localization, and microvoid coalescence is typical for the III region. Endpoints of the da/dN - ΔK curve are important characteristics of the fatigue resistance of material [1]: (1) threshold range of SIF ΔK_{th} ; (2) fracture toughness K_c .

These properties ΔK_{th} and K_c are often taken constant during calculation, but variable in practice. Though inaccuracy in taking K_c as an input value for calculation leads to the insignificant divergency of the test and prediction results of crack growth life till fracture of an order $10^2 \dots 10^4$ cycles, then inaccuracy in taking ΔK_{th} causes a huge error of an order $10^5 \dots 10^6$ cycles; thus, the precise ΔK_{th} value is a more critical factor at the high cycle fatigue.

2 Near-Tip Stress Model for ΔK_{th}

An interesting model of the variable ΔK_{th} was proposed by Sunder [3], which has found an empirical correlation between ΔK_{th} and the local stress at the distance r^* from the crack tip as a result of the tests with constant amplitude loading and periodical overloads to define ΔK_{th} for the aluminum alloy (Fig. 2). To avoid the stress singularity at the crack tip, Sunder estimated the local stress σ^* at the distance from the crack tip r^* obtained likewise correction of plastic zone derived by Irwin (Fig. 3a) [3]:

$$r^* = \frac{1}{2 \cdot \pi} \cdot \left(\frac{K_c^2}{\sigma_f \cdot \varepsilon_f \cdot E} \right). \tag{1}$$

where σ_f —local fracture stress, ε_f —local fracture strain.

Fig. 2 Relationship between the threshold range of SIF ΔK_{th} and the local stress near crack tip σ^* for the aluminum alloy 2024-T3 [3]

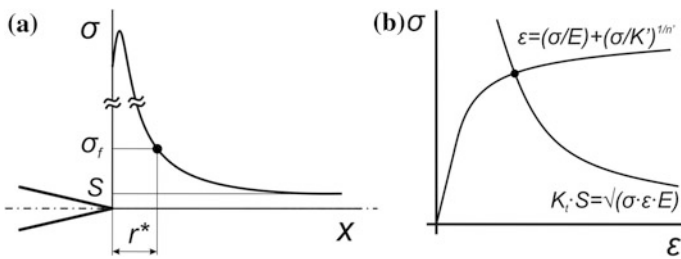
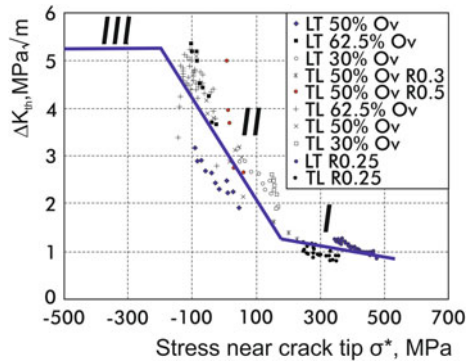


Fig. 3 Local stress σ^* near crack tip at the distance r^* (a); graphical representation of combination of the Neuber rule and Ramberg-Osgood equation (b)

Evidently, given estimation allows to look inside of the plastic zone, but restricted by the condition $\sigma^* \leq \sigma_f$. Using the Neuber rule [4] and the Ramberg-Osgood equation (Fig. 3b) [5], Sunder succeeded to associate the SIF K or its range ΔK with the local stress σ^* at the distance from crack tip r^* for monotonic and cyclic loading correspondingly [3]:

$$K = \sqrt{2\pi \cdot r^* \cdot E \cdot \sigma^* \cdot \left(\frac{\sigma^*}{E} + \left(\frac{\sigma^*}{K'} \right)^{\frac{1}{n'}} \right)}, \tag{2}$$

$$\Delta K = \sqrt{2\pi \cdot r^* \cdot E \cdot \Delta\sigma^* \cdot \left(\frac{\Delta\sigma^*}{E} + 2 \left(\frac{\Delta\sigma^*}{2K'} \right)^{\frac{1}{n'}} \right)}, \tag{3}$$

where K and ΔK —SIF and its range for the current point and load cycle correspondingly;
 E —elastic modulus;
 σ^* и $\Delta\sigma^*$ —stress and its range for the current point and load cycle correspondingly;

n' и K' —factors of cyclic hardening in Ramberg-Osgood equation.

In such a manner, Sunder established the unambiguous relationship between the current loading and the threshold range of SIF ΔK_{th} . Above-mentioned formulas and relationships are sufficient to formulate the fatigue crack growth prediction model; therefore, the interest appears for comparison analysis of efficiency of proposed and existing models. Classical models of Elber, Barsom, Wheeler, Willenborg, and contemporary models of NASGRO [6] and FASTRAN [7] were elected for this analysis. The special interest is resided in the generalized and modified Willenborg models in NASGRO and the crack closure model in FASTRAN. The listed models belong to the following classes [8]: (1) crack closure model; (2) probabilistic models; (3) models considering plasticity close to the crack tip.

It is a common knowledge that overloads and underloads cause various influence on the fatigue crack growth rate da/dN . Overloads usually retard crack propagation, but underloads can accelerate it [9]. Overloads exert various influence on the crack opening force P_{op} and the threshold range of SIF ΔK_{th} (Fig. 4) [10]. Therefore, according to the contemporary crack closure models, an overload and an underload cause increases of the P_{op} , but ΔK_{th} grows after the overload and falls after the underload by the proposed model. As well as overloads and underloads cause various cyclic stress–strain response near the crack tip during the following loading (Fig. 5): mean stress during the baseline loading is less after overloads than after underloads and it is considered in the proposed model (Fig. 2). This various description must find its way in the crack growth life prediction for the fatigue crack growth. Correlation between ΔK_{th} and σ^* was obtained during the tests with

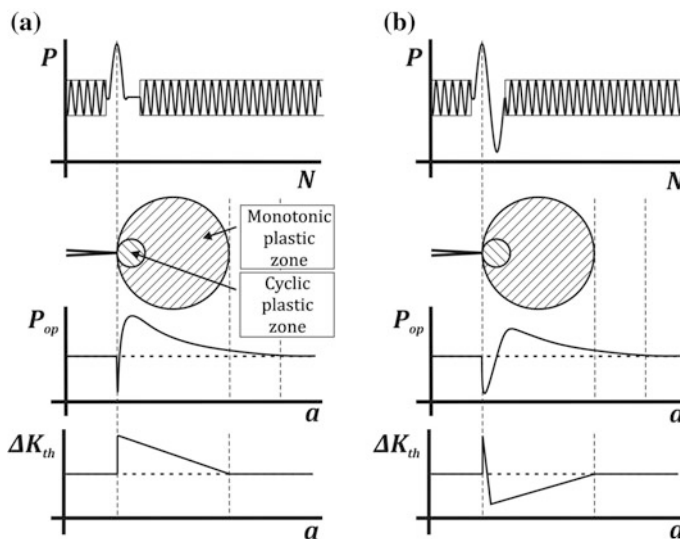


Fig. 4 Influence of various overloads on the crack opening force P_{op} and the threshold range of SIF ΔK_{th} [10]

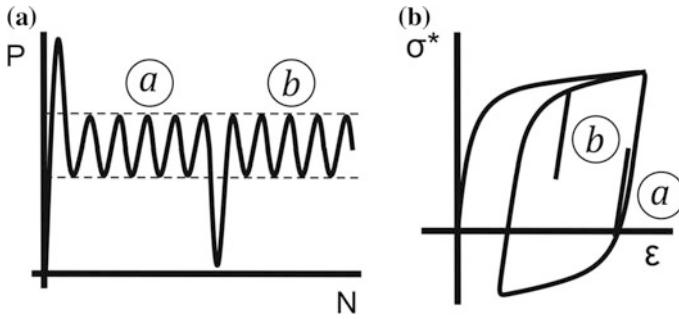


Fig. 5 Various cyclic stress–strain response near the crack tip during the baseline loading after overloads (a) and underloads (b)

overloads thus the interest appears to carry out similar tests with overloads of the various sequence.

Conventional aluminum alloy AA 2024-T3 was used as a test material, the duralumin of the Al–Cu–Mg dopant system. Besides, Cosmo Magna company has afforded the low carbon alloy steel for manufacturing of a suspension underframe in Ford Fiesta and Fusion automobiles. *C(T)*-specimens of the nonstandard geometry were used for the tests (Fig. 6a): (1) specimen thickness *B* is 5 mm instead of usual 12.5 mm; (2) hole diameter *D* is 6 mm instead of usual 12.5 mm.

It is suggested that the variable threshold range of SIF ΔK_{th} effects on crack growth life, but not the crack closure; thus, the high cycle ratio for the baseline block of the constant amplitude loading $R \geq 0.7$ and small overloads $K_{ol}/K_{max} \leq 1.5$ were applied. According to the above-mentioned recommendations for the aluminum alloy 2024-T3, the test schedule was planned, including: (1) tests with periodical underload–overload; (2) tests with periodical overload–underload; (3) constant amplitude loading. The tests with overloads and underloads consisted of overload cycle and baseline constant amplitude loading block. The tests were conducted for the following overload levels: (1) $K_{ol}/K_{max} = 1.5$, i.e., 50%;

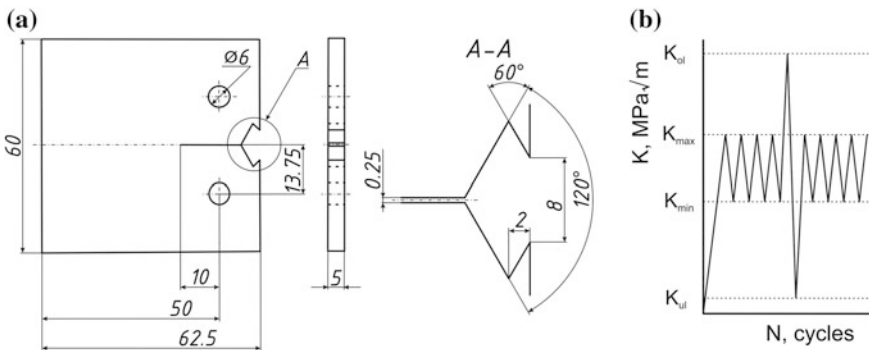


Fig. 6 Geometry of test specimen (a); load sequence with overload–underload (b)

(2) $K_{ol}/K_{max} = 1.4$, i.e., 40%; (3) $K_{ol}/K_{max} = 1.3$, i.e., 30%. The cycle ratio R and the maximal load P_{max} for the baseline loading block were different, but the load range was the same $\Delta P \approx 0.5$ kN due to the next conditions: (1) $R = 0.7$, $P_{max} = 1.7$ kN; (2) $R = 0.75$, $P_{max} = 2$ kN. After the overloads with frequency $F_{ol} = 0.1$ Hz, baseline loading was completed with the frequency $F_{bl} = 150$ Hz during $N_{bl} = 10^4$ cycles, and loading was repeated afterward. The underloads were in tensile loading zone ($K_{ul}/K_{max} = 0.15$). The constant amplitude loading was applied for the cycle ratios: (1) $R = 0.75$; (2) $R = 0.7$; (3) $R = 0.5$; (4) $R = 0.3$; (5) $R = 0.1$. However, the cycle ratio R varied, but the maximal load $P_{max} = 5$ kN of the baseline loading was constant at the tests with the low carbon steel: (1) $R = 0.75$; (2) $R = 0.7$; (3) $R = 0.5$. Applied designations are illustrated on Fig. 6b.

The preliminary calculation of ΔK_{th} at the proposed tests resulted in surface plots (Fig. 7) describing alteration of the threshold range of SIF ΔK_{th} and the effective range of SIF ΔK_{eff} at the various cycle ratio R and the overload level K_{ol}/K_{max} .

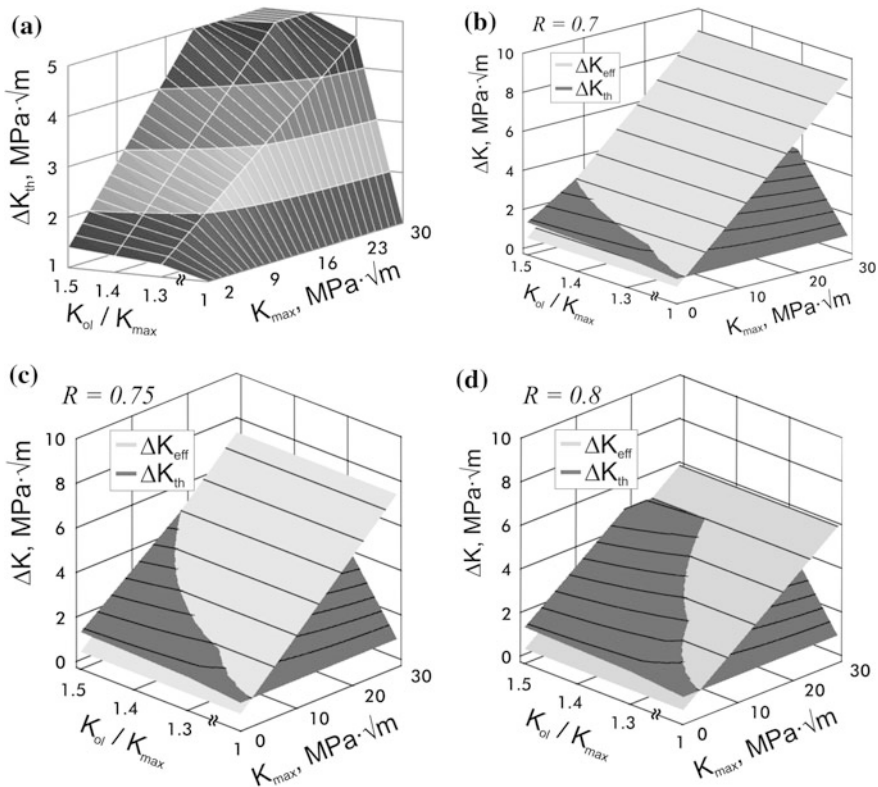


Fig. 7 Relationship between the threshold range of SIF ΔK_{th} , the overload level K_{ol}/K_{max} , and the maximal SIF of the baseline constant amplitude loading K_{max} (a); relationship between the effective range of SIF ΔK_{eff} and the threshold range of SIF ΔK_{th} at the cycle ratios for the baseline loading $R = 0.7$ (b), $R = 0.75$ (c), $R = 0.8$ (d)

during the crack propagation. The proximity of surfaces ($\Delta K_{eff} \rightarrow \Delta K_{th}$, $\Delta K_{eff} > \Delta K_{th}$) is typical for the near-threshold crack growth rates, where excess of surface for the threshold range of SIF ΔK_{th} ($\Delta K_{eff} \leq \Delta K_{th}$) means the crack growth delay.

As the results of all tests, the generalized $da/dN-\Delta K$ curves were obtained for the aluminum alloy 2024-T3 (Fig. 8) and the low carbon steel (Fig. 9). Fatigue crack growth rates for the tests with the last overload and underload at overload block differ approximately by an order. It leads to the significant divergence at the fatigue crack growth prediction and cannot be explained using the crack closure phenomenon.

For the crack growth rate estimation, the modified Forman-Mettu equation was used [6]:

$$\frac{da}{dN} = C \cdot \Delta K_{eff}^m \cdot \frac{\left(1 - \frac{\Delta K_{th}}{\Delta K_{eff}}\right)^p}{\left(1 - \frac{K_{max}}{K_c}\right)^q}, \tag{4}$$

where ΔK_{eff} —effective range of SIF. It is proposed in the tests with overloads that the crack closure influence is negligibly small, so we can accept $\Delta K = \Delta K_{eff}$.

The Paris factors c and m were defined during the constant amplitude tests, p and q —during tests with overloads and underloads. All these factors were constant during the crack growth life prediction unlike the ΔK_{th} . Assuming the variable character of p factor, it was found that the higher ΔK_{th} , the higher p value takes place as a result of the approximation procedure and vice versa. Moreover, the linear relationship between ΔK_{th} and p is typical for the tests with underload–overload sequence during the overload cycle. Thus, modification may appear for the further versions of the fatigue crack growth rate equation. Despite this fact for the purpose of forecasting averaged p factor value was chosen.

Fig. 8 Generalized $da/dN-\Delta K$ curve for the aluminum alloy 2024-T3

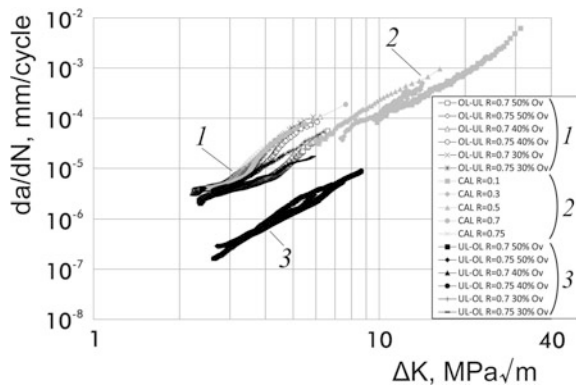
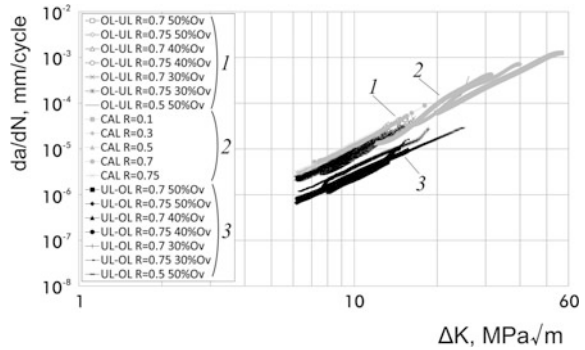


Fig. 9 Generalized $da/dN-\Delta K$ curve for the low carbon steel



Comparison of the prediction and experimental results by the various models is given on Fig. 10. Results are shown for the aluminum alloy on Fig. 10a, b and for the steel on Fig. 10c, d.

Correlation factors between the experimental and prediction results of the fatigue crack growth life are presented on Tables 1 and 2 for the aluminum alloy and the

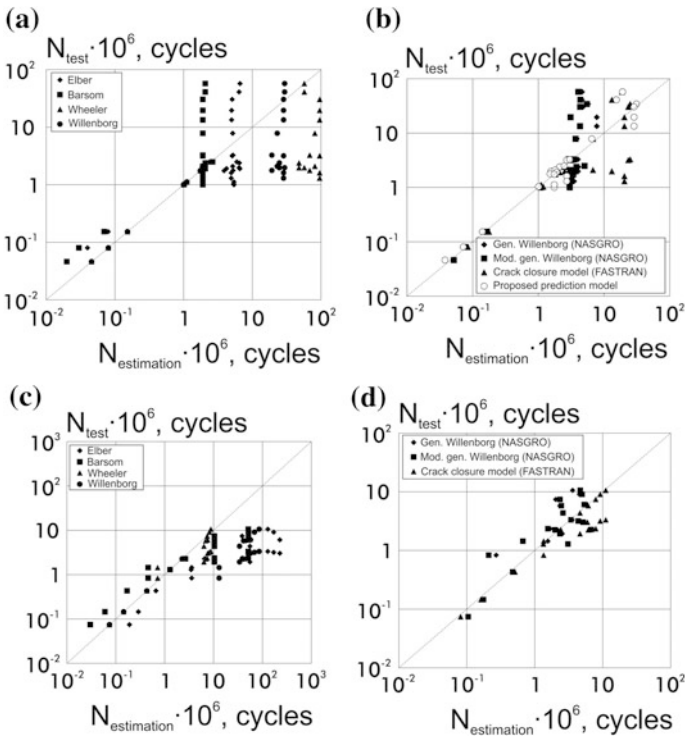


Fig. 10 Correlation between the experimental and estimation results of the fatigue crack growth life for the aluminum alloy 2024-T3 (a, b) and the low carbon steel (c, d)

Table 1 Correlation factors between experimental and estimation results of the fatigue crack growth life for the tests on the aluminum alloy 2024-T3

	<i>r</i>
Crack closure model (Elber)	0.346
Probabilistic model (Barsom)	0.267
Crack tip plasticity model (Wheeler)	0.387
Crack tip plasticity model (Willenborg)	0.507
Generalized Willenborg model (NASGRO)	0.52
Modified generalized Willenborg model (NASGRO)	0.537
Crack closure model (FASTRAN)	0.58
Proposed model for local stress estimation at the distance from crack tip	0.89

Table 2 Correlation factors *r* between experimental and estimation results of the fatigue crack growth life for the tests on the low carbon steel

	<i>r</i>
Crack closure model (Elber)	0.556
Probabilistic model (Barsom)	0.739
Crack tip plasticity model (Wheeler)	0.38
Crack tip plasticity model (Willenborg)	0.46
Generalized Willenborg model (NASGRO)	0.45
Modified generalized Willenborg model (NASGRO)	0.563
Crack closure model (FASTRAN)	0.751

steel correspondingly. Correlation factor for the tests on the aluminum alloy is greater for the proposed model than for others. The tests to define the threshold range of SIF ΔK_{th} at the steel are not accomplished yet, so the corresponding calculation results are not given. Crack closure model in FASTRAN seems to be also effective, but the fact that the proposed model showed the better accuracy than the commercial models reveals a very promising position of the first one.

3 Conclusions

1. The novel fatigue crack growth model based on the local stress estimation at the distance from the crack tip was formulated. The model predicts the fatigue crack growth life at the region of the near-threshold crack growth rates more effective than the existing models, assuming smallness of overloads.
2. Commercial software, for example, NASGRO and FASTRAN, uses hybrid models for fatigue crack growth life estimation to combine the advantages of various models and for the forecasts, which are more precise. Sometimes they work well, however, as it is shown at the current paper, some results leave much to be desired. Low values of the correlation factors between the forecasting and

experimental results of the crack growth life according to the NASGRO and FASTRAN models are represented.

Acknowledgments This paper was financially supported by RFBR grant 17-08-01648 A and RF President grant MK-943.2017.8.

References

1. J. Schijve, *Fatigue of Structures and Materials* (Springer, Delft, 2009), p. 623
2. R. Sunder, Unraveling the science of variable amplitude fatigue. *J. ASTM Int.* **9**(1), 32 (2012)
3. R. Sunder, Engineering application of threshold stress intensity, in *ASTM-ESIS Annual Symposium on Fracture Mechanics*, USA, FL, 2013, pp. 24–48
4. H. Neuber, *Kerbspannungslehre* (Springer, Berlin, 2000), p. 326
5. T. Siretanu, A. Mitu, M. Giuclea, O. Solomon, D. Stefanov, Analytical method for fitting the Ramberg-Osgood model to given hysteresis loops. *Proc. Roman. Acad. Series A.* **15**(1), 35–42 (2014)
6. J. Maierhofer, R. Pippan, H.-P. Gänser, Modified NASGRO equation for physically short cracks. *Int. J. Fatigue* **59**, 200–207 (2014)
7. M. Vormwald, Classification of load sequence effects in metallic structures. *Procedia Eng.* **101**, 534–542 (2015)
8. J.A. Bannantine, J.J. Comer, J.L. Handrock, *Fundamentals of Metal Fatigue Analysis* (Prentice Hall, New Jersey, 1990), p. 271
9. M. Sander, H.A. Richard, Fatigue crack growth under variable amplitude loading Part II: analytical and numerical investigations. *Fatigue Fract. Eng. Mater. Struct.* **29**(4), 303–319 (2006)
10. A.N. Savkin, A.V. Andronik, R. Abhilash, Crack closure detection using photometrical analysis. *Period. Polytech. Mech. Eng.* **59**(3), 114–119 (2015)

SHM—Prognostic Analysis of Tapered Attachment Lugs Under Fatigue Loading

K. Bharath, B. V. Sravan Kumar, L. Chikmath and B. Dattaguru

Abstract Over the years, the flight safety has become a matter of prime concern due to several fatigue failures of structural components and the need to prevent them. Among these, large number of fatigue failures was initiated at major discontinuities such as the inevitable structural joints. Due to this, structural health monitoring (SHM) at these critical locations has become a crucial aspect in the modern damage tolerance-based design concept. Lug joints are often preferred in large-scale structural components which act as primary load-carrying members and are more susceptible to failure due to high stress concentration and geometric irregularities. The primary issue in the analysis of these joints is the loss of contact between the pin-hole boundary during loading and possible change in contact conditions during fatigue loading. This paper deals with the behaviour of tapered attachment lug joints under fatigue loading and finally presents prognostic analysis to estimate remaining life of the joints at any instant of fatigue cycles.

Keywords Crack growth · Fasteners · Fatigue · Lug joints · Prognosis
SHM

Nomenclatures

$2a$	Hole diameter
a' and b'	Crack growth material constants
a_c	Critical crack length
b	Fatigue strength exponent
C and m	Material constants
c and s	Regions of contact/separation

K. Bharath · L. Chikmath (✉) · B. Dattaguru
Department of Aerospace Engineering, Jain University, Bengaluru, India
e-mail: lokamanyachikmath@gmail.com

B. V. Sravan Kumar
National Aerospace Laboratories, Bengaluru, India

G_I	Mode-1 Strain energy release rate
K_I	Mode-1 Stress intensity factor
K_{Ic}	Mode-1 Fracture toughness
K_t	Stress concentration factor
L and W	Length and width of the lug
P	Pin load
R and R_P	Stress and load ratios
R_i and R_o	Inner and outer radii of the lug
$\beta/2$	Taper angle
σ_t and σ_r	Tangential and radial stresses
σ_{br}	Bearing stress
$\tau_{r\theta}$	Shear stress

1 Introduction

Safety of an aircraft is a matter of grave concern in all forms of design concepts. Joints which are inevitable in large-scale structural systems like aircraft are often prone to failures predominantly under cyclic loading which drives the development of effective and reliable computational methods relevant to fatigue and fracture analysis. Hence, location of sensors for integrated vehicle health monitoring (IVHM) system at critical joints in aircraft structures has become one of the future requirements [1]. The science and technology of structural health monitoring (SHM), which is an important part of integrated vehicle health management (IVHM), comprises of two major aspects viz., one is the diagnosis, which deals with the detection of crack-like flaws in structures followed by prognosis, which involves the assessment of crack, crack growth behaviour and further estimation of residual strength and residual life of the structure [2].

Large-scale structural components are assembled in parts, and lugs are used for transferring loads at major joints such as the wing–fuselage junction. These lug joints are generally used as primary load-carrying members, and the ease of assembly and disassembly is an added advantage to prefer fasteners in metallic structures. In this current work, aluminium lug with push fit rigid pin is analysed, which nearly corresponds to a steel pin in an aluminium lug with the modulus ratio of pin to lug being equal to three. The effect of the relative rigidity of the pin and the lug on the stress intensity factor is negligible [3]. Unlike interference and clearance fits whose separation/contact regions between pin and the lug hole vary with varying pin load which leads to nonlinear moving boundary value problem, push fit poses a linear elastic problem with constant contact/separation region between pin and the lug for monotonically varying applied pin load [4]. However, in push fit too, load reversals during fatigue loading cause different contact configurations when the pin is pulled and pushed alternatively. The prognosis in these cases is

based on physical models, but it is interesting since one has to be aware that these are not simple linear problems, but they could be nonlinear.

The literature on lug joints is vast, and in this paper, only a few of those past contributions relevant to the current work are reviewed. The classical contribution of Bickley [5] is still valid, and most of the industry practices assume that the load transfer at the pin–hole interface is over half of the hole boundary, and the load is transferred in a cosine distribution. With the advent of finite element methods, more accurate contact stress analysis [6] showed that while Bickley’s assumptions are nearly valid for push fits, whereas for interference and clearance fit joints contact/separation zones need to be evaluated. Economic analysis using inverse formulations is presented in a series of papers, and these are reviewed in [3, 7]. For the current configuration of tapered lug joints (including the straight lug as a limiting case) with a push fit, results from the literature [8, 9] are used in the current work for comparative purposes.

Tapered attachment lugs with axially symmetric pin load are analysed in the current work. Generally, lugs are tapered in order to take the pin load effectively. Straight lug is the limiting case of zero taper, and the earlier studies [10] for straight lug will be used for comparison purpose. Most of these contributions have not addressed the issue of fatigue crack initiation and crack growth in these joints including the effect of changing contact conditions. The present work highlights the prognostic analysis of these lug joints and describes the computational methods to estimate residual life of these critical joints. Finite element (FE) method is used for this purpose with four-node quadrilateral elements in MSC PATRAN/NASTRAN [11] FE software package. Through the stress analysis, critical locations are identified in these lug joints, and the fatigue crack initiation life is estimated with help of Basquin’s relation, Goodman diagram and Miner’s rule [12, 13] for a prescribed load cycle using locally developed software. Further Paris law including Elber crack closure model [14] is adopted in computing crack growth life, and the fracture parameters required for crack growth formulae are estimated using Modified Virtual Crack Closure Integral (MVCCI) technique [15, 16].

2 Methodology

Tapered attachment lugs, with push fit where pin diameter is equal to the hole diameter of the lug, are analysed. The lug joints are analysed for loads along positive x -axis (called Pull) loads and along negative x -axis (called Push) loads for different taper angles (Fig. 1). There is partial loss of contact for an infinitesimally small pin load, and these contact/separation regions do not change with monotonically increasing load level either in Pull or Push loads leading to linear elastic problems. However, the regions of separation/contact change when the fatigue loading is of Pull–Push type with $R < 0$.

Pin is assumed to be rigid and the lug is of aluminium T3 2024. The rigid pin nearly corresponds to a steel pin in aluminium lug. Further, the interface between the pin and the hole is assumed to be smooth. Fatigue analysis for the above lug models for different taper angles is conducted for the Pull–Pull ($R_p \geq 0$) and the Pull–Push load cycles (with $0 > R_p > 1$), and the fatigue crack initiation life is estimated at critical locations identified from the stress analysis. Typical load cycles applied are shown in Fig. 2. The variation of contact/separation region between the lug and the pin for Pull and Push pin load cases is shown in Fig. 3. In case of push fit, the contact/separation regions for any load level are nearly 180° [4].

2.1 Boundary Conditions and Finite Element Modelling

The region of contact/separation between the hole and the pin remains invariant with monotonic increasing pin load, and this region of contact is nearly between $90^\circ : 0^\circ : -90^\circ$ and $90^\circ : 180^\circ : -90^\circ$ for Pull and Push pin loads, respectively, for axial loading. In the remaining region, the pin and the hole boundary separate from each other. The far end of the lug joints are supported by rollers, and the rigid body motion is suppressed at point A in both x - and y -directions (Fig. 1). The boundary conditions are as given below.

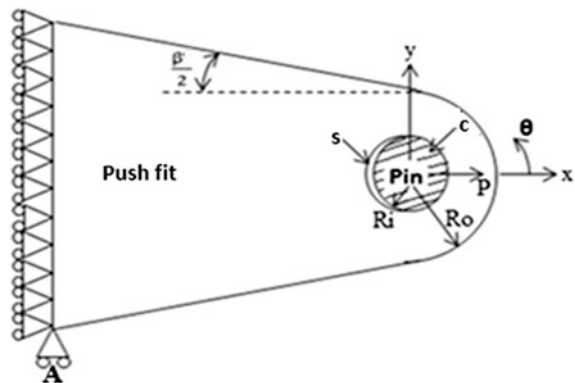
$$\text{Region of contact } (\theta_c) \quad 90^\circ : 0^\circ : -90^\circ \quad U_x = U_o, \quad \tau_{r\theta} = 0 \quad (1)$$

$$\text{Region of Separation } (\theta_s) \quad 90^\circ : 180^\circ : -90^\circ \quad \sigma_r = 0, \quad \tau_{r\theta} = 0 \quad (2)$$

The inequality constraint in contact region is $\sigma_r \leq 0$ and in the separation region is $U_r \geq 0$.

$$\text{At the far end at } x = -L \quad U_x = 0 \quad \text{and} \quad \tau_{xy} = 0 \quad (3)$$

Fig. 1 Typical tapered attachments lug



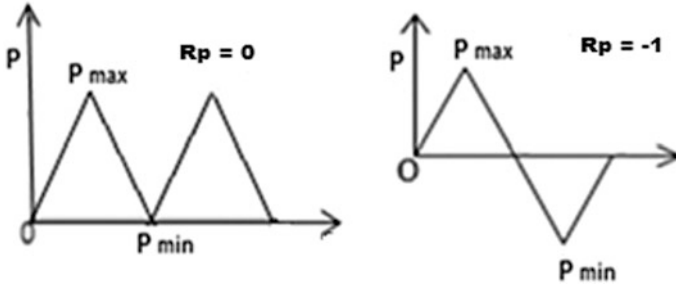


Fig. 2 Typical load cycles applied on the lug

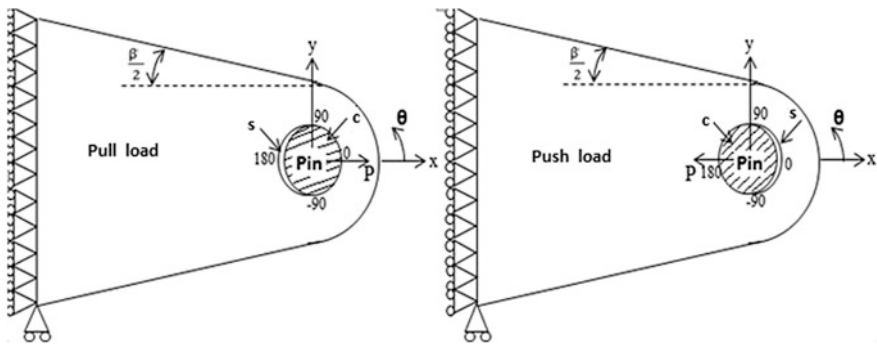


Fig. 3 Contact/separation regions *c* and *s* for pull and push loads

$$\text{Equilibrium eqn : } \int_{-\frac{\pi}{2}}^{\frac{\pi}{2}} \sigma_r r t \cos \theta d\theta = \pm P, \quad +P = \text{Pull load}, \quad -P = \text{Push load} \tag{4}$$

The regions of contact and separation are determined by the satisfaction of the inequality constraints. Even though the region of separation/contact is specified from literature as given in the above equations, the inequality constraints are checked during the analysis.

For the case of Push loading, the region of contact changes to 90° : 180° : -90° and the region of separation will be 90° : 0° : -90° . The boundary conditions in the region of contact and separation remain the same except the regions contact/separation are to be interchanged as in Eqs. (1) and (2) given above. U_o is the rigid body displacement of the pin. Boundary conditions at the far end are given in Eq. (3). Equilibrium equation for Pull and Push load case is given in Eq. (4). For each specified values of the load P in x -direction, the equilibrium is checked by summing up the x reactions at the far end.

Table 1 Convergence study of FEM

Tapered lug (Taper angle 22.5°)	
No. of nodes	Normalized maximum stress ($\sigma_{\max}/\sigma_{br}$) for the pin load, 1000 N
9112	4.785
10,008	5.196
10,856	5.442
11,789	5.686
12,052	5.812
12,071	5.8912
12,078	5.9304
12,082	5.9304
12,085	5.9306
12,089	5.9312

Finite element modelling of the above lug models is carried out in MSC NASTRAN/PATRAN [11] finite element software package using four-node quadrilateral shell elements. The load on the pin is applied by using RBE-2 elements in NASTRAN/PATRAN package. This imposes a multipoint constraint (MPC) on all the nodes in contact with the hole boundary with total load on all the nodes in x -direction is imposed as P , the specified total load on the pin. The movement of the centre of the pin yields the rigid body displacement of the pin U_o which can be estimated from the results. Convergence study was carried out on a tapered lug of taper angle 22.5° to select suitable number of degrees of freedom. Convergence study results are given in Table 1, and it was decided to run all tapered lugs with 12,078 nodes. The typical finite element model of the taper attachment lugs is shown in Fig. 4.

2.2 Fatigue Crack Initiation Life

Fatigue crack initiation life analysis is carried at the critical nodes identified from the stress analysis using well-known equations, and they are reproduced here for the sake of continuity. Typical crack initiation location is shown in Fig. 5. The elastic part of the Basquin's relation (Eq. 5) is used to estimate the damage per cycle, considering the mean stress effect and S-N life approach for the respective fatigue load cycles [12, 13] as given below.

$$N_f = \frac{1}{2} \left[\frac{\sigma_a}{\sigma'_f - \sigma_m} \right]^{(\frac{1}{b})} \quad (5)$$

Fig. 4 FEM model of tapered lug (taper angle 22.5°)

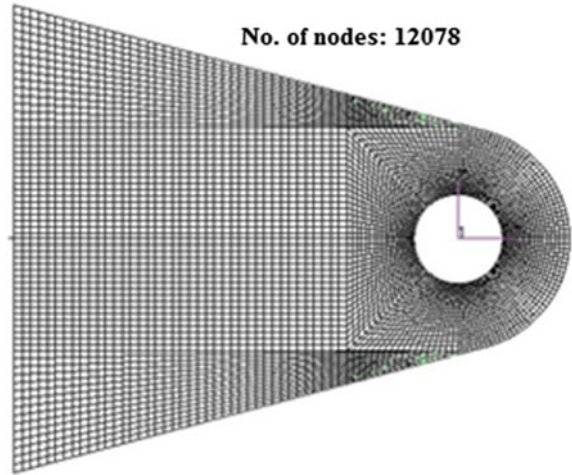
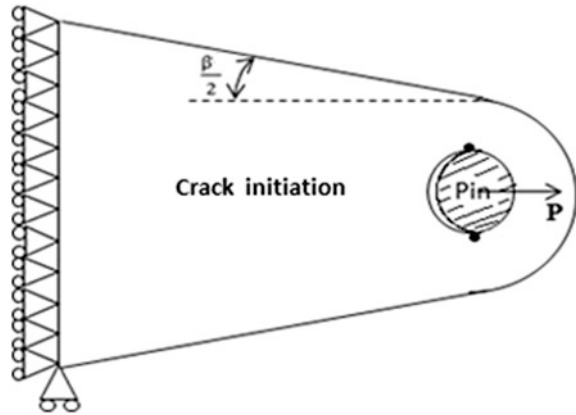


Fig. 5 Crack initiation location



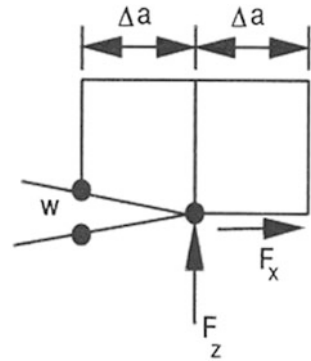
where b is fatigue strength exponent, and σ_f' is fatigue strength coefficient [8].

Fatigue crack initiation life is estimated for the load ratio (P_{min}/P_{max}) $R_p = 0$, $R_p = -1$ and $R_p = -2$ until the cumulative damage index at the critical node for these applied load cycles becomes one. Damage index is estimated using Miner's rule [13] given in the Eq. (6).

$$D = \sum_{i=1}^N \frac{n_i}{N_i} \tag{6}$$

where n is the number of alternating stress of i types, and N_i is total number of cycles to failure of i types, and damage occurs when the damage index reaches the value of one.

Fig. 7 Quad element at the crack tip to estimate fracture parameters



3 Results and Discussions

3.1 Variation of Maximum Tensile Stress

The effect of taper on the maximum tensile stress for both Pull and Push loadings is shown in Fig. 8. The results for straight lug [10] are also plotted in these and subsequent figures to visualize the results for the limiting case of $\beta = 0$. It is seen from the figure that as expected the maximum tensile stress is linear with applied loading confirming that the push fit case is a linear problem. However, the primary result is that the maximum tensile stress decreases with the angle of taper for the case of Pull loading. The same trend is followed even in case of Push loading, wherein it is noticed that lug joint with higher taper angle possesses lesser tensile stresses followed by the lower taper angles. Also it is important to notice that the stresses are too low for Push load to that of Pull load. The results for straight lug [10] are also plotted in the subsequent figures to visualize the results for the limiting case of $\beta = 0$.

3.2 Stress Concentrations Effects

Stress concentration factor (SCF) ($\sigma_{\max}/\sigma_{\text{br}}$ where bearing stress $\sigma_{\text{br}} = P/2R_i t$ and $t =$ thickness) due to applied pin load (both Pull and Push) for different R_o/R_i ratios of the lug is estimated. Since the SCF is obtained by normalizing the maximum stress value with bearing stress it could have a high value. So it is shown in a logarithmic (natural log) scale along the y-axis. For Pull loading (Fig. 9a), it is seen that with increasing R_o/R_i (keeping R_o constant and making the hole smaller) ratios the stress concentration factor decreases due to increase in bearing stress as R_i decreases ($\sigma_{\text{br}} \propto 1/R_i$). From Fig. 9a, it is observed that the straight lug has higher stress concentration factor in comparison with tapered attachment lugs for Pull loading. Obviously, when the taper angle is increased keeping R_o constant, the load

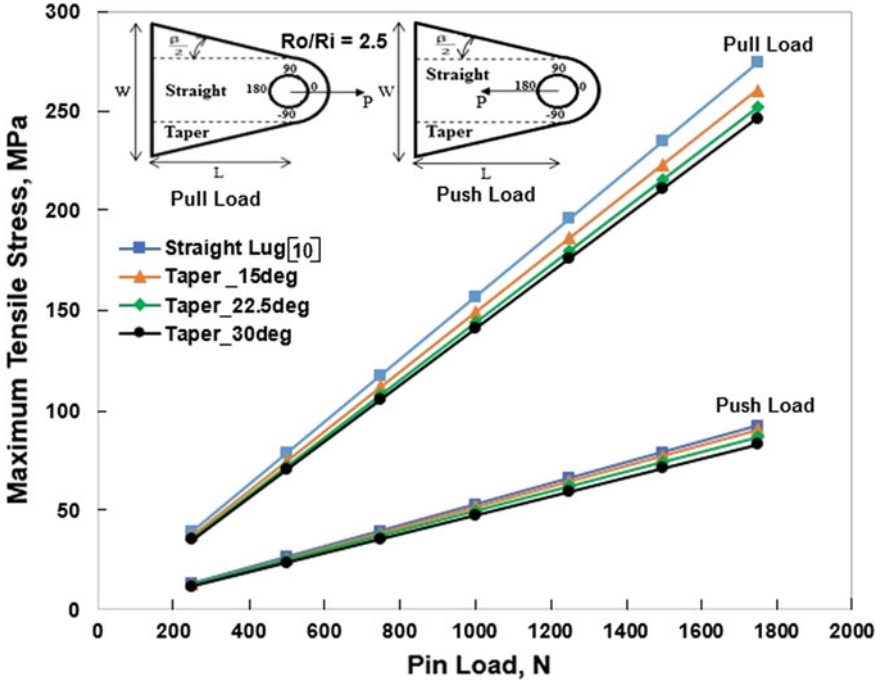


Fig. 8 Variation of maximum tensile stress for applied pull and push load cases

flow will be smoother into a wider lug, and this causes lesser SCF. For the Push load case (Fig. 9b) too, SCF decreases with increase in taper angle. It is also seen that there is decrease in SCF with increase in R_o/R_i ratios as in case of Pull load. Also there is significant drop in SCF in Push load case when compared with Pull load. Figure 9c shows the comparison between empirical solution available in the literature given in the Eq. (11) for the lug joints and the current results for tapered lug for the taper angle of 22.5° . The results of FEM vary within the 2.5% of actual values of literature and empirical solutions [9].

$$K_t = \frac{\sigma_{\max}}{\sigma_{br}} = \left(2.75 - \frac{\beta^0}{135} \right) \left(\frac{R_o}{R_i} - 1 \right)^{-\left(0.675 - \frac{\beta^0}{1000} \right)} \tag{11}$$

3.3 Radial and Tangential Stress Distributions

Radial stress distributions (normalized with σ_{br}) around the pin—the lug—hole interface are plotted in (Fig. 10a, b) for Pull and Push loads, respectively, for different taper angles and R_o/R_i equal to 2.5. For Pull loading (Fig. 10a), radial

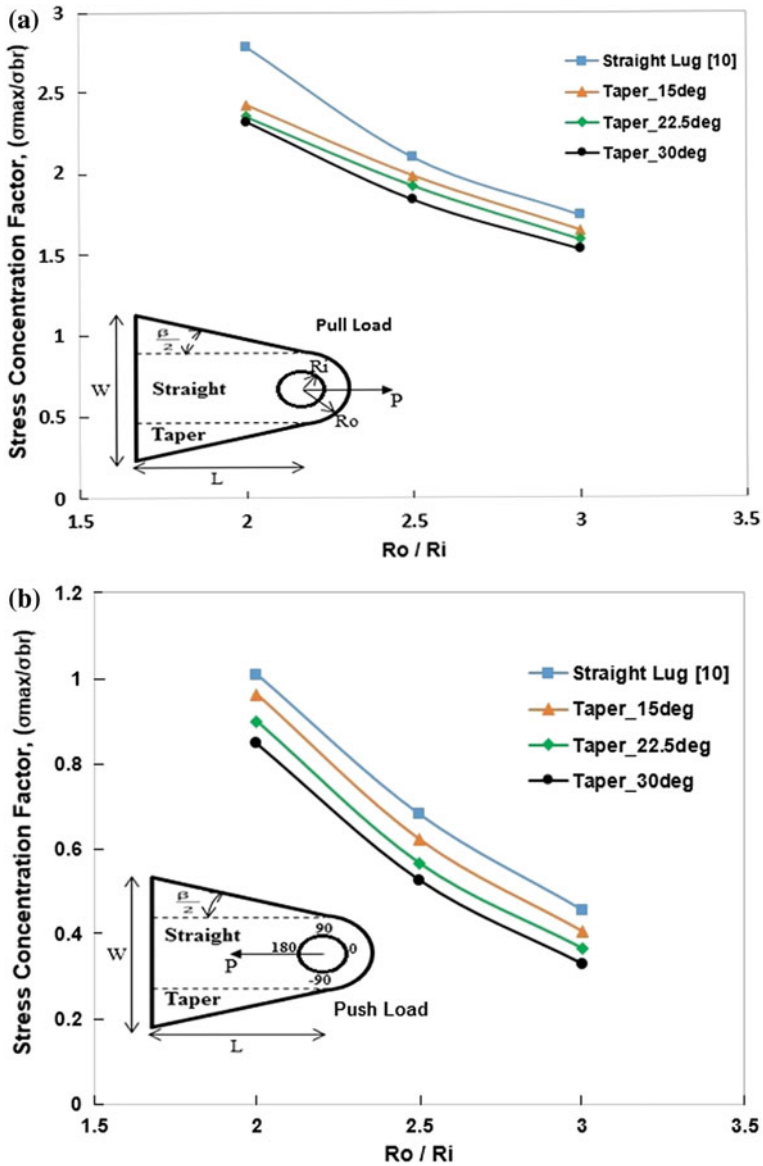


Fig. 9 a SCF for pull load, b SCF for push load, c comparison of SCF for taper lug

stress distribution is throughout smaller for higher taper angles in the contact region in comparison with smaller taper angles. A similar trend is seen in case of Push loading also (Fig. 10b). The results taken from Ref. [10] straight lug show highest radial stress distribution in the contact region in comparison with tapered lugs

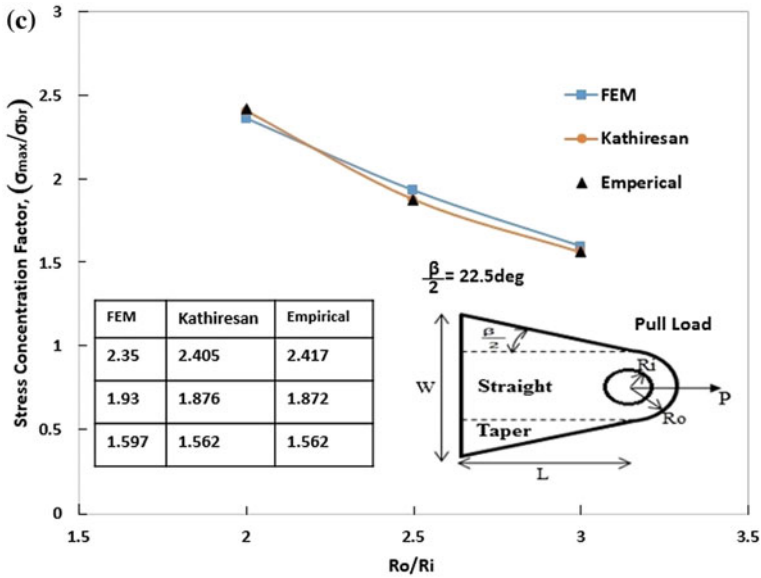


Fig. 9 (continued)

irrespective of pin loading directions. The radial stresses for the case of Push loads are larger compared to the case of Pull loads for the same load level.

Tangential stresses (hoop stresses) are computed around the pin-hole interface and are normalized with the bearing stress for Pull and Push load cases (Fig. 11a, b). In case of Pull load shown in Fig. 11a, there are two points at 90° and -90° where the tangential stresses are the highest. At these maximum tensile tangential stress points, straight lug has higher values in comparison with tapered lugs. These peak values decrease with taper angle. Figure 11b shows the distribution of tangential stress around the pin-hole interface for Push loading which also has two major peak points of stress at same locations, but their magnitude is much smaller than for the case of Pull load, which is again higher for straight lug and decreases with increase in taper angle. The fatigue loading with Pull-Push type will be stressed alternating between the two peaks from Fig. 11a, b with the configuration of contact/separation changing when the load passes through zero value.

3.4 Fatigue Crack Initiation Life

Stress history at a point is monitored due to applied load/displacement for which the fatigue analysis is carried out till the crack initiation. The critical locations are identified through the stress analysis in particularly from the tensile tangential stress

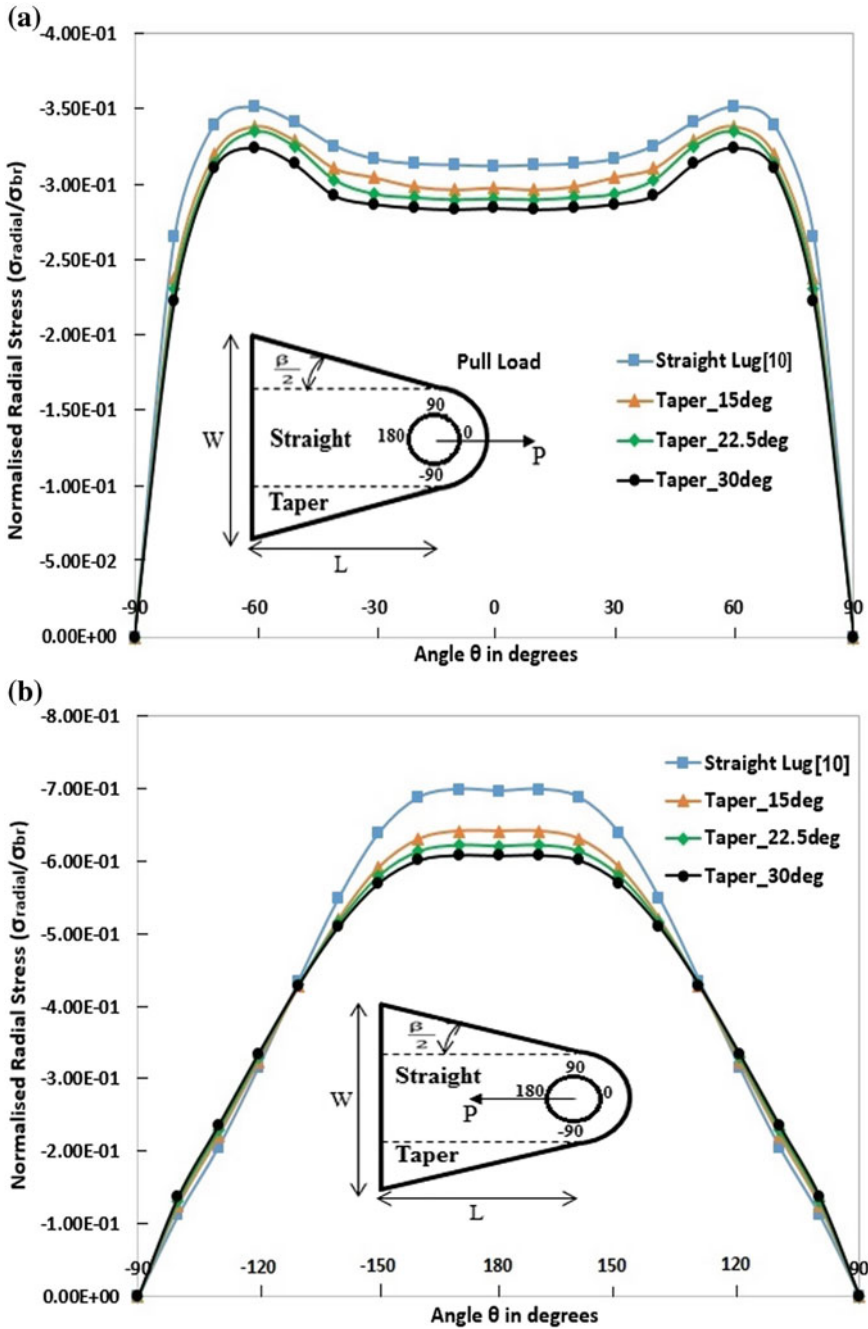


Fig. 10 **a** Radial stress distribution at the hole boundary for pull load, **b** radial stress distribution at the hole boundary push load

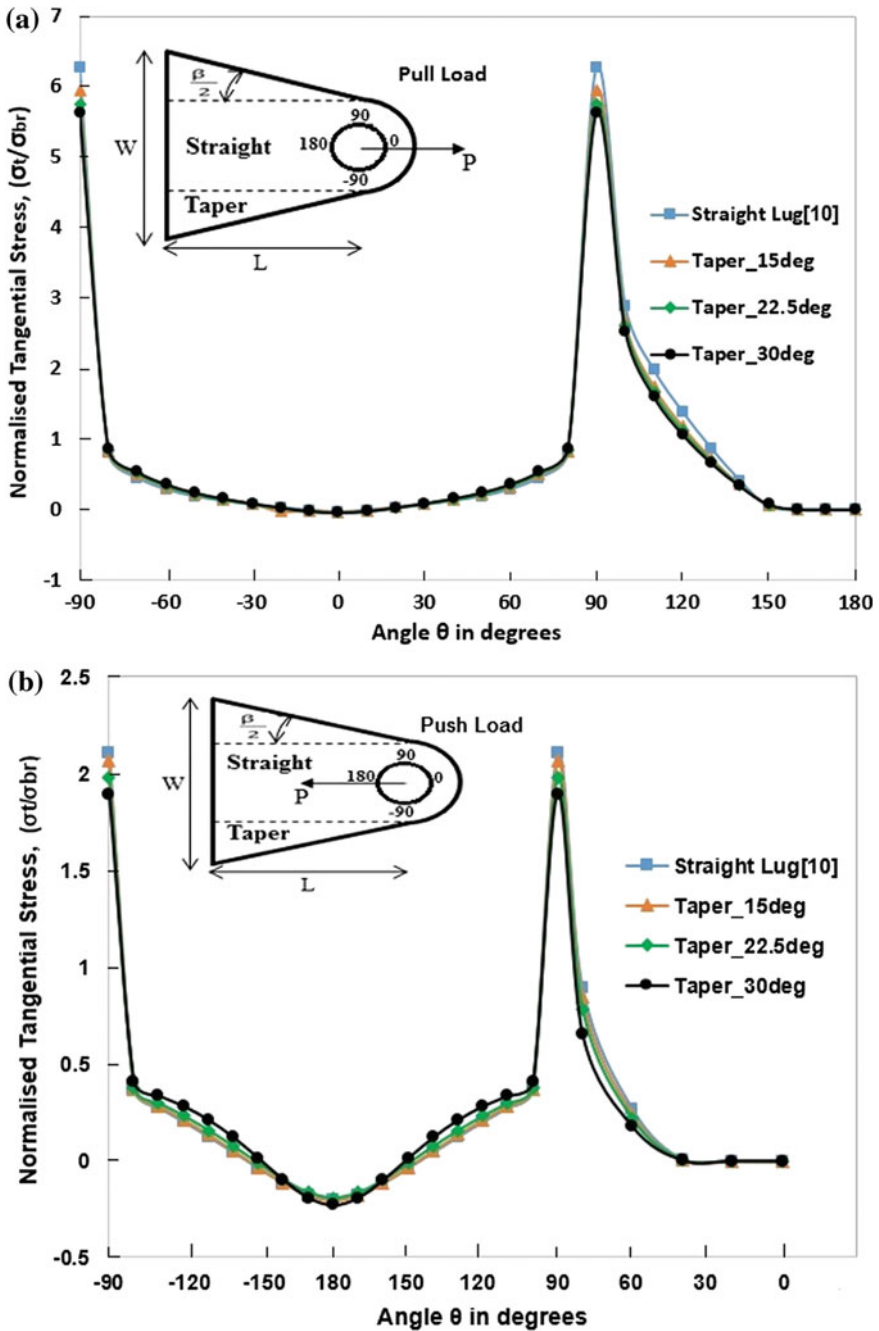


Fig. 11 a Tangential stresses around the hole boundary for pull load, b tangential stresses around the hole boundary for push load

distributions around the lug–hole interface (Fig. 11a, b). From these distributions, the maximum tensile tangential stress points are identified as the potential crack initiation and crack growth locations. Figure 12 shows load cycles for $R_p = 0$ and -1 . Respective local stress variation due to these load cycles at the maximum tensile stress locations are qualitatively shown in the figures. It is seen for both Pull and Push loadings, the tangential stress at the critical locations is tensile, but of a smaller magnitude for Push loads. It is observed that for $R_p = -1$, the local maximum tensile stress at the critical nodes is too small for the Push load in comparison with Pull load, and hence in case of $R_p = -1$, the contribution towards the fatigue failure is not significant. The crack initiation life is shown only for $R_p = 0$, and it is verified that it does not vary in a significant manner with the negative R_p ratios.

The lug configurations are analysed for varying P_{\max} with $R_p = 0$, and the results are compared for various taper angles. Initially, for lower loads, all the lugs possess very high life and damage is negligible. With the progressively increasing load P_{\max} , there is a drop in the fatigue life with increase in damage. Straight lug shows less fatigue life in comparison with tapered lugs. The life estimation is shown only for $R_p = 0$ in Fig. 13. It is seen that there is clear though not significantly large increase in fatigue crack initiation life with increase in taper angle.

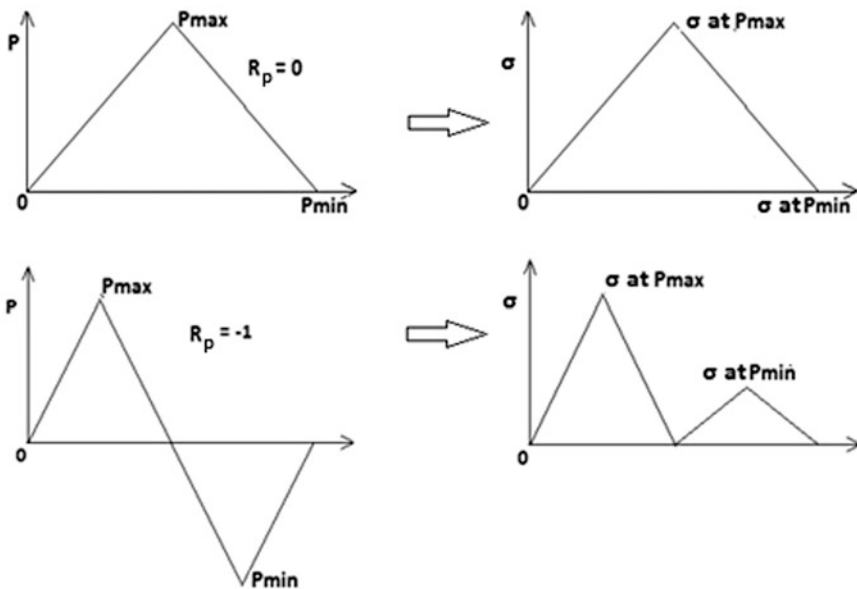


Fig. 12 Local stress variations due to applied fatigue load cycles [$R_p = P_{\min}/P_{\max}$]

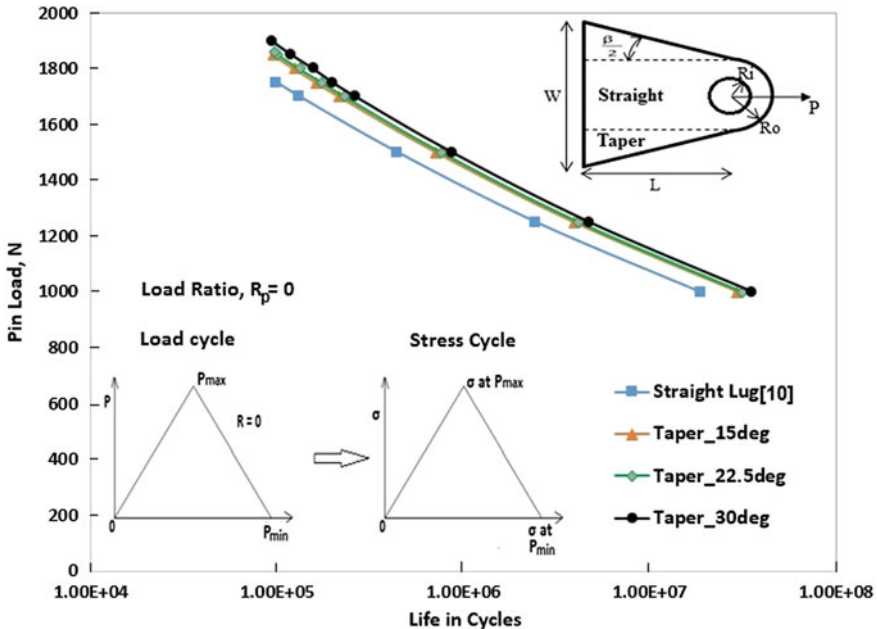


Fig. 13 Fatigue crack initiation life for load ratio $R = 0$

3.5 Crack Growth Analysis

The contribution of Push load to crack growth is negligible compared to Pull load. So the crack growth results are presented for the case of $R_p = 0$. The results are mainly directed to bring out the effect of taper angle which is the main parameter in the current paper. Initial crack length of 2 mm is assumed as mentioned earlier as the crack length which can be detected with 95% confidence level. The analysis is carried out for a fixed P_{max} and for the load cycle ($R_p = 0$). The critical crack length for unstable crack growth is plotted for different taper angles in Fig. 14, and the crack growth life is shown in Fig. 15. It is seen that critical crack length for straight lug is relatively small when compared with tapered lugs since the effect of stress intensity factor range (ΔK) decreases with taper angle. In Fig. 15, it is seen that straight lug has the least crack growth life, and the crack growth life increases with taper angle due to higher stress concentration factors in straight lug compared to tapered lugs.

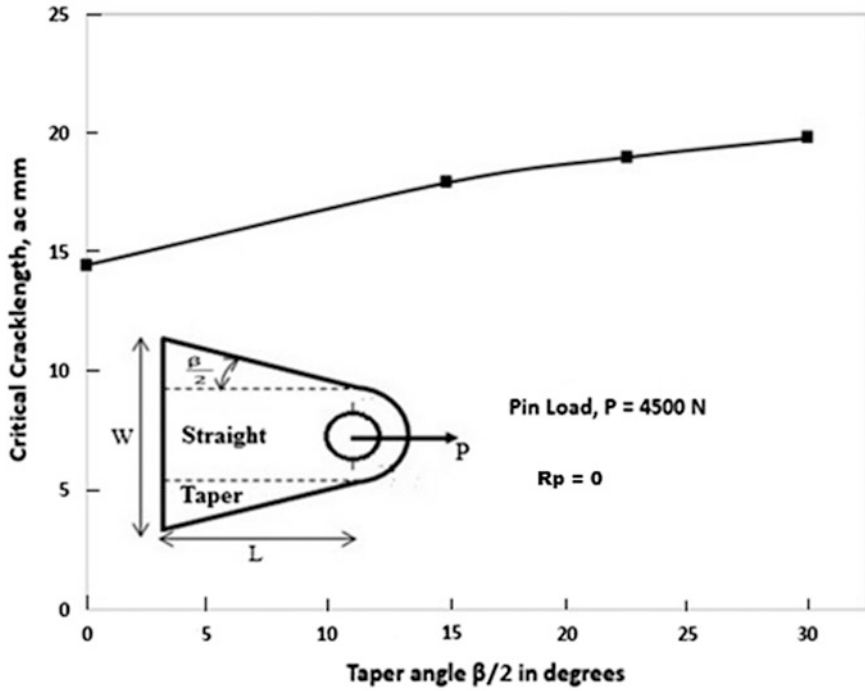


Fig. 14 Critical crack length for different taper angles of the lug

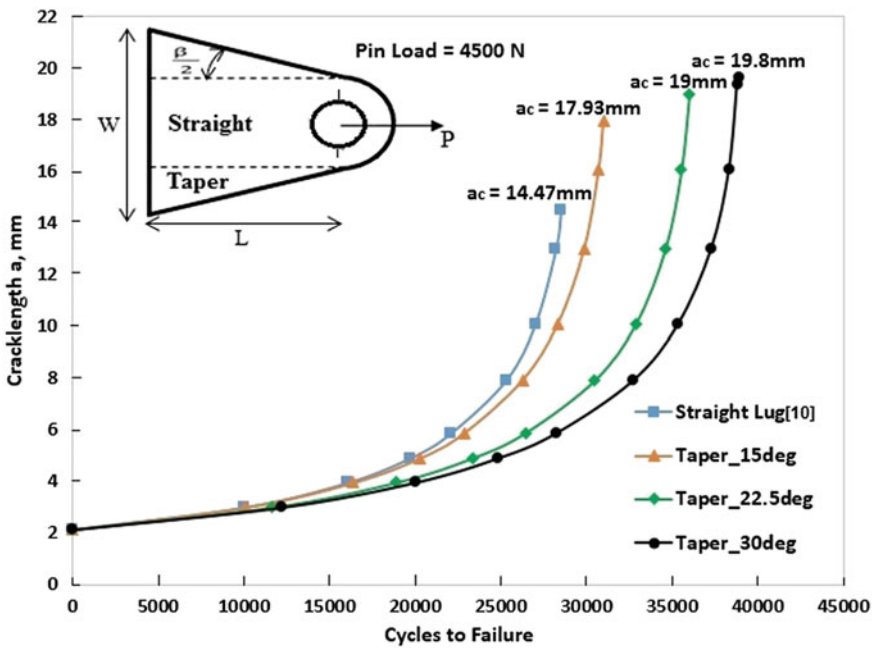


Fig. 15 Crack growth life

4 Conclusion

Lug joints play the key role in large-scale structural components which are used as primary load-carrying members. Health monitoring of these lug joints seeks major attention since their failure can be catastrophic. Tapered attachment lugs with rigid pin are analysed for the push fit case where in contact/separation region do not change with monotonically varying pin load. The major issue in the analysis is the loss of contact between the pin and the hole. During load reversals, the contact angles will change, and this has to be accounted in the analysis. Critical locations where maximum tensile tangential stresses occur are identified from finite element analysis.

The SCF with respect to bearing stress decreases in the case of both Pull loading and Push loading with (R_o/R_i). The fatigue crack initiation life and crack growth life are estimated from which one can derive the remaining life of the structure at any given instant during fatigue loading. The stress concentration around the lug decreases with taper angle. This results in tapered lugs with higher taper angle show that better crack initiation and crack growth life are achievable when compared with straight lugs.

Acknowledgements The work presented in this paper is carried out under the project Structural Damage Mitigation sanctioned by Aeronautical R&D Board. The investigators profusely thank the Structures Panel, Aeronautical R&D Board, India, for sanctioning the project.

References

1. M. Esperon-Miguez, P. John, I.K. Jennions, A review of integrated vehicle health management tools for legacy platforms: challenges and opportunities. *Int. J. Prog. Aerosp. Sci.* **56**, 19–34 (2013)
2. S. Gopalkrishnan, M. Ruzzene, S. Hanagud, *Computational techniques for structural health monitoring*. Springer, London (2011)
3. P.D. Mangalgiri, T.S. Ramamurthy, B. Dattaguru, A.K. Rao, Elastic analysis of pin joints in plates under some combined pin and plate loads. *Int. J. Mech. Sci.* **29**(2), 577–585 (1987)
4. W.G. Bickley, The distribution of stress round a circular hole in a plate. *Philos. Trans. R. Soc. Lond. Ser. A*, **227**(128), 383–415
5. H.G. Harris, I.U. Ojalvo, R.E. Hooson, Stress and deflection analysis of mechanically fastened joints. *AFFDL-TR-70-49* (1971)
6. A.K. Rao, Elastic analysis of pin joints. *Comput. Struct.* **9**, 125–144 (1978)
7. B. Dattaguru, Effect of non-linear behaviour of joints on the damage tolerance analysis in aerospace structures. *Proc. Indian Natl. Sci. Acad. (Special Issue—Part A)* **79**(6), 553–562 (2013)
8. K. Kathiresan, T.R. Brussat, J.L. Rudd, Damage tolerance assessment of aircraft attachment lugs. *J. Eng. Fract. Mech.* **23**(6), 1067–1084 (1986)
9. T.M. Hsu, Analysis of cracks at attachment lugs. *J. Aircraft* **18**(9), 755–760 (1981)
10. L. Chikmath, Prognostic analysis of fastener in lug joints. Ph.D. Thesis, Department of Aerospace Engineering, Jain University, Jakkasandra, 562112, India (2017)
11. The MSC NASTRAN Documentation. MSC Software Corporation, CA, USA (2005)

12. S. Suresh, *Fatigue of materials* (Cambridge University Press, UK, 1998)
13. T.L. Anderson, *Fracture mechanics: fundamentals and applications* (CRC Press, Taylor & Francis Group, Boca Raton, 2005)
14. W. Elber, The significance of fatigue crack closure. In: *Damage tolerance in aircraft structure*. ASTM STR **486**, 230–242 (1971)
15. E.F. Rybicki, M.F. Kanninen, A finite element calculation of stress intensity factors by a modified crack closure integral. *J. Eng. Fract. Mech.* **9**, 931–938 (1977)
16. T.S. Ramamurthy, T. Krishnamurthy, K. Badrinarayana, K. Vijaykumar, B. Dattaguru, Modified crack closure integral method with quarter point elements. *Mech. Res. Commun.* **13** (4), 179–186 (1986)
17. J. Haapalainen, E. Leskela, Probability of detection simulations for ultrasonic pulse-echo testing. In: *18th World Conference on Non-destructive Testing*, Durban, South Africa, pp. 16–20, Apr 2012
18. J. Gilbert Kaufman, *Properties of aluminum alloys—fatigue data and the effects of temperature-product form and processing*. ASM International Data Handbook (2008)

Experimental Study on Fatigue–Vibration Interactions of Cyclically Loaded FRP Composite Cantilever Beams Made of Glass/Carbon-Layered Arrangements

R. Murugan, R. Ramesh and K. Padmanabhan

Abstract Woven fabric-reinforced polymer composites are widely used in the structural applications like aircraft, automotive, marine and machine tool structures due to their excellent integrity, conformability and balanced mechanical properties within the fabric plane. It is observed that the structural members used in such applications experiencing vibration and considerable cyclic loading in operations are inevitable in dynamic conditions. Therefore, the study of the interaction of vibration characteristics of composite structures due to the fatigue loading needs much attention to meet the industrial requirements. In this study, the interaction of fatigue loading and vibration characteristics of epoxy-based glass/carbon hybrid beams was evaluated by measuring the variation in the modal stiffness. The two types of hybrid layer arrangements using glass and carbon woven fabrics, GCCG and CGGC, are preferred for the present investigation, by considering the balanced modulus property in longitudinal and transverse direction of the specimens. A displacement-controlled fully reversed flexural fatigue testing rig was designed and developed with required control circuits and test specimens to find the interaction of flexural fatigue loading on vibration characteristics of fibre-reinforced composite beams. The vibration characteristics and interaction of fatigue loading on vibration characteristics of thin-walled woven fabric glass/carbon hybrid composite beams made of different stacking sequences for promoting good dynamic stability were investigated.

Keywords Hybrid composite • Stacking sequence • Vibration characteristics
Interaction of fatigue loading on vibration characteristics

R. Murugan
Panimalar Institute of Technology, Poonamallee, Chennai 600123, India

R. Ramesh (✉)
Sri Venkateswara College of Engineering, Sriperumbudur 602117, India
e-mail: rameshraj@svce.ac.in

K. Padmanabhan
School of Mechanical and Building Sciences, VIT University, Vellore 632014, India

1 Introduction

Fibre-reinforced polymeric (FRP) composites are widely used in the structural applications like aircraft, automotive, marine and machine tool structures due to its high strength/stiffness-to-weight ratio. The recent fabrication of structures in polymer composites contains reinforcing fibres in the form of fabrics and properly formulated polymeric matrices. In woven fabrics, the fibre rovings are interlaced with two mutually orthogonal directions to one another which promote excellent integrity and conformability and balanced mechanical properties within the fabric plane. Due to these advantages, woven fabric composites become popular and widely used in all such mentioned applications. It is also observed that the structural members used in such applications experiencing vibration and considerable cyclic loading in operations are inevitable in dynamic conditions. Therefore, it is very important to understand and evaluate the influence of cyclic loading on vibration characteristics in terms of improving its dynamic stability of composite structures.

The anisotropic nature of FRP material makes the evaluation of its fatigue behaviour more complicated. This heterogeneous and anisotropic nature of FRP leads to the formation of different stress levels within the material during cyclic loading and thereby forms the various combinations of damage modes such as matrix cracking, fibre breakage, delamination, debonding and ply failure [1]. It is commonly accepted that FRP degradation of performance during cyclic loading is associated with a reduction in the composite material stiffness [2]. Research on fatigue of composite materials is conducted earlier by performing tension–tension fatigue and tension–compression fatigue, since damage is developing more or less equally in all layers of the composite specimen.

Very few authors only reported the bending fatigue experiments. Weber and Schwartz [3] monitored the bending fatigue behaviour of unidirectional carbon/epoxy composite strands using the changes in resistivity and in bending modulus [3]. Van Paeppegem and Degrieck [4] investigated the fatigue performance of plain woven glass/epoxy composite specimens with two different configurations such as $[\#0^\circ]_8$ and $[\#45^\circ]_8$. They showed that the two specimen types, although being made of the same material, have quite different damage behaviour and that the stiffness degradation follows a different path [4]. Belingardi et al. [5] performed displacement-controlled bending fatigue tests with stress ratio of $R = 0.1$ up to 1 million cycles on a carbon–glass hybrid composite beams. It was found that the amount of stiffness reduction was a function of the magnitude of applied fatigue loading on the specimen [5]. Lian and Yao [6] experimentally studied the fatigue behaviour of six kinds of E-glass/epoxy composite laminates with different lay-up sequences and obtained the stiffness degradation models in longitudinal, transverse and in-plane shear direction [6].

Most of the earlier investigations have been concerned with damage-induced changes in stiffness as found from observed variations in resonant frequencies of composite specimens. Little work was done in continuously monitoring the variation in stiffness as a function of the number of cycles to failure. The main objective



of the present work is to investigate the vibration characteristics and the interaction of fatigue and vibration characteristics on thin-walled woven fabric glass/carbon hybrid composite beams used for automotive and aircraft structural applications.

2 Fabrication of Hybrid Composite Specimen

The hybrid composite specimens were fabricated using hand lay-up method. E-Glass and T300 carbon fibres in plain woven fabric form with areal density of 600 g/m^2 were used as reinforcement. Thermoset resin of grade LY556 was preferred as matrix. A uniform volume fraction of $V_f = 0.5$ was controlled for the two types of hybrid laminates. The casting was cured for 24 h in a compression moulding machine with a nominal pressure of 2.5 MPa at room temperature. After curing, the hybrid laminates were cut into beam of size $250 \times 25 \times 2.4 \text{ mm}$.

Two different layer sequences H1 and H2 as shown in Table 1 were preferred in fabricating hybrid laminates. In hybrid layer arrangement, H1, the two inner layers are preferred as carbon fabrics and two outer layers as glass fabrics. For H2 hybrid arrangement, the layering control was done by placing two carbon fabrics in outer layers and two glass fabrics in inner layers. The layer arrangement of hybrid laminate was selected in consideration of balanced modulus property along the longitudinal and transverse direction with respect to neutral axis of the plate. Figure 1 shows the fabricated four-layered woven fabric hybrid composite beams made up of glass and carbon fabrics. Table 1 shows the dimensions and symbols used for the hybrid composite specimens considered.

Table 1 Symbol used and its corresponding layer arrangement of glass/carbon hybrid composite beams

Symbol	Specimen description	Layer sequence	Dimensions ($l * w * t$) (mm)
H1	Four-layered hybrid laminate Outer—glass and inner—carbon	 GCCG	250 * 25 * 2.4
H2	Four-layered hybrid beam Outer—carbon and inner—glass	 CGGC	250 * 25 * 2.4

l —length; w —width; t —thickness



Fig. 1 Image showing the two types of woven fabric glass/carbon hybrid composite beams fabricated by hand lay-up technique

3 Experimental Conditions

3.1 Static Deflection and Flexural Test

For measuring the static deflection, the beam specimen is fixed firmly by using clamping device on the work table. The standard weights are applied at the free end in different magnitude levels. This experimental arrangement is used to find the optimum span length for fatigue study of the hybrid samples and also to measure the loss of stiffness of the hybrid beams subjected to fatigue load.

Flexural test was performed as per ASTM D790 for all samples with a recommended span-to-depth ratio of 16:1 [7]. The size of the specimen is 127 mm \times 12.5 mm \times 2.4 mm. The flexural test was conducted on closed-loop servo-hydraulic universal testing machine INSTRON 3382 with feed rate of 1.2 mm/min at room temperature. Five specimens were tested for each type of laminate, and the average value was calculated.

3.2 Impulse Response Test

The vibration characteristics of the hybrid composite beams measured using impulse excitation technique [8]. Figure 2 shows the arrangement and equipment involved in conducting the vibration test. For conducting the vibration test, one end

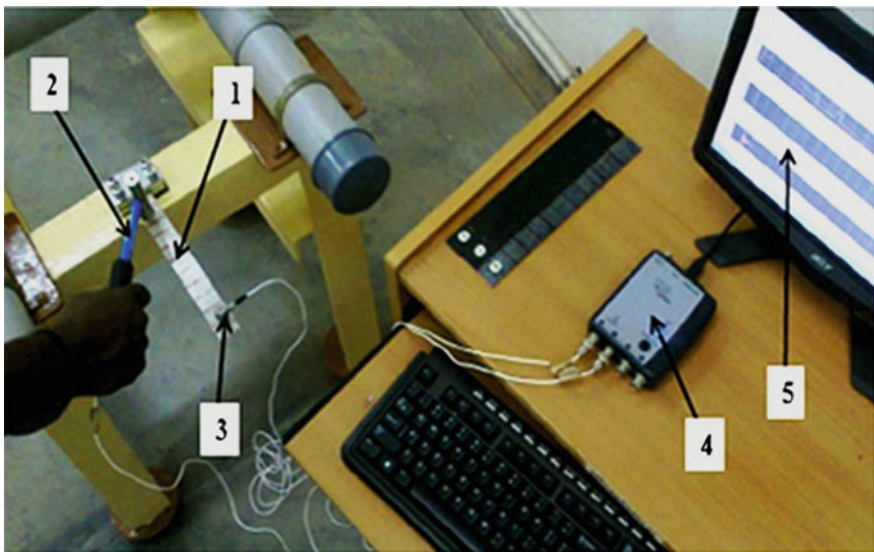


Fig. 2 Photograph showing experimental test set-up for vibration measurement (1) composite specimen (2) impact hammer (B&K Type 5800B4) (3) accelerometer (B&K Type 3055B2) (4) data acquisition card (B&K Type Photon+) (5) PC with RT Pro Software showing FRF

of the specimen is rigidly fixed by work clamping device and the other end was left as free end for offering fixed-free boundary condition. A beam length of 136 mm was set as suspended length for impulse testing. An instrumented impact hammer (B&K Type 5800B4) with a load cell was used to excite induce the excitation of flexural vibrations of the beam. The response of the structure was measured using an accelerometer (B&K Type 3055B2) at the free end of the beam as shown in Fig. 2. The signals of the impact hammer and the accelerometer were amplified and digitised through a high-speed data acquisition board (B&K Type Photon+) and finally processed using FFT software (RT Pro Photon+), to obtain frequency response functions (FRFs) of the tested component. The measured FRFs were used to extract the modal frequency values of each vibration mode.

3.3 Imposing Reversed Cyclic Bending

The experimental set-up developed specially for flexural fatigue tests on cantilever beam specimens is shown in Fig. 3. The outcoming shaft of the motor has a rotational speed of 1440 rpm. The power is transmitted by a single-stage gearbox to a second shaft, which provides a fatigue testing frequency of 10 Hz. The influence of frequency on fatigue loading can be assumed to be small in this range of values [8]. To investigate the effect of fatigue load on vibration characteristics of the two different stiffness samples, H1 and H2, an optimum span length of the composite specimens was arrived as 136 mm by conducting static deflection test. In the present investigation, stress-controlled fatigue test is preferred to compare the effect

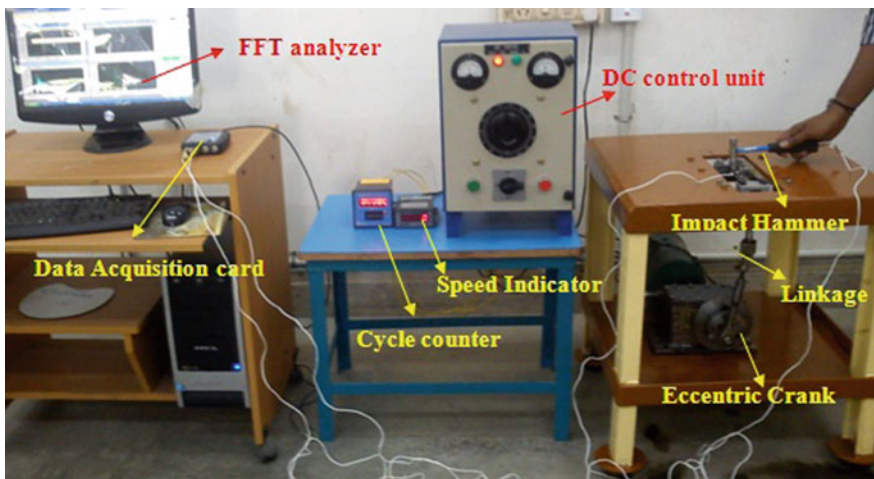


Fig. 3 Experimental test set-up for applying completely reversed bending fatigue load on hybrid composite specimen

Table 2 Experimentally evaluated flexural properties of woven fabric laminates [9]

Specimen	Flexural strength (MPa)	Flexural modulus (GPa)	Area MOI (mm ⁴)	Flexural rigidity (N mm ²) × 10 ⁶
H1	491	21.23	28.8	0.62
H2	507	42.08	28.8	1.23

of fatigue load on vibration characteristics of the hybrid beams with two different stacking sequences H1 and H2. Since the flexural strength of two hybrid beams is approximately equal to 500 ± 10 MPa, 20% of flexural strength of hybrid beams, i.e. 100 MPa, is taken as the limiting stress for stress-controlled fatigue test. However, the flexural modulus values are different for the hybrid beams H1 and H2 as shown in Table 2; to achieve the reference stress range for the two hybrid beams, deflections of the beam set in the test rig need to be controlled properly. Deflections for the two hybrid beams are theoretically calculated by using the standard beam deflection formula and bending equation. The experimental test conditions for fatigue loading are as follows:

Test specimen type	H1 (GCCG) and H2 (CGGC)
Free length, L	136 mm
Test frequency, f	10 Hz
Induced deflection, δ	± 17 mm for H1 and ± 12 mm for H2
Induced bending stress, σ_b	-100 to +100 MPa
Stress ratio, $R = \sigma_{\max}/\sigma_{\min}$	-1

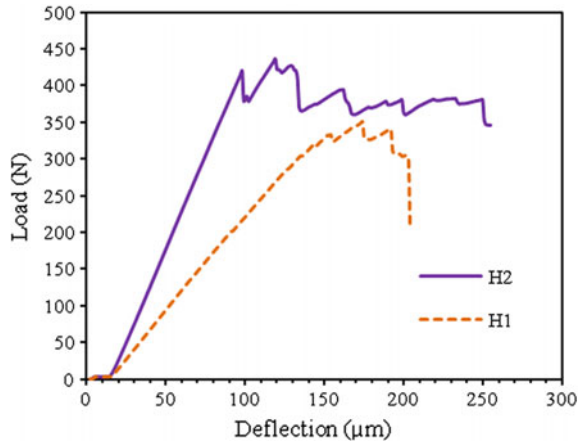
In this experiment, the vibration characteristics were measured after every 5,000 cycles up to a limited number of 200,000 cycles. The modal frequency values were measured experimentally by impulse excitation technique for all 5,000 cycles and tabulated.

4 Results and Discussion

4.1 Flexural Properties of Hybrid Composite Laminates

The experimental flexural properties of hybrid samples are reported in Table 2 based on the earlier investigation by Murugan et al. [9]. Figure 4 shows the load–deflection curves of hybrid composite laminates obtained by flexural test. Flexural modulus (E_b) and flexural rigidity ($E_b I$) were evaluated for the tested laminates and reported in Table 2. The variation in the flexural rigidity of hybrid laminates confirms that the stacking sequence controls the flexural rigidity. In case of hybrid

Fig. 4 Load–deflection curves of hybrid composite laminates obtained from flexural test



laminates, the layer arrangement H2 offered a noticeable increase in flexural modulus as compared to the other arrangement H1. The load–deflection characteristic curves of H1 and H2 samples tested confirm its variation in performance. In transverse bending, the flexural modulus of outer layer of composite beam plays an important role [10]. Hybrid laminate with carbon fibre plied as external layer (H2) offers high resistance against bending.

4.2 Analysis of Static Deflection

Loss of stiffness due to fatigue loading of the hybrid beams, H1 and H2, was measured by static deflection test set-up. Deflection of the hybrid beam at free end for common load of 0.5 kg was measured before and after subjected to 2×10^5 cycles of fatigue load. Table 3 shows the corresponding deflection values and calculated beam stiffness values. The percentage loss of stiffness evaluated from experimental deflection after 2×10^5 cycles found to be 76.03% for H1 beam and 45.14% for H2 beam. Table 3 reveals that loss of stiffness of hybrid beam H1 is nearly twice that of hybrid beam H2. It reveals the improved dynamic stability of hybrid beam H2 over the other hybrid arrangement H1.

Table 3 Stiffness degradation evaluated and compared at known 0.5 kgf load level

Specimen	Measured deflection at 0.5 kgf load (mm)		Stiffness performance at 0.5 kgf load (N/mm)		Stiffness degradation (in %)
	At 0 cycle	After 2×10^5 cycle	At 0 cycle	After 2×10^5 cycle	
H1	3.88	16.2	1.264	0.303	76.03
H2	2.94	5.36	1.668	0.915	45.14

4.3 Evaluating the Modal Stiffness of Hybrid Composite Beams Subjected to Limited Fatigue Loading

Figure 5 shows the comparison of frequency response plots of hybrid beams, H1 and H2, evaluated at various interval of fatigue loading. It reveals that the vibration response of hybrid beams changed due to fatigue loading and lowers the modal frequency values. Frequency response function plots of both beams were shifted towards left due to fatigue load which indicates the fall in vibration response of hybrid beams tested. Table 4 shows the variation of vibration characteristics such as modal frequency of hybrid beams H1 and H2 for first three modes arrived from experimentally recorded FRF function for all 5,000 cycles of fatigue loading. The frequency at which the resonant set attained for hybrid beam H2 shows higher range than other beam H1 for all levels of fatigue loading. It reveals that the stacking sequence of glass and carbon fabric layers influences appreciably its vibration characteristics during fatigue loading. Figure 6 shows the modal stiffness decay in

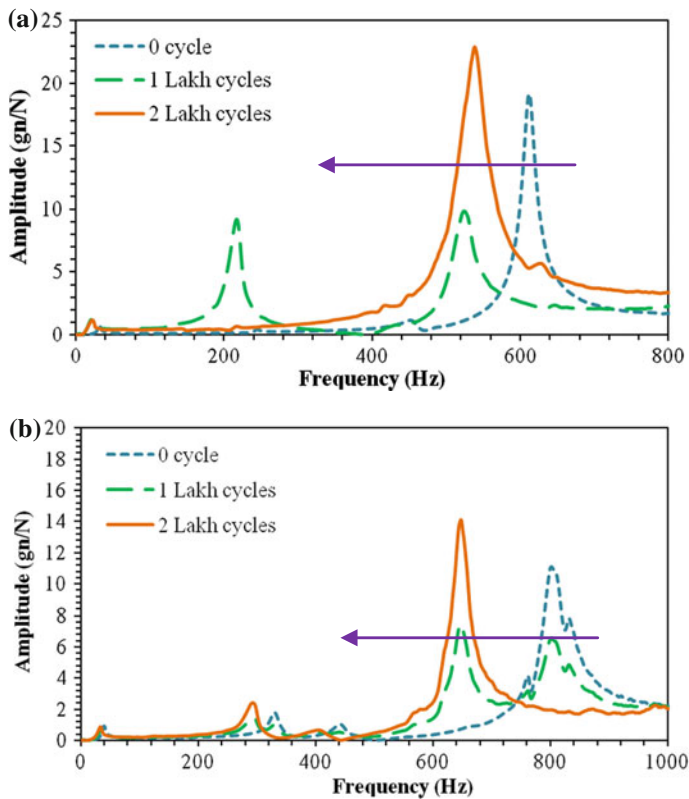


Fig. 5 Comparison of FRF plots of hybrid beams obtained at 0 cycles, after 1×10^5 cycles and 2×10^5 cycles of fatigue loading **a** FRF plots of H1 beam **b** FRF plots of H2 beam

Table 4 Variation of modal frequency values at successive modes of H1 and H2 hybrid beams subjected to a limited fatigue cycling of 2×10^5 cycles

No. of cycles ($\times 10^5$)	Mode 1		Mode 2		Mode 3	
	Frequency (Hz)		Frequency (Hz)		Frequency (Hz)	
	H1	H2	H1	H2	H1	H2
0.0	33.9	46.9	302.5	386.8	858.5	962.4
0.5	23.9	45.4	265.0	383.5	632.5	888.8
1.0	22.5	43.1	266.3	366.2	648.5	823.2
1.5	22.5	38.1	255.0	342.9	620.0	805.7
2.0	20.0	36.6	248.5	339.8	698.5	883.8

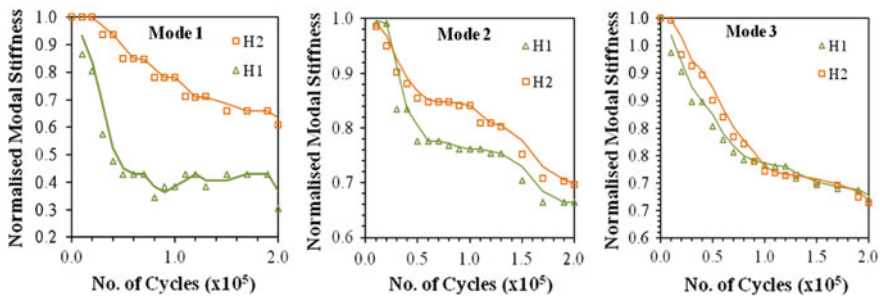


Fig. 6 Comparison of experimental modal stiffness decay curves at successive modes of hybrid beams H1 and H2 during fatigue loading

woven fabric hybrid composite beams, H1 and H2, due to limited fatigue loading. A rapid drop in modal stiffness was observed at the beginning stage of the fatigue loading for both the hybrid beams and followed by a region of gradual reduction region.

The bending stiffness of composite structures decreased steadily with increasing number of fatigue cycles because of diminishing elastic properties of the constituent materials during fatigue [11, 12]. The percentage loss of stiffness evaluated from experimental static deflection test of hybrid beams after limited fatigue loading in Sect. 4.2 also confirms this attribute. The degree of degradation of modal stiffness of H1 specimen during cyclic loading in all successive modes was higher than the other hybrid layer arrangement H2. In the H1 specimens, several fibres are broken at the clamped end of the specimen and a sort of ‘hinge’ is formed [13]. On the other hand, the damage level at the clamp end of H2 specimen is not observed to be as severe as the H1 specimen. High flexural strength and stiffness of the hybrid layer arrangement H2 (Table 3) offer more resistance against the flexural bending than the other layer arrangement H1. In this study, effect of fatigue loading on the free vibration characteristics of hybrid beams was both understood and evaluated in terms of the modal stiffness decay. It was found that the change in vibration

characteristics of composite specimens could be considered as an indication of variation in the strength and stiffness of the composite beams due to fatigue loading.

4.4 SEM Observation and Analysis of Damage Over Glass/Carbon Hybrid Beams After Subjected to Limited Fatigue Load

A scanning electron microscopy (SEM) analysis was performed on samples from tested specimens under completely reversed bending fatigue loading. Figure 7 shows the closer view of fractured surfaces obtained from optical microscopy at the fixed end after the fatigue tests of the hybrid beams H1 and H2, respectively. From these macroimages of failed surfaces, it is revealed that damage during bending fatigue is immense at the fixed end due to the occurrence of high bending stresses. The samples were obtained from this fixed end of the hybrid composite beams H1 and H2 for SEM analysis. SEM images of failed surfaces are shown in Fig. 8. Earlier investigation by Dew-Hughes and Way [14] revealed that the possible stages of fatigue damage in FRP materials are local debonding, joining up of debonds, matrix cracking and fibre fracture where debonding is considered as the main criterion for failure [14].

Figure 8a, b show SEM images of surface damage induced at the fixed end of hybrid beam H1 due to limited cycles of fatigue loading. During fatigue loading, first fibre breakage occurs at stresses exceeding the strength of the weakest fibre. An isolated fibre breakage causes shear stress concentration at the interface around the tip of the broken fibre. The interface may then fail, leading to debonding of the fibre from the surrounding matrix. Figure 8a shows the fibre–matrix debonding, severe delamination of the matrix and more numbers of longitudinal fibre breakages near

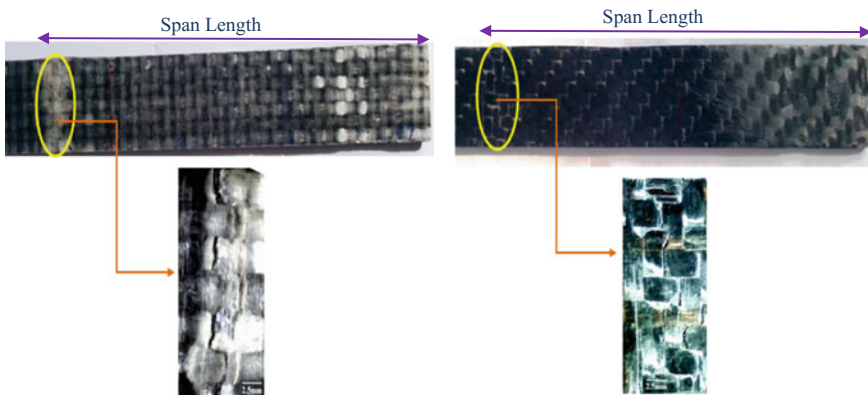


Fig. 7 Macroimages showing failure surfaces of hybrid beams H1 and H2 at the fixed end after limited fatigue load

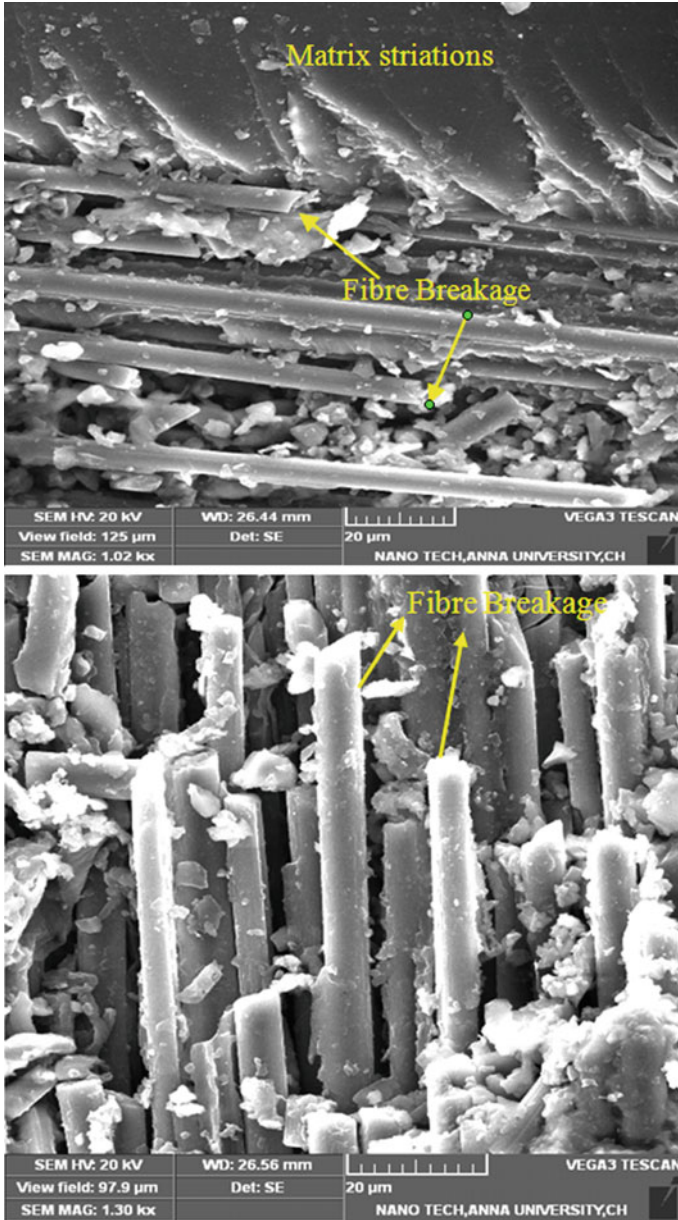


Fig. 8 SEM images of the fractured surfaces of hybrid composite laminate H1 after 2×10^5 cycles of flexural fatigue loading

the fixed end of hybrid beam H1. Figure 8b reveals the transverse fibre breakage of H1 specimen and transverse matrix striations in agreement with fatigue loading. The presence of high strength carbon fibres at the surface of H2 beam promotes the fibre breakage and crack propagation predominantly through the epoxy matrix. SEM images of the fatigue-damaged surfaces of hybrid composite beams revealed that hybrid sample H1 (GCCG) had relatively severe fibre breakages than H2 (CGGC) samples. The microstructural damages such as matrix cracking, fibre breakage and fibre–matrix debonding formed during fatigue loading caused the degradation of modal stiffness in the initial stage. SEM analysis of failed surfaces of hybrid beams H1 and H2 confirms the presence of all types of damages due to fatigue loading. Earlier research on fatigue behaviour of FRP composites by Manjunatha et al. [15], Wicaksono and Chai [16] and Sudevan et al. [17] showed a similar trend for the stiffness decay curve [15–17].

5 Conclusions

Completely reversed bending fatigue experiments were successfully conducted to understand the interaction between fatigue and vibration of the hybrid beams H1 and H2. The modal stiffness of both hybrid composite beams decreases with increasing number of fatigue cycles. Comparative results showed that the degree of degradation of modal stiffness in H1 beam is higher than the other arrangement H2. The stiffness loss evaluated by experimental static deflection test for fatigue imposed hybrid beam also confirms the appreciable difference in stiffness degradation. The morphology study clearly revealed that the localised variation in damage intensity among the two different stacking sequences caused the difference in vibration performance. Evaluation of free vibration characteristics of hybrid beams before and after fatigue damage shows that the carbon fabric plied as outermost layers offered enhanced dynamic stability than the outer layers replaced by low modulus glass fabric (GCCG). The obtained fundamental layering sequence, CGGC, is effective and beneficial for structural applications and should be extended by this plying form condition to meet out the designed dimension.

References

1. P.K. Mallick, *Fibre Reinforced Composites, Materials and Manufacturing and Design*. CRC Press, Taylor & Francis Group (2008)
2. Raif Sakin, Irfan Ay, Ramazan Yaman, An investigation of bending fatigue behavior for glass-fiber reinforced polyester composite materials. *Mater. Des.* **29**, 212–217 (2008)
3. Ingo Weber, Peter Schwartz, Monitoring bending fatigue in carbon-fiber/epoxy composite strands: a comparison between mechanical and resistance techniques. *Compos. Sci. Technol.* **61**, 849–853 (2001)

4. W. Van Paepegem, J. Degrieck, Experimental set-up for and numerical modelling of bending fatigue experiments on plain woven glass/epoxy composites. *Compos. Struct.* **51**, 1–8 (2001)
5. G. Belingardi, M.P. Cavatorta, C. Frasca, Bending fatigue behavior of glass–carbon/epoxy hybrid composites. *Compos. Sci. Technol.* **66**, 222–232 (2006)
6. Wei Lian, Weixing Yao, Fatigue life prediction of composite laminates by FEA simulation method. *Int. J. Fatigue* **32**, 123–133 (2010)
7. ASTM Standard D790-10, *Standard Test Method for Flexural Properties of Unreinforced and Electrical Insulating Materials*. ASTM International, West Conshohocken, PA (2003)
8. D.J. Ewins, *Modal Testing: Theory, Practice and Application*. Research Studies Press, Hertfordshire (2000)
9. R. Murugan, R. Ramesh, K. Padmanabhan, Investigation of the mechanical behavior and vibration characteristics of thin walled glass/carbon hybrid composite beams under a fixed-free boundary condition. *Mech. Adv. Mater. Struct.* **23**(8), 909–916 (2016)
10. K.S. Pandya, C. Veerajay, N.K. Naik, Hybrid composite made of carbon and glass woven fabric under quasi-static loading. *Mat. Design* **32**, 4094–4099 (2011)
11. S. Mahdi, A.J. Kinloch, F.L. Matthews, M.A. Crisfield, Fatigue performance of undamaged and repaired composite sandwich beams. *Proc. Inst. Mech. Eng. Part L: J. Mater. Design Appl.* **217**, 229–246 (2003)
12. A. El Mahi, A. Bezazi, Describing the flexural behaviour of cross-ply laminates under cyclic fatigue. *Appl. Compos. Mater.* **16**, 33–53 (2009)
13. W. Van Paepegem, I. De Baere, E. Lamkanfi, J. Degrieck, Monitoring quasi-static and cyclic fatigue damage in fibre-reinforced plastics by Poisson’s ratio evolution. *Int. J. Fatigue* **32**, 184–196 (2010)
14. D. Dew Hughes, J.L. Way, Fatigue of fibre—reinforced plastics: a review. *Composites* **4**(4), 167–173 (1973)
15. C.M. Manjunatha, Taylor A.C. Sprenger, A.J. Kinloch, The tensile fatigue behaviour of a glass fibre reinforced plastic composite using a hybrid toughened epoxy matrix. *J. Compos. Mater.* **44**(17), 2095–2109 (2010)
16. S. Wicaksono, G.B. Chai, A review of advances in fatigue and life prediction of fibre-reinforced composites. *J. Mater. Design Appl.* **227**(3), 179–195 (2012)
17. Deepika Sudevan, Raghu V. Prakash, M. Kamaraj, Post-impact fatigue response of CFRP laminates under constant amplitude and programmed FALSTAFF spectrum loading. *Procedia Eng.* **101**, 395–403 (2015)

Investigation of Cyclic Stress–Strain Behavior in FCC Single Crystals

Nipal Deka and Krishna N. Jonnalagadda

Abstract The plastic behavior in polycrystalline materials depends on the deformation of individual grains or single crystals. In this work, cyclic stress–strain behavior was studied in single crystal FCC material to understand the effect of strain localization. Numerical studies were accomplished utilizing crystal plasticity finite element method (CPFEM) on a single crystal with a notch. Under, two types of localization modes, namely growth of extrusion–intrusion bands and the strain accumulation in shear localized regions near the crack tip, are commonly noticed. The process of continuous strain accumulation in one certain direction is often termed as strain ratcheting. Importantly, this particular behavior is generally counted as one of the major causes of fatigue damage and also considered as very vital in understanding the fatigue crack nucleation and its propagation. In the current work, the strain ratcheting behavior of FCC single crystals with a notch subjected to cyclic loads was studied using CPFE methodology with suitable incorporation of nonlinear kinematic hardening law.

Keywords Cyclic loading · *T*-stress · FCC single crystal · CPFE

Nomenclature

$\dot{\gamma}_0$	Reference shear rate
τ^α	Resolved shear stress of the slip system α
χ^α	Back stress for the slip system α
g^α	Critical resolved shear stress
m	Rate sensitivity parameter
$h_{\alpha\beta}$	Hardening matrix
h_0	Initial hardening rate
h_s	Saturation hardening rate
τ_0	Initial strength of the slip system

N. Deka (✉) · K. N. Jonnalagadda
Department of Mechanical Engineering, Indian Institute of Technology Bombay,
Mumbai 400076, India
e-mail: nipal_deka@iitb.ac.in

τ_s	Saturation strength of the slip system
E	Young's modulus
ν	Poisson's ratio
K_1	Stress intensity factor
T	T -stress
$\log(\lambda_1^p)$	Maximum principal logarithmic plastic strain

1 Introduction

Metals are most extensively used in many engineering applications such as aerospace structures, automobile components, nuclear reactors, and micro-electromechanical systems. At the microscopic level, all these metals consist of crystals, which are mechanically anisotropic. Constitutive behavior at the scale of the microstructure plays a significant role in many important phenomena including fatigue failure, fracture. It is also well acknowledged that factors like single crystal behavior and distribution of grain orientation control the local stress–strain field [1]. While the first one controls the microscopic stress–strain response, second one controls the macroscopic response of metals. It is well understood that under fatigue loading microscopic deformation results in the nucleation and growth of cracks. At the microscale level, crack growth occurs through grains or along grain boundary in more commonly employed polycrystalline materials. The fracture behavior in polycrystalline materials is governed by the stress and plastic strain fields existing near a stationary crack tip in elastic–plastic solid [2]. And if the crack opening displacement is far smaller than the size of the grain, the process zones are limited within a single grain [2]. The need to understand the fracture mechanisms in polycrystalline materials under fatigue loading also requires the study of plastic deformation around the crack tip in a single crystal. An enhanced outlook of the deformation and stress fields near the crack in a single crystal would certainly assist the appreciation and forecast of the fracture of those materials under fatigue loading. Therefore, the study of consequences of local stress–strain field on phenomena like fatigue and fracture in the context of single crystal is very essential so as to forecast the overall behavior of the polycrystal. Beyond nucleation, the growth of fatigue cracks is also affected by the stress state near the crack tip. In order to understand the effect of constraint on the crack tip fields, mode I finite deformation elastoplastic simulations need to be conducted.

Generally, two types of events namely the growth of extrusion–intrusion bands [3] and the strain accumulation in shear localized regions near the crack tip [4] are commonly noticed under cyclic loading. The process of continuous strain accumulation in one certain direction is often termed as “strain ratcheting” [3]. Most importantly, this particular behavior is generally accounted as the major cause of fatigue damage and considered as very vital in understanding the fatigue crack

nucleation and its propagation. In the current work, cyclic stress–strain behavior for aluminum single crystal under zero-tension cyclic load was studied with crystal plasticity finite element (CPFE) framework with suitable incorporation of nonlinear kinematic hardening rule. By including the T -stress in the modified boundary layer simulation, the effect of constraint on the development of stress and strain fields under cyclic load was analyzed.

2 Crystal Plasticity Model

The computational advantages of crystal plasticity finite element (CPFE) models to solve crystal plasticity problems under complex loading conditions and deformation mechanisms have developed CPFE as one of the most versatile tools. The flexibility to incorporate a variety of constitutive formulations for plastic flow and hardening enables CPFE to capture small-scale deformation mechanisms like slip, twinning, in simulation.

2.1 Constitutive Model

The cyclic evolution of back stress component was modeled implementing the flow rule as [5],

$$\dot{\gamma}^\alpha = \dot{\gamma}_0 \left| \frac{\tau^\alpha - \chi^\alpha}{g^\alpha} \right|^{1/m} \text{sign}(\tau^\alpha - \chi^\alpha) \quad (1)$$

where τ^α was resolved shear stress of the slip system α , χ^α represented the back stress component of the slip system α , and initial value of it was chosen to be zero. The term $\dot{\gamma}_0$ was the reference shear rate. The exponent m was the rate sensitivity parameter. The value of m tending to zero reduced the model to be rate independent and g^α could be interpreted as critical resolved shear stress.

Rate of hardening of slip system will depend upon shear rate on slip systems, which was given as follows:

$$\dot{g}^\alpha = \sum_{\beta=1}^{12} h_{\alpha\beta} |\dot{\gamma}^\beta| \quad (2)$$

The term $h_{\alpha\beta}$ was the hardening matrix. The diagonal terms of this matrix signified self-hardening while non-diagonal terms signified latent hardening. Thus, hardening matrix captured the interaction between different slip systems.

PAN model [6] was used to define isotropic hardening which was implemented as follows:

$$h_{\alpha\beta} = h(\gamma)[q + (1 - q)\delta_{\alpha\beta}] \quad (3)$$

where $h(\gamma)$ takes the form given by [6],

$$h(\gamma) = h_s + (h_0 - h_s)\operatorname{sech}^2\left[\frac{(h_0 - h_s)\gamma}{\tau_s - \tau_0}\right] \quad (4)$$

with γ was the total slip accumulated on all the active slip systems and q was the latent hardening ratio. The initial and the saturation hardening rates were represented by material parameters h_0 and h_s , respectively. τ_0 and τ_s represented the initial and saturation strength of the slip system, respectively.

The evolution of back stress on each slip system, χ^α , was modeled according to the nonlinear kinematic hardening rule [5],

$$\dot{\chi}^\alpha = C_{\text{rate}}(C_{\text{sat}}\dot{\gamma}^\alpha - \chi^\alpha|\dot{\gamma}^\alpha|) \text{ no sum on } \alpha \quad (5)$$

where the rate of growth and the saturation of the back stress were controlled by C_{rate} and C_{sat} , separately.

2.2 Numerical Simulation Using CPFEs

A large circular disk along with a notch is modeled considering a very large value of the ratio of the radius of the disk to the notch diameter, $\frac{R_0}{b_0}$ such as 70,000 with notch diameter, $b_0 = 1$ unit [2]. The displacement components based on the elastic mode I, plane strain crack tip field [7] are applied on the outer boundary of the circular disk which are functions of stress intensity factor, K_I and T -stress, are given by,

$$u_1 = \left(\frac{R_0}{2\pi}\right)^{\frac{1}{2}} \left(\frac{1+\nu}{E}\right) K_I \cos \frac{\theta}{2} \left(\kappa - 1 + 2 \sin^2 \frac{\theta}{2}\right) + \left(\frac{1-\nu^2}{E}\right) TR_0 \cos \theta \quad (6)$$

$$u_2 = \left(\frac{R_0}{2\pi}\right)^{\frac{1}{2}} \left(\frac{1+\nu}{E}\right) K_I \sin \frac{\theta}{2} \left(\kappa + 1 - 2 \cos^2 \frac{\theta}{2}\right) - \frac{\nu(1+\nu)}{E} TR_0 \sin \theta \quad (7)$$

where E and ν are Young's modulus and Poisson's ratio and $\kappa = 3 - 4\nu$ for plane strain. In the present simulation, a FCC single crystal (aluminum) was considered and the crack geometry was chosen to be (010) [101] with the crack on plane (010) and the crack propagation direction to be [101], which was same as Rice's analytical analysis [8].

Cyclic displacements were applied on the remote boundary where K_I and T -stress were varied from zero to K_{max} and zero to T_{max} , respectively, as displayed in Fig. 1b. The normalized value for K_{max} was considered to be $K_{\text{max}}/(\tau_0\sqrt{b_0}) = 80$

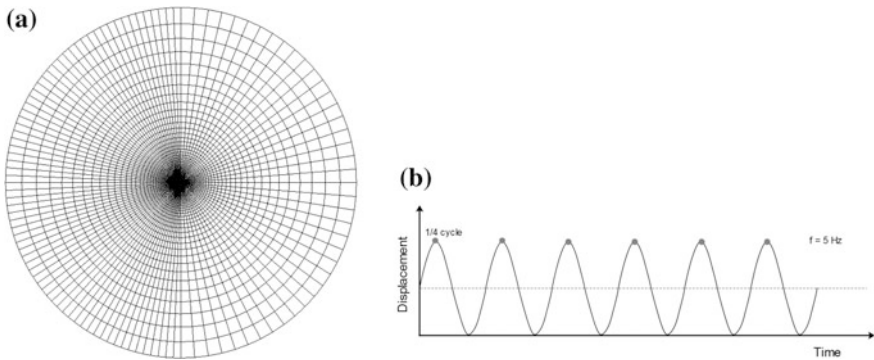


Fig. 1 **a** Circular disk used in the FE analysis. **b** Displacement applied in the modified boundary layer analysis for cyclic case

[2] and three different values of normalized T_{\max} , $T_{\max}/\tau_0 = -1, 0$ and $+1$, which include the T -stress span for numerous fracture geometries [9].

A User Material (UMAT) code was written with finite element analysis software, ABAQUS [10] by implementing these flow rules and hardening laws. Results of the finite element analysis are presented in the following section.

3 Results and Discussions

Cyclic evolution of plastic strain fields close to the crack tip is presented in Fig. 2 by plotting the maximum principal values of logarithmic plastic strain, $\log(\lambda_1^p)$ simulated after completing 20 cycles for three values of T -stress. It can be observed that the negative values of T -stress affected drop of constraint around the crack tip with the increase of plastic strain accumulation. Strain accumulation was quite substantial in the localization band at 55° in comparison to the other two bands at 90° and 125° . Very small accumulation was observed in the band oriented at 90° for negative magnitude of T -stress. However, there was fairly noticeable strain accumulation at 90° and 125° band for nonnegative T -stress. In fact, the contribution of 125° band in the plastic strain distribution was more visible for the $T = \tau_0$ case. Again, there was barely any plastic strain near the crack face for negative T -stress, which was certainly not the case for zero and positive T values. It was also witnessed that the strain accumulation along the slip band at 55° for negative T -stress was relatively high in magnitude and was reduced with the increase of T -stress. This kind of accumulation of strain in the slip bands in one direction with number of cycles was affiliated to “strain ratcheting.”

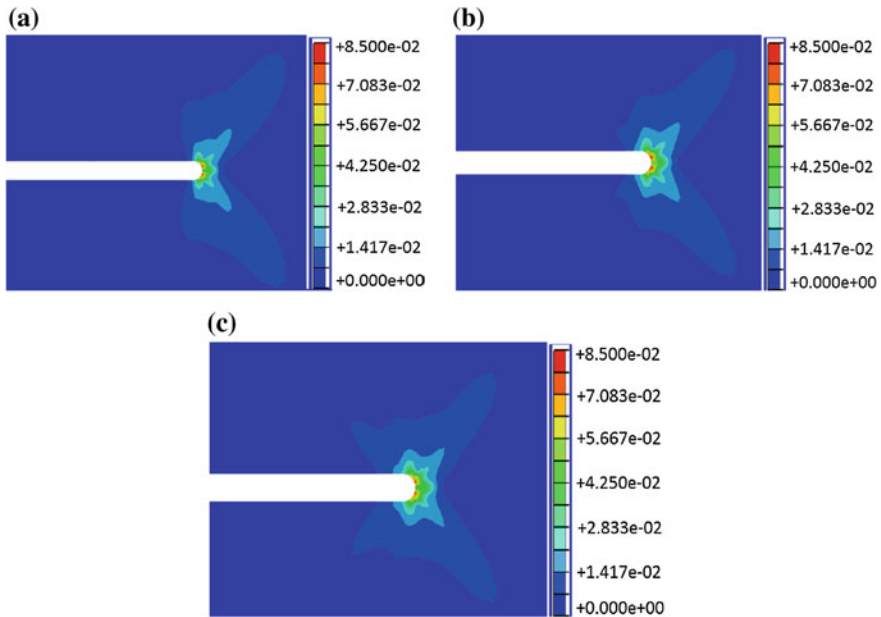


Fig. 2 Contour plots of plastic strain, $\log(\lambda_1^p)$ (for three different cases of T , **a** $T = -\tau_0$, **b** $T = 0$, and **c** $T = \tau_0$ after 20 cycles

References

1. F. Roters, P. Eisenlohr, L. Hantcherli, D. Tjahjanto, T. Bieler, D. Raabe, Overview of constitutive laws, kinematics, homogenization and multiscale methods in crystal plasticity finite-element modeling: theory, experiments, applications. *Acta Mater.* **58**(1), 1152–1211 (2010)
2. S.D. Patil, Constraint effects on stationary crack tip fields in ductile single crystals. Ph.D. thesis, IISC, 2009
3. J.M. Finney, C. Laird, Strain localization in cyclic deformation of copper single crystals. *Phil. Mag.* **31**(2), 339–366 (1975)
4. S. Flouriot, S. Forest, L. Remy, Strain localization phenomena under cyclic loading: application to fatigue of single crystals. *Comput. Mater. Sci.* **26**, 61–70 (11th International workshop on computational mechanics of materials)
5. J.D. Clayton, Homogenization and incompatibility fields in finite strain elastoplasticity. Ph.D. thesis, Georgia Institute of technology, 2002
6. D. Peirce, R.J. Asaro, A. Needleman, Material rate dependence and localized deformation in crystalline solids. *Acta Metall.* **31**, 1951–1976 (1983)
7. M.L. Williams, On the stress distribution at the base of a stationary crack. *J. Appl. Mech.* **24**(1), 109–114 (1957)
8. J. Rice, Tensile crack tip fields in elastic-ideally plastic crystals. *Mech. Mater.* **6**(4), 317–335 (1987)
9. J. Rice, Limitations to the small scale yielding approximation for crack tip plasticity. *J. Mech. Phys. Solids* **22**(4), 17–26 (1974)
10. ABAQUS, *ABAQUS documentation* (Dassault Systmes, Providence, RI, USA, 2011)

Analysis of the Plastic Zone Size Ahead of the Crack Tip in Notched Components and Its Application to Fatigue Problems

Masahiro Endo and Keiji Yanase

Abstract A method based upon the Dugdale model is proposed to calculate the plastic zone size (pzs) at the crack tip of a Mode I crack emanating from notch of arbitrary shape. To provide a generalized method, a crack at the notch root was modeled as an edge crack in a semi-infinite plate subjected to the same stress as that generated near the notch root in the absence of a crack. The calculated pzs ahead of the tip of the crack emanating from circular and elliptical holes was in reasonable agreement with the accurate values reported in the literature. By making use of the calculated pzs, the near-threshold behavior of crack emanating from notch under cyclic loading condition was simulated by using McEvily's fatigue crack growth equation. Subsequent comparison with the available experimental data revealed that the proper consideration of plastic zone size can capture the phenomena and trends observed in the experimental data with reasonable accuracy.

Keywords Dugdale model · pzs · Stress intensity factor · Notch effect
High-cycle fatigue

1 Introduction

In principle, there is a finite, albeit small, region around a crack tip in which the state of stress is adequately characterized by the stress intensity factor (SIF). In essence, the linear elastic stress analysis of crack predicts infinite stresses at the crack tip. In real materials, however, stresses at the crack tip are finite due to inelastic material deformation, such as plasticity in metals, which leads to the relaxation of crack-tip stresses. It is well established that, under small-scale yielding

M. Endo (✉) · K. Yanase
Department of Mechanical Engineering, Fukuoka University, Fukuoka City 814-0180, Japan
e-mail: endo@fukuoka-u.ac.jp

M. Endo · K. Yanase
Institute of Materials Science and Technology, Fukuoka University, Fukuoka City 814-0180,
Japan

conditions, SIF can reasonably account for the extent of stress intensity in the vicinity of cracks. Therefore, SIF is widely used to characterize the crack growth behavior in the high-cycle fatigue regime. In practice, there are circumstances in which the small-scale yielding condition is not satisfied. For instance, applying SIF to small cracks emanating from the notch root may lead to a hazardous prediction because the plastic zone size (pzs) is comparable to the crack length (i.e., small-scale yielding condition is not satisfied), due to the fact that the notch root is highly stressed by the stress concentration.

In reality, the stresses, strains, and displacements in the vicinity of crack associated with the plastic deformation are difficult to calculate. The finite element method (FEM) is a convenient tool, but a special care to obtain reliable results must be exercised for the mesh size, loading step, etc. On the other hand, applying simple corrections to linear elastic fracture mechanics is a very convenient and attractive alternative. Concerning Mode III, a modified crack length, c_{mod} , which is the sum of physical crack length c and half of the pzs, ω (i.e., $c_{\text{mod}} = c + \omega/2$), can account for the effect of plasticity [1, 2]. Strictly speaking, this relation does not hold for Mode I and II cracks. Nonetheless, this and similar approaches are widely used to address crack problems in the presence of plasticity. For instance, in the Dugdale model [3], the elastic–plastic behavior is modeled by superposing two elastic solutions: a through crack under remote tension and a through crack with closure stresses at the crack tip. In the literature, the Dugdale model was applied for a center crack in an infinite plate [3], an edge crack in a semi-infinite plate [4], and a crack emanating from a circular hole [5].

The procedures for analyzing constant amplitude fatigue under small-scale yielding condition are well established, though a number of uncertainties remain. For instance, large-scale yielding and short cracks introduce additional level of complexities that are presently not fully understood. In this work, a generalized method is proposed based on the Dugdale model, which is an effective approach for studying the elastic–plastic behavior of crack emanating from notch. As an application, the proposed method is combined with McEvily's equation [6] to simulate the fatigue crack growth behavior emanating from a circular hole in the high-cycle fatigue regime. As will be shown, the proper consideration of plastic zone size can capture the phenomena and trends observed in the experimental data with reasonable accuracy.

2 Dugdale Model for Notch Problem

2.1 Dugdale Model

In the Dugdale model [3], a long, slender plastic zone at the crack tip in a non-hardening material is considered. This strip-yield plastic zone is modeled by assuming a crack length $2(c + \omega)$, where ω is pzs, with a closure stress equal to

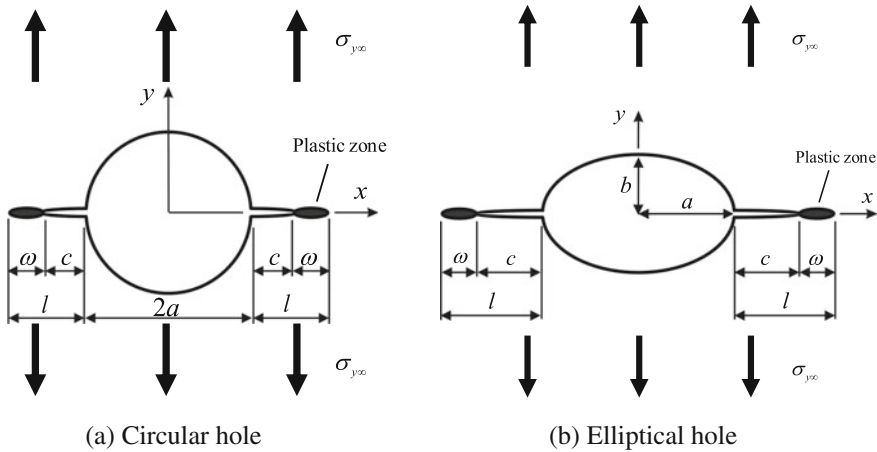


Fig. 1 Crack emanating from a hole and plastic zone

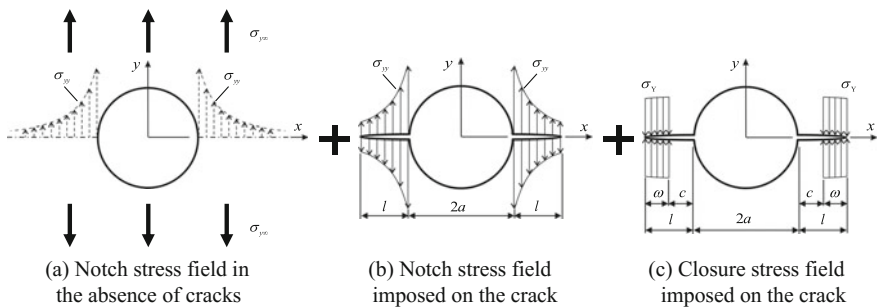


Fig. 2 Application of linear superposition with Dugdale model for Fig. 1a

yield stress of the chosen material, σ_Y , at the crack tip. Since the stresses are finite in the plastic zone, there cannot be a stress singularity at the crack tip. Accordingly, the value of ω must be calculated, such that SIFs due to remote tension and closure stress cancel each other.

Let us consider an extension of the Dugdale model for notch problem. Figure 1 shows a crack emanating from a circular hole and an elliptical hole, respectively. By using the principle of linear superposition, Fig. 1a can be effectively decomposed into the respective figures in Fig. 2. Given that only Fig. 2b, c contains the crack, the following condition for SIF must be satisfied according to the Dugdale model:

$$K_A + K_B = 0 \tag{1}$$

where K_A is the SIF due to the notch stress field of σ_{yy} (Fig. 2b) and K_B is the SIF due to the closure stress of σ_Y (Fig. 2c). By solving Eq. (1), the value of pzs or ω can be calculated. In practice, for an arbitrary notch shape, it is difficult to calculate ω since the closed-form solution for Eq. (1) is not available. Therefore, in what follows, an approximate method is presented by making use of the solution for an edge crack in a semi-infinite plate.

2.2 Approximation with an Edge Crack in a Semi-Infinite Plate

For the circular hole (Fig. 1a), the notch stress field on the x -axis is given as [7]:

$$\sigma_{yy}(x) = \sigma_{y\infty} \left[1 + \frac{a^2}{2(x+a)^2} + \frac{3a^4}{2(x+a)^4} \right] \tag{2}$$

where $\sigma_{y\infty}$ is the remote tensile stress and the origin of x -axis is, for convenience, moved to the edge of hole. It is noted that when $l \ll a$, the problem of Fig. 2b is equivalent to that of Fig. 3. To correctly account for the arbitrary notch stress field, the following calculation with a pair of concentrated forces, P , is convenient [8] (Fig. 4):

$$K = \frac{2P\sqrt{\pi l}}{\pi\sqrt{l^2 - x^2}} \{1 + f(\chi)\} \tag{3}$$

Fig. 3 Approximation of the edge crack with notch stress field by a circular hole

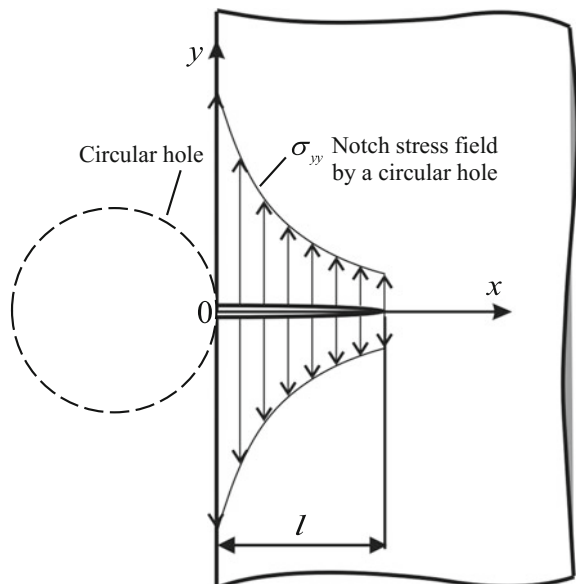
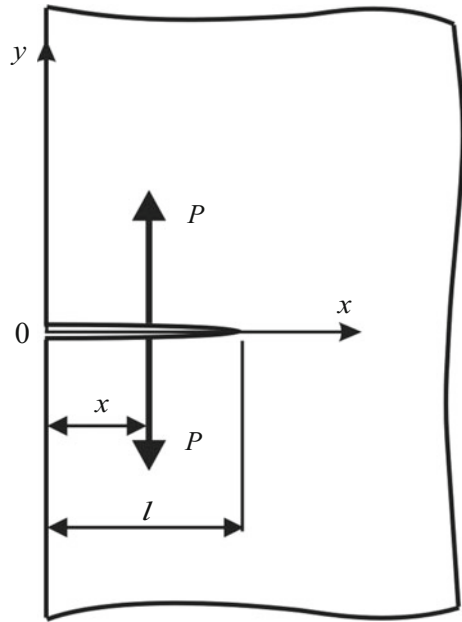


Fig. 4 Edge crack with a pair of concentrated forces [8]



where

$$f(\chi) = (1 - \chi^2)(0.2945 - 0.3912\chi^2 + 0.7685\chi^4 - 0.9942\chi^6 + 0.5094\chi^8); \quad (4)$$

$$\chi = x/l$$

Therefore, by substituting Eq. (2) into Eq. (3), K_A for Fig. 2b is calculated as:

$$K_A = \int_0^l \frac{2\sigma_{yy}(x)\sqrt{\pi l}}{\pi\sqrt{l^2 - x^2}} \{1 + f(\chi)\} dx \quad (5)$$

Similarly, K_B for Fig. 2c is given as:

$$K_B = - \int_c^l \frac{2\sigma_Y\sqrt{\pi l}}{\pi\sqrt{l^2 - x^2}} \{1 + f(\chi)\} dx \quad (6)$$

By substituting Eqs. (5) and (6) into Eq. (1), ω can be calculated via a numerical method (e.g., bisection method). To correctly address the presence of an elliptical hole (Fig. 1b), the following expression [9] can be used for Eq. (5):

$$\sigma_{yy}(x) = \sigma_{y\infty} \left[\frac{1}{\zeta^2 - 1} \left(\zeta^2 + \frac{\lambda}{\lambda - 1} \right) - F_1(\zeta) - F_2(\zeta) \right] \tag{7}$$

where

$$F_1(\zeta) = \frac{1}{(\zeta^2 - 1)^2} \left\{ \frac{1}{2} \left(\frac{\lambda - 1}{\lambda + 1} - \frac{\lambda + 3}{\lambda - 1} \right) \zeta^2 - \frac{\lambda + 1}{(\lambda - 1)^2} \right\}; \tag{8}$$

$$F_2(\zeta) = \frac{4\zeta^2}{(\zeta^2 - 1)^3} \left(\frac{\lambda}{\lambda^2 - 1} \zeta^2 - \frac{\lambda}{(\lambda - 1)^2} \right)$$

$$\lambda = \frac{a}{b}; \quad \zeta = \frac{x + \sqrt{x^2 - \xi^2}}{\xi}; \quad \xi = \sqrt{a^2 - b^2} \tag{9}$$

Figure 5 shows the results for a circular hole (Fig. 1a). Overall, the present calculation shows a moderate agreement with the accurate results reported by Rich and Roberts [5]. Further, Fig. 6 shows the results for the elliptical hole (Fig. 1b), in which ω is calculated in the absence of crack (i.e., $l = \omega$ in Fig. 1b). In other words, the pzs due to the stress concentration by an elliptical hole is calculated in Fig. 6. Compared to the accurate results reported by Nisitani [10], a good agreement is observed.

The pzs of a center crack in an infinite plate under remote tension is analytically given as [3]:

Fig. 5 Plastic zone size with a circular hole [5]

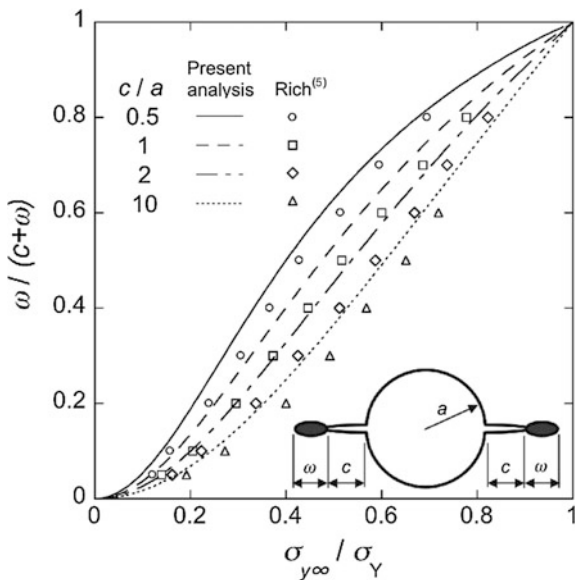
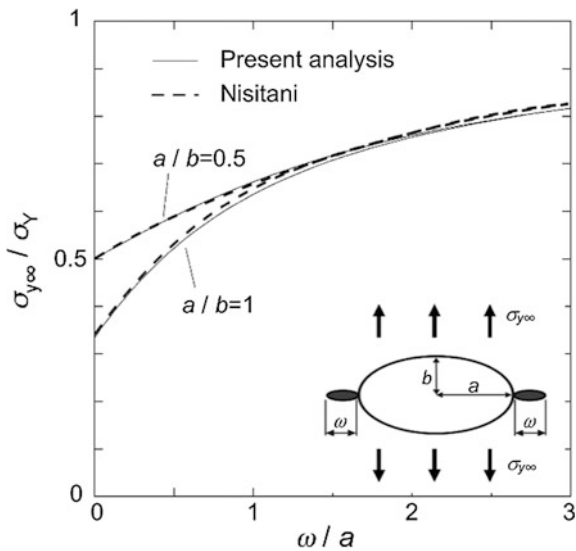


Fig. 6 Plastic zone size with an elliptical hole [10]



$$\omega_{\text{center}} = c \left[\sec \left(\frac{\pi \sigma_{y\infty}}{2 \sigma_Y} \right) - 1 \right] \tag{10}$$

On the other hand, the pzs of an edge crack in a semi-infinite plate is analytically given as [4]:

$$\omega_{\text{edge}} = 1.1215^2 \times c \left[\sec \left(\frac{\pi \sigma_{y\infty}}{2 \sigma_Y} \right) - 1 \right] \tag{11}$$

In principle, at $c/a \rightarrow 0$, $\omega = \omega_{\text{edge}}$ should hold (i.e., consideration of edge crack is proper). However, at $c/a \rightarrow \infty$, $\omega = \omega_{\text{center}}$ should hold (i.e., consideration of edge crack is no longer proper). The present calculation shows that $\omega = \omega_{\text{edge}}$ holds at both $c/a \rightarrow 0$ and $c/a \rightarrow \infty$ due to employing the solution for the edge crack (Figs. 3 and 4). This means that the following modification is necessary at $c/a \rightarrow \infty$ (cf. Eqs. 10 and 11):

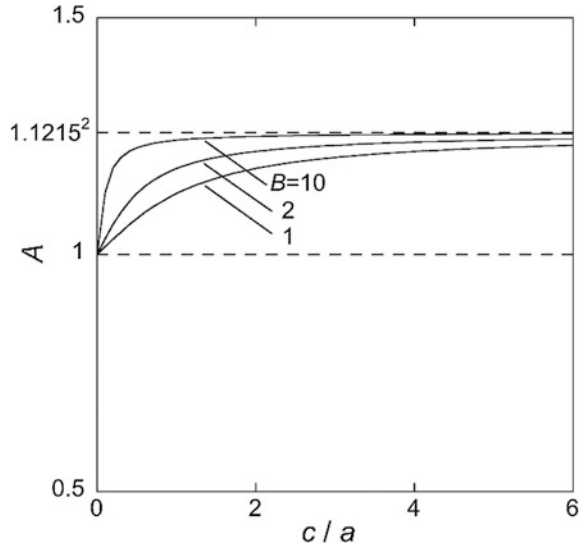
$$\omega_{\text{mod}} = \frac{\omega}{1.1215^2} \tag{12}$$

In this study, the following form is considered for convenience:

$$\omega_{\text{mod}} = \frac{\omega}{A}, \quad \text{where } A = \frac{2}{\pi} (1.1215^2 - 1) \tan^{-1} \left(B \frac{c}{a} \right) + 1 \tag{13}$$

As shown in Fig. 7, the parameter B governs the rate of convergence for A . For instance, by minimizing the error in Fig. 5, $B = 4$ is obtained for the circular hole.

Fig. 7 Variations of correction factor, A



As depicted in Fig. 8, a use of Eq. (13) provides results that are in good agreement with the accurate results reported by Rich and Roberts [5].

3 Fatigue Crack Growth Simulation with the Extended Dugdale Model

As an application of the extended Dugdale model, let us consider the fatigue crack growth behavior emanating from a circular hole in the high-cycle fatigue regime. According to McEvily et al. [6], the fatigue crack growth equation at a stress ratio of $R = -1$ is rendered as:

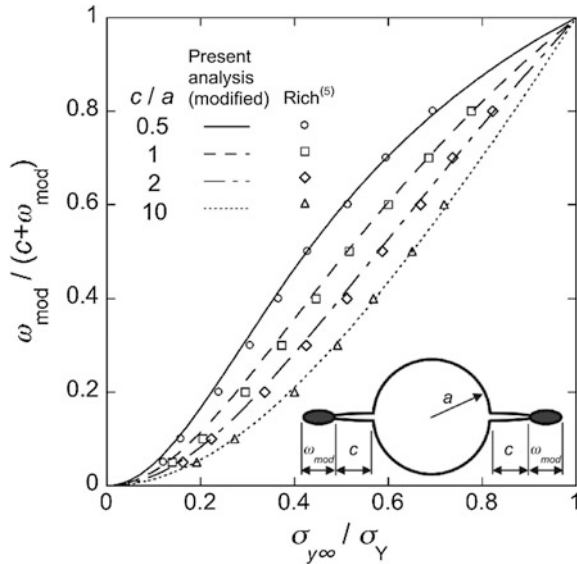
$$\frac{dc}{dN} = A \cdot M^2 \tag{14}$$

where

$$M = \left[\sqrt{2\pi r_e F} + Y\sqrt{\pi c F} \right] \sigma_a - \left(1 - e^{k(c-r_e)} \right) K_{opmax} - \Delta K_{effth} \tag{15}$$

Here, σ_a is the amplitude of remote cyclic stress, k is a material constant that governs the rate of crack closure development, K_{opmax} is a value of SIF when a macroscopic crack opens, and ΔK_{effth} is the effective range of the SIF at the threshold level. Based on Eq. (15), so-called inherent crack length, r_e , is estimated by considering the fatigue limit of a smooth specimen, σ_{w0} , at $R = -1$ as follows:

Fig. 8 Modified plastic zone size with a circular hole [5]



$$r_e = \left(\frac{1}{1.12\sqrt{\pi F_0}} \cdot \frac{\Delta K_{effth}}{\Delta \sigma_{w0}} \right)^2, \text{ where } F_0 = \frac{1}{2} \left[\sec\left(\frac{\pi}{2} \cdot \frac{\sigma_{w0}}{\sigma_Y}\right) + 1 \right] \quad (16)$$

In general, r_e is in the order of a few microns. Further, F is the elastic–plastic correction factor for crack length based on the Dugdale model (cf. Eq. 13):

$$F = 1 + \omega_{mod}/2c \quad (17)$$

Finally, Y is the geometric correction factor for SIF, which is illustrated for the circular hole in Fig. 9 [11]. In essence, Eq. (15) considers the effects of a crack tip of finite radius [12], the Kitagawa effect [13], and the crack closure. Based on Eq. (14), the threshold condition of $dc/dN = 0$ can be found by setting $M = 0$. Namely, by calculating the stress level of σ_a for a specific crack length of c to satisfy $M = 0$, the unique threshold behavior for a given notch geometry can be predicted.

The fatigue crack emanating from a circular hole was previously investigated by El Haddad et al. [14]. Table 1 provides the material constants used for the prediction, whereby comparisons between the present predictions and the experimental data are depicted in Fig. 10. It is noted that one prediction (respective solid lines) considers the effect of stress concentration for pzs (i.e., F in Eq. 15), while the other prediction (respective dashed lines) neglects such an effect. In the dashed prediction lines, the initial stresses (i.e., crack initiation stress) at $c = r_e$ denote the maximum threshold stress. This means that the crack initiation directly leads to fatigue failure without any evidence of crack arrest. On the other hand, concerning the solid prediction lines for $a = 0.2$ and 0.48 mm, the maximum stresses at the points A and

Fig. 9 Variations of geometric correction factor, Y [11]

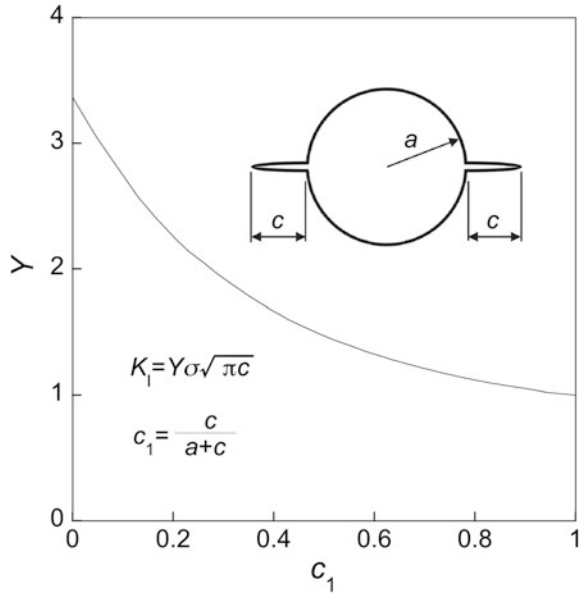
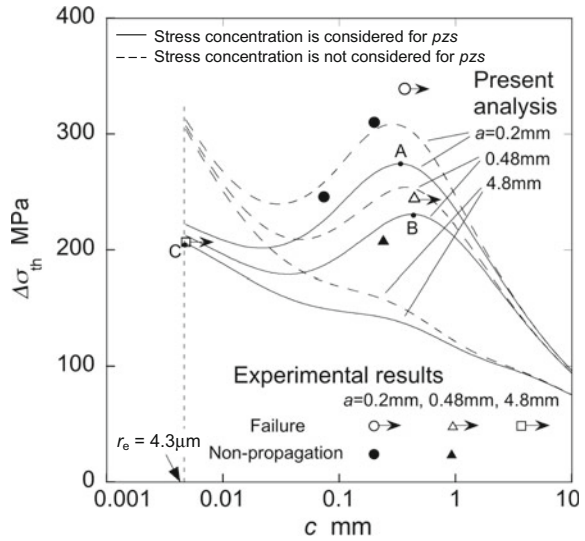


Table 1 Material constants (Material: CSA G40.11 steel)

K_{opmax} (MPa√m)	ΔK_{effth} (MPa√m)	σ_Y (MPa)	σ_{w0} (MPa)	k (m ⁻¹)
5.5	3.0	376	276	6000

B are greater than the respective crack initiation stresses (i.e., stresses at $c = r_e$). This finding indicates that the crack initiation does not lead to fatigue failure and the non-propagating crack exists. However, when the hole radius is large ($a = 4.8$ mm), the crack initiation leads to fatigue failure because the crack initiation stress itself is the maximum threshold stress. Consequently, non-propagating cracks are not observed for $a = 4.8$ mm. Accordingly, in Fig. 10, the points A, B, and C represent the predicted fatigue strength for the respective hole radii. Overall, the findings reported here confirm that the proper consideration of plastic zone size (i.e., the solid line) captures the phenomena and trends in the experimental data with reasonable accuracy.

Fig. 10 Comparisons between the predictions and experimental data [14]



4 Conclusion

In this study, the Dugdale model was extended and was applied in order to investigate the notch problem in the high-cycle fatigue regime. In principle, the proposed method takes advantage of the solution for an edge crack to calculate the plastic zone size. As an application, the proposed method was combined with McEvily’s equation to simulate the fatigue crack growth behavior emanating from a circular hole in the high-cycle fatigue regime. The present prediction captures the phenomena and trends observed in the experimental data with reasonable accuracy.

References

1. G.R. Irwin, Naval research laboratory report No. 5486, Naval Research Laboratory, Washington, D.C. (1960)
2. C.K.H. Dharan, B.S. Kang, I. Finnie, *Finnie’s Notes on Fracture Mechanics* (Springer, New York, 2016)
3. D.S. Dugdale, Yielding of steel containing slits. *J. Mech. Phys. Solids* **8**, 100–104 (1960)
4. H. Nisitani, Y. Murakami, Interaction of elasto-plastic cracks subjected to a uniform tensile stress in an infinite or a semi-infinite plate. *Proc. Int. Conf. Mech. Behav. Mater.* **1**, 346–356 (1972)
5. T. Rich, R. Roberts, Plastic enclave sizes for internal cracks emanating from circular cavities within elastic plates. *Eng. Fract. Mech.* **1**, 167–173 (1968)
6. A.J. McEvily, D. Eifler, E. Macherlauch, An analysis of the growth of short fatigue cracks. *Eng. Fract. Mech.* **40**, 571–584 (1991)
7. S.P. Timoshenko, J.N. Goodier, *Theory of Elasticity* (McGraw-Hill International, New York, 1982)

8. R.J. Hartranft, G.C. Sih, Alternating method applied to edge and surface crack problems. *Mech. Fract.* **1**, 179–238 (1973)
9. Y. Murakami, *Theory of Elasticity and Stress Concentration* (Wiley, West Sussex, 2017)
10. H. Nisitani, Elastic-plastic stress in a semi-infinite plate having an elliptical arc notch with an edge crack under tension or longitudinal shear, *Proc. Int. Cong. Fract.* **2**, 1–513 (1973)
11. Y. Murakami et al., *Stress Intensity Handbook* (Pergamon Press, Oxford, 1987)
12. G.R. Irwin, *First Symposium on Naval Structure and Mechanics* (Pergamon Press, Oxford, 1960), pp. 557–594
13. H. Kitagawa, S. Takahashi, Applicability of fracture mechanics to very small cracks or the cracks in the early stage. *Proc. Int. Conf. Mech. Behav. Mater.* 627–631 (1976)
14. M.H. El Haddad, T.H. Topper, K.N. Smith, Prediction of non-propagating cracks. *Eng. Fract. Mech.* **28**, 573–584 (1979)

Effect of Loading Frequency on the Fatigue Crack Growth Rate of Type 304L(N) Material

Mukhar Sharma, Punit Arora, P. K. Singh, D. K. Sahoo, Gargi Choudhuri and V. Bhasin

Abstract The aim of this study was to study the effect of loading frequency on the fatigue crack growth rate (FCGR) behaviour of Type 304L(N) austenitic stainless steel material. Compact tension ($C(T)$) specimens machined from the solution annealed pipe were used for carrying out the FCGR tests as per the standard procedure of ASTM E647. Constant amplitude loading method with varying frequency (0.01–10 Hz) was followed for cyclic loading during the tests. The tests were carried out at load ratio 0.1 and ambient temperature. Experimental results show that FCGR increases with decrease in frequency for a given stress intensity factor range. Increase in FCGR is very significant from high to low frequency. Fracture surface examinations of tested specimens were carried out using scanning electron microscope to understand the increased crack growth at lower frequency. The fracture surfaces revealed the presence of facets which have feature of brittle fracture. These facets could be the locations for the formation of deformation-induced-martensite (DIM). The facets are relatively harder (320 HV) as compared to matrix of the material (155 HV) which may have led to higher crack growth rate. Area covered by these facets is more for fracture surface tested at lower frequency. FCGR of present test study is also compared with FCGR curve for austenitic stainless steel given in ASME Section XI. ASME FCGR curve is comparable with that of the FCGR curve of loading frequency 10 Hz. However, ASME FCGR would lead to over-prediction of fatigue crack growth life for lower loading frequency scenario.

Keywords Fatigue crack growth rate • Deformation-induced martensite
Loading frequency

M. Sharma · D. K. Sahoo
Board of Radiation and Isotope Technology, Navi Mumbai 400703, India

P. Arora (✉) · P. K. Singh · G. Choudhuri · V. Bhasin
Bhabha Atomic Research Centre, Mumbai 400085, India
e-mail: punit@barc.gov.in

Nomenclature

$C(T)$	Compact tension
TPB	Three-point bend
FCG	Fatigue crack growth
FCGR	Fatigue crack growth rate
DIM	Deformation-induced martensite
a	Crack length
W	$C(T)$ width
K	Stress intensity factor (SIF)
ΔK	Stress intensity factor range
HCF	High-cycle fatigue
SEM	Scanning electron microscope
L	Longitudinal
C	Circumferential
P_{\max}	Maximum load in one cycle
P_{\lim}	Limit load
ΔP	Load range
OD	Outer diameter
R	Load ratio
N	Number of cycles
da/dN	Crack growth rate
COD	Crack opening displacement
σ_y	Yield strength
σ_u	Tensile strength
σ_f	Flow strength ($0.5 \times (\sigma_y + \sigma_u)$)
SS	Stainless steel

1 Introduction

Fatigue causes progressive and localized damage in a material due to repeated or fluctuating strains, at the nominal stresses that have maximum values less than the yield strength of the material. The cracks in the piping components of nuclear power plants (NPP) may get generated in due course of their service life or might have gone undetected during the pre-service inspection of components. The accurate assessment of residual fatigue crack growth life of cracked components serves two objectives that are life extension programme of power plants and demonstration of leak before break criterion. In NPP, different service level loads are categorized based on the frequency of their occurrence during its design life.

The studies are required to generate fatigue crack growth rate (FCGR) parameters on small-scale specimens such as compact tension ($C(T)$), three-point bend (TPB) specimens under different loading frequencies.

Over recent years, austenitic stainless steels have been extensively used for various engineering components specially in nuclear power plants because of their high corrosion resistant and an excellent combination of mechanical properties like high strength and high ductility. Now-a-days, Type 304L or Type 304L(N) stainless steel is being used in place of Type 304 stainless steel as these low carbon grades are less susceptible to formation of chromium carbide which may lead to failure due to the intergranular stress corrosion cracking. Due to metastable nature of austenitic stainless steel, it tends to form relatively harder martensite upon large deformation.

The strain that occurs ahead of the crack tip during fatigue crack growth in a metastable material induces a partial transformation to martensite, which alters both the microstructure and the stress state at the crack tip and should, therefore, change the fatigue crack growth rate. The martensite deformation causes a deformation in shape that is substantiated by surface relief effect [1] and a volume change that is dependent on composition and is $\approx 2\%$ in 304-type stainless steels [2, 3]. Deformation-induced martensite formation is influenced by many factors like steel chemistry, deformation mode, strain, stress, strain rate, grain size, grain orientation and temperature [4]. Although, researchers have concluded that there is no effect of frequency on the fatigue crack growth rate in air environment and room temperature. There have been research studies on the influence of the deformation-induced martensite transformation under monotonic tensile loading and low-cycle fatigue in 304 series of materials. Das et al. [4] investigated the behaviour of this material under cyclic loading, with increase in strain amplitude, the formation of deformation-induced martensite increases. Roa et al. [5] studies showed that formation of deformation-induced martensite is deleterious for low-cycle fatigue regime but small amount of deformation-induced martensite (DIM) is beneficial for high-cycle fatigue (HCF) regime. While in another study by Das et al. [6], under monotonic loading at lower strain levels, the amount of martensite increases very rapidly with increase in true strain in a linear proportional manner, whereas it is observed that at low true strain value, higher the strain rate, more is the martensitic transformation, while at high true strain value, reduction in strain rate favours the formation of deformation-induced martensite. But the effect of the influence of loading frequency (or strain rate) on fatigue crack growth rate behaviour is not studied much and is an open area for investigations.

For better understanding and accurate assessment of FCG life of austenitic stainless steels, influence of loading frequency/strain rate on its fatigue behaviour must be established. In this context, the aim of present paper is to study the effect of loading frequency/strain rate on fatigue crack growth rate (FCGR) behaviour of Type 304L(N) stainless steel material. Experiments are conducted on Type 304L(N)SS material using constant load amplitude method of standard ASTM E647 procedures [7]. The effect of cyclic loading frequency on FCG life is brought out.

Table 1 Chemical composition of present Type 304L(N) stainless steel (in wt%)

Cr	Ni	Mn	C	Si	P	S	N	Fe
18.26	8.45	0.79	0.021	0.33	0.004	0.003	0.1	Remainder

Table 2 Tensile properties of Type 304L(N) material

σ_y (MPa)	σ_u (MPa)	% El
240	560	64.2

% El: total percentage elongation

2 Experimental Procedures

2.1 Material Details

Austenitic stainless steel, Type 304L(N) stainless steel in the form of extruded pipe of outer diameter (OD) 324 mm and thickness 25 mm in the solution annealed condition as per the specification of ASME Section II [8] was used for machining of standard compact tension ($C(T)$) specimens.

The chemical composition and tensile properties of the material are shown in Tables 1 and 2, respectively.

2.2 Specimen Details

The $C(T)$ specimens were designed as per the standard test procedure of ASTM E647 [7]. The machined notch was put in circumferential direction with respect to pipe axis and was named as LC orientation. The LC orientation means loading direction is in longitudinal (L) direction, and crack growth is in circumferential (C) direction with respect to axis of the pipe. The $C(T)$ specimen with its dimensions is shown in Fig. 1a, and orientation with respect to pipe axis is shown in Fig. 1b.

2.3 Fatigue Pre-cracking

The pre-cracking for all the specimens was carried out as per the requirements of ASTM E647 [7]. The pre-cracking and subsequent fatigue crack growth rate (FCGR) tests were carried out at servo-hydraulic machine of maximum load capacity as ± 100 kN and travel of ± 60 mm. The loading frequency was maintained as 10 Hz, and the load ratio (R) (the ratio of minimum load to maximum load in a cycle) was kept as 0.1. The maximum stress intensity factor (K) during

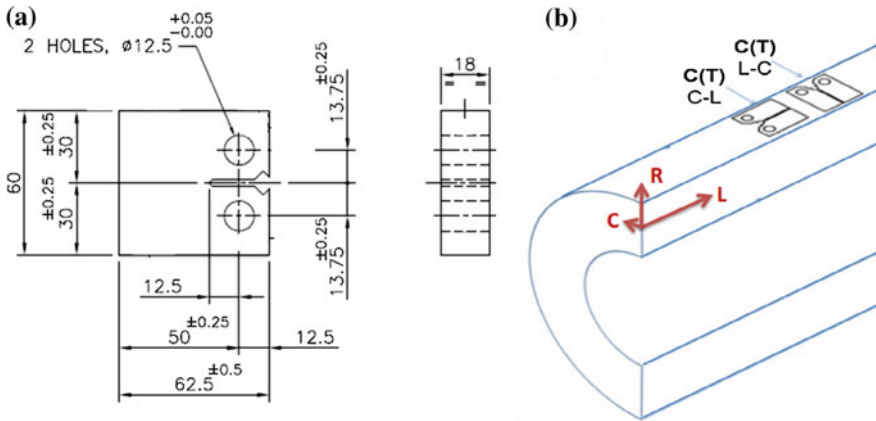


Fig. 1 a Typical schematic of C(T) specimen and b layout of the C(T) specimen as machined from full-scale pipe of 324 mm OD and 25 mm thickness of Type 304L(N) material

pre-cracking was less than that during FCGR test to rule out retardation effects. The stress intensity factor range at the end of pre-cracking was varying from 19 to 22 MPa-√m for various tests. The ratio of crack length (*a*) to width (*W*) was nearly 0.3 after pre-cracking.

2.4 Fatigue Crack Growth Rate (FCGR) Tests

FCGR tests were conducted on pre-cracked specimens using constant load amplitude method with a maximum and minimum load values of 16 and 1.6 kN, respectively. The test loading frequency was varied from 0.01 to 10 Hz to bring out the effect of loading frequency on the fatigue crack growth rate. The crack length (*a*) based on the compliance-crack size correlation [7] was recorded with number of fatigue cycles (*N*). The derived FCGR parameter (*da/dN*) from a-Vs-N curve was then correlated with crack driving force, that is, stress intensity factor range (ΔK). The stress intensity factor range (ΔK) was calculated from the crack length, cyclic load and geometric factor [9]. Test parameters are shown in Table 3.

3 Results and Discussion

The crack length (*a*) with number of cycles (*N*) curves for different loading frequencies are plotted in Fig. 2. All the curves are plotted from the data generated in the tests, considering same initial reference crack length as 17 mm. This figure shows that the crack growth life under slower loading frequency (0.01 Hz) is significantly shorter than that under 10 Hz frequency.

Table 3 Tests and loading parameters for the fatigue crack growth rate tests

	Test name	Units	SSB-f10	SSB-f1	SSB-f0.1	SSB-f0.01
	Test temperature	°C	25–27 °C	25–27 °C	25–27 °C	25–27 °C
Notch geometry	<i>r</i> (tip radius)	mm	0.2	0.2	0.2	0.2
	<i>a</i> ₀ (initial notch depth)	mm	12.5	12.5	12.5	12.5
	<i>W</i> (total width)	mm	50	50	50	50
	<i>b</i> (remaining ligament)	mm	37.5	37.5	37.5	37.5
	<i>B</i> (thickness)	mm	18	18	18	18
Material Properties	σ_y (yield strength)	MPa	240	240	240	240
	σ_u (ultimate strength)	MPa	560	560	560	560
	σ_f (flow stress)	MPa	400	400	400	400
	η^*	–	0.277	0.277	0.277	0.277
	<i>P</i> _{lim} (limit load)	kN	108.8	108.8	108.8	108.8
FCGR test parameters	<i>P</i> _{max}	kN	16.00	16.00	16.00	16.00
	<i>R</i> (stress ratio)	–	0.1	0.1	0.1	0.1
	<i>P</i> _{min}	kN	1.60	1.60	1.60	1.60
	Frequency	Hz	10	1	0.1	0.01
	Number of cycles	ΔN	113,347	26,780	6594	4680
	<i>a</i> _i (initial crack length)	mm	14.5	17	16	14.6
	<i>a</i> _f (final crack length)	mm	25.00	26.25	25.50	20.25
	ΔK_i (initial ΔK)	MPa- \sqrt{m}	19.6	22.3	21.2	19.7
	ΔK_f (final ΔK)	MPa- \sqrt{m}	34.6	37.4	35.6	26.4

$$*\eta = \sqrt{\left(\frac{2a}{b}\right)^2 + \frac{4a}{b} + 2 - \left(\frac{2a}{b} + 1\right)}$$

Figure 3 shows the variation of fatigue crack growth life for same initial crack length and final crack length with loading frequency. This comparison is made for the initial crack size of 17 mm to final crack size of 21 mm, subjected to load range (ΔP) of 14.4 kN and *P*_{max} as 16 kN (i.e. *R* = 0.1). This figure shows that the effect of frequency on FCG life becomes predominant as we decrease the loading frequency from 10 Hz (high-frequency regime) to 0.01 Hz (low-frequency regime). There is approximately 70% reduction in FCG life on lowering the frequency from 10 Hz to 1 Hz.

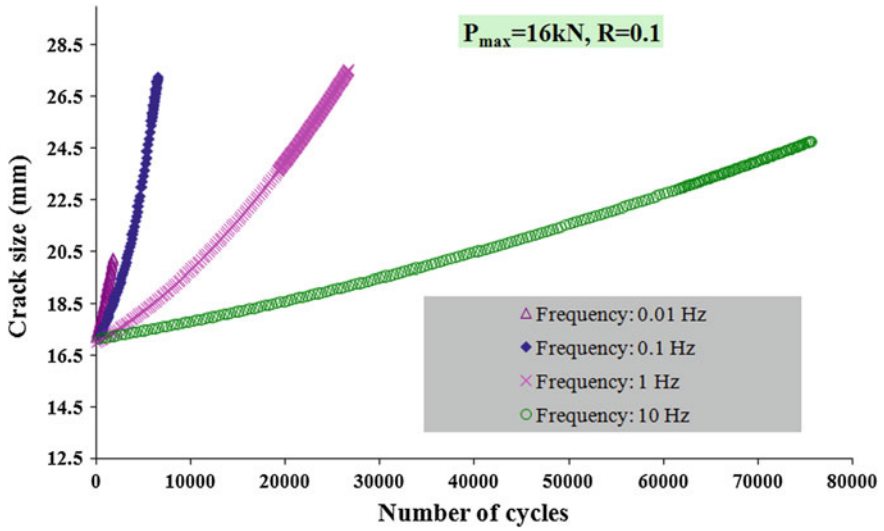


Fig. 2 Crack size (a) versus the number of load cycles (N) curves for different loading frequencies

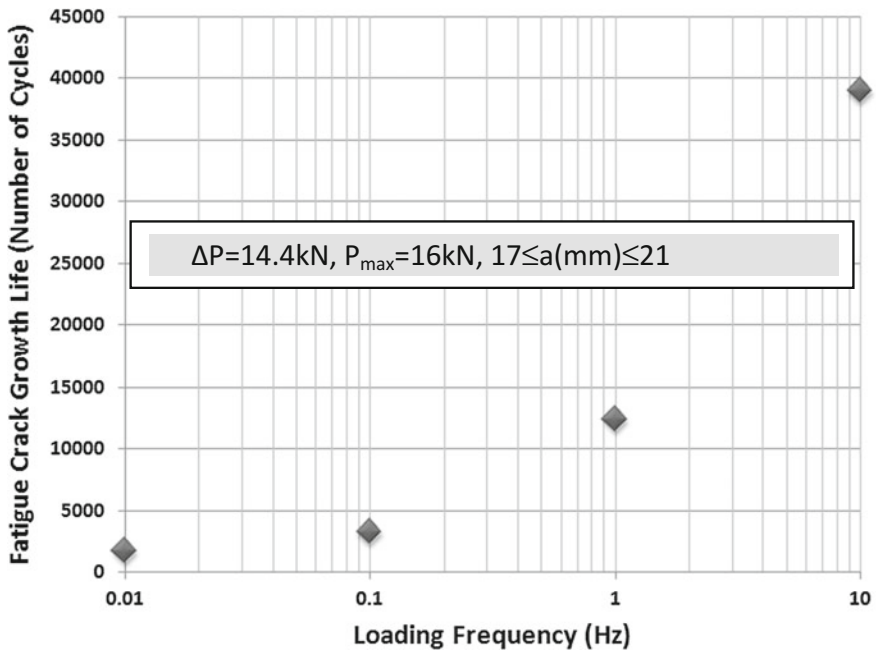


Fig. 3 Fatigue life for the same crack growth (starting from 17 to 21 mm) with the loading frequency

The fatigue crack growth rate (da/dN) is plotted with crack driving force (ΔK) in Fig. 4, for different frequencies. It is apparent from this figure that FCGR under slow frequency is significantly higher as compared to that under high frequency. This test investigation is in line with the tensile test studies carried out by Das et al. [6]. Das et al. have brought out in their studies that for higher true strain value, the decrease in the strain rate favours the formation of deformation-induced martensite. Although the above study is for the monotonic tensile loading and there is no direct correlation with the cyclic loading, but in an approximate way, similar observation was found in the present test results. This implies that the formation of martensite promotes the crack growth rate by providing a brittle facet to the crack. Model proposed by James and Jones [10] also shows that in ASS at room temperature, there is a slight increase in FCGR on decreasing the loading frequency. In subsequent studies, Shih and Chen [11] also proposed a modified power law relation for ASS and concluded increase in FCGR with decrease in loading frequency. This is also supported by the study of Khan [12] that mentioned the strain hardening effect generated due to the formation of deformation-induced martensite accelerates the crack growth rate. However, Khan studies were carried out on Type-301 stainless steel material. The present test results are consistent with the literature data.

Subsequent to FCGR test studies, the cause of higher crack growth rate was brought out through microstructural investigations using SEM. Specimens were cut open, and the fatigue fracture surface was examined under scanning electron microscope. The microscopic examinations of fatigued surfaces revealed the

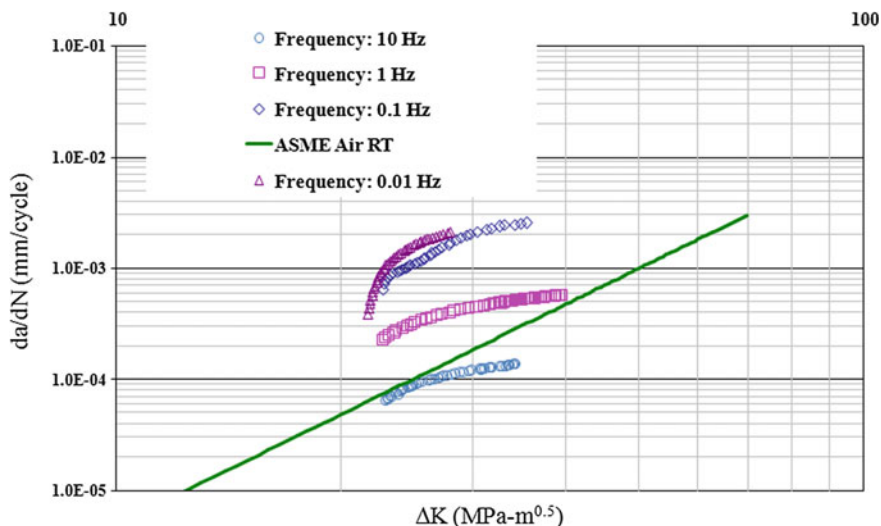


Fig. 4 Fatigue crack growth rate (da/dN) versus stress intensity factor range (ΔK) under different frequencies

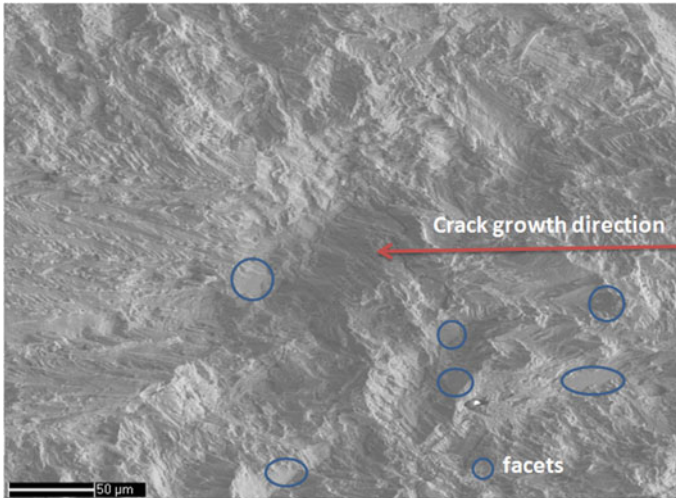


Fig. 5 Typical SEM image of microstructure of fracture surface of specimen tested under 10 Hz frequency

presence of discrete planar facets. These facets typically indicate the occurrence of brittle mode of fracture at the localised regions. Figures 5 and 6 show the typical SEM images of the fractured surfaces tested under loading frequency of 10 and 1 Hz, respectively. Figure 6 denotes typical brittle facets, and they are found to be occupying more area than that under 10 Hz frequency (Fig. 5) for same ΔK viz. same location from notch tip for given load range of 14.4 kN (Table 3). The hardness of region near to fracture plane was measured to be 320 HV in SSB-f0p1 specimen (0.1 Hz test) on transverse free surface plane. However, untested specimen had hardness of nearly 150 HV. The facet-like features on fracture surface (Figs. 5 and 6) and hatched-like impressions on transverse etched planes (Figs. 7 and 8) near to fracture plane have been characterized as DIM [4]. These observations indicate the formation of DIM near to crack plane leading to higher crack growth rate for low rate of loading tests. The features belonging to deformation-induced martensite are clearly visible as hatched region on the transverse free surface plane (perpendicular to crack surface) using optical microscopy in Fig. 7 for 10 Hz loading frequency test. These features are depicted in Fig. 8 for 0.1 Hz loading frequency test. Here also, the extent of DIM (hatched region) is higher for lower loading frequency. The results of optical microscopy are consistent with facets observed under SEM.

The ASME Section XI has the fatigue crack growth rate curve for austenitic stainless steel material in air environment at room temperature [13]. The fatigue crack growth rate as per ASME Section XI lies below the tests conducted under lower frequency range (0.01–1 Hz). This comparison is shown in Fig. 4. For any engineering component having part through thickness crack subjected to

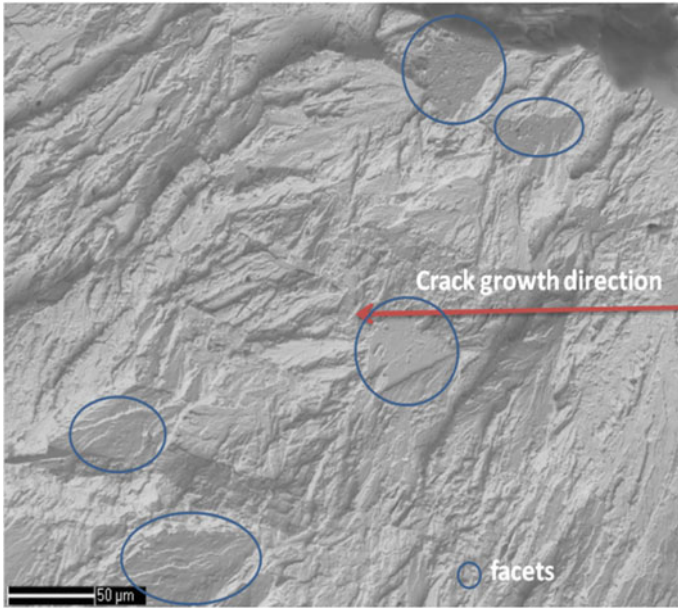


Fig. 6 Typical SEM image of microstructure of fracture surface of specimen tested under 1 Hz frequency showing facets

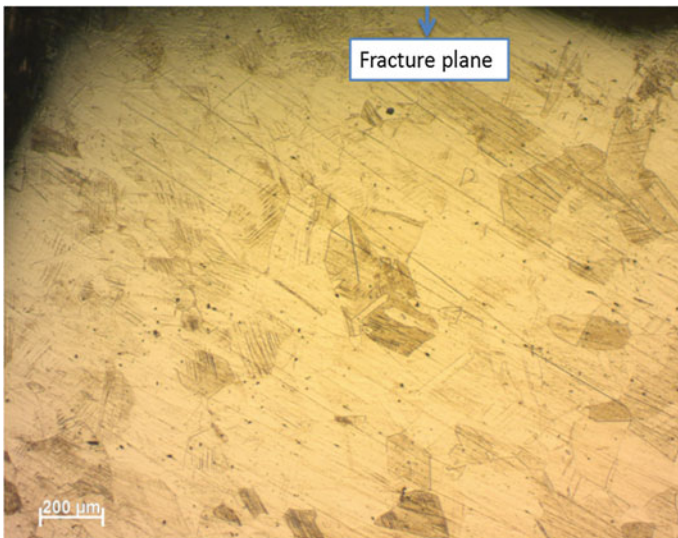


Fig. 7 Typical optical image of etched transverse free surface (perpendicular to crack surface) of specimen tested under 10 Hz frequency at 12 mm location from notch tip

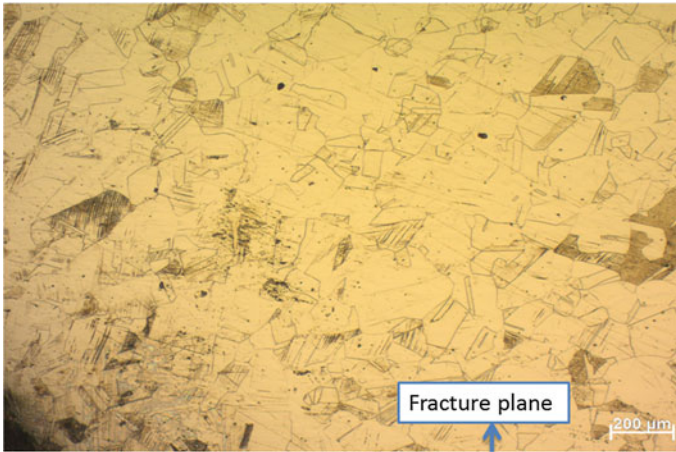


Fig. 8 Typical optical image of etched transverse free surface (perpendicular to crack surface) of specimen tested under 0.1 Hz frequency at 12 mm location from notch tip

low-frequency fatigue loading, if fatigue life is predicted using ASME prescribed FCGR curve, this would lead to over-prediction of fatigue crack growth life of cracked component.

4 Conclusions

Study on the effect of loading frequency on fatigue crack growth rate (FCGR) behaviour of Type 304L(N) austenitic stainless steel material can be summarized as:

1. FCGR increases with decrease in frequency for a given stress intensity factor range. Increase in FCGR is very significant from high to low frequency.
2. Fracture surface examinations revealed the presence of facets which have feature of brittle fracture. These facets could be the locations for the formation of deformation-induced martensite (DIM). Area covered by these facets is more in the specimens tested at lower frequency.
3. ASME FCGR curve is comparable with that of the FCGR curve of loading frequency 10 Hz. ASME FCGR curve lies below the FCGR curves generated for frequencies 0.01–1 Hz in present study. Use of ASME FCGR curve for application where loading frequency is lower would lead to over-prediction of FCG life.

References

1. J.F. Breedis, W.D. Robertson, *Acta Metall.* **10**, 1077–1088 (1962)
2. H. Fiedler, B. Averbach, M. Cohen, *Trans. ASM* **47**, 276–290 (1955)
3. R. Read, *Acta Metall.* **10**, 865–877 (1962)
4. A. Das, S. Sivaprasad, P.C. Chakraborti, S. Tarafder, Morphologies and characteristics of deformation induced martensite during low cycle fatigue behaviour of austenitic stainless steel. *Mater. Sci. Eng. A* **528**(2011), 7909–7914
5. J.J. Roa, G. Fargas, E. Jimenez-Pique, A. Mateo, Deformation of mechanism induced under high cycle fatigue tests in austenitic stainless steel. *Mater. Sci. Eng. A* **597**, 232–236 (2014)
6. A. Das, S. Das, Experimental investigation on martensite transformation and fracture morphologies of austenitic stainless steel. *Int. J. Plast.* **25**, 2222–2247 (2009)
7. Standard Test Methods for Measurement of Fatigue Crack Growth Rate, ASTM E 647-05
8. ASME, *Boiler Pressure Vessel Code, Section II: Materials*. Edition 2001
9. T.L. Anderson, *Fracture Mechanics, Fundamental and Applications* (Taylor and Francis Publishers, Oxford, 2005)
10. L.A. James, D.P. Jones, Fatigue crack growth correlations for austenitic stainless steels in air, in *Conference on Predictive Capabilities in Environmentally Assisted Cracking*, ASME PVP, vol. 99, 1985, pp. 353–414 (Presented at the Winter Annual Meeting of the American Society of Mechanical Engineers)
11. Y.S. Shih, J.J. Chen, The frequency effect on the fatigue crack growth rate of 304 stainless steel. *Nucl. Eng. Des.* **191**(1999), 255–230
12. Z. Khan, Stress-induced martensitic transformation in metastable austenitic stainless steels: effect on fatigue crack growth rate. *ASM Int. JMEPEG* **5**, 201–208 (1996)
13. ASME Boiler Pressure Vessel Code, *Section XI, In-service Inspection of Nuclear Power Plant Components*, Edition 2010

Fatigue Life Characterization of Additively Manufactured Acrylic like Poly-Jet Printed Parts

J. A. Suresh, Gurunathan Saravana Kumar, Palaniappan Ramu and Jayaganthan Rengaswamy

Abstract Application of additively manufactured components is gaining popularity in functional application. Several polymer-based additive manufacturing processes such as fused deposition modelling (FDM), selective laser sintering (SLS), stereolithography apparatus (SLA) and poly-jet printing to name a few cater to automotive to medical applications. Reliability in service of these components has to be ascertained for using them for functional application. The components made from additive manufacturing have inherent anisotropy due to the process characteristics such as build orientation and laser scanning/deposition tool paths. Literature reports fatigue life characterization mostly in FDM parts. In this work, a fatigue life analysis was carried out on components manufactured by poly-jet printed parts. Also, two build orientations were used to study the effect of this process parameter on the tensile strength and fatigue life. Other process parameters such as layer thickness, finishing type and polymer material were kept constant. A standard test specimen as per ASTM standard D7791–12 was prepared using Stratasys® Eden 350 V™ poly-jet printer using Veroclear 720™ material in two build orientations. The specimens were tested for tensile test and tensile–tensile fatigue cycles to failure at different stress levels. The test results were analysed to understand the fatigue life characteristics, and it was found that the process parameter variation has significant effect on the part strength (tensile) and reliability (fatigue failure). The fractured surface was analysed using SEM images to corroborate the inferences from test results.

J. A. Suresh · G. S. Kumar (✉) · P. Ramu · J. Rengaswamy
Department of Engineering Design, Indian Institute of Technology Madras,
Chennai 600036, India
e-mail: gsaravana@iitm.ac.in

J. A. Suresh
e-mail: rajsresh@iitm.ac.in

P. Ramu
e-mail: palramu@iitm.ac.in

J. Rengaswamy
e-mail: metarj@iitm.ac.in

Keyword Additive manufacturing • Mechanical test • Fatigue
Part build orientation

1 Introduction

Additive manufacturing (AM) is a unique alternative to traditional manufacturing techniques that embraces the concept of reducing product development cycles and shortening the time-to-market of new products [1]. AM has become a popular method to produce not only prototypes and moulds, but increasingly AM is being used to fabricate components for engineered products for a range of industrial applications. AM production of multimaterial components and devices is of considerable interest, as it allows the fabrication of elastomeric hinges, integrated grips and other products where material changes can achieve enhanced functionality [2], reduced part counts and streamlined assembly. The ability to selectively use several materials with different mechanical properties offers design freedom for producing final parts with tunable failure locus and resistance to fracture. Reliability in service of additively manufactured components has to be ascertained for using them for functional application. The components made from additive manufacturing have inherent anisotropy due to the process characteristics such as build orientation and laser scanning/deposition tool paths which lower the mechanical strength [3]. Also, since the part is fabricated layer by layer, staircase effect [4] reduces the surface finish [5] and also causes poor form tolerance [6].

The poly-jet direct 3D printing (PJD-3DP) system is an AM process that builds physical models from computer models with good surface finish by adding layers of photopolymer resin. This process uses simultaneous jetting of modelling materials to create physical prototypes [7]. The Stratasys[®] poly-jet process is a direct 3D printing process (direct 3DP) in which layers of photopolymer are printed onto the build platform via inkjet print heads (as described in Fig. 1). During printing, UV lamps (located on either side of the print head) cure the recently deposited photopolymer. The direct 3DP process differs from the more common indirect 3DP processes in that the build material is being jetted, rather than jetting a binder into a bed of build material.

Because there is no powder bed in direct 3DP processes, multiple materials can be printed in the same build—similar to the manner in which multiple colours can be printed with traditional inkjet printers. Stratasys[®] has developed a number of different photopolymers with differing degrees of stiffness, strength and transparency for various applications [8]. Several literatures are available in characterization of parts fabricated with poly-jet process such as surface finish [5] and part strength [4], to name a few. Literature reports fatigue life characterization mostly in FDM parts [9]. Since the literature on fatigue life analysis of poly-jet parts is limited [10], the present work was carried out to understand the same. Tensile and fatigue tests were carried out on ASTM D7791–12 specimens fabricated using Veroclear 720™ model material. Veroclear 720™ is a rigid photopolymer, nearly colourless

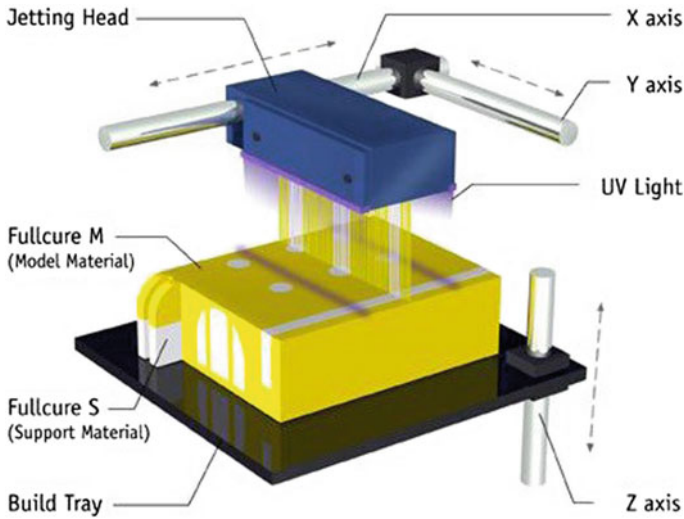


Fig. 1 Additive manufacturing using poly-jet process. Courtesy Stratasys®

material featuring proven dimensional stability for general purpose, fine-detail model building and visual simulation of transparent thermoplastics like PMMA. The authors also evaluated the effect of two different orientations on tensile and fatigue life for comparison. Rest of the paper discusses the details of methodology, results and inferences from the study.

2 Materials and Methods

Stratasys® Eden 350 V™ rapid prototyping machine was used to build parts to study tensile and fatigue characteristics and the effect of two part build orientation on the same. The models were built with the photopolymer Fullcure Veroclear 720™ model material and Fullcure 705™ support material supplied by Stratasys® company. Process parameters such as layer thickness, type of finish and build orientation are important factors affecting the surface finish and mechanical characteristics of poly-jet AM components [11]. Out of these factors, only build orientation is considered for the present study. Thus, for the present experimental study, these parameters were chosen as described in Table 1. The machine can

Table 1 Process parameters chosen for experiment and their levels

S. No.	Factors	Level-1	Level-2
1	Layer thickness, t (μm)	16	–
2	Type of finish	Matte	–
3	Build orientation, θ ($^\circ$)	0, 90, 0	90, 0, 0

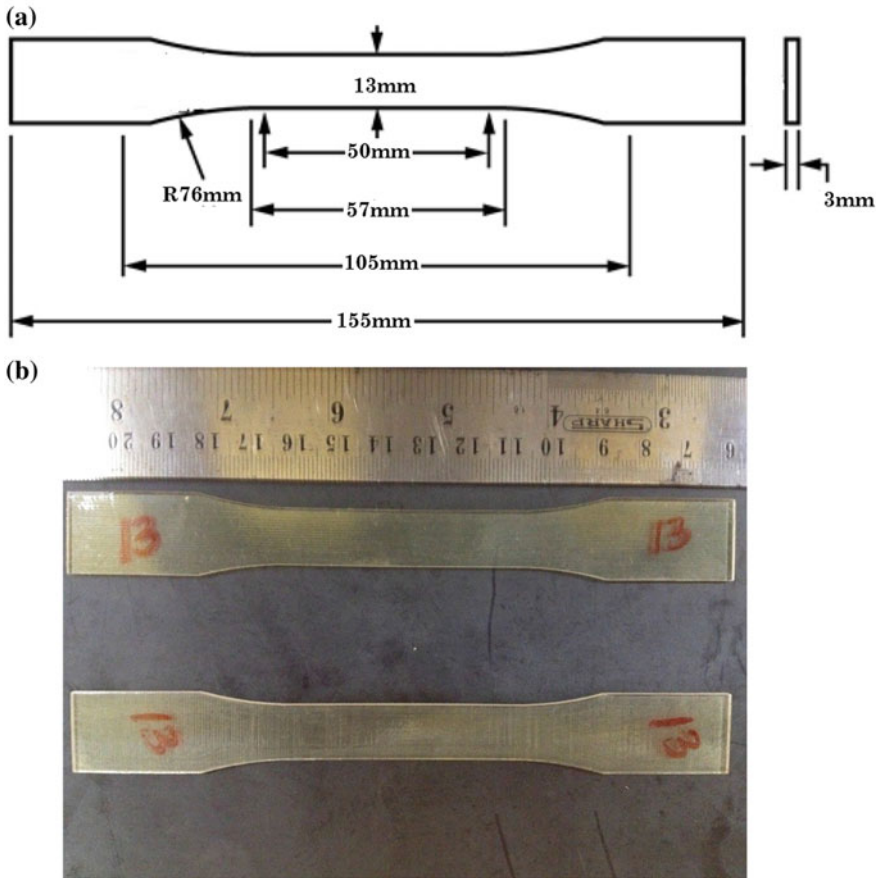


Fig. 2 a CAD model of tensile and fatigue coupon, b samples fabricated corresponding to two orientations (L1 and L2)

build parts in two layer thicknesses (16 and 32 μm) and two different finish types (matte and glossy). The parts (in this case tensile coupons) were built in two orientations as described in Table 1. The angle θ in ($^{\circ}$) is a vector that describes the built orientation; angle made by the longitudinal axis (pull direction) of the samples to the build table axes (X, Y and Z). In all two combinations of layer thickness, types of finish and build orientation were obtained. Henceforth, specimen built with level-1-built orientation (specimen axis parallel to X-axis) will be designated as L1 and the other as L2. The size of the specimens (shown in Fig. 2a) was designed as per ASTM D7791–12. The fabricated parts are shown in Fig. 2b. For each combination (L1 and L2), two parts (A and B) were built to get statistical concurrence.

The uniaxial tensile test was conducted using displacement controlled testing with a controlled ramp rate of 2 mm/min in a servo-hydraulic UTM. The fatigue tests were conducted with force-controlled tension–tension mode. The load form

chosen was sine wave with a frequency of 20 Hz. The fatigue tests were conducted till the failure, and the fractured surfaces were examined by SEM analysis to reveal the fracture details.

3 Results and Discussion

3.1 Tensile Strength

The tensile tests were performed at ambient conditions to obtain the tensile properties. The specimens used for this study were prepared to ASTM D638 standard as shown in Fig. 2. The specimens were first cleaned thoroughly to be free from the support material and any other foreign material. Two samples were tested in each case.

The results of tensile tests are provided in Table 2, and the stress strain graph is shown in Fig. 3. It can be observed that poly-jet printed parts exhibit very close UTS and yield point stress. It is also observed that the UTS of the L2 samples (built in perpendicular orientation L2) has slight improvement when compared with L1 sample (built in parallel orientation). The elongation of L1 specimens is longer than the L2 samples. This could be attributed to continuous polymerization of L1 along the axis of the specimen as compared to discontinuous polymerization (more than one pass) for the L2 samples.

3.2 Fatigue Strength

Fatigue strength of the material for both orientations was tested under tension-tension with force-controlled loading cycles axially. S-N plots were obtained from these tests. The fatigue experiments were carried out using a servo-hydraulic universal testing load frame. The test system is computer controlled with provision for data acquisition. The experiments were conducted in the ambient conditions. The tensile test results were used to select the stress levels for the fatigue tests. The R-ratios (ratio of the minimum stress over the maximum stress in a loading cycle) were selected in the range from 0.05 to 0.1 for the experiments. The specimen was tested until 10^6 loading cycles to obtain the fatigue limit at chosen stress levels.

Figure 4 shows the S-N curve for the L1 and L2 oriented samples. Four alternating stress levels were used in steps. Three samples were tested for each stress levels for both types of orientations. The fatigue limit is obtained at 8 MPa for the parallel-oriented specimens as against 9 MPa for perpendicular-oriented samples. Hence, there is a small improvement in fatigue life in perpendicular-oriented samples.

Table 2 Tensile properties of poly-jet printed parts

Specimen	Repeat code	Yield strength (MPa)	Average yield strength (MPa)	Tensile strength (MPa)	Average tensile strength (MPa)	% Elongation	Average % elongation
L1 (parallel orientation)	A	31.85	31.88	32.72	32.57	127	126.5
	B	31.92		32.43		126	
L2 (perpendicular orientation)	A	34.15	34.13	34.35	34.31	113	113.5
	B	34.12		34.27		114	

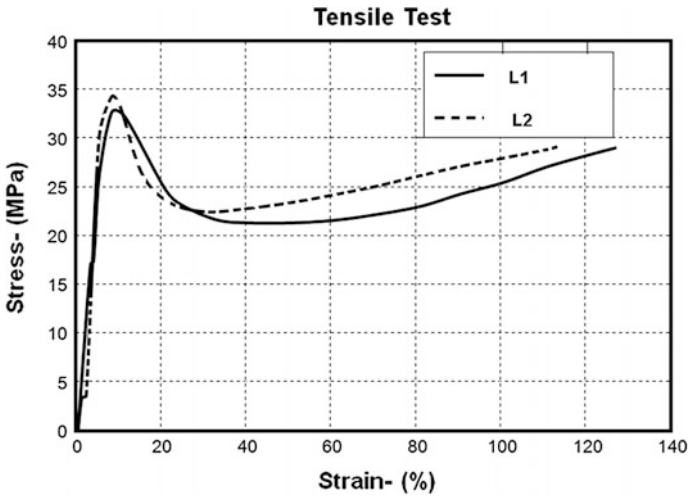


Fig. 3 Stress-strain (engineering) characteristics of poly-jet printed parts

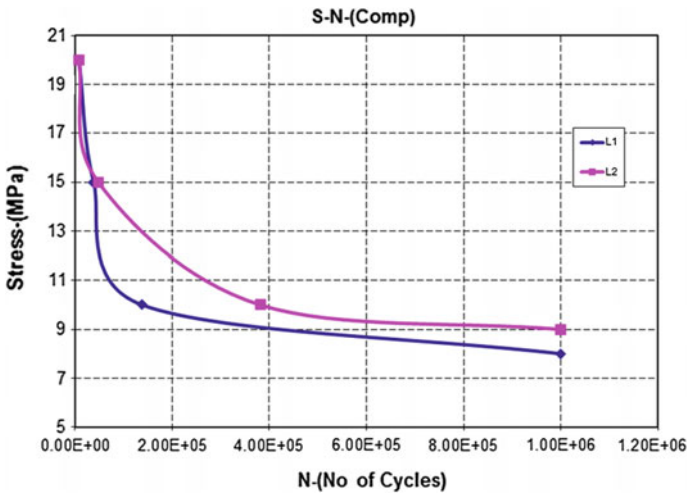


Fig. 4 S-N plot of poly-jet printed parts

3.3 Microstructural Observations

The samples for optical microscopy were sectioned from the printed samples for both parallel and perpendicular orientation of the samples. The sectioning of the samples was made methodically to preclude any damage or scratches that could occur on surface of the printed samples. The microstructure of the samples was characterized by an optical microscope (Carl Zeiss Axioskop series). The

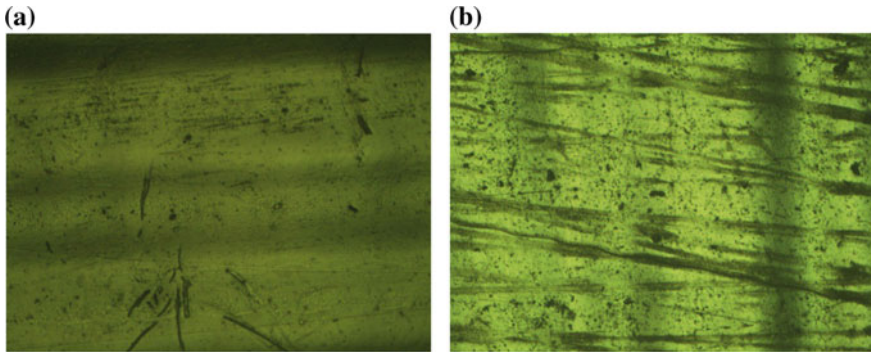


Fig. 5 Microstructure of printed samples at $50\times$ **a** parallel and **b** perpendicular oriented

calibration of the microscope was done as per the ASTM E1951–02 requirements. The samples were viewed at various magnifications to understand the influence of surface characteristics on fatigue strength of the printed material. The images obtained under different magnifications are shown in Figs. 5 and 6. The optical micrographs in Fig. 5a, b reveal the horizontal and vertical shades representing the L1 (parallel oriented) and L2 (perpendicular oriented) samples, respectively. The shades indicate the parallel and perpendicular micro-irregularities on surfaces of the samples. However, the optical micrographs in Fig. 6a, b show the presence of surface irregularities in both orientation of the samples, and especially microcracks were observed at the parallel-oriented samples. The microcracks were observed on entire surface on both sides of the sample.

The cross-sectional SEM images taken at parallel- and perpendicular-oriented samples are shown in Fig. 7a, b. It reveals that the irregularities such as tiny voids and microcracks are relatively less accounting for higher tensile and fatigue strength of the printed samples in the perpendicular-oriented samples as compared to parallel-oriented samples.

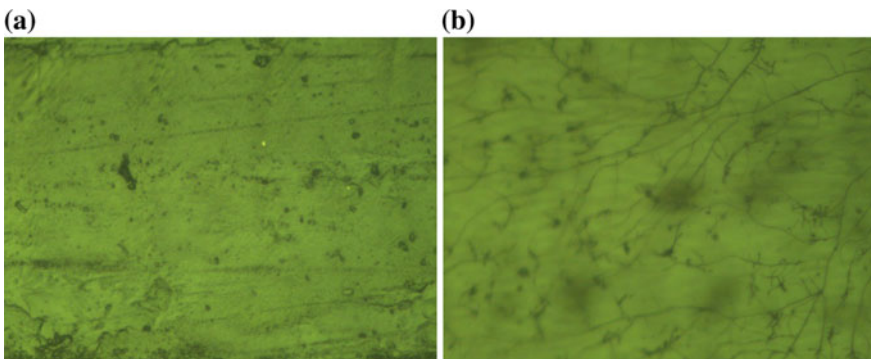


Fig. 6 Microstructure of printed samples at $400\times$ **a** parallel and **b** perpendicular oriented

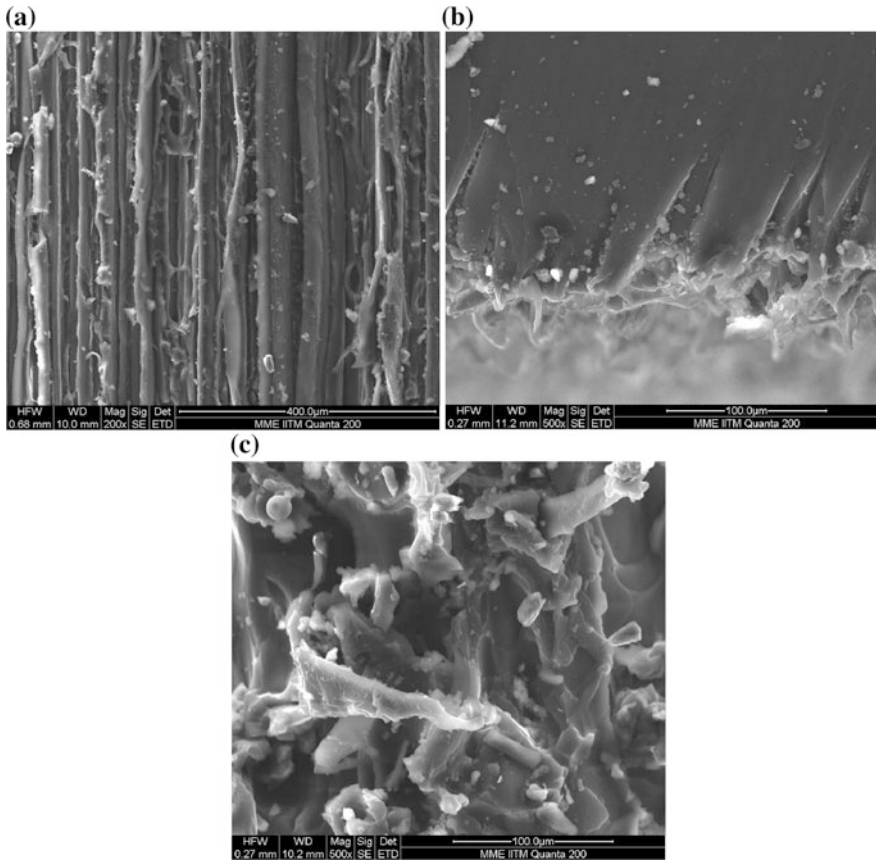


Fig. 7 SEM images of fatigue fracture surface **a** parallel oriented, **b** perpendicular oriented and **c** higher magnification of fracture surface

Since the printing is carried out layer-by-layer deposition of Veroclear in the present work, the interface with various geometrical features and irregularities is inevitable as observed in the present work. The orientation of cracks and applied load in the parallel-oriented samples could facilitate the crack propagation rate slightly faster than the perpendicular-oriented samples. The crack branching and fibre pull out and its misorientation could slow down the crack movements in perpendicular-orientated samples as evident from the SEM cross-sectional samples.

4 Conclusion

Poly-jet printer was used to fabricate three-dimensional parts using Veroclear polymer in two different build orientations in the present work. The tensile and fatigue tests of the printed samples were performed to evaluate its strength and fatigue life in both parallel and perpendicular orientations. The mechanisms of improvement in strength and fatigue life of samples were substantiated using optical and SEM characterization of surface morphology and fracture surface. The perpendicular-oriented samples exhibit higher tensile and fatigue strength as compared to parallel-oriented samples as evident from the surface morphological and cross-sectional characterization of samples made by SEM. The multipass deposition and polymerization of printed resins in the poly-jet printing accounts for the anisotropy in strength and fatigue life seen in the present work. The interface with varying surface roughness and voids' formation in the printed parts ought to be tailored for improving the fatigue life. The study is a pilot study, and the results need to be augmented with experiments involving larger sample size for statistical validity.

References

1. Objet Inc., 3D printing & rapid prototyping by Objet Ltd., in *3D Printing & Rapid Prototyping by Objet Ltd.* (2012). Available: <http://www.objet.com/>. Accessed 12 July 2012 (Online)
2. I. Gibson, D.W. Rosen, B. Stucker, *Additive Manufacturing Technologies: Rapid Prototyping to Direct Digital Manufacturing* (Springer, 2009)
3. B. Caulfield, P. McHugh, S. Lohfeld, Dependence of mechanical properties of polyamide components on build parameters in the SLS process. *J. Mater. Process. Technol.* **182**, 477–488 (2007). ISSN 0924-0136
4. O.S. Es-Said, J. Foyos, R. Noorani, M. Mendelson, R. Marloth, Effect of layer orientation on mechanical properties of rapid prototyped samples. *Mater. Manuf. Process.* **15**(1), 107–122 (2000)
5. D. Ahn, J.H. Kweon, S. Kwon, J. Song, S. Lee, Representation of surface roughness in fused deposition modeling. *J. Mater. Process. Technol.* **209**, 5593–5600 (2009)
6. B. Lee, J. Abdullah, Z. Khan, Optimization of rapid prototyping parameters for production of flexible ABS object. *J. Mater. Process. Technol.* **169**, 54–61 (2005). ISSN 0924-0136
7. S. Ashley, Rapid prototyping systems. *Mech. Eng.* **113**(4), 34 (1991)
8. T. Wohlers, T. Gornet, *History of Additive Manufacturing*. Wohlers Report (2014). <http://wohlersassociates.com/history2014.pdf>
9. J. Lee, A. Huang, Fatigue analysis of FDM materials. *Rapid Prototyp. J.* **19**(4), 291–299
10. E. Brandl, U. Heckenberger, V. Holzinger, D. Buchbinder, Additive manufactured AlSi10 Mg samples using selective laser melting (SLM): microstructure, high cycle fatigue, and fracture behavior. *Mater. Des.* **34**, 159–169 (2012)
11. K. Puebla, K. Arcaute, R. Quintana, R.B. Wicker, Effects of environmental conditions, aging, and build orientations on the mechanical properties of ASTM type I specimens manufactured via stereolithography. *Rapid Prototyp. J.* **18**(5), 374–388 (2012)

Part IX
Material Processing

Influence of Machining Process on Surface Integrity and Fatigue Life of a Turbine Rotor Blade

Benudhar Sahoo, S. K. Panigrahi and R. K. Satpathy

Abstract Turbine blades of a military gas turbine are one of the most safety-critical components as per MIL-STD-1783 as its failure cannot be contained by engine casing in case of failure. Statistic tells, the major failure of the turbine blade is due to fatigue. Further, both the surface integrity and structural integrity of a turbine blade only can be assessed by full-scale testing. This study deals with a turbine blade made of a wrought nickel base alloy AP220BD of a military gas turbine engine. The primary shape of the blade is achieved by closed die forging followed by machining of the aerofoil profile. Two machining processes, namely (i) Non-conventional machining ECM process and (ii) Conventional CNC milling, have been adopted to get the finished shape of the blade. Aluminising coating by pack cementation method was deposited to provide oxidation resistance. Surface integrity of the blade has been evaluated by visual inspection of the surface, roughness, surface residual stress and microhardness survey from the surface to subsurface. X-ray diffraction method has been adopted to measure the residual stress. Full-scale fatigue testing of the turbine blades machined by both the processes has been conducted following incremental amplitude Armstrong method. Comparison of fatigue life has been carried out statistically using Student's t test. The fractographic study has been made both under low magnification and high magnification. SEM could reveal the initiation point and crack propagation mode. Turbine blades machined by ECM gave a higher tensile surface residual stress and lower fatigue life. Blades machined by ECM reveal multiple crack initiation while blades machined by CNC milling shows few cracks. There is a distinct separation of progressive and overload failure region during the fractographic study. However, the ECM process needs to be optimised, and subsequent surface treatments also need to be improved to have enhanced fatigue life.

B. Sahoo (✉) · R. K. Satpathy
DRDO, RCMA, Sunabeda, Koraput 763002, India
e-mail: bsahoo543@gmail.com

S. K. Panigrahi
Defence Institute of Advanced Technology (DU), Pune, India

Keywords Turbine rotor blade • High cycle fatigue • Electrochemical machining
Residual stress • Armstrong method • HCF • ECM • CNC

Nomenclature

HCF High cycle fatigue
ECM Electrochemical machining
CNC Computer numerical control

1 Introduction

Turbine rotor blades of a military gas turbine are designed against high cycle fatigue (HCF) with the major source of HCF is vibration [1]. As per MIL-5007E, the rotor blades are subjected to vibration fatigue test at its resonance condition for 2×10^6 cycles for qualifying blade life [2]. Turbine rotor blades are made of nickel-base alloys for their outstanding high-temperature strength and excellent manufacturability. Because of the lengthier configuration of low-pressure turbine rotor (LPTR) blade, undue loading due to vibration is an important consideration for its life. Non-conventional machining process such as electrochemical machining (ECM) was adopted as a metal removal process for its faster removal rate. With the significant advancement in computer numerically controlled (CNC) machining process, it is replacing the non-conventional machining process for its improved accuracy and repeatability. Also, it is becoming an alternative as a green manufacturing process against the malign effect of ECM process on the environment.

The present investigation deals with the influence of ECM process and CNC milling process on surface integrity and fatigue life of a turbine rotor blade.

2 Experimental Detail

Wrought nickel base alloy AP220BD of Russian origin having a typical chemical composition in weight percentage: Ni-15Co-10Cr-6Mo-6 W-2.5Ti-4.3Al-0.6 V- 0.03C in the cold-rolled condition has been used for manufacturing the LPTR blade by envelope forging. Two machining processes, namely ECM and CNC milling, have been adopted to generate the aerofoil profile from the blade forging. In ECM process, both the suction surface and pressure surfaces are machined at the same setting followed by grinding to remove the surface unevenness. Sodium chloride is being used as the dielectric fluid during ECM process with the stainless steel electrodes. Aerofoil surface of turbine rotor blade has been generated by 5-axis CNC milling process using a machine of make HX-253S Switzerland with the help of rigidid cam software (RCS). The finished shape was achieved in three passes using carbide

tool followed by buffing to achieve a mirror finish. The blades are provided with an aluminising coating of 30–40 μm thickness to resist oxidation and high-temperature corrosion. The coating was deposited by diffusion technique using low-activity pack cementation process. The turbine blades are put in a metal retort in a pack consists of inert oxide Al_2O_3 , halide salt NH_4Cl and FeAl powder [3].

Vibration fatigue testing of blades using incremental amplitude method suggested by Dr. Armstrong is based on Miner's hypothesis. The stress is simulated by the af level where a —amplitude of vibration and f —frequency of vibration. The initial af is 1.0 ft/s while the each increment af is 0.5 ft/s and the dwell period at each " af " level is 30 min. The test is continued till failure of the blade.

2.1 Test and Checks

As fatigue is predominantly a surface phenomenon, surface roughness and microhardness checks have been carried out to characterise the surface [4–6]. Full-scale fatigue testing of a turbine blade by vibration fatigue method following Armstrong staircase has been adopted to evaluate its life.

3 Results and Analysis

The topography of the surface of the blade influences HCF life most. The surface texture is also affected by the machining parameters. The undulation in the surface acts as a stress concentrator and initiates fatigue failure. The hardness of the blades indicates the strength and the surface residual stress. The two critical surface features influencing fatigue life, i.e. surface roughness and microhardness were measured on the blades manufactured by both the routes.

3.1 Surface Roughness

See Table 1.

3.2 Microhardness

The full aerofoil profile was covered by measuring hardness at seven locations as depicted in Fig. 1 using microhardness tester make: TUKON TM1162 with a load of 100 g. The hardness survey was carried out from the top of the coating into the blades at a depth of 20 μm till attaining 100 μm as shown in Fig. 2, and the

Table 1 Surface roughness of blades produced by ECM and CNC milling process

<i>(a) ECM process: surface roughness (Rz) in μm</i>			
	Root	Middle	Top
Suction surface	2.055–2.51	1.65–1.829	3.737
Pressure surface	1.432–1.80	2.418–2.665	3.63
<i>(b) CNC milling: surface roughness (Rz) in μm</i>			
	Root	Middle	Top
Suction surface	0.915	1.13–1.865	1.34
Pressure surface	1.201	1.073	2.46–2.82

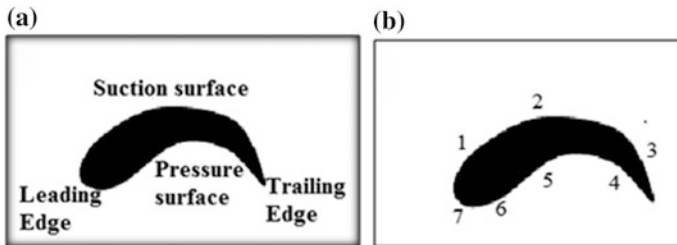


Fig. 1 Sketches showing blade aerofoil for hardness measurement **a** sections of blade and **b** locations for hardness measurement

hardness impressions are shown in Fig. 3. Pressure surface exhibited higher hardness compared to the suction surface. The maximum hardness on suction surface and pressure surface is found to be 758 and 830 HV, respectively. Maximum hardness was observed on the coating layer. The maximum hardness and hardness gradient over the blades manufactured by ECM are found to be more compared blades machined by CNC milling process as reflected in Fig. 2.

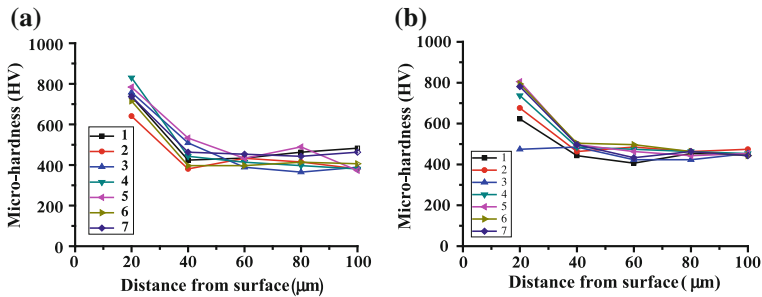


Fig. 2 Variation of microhardness in the aerofoil of turbine rotor blades **a** electrochemical machining **b** CNC milling

Aluminising coating being brittle provides the highest hardness in comparison with the substrate, i.e. nickel base wrought alloy AP220BD. Aluminising coating gets deposited by a diffusion process, and the surface energy of the substrate does influence the rate of diffusion. As ECM and CNC milling yield different levels of surface energy, the same will be reflected in the coating and to a lesser degree in hardness. But HCF life gets significantly affected by the surface and subsurface condition, therefore, different machining operations such as ECM and CNC milling results in different fatigue performance.

3.3 Residual Stress

Surface residual stress was determined by the X-ray diffraction residual stress analyser, Proto automated XRD system and service manufacturing, using Mn-K α tube with detector angle of 156.32° and collimator of higher diameter in the range of 3–5 mm. The turbine rotor blade was divided radially into three sections, namely root, middle and tip. Also, it was divided laterally into three sections, namely leading edge, trailing edge and middle portion as shown in Fig. 4. A full profile of the blade has been mapped for residual stress measuring nine points each on pressure surface and suction surface.

Residual stress on the pressure surface ranges from –93 to 277 MPa for blades produced by ECM route and from –685.5 to 176.4 MPa for blades produced by CNC milling. Residual stress on the suction surface varies from –83 to –225 MPa and –131.8 to –368.9 MPa for blades produced by ECM route and CNC milling routes, respectively. The maximum stress was observed near the fir-tree root towards the leading edge. Ozel and Ulutan reported that residual stress increases with an increasing cutting tool radius and coated tools show less residual stress at the surface than at subsurface [7]. Residual stress varies during lifetime and depending on thermal energy or mechanical energy imparted to the surface. Under the application of mechanical and thermal energy, elastic deformations associated

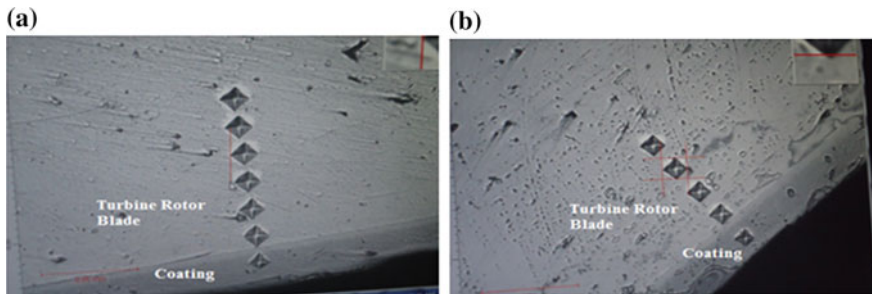


Fig. 3 Microhardness impressions on turbine rotor blades showing coating and blade **a** electro-chemical machining **b** CNC milling

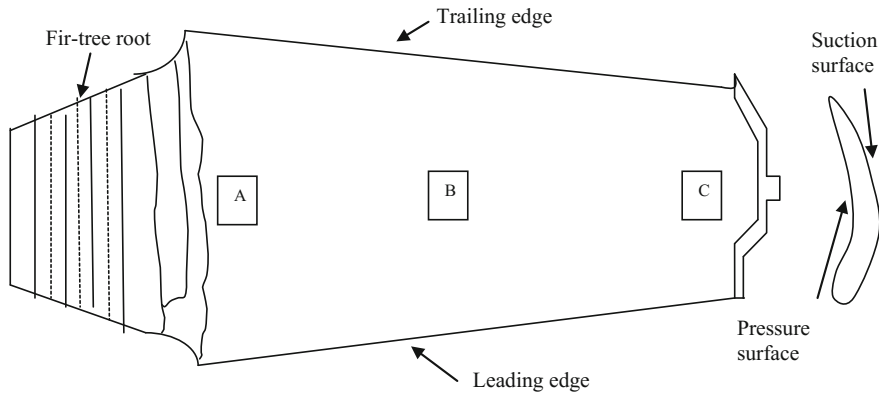


Fig. 4 Schematic diagram showing section of a turbine blade for residual stress measurement

with residual stress relax in case of plastic deformation. Under the application of elastic load, tensile strength remains stable but this increases when the load is increased close to yield strength of the material [8].

3.4 Fatigue Life Evaluation of Turbine Rotor Blades

Various machining processes modify the surface in terms of residual stress pattern, plastic deformation, micro-cracking, etc. which in turn influence the fatigue life. The turbine rotor blade is subjected to vibratory fatigue testing in bending mode under constant stress. It has been reported by Pervey and Koster that relative behaviour of materials under combined tension–tension loading is approximate to the cantilever bending [9]. Full-scale fatigue testing under resonance condition is a well-proven method for evaluating the HCF life of turbine blades [10]. The maximum stress at the root of a turbine rotor blade during fatigue testing under cantilever loading is expressed in Eq. (1) [11] by

$$\sigma_{\max} = 2\pi y k \sqrt{E\rho} a f \quad (1)$$

where

- a leading edge tip amplitude
- f frequency of vibration
- k radius of gyration of the root section of the blade
- y distance from neutral axis to the point of maximum stress
- E Young's modulus
- ρ density

Table 2 Fatigue test results of blades **a** ECM and **b** CNC milling process

<i>(a) ECM process</i>			
S. No.	Frequency (Hz)	Failing “ <i>af</i> ”	Time at failed <i>af</i> (min)
1	334.7	3	25
2	335	3.5	15
3	335.5	3	10
4	334.4	3	20
5	331.7	3	25
6	331.5	3	10
<i>(b) CNC milling</i>			
1	328	3	25
2	344	3.5	10
3	341	3.5	15
4	333	3.5	10
5	337	3	20
6	337.5	3	30

Therefore, “*af*” (amplitude × frequency) is a convenient way of comparing the fatigue life of blades produced by different manufacturing process suggested by Armstrong [11]. Full-scale fatigue testing under resonance condition is a well-proven method for evaluating the HCF life of turbine blades [9]. The turbine rotor blade has been subjected to fatigue testing by Armstrong incremental amplitude method. It is based on cumulative damage rule of Miner’s hypothesis. In this method, a single specimen is tested till failure with incremental amplitude having subjected to an equal number of cycles at each test amplitudes. In the present investigation, the initial “*af*” level was 1 ft/s. The natural frequency failing *af* and time at failed “*af*” has been tabulated at Table 2 for blades produced by ECM and CNC milling routes, respectively.

3.4.1 Estimation of Fatigue Life

The fatigue life has been evaluated by incremental amplitude Armstrong method. Using Miner’s hypothesis of cumulative damage rule, incremental amplitude fatigue life has been converted into life at constant “*af*” in Eq. (2) [12].

$$S \times N^c = S_r \times N_s^c \left[(N_r/N_s) + \left((r - 1/r) \right)^{\frac{1}{c}} + \left((r - 2/r) \right)^{\frac{1}{c}} + \dots + \left((2/r) \right)^{\frac{1}{c}} + \left((1/r) \right)^{\frac{1}{c}} \right]^c \tag{2}$$

where

- S Stress level at which life is calculated, here 1 ft/s
 N Life at constant stress level S
 S_r Final or failure amplitude level in ft/s
 N_r No. of reversal completed at failure amplitude
 N_s No. of reversal completed at other incremental amplitude
 r No. of steps from 1.0 “ af ” to failure, i.e. (maximum amplitude/incremental amplitude)
 $(1/c)$ fatigue exponent coefficient.

3.4.2 Sample Calculation for Log Life of Blade

The blade sl no. 1 produced by ECM process was having its natural frequency of vibration as 334.7 Hz, and the failed “ af ” was 3.0 ft/s with a dwelling for 25 min at the failed amplitude. Using Eq. (2), the log life at unit “ af ” level was found to be 9.194103.

Similarly, the fatigue log life for all the sample six blades produced by ECM and CNC milling batch has been calculated.

3.4.3 Statistical Analysis of Fatigue Life

The fatigue life lies in a log-normal distribution and the sample size, i.e. six (06) is small compared to the population size of the blades. Therefore, the analysis of variance (Students “ t ”-value) has been adopted to compare the fatigue life of the blades produced by both the processes.

The “ t ” value is calculated using Eq. (3) [12] with the mean and standard deviation (SD) of the turbine rotor blades produced by both the routes

$$t = \frac{(\bar{X}_a - \bar{X}_b)}{\sqrt{\left(\frac{1}{N_a} + \frac{1}{N_b}\right) \left[\sqrt{\left(\frac{N_a \times SD_a^2 + N_b \times SD_b^2}{N_a + N_b - 2}\right)} \right]}} \quad (3)$$

- \bar{X}_a Mean life of blades produced by ECM
 \bar{X}_b Mean life of blades produced by CNC Milling
 SD_a Standard deviation of blades produced by ECM
 SD_b Standard deviation of blades produced by CNC Milling
 N_a Sample size of blades produced by ECM
 N_b Sample size of blades produced by CNC Milling

The mean log life (\bar{X}_a) and standard deviation (SD_a) of the blades produced by ECM process are 9.251717 and 0.507564, respectively. The mean log life (\bar{X}_b) and standard deviation (SD_b) for the blades produced by CNC milling process are 9.713233 and 0.528702, respectively. The degree of freedom is ten.

The “*t*” value with 95% probability and degree of freedom ten is found to be from the statistical chart as 2.23. The calculated value of “*t*” for the blades produced by ECM route and CNC milling (for 1 in 10,000 at 95% confidence intervals) is found to be 1.24 and 1.24, respectively. This is less than the reference value of 2.4 indicating that there is no significant difference in fatigue life of the blades produced by both the routes.

Statistically, both the processes are comparable; however, the blades produced by CNC route provide superior fatigue life in comparison with blades produced by ECM route. It is also confirmed from the literature that there is approximately 30–40% reduction in fatigue life of components produced by ECM process.

4 NDT of Turbine Blade Post-fatigue Test

Blades after fatigue test have been subjected to FPI (Fluorescent penetrant inspection) to reveal the cracks. It was found that cracks are initiating near the root of the blade on the LE (leading edge) on all the twelve blades as shown in Fig. 5.

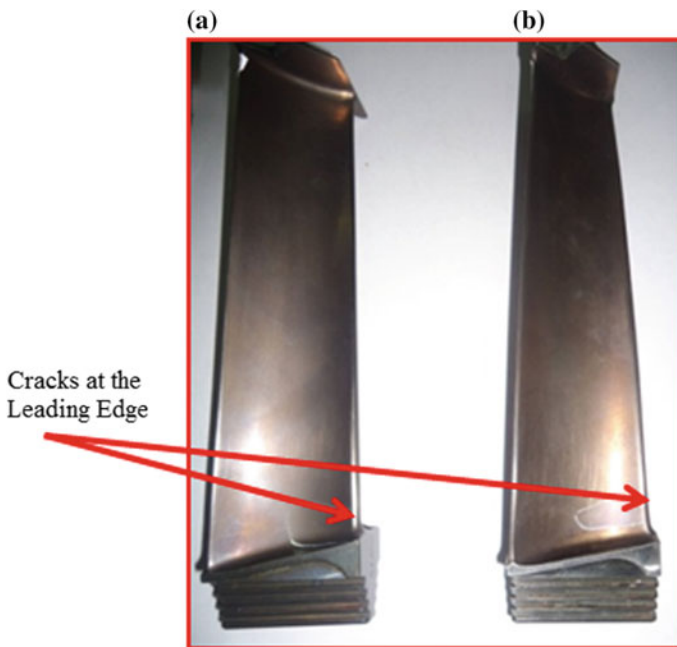


Fig. 5 Cracks at the leading edge on failed blade after vibration fatigue test **a** ECM, **b** CNC milling

5 Fractography

Turbine blades post-fatigue test were cut along the failed plane to examine the fatigue origin and crack propagation. There is a separation between progressive failure region and overload failure region. The progressive failure is designated as fatigue failure region as shown in Fig. 6. There is a half-moon cut region of the blade where fatigue crack propagated and fatigue is the dominant damage mechanism. The origin of fatigue is at the pressure surface near leading edge. The magnified view of the fatigue cracks was shown in Fig. 7 for clarity.

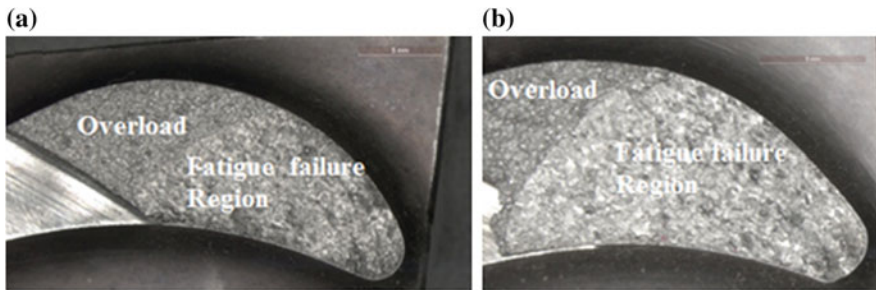


Fig. 6 Fracture surface of the blade after fatigue test for both the manufacturing processes at low magnification a ECM and b CNC milling

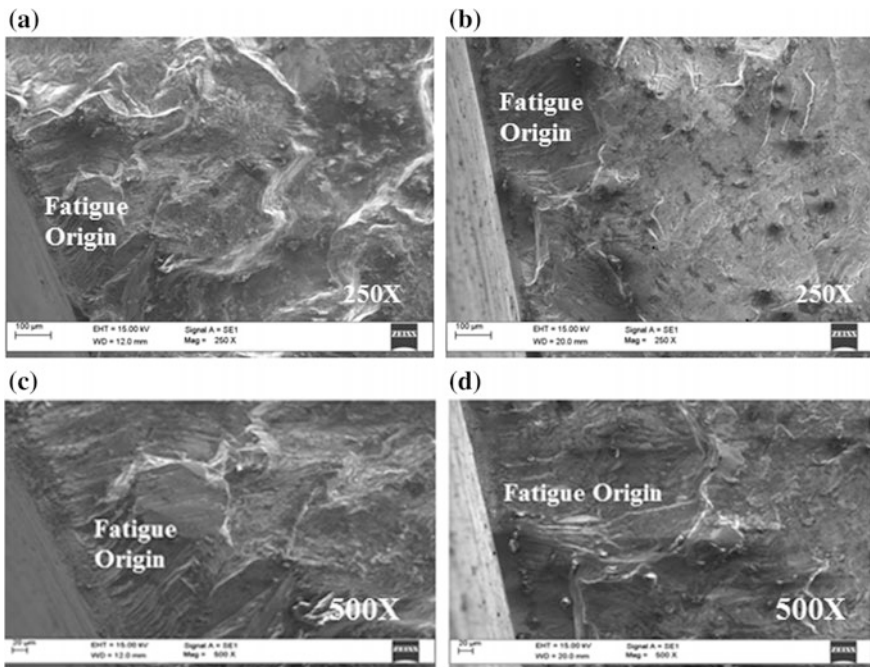


Fig. 7 Fatigue origin in turbine blade of different machining processes a and c ECM and b and d CNC milling

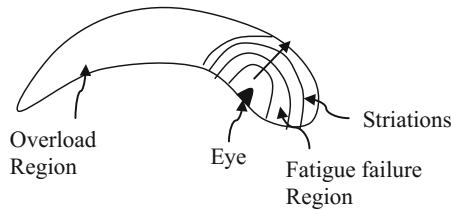


Fig. 8 Sketch showing various features of fatigue failure of turbine blade observed under SEM with arrow showing direction of propagation of fatigue crack

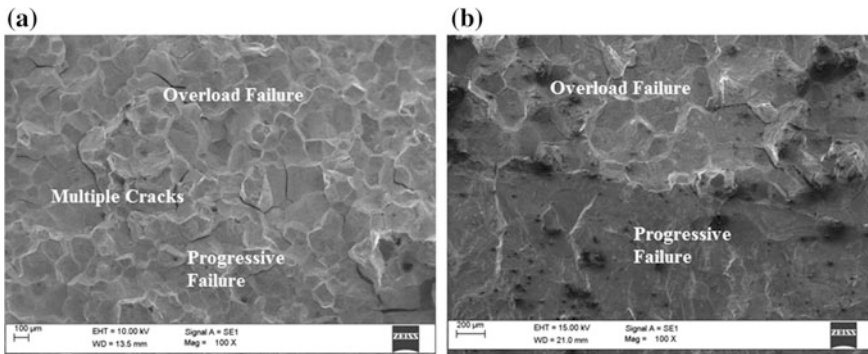


Fig. 9 SEM fractograph showing cracks in turbine blades manufactured by different machining processes **a** ECM showing multiple cracks and **b** CNC milling showing only one crack

Sketch showing fatigue failure region, overload failure region and a half-moon cut shape of the fatigue region with its eye on the pressure surface near leading edge has been shown in Fig. 8. This is a typical fatigue feature of HCF failure.

Examination of overload region of turbine blade machined by ECM route revealed many secondary cracks compared only one crack in blade machined by CNC milling route as shown in Fig. 9.

The surface roughness of pressure surface of blades machined by ECM process is found to be less compared to the suction surface while the reverse trend was observed on blades machined by CNC milling process. However, in both the cases, fatigue failure has from the pressure surface near leading edge. From the above observations, it can be inferred that influence of surface roughness is not significant on fatigue life of turbine blade tested at room temperature. Similar findings have been reported by Pervey and Koster on HCF life [9]. Microhardness is influenced by the residual stress. The average microhardness of the suction surface is found to be less compared to that of pressure surface. Residual stress on the suction surface is of compressive in nature while that of pressure surface is tensile. The literature on the relation between residual stress with microhardness reveals that there is an increase in hardness value with compressive stress for medium carbon steel

investigated by Tosha [13]. However, the crack location by NDT is experiencing maximum the tensile stress of pressure surface. The origin of fatigue is at the region of maximum tensile stress. The fatigue failure region looks like a half-moon cut with its eye on the pressure surface confirms a typical HCF failure.

6 Conclusions

Following conclusions were made from the present investigation:

- (a) The maximum level of *af* the blades survived is 3.5 ft/s. Out of the six blades produced by ECM route, only one blade could survive up to *af* of 3.5, while four out of six by CNC Milling route.
- (b) The origin of fatigue is near the leading edge at the pressure surface. There is separation between progressive failure and over load failure region.
- (c) Higher level of residual tensile stress of the blades machined by ECM route caused lower fatigue life during blade testing.
- (d) The maximum stress location approximately coincides with the crack location as detected by dye penetrant test (DPT).
- (e) The half-moon cut region is a typical fatigue feature of turbine blades failing under high cycle fatigue (HCF).

Turbine rotor blades produced by CNC milling route are found to be superior in terms of fatigue life.

Acknowledgements The authors acknowledge the support rendered by HAL, Koraput. The encouragement and guidance from the Chief Executive (A) and Group Director (propulsion), CEMILAC, Bangalore, are sincerely acknowledged.

References

1. B.A. Coweles, High cycle fatigue in aircraft gas turbines-an industry perspective. *Int. J. Fract.* **80**, 147–163 (1966)
2. Military Specification, MIL-E-5007D, pp. 30–31 (1973)
3. C.T. Sims, W.C. Hagel, The super alloys. Chapter-(12), in *Coatings and Protection* (Wiley Science Publication), pp. 341–370
4. D. Ulutan, T. Ozel, Machining induced surface integrity in titanium and nickel alloys: a review. *Int. J. Mach. Tools Manuf.* **51**, 250–280 (2011)
5. M.C. Hardy, C.R.J. Herbert, W. Li, D.A. Axinte, A.R.C. Sharaman, A. Encinas-Oropesa, P.J. Withers, Characterising the integrity of machined surfaces in a powder nickel alloy used in aircraft engines. *Procedia CIRP* **13**, 411–416 (2014)
6. R.M. Saoubi, J.C. Outeiro, O.W. Dillon Jr, J.S. Jawahir, A review of surface integrity in machining and its impact on functional performance and life of machined products. *Int. J. Sustain. Manuf* **1**(1/2), 203–236 (2008)

7. T. Ozel, D. Ulutan, Prediction of machining induced residual stress in turning of titanium and nickel based alloys with experiment and finite simulation. *CIRP Ann.-Manuf. Technol.* **61**, 547–550 (2012)
8. A. Madariaga, D.J. Arrazoa, J.A. Esnaola, J. Ruiz-Hervias, P. Munoz, Evolution of residual stress induced by machining in a nickel based alloy under static loading at room temperature. *Procedia CIRP* **13**, 175–180 (2014)
9. P.S. Pervey, W.P. Koster, Effect of surface integrity of fatigue of structural alloys at elevated temperature. *ASTM STP* **520**, 522–531 (1973)
10. J. Tommy, J. Seidt, M.-H. Herman Shen, T. Nicholas, Development of a novel vibration-base fatigue testing methodology. *Int. J. Fatigue* **26**, 477–486 (2004)
11. E.K. Armstrong, R.E. Stevenson, *J. R. Aeronaut. Soc.* **64**(592), 117–130
12. Fatigue testing of turbine blade schedule Adour 811 Report No. E/EKA/34960
13. K. Tosha, Influence of residual stress on the hardness number in the affected layer produced by shot peening, in *Second Asia-Pacific Forum on Precision Surface Machining and Deburring Technology*, Seoul, Korea, pp. 48–54 (2002)

Spark Plasma Sintering Process as a Tool for Achieving Microstructural Integrity

P. Parameswaran, T. Ezhilarasi, Srinivasa R. Bakshi, V. Thomas Paul and E. Mohandas

Abstract The fact that real materials are not perfect crystals, is critical to materials engineering as the presence of crystalline defects is the most important feature of the microstructure which influences the mechanical properties. Exposure of materials to high temperature for long duration would result in structural failure, when a sub-size crack grows into a critical level. This paper concentrates on the novel application of spark plasma sintering (SPS) technique in achieving microstructural integrity of materials by crack closure using the superior capability of SPS for annealing the defects in materials. Due to the presence of applied compressive stress, expansion is restricted and brings about the closure of cracks. The crack surfaces then come in contact with each other, and energization between the crack surfaces causes them to bond. The presentation would bring about the nature of bonding achieved through SPS when two model systems, diffusion bonding of stainless steel discs and stainless steel with ferroboration powder, were considered and highlighted its applicability through systematic optimization.

Keywords Spark plasma sintering · Diffusion bonding · Microstructural integrity

P. Parameswaran (✉) · T. Ezhilarasi · V. Thomas Paul · E. Mohandas
Metallurgy and Materials Group, Indira Gandhi Centre for Atomic Research,
Kalpakkam 603102, Tamil Nadu, India
e-mail: param1961@gmail.com

T. Ezhilarasi
e-mail: ezhila.t@gmail.com

V. Thomas Paul
e-mail: thomaspauly@gmail.com

E. Mohandas
e-mail: mohandas.eladath@gmail.com

S. R. Bakshi
Department of Metallurgical and Materials Engineering, Indian Institute of Technology
Madras, Chennai 600036, India
e-mail: sbakshi.iitm@gmail.com

1 Introduction

The properties of materials are greatly affected by their microstructure, which may contain defects ranging from point defects to three-dimensional defects. Prolonged high-temperature exposure of materials may lead to structural failure, when a microcrack grows into a critical level. This paper concentrates on the novel application of spark plasma sintering (SPS) technique in achieving microstructural integrity of materials by crack closure using the superior capability of SPS for annealing the defects in materials through diffusion bonding.

Since the bonding process involved in crack closure that occurs between two different planar surfaces is basically driven by mass diffusion, model studies were carried out to simulate the crack closure problem. Diffusion bonding employing pressure and temperature, the interface region formed would exhibit a gradation in microstructure. This gradient could be reduced if the heating rate and holding time were reduced. In this respect, spark plasma sintering is expected to provide a good alternative method for diffusion bonding [1]. We have shown using model experiments that cracks could be closed by SPS by a diffusion bonding phenomena. Further, by using the process, composite discs of SS with ferroboron powders sandwiched in between are subjected to SPS in order to study the feasibility of obtaining compacts that have sufficient strength and porosity for use as control rod materials in fast reactors. The studies show that SPS can be a fast process for achieving these objectives.

Present study aims at manipulation of diffusion bonding parameters: temperature, holding time and applied pressure and examination on the achievement of structural integrity in terms of uniformity in microstructure and hardness.

2 Experimental Details

When spark discharge appears in the gap between the materials of compact, a local high-temperature state occurs. This causes vaporization and melting of the surfaces during the SPS process. Constricted shapes or “necks” are formed around the contact area between the particles. These necks gradually develop, and plastic deformation progresses during sintering resulting in a sintered compact of over 99% density. Since only the surface temperature of the particles rises rapidly by self-heating, particle growth of the starting powder materials is limited to a great extent.

A stack of 4 SS discs of 500 μm thickness was tightly held by an initial pressure by placing them in a graphite die. Experimentation was carried out in a vacuum chamber at different temperatures of 900, 1000 and 1100 $^{\circ}\text{C}$. A pressing force of 30 MPa is applied at the beginning of the SPS cycle and held constant throughout the process. The sample was heated to the desired temperature at the heating rate of 100 $^{\circ}\text{C}/\text{min}$ and held at that temperature for the dwell time of 5 min. For the second

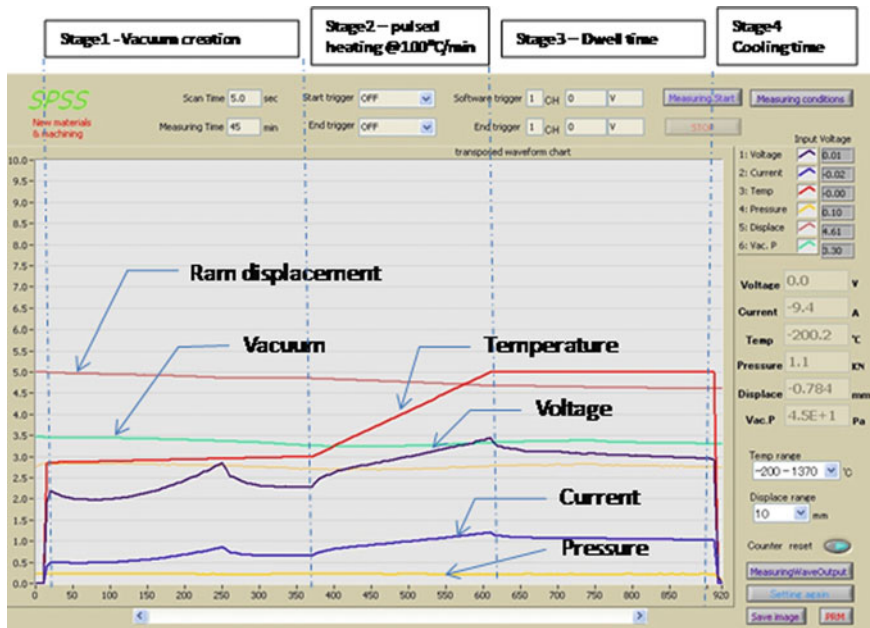


Fig. 1 Recording of process parameters

case, FeB powder is placed between stainless steel discs and sintered at a temperature of 900 °C keeping the other process parameters same as the previous experiment. A typical SPS processing schedule is shown in Fig. 1 along with the recording of process parameters during the process.

The bonded specimens were sectioned and prepared for metallography by conventional processes of successive grinding and polishing, followed with electrolytic etching in oxalic acid. Scanning electron microscopy (SEM) studies were carried out by M/s FEI-XL30 SEM. Further, a hardness profile across the sample was generated by measuring at an interval of 100 μm using Vickers microhardness tester employing an applied load of 100 g.

3 Results and Discussion

3.1 Case Study 1: Similar Materials

The process parameters during the experiment were monitored and given in Fig. 1, which clearly shows that the pressure and vacuum were constant throughout the process. On the other hand, a minor decrement in the ram displacement of $\sim 500 \mu\text{m}$ suggests that bonding is achieved as the initial height being 5 mm is reduced to 4.5 mm. When the discs were kept in contact, the gap was present which

gets closed and resulted in bonding. The overall reduction from the geometry of the compact in terms of the height is 500 μm which in comparison with original height of 2 mm indicates a 25% reduction. In order to assess the quality of the bonding, cross sections of the same were studied using SEM. Figure 2a–d depicts the secondary electron images of stainless steel discs treated at 900 $^{\circ}\text{C}$. It can be observed that bonding is present between the discs with uniform microstructure at the interface. However, presence of pores (Fig. 2b) is observed in the interface region.

A close SEM examination of grains at the regions proximate to edges of the specimen showed the evidence of sensitization as shown in Fig. 2d. Austenitic stainless steels which have undergone treatment in the temperature range between 500 and 900 $^{\circ}\text{C}$ or have been cooled slowly from annealing temperatures (1000–1200 $^{\circ}\text{C}$) become sensitized [2]. During extended exposure of the materials to this temperature range, chromium-rich carbides tend to precipitate at grain boundaries (GB). Significant carbide precipitation can result in severe chromium depletion near the grain boundary, referred to as sensitization. Exposure of sensitized material to aggressive environments can lead to a breakdown in passivity and consequent intergranular degradation termed as intergranular corrosion (IGC) and intergranular stress corrosion cracking (IGSCC).

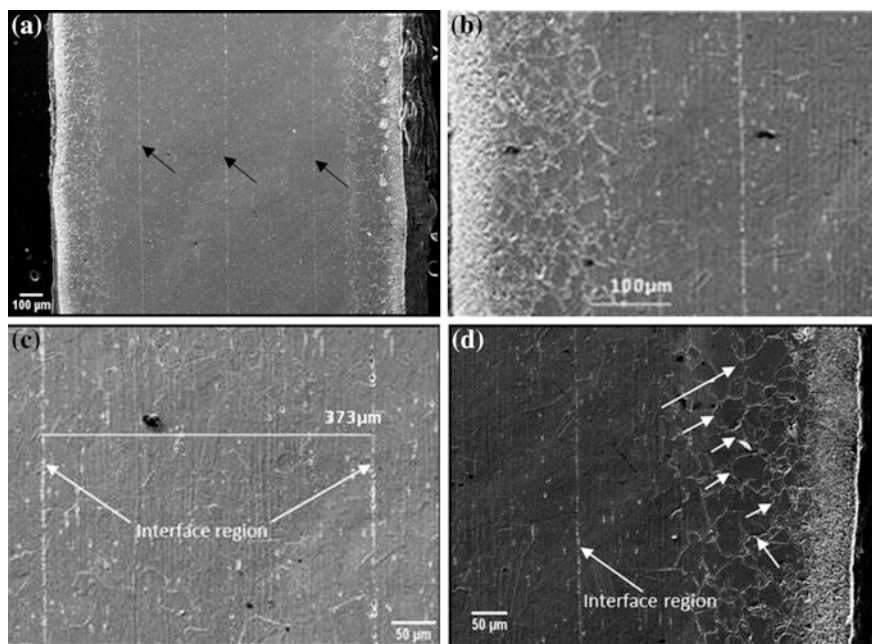


Fig. 2 Micrographs of diffusion bonding of SS discs sintered at 900 $^{\circ}\text{C}$ (pressure—30 MPa, heating rate—100 $^{\circ}\text{C}/\text{min}$ and holding time—5 min) showing: **a** overall view of the sectioned specimen, **b** and **c** interface region with pores, **d** grain boundary sensitization indicated by arrow

In order to understand the present observation, the chosen time of 5–10 min for SPS was compared with TTS diagram for SS316, which is a plot of exposure time versus temperature necessary for sensitization. The C-shaped curve [3] separates the sensitized and non-sensitized regions. The nose of this curve specifies the critical temperature at which the minimum time for sensitization (t_{\min}) which is 5 min in the present case. The hashed portion of the figure indicates the process window employed in the present experiment. It can be inferred that processing time falls within the sensitization region of the plot (Fig. 3).

Figure 4 shows micrographs from SS disc joints prepared by sintering at 1000 °C. It can be seen that bonding line is observed along the interface line with good adherence and absence of porosity (Fig. 4c). In the presence of pressure and electric current, localized necking occurs faster due to joule heating [4]. Consequently, the temperature rises very fast (faster than conventional sintering and hot pressing), and the densification is completed within few minutes. The coarse grain structure and twinning were also seen clearly. The evidence of grain boundary indicates the formation of metallic bonding between the atoms of each side of the interface [5]. Twinning indicates that the material is subjected to high amount of stress during the bonding process.

On comparing the micrographs Figs. 2d and 4d, it is clear that the severity of sensitization increases with sintering temperature. It is very clear that the sensitization has occurred up to a depth of about 150 μm from the surface of the specimen. This is due to the carbon transport at high temperature from graphite mould to steel specimen which is in intimate contact during the process, as similar to the

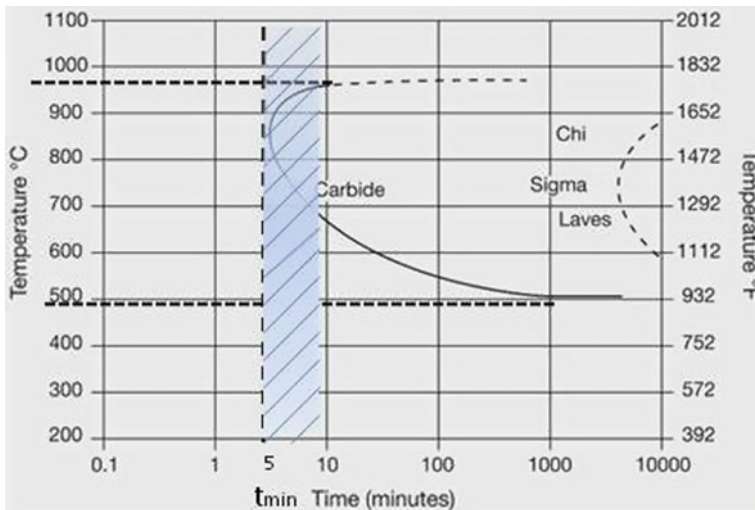


Fig. 3 TTS diagram for 316SS adopted from [3]; hashed area shows processing window of the present study

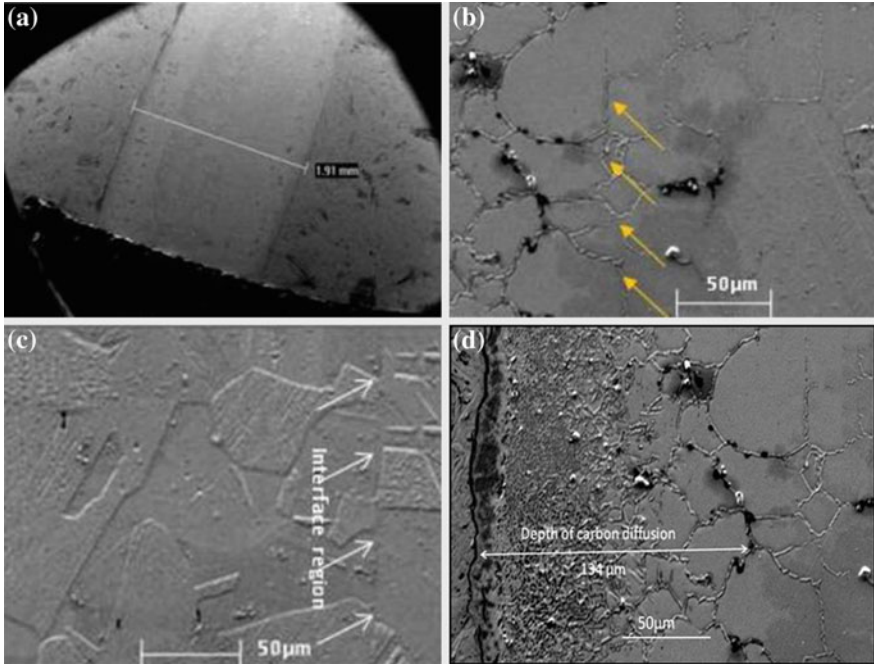


Fig. 4 Micrographs from diffusion bonded SS discs sintered at 1000 °C (pressure—30 MPa, heating rate—100 °C/min and holding time—5 min) showing **a** over all view of sintered joint at low magnification, **b** severely sensitized region at the edges, **c** interface with good bonding but, **d** coarse grains and annealing twins, **e** depth of carbon diffusion

carburization of stainless steel at temperatures above 595 °C reported in the literature [6, 7].

Additionally, extensive twinning was also present in the grains as indicated by arrows in Fig. 4c. Twinning indicates that the material is subjected to high amount of stress. The occurrence of annealing twins which is profound at higher processing temperature is beneficial to grain refinement. The twin boundary is a strong obstacle to dislocation slip, which provides an effective strengthening similar to grain boundaries. Twin boundaries prevent dislocation slip so that dislocation gets piled up at the twin boundaries. Thus, the presence of extensive twin boundaries would enhance the mechanical properties [8, 9].

Figure 5 shows the microstructural changes that occurred when the process temperature is 1100 °C. Figure 5a indicates fine grains suggesting imminence of recrystallization in the region proximate to the mould. Microcracks were also present in the region as marked by arrows. There was also an extensive grain growth along with twinning (Fig. 5b, c) in the central region of the final compacted specimen. Further, Fig. 5b indicates that at 1100 °C the specimen got heavily sensitized as depicted by formation carbide films along the grain boundaries. Irrespective of process temperature, the sensitization effect was at all temperatures.

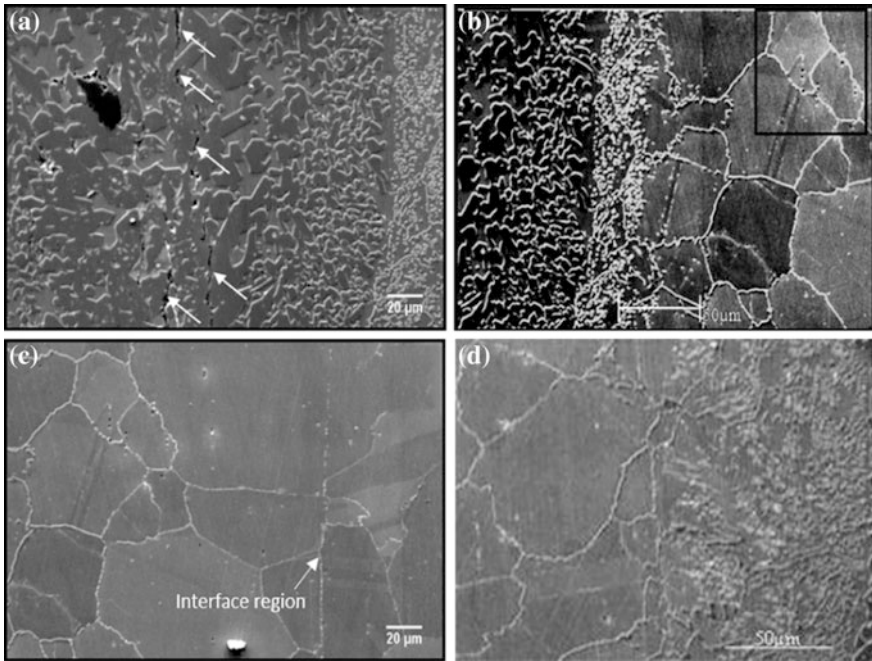


Fig. 5 Micrographs of SS discs sintered at 1100 °C (pressure—30 MPa, heating rate—100 °C/min and holding time—5 min) **a** heavily sensitized area with cracks (arrows) along the grain boundaries, **b** annealing twins, **c** good bonding in the interface region (box) along with grain growth (arrows)

It is apparent that carburization effect occurred through the surface areas close to graphite mould [6, 7].

Figure 6 gives the hardness profile measured across the sintered joints processed at three different temperatures. The effect of temperature on hardness was found to be marginal. Uniform hardness is seen in samples treated at 900–1000 °C in the central region. Also, it is observed that the average hardness value decreases with the increasing processing temperature. The low hardness values at high temperatures indicate that the material lost its strength due to sensitization effect. Based on microstructure and hardness values, it is optimized that 1000 °C is the best-suited process temperature considering the integrity of the joint. Similar results were reported by Li et al. [5], by carrying out through vacuum diffusion bonding. However, the present results demonstrate saving in time and reduced temperature of processing in comparison with diffusion bonding as it can be kept below 5 min with possible increase in pressure to 50 MPa which would form future studies [5]. Considering dominance of sensitization and grain growth in the steels studied, it is suggested that keeping the time of SPS less than 5 min with a temperature lower than 1000 °C to avoid grain growth would be optimum. In order to achieve better compaction, the pressure may be enhanced to ~50 MPa in future studies.

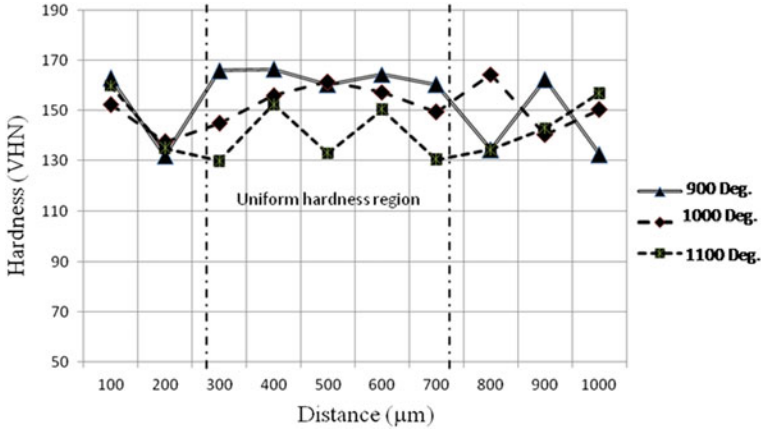


Fig. 6 Hardness profile across the bonded SS at different temperatures; note nearly uniform hardness seen in samples treated at 900–1000 °C

3.2 Case Study 2: Dissimilar Material

In the case of second part of the experiment, i.e. bonding of dissimilar materials of FeB with SS disc, sintering was carried out at 900 °C at a heating rate of 100 °C/min with a pressing force of 30 MPa for the duration of 5 min. Figure 7 depicts the microstructure of the sectioned specimen. Adherence was observed between SS and FeB at the interface regions of centrally located discs (marked R1 in Fig. 7a). However, the ends exhibited a poor adhesion (marked R2). The microstructure of FeB powder region exhibited lots of open and closed pores, which indicates that good compaction is not achieved, possibly due to insufficient pressure. However, at the interface region, the adhesion was good as no cracks or pores were seen (R1 in Fig. 7). Hardness profile across the bonded SS disc is given in Fig. 8. Profile showed a nearly constant hardness values throughout the region. Further studies have to be carried out with varying pressure and temperature to arrive at better integrity.

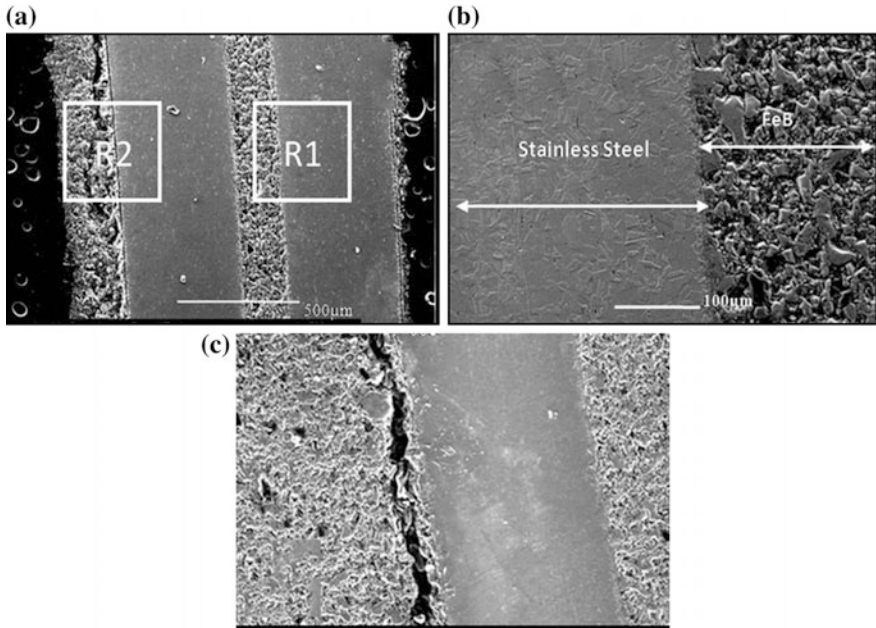
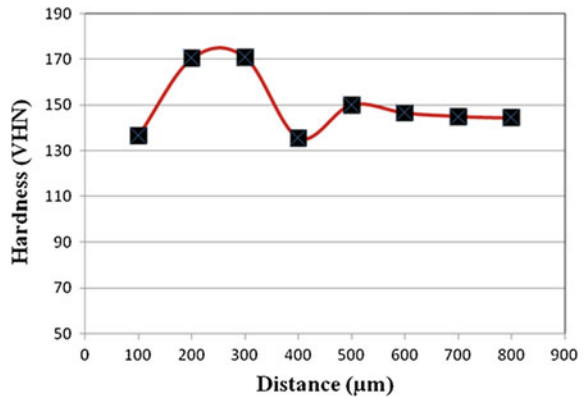


Fig. 7 Micrograph showing the cross section of dissimilar bonding of FeB with SS sintered at 900 °C (a) R1—defect free bonded region, R2—crack along the interface; details of R1 and R2 in (b and c), respectively

Fig. 8 Hardness profile along the FeB-SS bond measured at an interval of 100 µm



4 Conclusions

- Systematic studies of Spark Plasma Sintering have been carried out to understand the effect of sintering parameters on bonding on two systems. (i) With two similar materials of SS discs and (ii) with dissimilar materials (FeB and SS) of different forms namely metal and powder in nature.
- It was understood that the densification/bonding is influenced by the sintering parameters, i.e. temperature, pressing force and the holding time.
- When sintering on similar material was carried out at different temperatures, the overall compaction of 25% was achieved which is basically measured in terms of the reduction in the compact height before and after the experimentation.
- The integrity was understood in terms of distinct microstructural features like (i) sensitization, (ii) recrystallization and grain growth, (iii) formation of carbides films along the grain boundary, (iv) precipitation at the surface region and (v) hardness.
- Hardness profile indicates that the bonded region has the same strength as the base metal. A marginal variation in the hardness value was observed with varying process temperature.
- Considering sensitization and dominance of grain growth, it is suggested that keeping the time of SPS less than 5 min at a temperature lower than 1000 °C to avoid grain growth. In order to achieve better compaction, the pressure may be enhanced to ~50 MPa in future studies.
- In the case of dissimilar materials, a good adhesion was achieved at the central interface region. However, the microstructure of FeB powder region is found to have lots of open pores and closed pores which indicate that good compaction is not achieved. It could be due to insufficient pressure used in the process. Further experimentation with increase in applied pressure is essential

Acknowledgements The authors would like to thank Mr. Vasanth, Research Associate, Department of Metallurgical and Materials Engineering, Indian Institute of Technology Madras, Chennai for his sincere support in carrying out the sintering process. The authors thank Dr. A.K. Bhaduri, Director, Metallurgy and Materials Group, IGCAR, Kalpakkam for his constant encouragement and support during the course of the present work.

References

1. T. Hungria, J. Galy and A. Castro, Spark plasma sintering as a useful technique to the nanostructuring of piezo-ferroelectric materials, *Adv. Eng. Mater.* **11**(8) (2009)
2. M. Dománková, E. Kocsisová, I. Slatkovský, P. Pinke, The microstructure evolution and its effect on corrosion properties of 18Cr-12Ni-2.5Mo steel annealed at 500–900 °C. *Acta Polytech. Hung.* **11**(3) (2014)
3. Practical Guidelines for the Fabrication of High Performance Austenitic Stainless Steels, *ISBN 978-1-907470-10-3*. Published by the International Molybdenum Association (IMOA), London, UK

4. M. Gendre, A. Maitre, G. Troliard, A study of the densification mechanisms during spark plasma sintering of Zirconium (oxy-) carbide powders. *Acta Mater.* **58**, 2598–2609 (2010)
5. S.-X. Li, F.-Z. Xuan, T. Shan-Tung, Fatigue damage of stainless steel diffusion-bonded joints. *Mater. Sci. Eng. A* **480**, 125–129 (2008)
6. B. Fleischer, J.H. DeVan, J.H. Coobs, in *Graphite-Stainless Steel Compatibility Studies*, Doc. No. ORNL-TM-338 (1962)
7. S. Schwarz, R. Oberacker, M.J. Hoffmann, in *Microstructure and Mechanical Properties of Maraging Steel Processed by Spark Plasma Sintering (SPS)*, Euro PM 2008—Sintering
8. J.-H. Shin, J.-W. Lee, Effect of twin intersection on the tensile behaviour in high austenitic stainless steel. *Mater. Charact.* **91**, 19–25 (2014)
9. C.X. Huang, G. Yang, Y.L. Gaob, S.D. Wu, Z.F. Zhang, Influence of processing temperature on the microstructures and tensile properties of 304L stainless steel by ECAP. *Mater. Sci. Eng. A* **485**, 643–650 (2008)

Part X
Structural Health and Condition
Monitoring

On Increasing Quality of Measurement Results at Testing State of Construction Materials

I. P. Miroshnichenko and I. A. Parinov

Abstract The results of the development of new software for processing the results of measuring the intensities of optical fields of interference patterns, created by optical means for measuring small linear and angular displacements of control object surfaces, are discussed. These measurement means are proposed on the base of a laser two-way interferometer with aligned branches; examples of their use are given. The offered software was certificated in Russia due to the state registration of corresponding computer programs. This software allows one to improve the quality of measurement results in solving various actual practical problems of studying the properties and processes of defect formation in new materials, diagnosing the state of construction materials of the power elements of goods by acoustic nondestructive testing at all stages of their life cycle.

Keywords Laser interferometer · Interference pattern · Measurement of small displacements · Control object surface

1 Introduction

At present, the introduction of modern methods and means of laser interferometry opens new possibilities in the solution of various actual practical problems of studying the properties and processes of defect formation in new materials (including layered, polymer, and composite) and also in the diagnostics of the state of construction materials for power elements of goods at all stages of their life cycle.

One of the most preferred for solving scientific and production problems is a laser two-way interferometer with combined branches, proposed in [1, 2]. Experimental studies of the functional characteristics of above-mentioned inter-

I. P. Miroshnichenko (✉)
Don State Technical University, Rostov-on-Don, Russia
e-mail: ipmir2011@yandex.ru

I. A. Parinov
Southern Federal University, Rostov-on-Don, Russia

ferometer, modified for the contactless measurement of the small displacements of control object surfaces in the diagnostics of the state of materials by acoustic nondestructive testing methods, were described in detail in works [3–5].

New mathematical models and original software for modeling the intensities of the optical fields of interference patterns, created by above interferometer, modified for solving measurement problems, were developed. This software was certificated in Russia due to the state registration of computer programs. Numerical simulation for various variants of optical schemes taking into account the features of their constituent parts (geometric characteristics, beam splitter type, etc.) was carried out, the results and analysis of which are described in detail in works [6, 7].

Based on the results of numerical and experimental modeling, new optical facilities for contactless measurements of small linear and angular displacements of the control object surfaces, methods, and means for recording the intensities of the optical fields of interference patterns, unambiguously associated with the measured displacements, were proposed. Moreover, the methods and means of protecting the developed measuring means from the influence of external and internal destabilizing influences on measurement results were developed. Technical solutions, implemented in the proposed measuring facilities, were patented in Russia. The functional characteristics of the prototypes of these measuring instruments were numerically and experimentally investigated and grounded. The results of the development and scientific calculation and experimental justification of the proposed optical measuring means were described in detail in works [8–10]. Works [11, 12] describe new scientifically grounded method and an optical device for measuring small spatial (linear and all angular) displacements of the surfaces of control objects. Works [9, 10] present technical solutions, patented in Russia, allowing the use of the developed optical means as components of mobile diagnostic setups and measuring controlled small displacements without loss of functional properties and accuracy of characteristics at the site of operation of the diagnosed objects.

The above-mentioned measuring facilities have been successfully used in experimental studies of defect formation processes in thin samples of tape high-temperature superconductors, as well as in the development of methods for monitoring their quality during manufacture. Descriptions of experimental measuring devices are given in the works [13, 14]. Experimental operation of the above optical measuring means has shown that one of the directions for improving the quality of measurement results can be the development and use of new software for processing the results of measuring the intensities of optical fields of interference patterns that are unambiguously associated with measurable small displacements of the surfaces of control objects.

This paper describes the results of the development and use of this software in solving measurement problems.

2 Software for Processing the Measurements Results of the Optical Field Intensities of Interference Patterns and Examples of Its Use

It is developed software in MathCad 2000 Professional and above versions for processing the measurement results of the optical field intensities of interference patterns. These patterns are created by optical means for measuring small linear and angular displacements of the control object surfaces, proposed on the base of a laser two-way interferometer with combined branches.

This software includes a set of computer programs, developed on the base of the same typical algorithm. These programs model a certain variant of information collection, connected with the intensity of optical field of interference pattern (a single photodetector device, a group of photodetectors, a matrix of photoreceivers with predetermined geometric characteristics, etc.). This information is collected from predetermined areas of the interference pattern (in one or several rings of the interference pattern, in the selected region of the interference pattern, and so on). The software also uses various methods of statistical processing of information obtained.

In each computer program of the software, a typical algorithm for simulating the process of measuring small displacements of the control object surfaces by optical interference measuring means is implemented. The essence of this algorithm can be visually shown in the simplest example of measuring a small linear displacement of the control object surface by a single photodetector device (e.g., a photodiode of FD9 type) installed in one of the rings of the interference pattern.

The initial data for processing is a set of images of interference patterns ($n = 1, 2, \dots, N$), presented in standard graphic formats. Each (n th) of them corresponds to a certain moment of measurement (to small linear displacement) during registration of the image of the interference pattern. In this process, it is performed a reproduction of the given value of a small linear displacement of the control object surface, as well as the geometric characteristics of the photodetector device.

In a whole, this algorithm, implemented in the software, consists of the following steps:

1. Visualization and analysis of the intensity of the optical field of the initial interference pattern ($n = 1$), characterizing the initial position of the surface of the control object, whose appearance is represented in Fig. 1.
2. Visualization and analysis of the intensities of optical fields of all interference patterns, included in a set of images ($n = 1, 2, \dots, N$, e.g., $N = 31$), corresponding to certain measuring moments (to linear displacements) during registration (the appearances of interference patterns $n = 1, 2 \dots 9$ are shown in Fig. 2).
3. The choice of the region in the initial interference pattern ($n = 1$), restricted by the given geometric characteristics of the photodetector device, by applying horizontal and vertical lines (marking) and its visualization (see Fig. 3).

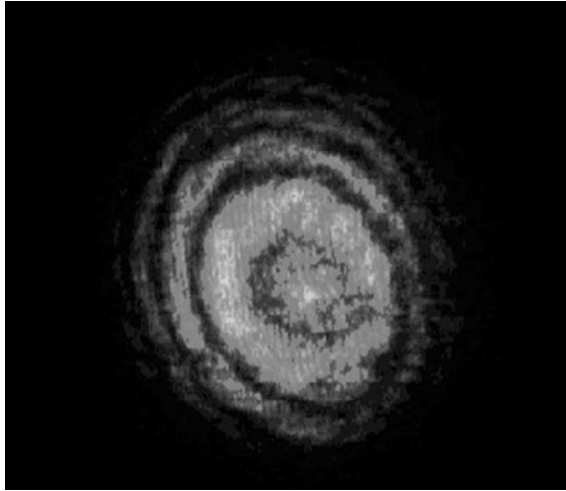


Fig. 1 Appearance of the original interference pattern ($n = 1$)

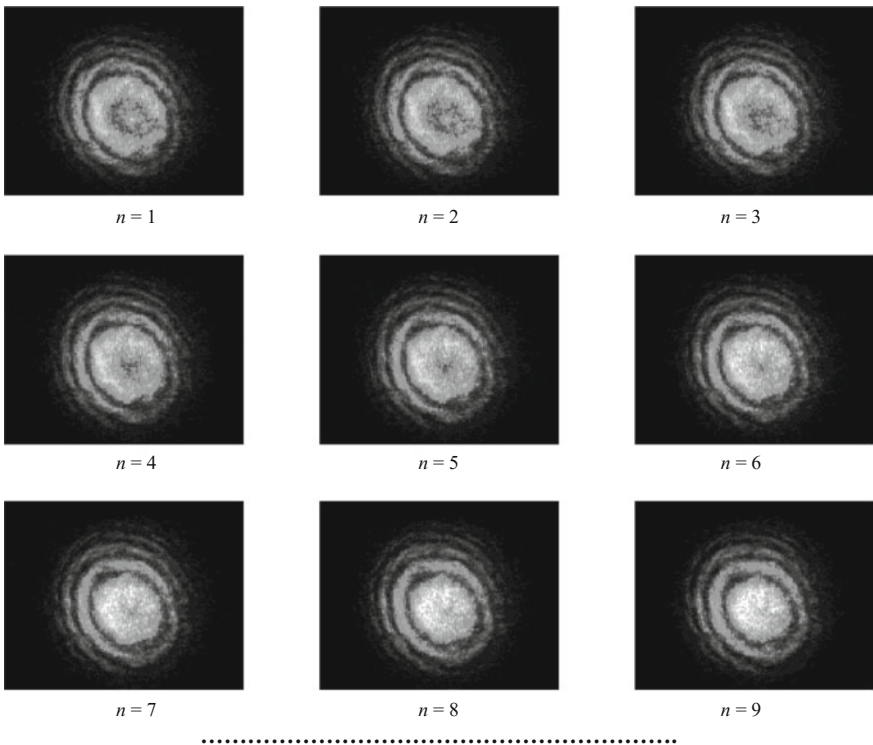


Fig. 2 Appearances of interference patterns $n = 1, 2, \dots, 9$

Fig. 3 Appearance of the marking on the original interference pattern ($n = 1$)

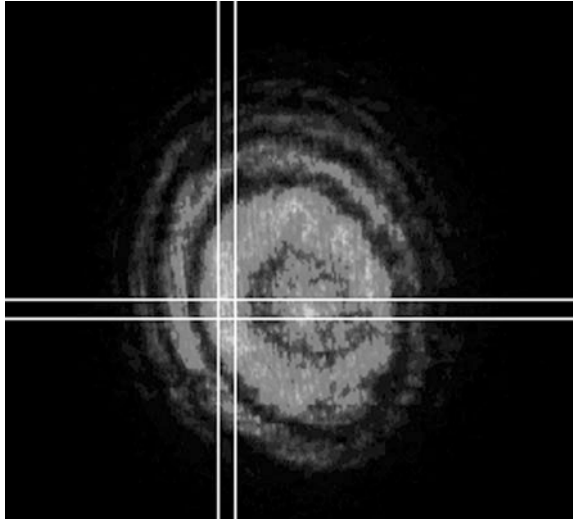
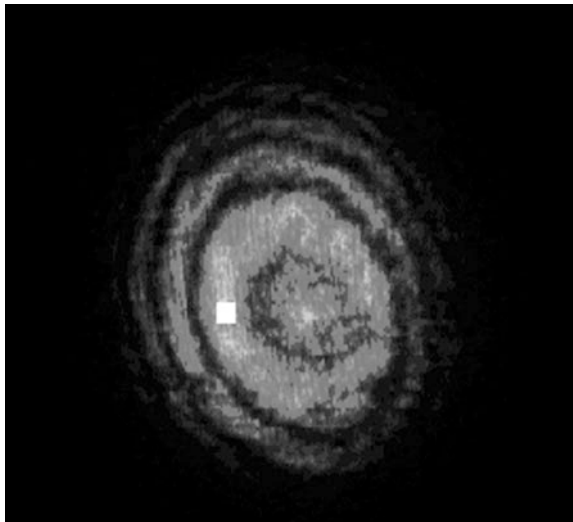


Fig. 4 Appearance of the original interference pattern ($n = 1$) with the selected region



4. Visualization of the selected region of the original interference pattern ($n = 1$), restricted by the given geometrical characteristics of the photodetector device (see Fig. 4).
5. Specification and visualization of the selected area in all interference patterns ($n = 1, 2, \dots, 31$), belonging the set by using the parameters of the original interference pattern (the appearances of the interference patterns $n = 1, 2, \dots, 9$ are shown in Fig. 5).

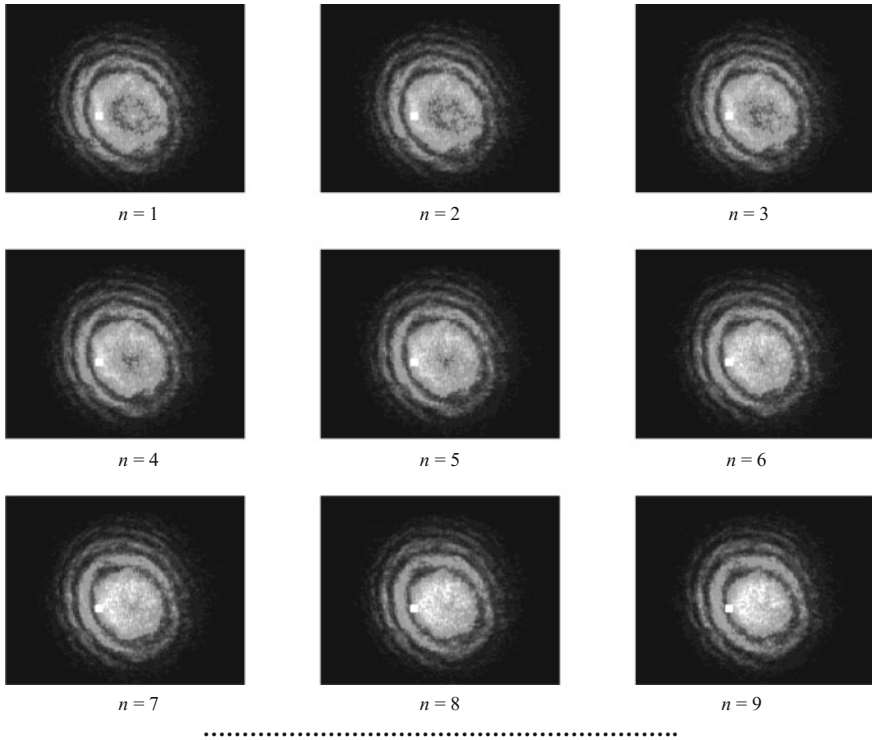


Fig. 5 Appearances of interference patterns $n = 1, 2, \dots, 9$ with selected areas

6. Determination of the summary intensity I_s for the chosen region for all interference patterns, belonging the set ($n = 1, 2, \dots, 31$), and constructing the dependence of the change in the calculated summary intensity I_s for the chosen region for each of the registration moments (see Fig. 6).
7. Processing the results obtained using, for example, various built-in tools that implement methods of statistical processing and forecasting and known software. Figure 7 shows, for example, the dependence of the summary intensity I_s for the selected region of interference patterns $n = 1, 2, \dots, 31$ after statistical processing using the built-in tools of MathCad 2000 Professional software.

The developed software also includes computer programs for processing the results of intensity measurements obtained with the aid of two photoreceivers, mounted in adjacent interference pattern rings (see Fig. 8), and also when recording the intensity from the selected region of the interference pattern, characterized by maximum contrast (see Fig. 9).

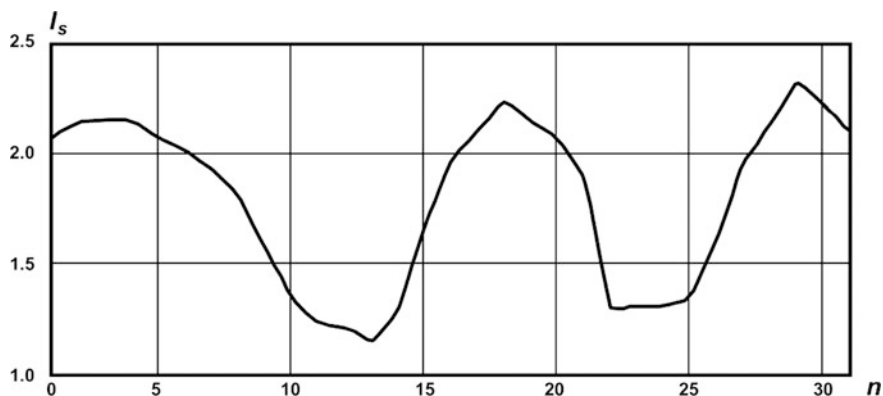


Fig. 6 Dependence of summary intensity I_s for selected region of interference patterns $n = 1, 2, \dots, 31$

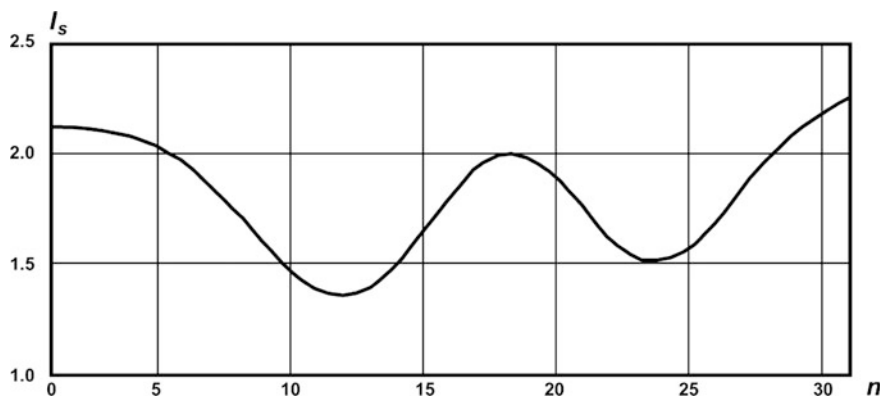


Fig. 7 Dependence of summary intensity I_s for selected region of interference patterns $n = 1, 2, \dots, 31$ after statistical processing

The programs described above, included in the software, have been tested and used in processing the results of experimental studies of the functional characteristics of promising optical measuring facilities.

Further development of the proposed algorithm and software will be connected with the improvement of standard unified algorithms for modeling various options for measuring and processing the results of measurements of small spatial displacements of control object surfaces and also will be directed to automation of the processing test data.

Fig. 8 Appearance of the original interference pattern ($n = 1$) with the selected regions for the registration variant using two photoreceivers

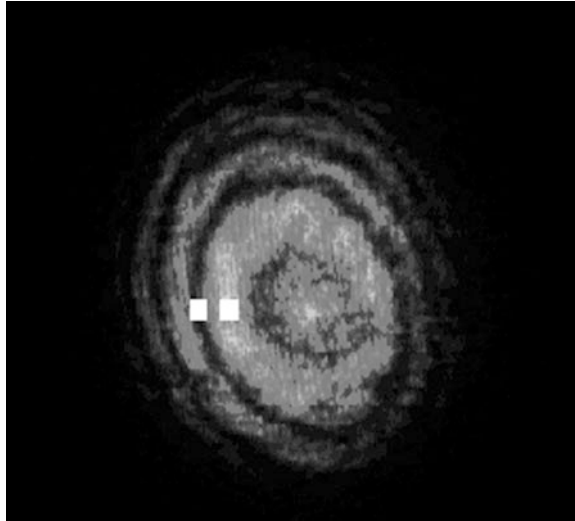
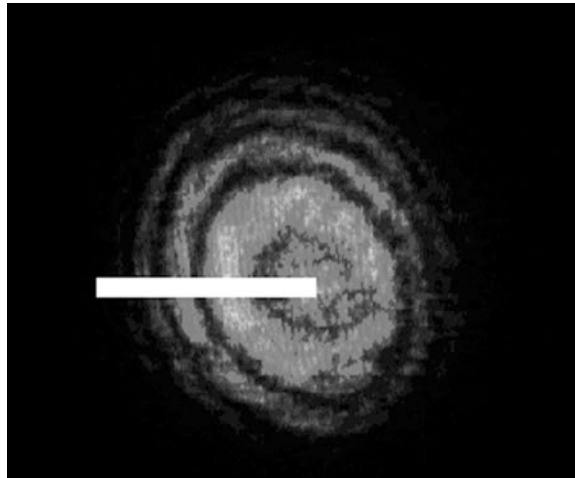


Fig. 9 Appearance of the original interference pattern ($n = 1$) with selected region for the registration variant of intensity from the selected area



3 Conclusions

New software has been developed for processing the measurement results of the optical field intensities of interference patterns, created by optical means, for measuring small linear and angular displacements of control object surfaces, proposed on the base of a laser two-way interferometer with combined branches.

The proposed software has been certified in Russia due to the state registration of corresponding computer programs and allowed improving the quality of measurement results by solving various actual practical problems of studying the

properties and processes of defect formation in new materials, diagnosing the state of construction materials of the power elements of goods by acoustic nondestructive testing methods of control at all stages of their life cycle.

The proposed software can also be successfully used to simulate the measurement of small linear and angular displacements of control object surfaces by creating new methods for processing the intensities of the optical fields of interference patterns, created by optical measuring means, developed on the base of laser interferometers of various types.

The software and technical solutions, described in the article, were presented at the International Innovation Salons INVENTIONS GENEVA 2017 (Switzerland) and EUROINVENT 2017 (Romania), where were awarded gold medals.

Acknowledgements The study was performed under partial support of the Russian Foundation for Basic Research (No. 16-08-00740). I. P. Miroshnichenko and I. A. Parinov acknowledge financial support of the Russian Ministry of Education and Sciences in the framework of “Organization of Scientific Research” Government Assignment.

References

1. A.N. Matveev, *Optics* (High School, Moscow, 1985), 351 p (in Russian)
2. A.S. Batrakov, M.M. Butusov, G. P. Grechka, *Laser Interferometry Systems* (Radiocommunication, Moscow, 1981), 456 p (in Russian)
3. I.P. Miroshnichenko, A.G. Serkin, *Meas. Tech.* **49**(5), 22 (2006)
4. I.P. Miroshnichenko, A.G. Serkin, *Russ. J. Nondestr. Test.* **43**(4), 234 (2007)
5. I.P. Miroshnichenko, A.G. Serkin, *Russ. J. Nondestr. Test.* **44**(5), 318 (2008)
6. I.P. Miroshnichenko, A.G. Serkin, V.P. Sizov, *Meas. Tech.* **50**(1), 10 (2007)
7. I.P. Miroshnichenko, A.G. Serkin, V.P. Sizov, *J. Opt Technol.* **75**(7), 437 (2008)
8. I.P. Miroshnichenko, I.A. Parinov, E.V. Rozhkov, A.G. Serkin, V.P. Sizov, in *Piezoelectrics and Related Materials: Investigations and Applications*, ed. by I.A. Parinov. (Nova Science Publishers, New York, 2012), p. 239
9. I.P. Miroshnichenko, I.A. Parinov, E.V. Rozhkov, V.P. Sizov, V.A. Shevtsov, in *Physics and Mechanics of New Materials and their Applications*, ed. by I.A. Parinov, S.-H. Chang (Nova Science Publishers, New York, 2013), p. 145
10. I.P. Miroshnichenko, I.A. Parinov, E.V. Rozhkov, S.-H. Chang, in *Advanced Materials—Manufacturing, Physics, Mechanics and Applications*, ed. by I.A. Parinov, S-H. Chang, V.Y. Topolov. Springer Proceedings in Physics, vol 175 (Springer Cham, Heidelberg, 2016) p. 341
11. I.P. Miroshnichenko, I.A. Parinov, *IOP Conf. Ser.: Mater. Sci. Eng.* **209**, 8 (2017)
12. I.P. Miroshnichenko, I.A. Parinov, J.-K. Wu, W.-L. Hong, M.-Y. Yeh, in *Advanced Materials—Techniques, Physics, Mechanics and Applications*, ed. by I.A. Parinov, S.-H. Chang, M.A. Jani. Springer Proceedings in Physics, vol. 193 (Springer Cham, Heidelberg, 2017), p. 591
13. I.P. Miroshnichenko, I.A. Parinov, E.V. Rozhkov, A.G. Serkin, *Metallurgist* **50**(7–8), 408 (2006)
14. I.P. Miroshnichenko, A.G. Serkin, *Metallurgist* **54**(3–4), 189 (2010)

Damage Growth Study in Unidirectional CFRP Composites Using Infrared Thermography

Sukanta Das, Naresh Reddy and Gangadharan Raju

Abstract Structural integrity evaluation of composite structures requires a comprehensive understanding of the various failure mechanisms like matrix cracking, fiber breakage, fiber-matrix interface failure, delamination, and their evolution across micro-to-macro scales. Non-destructive testing and evaluation (NDT&E) techniques are applied to composite structures for discerning the various damage mechanisms and provide information for numerical life estimation tools. Among the NDT methods, infrared thermography is one of the modern non-invasive techniques suited for real-time monitoring and gives in situ information regarding the onset of damages and its growth. In this work, the aim is to investigate damage initiation and progression in unidirectional carbon fiber reinforced plastic (CFRP) composite under static loading condition. The passive thermography (PT) and active thermography techniques are employed in damage growth studies in CFRP laminate using an infrared camera. The PT experiments were carried out to examine the damage information in the thermograms under monotonic ramp loading. Image processing of the thermal images obtained using thermography is used to get qualitative information about the damage evolution in unidirectional CFRP specimens.

Keywords Non-destructive testing and evaluation · Passive thermography
Damage study · Carbon fiber reinforced plastic

1 Introduction

Composite materials are increasingly used in the field of aerospace, marine, automobile, and wind energy applications due to their high specific strength, stiffness properties, and tailorability options to design efficient structures. Recently,

S. Das (✉) · N. Reddy · G. Raju
Department of Mechanical & Aerospace Engineering, Indian Institute of Technology
Hyderabad, Kandi, Telangana 502285, India
e-mail: me14mtech11036@iith.ac.in

© Springer Nature Singapore Pte Ltd. 2018
R. Prakash et al. (eds.), *Advances in Structural Integrity*,
https://doi.org/10.1007/978-981-10-7197-3_56

673

advanced carbon fiber-reinforced polymer matrix composites have been widely used in primary and secondary load-bearing aircraft structures. Composites usage in critical structures necessitates a clear understanding of their mechanical behavior under static and dynamic loading. Unlike metals, composite materials are inhomogeneous and anisotropic, which makes their failure more complicated, and understanding those failures leads to more efficient design.

Infrared (IR) thermography is one of the many techniques used to “see the unseen.” As the name implies, it uses the distribution (suffix -graphy) of surface temperatures (prefix thermo-) to assess the structure or behavior of what is under the surface [1]. Infrared thermography is one of the most modern, efficient non-destructive techniques, used in aerospace, mechanical, electrical, and civil engineering. The fundamental principle of this method is that the infrared sensor senses the emitted infrared radiation from the focused object and processes it in the form of a surface temperature distribution. Image processing of the acquired thermal images provides qualitative and quantitative information about the presence of damage in structures. With the advent of technology, thermal imaging has evolved and has become a useful tool to identify the critical zone well before the failure [1]. There are two approaches in infrared thermography: passive, in which the features of interest are naturally at a higher or lower temperature than the background and active, in which an external energy source is required to produce a thermal contrast (ΔT) between the area of interest and the background [2].

A good number of the researchers have worked on this topic, and most of them were interested in cross-ply glass fiber reinforced plastic (GFRP) under dynamic loading [3, 4], but very few researchers worked on unidirectional (UD) CFRP composite under static loading [5, 6]. In this work, the objective is to investigate damage initiation and progression in UD CFRP composite under static loading condition. The passive thermography experiments were carried out under monotonic ramp loading to examine the damage initiation information in the thermograms. The image processing of the recorded thermal images is adopted to get qualitative information about the damage evolution in UD CFRP samples. For the validation, the identified damages in the passive thermogram were correlated with the microscopic surface texture images for studying local micro-damages at the lamina.

2 Materials and Test Setup

2.1 Materials and Specimen Preparation

The material used in this study is a carbon/epoxy laminate with 60% volume fiber content. To maintain the material properties constant for all the test specimens, coupons are prepared from the same plate. The plate is made with eight layers of unidirectional dry woven fabric. An epoxy resin of Araldite CY230 mixed with the

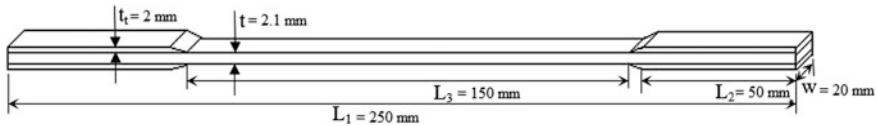


Fig. 1 Tensile test specimen's dimensions

hardener of Araldite HY951 in a ratio of 10:1 was used to impregnate the dry fabric. The laminated plate was fabricated using hand lay-up followed by vacuum bagging techniques to improve the fiber volume fraction. The sealed wet laminate was cured for 24 h at room temperature of 28.5 °C and a vacuum pressure of—87 kPa. The specimens were endowed with 2 mm-thick aluminum (t_1) adhesively bonded tabs, ensuring the shear forces transferred through the adhesive, and minimize any stress concentration due to the gripper pressure (700 psi). The schematic of the test specimen is shown in Fig. 1. For preparing the test coupon, carbide diamond-coated milling cutter of diameter 6 mm was used to reduce the machining effects at the edges of coupon.

2.2 Test Setup

The tensile test was carried out on unidirectional CFRP composite coupons under displacement control mode in MTS Landmark 370, having a maximum load capacity of 100 kN. During tensile testing, the IR thermal camera from FLIR SC5500 equipped with a cooled indium antimonide detector which facilitated to record the smallest of temperature differences. It is working in the waveband range of 2.5–5.1 μm and produces thermal images of 320×256 pixels. The camera has Focal Plane Array (FPA) InSb sensor with a capacity of 25 mK thermal sensitivity [7]. The micro-cracks, delamination, fiber damages, and also other damages were observed and recorded using this infrared (IR) camera.

For passive thermogram recording, the IR camera was placed approximately 510 mm far from the surface of the specimen loaded into the MTS machine. The experimental test setups are shown in Fig. 2. The camera was connected to a computer for recording the thermogram data. The recording and post-processing of the data were done using Altair software. This software allows highlighting the damaged zones by performing a pixel-by-pixel analysis of the temperature data. To reduce the environmental noise in the recorded thermogram, a non-transparent plastic sheet covered the whole experimental setup (i.e., MTS machine and the IR camera). The test room was maintained at a constant temperature of 23 °C.

For inspection of the damaged specimens, active thermography adopted using the same camera additionally used two halogen lamps having a maximum capacity of 2.5 kW for the heat wave. For all active thermography tests, the lamps and camera have been kept at a distance of 700 and 550 mm from the specimen, respectively. All the active thermography tests were conducted using IrNDT

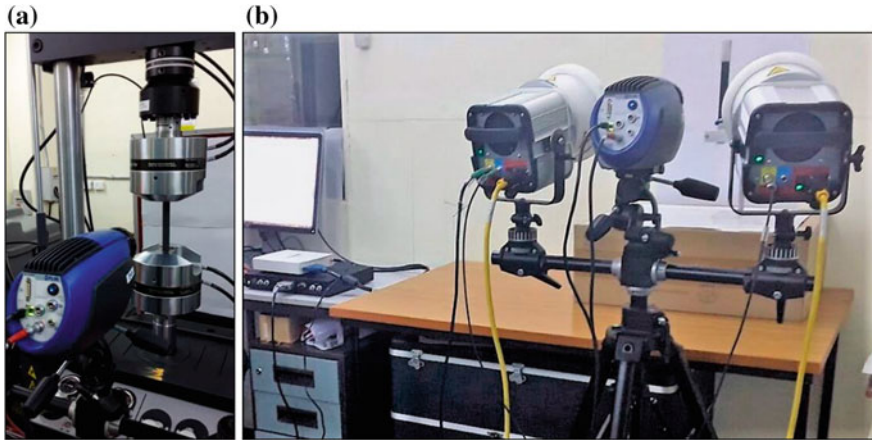


Fig. 2 Test setups **a** passive thermography, **b** Active thermography

software with lock-in and transient thermography module supported by automation technology.

For a microscopic analysis of the preidentified damage sections from the image processing thermogram, Olympus STM6 optical microscope with the objective lens “MPlanFL N 10×/0.30” having a capacity of 10× magnification with a numerical aperture value of 0.3 was used.

3 Experimental Tests

3.1 Static Loading

Static monotonic tensile tests were performed in the displacement control mode with a crosshead speed of 1 mm/min. The three specimens were loaded on an MTS universal testing machine, and during each tensile test, the surface thermogram of the specimens was recorded by the thermal camera. The aim was to capture any onset of micro-damages indication in the temperature trend and correlate it with the material’s stiffness. Three specimens were loaded up to stress level of 500, 700, and 900 MPa, respectively, and the corresponding temperature data acquisition frequency was set as 120, 85, and 55 Hz.

3.2 Active Thermography

After tensile loading, every loaded specimen was inspected through active (i.e., lock-in and transient pulse techniques) thermography to capture the macro-damages.

A set of different thermal excitation frequencies starting from 2, 1, 0.34, and 0.2 Hz with corresponding thermal periods of 5, 5, 4, and 4 was selected for the lock-in thermography. For transient pulse thermography, a rectangular pulse width of 1.5, 2.25, and 3 s with a period of 10, 15, and 20 s, respectively, was adopted. The recorded thermograms were evaluated using pulse phase techniques to plot the phase diagram. The image acquisition frequency of 300 Hz was chosen for both the techniques. The aim of these tests was to plot the phase diagrams of the loaded specimen and correlate phase delay response of the damage location with the passive thermogram's damage indications.

3.3 *Microscopic Analysis*

For the validation of the thermogram techniques, the specimens were cut along the transverse direction at passive thermogram's damage indications and inspected the sections under the optical microscope to capture the micro—macrodamage. The damage sections of the specimen were cut using carbide diamond-coated milling cutter of diameter 3 mm. To reduce machining defects, a different set of cutting parameters, i.e., cutting speed and depth of cut were chosen to be applied on an unloaded specimen. After analyzing all the microscopic images of different machining sections of the healthy specimen, it was concluded that the least number of defects was observed for the cutting speed of 1000 RPM with the 0.5 mm depth of cut. These optimum cutting parameters were adopted to cut the different loaded specimens for microscopic analysis.

4 Test Results and Discussions

4.1 *Experimental Results*

The tensile test result shows (Fig. 3) an approximately linear behavior of the stress–strain at the initial stage of the test. Later, the linear stress–strain relation starts changing its slope when the specimen reaches to a stress value of 270 MPa (Fig. 4). This change in slope phenomena can be correlated with the starting of different damage mechanisms, which continue until it reached the ultimate strength.

Thermogram of the loaded specimens is allowed to do both qualitative and quantitative analysis of the damages. For qualitative analysis, it was tough to locate the hottest zone of the specimen from the raw thermograms. At low-stress level, the raw thermograms did not indicate any the thermal contrast between damage initiation temperature and the specimen temperature. To enhance the damage zone, corresponding to the hottest zone of the specimen, an image processing was done. For image processing, thermograms were first normalized by dividing the first frame of the recorded film and then performed subtraction operation between the

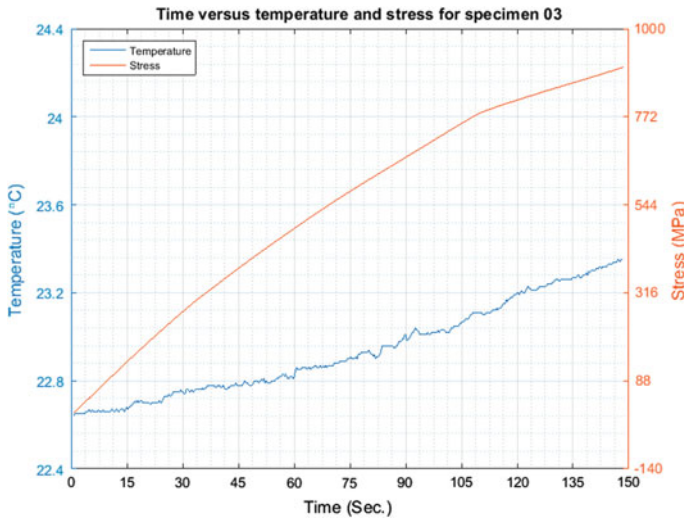


Fig. 3 Temperature and stress variation plot with respect to time for specimen 03

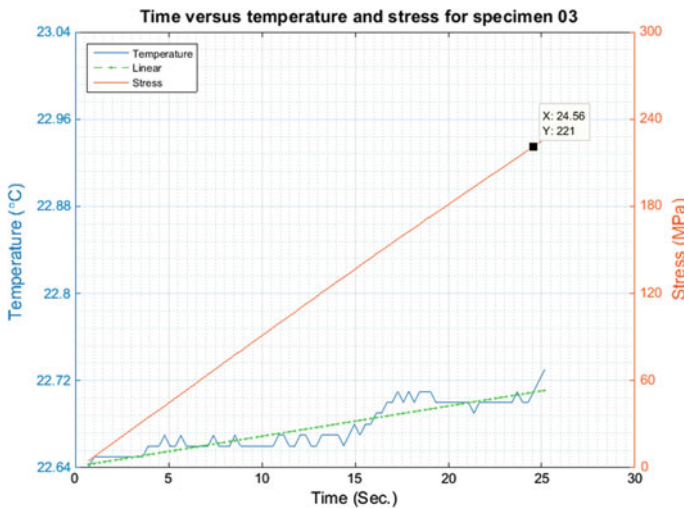


Fig. 4 Linear variation of stress and temperature in the first phase (thermoelastic effect)

current frame and the previous frame of the normalized film [5]. These arithmetic operations have been performed using Altair software. Figure 5 represents the maximum normalized subtracted temperature of the small area of interest (AoI) versus time. A threshold value of 0.006 of the “maximum normalized subtracted temperature” was chosen for identifying the damages in the specimen. All

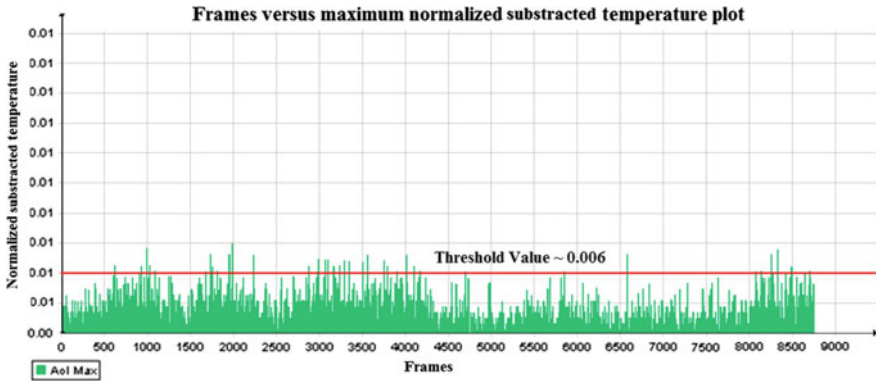


Fig. 5 Maximum normalized subtracted temperature timing graph for specimen 01

the frames which are above the threshold value were inspected for the hottest zone and calculated for the damage initiation. Figures 6, 7, and 8 represented the set of thermograms, which were above the threshold value specimens 01, 02, and 03, respectively. Every thermogram within Figs. 6, 7, and 8 represents the evolution of damages with time. For example, in Fig. 6 representing the key thermograms of specimen 1, the first thermogram represents the first critical temperature rise appear in the specimen at 20.12 s. This frame is considered for the damage initiation of the UD CFRP composite under static loading, and the corresponding stress value is considered as damage stress.

For quantitative analysis, temperature variation within the specimen due to the external load can be obtained using the thermoelastic effect. All the tested specimens showed a similar temperature variation with time. The temperature profile can be schematized in two phases. The *first phase* is characterized by an approximately linear variation of the temperature with time. The linear increase in temperature observed in CFRP specimens is in agreement with the thermoelastic effect ($\Delta T = -k_m T \sigma_m$), assuming the negative coefficient of thermal expansion (CTE) in the fiber direction. The *second phase* is characterized by a nonlinear variation in the temperature with time. This can be attributed to the initiation and growth of local micro-damages arising from the pre-existing manufacturing defects [3, 5, 6]. These damages can be confirmed by micrographic analyses using an optical microscope.

The temperature and the stress trends are represented together on the same graph to illustrate the thermoelastic effect due to an external load. In Fig. 4, the first phase is characterized by a linear trend, which can be described with an equation obtained through a linear regression analysis. The end of the first phase might be correlated to the end of the linear thermoelastic behavior of the material and beginning of the micro-damages in the material. Hence, the stress value corresponds to the end of the linear thermoelastic phase, considered as damage initiation stress. The average value, obtained from static tests, was equal to 221 MPa and represents the damage initiation stress point (σ_d) for the unidirectional CFRP specimens [3, 5].

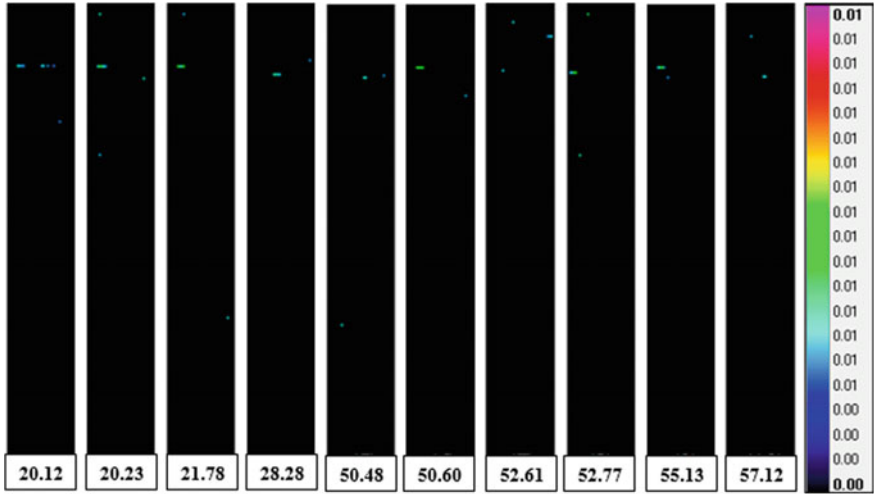


Fig. 6 Normalized subtracted thermogram with damage indications for specimen 01 at a different time (t)

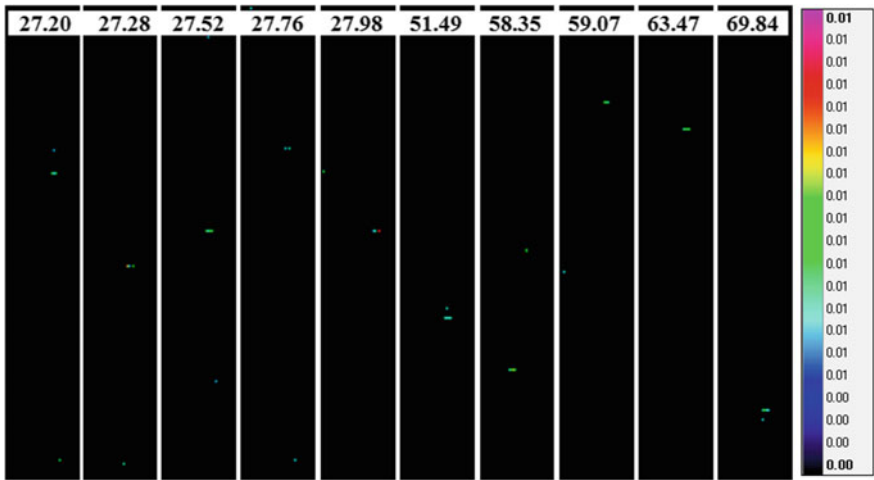


Fig. 7 Normalized subtracted thermogram with damage indications for specimen 02 at a different time (t)

For active thermography, both lock-in and transient pulse thermography were done for all specimens. The lock-in test result shown in Fig. 9a represents the phase information on loaded specimen 01 (500 MPa) and healthy specimen. It is clearly observed from the phase diagram of the loaded specimen and healthy specimen that damages are located the top portion of the specimen 01. After pixel-by-pixel analysis of the phase value, we summarize that the damages location of the

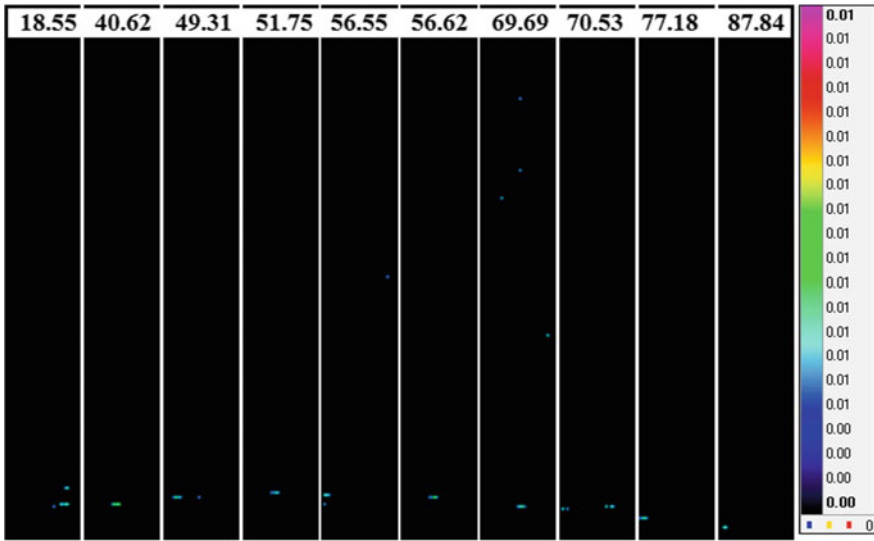


Fig. 8 Normalized subtracted thermogram with damage indications for specimen 03 at a different time (t)

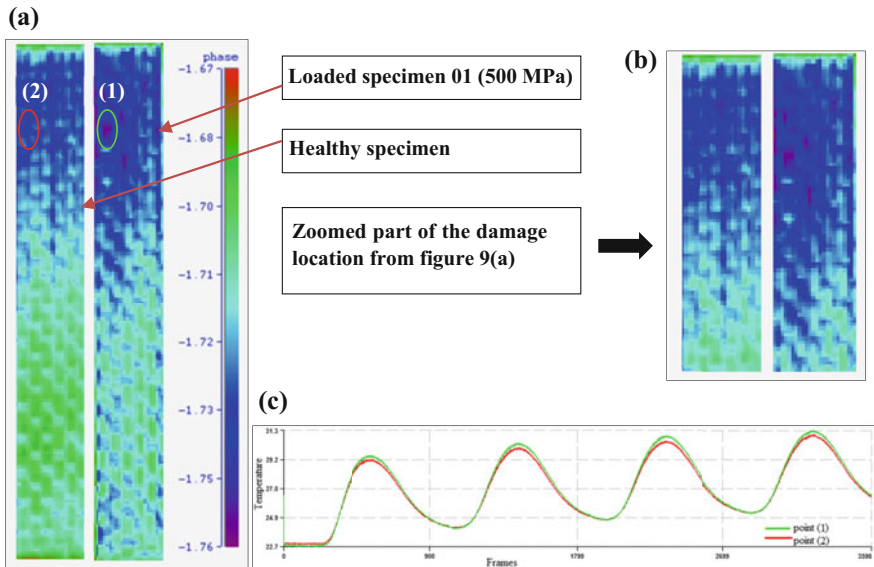


Fig. 9 Phase diagram and temperature variation of point (1) and (2) for specimen 01. **a** Phase plot using lock-in thermogram, **b** zoomed part of the damage location from the (a), **c** temperature variation of point (1) and (2) over time

Table 1 Damage dimensions from microscopic images for specimen 01

Section no.	Damage no	Damage length (pixel)	Damage length (mm)	Damage width (pixel)	Damage width (mm)
1	1	570	0.342	138	0.0828
	2	474	0.2844	234	0.1404
	3	504	0.3024	186	0.1116
	4	1392	0.8352	357	0.2142
2	1	951	0.5706	135	0.081
	2	705	0.423	189	0.1134
3	1	823	0.4938	159	0.0954
	2	816	0.4896	108	0.0648
	3	672	0.4032	273	0.1638

Microscopic damages (1 and 2) in section 1, Specimen 01 (500 MPa)

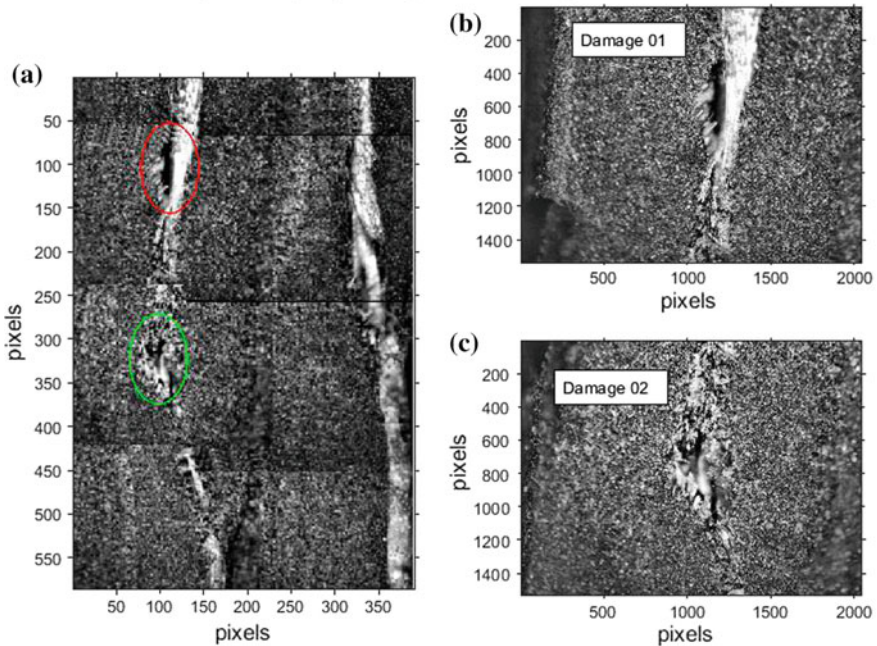


Fig. 10 Microscopic images. **a** Damage 01 and 02 after image stitching adjacent to damaged image **(b)** and **(c)**. **b** Microscopic image of damage 01 at 10× zoom for Sect. 1 of specimen 01. **c** Microscopic image of damage 02 at 10× zoom for Sect. 1 of specimen 01. Dimensions of the damages are given in Table 1

specimen 01 is nearly same with passive thermogram damage indications. The temperature variation in the damage point (1) and health point (2) corresponds to loaded specimen 01 and healthy specimen which is shown in Fig. 9c. The deviation in cooling profile between healthy and loaded specimen indicates the damage

present at the point (1). The above analysis clearly indicates the damages for the specimen 01 and agrees with the respective passive thermogram damage indications.

To validate passive thermogram damage indications, specimens were cut along the damage indications and inspected under a microscope. For specimen 01, a list of the damages and their corresponding dimensions were mentioned in Table 1. Figure 10 represents the microscopic image of one of the damaged sections of specimen 1. The microscopic image of the section was able to highlight local damages. In Fig. 10b, c, damages are representing the local damages.

5 Conclusions

Quasi-static tensile experiments were carried out on unidirectional CFRP specimens to study the damage initiation and progression using IR thermography. Both passive and active thermography techniques were used to monitor the damage progression in UD laminates. Passive thermography results were able to capture the thermo-elastic effect showing a temperature increase with loading within the elastic limit. Also, using PT, we were able to identify the damage initiation stress point (approximately 221 MPa) beyond which the temperature variation becomes nonlinear with load showing the growth of damage in CFRP specimens. Further, image processing operations were performed on thermograms acquired using PT, and a threshold value was adopted to identify the damages in the CFRP specimens. Active thermography techniques, namely lock-in and transient pulse thermography, were then used to validate the damage identified using PT. Finally, the specimens were cut at the damage location defined by PT, and the micrographic images were captured using an optical microscope. Also, an experimental study was carried out to determine the optimal cutting speed and depth of cut to minimize the machining damage. The microscopic images obtained at the damaged section agreed with the results achieved by PT.

Acknowledgements The authors wish to thank prof. (Asso.) M. Ramji, for allowing to access material characterization laboratory, IIT Hyderabad, and also like to thank Mr. M. Pravin, composite manufacturing Lab, for helping tensile specimen preparation, Swaraj Kumar Tripathy, M. Tech. student, IIT Hyderabad, and Divya Selvaraj, a summer intern student from NIT Trichy for helping in microscopic analysis.

References

1. X.P.V. Maldague, *Theory and Practice of Infrared Technology for Nondestructive Testing* (Wiley, New York, 2001)
2. X.P.V. Maldague, Introduction to NDT by active infrared thermography. *Mater. Eval.* **60**(9), 1060–1073 (2002)

3. C.C.F.L.L. Vergani, C. Colombo, F. Libonati, L. Vergani, Fatigue damage in GFRP. *Int. J. Struct. Integr.* **3**(4), 424–440 (2012)
4. W. Harizi, S. Chaki, G. Bourse, M. Ourak, Composites: part B mechanical damage assessment of glass fiber-reinforced polymer composites using passive infrared thermography. *Compos. Part B* **59**, 74–79 (2014)
5. B. Rodriguez, C. Galleguillos, R. Fernández, F. Lasagni, Passive infrared thermography for damage monitoring during structural testing of CFRP parts, in *Proceedings of 16th European Conference Composite Materials*, pp. 22–26 (2014)
6. N.I. Baurova, W. Hao, O. Xiao, Microstructure of carbon fiber and carbon reinforced plastic. *J. Mater. Sci. Chem. Eng.* **1**, 28–32 (2013)
7. FLIR® Systems, FLIR SC5000 Series. FLIR® Systems. Available: <http://www.flir.co.uk/cs/display/?id=42577>. Accessed 10 May 2016 (Online)

Online Damage Detection in Metallic Cylindrical Shells Using Guided Wave Modes by Time Reversal Method

P. Jayesh and Christudas R. Bijudas

Abstract Online damage detection and structural health monitoring (SHM) of aerospace structures are having great scientific and economical importance, since maintenance costs can be considerably reduced by introducing condition-based structural maintenance instead of time-linked preventive maintenance. Active structural health monitoring using guided wave modes is gaining importance after the introduction of lightweight piezoelectric wafer transducers (PWTs) since the mass penalty associated with these systems is considerably less. Multiple research papers are generated worldwide on the use of guided Lamb wave modes for active defect detection in thin platelike structures. Since so many civil and aerospace structures are cylindrical in shape, studies on the use of guided wave modes for SHM of cylindrical shells are gaining importance. Studies on the use of guided wave modes for SHM of cylindrical shells and pipes are done by a few authors by pulse echo method. In this chapter, the methods to generate different guided wave modes in metallic isotropic cylindrical shells, dispersion characteristics of wave modes in cylindrical shells, their interaction with defects, etc., are studied. Moreover, the structural health monitoring of cylindrical shells using the time reversibility concept adopted from guided Lamb wave mode is also studied. Numerical modelling of propagation of guided wave modes in plates and cylindrical shells is done using finite element methods, and comparisons are made. Experimental evaluation on the propagation of guided waves in cylindrical shells is carried out. Dispersion characteristics of guided wave modes in cylindrical shells and the signature of guided wave modes for different defects are studied by numerical modelling and experiments. A tomography scheme is worked out which can predict the presence of defects and its propagation, which can be used for condition-based structural maintenance of aerospace structures. A comparison between the numerical modelling and experimental studies is done, and damage indices based on time-reversed reconstruction are generated.

P. Jayesh · C. R. Bijudas (✉)

Indian Institute of Space Science and Technology, Thiruvananthapuram 695547, India
e-mail: jayeshpkalappila@gmail.com

Keywords Cylindrical shells · Guided wave modes · Structural health monitoring
Time reversibility · Tomogram

Nomenclature

SHM Structural health monitoring
PWT Piezoelectric wafer transducer

1 Introduction

Online damage detection and prognosis of cylindrical shells, especially pressurized vessels, fascinated the researchers worldwide over the last century. A breakthrough in structural health monitoring happened after the introduction of lightweight, cheap and extremely thin piezoelectric wafer transducers (PWTs). Guided wave modes can be generated by supplying electric signal to the PWTs. SHM systems consist of permanently embedded PWTs in structures, and the output signals are monitored and analysed to get the required information on the health of the structure. Giurgiutiu [1] earlier introduced the idea of embedded ultrasonic structural radar (EUSR) for damage detection in plates. In [2, 3], authors extended this concept to cylindrical shells. Muc and Stawiarski [4] give a comparison between experimental and numerical studies on the propagation of elastic guided waves in cylindrical shells. Li et al. [5] studied the effect of pressurized fluid in the wave propagation characteristics in cylindrical pressure vessels and also investigated the mode at which the attenuation due to interaction with fluid is less. Gresil et al. [6] give detailed guidelines on the usage of finite element method on the wave propagation problems. Ing and Fink [7] carried out experiments on self-focusing process of the time reversal mirrors and time recompression for detection of flaws. Poddar and Giurgiutiu [8] used a method to avoid boundary reflections in experimental studies, by applying modelling clay near the shell boundaries. Sohn [9] concluded that baseline data-based damage detection techniques will have limited practical applications unless otherwise new methods are discovered to correctly compensate for the environmental and operational variabilities. Qiang and Shenfang [10] filtered out the scattered signals from defect locations and time reversed it so that these waves got focused at scatterers. In order to separate the scattered signal, authors introduced a new unique PWT arrangement and a time window function is then used to separate out the scattered signals from the source and boundary reflection signals. Harley et al. [11] used time reversal technique to effectively remove the coherent noise and also to increase the signal-to-noise ratio. Doing this, the sensitivity of the damage detection technique is considerably increased. Park et al. [12] attempted the near perfect reconstruction of the original signal after time reversal. A narrowband excitation is used with limited frequency components, so that after time reversal reconstruction uniform scaling of different frequency

components is possible. Hence, the original input signal can be reconstructed. Wang et al. [13] described a synthetic time reversal imaging method for structural health monitoring of plates. Ying et al. [14] carried out time reversal wave propagation experiments in pipes, so that they could able to collect the signatures for different kinds of defects in a pipe. Ying et al. [14] experimentally simulated welded butt joints, effect of internal pressure in pipe, pipe with lateral defect, pipe with longitudinal defect and pipe with corrosion-like defect. In this chapter, the propagation characteristics of elastic guided waves in cylindrical shell structures in longitudinal and circumferential directions are evaluated experimentally, numerically and analytically. Time reversible recompression of guided waves is used as a basis for a new tomography scheme which can detect the presence and growth of damages in cylindrical shell structures.

2 Experimental and Numerical Studies

2.1 Experimental Studies

Experimental investigation is carried out on a cylindrical shell structure of diameter 0.6 m and length 1.2 m. The cylindrical shell is made of 1.5-mm-thick AA 8081 material in H14 temper condition. Agilent 33522A arbitrary wave form generator is used for generating the eight peaked tone burst. A Hanning window is used to get a narrow frequency band of the input signal. The oscilloscope used is Agilent DSO X2004A, while 0.5-mm-thick 7-mm² PWT 5A sourced from Sparkler Ceramics is used for exciting the waveform. PWT transmitter/receiver pairs are attached to the cylindrical shell in longitudinal and circumferential directions. Experimental set-up and schematic diagram showing the location of attached PWTs are shown in Fig. 1.

The output signal on careful analysis reveals that the input wave packet is divided into multiple submodes due to mode separation and dispersion. The first wave mode is a symmetric wave mode, and it is longitudinal L (0, 2) mode of the cylindrical shell. The second wave mode is an antisymmetric one, and it is the longitudinal L (0, 1) mode. This can be further understood by plotting the

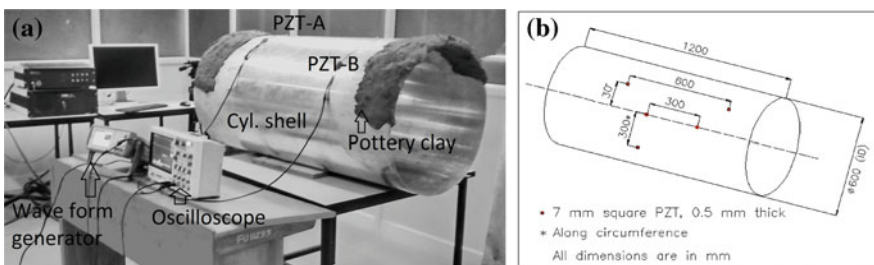


Fig. 1 a Experimental set-up and b locations of PWT in experimental set-up

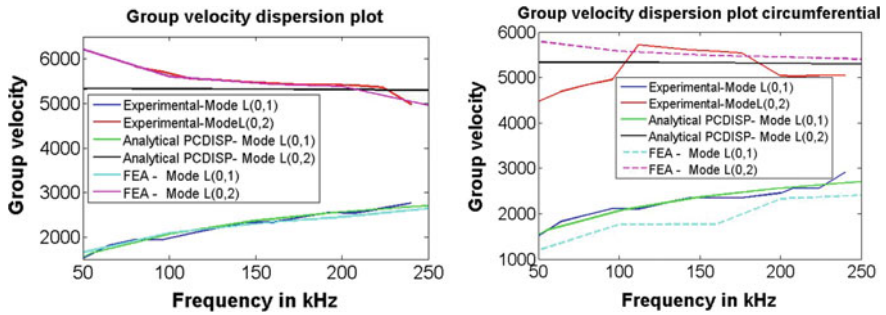


Fig. 2 Group velocity dispersion plot (left) and longitudinal (right) circumferential

displacement behaviour at two points, inside and outside the cylindrical shell. Group velocities of the wave modes for different frequencies are estimated and compared with the results of analytical [15] and experimental predictions as shown in Fig. 2. The analytical estimation of wave propagation characteristics in the cylindrical shell structure is done using a closed-form solution method as described by Sanderson [15]. Usually, the scatterings from the defects sink into the reflections from the boundaries and make it difficult to achieve the damage detection in cylindrical shell structures. The reflections from the boundaries are damped by placing pottery clay over the boundaries of the structure. The schematic diagram of the pottery clay attached to the boundaries of the cylindrical shell is given in Fig. 3. A typical plot showing comparison of output voltage signals after applying the clay

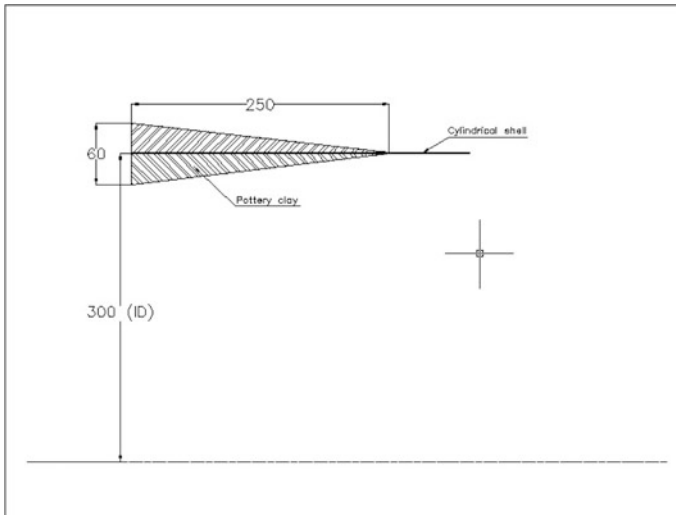
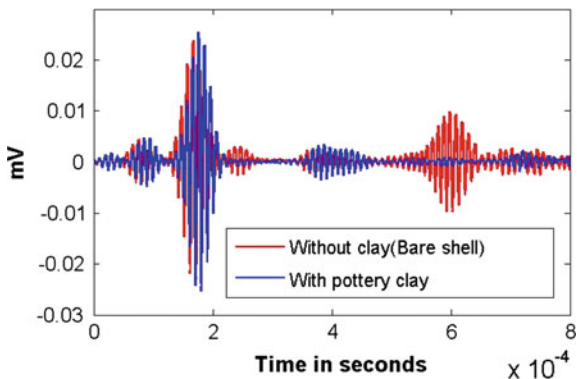


Fig. 3 Schematic diagram showing the application of pottery clay over the cylindrical shell boundaries

Fig. 4 Comparison for output voltage signals without and with pottery clay covered the boundaries—100 kHz



over the boundaries is shown in Fig. 4. It can be seen that the reflections from the boundaries are almost completely eliminated. Fast Fourier transform (FFT) of the output signals is done to estimate the frequency content, and it is confirmed that no higher multiples of the input frequency are present in the output signals. This is an indication of the damage-free structure.

Time reversal of the output wave components is carried out, and the amplified time-reversed signals are transmitted from the receiver PWT. It is found that the original input signal is reconstructed with near perfect accuracy. To compare the original signal and reconstructed signal, a quantity known as correlation factor is used which is defined as ‘correlation factor = Covariance(x, y)/(Sqrt(Variance(x)) * Sqrt(Variance(y)))’. The observed correlation factor for defect-free wave propagation paths is as high as 99.5%. Fully reconstructed recompressed signal along with the original initial input signal (amplitude normalized) is shown in Fig. 5.

An experiment is conducted on the proposed tomography scheme to detect the presence of damage on the cylindrical shell structure. For this, a 1.5-mm-thick 100-mm-square cylindrical shell piece is attached to the surface of the cylinder

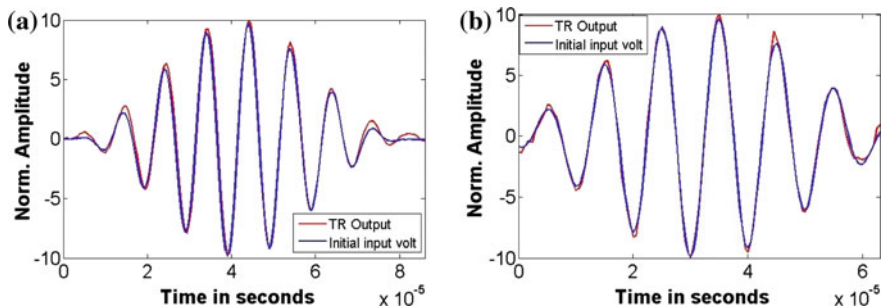


Fig. 5 Comparison between TR output signal and original input signal (for 300 mm **a** axial and **b** circumferential wave travel)—100 kHz

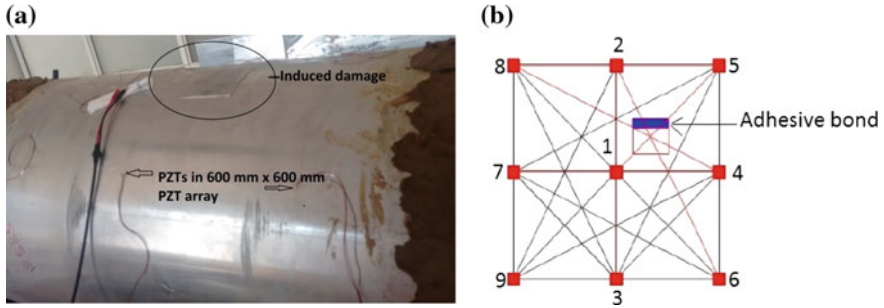
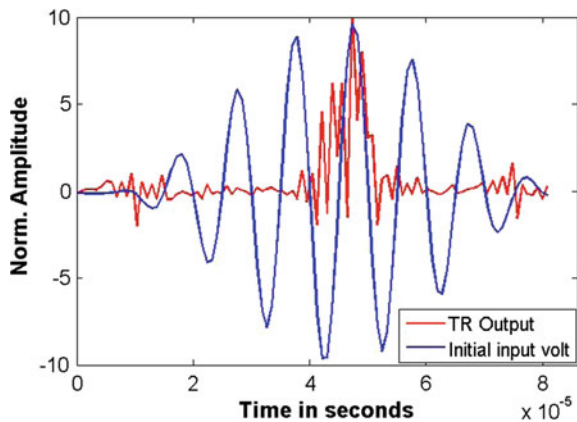


Fig. 6 a Experimental set-up with 600 mm × 600 mm 9 PWT array and b the possible wave propagation paths

using epoxy adhesive (Araldite) at one edge of the metallic piece (covering almost 25% of the surface area). The metallic piece is placed such that the two cylindrical surfaces are in contact. When a wave is propagating, there will be a slapping action between the metallic surfaces and it will simulate an intentionally introduced damage. Experimental set-up with 600 mm × 600 mm 9 PWT array is used as shown in Fig. 6a. The possible wave propagation paths between the PWT elements are given in Fig. 6b.

Time reversal reconstruction is attempted in all the wave paths, and it is found that the reconstruction is very poor in the case of paths with artificially introduced damages as shown in Fig. 7. The correlation factor observed for these paths is as less 15%, while it is more than 99% in case of all other defect-free paths. To enhance the imaging process, a numerical quantity labelled as inverse correlation factor (100-correlation factor in %) is used. A computer program is generated for this end use. Coordinate locations of the PWT array and the correlation factors for different paths are input to the program. The number of pixels in the cylindrical shell image constructed by the computer program can be adjusted across axial and

Fig. 7 Experimental time reversal reconstruction for a wave propagation path with damage



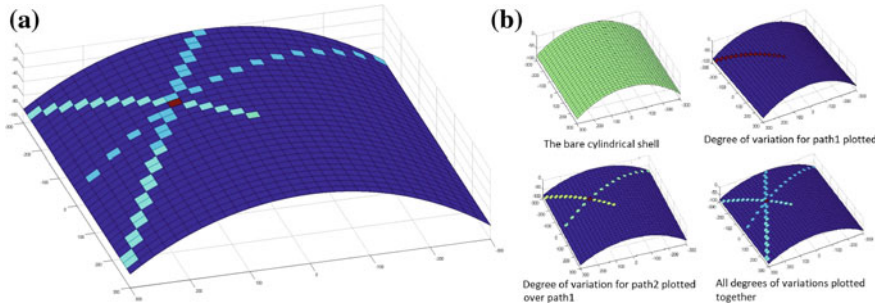


Fig. 8 **a** Constructed tomogram and **b** different steps in construction of the tomogram

tangential directions to change accuracy of damage imaging. The program will find the pixels through which each wave propagation paths are passing through and allot the corresponding inverse correlation factors to all the pixels associated with the path. Inverse correlation factors are assigned to pixels in other wave propagation paths also. The pixels at which the wave propagation paths are crossing, the inverse correlation factors will be added up. When multiple paths passing through a defect, all the inverse correlation factors will added up to a value higher than the surrounding pixels. Then, these pixels at the defect location will be highlighted with a different colour. The constructed tomogram is shown in Fig. 8a. The entire process is schematically shown in Fig. 8b. The tomogram gives the exact location and visualization of the defect.

2.2 Numerical Simulations Using Finite Element Method

Both axisymmetric and plane strain analyses are carried out using Ansys 14.5 FEM software. The 0.6-m-diameter, 1.2-m-long and 1.5-mm-thick cylindrical shell is modelled. Two PWTs are modelled on outer surface of the cylindrical shell. The bottom and top nodes of the piezoelectric devices modelled are voltage coupled. The load input is given as a voltage signal in one of the PWTs at the topside master node. The mode separation and dispersion characteristics as observed in experiments are reconfirmed using numerical modelling. The input wave packet is separated into multiple subwave modes. The first wave mode is $L(0, 2)$ mode, while the second one is $L(0, 1)$ mode. The group velocity dispersion plot is estimated from 2D FE analyses. FE analyses repeated with plane strain analyses. Propagation of waves in the circumferential direction can be better visualized using plane strain analysis. The FE models are shown in Fig. 9. The propagation of the wave packet at different time intervals is shown in Fig. 10 (both symmetric and antisymmetric modes are there, even though the antisymmetric mode is clearly visible due to large out of plane displacements). FE analyses are carried out to simulate the entire tomography experiment. All the wave propagation paths are modelled, and the time

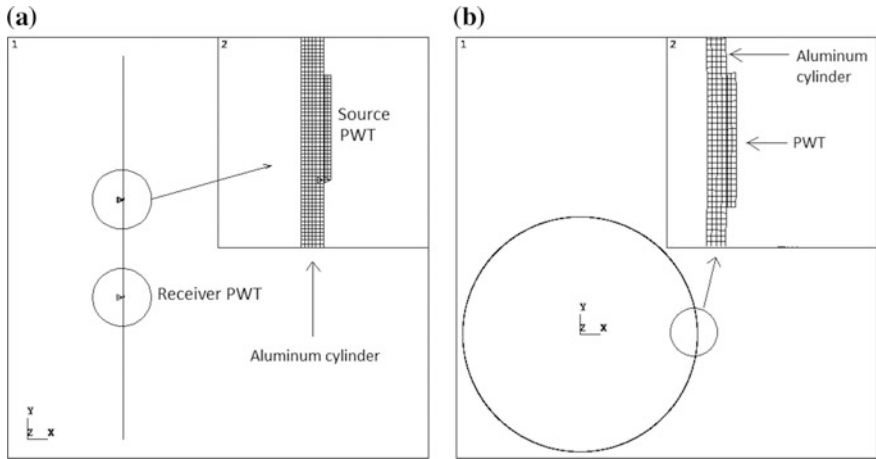


Fig. 9 FE models for **a** axisymmetric analyses and **b** plane strain analyses

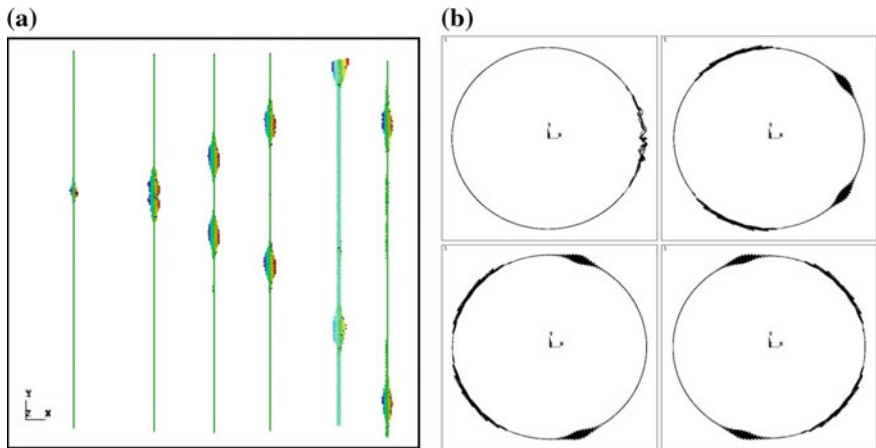


Fig. 10 Propagation of wave through the cylindrical shell at different time intervals for **a** axisymmetric analyses and **b** plane strain analyses

reversal reconstruction is attempted. The results are matching with the experimental predictions. FE model is shown in Fig. 11a. The propagation of wave packet through the defect is shown in Fig. 11b. Figure 12 shows the numerically simulated time reversal reconstruction attempted for a path with artificially introduced damages. It can be seen that the time reversal reconstruction is poor.

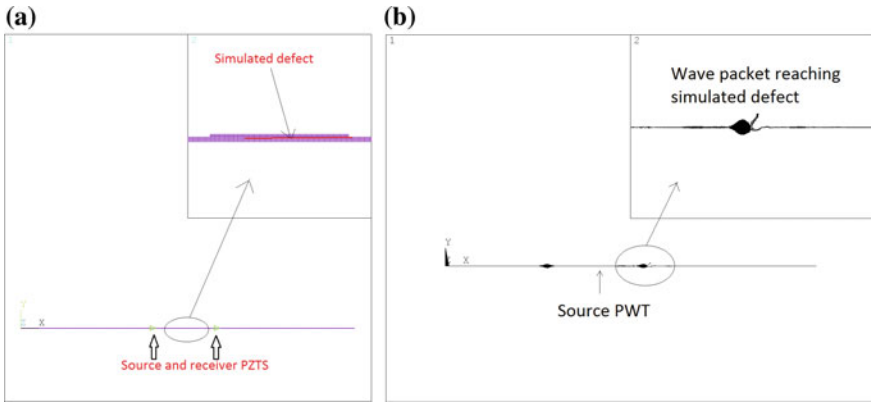
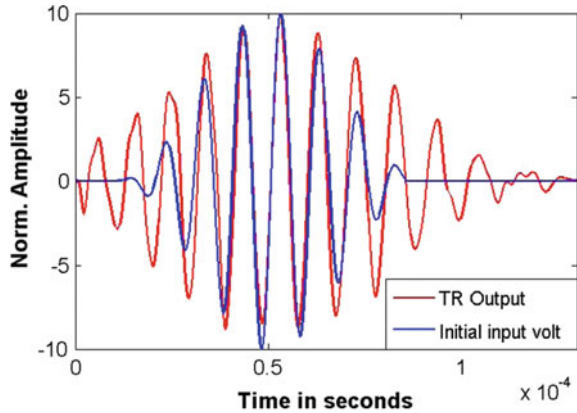


Fig. 11 FE analysis for the propagation of wave packet through the path with damage **a** FE model and **b** propagation of wave through the damage

Fig. 12 Comparison between the numerically simulated TR output signal and original input signal over a typical propagation path which contains the defect (poor reconstruction)



3 Conclusions

- Near perfect time reversal reconstruction by time recompression is carried out in cylindrical shell type structures.
- All the experimental wave mode packets are matching with the finite element predictions.
- Dispersion plot for the cylindrical shell structure considered is plotted using experimental evaluation and compared with analytical and numerical predictions. Group velocities of different modes are matching with FE predictions for all the frequencies considered.

- A tomography scheme is developed based on the time reversal reconstruction of guided wave modes which becomes a basis for a baseline-free structural health monitoring technique.

References

1. V. Giurgiutiu, Tuned lamb wave excitation and detection with piezoelectric wafer active sensors for structural health monitoring. *J. Intell. Mater. Syst. Struct.* **16** (2015)
2. V. Giurgiutiu, J. Bao, Embedded-ultrasonics structural radar for in situ structural health monitoring of thinwall structures, in *AIAA* (2004)
3. V. Giurgiutiu, L. Yu, Embedded ultrasonic structural radar with piezoelectric wafer active sensors for damage detection in cylindrical shell structures, in *AIAA* (2004)
4. A. Muc, A. Stawiarski, Modeling damage in cylindrical shells using elastic wave based techniques, in *18th International Conference on Composite Materials*
5. F. Li, F. Liu, X. Sun, H. Li, G. Meng, Propagation of guided waves in pressure vessels. *J. Wave Motion* (2014)
6. M. Gresil, V. Giurgiutiu, Y. Shen, B. Poddar, Guidelines for using the finite element method for modeling guided lamb wave propagation in SHM processes, in *6th European Workshop on Structural Health Monitoring*
7. R.K. Ing, M. Fink, Time reversed lamb waves. *IEEE Trans. Ultrason. Ferroelectr. Freq. Control* **45**(4) (1998)
8. B. Poddar, V. Giurgiutiu, Experimental validation of analytical model for lamb wave interaction with geometric discontinuity. *Proc. SPIE* **9437**, 795–803 (1997)
9. H. Sohn, Effects of environmental and operational variability on structural health monitoring. *Philos. Trans. Roy. Soc.* (2007)
10. W. Qiang, Y. Shenfang, Baseline free imaging method based on new PWT sensor arrangements. *J. Intell. Mater. Syst. Struct.* **20** (2009)
11. J. Harley, N. O'Donoghue, J. States, Y. Ying, J. Garrett, Y. Jin, J. Moura, I. Oppenheim, L. Soibelman, Focusing of ultrasonic waves in cylindrical shells using time reversal, in *Seventh International Workshop on Structural Health Monitoring, 2009*
12. H. Park, H. Sohn, K. Law, C. Farrar, Time reversal active sensing for health monitoring of a composite plate. *J. Sound Vib.* **302** (2007)
13. C. Wang, J. Rose, F. Chang, A synthetic time reversal imaging method for structural health monitoring. *Smart Mater. Struct.* (2003)
14. Y. Ying, J. Harley, J. Garrett, Y. Jin, J. Moura, N. O'Donoghue, I. Oppenheim, L. Soibelman, Time reversal for damage detection in pipes, in *SPIE conference* (2010)
15. R. Sanderson, A closed form solution method for rapid calculation of guided wave dispersion curves for pipes. *Wave Motion* (2014)

Author Index

A

Akshitha, G., 103
Alfaori, Qusay, 169
Andronik, A.V., 549
Anilchandra, A.R., 195
Arora, Punit, 611

B

Bade, Simhachalam, 303
Badikov, K.A., 549
Bakshi, Srinivasa R., 649
Balasubrahmanian, A.K., 395
Bharathanatha Reddy, R., 65
Bharath, K., 559
Bhasin, V., 419, 611
Bhat, Praveen, 385
Bhaumik, S.K., 65
Bijudas, Christudas R., 685
Biswas, Swati, 117
Bojja, Ramesh, 27, 195
Boniface, Vinodkumar, 279
Bose, S., 205
Bykov, Anton, 503

C

Chaitanya Sagar, T., 253
Chakraborty, D., 461
Chakraborty, Debaleena, 461
Chandan Reddy, V.R., 407
Chandra Kishen, J.M., 147
Chaudhry, V., 395
Chebanenko, V.A., 291
Chen, Zhen, 1
Cherpakov, A.V., 291
Chikmath, L., 559
Chinthapenta, Viswanath, 253

Choudhuri, Gargi, 611
Cinitha, A., 267, 437

D

Daga, Rajesh, 369
Das, Sukanta, 673
Dattaguru, B., 559
Deka, Nipal, 593
Dhiman, Abhijeet, 481
Dubey, P. N., 493
Duong, L.V., 291

E

Endo, Masahiro, 541, 599
Ezhilarasi, T., 649

G

Gandhi, P., 419
Gangadharan, R., 527
Glot, Irina, 451, 503
Goyal, Sunil, 353
Gujar, Shriram, 77

H

Holdsworth, Stuart R., 1, 341

I

Ikeda, Yuichi, 541
Ingole, S.M., 395
Iyer, Nagesh R., 157

J

Jagannathan, N., 27, 195
Jaladeen, S., 325
Jayaram, V., 205
Jayesh, P., 685

Jensen, Hanna, 169
 Jensen, Morten, 169
 Jonnalagadda, Krishna N., 481, 593

K

Kalyanasundaram, Valliappa, 341
 Kesavan, K., 437
 Khaderi, S.N., 315
 Khan, I.A., 419
 Kodag, Pradeep B., 215
 Kumar, Gurunathan Saravana, 623
 Kumar, Jivan, 117
 Kumar, Suranjit, 419
 Kumar, Suresh, 225

L

Laha, K., 353
 Lakshmana Rao, C., 303
 Lakshminarayana, H.V., 15
 Lakshminarayana, S.C., 93

M

Madan, M., 65
 Mahendra Babu, N.C., 15
 Manjunatha, C.M., 27, 39, 195
 Manjuprasad, M., 39, 77
 Master, Bakul, 385
 Miroshnichenko, I.P., 663
 Miyakawa, Susumu, 541
 Miyamoto, Nobuyuki, 541
 Mohandas, E., 649
 Mohan Kumar, M., 103
 Muktibodh, U.C., 395
 Murthy, K.S.R.K., 461
 Murugan, R., 579

N

Narendra Babu, S.N., 117
 Neergat, M., 481
 Nimje, Yashdeep P., 517
 Nishimura, Yoshiro, 541

P

Padmanabhan, K., 579
 Palani, G.S., 267
 Panbarasu, K., 225
 Panigrahi, S.K., 635
 Parameswaran, P., 353, 649
 Parinov, I.A., 291, 663
 Patil, Prataprao, 315
 Pavan Kumar, D.V.T.G., 39
 Prakash, R.V., 225

R

Raghava, G., 419
 Raghavan, Kotur S., 53
 Raghavendra, K., 65
 Raghu Prasad, B.K., 157
 Rahul, G.R., 205
 Raju, Gangadharan, 517, 673
 Ramachandra Murthy, A., 157
 Ramesha, H., 15
 Ramesh, R., 579
 Ramji, M., 235, 315, 527
 Ramu, Palaniappan, 623
 Ranganath, V.R., 225
 Ravi, S., 353
 Reddy, G.R., 493
 Reddy, Naresh, 527, 673
 Rengaswamy, Jayaganthan, 623
 Rozhkov, E.V., 291

S

Sahoo, Benudhar, 635
 Sahoo, D.K., 611
 Sahoo, Kanhu Charan, 353
 Sahoo, P.K., 77
 Sakthivel, K., 27
 Samal, Mahendra Kumar, 369
 Saravanan, M., 419
 Sarkar, Rosy, 325
 Satishkumar, V.N., 117
 Satpathy, R.K., 635
 Savkin, A.N., 549
 Saxena, Ashok, 169
 Schwarzkopf, Erik A., 469
 Sedov, A.A., 549
 Selvaraj, P., 407
 Seshadri, Matta, 235
 Seshagirachari, M., 195
 Shailesh Rao, A., 103
 Shardakov, Igor, 129, 451, 503
 Sharma, Anil Kumar, 407
 Sharma, Mukhar, 611
 Shepard, Michael J., 469
 Shestakov, Aleksey, 129, 451, 503
 Shuaib, Muhammad, 527
 Simon, Keerthy M., 147
 Singh, P.K., 419, 611
 Sivaranjani, T., 39
 Soloviev, A.N., 291
 Sravan, B.V., 559
 Srinivasan, N., 103
 Srivatsa, Shivashankar R., 183
 Sujata, M., 65

Suresh, J. A., [623](#)
Suresh Kumar, R., [407](#)

T

Thomas Paul, V., [649](#)
Tsvetkov, R., [129](#), [451](#)

U

Umesha, P. K., [267](#), [437](#)

V

Vaghela, Ajaysinh R., [137](#)
Varughese, Byji, [93](#)
Velusamy, K., [325](#), [407](#)

Venkatesh, S., [93](#)
Verma, R.K., [493](#)
Vesmawala, Gaurang R., [137](#), [215](#)
Vignesh, S., [303](#)
Vinayaka, H.L., [183](#)
Vishnuvardhan, S., [419](#)

W

Wasim, F.G.S., [481](#)

Y

Yanase, Keiji, [541](#), [599](#)
Yepin, V., [129](#), [451](#)

Subject Index

A

Actuator assembly, 96, 100
Additive manufacturing, 625
Aluminium alloy, 303–305
Aneurysm, 169–171, 176–178, 180
Aorta, 169–171, 173, 175–179
Armstrong method, 635, 641
ASME, 54, 55, 61, 63
AUSC, 354

B

Ballistic impact, 183–185, 191, 193
Band structure, 253, 255, 256, 261
Beach marks, 120
Bearings, 117, 118, 122, 124
Biaxial columns, 215, 216
Bi-metallic pipe weld joints, 421–426,
429–433
Bimorph, 291–293
Buckling, 279–281, 284–288, 528–531,
533–536
Bulkhead, 106, 107, 113, 114
Buttering, 420, 421, 429, 432, 433

C

Cantilever, 291–293, 295, 297
Carbon Fiber Reinforced Plastic (CFRP), 529,
530, 532, 533, 536, 673–675, 679, 683
Carbon nanotubes, 138
Catastrophic failure, 399, 405
CBR, 326, 335
CFRP composite laminates, 78, 79, 89
CFRP composites, 225, 232
Characterization, 158
Circumferential joint, 15–18, 20, 21, 23, 25
CMC, 470, 471, 477

Cohesive energy and second order elastic
constants, 253, 255, 256, 258, 259, 262,
263
Cohesive zone law, 235, 237
Collagen degradation, 169–171, 173–180
Compliance, 195, 197, 199
Composite, 94–97, 100, 195–197, 199, 201,
528
Composite laminate, 281, 518
Composite structure, 183, 184, 193
Compression member, 267, 268, 270, 274,
275, 277
Computer Numerical Control (CNC), 635, 636,
638, 639, 641–646
Concrete, 137, 138, 140, 141, 144, 147, 148,
151–155
Control object surface, 664, 665, 669, 670
Control plug, 325, 326, 330, 332, 334, 335,
337, 339
Corrosion, 267–270, 272–275, 277, 438,
443–445, 448
CPFE, 595, 596
Crack, 15–18, 21–26, 104, 107, 109–111, 113
Crack growth, 157, 159, 160, 163–165, 560,
561, 566, 573, 574, 576
Cracking, 216, 222
Crash cooling, 326
Crashworthiness, 304
Creep, 369, 370, 373–381
Creep cracking, 1, 3–11
Creep curve prediction, 348
Creep fatigue damage assessment, 370,
373–380
Creep-fatigue interaction, 341, 342
Creep strength degradation, 343
Critical microcrack, 147–149, 151–155

- Crushable foam, 304
 Cyclic loading, 594
 Cyclic softening, 342, 343, 347, 348
 Cylindrical shells, 685–693
- D**
 Damage study, 674
 Damage tolerance, 104, 105
 DBA, 54–56, 58
 Deformation induced martensite, 613, 618, 619, 621
 Deformation monitoring, 130, 131, 135
 Delamination, 195–198, 200–202, 279–288, 518–522, 524–526
 Design, 53–55, 57, 60–63
 Design in-place analysis, 386, 387, 391
 DFT, 253–258, 262
 Diffusion bonding, 650, 652, 655
 Digital Image Correlation (DIC), 235, 239, 487, 528, 531, 533–536
 Dimples, 121, 122
 Double ended cracks, 463, 467
 Double sided stepped lap joint, 235, 245–247, 249
 Dugdale model, 599–601, 606, 607, 609
- E**
 Electrical resistance strain gauge, 438, 442, 443, 445, 448
 Electro Chemical Machining (ECM), 636, 638, 639
 Electrolyte, 438, 443, 445
 Energy absorption, 304, 310–312
 Experimental stand, 452
- F**
 Failure analysis, 216
 Fast breeder reactor, 408, 415
 Fasteners, 560
 Fatigue, 65–68, 71, 73, 76, 117, 118, 121, 124, 125, 560–562, 564, 565, 570, 573, 574, 576, 624, 626, 627, 630–632
 Fatigue crack growth, 552, 555, 557
 Fatigue crack growth rate, 613–615, 618, 619, 621
 Fatigue life, 40, 48–51, 77–79, 84, 85, 87–90
 Fatigue limit, 543–547
 Fatigue loading, 157, 159, 163
 FCC single crystal, 596
 FE analysis, 100
 Feature level test, 94–97, 100
 FEM, 183, 185, 186, 191, 315, 318–321
 Fiber bragg grating sensor, 439
 Fiber reinforced polymer, 215
- Finite element analysis, 107, 355, 356
 Finite Element Method (FEM), 292
 Four point bending, 423
 Fractal dimension technique, 518, 520, 526
 Fractography, 226
 Fracture, 104, 105, 107, 114
 Fracture energy, 157–159, 164
 Fracture mechanics, 138, 453
 Frequency, 297–300
 FRP, 504, 507, 511, 513, 514
 Fuel cell, 482, 483, 490
 Full-scale testing, 452
 Fuselage, 15–17
- G**
 Gas turbine blades, 65, 66, 74
 Gas turbine engine, 118
 Glass fiber, 27, 29
 Goodman and Gerber mean stress corrections, 48–51
 Graphene, 253, 255, 256, 258–264
 Ground surface subsidence, 130
 Guided wave modes, 685, 686, 694
- H**
 Hanger and support, 369, 371, 372, 374, 379
 Hardness measurement, 355, 363
 Harmonics, 295
 Heat-affected zone, 421, 429, 432, 433
 High Cycle Fatigue (HCF), 408, 417, 600, 606, 609, 636, 646
 High energy piping, 369–371
 High-R, 1, 3, 5–11
 High temperature, 1, 3, 4, 6, 7, 9, 11, 470, 472, 473, 477
 Hybrid composite, 579–590
 Hydrostatic level, 130, 133, 134
- I**
 IC debonding, 504, 506
 Infrared thermography, 504
 Inner vessel, 325, 326, 330, 335, 337–339
 In situ tensile testing, 488
 Interaction of fatigue loading on vibration characteristics, 579
 Interfacial transition zone, 147
 Interference pattern, 664, 665, 667, 670
 Interlaminar fracture toughness, 226
 Intermediate Heat Exchanger (IHX), 325, 326, 330, 332, 337–339
 Irradiation damage, 396, 398
- J**
 Jacket structure, 386, 387, 389–394

K

Kinetic theory of fracture, 77, 78, 80, 83, 89
 ΔK_{th} , 1–11

L

Laser Doppler Vibrometer (LDV), 518, 524
 Laser interferometer, 671
 Leak Before Break (LBB), 403, 404
 Level fluctuation, 410, 411, 415
 Life prediction, 353, 359, 362, 366
 Loading frequency, 613–615, 617–619, 621
 Load sequence, 553, 555
 Local stress calculation, 550, 551
 Longitudinal joint, 15–17, 19, 21, 25
 Lug joints, 560–562, 568, 576

M

Main landing gear, 41–44, 44, 48–51
 Matrix cracking, 77, 78
 Maximum absolute principal stress, 50, 51
 Measurement of small displacements, 664, 665
 Mechanical properties, 138
 Mechanical test, 625
 Metals, 470, 477
 Microstructural integrity, 650
 Mode I SIF, 462, 465–467
 Monotonic fracture, 426, 429
 Multiaxial creep, 363, 366
 Multicontinuum theory, 77, 78, 80, 83, 89

N

Non-destructive Testing and Evaluation
 (NDT&E), 673
 Nonlinear Finite Element Analysis, 183, 193
 Notch effect, 542, 545, 546, 548, 600, 601

O

OGDHR, 325, 326, 329, 338
 Onset-of-growth, 195–197, 199–201
 Orthotropic laminate, 462, 463, 467
 Overheating, 65, 75
 Oxide induced crack closure, 1, 3, 5, 6, 9, 11

P

Part build orientation, 625
 Passive thermography, 673, 674, 683
 Piezoelectric generator (PEG), 291–300
 Piping code, 369, 371, 378, 379
 Pitting corrosion, 267, 268, 273, 274, 277
 Plastic collapse, 396, 400, 405
 PMC, 470–472, 477
 PMMA, 205, 206, 208, 209, 212–214
 Poly (2,5-Benzimidazole), 481
 Polymer composite, 28, 33

Polymer electrolytic membrane, 482, 483, 490
 Power, 291, 292, 296, 297, 300
 Prediction models, 552
 Prognosis, 560
 Proof mass, 291–297, 299, 300
 Pzs, 599, 600, 602, 604, 605, 607

Q

Quantum Espresso, 253, 256–258, 260, 261,
 263

R

RC beams, 504
 Reinforced concrete, 451, 452, 458, 459
 Remaining life, 157, 158, 160, 163–165
 Residual strength, 15–17, 22, 23, 25, 26, 109
 Residual stress, 635, 637, 639, 640, 645
 Resin infusion, 225–229, 232
 Retrofitting, 215
 Rigid line inclusion, 315–317, 319–322
 RSR, 385, 389
 Rupture, 169–171, 173, 175–178, 180

S

Scratch, 541, 542, 548
 Shake table, 493, 498, 500
 SHM, 560
 SHPB, 304, 306–308
 Silica nanoparticle, 27–30, 34, 37
 Sine-sweep test, 493, 498
 Single Edge Notched Clamped Beam
 (SENCB), 205–207, 209, 213
 Singularity, 315, 317, 319, 320
 Site-specific ground response spectrum, 498
 Slow crack growth, 206, 213
 Snubber, 493, 494
 Spark Plasma Sintering (SPS), 650, 658
 Spectrum fatigue, 27, 28, 31–33, 35, 37
 Spectrum load, 196–201
 Spring steel, 541, 548
 Stacking sequence, 579, 584, 586, 590
 Strain energy release rate, 235, 237, 238,
 241–243, 249
 Strain gage, 462, 464, 466, 467
 Strain intensity factor, 316–319, 321, 322
 Strength, 53, 54, 56–58, 60, 62, 63
 Strengthening, 504, 506
 Stress analysis, 369–371, 373–376, 378
 Stress intensity factor, 15–17, 21–24, 205–209,
 211–214, 599
 Stress linearization, 55–57, 59
 Stress relaxation, 341–350
 Stress rupture, 65, 74, 75
 Stress spectra, 46, 48–51

Striations, 121
Structural health monitoring (SHM), 685–687, 694
Structural integrity, 16, 415, 417
Superalloy, 67, 68, 73, 74

T

Tearing instability, 396, 400, 402, 405
Tear strap, 107, 109–113
Tension softening, 157, 158, 160, 164, 165
Test design, 94
Thermal movement, 369, 372, 379
Through-wall notch, 423, 424
Time reversibility, 685
Tomogram, 691
T-stress, 595–597
Turbine rotor blade, 636, 638–642, 646

U

Ultimate strength analysis, 387–389
Ultra High Strength Concrete (UHSC), 157–159, 159, 160, 164
Uniform corrosion, 267, 268, 272, 273

V

Vibration characteristics, 579–584, 586–588, 590
Visco-elastic damper, 493–495, 496–500
V(K) curve, 206
Voltage, 291, 296–300

W

Wind turbine blade, 280, 281, 288